MAX-PLANCK-INSTITUT FÜR PLASMAPHYSIK
GARCHING BEI MÜNCHEN

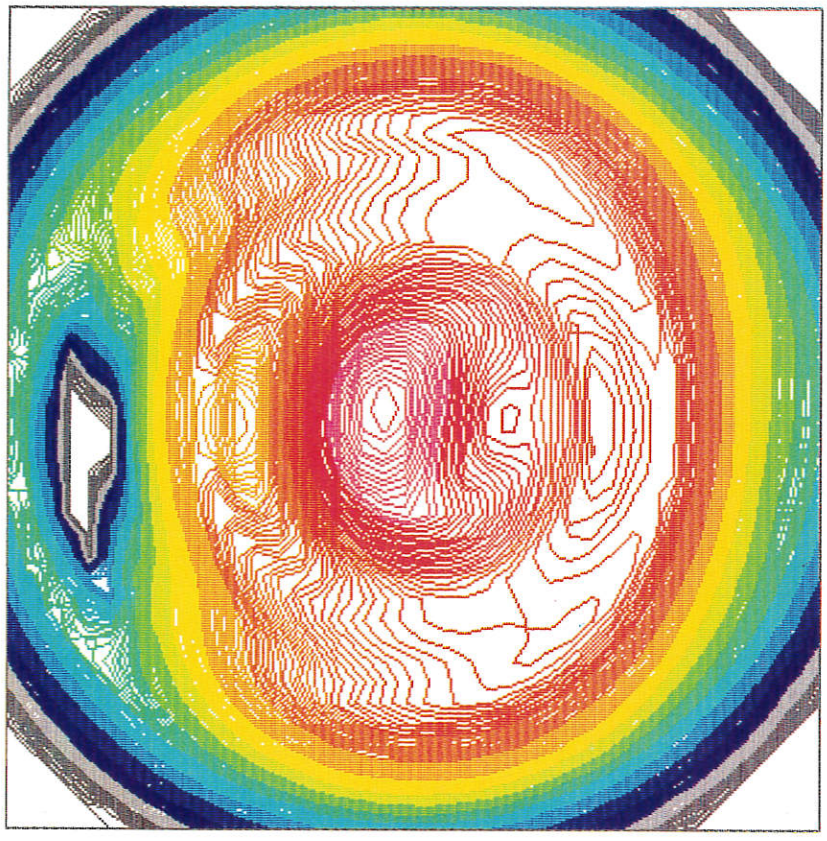

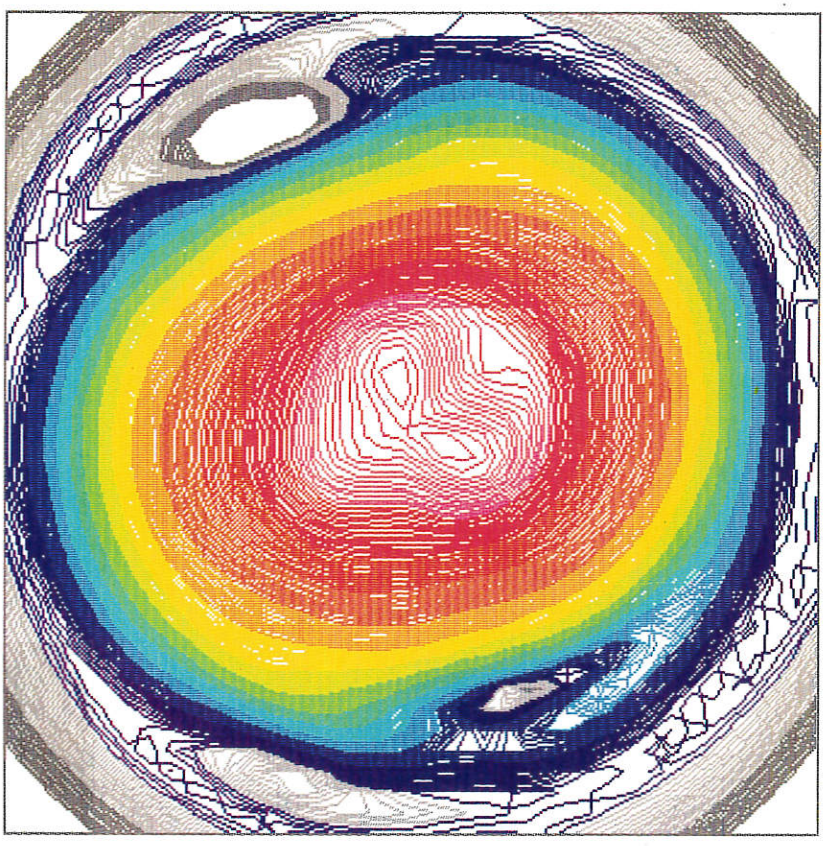

ANNUAL REPORT 1984

IPP AR/1984

COVER ILLUSTRATION

The upper figure shows surfaces of constant X-ray emission of the ASDEX tokamak high-β plasma during neutral beam heating. The 15 colours denote the various intensities ranging from 2×10^{-3} to 0.5 W/cm^3 on a logarithmic scale. The structure is obtained from the data of two pinhole cameras by tomographic reconstruction. Even in clean plasmas, X-ray emission is predominantly due to collisions of electrons with impurity ions and depends on T_e, n_e, n_z. It is therefore believed that the picture shows the distribution of the impurities along the magnetic surfaces, these being driven to the outside of the torus (right-hand side of the picture) by the centrifugal force of the plasma rotation caused by neutral injection.

The lower figure shows the deformation of the plasma cross-section in the Wendelstein VII-A stellarator. In a tokamak-like mode of operation with a plasma current of 20 kA and a low external rotational transform the additional neutral beam injection destabilizes the (2,1) tearing mode and leads to disruption. The disruption is believed to be due to radial overlapping of various tearing modes. There is indeed evidence of other growing modes: (2,2), (3,2) and a (3,1). The emission scales logarithmically from 10^{-4} to 0.15 W/cm^3.

MAX-PLANCK-INSTITUT FÜR PLASMAPHYSIK
GARCHING BEI MÜNCHEN

Annual Report 1984

C O N T E N T S

Contents

P R E F A C E

The year 1984 was a very successful one for IPP, as testified to by this report. The scientific activities of our institute comprise two programmes, Tokamaks and Stellarators, the main results of which are summarized in two overviews introducing the corresponding sections in the body of the report. Just a few highlights shall be mentioned here: in ASDEX the H-regime was further investigated, resulting in detection of a quiescent phase with very long confinement times; of equal importance in ASDEX was the exploration of the beta limit; with respect to heating, recharging of the transformer by LHRH current drive was demonstrated and the ICRH system was commissioned without complication; in the stellarators, electron cyclotron heating with 28 GHz and later 70 GHz was applied, which not only resulted in the production and heating of stellarator plasmas but also gave a deeper insight into the transport properties of the plasma electrons.

The scientific work at our institute is firmly integrated into a network of cooperation. In Germany, we collaborate with Kernforschungszentrum Karlsruhe in the "Entwicklungsgemeinschaft Kernfusion"; of the collaboration with universities the most successful has been that with Stuttgart on ECRH. We are now establishing a new joint research effort with the University of Bayreuth in the field of plasma-wall interaction.

The IPP programme forms an integral part of the European fusion programme. As stated in the report of our Fachbeirat 1983, "the European fusion efforts depend entirely on Garching for certain important questions (divertor, stellarator)".

On an even larger scale, implementing agreements with the US are ready to be approved to cover international use of ASDEX and ASDEX Upgrade and draw up a coordinated international programme on stellarators, the Wendelstein activities being a major contribution. These agreements are devised to afford Japan the possibility of joining somewhat later. In this way, world resources will be put to the most efficient use.

The essential programmatic elements of fusion research are decided in the European programme: The JET joint European experiment, the basic tokamak programme, to which our contributions are ASDEX and ASDEX Upgrade, and the alternative lines with the Wendelstein VII-A, and VII-AS stellarators aiming at the reactor-relevant Wendelstein VII-X. They are funded, are being exploited or are under construction. With this programme the investigations of fusion will continue with, it is hoped, as much success as hitherto.

Klaus Pinkau

Part A:
Projects

Tokamaks

Most of the capacity at IPP is devoted to investigating magnetic confinement in the tokamak configuration, this line still being the furthest advanced towards application in a fusion reactor. With ASDEX and ASDEX Upgrade, which is now under construction, IPP have concentrated their tokamak research on the divertor principle.

Meanwhile, the divertor has proved especially successful both for solving problems characteristic of the edge plasma and for controlling the central plasma. The edge plasma can be kept hotter because the divertor shifts contact between the wall and plasma to a region far from the central plasma. Furthermore, the energy is deposited on the divertor plates at much lower temperatures. On the one hand, the hot edge plasma results in good confinement of the central plasma (discovery of the H-regime in ASDEX); on the other, the shift of wall contact limits wall erosion and any impurities still being produced find it harder to reach the central plasma. The divertor also affords some other advantages, e.g. improved helium pumping can be expected and it is easier to control the plasma position.

This year the H-regime was again to the forefront of interest. Despite the relatively low heating power available to ASDEX, its excellent confinement properties and the advent of neutral beam injectors with higher powers and longer confinement times made it possible in ASDEX to investigate ß-limits, which were the centre of attention throughout the world, and to obtain a large measure of agreement with numerical calculations and other experiments. Essential results for clarifying the H-regime were also obtained. The confinement behaviour in all regimes observed was further investigated and the control of impurities by the divertor was studied.

Lower hybrid waves failed to heat the plasma ions because it was just the poorly confined high-energy ions that were additionally heated and the waves were subject to parametric decay. By coupling the waves to the electrons it was possible, however, not only to maintain the plasma current, but also to demonstrate for the first time re-charging of the OH transformer. Towards the end of the year the ion cyclotron heating was put into operation without trouble and first results were obtained.

Experimental success with ASDEX and other divertor experiments and increasing know-how have made the poloidal field divertor the first option for solving plasma boundary problems in NET. For technical reasons, however, the magnetic configuration of the divertor will have to be modified - in relation to that in the ASDEX device. To ensure proper functioning of such an "open" divertor in NET and allow experiments in which the values of major parameters are equivalent to those in the boundary layer of a reactor, an upgraded version of ASDEX was needed to provide NET with definitive solutions of plasma boundary layer problems. IPP have secured approval from EURATOM for such an ASDEX Upgrade experiment. Besides having a reactor-relevant divertor, ASDEX Upgrade is characterized by a strongly enhanced plasma current which should provide access to much improved plasma parameters. In addition to the actual objectives of the boundary layer investigations, it is also possible to tackle other important problems such as current drive and ß-limits in the case of non-circular cross-sections. As its magnetic field configuration is very similar to that of NET, ASDEX Upgrade will also make a major contribution to the study of reactor plasma control.

In 1984 construction of the shielding structure for ASDEX Upgrade was started and most of the components for the tokamak system were ordered. The experiment is scheduled to go into operation in 1987.

Besides conducting their own tokamak experiments, IPP have been involved in JET, the joint large-scale project at Culham (U.K.), since the planning phase. After the first experiments in 1983, JET conducted a major experimentation programme in 1984, without additional heating for the time being. A plasma current of 3.7 MA was reached, which exceeded the target value for the basic stage. It was demonstrated at least in discharges with ohmic heating that the energy confinement time scales very favourable with the size of the plasma and attained a record value of 0.7 s.

JET, however, is a limiter experiment based on the knowledge available at the time the decision to build it was taken. Unlike a divertor, a limiter bounds the plasma direct with a material surface. This may entail prolems in achieving good plasma confinement without impurities. It is therefore essential that JET be supplemented and backed up by ASDEX and ASDEX Upgrade.

As the investigations in JET are so important, IPP are contributing to it by providing funds, seconding personnel and developing diagnostic facilities. IPP are also participating direct by periodically sending scientists to take part in the experimental investigations, thus benefitting from the know-how being acquired.

Just as JET was nearing completion, the EURATOM partners initiated joint studies on the NET device to succeed it. These studies are being conducted by the European NET Group at Garching, to which IPP have delegated personnel and are lending scientific support.

ASDEX PROJECT

Head of Project: M. Keilhacker

1. EXPERIMENTAL RESULTS AND COMPARISON WITH THEORETICAL INVESTIGATIONS

G. Becker, K. Bernhardi, H. Brocken, A. Eberhagen, U. Ditte, G. Fussmann, O. Gehre, J. Gernhardt, G. v. Gierke, E. Glock, T. Grave[1], O. Gruber[2], M. Hesse[3], G. Haas, K. Hübner[4], G. Janeschitz, A. Izvozchikov[5], F. Karger, M. Keilhacker, S. Kissel[6], O. Klüber, M. Kornherr, P. Kotzé[7], K. Lackner[2], M. Lenoci[8], G. Lisitano, H. M. Mayer, K. McCormick, D. Meisel, V. Mertens[9], E.R. Müller, H. Murmann, H. Niedermeyer[10], W. Poschenrieder[11], F. Ryter[3], H. Rapp, G. Siller, P. Smeulders, F. Söldner, E. Speth[12], A. Stäbler[13], K. H. Steuer, Z. Szymanski[14], G. Venus[11], O. Vollmer[12], F. Wagner, D. Zasche[15]

1.1 Overview

In 1984 there were increased indications that the theoretically predicted ß-limit exists for all tokamaks. Very good agreement was found between the scaling and absolute values of theoretical ß-limits (resulting from linear ideal MHD stability analysis) and those of experiments in ASDEX and other tokamaks. In ASDEX it was possible to test the ß-limits even at relatively modest beam powers over a wide range of magnetic fields, because the energy confinement factor typical of H-mode discharges is larger than in other tokamaks. The now practically certain fact that all tokamaks with sufficiently high neutral injection power run up against a ß-limit showing impaired confinement or loss of stability has two consequences: On the one hand, the conception of future large machines will have to be somewhat revised with respect to the size and shape of the cross-section; on the other, the unexpectedly good agreement between theory and experiment has made the basis for reactor calculations more reliable.

In ASDEX the maximum ß-values are obtained in a transient state and decay to a lower equilibrium value in a time of the order of 1 s. This is interpreted as being a consequence of changes in the current density profile (affecting the ß-limits for kink and ballooning modes) that adjust to the H-mode profiles on a resistive time scale. Corroborative evidence of this effect is afforded by results of beam heating experiments with simultaneous plasma current variation: Experiments with decreasing current and presumably more peaked current density distribution reached higher ß-limits at given q than those performed with stationary or rising plasma current. This, however, also gives grounds for hoping that further optimization can be achieved by specific current profile shaping.

Besides the 4.2 MW deuterium injection for measuring the ß-limit, neutral beam heating was predominantly used for studying the possible reasons for the degradation of confinement in the L-mode and the sudden improvement after the H-transition. Deeper insight into the intrinsic confinement and

---

1 Up to June 1984
2 Tokamak Physics group
3 CEN Grenoble, France
4 University of Heidelberg, Germany
5 Academy of Sciences, Leningrad, USSR; up to February 1984
6 Up to August 1984
7 Nuclear Development Corp. of South Africa, Pretoria; since July 1984
8 Frascati, Italy; since November 1984
9 ASDEX-Upgrade group
10 Assigned to JET up to July 1984
11 Plasma-Wall Interaction group
12 Neutral Injection group
13 Neutral Injection group, assigned to JET since May 1984
14 Institute of Fundamental Technological Research, Warsaw, Poland; up to April 1984
15 JET Diagnostic and Pellet group

transport properties of the H-mode was gained after finding means of suppressing edge-localized modes, which were previously a characteristic feature of this superior confinement regime. These modes, which periodically expel particles and energy from the peripheral plasma, could be reproducibly avoided for periods of up to 130 ms by displacing the plasma column a few cm outwards. During this quiescent H-mode period the power flow into the divertor is very small. This, together with the steep density and temperature gradients observed at the plasma edge, points to a transport barrier at the plasma boundary. The location and extent of this barrier are shown to coincide with the zone of increased shear specific to the divertor configuration. Without the edge-localized modes a global energy confinement time of ~120 ms is achieved, a value which clearly surpasses those of ohmic discharges. The virtue of this discharge type, however, is hampered by the fact that the superior confinement applies to impurities as well, giving rise to a serious radiation problem in the course of the quiescent H-phase.

Impurity transport and recycling studies were made using argon gas puffs into the main discharge vessel and into the divertor chamber of ASDEX. They showed that the impurity transport is unfavourably modified with neutral injection, leading to higher concentrations in the plasma. This can be interpreted either by improved particle confinement in the bulk plasma or - more likely - by a change of transport in the scrape-of layer, resulting in a reduction of the divertor retainment.

By using two ultra-soft-X-ray cameras and a tomographic inversion technique iso-emission contour lines for successive times were obtained. The detailed effect of an edge-localized mode on the impurity distribution was thus documented.

Whereas ion heating with lower hybrid waves in ASDEX and other large tokamaks was unsuccessful, the investigations on current drive with lower hybrid waves yielded positive results. Besides achieving a rise in the plasma current already with relatively low HF powers, like other machines, ASDEX was the first tokamak to simulate a reactor scenario in which the OH transformer was recharged at a constant plasma current. This demonstration is important for possible steady-state operation of a future tokamak reactor.

The ion cyclotron resonance heating, which was put into operation in November, attained 550 kW/1 s and 700 kW/0.4 s within a few experimental days. As in other tokamaks, impurities were found to increase with the onset of HF heating. It is interesting to note that the degree of contamination depends sensitively on the position of the resonance layer relative to the divertor entrance. This is another example which shows that the special properties of the divertor create very exactly defined conditions, thus making many physical effects transparent.

The plans to extend ion cyclotron and neutral injection heating to the 10 s pulse length range at a total power of around 6 MW call for some modifications of the divertor. The design of this "hardened" version has been completed and the progress in manufacture will allow installation early in 1986.

1.2 Confinement Studies with Neutral Injection

1.2.1 Confinement and transport scaling

Global confinement analysis

In our confinement studies, we could investigate the scaling of τ_E with external parameters I_p, P_{tot}, $\bar{n}_e$, B_T, the atomic mass A and charge Z of the target gas. The results of the scaling experiments can be summarized as follows /222/.

$$\tau_E^* = K \cdot \bar{n}_e^{\,u} \cdot I_p^{\,v} \cdot P_{tot}^{\,w} \cdot B_T^{\,x} \cdot (A^y/Z^z) \quad (1)$$

with u = x = o, v = 1, w(H) = o, w(L) = -1/3, y = 1/2, $1/2 \leq z \leq 1$. For H^o-injection into D^+-plasmas, the constant of proportionality is calculated as: $K(H) = 1.1 \cdot 10^{-7}$ s $\cdot A^{-1}$ and $K(L) = 8 \cdot 10^{-8}$ s $\cdot A^{-1} \cdot MW^{+1/3}$, respectively, resulting in $\tau_E^H \simeq 2 \cdot \tau_E^L$ for P_{tot} = 3 MW and otherwise unchanged parameters. The L-mode scaling is in general agreement with the scaling found with other experiments. The H-mode scaling, however, does not show any dependence on the heating power far from the ß-limit (see Sec. 1.3).

The leading term in the confinement scaling with NI is the proportionality of τ_E to I_p (see Annual Report 1983). In L-type discharges, there is clearly no density dependence. A definite conclusion on the density scaling in the H-phase is premature. It is interesting to note that the proportionality of τ_E to n_e which applies to current-heated discharges is replaced by $\tau_E \sim I_p$ in discharges without predominant current heating. Just as Ohmic plasmas become neoclassical at high densities owing to the prevailing ion transport contribution, there are indications that H-mode plasmas follow the same trend at high plasma currents.

Local transport analysis

For the L and H-regimes empirical scaling relations for the cross-field electron heat diffusivity χ_e, the diffusion coefficient D and the inward drift velocity v_{in} were determined / 13 /. Flux-surface-averaged transport was analyzed by computer modelling of many series of L and H-discharges with modified versions of the BALDUR tansport code. The deduced transport coefficients hold for deuterium plasmas and tangential co-injection of hydrogen.

In the Ohmically heated phases the OH scaling

$$\chi_e = (1.9 - 2.5) \times 10^{17}\, n_e^{-1}\, T_e^{-1}\, q^{-1}\ \mathrm{cm}^2 \cdot \mathrm{s}^{-1} \quad (2)$$

$$D = 0.2\, \chi_e \quad (3)$$

is found, where n_e is in cm^{-3} and T_e in keV. The range of numerical factors results from using different coefficients in the scrape-off zone.

With neutral injection, a distinction has to be made between the L-regime, the H-regime with high-frequency ELMs, and the H*-regime without ELMs (see Sec. 1.2.3). In these regimes, the following empirical scaling relation, which can be expressed in dimensionless quantities, yields a good fit to all series of ASDEX discharges analyzed so far:

$$\chi_e = C_R\, r_n^{-1/2}\, T_i^{1/2}\, rB_p^{-1} \quad cm^2 \cdot s^{-1} \qquad (4)$$

$$D = 0.2\, \chi_e \qquad (5)$$

with C_R equal to $C_L = 2.3 \times 10^4$, $C_H = 9.2 \times 10^3$ and $C_H^* = 4.9 \times 10^3$.

Here, C_R is a regime-dependent factor, $r_n = -n/(dn/dr)$ is in cm, T_i in keV, B_p is in kG and $rB_p^{-1} = R_o q B_t^{-1}$, with the major radius R_o in cm. The outstanding features are the lack of an explicit density dependence and the inverse B_p scaling. At present, the accuracy of the experimental data and the range of parameter variation are not sufficient to exclude modified representations of $\chi_e(r)$, e.g. by other profile scale lengths.

Comparing the results shows that a large change in scaling and probably also in the transport mechanism takes place between the OH regime and the regimes with NI.

Since the dominant power loss is due to electron heat conduction, χ_e essentially determines the global energy confinement time τ_E. Both χ_e and τ_E are independent of density in regimes with NI. The local parameters B_p and T_i in the χ_e scaling correspond to plasma current and injection power, respectively, in the τ_E scaling.

The ion heat diffusivity χ_i is found to be neoclassical in the Ohmic, L and H-regimes.

Regarding the anomalous inward drift velocity, the thermoelectric-type relation is found to work in all regimes:

$$v_{in} = -0.54\, D(a/2)\, T_e^{-1}\, \frac{\partial T_e}{\partial r} \quad cm \cdot s^{-1} \qquad (6)$$

where D is in $cm^2 \cdot s^{-1}$ and a is the separatrix radius. The anomalous inward drift is applied instead of the Ware pinch.

For a well-diagnosed series of H-discharges local transport in the whole plasma including the scrape-off region was analyzed (I_p = 380 kA, P_{NI} = 3.2 MW). Applying the empirical scaling relations yields agreement with the electron density and temperature profiles (see Fig. 1a) and with the measured β_p = 1.5 and τ_E = 55 ms. The corresponding profiles for χ_e, D and v_{in} are shown in Fig. 1b.

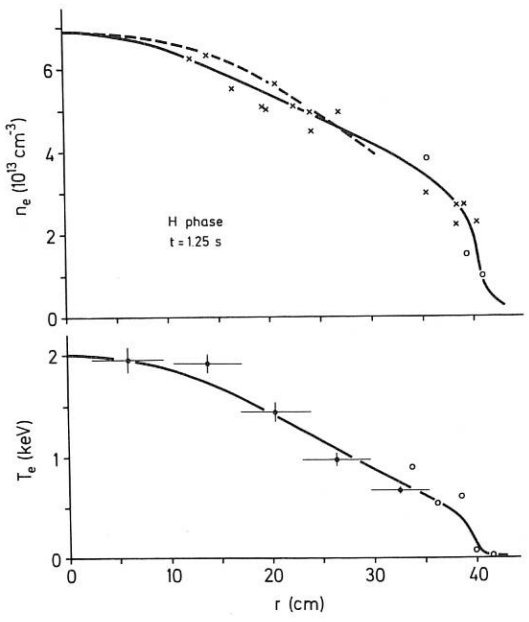

Fig. 1a: Computed $n_e(r)$ and $T_e(r)$ (solid curves) compared with the density profile measured by HCN laser interferometry (dashed curve), quasi-stationary laser scattering (crosses) and Thomson scattering (circles), and with the T_e profile from ECE diagnostic (points) and Thomson scattering (circles).

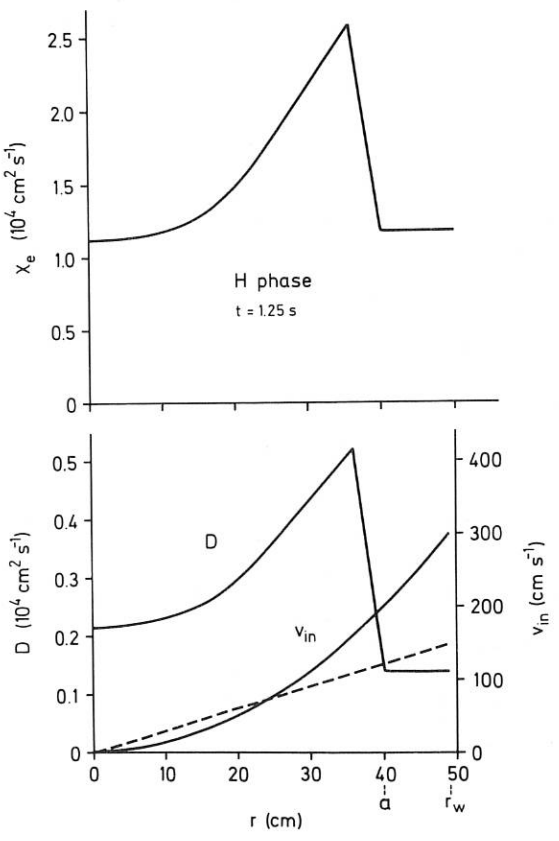

Fig. 1b: Profiles of χ_e, D and v_{in} during the H phase. For comparison the v_{in} profile in the OH phase is shown as a dashed curve.

Comparison and application of the scaling results

Combining the assembled scaling results from different devices (ASDEX, PDX, DIII, ISXB, DITE /101/) with ß-values below the theoretically predicted MHD-limit $ß_t = 0.03\ I/aB_t$[MA, m, T][1], one can try to use the Connor-Taylor constraints to obtain information about the size scaling, since the latter cannot be inferred from a single machine and is even hard to deduce from differences between the above mentioned five devices. Assuming power laws the confinement scaling of eq. (1) is supplemented with the geometrical parameters $a^r R^s (b/a)^t$.

Applying the Connor-Taylor constraints of the reduced tokamak equations one obtains a scaling law for L-discharges

$$\tau_E = 0.033\ \bar{n}^{-1/9}\ a^{-2/9}\ R^{10/9}\ (b/a)^{1/2} \cdot B_t^{-1/9}\ P_H^{-1/3}\ I\ A_i^{1/3} \qquad (7)$$

[s, 10^{20} m^{-3}, m, T, MW, MA]

The density and field scaling is well within experimental error bars and the dimensional scaling is in remarkable agreement with the results from other devices.

Using the definition $P_H = 3 \langle nkT \rangle 2\pi^2 Rab/\tau_E$ yields $\tau_E \sim I^{3/2}\ T^{-1/2}\ \bar{n}^{-2/3}$. Compared with the scaling given by Goldston[2], our power and correspondingly T scaling rely more on the PDX and ASDEX results and are more favourable, while the size scaling is weaker.

In the H-mode divertor discharges, different scalings result if either all data points are used in the τ_E^* versus P_H plot or only cases with ß-values clearly below the ideal MHD limits. A size scaling is hard to deduce, since the dimensions of the ASDEX, PDX and DIII experiments are close together. Data taken below the MHD limit or at lower heating powers do not contradict the L-mode size scaling given above, so that an approximate scaling

$$\tau_E \text{ (H with ELMs)} = 0.065\ I\ R\ A_i^{1/2} \text{ [s, MA, m]} \qquad (8)$$

is well within experimental errors.

The extrapolation to TFTR and JET, these being limiter tokamaks, has to be done on the basis of L-mode scaling. From eq. (7) one obtains $\tau_E(L) = 0.3$ s for JET-parameters. Extrapolating even further to INTOR yields τ_E (L) = 0.4 s, preventing ignition. If JET and INTOR were to operate in the H-mode, $\tau_E(H) = 1.9$ s and 3 s, respectively, could be expected. The H-mode confinement times might be just sufficient for ignition even without an additonal favourable scaling with dimensions.

[1] F. Troyon et al., Plasma Physics and Controlled Fusion 26 (1984) 209

[2] R.J. Goldston, Plasma Physics and Controlled Fusion 26 (1984) 105

1.2.2 Investigation of possible reasons for the confinement deterioration

Variation of the neutral beam deposition profile

It has been speculated that good confinement is achieved when the power deposition profile matches the plasma profiles (canonical profiles[3]). Such an agreement may prevail in Ohmic discharges because the heating profile is linked to the plasma profiles via the electron temperature. With auxiliary heating, however, the deposition profile can be set independently and may deviate from the Ohmic profile. The link between the plasma and power deposition profiles are the transport characteristics of the plasma. Under unfavourable circumstances the transport might be enhanced.

In order to study the role of the beam deposition profile, we performed hydrogen and deuterium injection at the full injection voltage (40 - 45 kV) and additionally deuterium injection at 29 kV (for details see Sec. 5.1.2). The Ohmic target plasma parameters were the same for all cases and, by choosing the appropriate number of heating sources, the heating power was kept constant (1.1 - 1.3 MW).

The two extreme power deposition profiles (calculated with the FREYA-code) of this study are shown in Fig. 2b. 40 keV H^o-injection gave rise to a peaked profile; the one for electrons (ion transfer neglected) matches well the deposition profile of the preceding Ohmic phase. 29 keV D^o-injection yields a very broad profile.

The major result of this study is plotted in Fig. 2a which shows the variation of the global energy confinement time τ_E of L-type discharges with mean ($\langle E \rangle$) and maximal (E_o) beam energy. τ_E is found to be fairly insensitive to the shape of the deposition profile. Even the case 40 keV, H^o with an electron deposition profile which hardly deviates from the Ohmic profile yields L-type confinement. These results raise doubts as to whether the degradation in confinement in L-type discharges is caused by the peculiarities of the energy deposition profile of beam-heated discharges.

Effects of increased $ß_p$ and T_e

The degradation in confinement could be caused by the increased plasma pressure or the rising electron temperature. The rising pressure affects plasma stability (at low power locally and at high power the global plasma) causing additional instabilities which enhance transport. The rising electron temperature may allow new types of fluctuations as soon as the plasma becomes collisionless, with the free energy of banana particles causing destabilization. Furthermore, the degradation of

[3] B. Coppi, Comments Plasma Phys. Cont. Fusion 5 (1980) 261

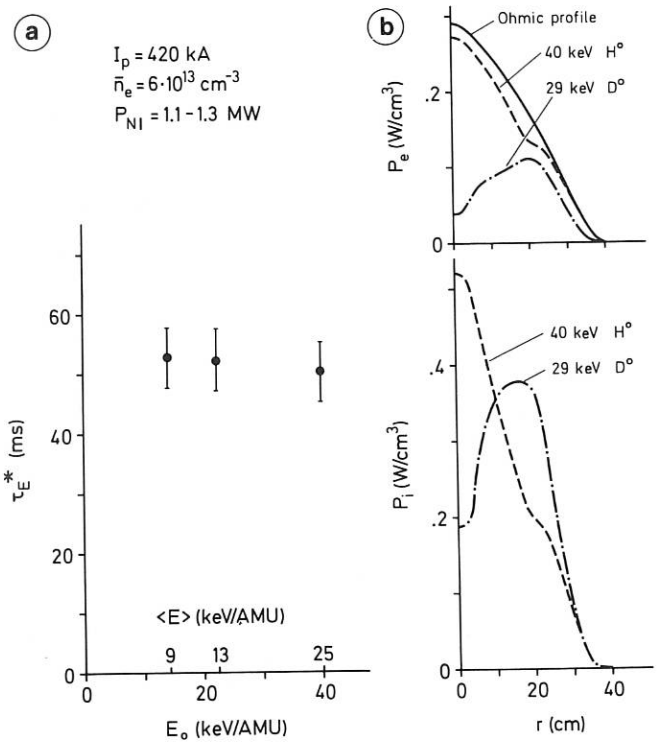

Fig. 2a: Energy confinement time τ_E^* (derived from $\beta_{p\perp}$) versus full beam energy E_o and species-averaged beam energy <E>, respectively.

Fig. 2b: Power density P to the plasma versus radius as computed for experimental plasma parameters and for two beam energies <E> = 25KeV/AMU and <E> = 9KeV/AMU. P_i = power to ions; P_e = power to electrons. P_e is compared with the Ohmic power deposition profile.

---

confinement with rising electron temperature may be an inherent plasma property unnoticed by the study of Ohmic discharges.

A reduction in τ_E is already noted at low beam power. Operation with one source roughly doubles the power input, while β_p rises by only 30 % yielding a drop of τ_E to about 2/3 of the reference Ohmic value. At high plasma current, β_p-values as low as 0.2 can be achieved with low heating power which, nevertheless, clearly carry the signature of degraded confinement. Such β_p-values are easily reproduced in Ohmic discharges (by operation at lower plasma current) without any effect on confinement (if q_a is kept constant), indicating that β_p, as a global parameter, does not cause the degradation in confinement.

The concept of ideal ballooning modes causing the deterioration in confinement of beam-heated discharges[1] has been analyzed quantitatively. Figure 3 shows the expected variation of τ_E (normalized to the Ohmic value) plotted basically versus beam power. The theoretical dependence is compared with the experimental results. Degradation in confinement is found to already set in at low heating power when ideal ballooning modes are not yet unstable. The same result is obtained by directly comparing the pressure gradient of L-type discharges with the critical one for ballooning stability. The prevailing gradient (including the contribution from the beam ions) of a high power L-discharge is still below the critical one by a factor of about 2. Thus - on the basis of the existing theory - ideal ballooning modes have to be excluded as reason for the confinement degradation.

Though the stability criterium for ideal ballooning modes is not violated in L-discharges, resistive ballooning modes could nevertheless be unstable. The empirical confinement law (eq. 7) can indeed be transformed into the functional form of the reduced tokamak equations

$$\tau_E = \tau_R \cdot f\left(\frac{\beta q^{*2}}{a} R, \frac{\tau_R}{\tau_{Ap}}, q^*\right) \qquad (9)$$

which is closely related to the growth times of resistive ballooning modes. A theory based on resisitive ballooning modes could explain the experimentally observed radial dependence of the thermal diffusivity and the degradation in confinement in case of ISX[2].

The application of the theoretical thermal diffusivity in ASDEX tansport calculation, however, gives poor agreement with the experimental results (a 10-100 times higher χ_e is required for agreement) and does not confirm the resistive ballooning mode hypothesis. Moreover, the predicted scaling relations disagree with our empirical results.

The possibility that the degradation in confinement with beam-heating is invariably caused by the

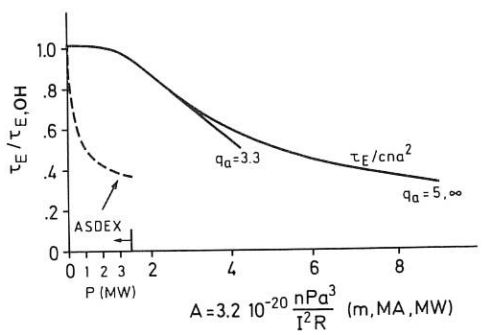

Fig. 3: Variation of the energy confinement time τ_E normalized to that of the Ohmic plasma τ_E^{OH} versus beam power. The theoretical dependence is compared with the experimental result.

---

[1] J.W. Connor, J.B. Taylor and M.F. Turner, Nucl. Fus. 24 (1984) 642

[2] B.A. Carreras et al., Phys. Rev. Lett. 50 (1983) 503

rising electron temperature was experimentally tested by comparing an Ohmic discharge with beam heated discharges of the same peak T_e-values. $T_e(o)$ was kept constant by operating the beam-heated discharges at elevated plasma density. Fig. 4b compares the fits to the T_e-profiles of the Ohmic discharge with two beam heated discharges. For the Ohmic discharge the individual data points are given to demonstrate that within the experimental resolution not only is the peak T_e-value the same for the three cases but also the full temperature profiles. Though the T_e-profiles are kept invariant, τ_E degrades with beam heating as documented by Fig. 4a. We conclude from these investigations that the deterioration in confinement is not caused by the T_e-rise alone. If τ_E varies with T_e then in the form $T_e^{\alpha}\ \bar{n}_e^{\beta}$. As the power and $\bar{n}_e$ were changed simultaneously, such a dependence cannot be excluded.

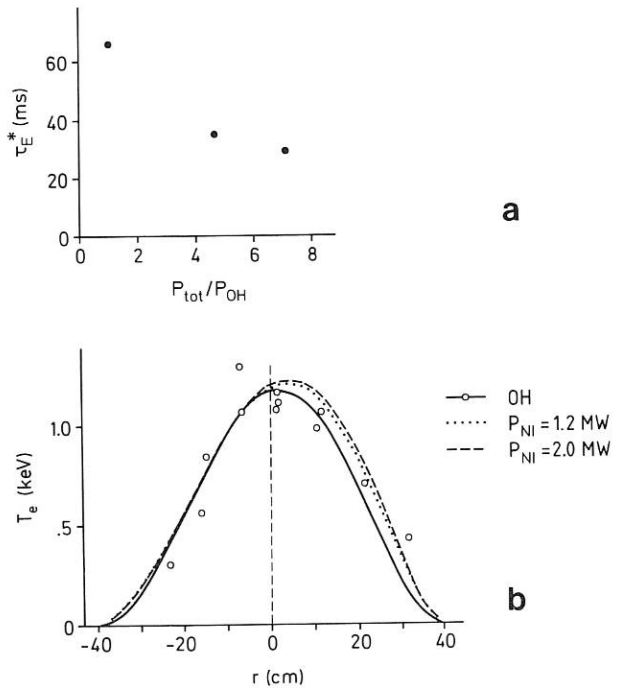

Fig. 4: Variation of the energy confinement time τ_E^* with normalized heating power (a). The electron temperature profile (b) is kept constant for the three cases (individual data points are shown for the Ohmic case) by increasing the density with power (OH : $\bar{n}_e$ = 2.1 x $10^{13}cm^{-3}$, 1.2 MW : $\bar{n}_e$ = 3.4 x $10^{13}cm^{-3}$, 2.0 MW : $\bar{n}_e$ = 4.2 x $10^{13}cm^{-3}$).

The effect of plasma profiles on confinement

The effect of the profiles on the transport characteristics of the plasma can be comprehended by the qualitative analysis of the sequence of confinement regimes caused by NI into an Ohmic discharge. The plasma first reacts with reduced confinement typically 10 ms after the beams have been fired. About 50 ms later, a diverted plasma transits into the H-mode (if the operational conditions prevail). The duration of the preceding L-phase is shortened by increasing beam power. This dependence on beam power favours the concept of a threshold which has to be surpassed or a stability criterion which has to be met in order to reach the H-phase. As reported in detail in the Annual Report 1983 the transition into the H-mode requires the electron temperature (or electrical conductivity) in the plasma periphery to surpass a threshold of ~300 eV. When the beams are switched off, the plasma stays in the H-mode typically for 30 ms before it flips back again into the L-mode, from where it gradually becomes an Ohmic discharge. The profile shapes thus again have to run through the same sequence as during the initial phase but in reversed direction. This remarkable symmetry in confinement properties can be seen from the parameter variation shown in Fig. 5. The second L-phase again causes an increase in particle outflux from the main plasma, which is manifested as a sudden decrease in $\bar{n}_e$ and a sharp rise in the atom flux ϕ_a of ions neutralized at and backscattered from the neutralizer plate. The reduced energy confinement time gives rise to a discontinuity in the slope of $\beta_{p\perp}$. After termination of the beams the H-phase remains for more than an ion-slowing down time (~10 ms). The delay time of about 30 ms is a typical confinement time. In particular, it is the time the ion temperature needs to fall below the electron temperature. It is possible that the edge electron temperature is temporarily kept above the transitional threshold by the energy transfer from the ions.

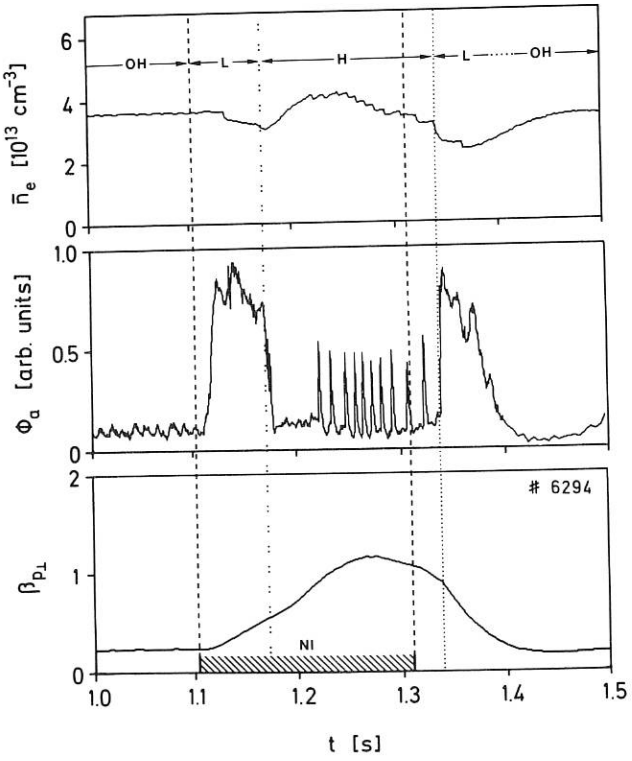

Fig. 5: Variation of the line averaged electron density $\bar{n}_e$, the atom flux Φ_a emerging from the neutralizer plate and $\beta_{p\perp}$ from the diamagnetic loop during the NI phase (hatched time interval) for the different confinement regimes L and H.

The invariable sequence of confinement regimes and, in particular, the appearance of a second L-phase in the transitional phase from a beam-heated to an Ohmically heated discharge clearly document that the plasma profiles determine the type of confinement: When the second L-phase begins, the beam ions are already slowed down and have merged into the bulk plasma. Both L-phases may be caused by peaked profiles. At the beginning of NI, the profile peaking may be caused by central deposition. When the beams are switched off the profiles may peak again because of the lower confinement at the edge than in the centre.

Transition from the Ohmic plasma to the L-phase

The study of the transition from an Ohmic plasma to the beam-heated phase with degraded confinement may elucidate the nature of the mechanisms which additionally affect confinement. Figure 6 displays the initial phase of NI with the transition from Ohmic to L-behaviour and then, at 1.18 s, the sudden transition to the H-phase. When the beams are fired, this has no effect first on the line average density $\bar{n}_e(0)$ and $\bar{n}_e(a/2)$, on the hard X-ray radiation ϕ_x (indicating the loss rate of runaway electrons), on the $D\alpha$- radiation in the divertor chamber (being a measure of the energy outflux) and on the atom flux from the target plate ϕ_a (correlated to the particle confinement). The total power transferred to the plasma P_{tot} rises and the energy content of the plasma increases at a rate dE/dt. dE/dt as derived from the plasma equilibrium ($\beta_p + 1_i/2$) contains plasma rotation and beam energy and therefore rises approximately as P_{tot}; dE/dt from the diamagnetic loop ($\beta_{p\perp}$) gives the rate with which the thermal energy content rises.

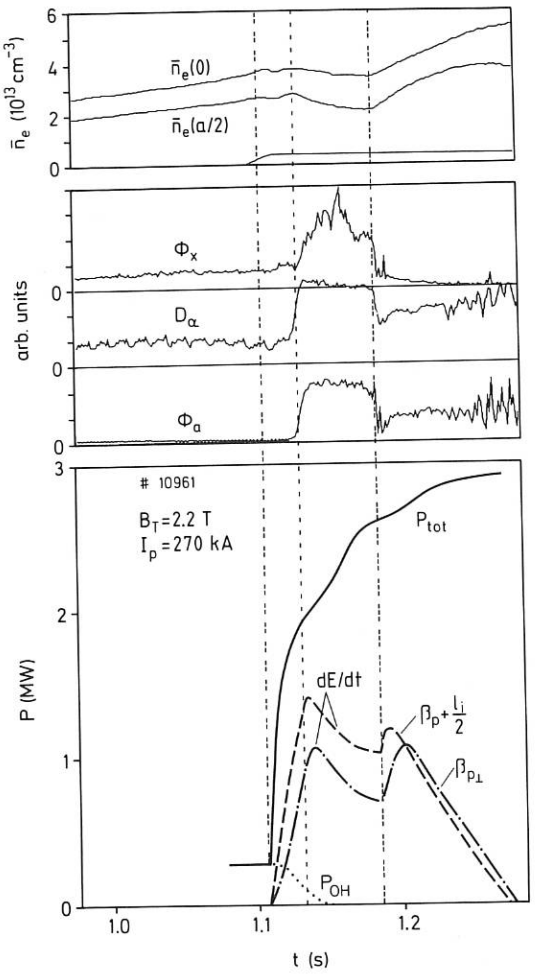

Fig. 6: Variation of the line averaged electron density $\bar{n}_e(o)$ and $\bar{n}_e(a/2)$, the hard x-ray radiation Φ_x, the D_α-radiation in the divertor chamber, the atom flux Φ_a emerging from the target plate, the total heating power P_{tot} and the rate of energy change dE/dt of the plasma deduced from the equilibrium (β_p + 1i/2) and the diamagnetism ($\beta_{p\perp}$), respectively.

25 ms after the beginning of NI, the confinement properties of the discharge, documented in Fig. 6, suddenly change. The decrease in plasma particle content ($\bar{n}_e$) and the increase in ion outflux (ϕ_a) indicate a sudden reduction of particle confinement. Simultaneously, the global energy confinement deteriorates: Though the heating power still increases, dE/dt suddenly decreases after a maximum and decouples from P_{tot} indicating enhanced losses. The increased energy flux into the divertor chamber changes the local recycling equilibrium there with the consequence that the ionization rate and $D\alpha$-radiation are increased. Simultaneously to the confinement of the thermal plasma that of the runaway electrons deteriorates, causing ϕ_x to rise.

It can be concluded from these observations that there exists a well-defined condition for the change in confinement which is met 25 ms after initiation of the beams in the phase of rising temperatures. The change in confinement affects both the thermal plasma, the non-thermal electrons, and the particle and energy contents. (Exactly the opposite observations - corollary to the improvement in confinement - are made on the following H-transition.)

The correlation between particle and energy confinement points to electrostatic turbulence as the origin of the degradation; it may be doubted whether it is the collisionality aspect of the plasma which changes the drift wave pattern with beam heating. γ_e^* of the discharge sequence shown in Fig. 6 is below 1 for the Ohmic case with good confinement and rises with beam power because of increased density at constant T_e. Nevertheless the confinement decreases. The strong effect on runaway electrons may indicate a strong magnetic component of the fluctuation causing the L-phase.

Is the L-regime determined by a local or global condition

It is of importance to know whether the degradation in confinement is determined by a global (like β_p) or a local (e.g. a gradient) condition. To explore this, the transition from Ohmic scaling ($\tau_E \sim \bar{n}_e q_a$)

to that of beam-heated plasmas ($\tau_E \sim I_p$) was studied. Figure 7 shows the density and current scaling of τ_E^* for the Ohmic phase as a reference and then with one source and two sources, respectively. These results are further compared with the high-power scaling limits.

With increasing beam power, a gradual transition from the Ohmic confinement scaling to that of beam-heated plasmas is observed. In the transitional power range, the local transport coefficients may depend on both the plasma density and current density (or poloidal field) so that the change in global confinement scaling may be the result of a modification of χ_e everywhere in the plasma. On the other hand, the results of Fig. 7 can also be interpreted in the sense that the transport is only modified in part of the plasma cross-section and is governed there by NI confinement, while the other parts still follow the OH scaling. With increasing beam power the modified part expands at the expense of the unchanged part, giving rise to a gradual transition from Ohmic to NI scaling.

From the scaling properties alone, it is not possible to decide definitely between the two possibilities - global or local change in transport characteristics. A preliminary analysis shows that the global condition does not reproduce the density scaling of τ_E (see Fig. 7) well, in particular the still prevailing linear $\bar{n}_e$-variation, while the local condition reproduces this property. Additionally, a local change in transport can give rise to an improvement in τ_E when the high Ohmic transport at low density (particularly at the plasma edge) is replaced by the superior beam transport at high plasma current.

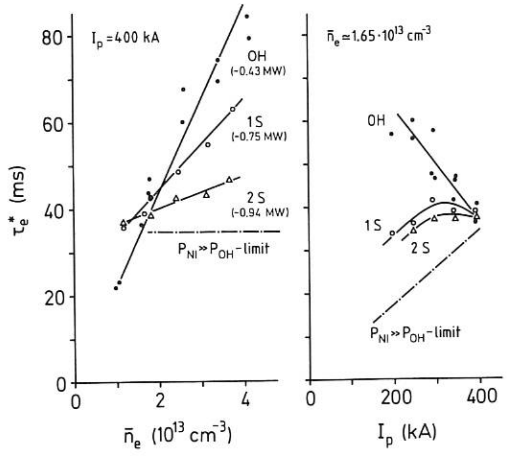

Fig. 7: Scaling of the energy confinement time τ_E^* with density $\bar{n}_e$ and plasma current I_p of the Ohmic plasma and with low beam power. The results are compared with the high beam power scaling limit.

1.2.3 Confinement of the H-phase

Development of a transport barrier at the H-transition

The H-regime is of great importance for meeting the ignition conditions in a tokamak reactor. For the design of future near-reactor tokamak experiments, the distinguishing feature between the divertor configuration (allowing the H-mode) and the limiter tokamak (which only operates in the L-mode) has to be identified. Deeper insight into the conditions for the H-phase was afforded by studying the dynamics of the H-transition.

As already documented in the Annual Report 1983, the H-mode can be initiated by the arrival of an energy pulse of sufficient magnitude in the proximity of the separatrix. Such pulses arise spontaneously after an internal disruption (sawtooth event) when a fraction of the energy, stored inside the q = 1 surface, is suddenly released and propagates outwards. Operation close to but below the power threshold for the H-transition causes an L-discharge. With large sawteeth short transient H-phases can occur, which, however, cannot be sustained permanently because of the low quasistationary power level.

Figure 8 plots the line average density $\bar{n}_e$, the Dα-radiation in the divertor chamber and the electron temperature T_e at four different radii of a marginal L-discharge with large sawteeth. The sawteeth modulate T_e in the known form of a reduction within the q = 1 surface and a pulse like variation outside it caused by the thermal wave travelling to the plasma surface. The plasma density is modulated in a similar way. Sawteeth also modulate the Dα-signal in the divertor chamber, causing a signal rise there which is very conspicuous during the beam heating phase.

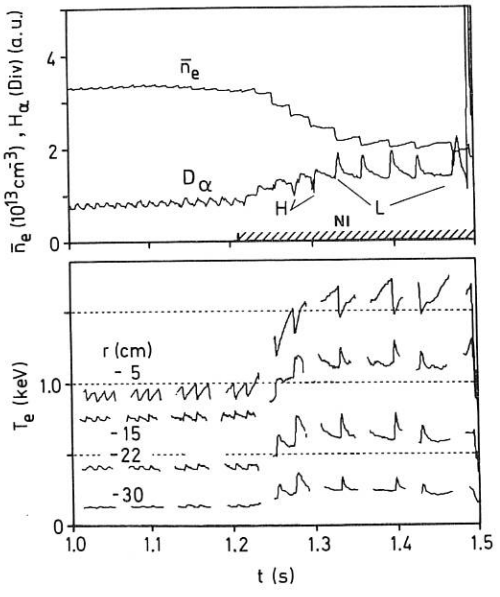

Fig. 8: Line averaged density $\bar{n}_e$, Dα-radiation in the divertor chamber and ECE-electron temperature T_e during an L-discharge with large sawteeth. Two sawteeth give rise to a short H-phase.

There are two exceptions as noted in Fig. 8. These are large sawteeth (only one is documented by the T_e-diagnostic), which cause an H-transition with the consequence of a decrease in D_α-radiation. The comparison of the T_e-variation caused by a sawtooth in the L-phase with that of a sawtooth triggering the H-phase reveals a distinct difference in the outer plasma zones but rather similar behaviour in the plasma core.

The detailed development of the H-transition triggered by a sawtooth under marginal conditions (P_{NI} = 0.8 MW) was studied by using the superior time and space resolutions of the soft X-ray (SX) diode array. As an example, two traces are shown in Fig. 9. Diode 1 views the scrape-off layer and diode 2 mostly the plasma inside the scrape-off layer. The distance between the two viewing lines is 2.5 cm. The same technique of comparing a regular sawtooth with one causing the H-mode is again adopted. As these two events occur in sequence only 50 ms apart, the dynamics of the H-transition become evident in a comparison of the parameter changes /246/.

The thermal wave of a sawtooth during the L-phase causes T_e to increase first in the main plasma periphery (as shown by Fig. 8), subsequently in the scrape-off layer where the T_e-variations modulate the SX signal (Fig. 9), and finally inside the divertor chamber, where it temporarily increases the D_α-radiation (Fig. 8).

The large sawtooth (H), which triggers an H-phase transition, gives rise to a totally different behaviour: The edge electron temperature does not show the transient variations caused by a passing thermal wave. The transition occurs during the sawtooth rise, which is initially still resolvable. At the instant of transition, the signal of the SX-diode, viewing the scrape-off layer, decreases sharply. Within the separatrix, the sawtooth, triggering the H-phase, causes a continuously rising signal.

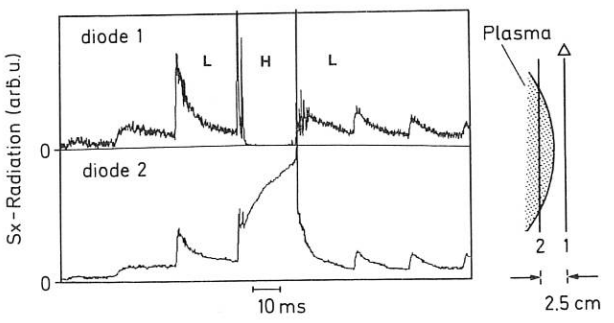

Fig. 9: Soft x-ray radiation during the L-phase with large sawteeth. Diode 1 views the scrape-off layer, diode 2 mostly the plasma within the separatrix. One sawtooth gives rise to a transient H-phase.

Comparison of the different parameter variations during the two subsequent sawtooth events clearly demonstrates that the arrival of a thermal wave of sufficient intensity in the edge region causes there a reduction of the anomalous transport coefficients and provides an effective barrier to both energy and particle fluxes. The reduction causes the decrease in the SX-signals from the scrape-off layer and of the energy (D_α) and particle flux into the divertor. Inside the separatrix, energy and particle flow stagnate, causing good confinement and a continuous rise of the SX-signal and the total energy content.

The consequence of an edge barrier with low transport coefficients is that steep gradients develop at the plasma edge (see Annual Report 1983) and that the energy losses from the main plasma are transiently modified. The power which is transported into the divertor chamber (predominantly by parallel electron heat conduction) shows a sharp reduction at the H-transition. Figure 10 plots the variation of the power deposited on the neutralizer plates P_{DEP} (measured by infrared thermography) and the power radiated within the divertor chambers P_{RAD} (from a bolometer). In this case a power of 3 MW is injected, giving rise to a fully developed H-phase. The transport losses across the separatrix $P_{DIV} = P_{DEP} + P_{RAD}$ which amount to more than 70 % of the power input during the Ohmic and L-phases drop to 8 % after the H-transition. Despite the high power input, the accounted transport losses of the plasma are comparable to those during the Ohmic phase!

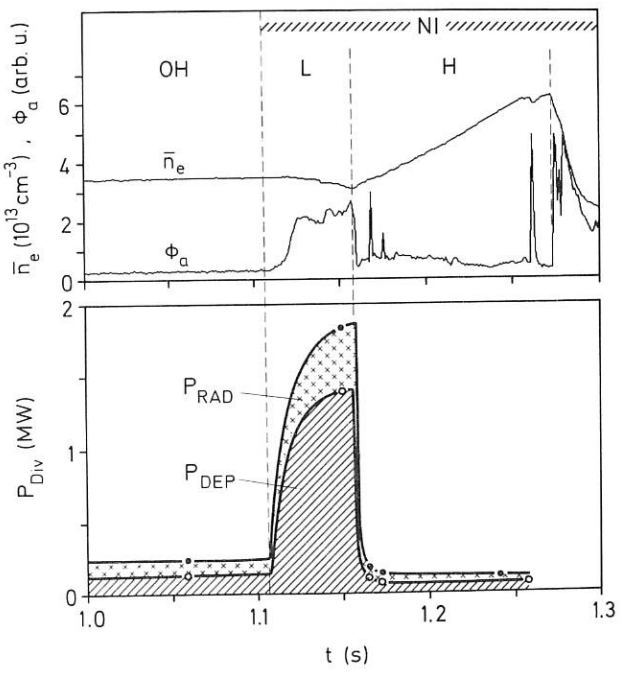

Fig.10: Line averaged density $\bar{n}_e$, atom flux Φ_a from the target plate and total power measured within the divertor chamber P_{Div} (energy deposition onto the target plate P_{DEP} plus radiated power P_{RAD}). Note the sharp transition into the H-phase.

The exclusive observation of the H-mode in divertor discharges, the narrow extent of the transport barrier of a few cm, and its proximity to the separatrix suggest that it is linked to the specific field topology at the stagnation point, giving rise to long field lines and high shear.

Transport characteristics of intrinsic H-discharges

A characteristic feature of an H-discharge is the occurrence of so-called ELMs (edge localized mode), which repetitively expel particles and energy from the plasma periphery, causing saturation of the global particle and energy confinement time (see Annual Report 1983).

A method of suppressing ELMs by moving the plasma column to the outer wall was found. The major radius has to be increased by 7 cm, which reduces the plasma-to-wall distance (to 4 auxiliary limiters) to ~4 cm. It is not yet clear why the instability condition for ELMs is affected by this displacement. A possibility is stabilization due to the proximity to the wall. An indication of this stabilization mechanism might be the observation that ELMs occur during the beam pulse as soon as the plasma is moved away from the wall.

Without ELMs (quiescent H-mode, H^*), the intrinsic confinement properties of the H-mode could be studied. Figure 11 compares the density development of an H^*-discharge with an L-discharge. The remarkable particle confinement properties of the H^*-discharge are illustrated by the fact that the density rise does not require any external molecular gas fuelling. The virtue of this discharge type, however, is hampered by the fact that the superior confinement applies to impurities as well, giving rise to a serious radiation problem in the course of the quiescent H-phase.

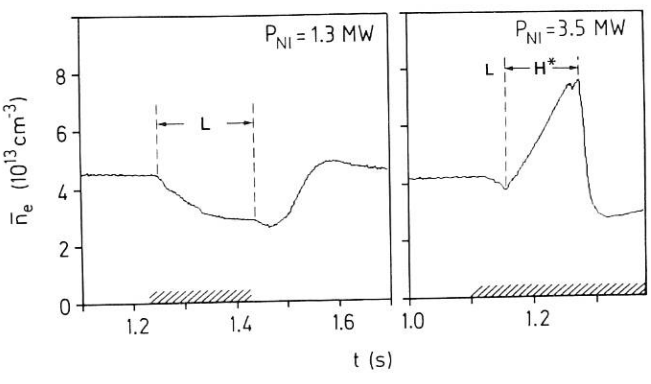

Fig.11: Comparison of the line average density of an L and an H^*-discharge (without ELMs).

Impurity accumulation

In an H-discharge with ELMs the bolometrically measured radiation from the plasma centre settles to the stationary value of 0.16 W/cm^3. In the case of the H^* discharge the volume-integrated and the central radiation losses attain extremely high levels of 3 MW and 3 W/cm^3, respectively. The volume-integrated heating power is 3.4 MW, with a calculated central value of only 1 W/cm^3. These radiation losses explain most of the observed decrease in beta and the decrease of the central electron temperature from 2 keV to 0.6 keV before and at the end of the accumulation phase.

Figure 12 shows the development of the ultra soft X-ray (USX) radiation during a quiescent H-phase with the exponential rise up to 2 W/cm^3. The local radiation is determined after Abel inversion of the line integrals assuming poloidal symmetry. The use of a further USX-ray camera viewing the plasma from a different poloidal angle allows tomographic inversion. Contour plots of constant emissivity can thus be constructed and poloidal asymmetries are detected.

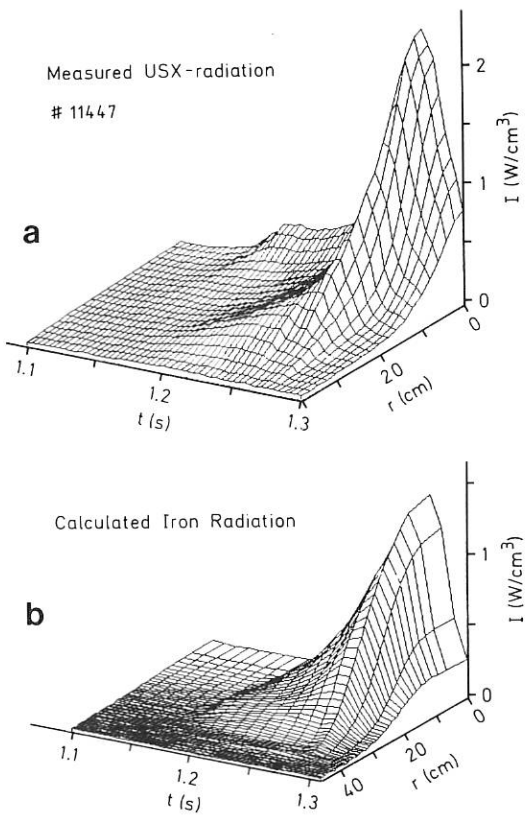

Fig.12: Measured ultra soft x-ray radiation (a) and calculated iron impurity radiation (b) during a quiescent H^*-phase.

The accumulation of impurities in the quiescent H-phase is not directed symmetrically to the magnetic axis but is found to be largely a contraction in the poloidal plane towards the outside of the torus. Unlike the Ohmic phase (see Sec. 1.4.1) the H^*-phase shows remarkable up-down symmetry.

Figure 13 shows the iso-emission contour lines during the accumulation process for two moments in the discharge: at the β_p-maximum (t = 1.225 s) and in the middle of the accumulation phase (t = 1.25 s) when the radiation losses start to affect the plasma performance and β_p and the temperatures quickly decrease. The role of the emission pattern can better be judged from a comparison with normal H-discharges with ELMs. The poloidal shoulder that develops after the H-transition (see Fig. 14) is found to exist also in a normal H-discharge. However, each ELM removes large parts of the impurity shoulder, thereby preventing the impurity accumulation and the final collaps of the discharge into a transitional L-phase (this L-phase after the radiaton collapse serves to remove all impurities; thereafter the plasma performs a second H-transition).

The detailed action of an ELM on the impurity distribution is documented by Fig. 14. Figure 14a shows a 3-D profile of the USX-radiation just prior to an ELM. Note the steep gradients at the inside of the separatrix. These gradients might well represent steep T_e and n_e-gradients and point to the actual cause of an ELM instability. No such steep gradients are observed in H^*-discharges. Figure 14b represents the situation after an ELM event: The steep gradients near the separatrix have disappeared but also the poloidal asymmetries, the inner low emission region, the poloidal shoulders and the width of the banana-shaped central part are strongly reduced.

Spectroscopic measurements reveal that the enhanced radiation losses predominantly originate from iron line radiation. Artificially introduced gaseous impurities (Ar, H_2S) are subjected to the same accumulation process accompanied by an exponentially rising line radiation. This observation clarifies that the enhanced radiation is not due to increased impurity influx but is the consequence of the improved confinement properties of the H^*-phase.

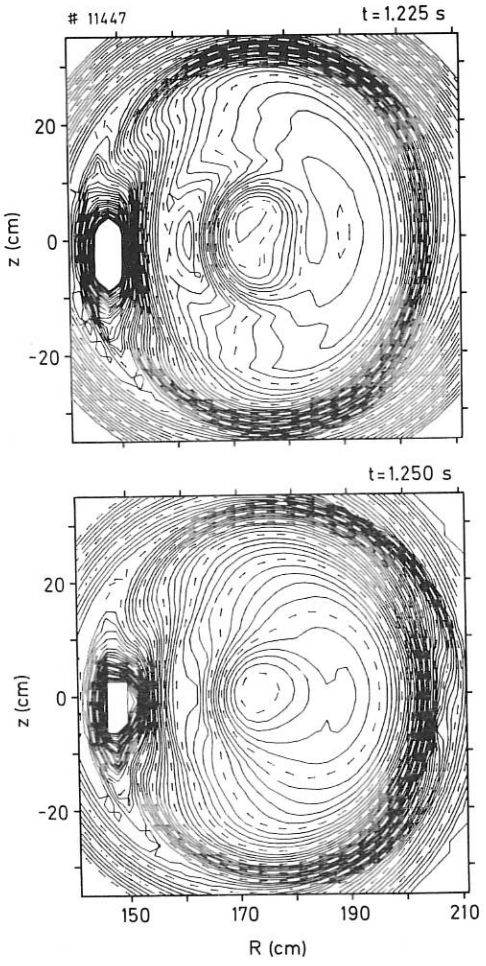

Fig.13: Iso-emissivity lines showing the plasma cross-section in ultra soft x-ray light for maximum beta (t = 1.225 s) and later in time during the impurity accumulation phase (t = 1.25 s). I(r = o) increases from 0.5 to 1.5 W/cm^3 during this phase.

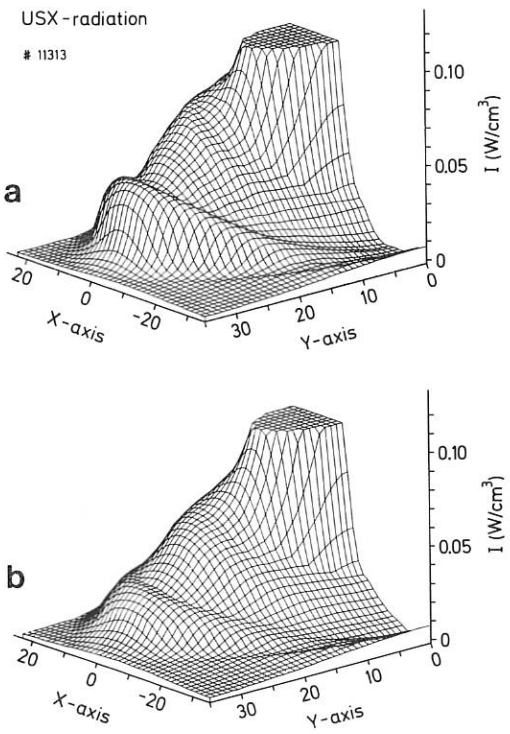

Fig.14: The ultra soft x-ray emissivity over the plasma cross-section before (a) and after (b) an ELM. Note the decay of the shoulder at the plasma edge.

The transport characteristics of impurities in the quiescent H-phase were studied by means of an impurity transport code. The background plasma is described by experimental T_e and n_e-profiles. Diffusion coefficient and inward velocity are varied so that the measured line radiation profiles are reproduced. The code assumes poloidal radiation symmetry, which does not prevail as the tomographic studies have shown. Therefore, the results rather indicate the general trend.

Because of the unprecedented confinement properties of the H^*-mode, neoclassical transport was tested first. But no satisfactory modelling of the experimental profiles was achieved. The main reason is that the neo-classical inward drift, due to the density gradient, is overcompensated by the outwardly directed drift caused by the steep temperature gradient at the plasma edge.

Satisfactory agreement was achieved on the assumption of an anomalous diffusion coefficient D and a superimposed inward velocity $v_{in} \sim r^2$. The preceding L-phase is modelled with D = 10000 cm^2/s and $v_{in}(a)$ = 230 cm/s ($v_{in} \sim r$). (The thermal plasma requires the same radial dependence in the L- and H-phases for successfully modelling the density profiles.) The H^*-results are reproduced with the same quality of agreement either by a constant D = 2000 cm^2/s or D = 1000 cm^2/s at the plasma periphery where the location of the transport barrier is expected ($0.9 \leq r/a \leq 1$) and D = 3000 cm^2/s elsewhere. The inward velocity has to be increased to $v_{in}(a)$ = 1800 cm/s. Figure 12 compares the calculated total iron radiation during the accumulation phase with the experimental SX-profiles. An iron-concentration of ~ 1 % causes the maximum power loss of 3 MW. The computations further reveal that the H-phase displays reduced impurity screening due to the steeper density and temperature gradients in the scrape-off layer.

Transport characteristics of the thermal plasma in the quiescent H-phase

The local transport of the plasma in quiescent H-phases was investigated by computer modelling. Discharges with a moderate iron impurity content were chosen, since they are expected to yield the most reliable transport coefficients (I_p = 380 kA, P_{NI} = 2.9 MW for 200 ms).

The scaling relations for χ_e, D and v_{in} are successfully applied. In Fig. 15 measured profiles of the electron density and temperature in the H^*-phase are compared with the simulation. The computed iron density profile n_{Fe} exhibits a weak increase to the edge. Measured time developments of the central ion temperature and of β_p are also correctly modelled. The diffusivities $\chi_e^{H^*}$ and D^{H^*} are found to be about twice as small as those in ordinary H-discharges, where additional energy and particle losses are caused by ELMs ($\chi_e^{H^*}$ (2 a/3, 1.3 s) = 1.0 x 10^4 cm^2 s^{-1} and $D_e^{H^*} = 0.2\ \chi_e^{H^*}$). The approximate ratio of the local coefficients $\chi_e^L : \chi_e^H : \chi_e^{H^*} \approx 4 : 2 : 1$ reflects the ratio of global energy confinement times at r = a, namely

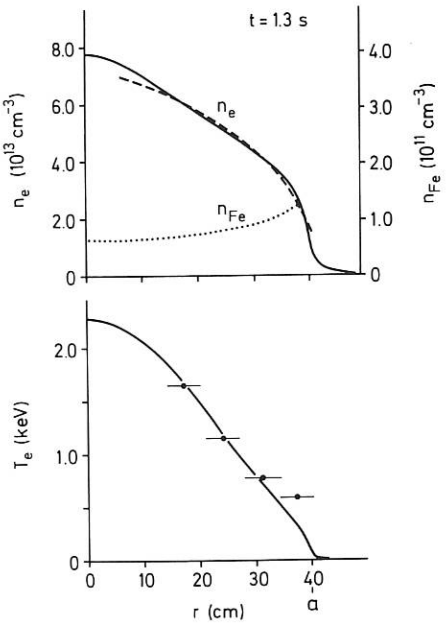

Fig.15: Computed $n_e(r)$ and $T_e(r)$ (solid curves) compared with the density profile measured by HCN laser interferometry (dashed curve) and with the T_e profile from ECE diagnostic (points). The dotted curve is the computed iron density profile.

τ_E^L = 30 ms, τ_E^H (1.2 s) = 65 ms and $\tau_E^{H^*}$ (1.3 s) 120 ms. Here τ_E is defined as the thermal energy content in the plasma divided by the conductive and convective energy fluxes due to electrons and ions. It should be mentioned that $\chi_e^{H^*}$ (r, 1.3 s) is a factor of about three lower than the values derived from the OH scaling. In the H regimes with and without ELMs the scaling of Ohmically heated plasmas is not recovered. Qualitatively, the confinement in the unperturbed H-phases does not differ from that with high-frequency ELMs.

1.3 Beta Limit Studies /122/

During the last year a remarkable consensus has been reached on the scaling and absolute values of theoretical ß-limits resulting from linear ideal MHD stability analysis. It was found that the limit for the toroidal ß can be described by the simple formula

$$\beta_{T,max} = g(\text{shape}) \frac{I}{a \cdot B_T} \quad [\%, \text{MA}, \text{m}, \text{T}], \qquad (10)$$

where g is only a weak function of the plasma cross-section as long as circular or "normal" D-shaped plasmas are considered. Troyon et al.[1] found

[1] Troyon, F., et al., Plasma Physics and Controlled Fusion 26 (1984) 209

that g = 2.4 to 3.1 is required for stability against kink and ballooning modes, while an optimization by Sykes et al.[1] for ballooning modes alone (and $q_o = 1$) resulted in g = 4.0.

On the other hand, the ß-values attainable with a given heating power $P_{tot} = P_{OH} + P_{NI,abs}$ for a non-circular cross-section with minor radii a and b are

$$ß_T \sim \frac{P_{tot} \cdot \tau_E}{a.b.R.B_T^2} \quad . \qquad (11)$$

Combining (10) and (11) and making use of the general experimental finding that for NI-heated plasmas $\tau_E = f \cdot I$ (evaluated at the ß-maximum), yields

$$\frac{ß_T}{ß_{T,max}} \sim \frac{f \cdot P_{tot}}{b \cdot R \cdot B_T} \quad . \qquad (12)$$

Because of the large energy confinement factor typical of H-mode discharges ($f = 1.6 \times 10^{-7}$ s/A for ASDEX H-mode discharges in deuterium) it was possible in ASDEX even with relatively modest beam powers (3.4 MW for H^o- and 4.2 MW for D^o-injection) to test the ß-limits over a wide range of magnetic fields ($1.24\ T \leq B_T \leq 2.63\ T$). All ß-values presented in the following are from "normal" H-mode discharges with ELM's where radiation losses can be neglected in the global energy balance.

Figure 16 summarizes the maximum $ß_T$-values obtained so far as a function of the normalized plasma current $I_N = I/(a\ B_T)$. The ß-values labelled $ß^{equ}$ are deduced from equilibrum measurements and contain the contribution of the orbiting ions and the plasma rotation while those labelled $ß^{dia}$ are obtained from diamagnetic loop measurements. The latter are typically 20 - 30 % smaller and their maximum values $ß_T^{dia}$ lie close to the limit due to kink and ideal ballooning modes with free boundary $ß_T = 2.8 \times I_N$ (Troyon et al.).

Most points in Fig. 16 represent maximum $ß_T$-values obtained in a power scan at fixed plasma current I and toroidal magnetic field B_T. At a larger magnetic field Δß increases linearly with neutral beam power P_{NI} up to the highest powers available, whereas at a lower field ß tends to saturate for $P_{NI} \simeq 3$ MW, indicating a soft ß-limit. For small and moderate plasma currents (I = 170 and 270 kA in Fig. 16) such a saturation in ß was observed up to the highest toroidal fields used. At the larger plasma currents, however, the maximum ß-values achieved so far have been limited by the available beam power (this may explain why for I = 410 kA the maximum $ß_T$-values increase faster than linearly with I_N). It is worth noting that except for discharges with $q_{cyl} \leq 3$ or with very high power input, which are terminated by a disruption, the ß-limits are "soft".

[1] Sykes, A., et al., "Controlled Fusion and Plasma Physics" (Proc. 11th Europ. Conf. 1983), Part II, p. 363

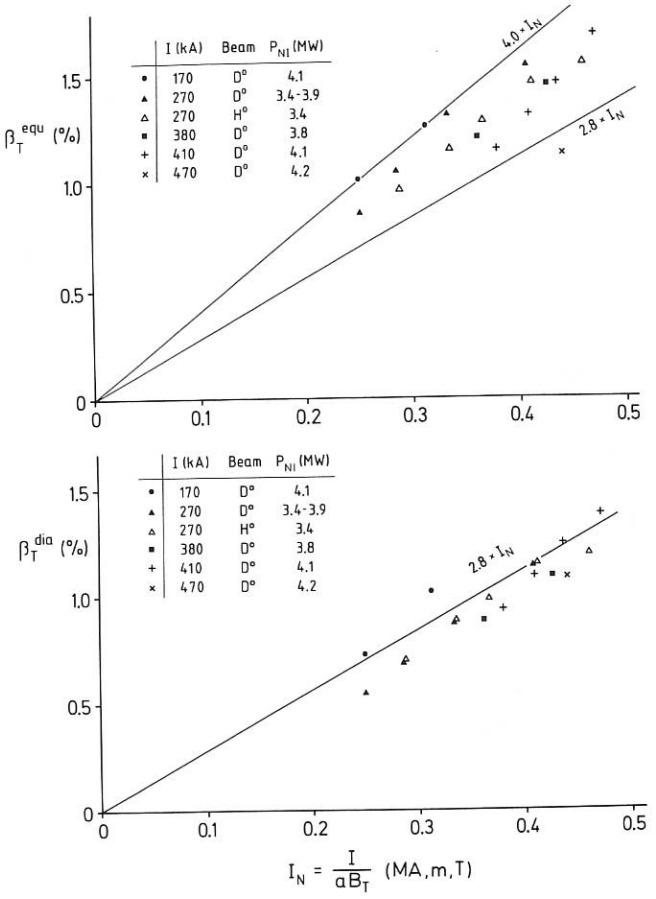

Fig.16: Maximum $ß_T$-values derived from equilibrium ($ß_T^{equ}$) and diamagnetic ($ß_T^{dia}$) measurements, respectively, as a function of normalized plasma current $I_N = I/(aB_T)$. Also shown are theoretical $ß_T$-limits $ß_T = 2.8$ and $4.0 \times I_N$, respectively.

Equation (12) can be used to represent the measured ß-values in a normalized plot. Figure 17 shows such a plot of $ß_T$ versus P_{tot}/B_T for all analyzed discharges with D^o-injection. To extend the data to lower P_{tot}/B_T values, results from H^o-injection have been included. The striking feature is the bending over of the $ß_T$-points at large P_{tot}/B_T either due to a deterioration of the confinement time or (in the region marked "disruptive") due to a disruptive end during a phase of still finite dE/dt. The maximum $ß_T$-values reached are close to the ideal MHD ß-limits.

Close to the limiting ß both the energy and the particle confinement is found to deteriorate. The measured time developments of ß, of the D_α signal and of the density and temperature profiles show the enhanced energy and particle transports. These additional losses are likely due to ideal MHD modes which grow unstable at least locally when the ß-limit is approached. On the other hand, discharges well below the limiting ß are found to be ideal-MHD-stable, i.e. kink and ideal ballooning modes cannot impair their confinement. These discharges exhibit the transport behaviour of the H-regime

with high-frequency bursts. Their flux-surface-averaged transport can be described by the empirical scaling relations for the transport coefficients χ_e, D and ν_{in} presented in Sec. 1.2.1.

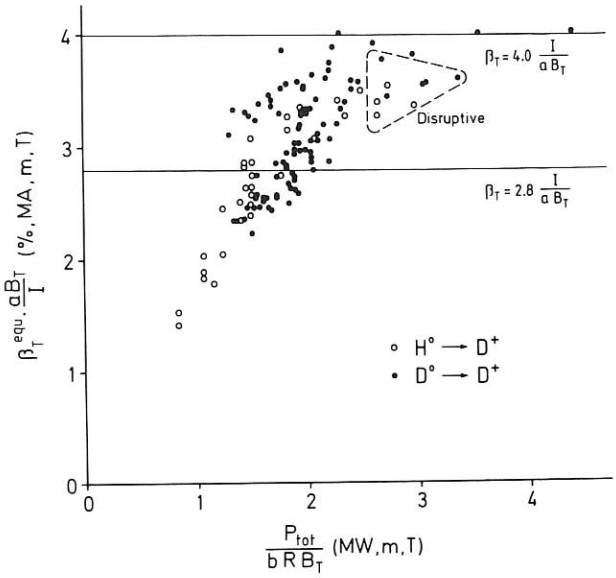

Fig.17: Normalized plot of β_T^{equ} versus heating power P_{tot}/B_T showing a saturation of ß with heating power.

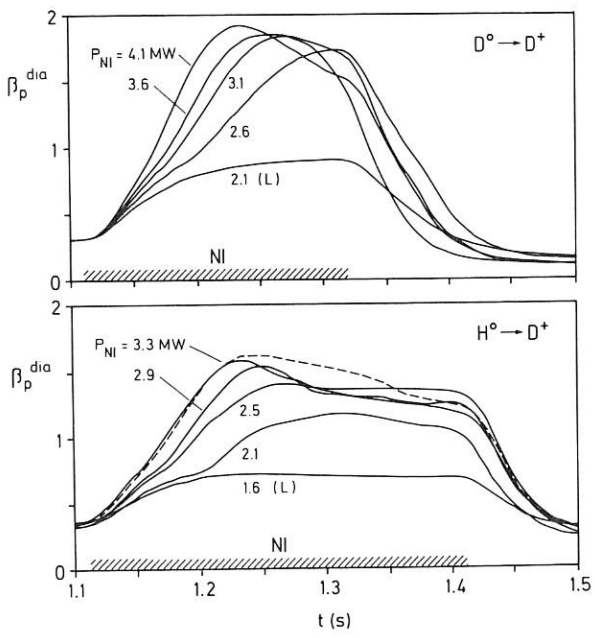

Fig.18: Time development of β_p^{dia} for two typical sets of discharges with varying beam power P_{NI}, showing first a linear increase $d\beta_p/dt \sim P_{NI}$ and then a characteristic decay which is probably due to changes in the current density distribution.

So far we have always quoted the maximum ß-values obtained during a discharge. ß cannot, however, be kept at that maximum value but rather decays with a time constant of about 1 s, and this cannot be explained by radiation losses. To illustrate this further, Fig. 18 displays two typical sets of discharges in which the neutral injection power P_{NI} was varied: Most striking is the almost linear rise in β_p with time and its sudden termination. Furthermore, the shots with lower heating power reach their maximum ß at later times and at an absolute value to which the discharges with higher heating power have decayed in the meantime, indicating that the maximum attainable ß depends on a time-varying parameter.

An obvious possibility is the current density distribution, which will adjust to the H-mode temperature profiles only on a resistive time scale: At fixed plasma currents the ultimately resulting q-profiles would allow only smaller stable ß-values. Estimates taking into account the actual variation of T_e-profiles, the dependence of the critical ß for ballooning modes on the current density distribution and the possible extent of the resistive adjustment of the latter indicate that this effect could account for a decay of ß by about 10 % within 50 ms. Corroborative evidence for the effect of current density profiles on ß-limits might be taken from results of beam heating experiments with simultaneous plasma current variation: Experiments with decreasing current and presumably more peaked current density distribution reached higher ß-limits at given q_a than those performed with stationary or rising I(t) (the latter gave even lower ß-values).

1.4 Edge Plasma and Divertor

1.4.1 Impurity transport[1]

Impurity retainment of the divertor in neutral injection heated discharges

In 1984 we resumed the experiments on the retainment of gaseous impurities in the divertor[2] (see Annual Report 1983). The previous experiments had indicated that the smallness of the plasma streaming velocity in the throat region of the scrape-off could cause the observed degradation of impurity retention during the NI heating phase. For this reason, enhancement of the streaming velocity was desirable. This was accomplished by Ti-gettering in the lower divertor chamber, thus increasing asymmetrically the flow velocity into this chamber. We then puffed small amounts of argon (8×10^{16} atoms/puff, pulse length 10 ms) into the three different chambers. The experiments were performed in the symmetric double-null configuration with wide divertor throats. In Fig. 19 we present spectroscopic measurements taken in the main chamber for the high-density case $\bar{n}_e = 5 \times 10^{13}$ cm^{-3} (I_p = 420 kA, B_t = 2.2 T).

[1] Further studies on impurity transport during NI and RF-heating are discussed in Secs. 1.2.3 and 1.6

[2] G. Fußmann, W. Poschenrieder, et al., Jour. of Nucl. Mat. 121 (1984), 164

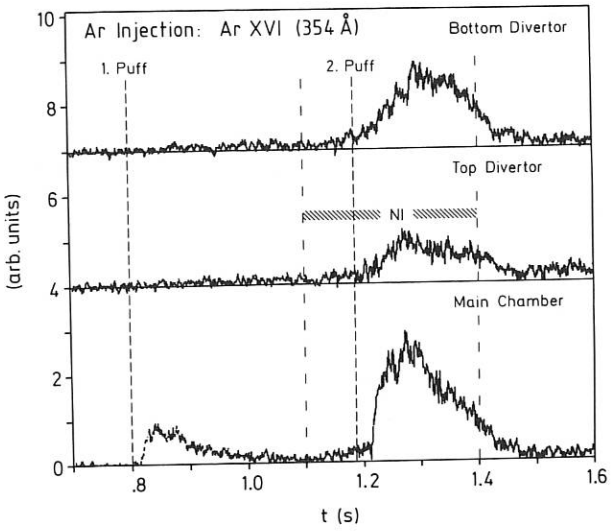

Fig.19: Intensity of ArXVI line emission from the bulk plasma during argon blow-in experiments. For the three cases shown, Ar-puffs were applied in either the bottom or top divertor or the main plasma chamber.

Two equal puffs were injected into the ohmic phase at t = 0.8 s and into the H-phase of NI (with bursts; $H^0 \rightarrow D^+$; 3.4 MW) at t = 1.2 s. As seen from Fig. 19, there is obviously good retainment in the divertor chambers during the ohmic phase: detectable intensities of Ar XVI (maximum emission at r/a ~ 0.5) are obtained only in the case where the gas is blown into the main chamber. Conversely, we obtain signals of comparable magnitude during the NI-phase for all three locations of Ar influx. From simulation calculations using an impurity transport code it is to be concluded that the observed increase of the Ar XVI signals even understates the actual changes of the argon content in the plasma with the transition from the ohmic to the NI-phase.

Obviously, the impurity transport is unfavourably modified with NI, leading to higher concentrations in the plasma. This can be interpreted either by improved particle confinement in the bulk plasma or - more likely - by a change of transport in the scrape-off resulting in a reduction of the divertor retainment. Such a degradation of retainment with NI is not unexpected for two reasons: The higher power flow into the divertor increases the pressure in the divertor scrape-off, thus reducing the flow velocity in the throat regions. Furthermore, with steeper temperature gradients along the scrape-off, the thermal forces, which tend to drive the impurities towards the bulk plasma, are of increasing importance (see Annual Report 1983 and Ref. /176/). An assessment, however, whether one or both of these effects are essential in the experiments cannot be made on the basis of our hitherto existing measurements.

Asymmetric impurity transport

For understanding the impurity transport in the scrape-off plasma, up-down asymmetries could be of crucial importance. The asymmetries are observed in the plasma boundary emission as well as by mass spectrometer measurements in the divertors. Very pronounced asymmetries (bottom-top Ar-pressure ratios of up to 5) have been found during the OH-phase[1]. More recently, a change in the asymmetry with NI was observed. While for the chosen direction of the toroidal field the impurities were found to concentrate in the bottom divertor during the OH-phase, they accumulate in the top divertor during the neutral injection phase. The same transition is observed in the soft X-ray ($h\nu > 40$ eV) boundary radiation of the bulk plasma. In Fig. 20 the intensity ratio measured along chords in the upper and lower boundaries (r = ± 38 cm) is plotted versus the number of NI-sources (0.4 MW/source, $H^0 \rightarrow D^+$). As seen from the figure, the asymmetry changes at power levels where the transition from the L to the H-phase occurs. With vertical plasma shifts of 1 cm the intensity ratio of the two chords changes from 2 in the unshifted case to 1. As a matter of interest it should be noted, however, that practically no asymmetries were found in the case of the quiescent H-mode (see Sec. 1.2.3). The preference of the impurities to stream into the upper divertor during the normal H-phase was even observed in the case of the above-mentioned experiments with enforced flow into the bottom divertor. Our spectroscopic signals in Fig. 19 confirm this behaviour: comparing puffing into the top and bottom divertor, we find a smaller amount of argon in the plasma in the former case.

The physical mechanisms leading to the asymmetries are still unclear. A possible explanation may be given in terms of neoclassical transport[2]. In addition, poloidal plasma rotation may be important whereas a large influence of toroidal rotation is unlikely because of the diasppearance of the

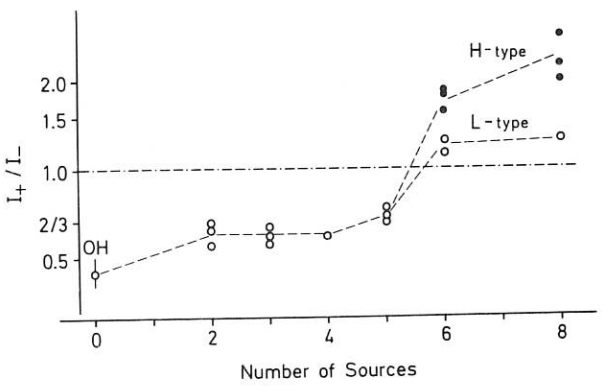

Fig.20: The ratio of upper to lower boundary radiation is plotted in logarithmic scale versus number of NI-sources.

[1] G. Fußmann, W. Poschenrieder, et al., Jour. of Nucl. Mat. 121 (1984), 164
[2] W. Feneberg, A. Samain, private communication

asymmetries during the quiescent H-phase. Moreover, an asymmetric energy flow would lead to pressure differences in the divertor scrape-off regions and thus influence the plasma streaming pattern. There is, however, too little information from the experiments on a possible up-down asymmetry of the energy fluxes. The well documented preference of the outer separatrix for the energy flow, however, is probably of general importance for impurity retainment. Thus, in the case of high energy fluxes, impurities may be exhausted along the inner separatrix but driven into the bulk plasma along the outer one.

1.4.2 Modelling of edge plasma and divertor

(R. Chodura, K. Lackner, J. Neuhauser, K.-G. Rauh, W. Schneider, R. Wunderlich; Tokamak Physics Group)

Effect of nonlocal heat conduction on fluid model results

The description of mass flow and energy transport along the field lines in terms of fluid equations and the usual collisional transport relations is a realistic model for the plasma in the scrape-off layer as long as the mean free path λ of the electrons is small compared with the characteristic length-scales along the field lines. This is, however, only marginally satisfied for certain ASDEX scrape-off layer parameters, especially concerning the hot electrons carrying most of the energy ($\lambda \sim E^2/n$).

An increase of λ first leads to deviations from the classical Spitzer-Härm heat flux. In order to account for this fact, we have implemented the non-local electron heat flux formulation proposed by Luciani et al.[1] together with an appropriate modification in the vicinity of the target plates in the SOLID hydrodynamic scrape-off layer code.

Compared with the classical case, the resulting electron temperature profile T_e along the field lines clearly shows an increase of T_e at mid-plane for the same density and power input, as demonstrated in Fig. 21. This implies a reduced effective heat conductivity compared with the classical one. On the other hand, the effective energy transfer per electron, $\delta_{eff} = q_{ed}/(kT_{ed} \cdot \Gamma_{id})$, into the electrostatic sheath at the target plate is increased, since in addition to local tail electrons a small number of very fast electrons originating from hotter plasma regions can immediately reach the target plates. This result is illustrated in Fig. 22, where δ_{eff} is plotted as a function of the divertor density with the input power as parameter. δ_{eff} clearly increases over the classical value ($\delta_{eff} \simeq 4$) if the density is decreased or the power increased, both causing an increasing mean free path. The range of validity of this approach and possible improvements are being investigated by the elaborate particle simulation code described in the following section.

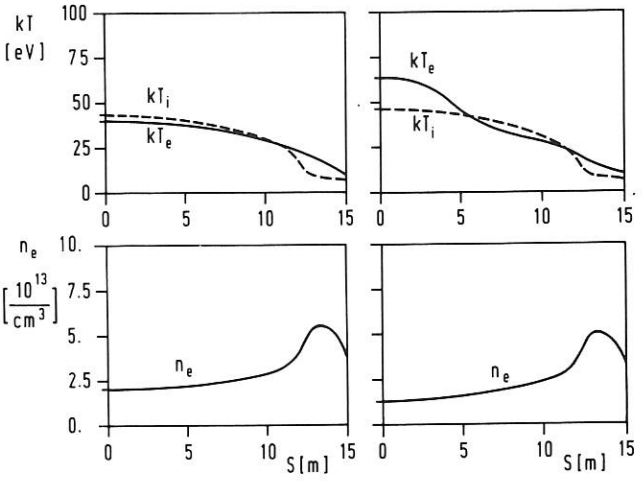

Fig.21: Plasma parameters along scrape-off field lines between mid-plane (s = 0) and target plate (s = 15 m) for ASDEX gemometry using either the classical electron heat conductivity (left) or a nonlocal heat flux model (right).

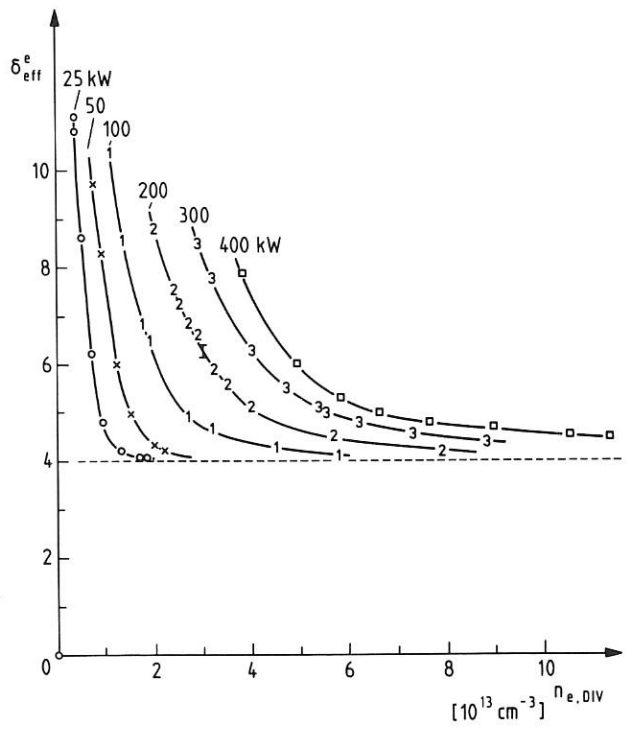

Fig.22: Effective electron energy transfer coefficient δ^e_{eff} according to SOLID calculations using a non-local heat flux model, as function of the electron density in the target plate vicinity and energy flux into each divertor channel.

[1] Luciani, et al., Phys. Rev. Lett. 51 (1983) 1664

Kinetic description of the electrostatic sheath and presheath region including collisions

From a kinetic model of the sheath ahead of an absorbing wall it is possible to derive implications for the hydrodynamic flow upstream from the sheath. The electron energy flow required by the sheath (which is determined by the sheath potential) is larger than the energy flow convectively transported to the sheath. The difference must be transported by electron heat conduction. Depending on the distribution of ionization in the scrape-off layer this heat conduction may lead to a supersonic flow velocity at the sheath edge. Furthermore, the high electron heat conduction required by the sheath violates the applicability of the usual classical conductivity coefficient as described in the previous section. Instead of this a non-local kinetic description of the electron heat conduction, at least in the vicinity of the sheath edge, must be applied. The energy flow of ions at the sheath edge, on the other hand, is only partly determined by the sheath, via the so-called Bohm condition. This condition originally formulated for an unmagnetized plasma and cold ions has been generalized analytically to the case of an oblique magnetic field and ions of finite temperature. As in the case of the electrons, a complete description of the ions in the vicinity of the sheath demands a kinetic treatment including collisions.

This is attempted by extending our collisionless one-dimensional particle code to include collisional (Fokker-Planck) friction and diffusion in velocity space. In a first approach the collision terms are restricted to nearly Maxwellian particle distributions. The code will be used to study the non-local transport and the plasma-sheath transition in the scrape-off layer at different collisionality. Furthermore, the kinetic code is being used to calculate current-voltage characteristics of the electrostatic sheath (or equivalently the probe characteristic of a plane Langmuir probe) for different angles of incidence of the magnetic field.

Improved SOLID-DEGAS coupling and automatic grid mapping

In addition to the implementation of a new version of the DEGAS code a new coupling algorithm between SOLID and DEGAS has been implemented: instead of the profiles n_H, T_H of the neutrals the actual particle and energy source and sink terms computed by DEGAS are transferred to SOLID. This procedure is superior to the previous one since the DEGAS code uses a more elaborate atomic physics package and also guarantees consistency between the particle balances of the two codes.

A semi-automatic procedure for generating the 2D mesh of DEGAS was further developed. The code uses the flux coordinates obtained from an equilibrium code together with the coordinates of the walls and target plates as additional input. The procedure was adapted for the ASDEX divertor, and the ASDEX Upgrade configuration.

Expected performance of the ASDEX-divertor after hardening

To investigate the recycling characteristics of the ASDEX divertor chamber after the modifications required for long pulse heating (see also Sec. 4.2) a nearly identical plasma profile was used in the two configurations; the neutral particle time constants and neutral gas profiles were calculated with the DEGAS Monte Carlo code. Due to the reduced volume of the divertor its neutral hydrogen time constant will be reduced by a factor of nearly 20. This, however, will not directly affect the intensity of divertor recycling, which in the calculations described above is best measured by the fraction of atoms, produced by recombination at the target plates which escape through the slits without being once ionized: this fraction is just weakly enhanced. From this no strong changes in the scrape-off parameters are to be expected, a conclusion also supported by the results of SOLGAS calculations iterated to full consistency between neutral particle and scrape-off plasma dynamics.

Poloidal thermal stability of the tokamak edge plasma

Usually, the temperature and density are assumed to be constant on closed flux surfaces because of the fast transport along magnetic field lines. Experimentally, however, strong poloidal variations are observed in ASDEX ohmic dischargs near the density limit (see Annual Report 1983, Sec. 1.3) and, in modified form, in several other tokamaks (e.g. JET). A poloidal thermal instability and poloidal asymmetries in radial heat transport and particle flow were considered as explanations.

In order to get a more quantitative understanding, we studied poloidal thermal equilibria and their stability analytically and numerically by solving the hydrodynamic equations along field lines. Cross-field transport was included qualitatively by appropriate diffusion time constants.

First the general dispersion relation of a homogeneously radiating plasma sheath was derived, it being assumed that the impurities are strongly coupled to the hydrogen. Unstable eigenvalues are found if the parallel electron heat conduction time becomes larger than the radiation cooling time, provided that the cooling rate increases more slowly than quadratically with temperature. A non-local expression for the electron heat flux had to be used for typical edge parameters because of the long mean free path of the heat conduction electrons.

Numerical solutions of the full nonlinear problem were obtained from a modified version of the SOLID hydrodynamic code, coupled with a multifluid impurity code providing the correct impurity transport and radiation cooling (see Annual Report 1983). The analytic stability criterion was verified, and highly asymmetric, nonlinear equilibria were found with subsequent slow redistribution of the impurities. The nonlinear state closely resembles the poloidal structure observed in ASDEX.

1.4.3 Parametric investigation of the scrape-off layer density profile

The dependence of the scrape-off layer (SOL) density profile on plasma current during Ohmic heating was ivestigated with the aid of the neutral lithium beam diagnostic (see Annual Report 1983, p. 25). Figure 23 shows the Li[2p-2s] light intensity along the beam in the SOL of a diverted discharge at three time points corresponding to three different current (I_p) plateaus of 235, 305 and 385 kA: It is immediately apparent that increasing the current leads to steeper profiles. Quantitatively (after correcting the Li-beam profiles for systematic errors associated with the method), the density e-folding length λ_n near the separatrix is found to be approximately 2.2, 1.9 and 1.5 cm respectively, which corresponds to a scaling $\lambda_n \sim I_p^{-0.75}$. Most of this dependence can be ascribed to the variation of the SOL field connection length to the divertor plates L with the safety factor q ($L \sim q \sim I_p^{-1}$). Using the relation $\lambda_n = \sqrt{D_\perp L / v_\parallel}$, where $D_\perp$ is the perpendicular diffusion coefficient and $v_\parallel$ a global streaming velocity in the SOL, we get $v_\parallel / D_\perp \sim I_p^{0.5}$. Owing to the preliminary nature of these measurements, the exact determination of the dependence of $v_\parallel / D_\perp$ on I_p (or q) must be a subject of further studies.

The SOL n_e profile may be strongly influenced by the choice of limiter configuration. Figure 24 illustrates the difference in the SOL Li-beam light profiles for the case of a mushroom limiter placed at a radius r = R - 165 = 35 cm with the divertor coils (MP) activated (#9277) and not activated (#9278). In both cases $\bar{n}_e = 2 \times 10^{13}$ and I_p = 245 kA. The limiter SOL $\bar{n}_e$ profile can be described by $\lambda_n \simeq 5$ cm for $35 < r < 43$ cm and $\lambda_n \simeq 2.5$ cm for $r \geq 43$ cm, this latter transition point originating from the intersection of field lines with structural components of ASDEX, leading to a shorter

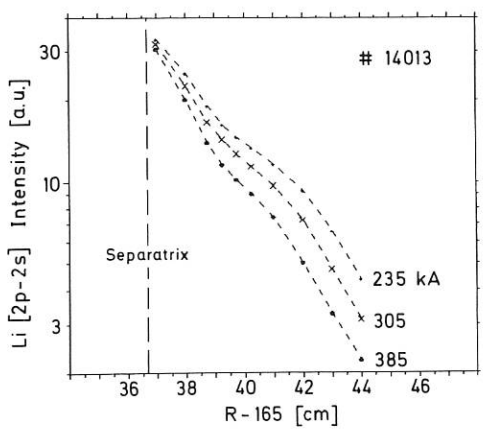

Fig.23: Li[2p - 2s] light intensity profiles along the beam in the plasma midplane for a double-null diverted, ohmically-heated discharge with three current plateaus. H_2, B_T = 2.17 T, $\bar{n}_e = 1.9 \times 10^{13} cm^{-3}$, R_p = 163 cm, I_{mp}/I_p = 0.1.

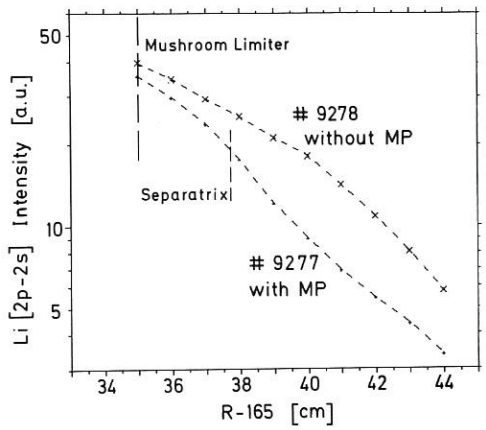

Fig.24: Li[2p - 2s] light intensity profiles for the cases of an ohmically-heated mushroom limiter discharge with the divertor coils (mp) activated (#9277, I_{mp}/I_p = 0.1) and deactivated (#9278). H_2, B_T = 2.17 T, $\bar{n}_e = 2 \times 10^{13} cm^{-3}$, I_p = 245 kA, R_p = 164 cm.

---

field connection length. In contrast, the discharge with MP exhibits approximately the same SOL profile as in a pure divertor discharge, with $\lambda_n \simeq 2.2$ cm in the vicinity of the separatrix. Experiments carried out with the mushroom limiter placed approximately at the position of the separatrix reveal no differences in density profile, regardless of whether the limiter is present or not. In other words, a mushroom ("point") limiter appears to produce a much less sharply defined boundary, i.e. it is less effective in comparison to a divertor configuration of the ASDEX type. On the other hand, a poloidal limiter which subtends a larger sector at the plasma edge has been found to yield profiles with $\lambda_n \simeq 2$ cm. As above, most of these differences can probably be accounted for by consideration of the field connection length L.

1.4.4 Contributions from the Plasma-wall Interaction Group

Intense auxiliary heating using neutral injection, lower hybrid and ion cyclotron resonance heating has led in the past year to increased impurity production in ASDEX as in other large tokamak experiments. In phases of improved particle confinement the accumulation of impurities ultimately limits further improvement /93/. The identification of impurity sources and erosion mechanisms, which has been the central topic of the PWW group for several years, is therefore of increasing importance.

The investigations include the determination of plasma ion, charge exchange neutral and energy fluxes to the wall structures and divertor plates as well as direct erosion measurements at representative positions in the main chamber and in the divertor. These data together with simulation

experiments are used to identify the dominant erosion process. Finally, the redistribution of the eroded material on the poloidal limiter and graphite armour blocks is examined.

The results may allow estimates for the impurity production in quiescent plasma phases, while during other phases, especially during HF heating, further investigations are needed to develop a comprehensive model.

Fluxes of plasma ions

With the start of the year a new sniffer probe was incorporated in the mass spectrometric diagnostic system on the plasma chamber of ASDEX. It consists of a tube 7 cm in diameter which is moved radially into the scrape-off range by means of a manipulator. A rotatable slit (1 x 3 cm^2) at the end near the plasma probes either the toroidal or poloidal particle fluxes. About 40 % of the flux entering the slit reaches the differentially pumped quadrupole mass analyzer at the far end of the tube and a simple calibration procedure affords absolute flux measurements. The response time of the total arrangement is 100 ms.

Typical data are shown in Fig. 25 as a function of the radial distance from the main axis, and the position of the protective limiter is marked by SL. The plasma centre was positioned at R_S = 169 cm and the distance from the protective limiter to the separatrix was about 8 cm. One observes a roughly exponential decay of the flux of D with a decay length λ = 1 cm. The flux with the slit looking in the toroidal direction is much larger than when it is directed poloidally. Obviously, the flux consists of ions following the toroidal magnetic field. In the ohmic phase a marked asymmetry is seen between the electron drift (ES) and ion drift side (IS), which is less pronounced during neutral injection. Since fluxes near the wall depend in a complicated way on the connection length of magnetic field lines and localization of sources, the cause of the asymmetry is not yet clear. All measurements were taken well within the shadow of the protective limiters to avoid damage to the probe. Particle fluxes can be extrapolated to 1 x10^{18} cm^{-2} s^{-1} at the tip of the fixed limiters (position SL). The integral ion flux hitting the fixed limiter and other wall structures is about 1 x 10^{20} ions/s.

A significant result is obtained by comparing the ion fluxes measured with the sniffer probe with those obtained by the collection of plasma ions in carbon strips (also indicated in Fig. 25). Though the latter strongly depend on the plasma parameters and probe position, it can be seen that the measured fluxes are more than an order of magnitude lower than those obtained with the sniffer probe.

The discrepancy can be resolved by assuming the mean energy of the ions to be below 10 eV, where the sensitivity of the collector probe method is very low owing to saturation effects. The ion

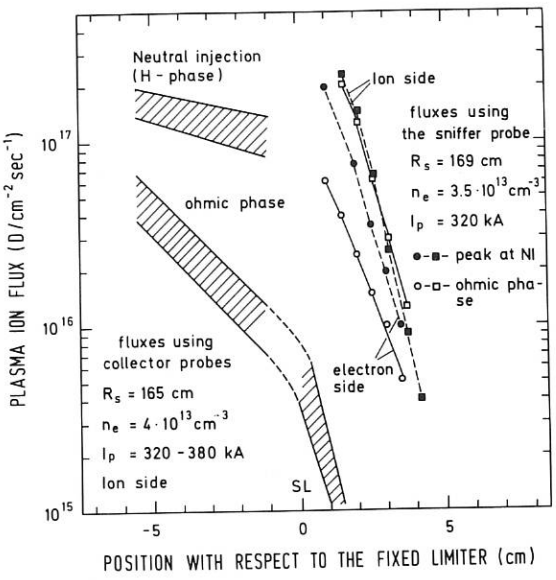

Fig.25: Comparison of the plasma ion fluxes measured with the sniffer probe with the range of fluxes obtained by the collector method for comparable plasma parameters.

energies extracted from the saturation behaviour and the depth distribution of injected hydrogen range from 20 to 60 eV and may represent a minority of high-energy ions which, however, contribute substantially to erosion processes such as sputtering.

The application of mass spectrometry also permits one to follow the development of the isotope fluxes during a discharge (Fig. 26). After a change from discharges in H_2 to D_2 large amounts of H_2 still appear to recycle at the plasma edge. The large

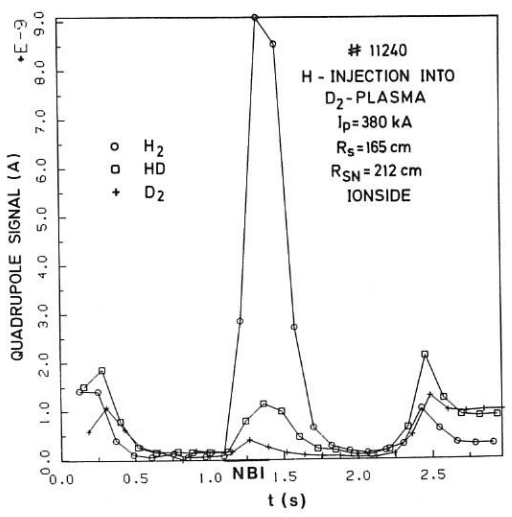

Fig.26: Hydrogen ion isotopes in the plasma boundary during a discharge with neutral injection.

peak of H_2 during NBI was also found to be due to desorption and not primarily to the injection of H^o. (W. Poschenrieder, G. Venus, G. Wang)

The origin of the large decay length of the flux of plasma ions in the H-phase during neutral injection was investigated with a collector probe /155/. In discharges with L-phase during NBI the decay length in front of the fixed limiter is about 2 cm, while in discharges with H-phase a decay length of 8 cm is measured. A comparison with the density decay length λ_n measured with the lithium beam diagnostics[1] showed that similarly large decay lengths are observed during bursts, so-called ELMs, which frequently interrupt the H-phase (see Sect. 1.2). During these ELMs the flux of ions with energies larger than 40 to 50 eV is drastically enhanced in the plasma boundary and may lead to severe erosion of the protection limiter or divertor throat. The low confinement during these periods leads, however, to fast transport of impurities into the divertor chamber before they enter the main plasma (see Annual Report 1983). (A.P. Martinelli, J. Roth)

Low-energy neutral particle analysis

The low-energy neutral particle analysis (LENA) system has been operated throughout experimentation with ASDEX. During one ASDEX shot up to 32 energy distributions of the neutral particles impinging perpendicularly on the wall can be taken in the energy range of 20 to 2000 eV/amu. The usual time resolution during a shot is 100 ms, but 20 ms is possible with acceptable statistical errors. In a different mode of operation the neutral flux within a certain selected energy interval is recorded over the entire discharge. In this mode a time resolution of 1 ms is possible.

In all energy spectra observed so far the intensity of the neutrals increases monotonically as the energy decreases. All spectra are curved in the log-plot, i.e. they cannot be fit by single-temperature Maxwellians (except during the plasma start-up phase). From the steep rise of the neutral flux at low energies it can be deduced that 80 % of the impurity production by neutral particle sputtering is due to neutrals with energies of below 200 eV.

During neutral injection one generally observed a large increase of the neutral flux at energies of above 100 eV, which strongly depends on the position of the plasma in the vacuum vessel. With the onset of LH heating an instantaneous increase of the neutral flux and return to the original flux level with shut-off was observed for neutral particle energies >150 eV. No effect was observed for the neutrals with energies of below 150 eV. This shows the heating of the plasma edge due to the LHRH. Assuming complete toroidal and poloidal symmetry, 2 % of the LH-power is lost to the walls by the low-energy neutrals. During ICRH with 100 kW a slight increase of the neutral flux at energies of below 300 eV could be observed. (H. Verbeek)

[1] K. McCormick, H. Murmann, M. El Shaer, ASDEX and NI-Team, J. Nucl. Mat. 121 (1984), 48

Energy flux measurements

The heat flux in the edge plasma is investigated to determine the power deposition on limiters, divertor plates and the wall and possible contributions from nonthermal ions during auxiliary heating. Measurements with the combined calorimeter-Langmuir probe in the edge plasma of the main chamber yield time-resolved profiles of the parallel energy flux, electron temperature and plasma density.

The deposited power on a floating probe can be written approximately as

$$P_f = P_e + P_i = \Gamma_f ((2\,kT_e + (1-R_E)(2\,kT_i + 3\,kT_e) + E_i + (1-R_N)\,(E_R - 0.5\,E_D))$$

($\Gamma_f = \Gamma_e = \Gamma_i$: particle flux to the floating probe, R_E: energy reflection coefficient, R_N: particle reflection coefficient, E_i: ionization energy (13.6 eV), E_R: recombination energy per H-atom (2.2 eV), E_D: desorption energy per molecule (0.5 eV)).

Typical of all shots observed is the rise of the energy flux at the start and end of the discharge (Fig. 27). In ohmically heated discharges a decay length of 1.2 cm is found for the energy flux in the region investigated (3.5 to 6 cm from the separatrix).

The mean electron temperature as deduced from the Langmuir measurements is about 10 eV at a distance of 5 cm from the separatrix and about 14 eV at a distance of 3.5 cm. No exponential decay of T_e is found in this region. If it is assumed that $T_i = T_e$, a decay length of about 1.6 cm is obtained for the density (Fig. 28). However, the measured energy flux does not correlate with the Langmuir probe data. Inserting the probe data and the energy flux into the above equation would yield negative ion temperatures. This shows that electron temperatures deduced from Langmuir measurements are too high. Comparison with other diagnostics showed that measured electron temperatures may be a factor of more than 2 too high (see last Annual Report 1983, Sec. 1.2.1).

LHRH discharges are identical with OH discharges. Discharges with otherwise equal parameters lead to identical energy flux curves for both OH and LHRH shots.

Characteristic of NBI-heated discharges is a strong increase of the energy flux on the ion side compared with a much smaller increase on the electron side during NBI. With absolute values of up to 2 kW/cm^2 on the ion side during 3.4 MW NBI the asymmetry of the energy fluence between the ion and electron sides is a factor of 10 to 50. This may indicate a toroidal plasma rotation due to the tangential neutral injection. A simple model for the steady-state case neglecting momentum confinement and burst activity gives toroidal particle energies of 1.6 keV. If the main part of

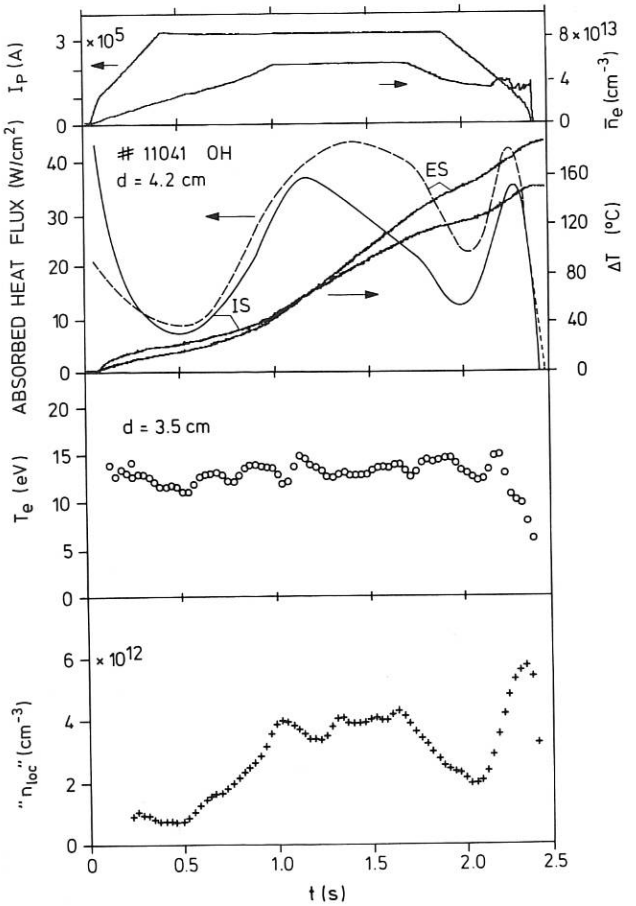

Fig.27: Temporal profiles for a OH double-null divertor H^+-discharge. Top to bottom: plasma current, density, calorimetric temperature and absorbed heat flux at ion and electron drift sides, from Langmuir probe deduced electron temperature and density ($T_i = T_e$ assumed).
IS: ion drift side ES: electron drift side.

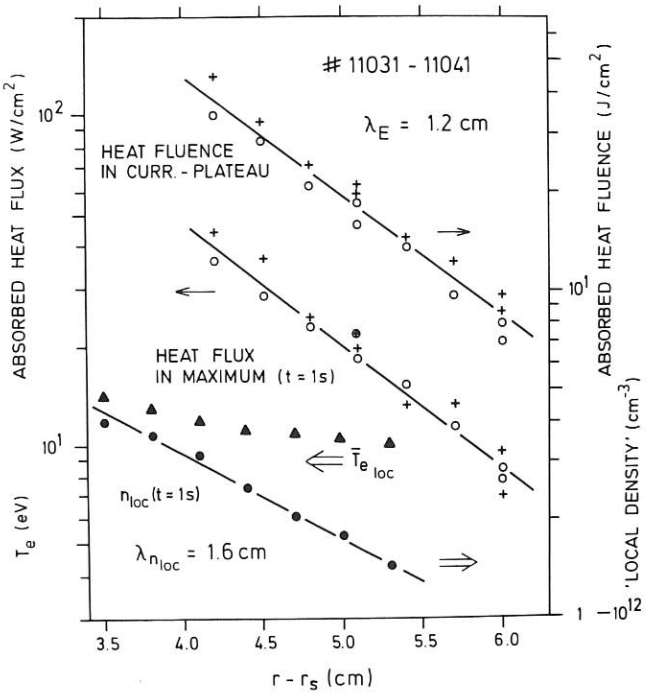

Fig.28: Radial profiles for LH -heated discharges (no difference is found for OH discharges with otherwise equal parameters): Absorbed heat flux in the maximum at t = 1s, heat fluence during current plateau, Langmuir electron temperature and density.

---

the momentum is carried by a particle minority, this estimate of the toroidally directed energy is a lower limit /35/. (K. Ertl)

Wall erosion in the main chamber

The erosion at the wall was measured at two different positions G and O in the midplane of the main plasma chamber of ASDEX. Position G was close to the gas feed valve and the second position O was opposite to it. To measure the erosion a collection method was used: atoms eroded from an initially clean Ni-target are collected on a Papyex strip and are subsequently detected by surface analysis, mainly by electron-induced X-ray analysis.

The present detection limit of about 0.1 monolayers allows one to measure erosion rates of metals as small as 8×10^{14} at/cm^{2}s integrating over one second. Smaller erosion rates can be measured by integration over a correspondingly longer time interval.

The results of two measurements at position O are shown in Fig. 29. The erosion rate at the wall is 1.8×10^{13} at/cm^{2}s, i.e. 10^{-2} monolayers per second. To measure such low erosion rates requires an integration time of about 40 s (about 12 to 20 discharges).

In order to determine the erosion yield, the energetic deuterium flux in the same position and geometry was measured simultaneously with a double carbon resistance probe[1]. The evaluation yields a deuterium flux of 6.3×10^{14} deuterium/cm^{2}s with a mean energy of 150 eV. Hence, an erosion yield of $Y_E = 2.8 \times 10^{-2}$ Ni/D is found in agreement with sputtering yield data.

For the same series of discharges measurements were made at position G close to the gas valve. It is found that the erosion rate is more than one order of magnitude higher than at position O (Fig. 29).

[1] W.R. Wampler, J. of Nucl. Mater. 128 & 129 (1984), 951

In both cases the sample was positioned radially close to the wall, between the two protective limiters, where the dominant species hitting the wall are charge exchange neutrals. The order-of-magnitude difference in sputtering at the two positions is due to an order-of-magnitude difference in charge exchange neutral flux, as measured in the vicinity of the gas valve and the limiter /247/.

Neglecting toroidal and poloidal asymmetries, we obtain as a mean value over a large number of discharges and a variety of discharges conditions a flux $\Phi^{o} = 7 \times 10^{18}$ (FeCrNi)/s released from the wall and, in addition, a flux $\Phi^{G} = 4 \times 10^{18}$ (FeCrNi)/s released from a wall area in the vicinity of the gas valve, if we assume the same sputtering yield at the wall as from the Ni samples. (G. Staudenmaier)

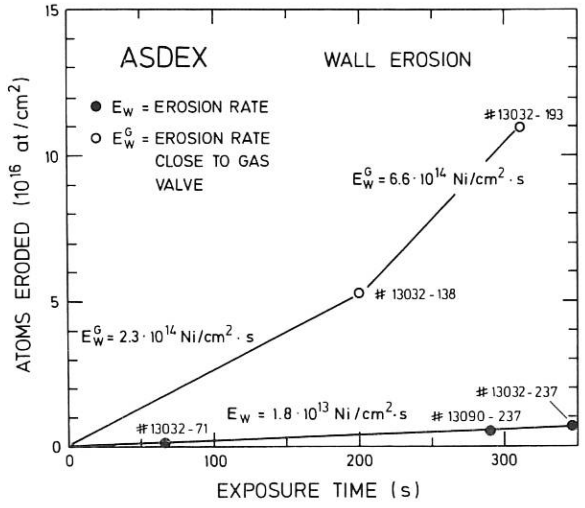

Fig.29: Atoms eroded from wall probes as a function of the exposure time for a position close to the gas valve and opposite to it. The erosion rates indicated are calculated assuming a cosine angular distribution of the sputtered atoms.

The surfaces of the toroidal and poloidal carbon limiters have been identified as another source of heavy impurities in the main chamber. Segments of the poloidal carbon limiter were removed and sputtering was simulated in the high-current ion source using a 2 keV D^+ ion beam. The sputtered iron flux was determined by laser-induced fluorescence (see Sec. 4. PWW). In Fig. 30 the dose dependence of the Fe sputtering yield is compared with the sputtering of a Fe film evaporated onto carbon, without annealing and after annealing at 700° C.

The thickness of the evaporated iron layer was chosen to conform to the amount of iron found on the limiter material. The initial sputtering yield from the limiter sample is about 1/3 of the

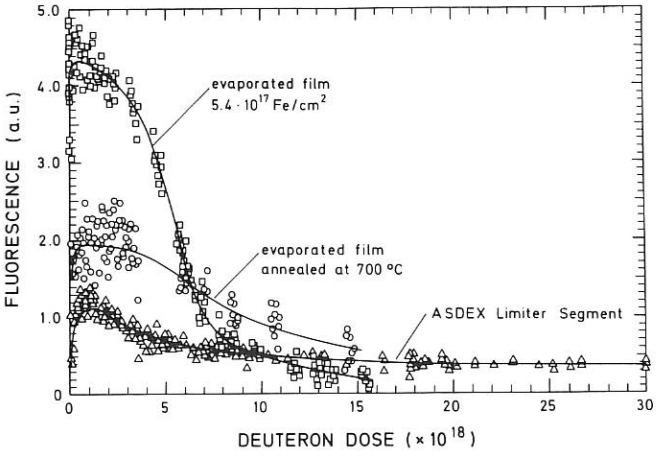

Fig.30: Comparison of the dose dependence of Fe sputtering from an ASDEX limiter segment and an evaporated iron film with the same areal iron density.

---

bulk iron yield, but it persists to much higher doses than equivalent for total erosion of the evaporated film. It is very similar to the sputtering of the Fe-film after 700° C annealing, as a result of which the film agglomerates to islands and drops. This is in fact the iron distribution observed on the limiter samples in the scanning electron microscope (SEM). After prolonged sputtering a stable yield is established at about 10 % of the yield for bulk iron. In this stage ion beam and SEM analysis indicate that 50 % of the initial amount of Fe is still hidden in deep pores in the form of small droplets. (J. Appelt, J. Berthold, J. Bohdansky, J. Roth)

Erosion in the divertor chamber

The erosion and impurity deposition were studied simultaneously by using a carbon probe implanted with a ^{13}C marker /200/. Carbon erosion and deposition were determined from changes in the depth distribution of the ^{13}C, and impurity accumulation was also monitored by ion backscattering. In the boundary layer of the main plasma 8 cm from the separatrix erosion could hardly be measured, being 10 A/s in the plateau phase of the discharge. In the divertor plasma erosion and deposition were clearly detectable, as shown in Fig. 31. Fe and Ti are deposited particularly at the beginning and during neutral injection.

Infrared measurements show that the power deposition on the neutralizer plates during NBI is 200 to 400 W/cm^2 (the magnetic field lines intersect these plates at an angle of ≃5 degrees). Much higher power deposition occurs on the probe surface, since it is perpendicular to the magnetic field lines. The observed erosion is consistent with a sputtering yield of ≃0.1 for estimated fluxes of energetic ions /247/ to the probe. This would correspond to the erosion yield for 100 eV hydrogen ions on graphite at 1500° C (see Sec. 4 PWW).

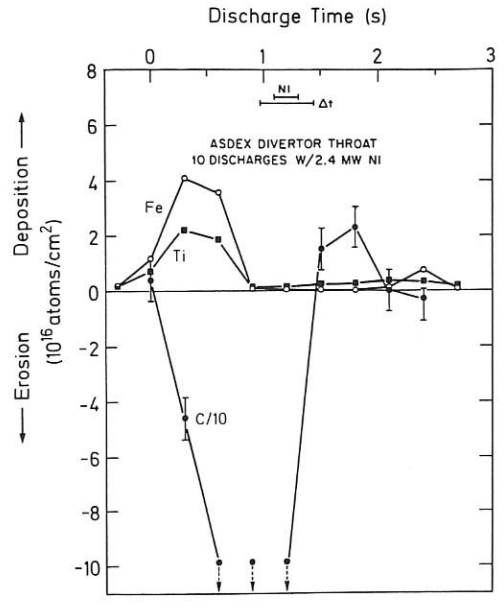

Fig.31: Erosion of carbon and deposition of Fe and Ti during a neutral beam heated discharge on a probe in front of the divertor plate.

The simultaneous deposition of plasma impurity ions, at least at high surface temperatures, does not substantially reduce graphite substrate erosion for typical impurity fluxes in the plasma edge. This result is consistent with laboratory measurements of the sputtering of graphite at high temperature during simultaneous Ti /204/ evaporation onto the sample.

The use of ^{13}C-enriched graphite probes is an effective means of measuring erosion/deposition at high heat/particle fluxes in the plasma edge. It is expected that similar techniques will prove to be useful for monitoring erosion in other materials.
(J. Roth, J.B. Roberto, E. Taglauer)

The behaviour of TiC and TiN coatings on graphite and Mo exposed to the divertor plasma in ASDEX was studied in relation to surface modifications and overall capacity to resist the plasma action. Such coatings are used for the ICRH antennae in ASDEX. The samples were exposed in front of the upper outer divertor plate with their surfaces perpendicular to the magnetic field lines. During neutral beam injection a sample temperature of 950° C was measured as a lower limit.

Near the separatrix the main effect of the plasma arises from the large heat load, which causes partial disruption of the coatings and segregation of carbon and sulphur on the surface. In addition, plasma impurities such as C, O, and Fe are deposited. The flux of plasma particles also causes preferential sputtering of the lighter constituent, i.e. C or N (see Fig. 32).

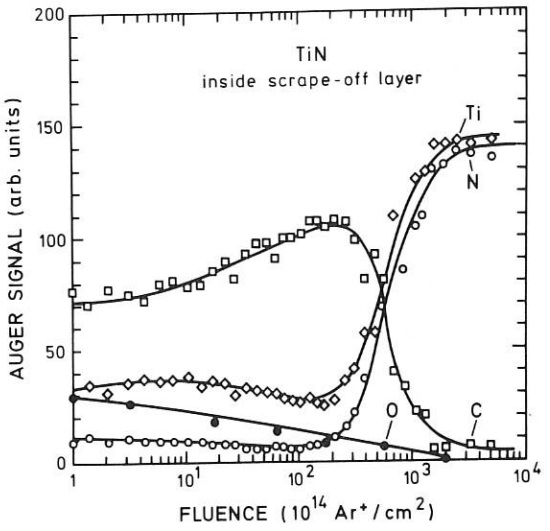

Fig.32: Elemental depth distribution of a TiN coating exposed to one discharge. 10^{17} Ar^+/cm^2 corresponds approximately to a depth of 200 nm.

From the surface concentration and depth distribution of the preferentially sputtered layer it can be estimated that the deuterium fluence during one discharge is above 10^{17} cm^{-2} with energies below a few hundred eV, which is equivalent to the flux of fast ions to the divertor plates /247/.
(E. Taglauer, K. Ertl, P. Varga)

Composition and spatial distribution of the metal deposits on graphite structures

The surfaces of several segments of the poloidal graphite limiter used in ASDEX for about 150 mostly NBI-heated plasmas were investigated in some detail. The spatial distribution of the metal was measured by Proton induced X-ray emission (PIXE). The compounds of Fe, Ni and Cr were found in nearly the same composition as in the SS 304 used for the wall, while Ti and Mn show very different concentrations.

On most tiles the Fe, Ni, Cr deposition shows a strong maximum at the centre, i.e. the area most closely exposed to the plasma, followed by deep local minima on both sides (Fig. 33a). The minimum is much broader on the ion drift side than on the electron drift side. It is followed by a maximum with a deposition comparable to that in the centre. At the very sides the intensity decreases again. The titanium does not show such variation but is almost uniformly distributed.

The relative abundance of Mn in the deposited materials was found to vary between 0 and 20 % in contrast to ≃ 2 % in the bulk SS. An example is shown in Fig. 33b. There is no clear correlation between the relative Mn content and the integral areal coverage of the limiter. The large variations

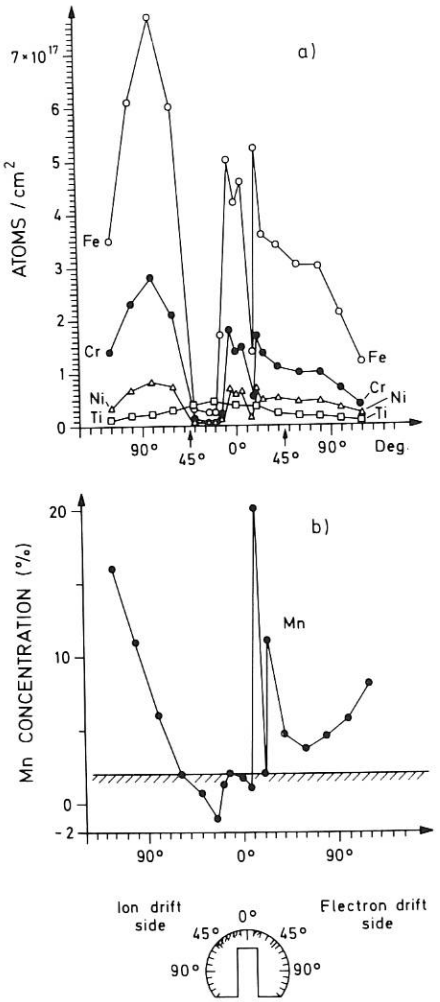

Fig.33: a) Concentration distributions of various elements on the limiter tiles as measured by PIXE
b) Relative Mn content of the SS deposit.

---

in the Mn content of the deposited metal layer clearly indicate thermal effects in the erosion on the wall and redistribution on the limiter. In austenitic steels near the melting point the vapour pressure of Mn is several orders of magnitude higher than that of the other components (Cr, Ni, Fe).

At the maxima the deposited Fe, Ni, Cr is contained in small droplets about a few 100 nm in diameter on the very rough surface of the carbon tile. The state of these droplets was investigated by Mössbauer spectroscopy, which yielded a cementite composition $(Fe, Ni, Cr)_3C$ /16/. The deep minima are most likely caused by evaporation due to plasma impact, in agreement with the low Mn concentration. (P. Børgesen, J. Ehrenberg, B.M.U. Scherzer, B. Sawicka, J. Sawicki, R. Behrisch).

Representative examples of the graphite blocks protecting the divertor entrance slits were analyzed with respect to metal deposition and hydrogen isotope retention. On all 4 blocks a large variety of elements were observed by means of PIXE. Most dominant were the stainless-steel components, while Ti was an order of magnitude lower and traces of S, Cu, K, Ca, Se, In, Zn were detected. Most of the deposited material was in the form of droplets which, especially at the side of the blocks near the plasma, accumulated in deeper pores. The composition of the drops was mainly SS, some W/Se, Cu/Zn and Ti. On all 4 blocks surrounding the main plasma the iron areal density was around 1 x $10^{17}/cm^2$, that of Ti 1 x $10^{16}/cm^2$. The distribution showed only small lateral variations with iron maxima on all blocks at the far end from the plasma. Ti, however, showed shallow maxima closer to the plasma. The amount of Ti on the graphite blocks and the limiter indicates a wall coverage of about 10 % and an equivalent contribution to the impurity concentration in the plasma.

In contrast to the rather uniform behaviour of the metallic deposits, there was a pronounced top-bottom asymmetry as regards the hydrogen isotopes. While the areal density of hydrogen and deuterium on the outer top block were about equal at 1 x $10^{17}/cm^2$, mainly hydrogen (3 x $10^{17}/cm^2$) and very little deuterium (3 x $10^{16}/cm^2$) were detected on the bottom block. The same asymmetry was found on the inner protection blocks with strongly decreasing hydrogen coverage into the divertor throat. The origin of this asymmetry may be due to the fact that in many discharges the plasma was shifted upwards slightly. (J. Roth, A.P. Martinelli)

Estimates on impurity sources and erosion rates

The experimental results from measurements in ASDEX as well as from laboratory experiments have led to an attempt to identify impurity sources and fluxes during different phases of the discharge.

As already reported in the Annual Report 1982, the Fe impurity concentration in the plasma shows a dependence on the plasma density very similar to that of the flux of charge exchange neutrals to the wall. Charge exchange fluxes of down to 20 eV and information on the angle of incidence are now available, and in Fig. 34 charge exchange fluxes were used to calculate sputtered impurity fluxes. From Fig. 34 it can be seen that the highest erosion yields are due to CX neutrals with energies of around 150 eV, and that 80 % of the sputtered iron atoms originate from hydrogen atoms with energies of below 500 eV.

The total sputtered atom flux of about 4 x 10^{12} Fe/cm^2s as obtained from Fig. 34 would lead to an impurity concentration in the plasma of about 5 x 10^8 Fe/cm^3 in good agreement with spectroscopic measurements. This is a factor of 4 smaller than the experimentally determined erosion yield integrated over many discharges, which is probably due to higher erosion yields during auxiliary heating and in transient phases of the discharges.

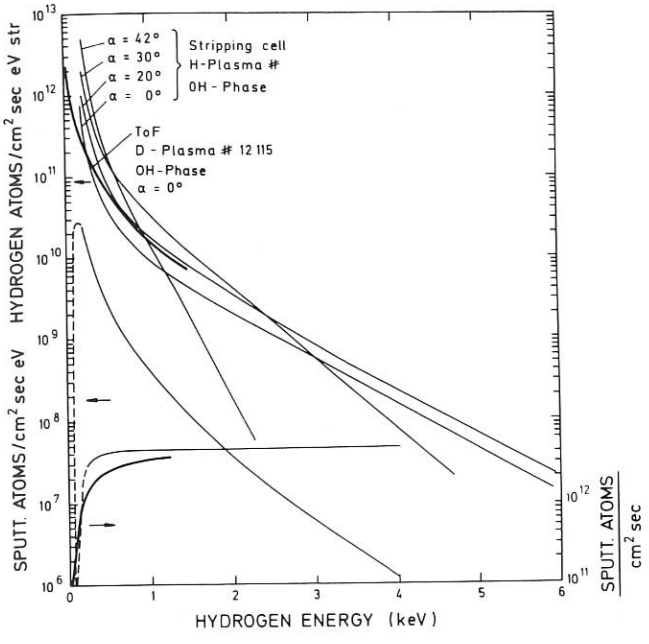

Fig.34: Energy distribution of the charge exchange hydrogen atoms for different angles of incidence on a wall position of ASDEX. The flux of sputtered iron atoms was calculated by folding with the sputtering yield.

On the assumption that charge exchange sputtering dominates the impurity influx, at least in the ohmic phase, it has been concluded on the basis of charge exchange cross-sections that in He discharges the impuritiy production should be reduced by more than one order of magnitude. Figure 35 shows the time dependence of the Fe impurity line radiation for He and D_2 discharges with comparable plasma parameters T_e and n_e. The spectroscopic signals in Fig. 35 are thus representative of the Fe concentrations.

During the ohmic phase before NBI the Fe concentrations are very similar at about 5×10^8 cm^{-3}. This indicates - assuming no difference in impurity screening, i.e. unchanged scrape-off parameters - approximately the same impurity influx to the plasma both for D_2 and He discharges.

Besides being produced by charge exchange neutrals, the heavy impurities may also be due to plasma ions hitting the wall in the main chamber. Neglecting charge exchange neutrals for the case of He discharges and on the assumption that the fraction A of ions hitting the wall of the main chamber is the same in D_2 and He discharges, one gets for A

$$A = \frac{Y_1 \, \phi_{cx}}{(Y_3 - Y_2) \, \phi_{ion}}$$

where ϕ_{cx} is the flux of charge exchange deuterium hitting the wall with a sputtering yield of Y_1, ϕ_{ion} is the flux of ions diffusing through the separatrix and Y_3 and Y_2 are the sputtering yields

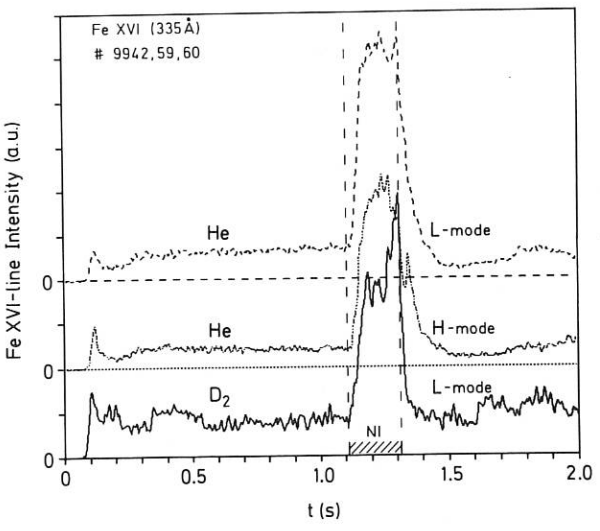

Fig.35: Fe XVI line intensities (λ = 335 Å) in He- and D_2-discharges ($\bar{n}_e \sim 2 \times 10^{13}$ cm^{-3}). In case of He the L and H-mode could be realized during the NI-phase (2.2 MW absorbed power). For comparison, in particular the two L-mode discharges should be considered.

---

for He^{++} and D^+ ions, respectively, after acceleration in a sheath potential. Within a factor of 2 the fluxes were determined to be $\phi_{cx} = 3 \times 10^{20}$ s^{-1}, $\phi_{ion} = 3 \times 10^{21}$ s^{-1} with sputtering yields of $Y_1 = 5 \times 10^{-3}$, $Y_2 \lesssim 10^{-4}$ and $Y_3 \simeq 2 \times 10^{-2}$. Inserting these into the above equation, we find that only 2.5 % of the ions have to hit wall structures in the main chamber (97.5 % are lost to the divertor) to produce the same Fe fluxes in the two cases. As Y_2 is much smaller than Y_1, the erosion of this small percentage of ions is negligible compared with charge exchange sputtering for the case of discharges in D_2. For the case of He discharges ions alone easily account for the whole impurity concentration. Actually, to account for 5×10^8 Fe/cm^3, a flux of just 6×10^{19} He^{++}/s to the wall would be necessary, which is again of the order of 2 % of the total ion flux. It is also in good agreement with the ion flux measured directly with the sniffer probe (see Fig. 25).

The dominance of the charge exchange sputtering during D_2-discharges explains why covering the divertor throat and the fixed limiter with carbon blocks did not markedly influence the heavy impurity content. For He discharges a stronger influence would be anticipated. Since the carbon tiles are partly covered with metallic impurities, however, ion sputtering will cause here a considerable heavy impurity influx. At the actual coverage of the graphite blocks a reduction of the sputtered metal flux to 10 % would take 2000 full ohmic discharges (see Fig. 30).

No comprehensive picture is available for the impurity production during auxiliary heating. During NBI the ion flux in the edge plasma increases, especially during the ELMs, but in this period

the impurities are badly contained and are transported into the divertor. The charge exchange flux is seen to increase drastically at energies of above several 100 eV. This may explain the increased impurity influx (see Fig. 35), but more measurements on the energy dependence of charge exchange neutrals below 500 eV are necessary for quantitative comparison. The problems of impurity production processes during HF heating are discussed in the respective sections. (J. Roth, G. Staudenmaier, G. Fussmann)

1.5 Lower Hybrid Experiments

(in collaboration with D. Eckhartt, M. Brambilla, H. Brinkschulte[1], H. Derfler, M. Hesse[2], F. Leuterer, R. Magne[3], M. Münich, F. Ryter[2], K.H. Schmitter, T. Vien, F.v.Woyna, M.Zouhar; Lower Hybrid Group (Technology Division))

Lower Hybrid (LH) experiments at 1.3 GHz were carried out in a routine manner with HF powers of up to 800 kW lasting 1,5 s /76/. The 8-waveguide grill coupler was used with three different front-pieces to emit LH-power spectra centred around $N_{\parallel} = 3$ and 4, resp., and, for a few initial runs, $N_{\parallel} = 6$. No bulk plasma heating was observed when exploring that portion of the parameter space where qasilinear theory predicted ion heating by stochastic acceleration or mode conversion. The main emphasis was placed on experiments with plasma current generation by LH waves and the interaction of these LH-driven currents with the "normal" current induced by the OH transformer. It was demonstrated for the first time that with constant plasma current, the rate of change of the current through the primary coil could be reversed, thus "re-charging" the OH transformer /142/. Difficulties were encountered when raising the total LH power above the level mentioned above. The reason(s) for this power limit have not yet been found.

1.5.1 Ion heating regime

After combining the numerical codes for computing the grill spectra with those for ray-tracing and for quasilinear absorption of LH power[4], and using the measured plasma density profiles, it was possible to predict different parameter sets for target plasmas where LH power should be absorbed and transferred into perpendicular kinetic energy of the ions. (The validity of this approach was checked by comparing similar calculations for WEGA III with the experimental data[5].) These parameter sets included conditions such as

- moderately high densities ($\bar{n}_e \simeq 6 \times 10^{13}$ cm^{-3}) with ohmic heating alone
- lower densities and higher temperatures produced by ohmic heating and neutral injection heating
- "minority heating" in a deuterium plasma with neutral injection heating by energetic H^0-particles.

However, no significant heating effects could be observed on the diamagnetic signal or with the perpendicular charge exchange analyzer in any of these target plasmas. The simultaneous use of NI and LH proved somewhat tricky since it is difficult to detect the effects of 0.8 MW of LH power in the presence of four times as much NI power.

The absence of bulk ion heating in the predicted range of plasma parameters is in line with the findings of other "big" machines[6] or high-density experiments[7]. It is not clear whether the LH waves are unable to penetrate into the plasma interior or whether they decay at the plasma edge owing to parametric instabilities: HF activity is observed with up to 15 side-band lines whose frequency spacing, if attributed to the local ion cyclotron resonance, corresponds to a location about 1 to 3 cm in front of the grill, i.e. 2 to 5 cm outside the separatrix.

When one starts at less than half the plasma density where mode conversion is expected in an ohmically heated discharge, an intense flux of ions with energies of above 3 to 5 keV is observed in the prependicular charge exchange analyzer. The main features of this energetic ion population are:

- It forms a hot "tail" in the charge exchange spectra having a Maxwellian-type energy distribution with an equivalent temperature T_{ih} which can go up to 4 keV, depending on the plasma density and HF power.
- The intersection point of the fast ion tail with the bulk ion distribution in the charge exchange spectrum is located at low energies, indicating that the perpendicular wave numbers which are associated with the generation of these fast ions are about twice as high as would be expected at the turning-point of the LH wave deep inside the plasma.
- The fast ions are generated as soon as the HF is switched on and have a decay time shorter than 1 ms after the HF is turned off, indicating that they are not confined.
- The fast ion fluxes appear above a certain density limit of about 2×10^{13} cm^{-3} and grow with density to about 4.5×10^{-3}, where they tend to saturate or even decrease.

---

[1] Till 31.8.1984
[2] CEN Grenoble
[3] CEN Grenoble, till 31.7.1984

[4] M. Brambilla, Chen Yan Ping, Proc. 3rd Internat. Symp. on Heating in Toroidal Plasmas, Grenoble, 1982, EUR 7979 EN, Vol. II, p. 565
[5] C. Gormezano, et al., Proc. 3rd Internat. Symp. on Heating in Toroidal Plasmas, Grenoble 1982, EUR 7979 EN, Vol. II, p. 439
[6] W. Hooke et al., Proc. 9th Intern. Conf. Plasma Physics and Controlled Nuclear Fusion Research, Baltimore 1982, Vol. 1, p. 239
[7] M.Porkolab et al. Proc. 4th Intern. Symp. on Heating in Toroidal Plasmas, Rome, 1984, Vol. 1, p. 529

- The energy contained in these hot ions, E_{ih}, increases with density whereas T_{ih} decreases (see Fig. 36).

- Tilting the charge exchange analyzer reveals an up-down asymmetry, with much higher fluxes being received from the edge of the plasma than from its centre; this asymmetry inverts when the direction of the main magnetic field is reversed.

- The fluxes received in the strictly perpendicular direction are much lower than those from slightly inclined, quasi-perpendicular directions (see Fig. 37).

These results can be qualitatively interpreted as follows:

The fast ions have large perpendicular kinetic energies and are generated well off the plasma centre. They are either locally trapped in the ripples of the main magnetic field and drift vertically out of the plasma, or they are barely confined on the fattest banana-orbits and reach the walls very fast. In either case the energetic ions do not have enough time to interact with the bulk plasma, hence no heating can be observed. The location of the intersection points in the charge exchange spectra, mentioned above, suggests that the fast ions could be generated by other modes such as parametric decay waves.

There is no information about the toroidal distribution of the fast ion fluxes or the impurity radiation they produce. If symmetry around the torus is assumed, the bolometer signals would account for more than half of the HF power delivered to the plasma.

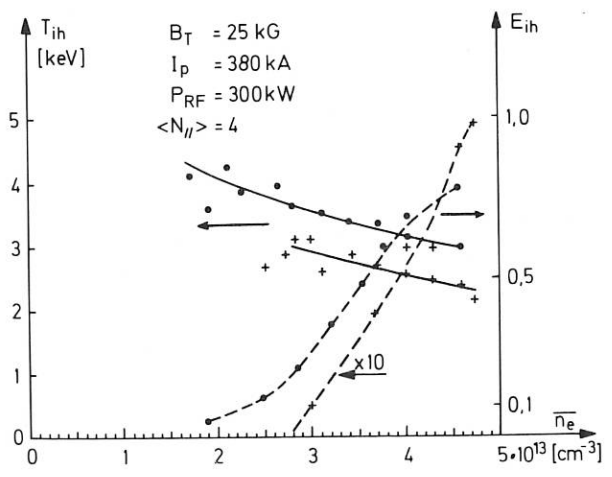

Fig.36: Equivalent temperature T_{ih} (full lines) and energy content E_{ih} (in relative units, broken lines) of the energetic ion population as a function of plasma density for two different inclinations of the charge exchange analyzer: (+) through the plasma centre, (o) tangent to a circle with radius 39,5 cm in the minor plasma cross-section.

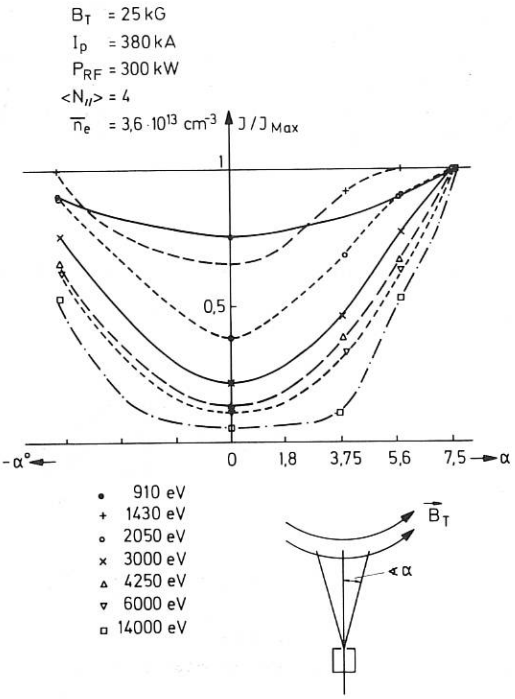

Fig.37: Normalized fluxes of energetic neutrals leaving the plasma in the equatorial plane under different angles with respect to the direction of the main magnetic field lines (see insert).

1.5.2 Current drive experiments /142/

In the current drive experiments the tokamak plasma was set up in the usual way by ohmic heating. As soon as a stationary state was reached, the primary current through the OH-transformer was kept at a constant value, $I_{OH}(t > t_o)$ = const. Thus no electromotive force is induced in the plasma. The plasma current I_p decays with its characteristic time $\tau_p = L_p/R_p$, where L_p and R_p denote the inductance and resistance, respectively, of the plasma ring. In ASDEX τ_p is of the order of 1 s. During this time the plasma dissipates the magnetic energy stored in L_p.

If, at the time t_o, an HF driven current I_{HF} is switched on (this happens in a time interval very short compared with τ_p) only a fraction of the magnetic flux has to be removed. We then have

$$I_p(t) = (I_p(t_o) - I_{HF})e^{-t/\tau_p} + I_{HF}$$

and

$$\dot{I}_p(t) = -\frac{I_p(t_o) - I_{HF}}{\tau_p} e^{-t/\tau_p} .$$

A series of experiments along these lines is shown in Fig. 38: with increasing HF power the decay of the plasma current is slowed down until the full current can be maintained or even increased at sufficiently high HF powers. In Fig. 39 the results of such runs are shown for different plasma dens-

ities. At lower densities the same current can be maintained with less HF power. It is seen that I_p rises very sharply at low HF powers (P_{HF} < 100 kW) whereas it increases more slowly at higher powers. Assuming I_{HF} proportional to P_{HF}, as predicted by collisional theory, the nonlinear dependence of I_p on P_{HF} can only be explained by an increase of τ_p under the influence of the HF power. This seems to be plausible since the electron energy distribution during current drive strongly deviates from a thermal distribution, as is clearly observed in the spectra of X-rays and of ECE radiation.

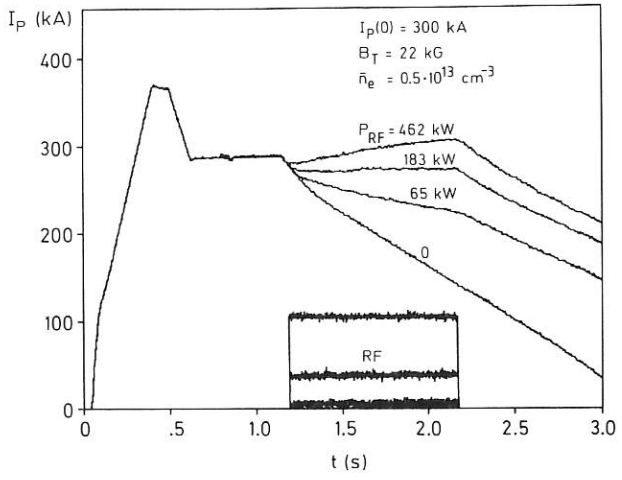

Fig.38: Plasma current I_p as a function of time for different rf powers. For $t > t_o$ = 1,17 s the primary current I_{OH} through the OH-transformer is set constant.

Figure 40 shows measurements for different densities in H^+ and D^+-plasmas at constant HF power. For low denisities the same $\dot{I}_p$ is obtained in both gases. With increasing densities a change in $\dot{I}_p$ due to HF driven currents is observed in H_2 only up to a density of $\bar{n}_e \simeq 2 \times 10^{13}$ cm^{-3}, whereas in D_2 this region extends up to about 3×10^{13} cm^{-3}. These numbers roughly agree with a theory on the density limit of current which assumes that, with rising density, the wave interaction with ions is the limiting mechanism[1].

At sufficiently high HF powers a rise in the plasma current can be achieved (see Fig. 38) for $t > t_o$. The loop voltage then becomes clearly negative. In this case the energy stored in the poloidal magnetic field of the plasma ring current is increased. This increase in magnetic energy will be released when the plasma current is allowed to decrease at a later time.

A recharging of the primary windings of the OH transformator can be accomplished by clamping the plasma current. In order to prevent the plasma current from increasing when a high HF power is applied, a counter-voltage must be induced. This leads to re-charging of the primary side of the OH transformer. Such a shot is shown in Fig. 41, where

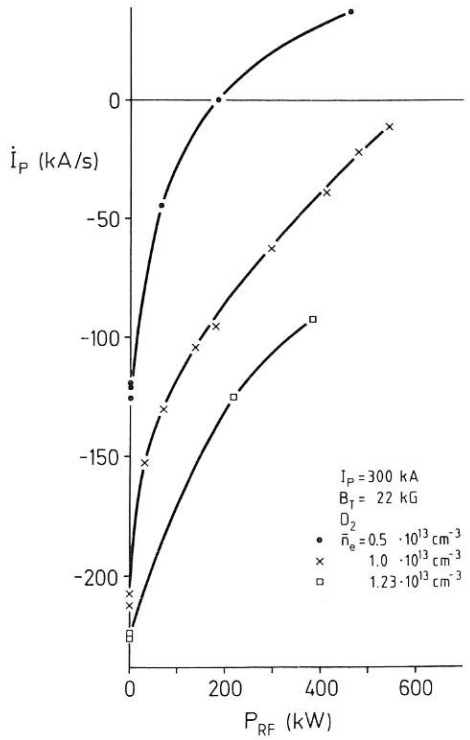

Fig.39: Plasma current decay rate $\dot{I}_p$ as a function of rf power for different plasma densities.

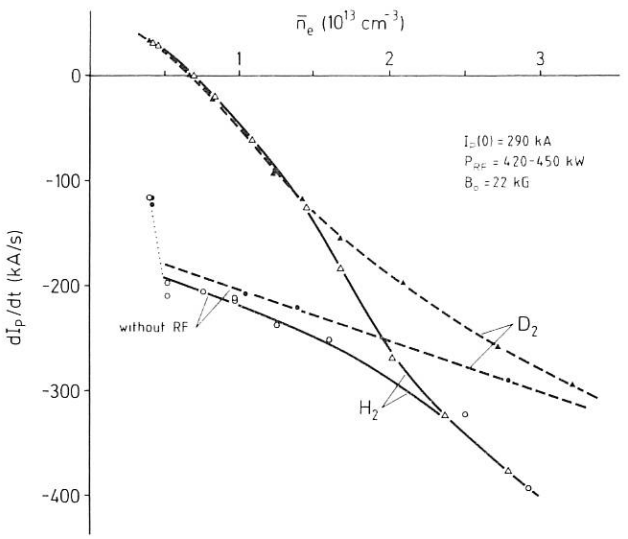

Fig.40: Plasma current decay rate $\dot{I}_p$ as a function of density in H^+ and D^+-plasmas.

[1] J.G. Wegrowe and G. Tonon, Proc. IAEA Techn. Com. Meeting, Culham, 1983, Vol. II, p. 343

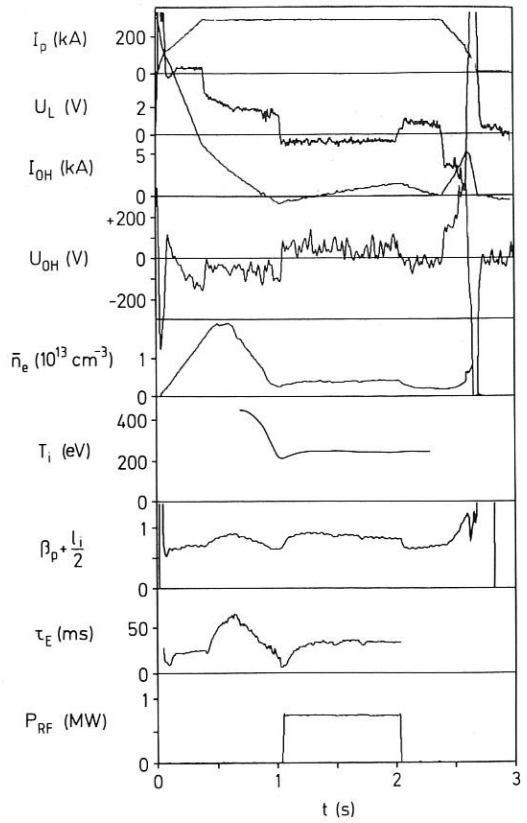

Fig.41: Recharging the OH-transformer by an increase in primary current I_{OH} with constant plasma current I_p.

---

the primary current I_{OH} is again raised during the LH current drive. The amount of re-charging in this shot corresponds to a flux swing of 0.2 Vs. The re-charging efficiency has been rather low in the experiments performed up to now. A maximum of about 13 % of the HF energy expended could be stored as useful magnetic energy in the OH transformer. The remainder is used to maintain and further heat the plasma.

The energy content of a discharge where the current is maintained by LH waves alone is higher than in an OH-produced discharge with the same current and density, indicating that the energy confinement in LH-driven discharges is improved. This is also expressed by a steepening of the density gradient at the plasma edge as observed by the Li-beam diagnostics.

1.5.3 Coupling studies; HF power limits

In general, the coupling of LH power is good and agrees rather well with theoretical predictions even for asymmetric power spectra.

As soon as the total power through the grill approached the 1 MW level, the number of power trips caused by enhanced reflections increased and the pulse lengths became shorter and shorter. No systematic study of this power limitation could be made up to now. But it appears as if the power transport through the grill antenna with its coated grill waveguides /67/ occurs without problems.

There are, however, a number of observations relating to the grill-plasma interface which could not yet be made to form a consistent picture:

- The HF power density could be raised by nearly a factor of two when only the two central waveguides were fed.
- The power limit seems to be lower for higher plasma densities.
- High-speed cine pictures show a luminous seam along the vertical side-walls and the lower horizontal contour of the grill boundary plasma which appears and vanishes with the HF.
- This luminous seam switches from the lower to the upper horizontal side when the main magnetic field is reversed, its orientation being as if it were caused by grad B-driven ions releasing neutral gas when they impinge on the grill walls.
- Along the upper edge of the grill front-plate a large number of small arc traces was found after removing the grill antenna.
- When the light from the grill boundary plasma was observed the long way through the individual grill waveguides, the light signals all showed the same time evolution, indicating some type of collective behaviour in front of the grill.

More relevant information is expected soon from a microwave interferometer measuring the electron density in front of the grill.

1.6 First Experimental Results of ICRH on ASDEX

(In collaboration with F. Wesner, J. Bäumler, F. Braun, R. Fritsch, F. Hofmeister, E. v. Mark, J.-M. Noterdaeme, S. Puri, M. Söll, K. Steinmetz, H. Wedler; ICRH Group (Technology Division))

The main topics of ICRH investigations in ASDEX are the heating efficiency and plasma confinement in various heating scenarios ($2\,\Omega_{CH}$ and D(H)-minority heating), and the role of the ASDEX divertor and its influence on impurity production and transport in ICRF-heated discharges.

1.6.1 Heating experiments

First experiments were started in November 1984 at

67 MHz, corresponding to second-harmonic heating in a hydrogen plasma at a magnetic field of about 2.2 T. A transmitted power of about 700 kW for 0.4 s with one antenna was reached by the end of 1984. The preliminary results described here were obtained mainly at a power of 450 to 550 kW with pulse lengths of about 1 s. Typical parameters of the Ohmically heated target plasma were:

I_p = 400 kA
$\bar{n}_e$ = 4 - 5 x 10^{13} cm^{-3}
$T_{eo} \simeq$ 630 eV
$T_{io} \simeq$ 500 eV
P_{OH} = 480 - 550 kW
$Z_{eff} \simeq$ 1.4

Already at relatively low powers plasma heating has been observed with a maximum β_p -increase of about 30 % at $P_{rf} \simeq$ 550 kW. Figure 42 shows the development of β_p while the ohmic heating power (plasma current and loop voltage) is kept constant. Since the density ($\bar{n}_e$ = 4.5 x 10^{13} cm^{-3}) does not significantly change, the observed β_p increase should be related to a rise of the electron and ion temperatures. The electron temperature rise (ΔT_e max. 100 eV) measured by ECE does not explain the β_p increase so that the ion temperature must also be enhanced. This is confirmed by first, not yet systematically performed CX-measurements indicating a temperature increase $\Delta T_i \simeq$ 200 eV. The preliminary heating efficiency $\eta \simeq$ 2.7 x 10^{13} eV/kW cm^3 compares well with other experiments if corrected for different plasma volumes and energy confinement times.

The total efficiency, which describes the HF-energy transfer from the antenna into stored plasma energy by heating ions and electrons, is found to be about 20 to 35 % under present discharge conditions if the additional input power $P_{HF} \simeq$ 450 kW is compared with the increment of the plasma energy content $\Delta E_p \simeq$ 5 kJ (τ_E = 30 to 50 ms). A complete energy balance has not yet been performed, but it seems to be of special importance to study particularly HF-induced energy loss channels, e.g. due to surface modes or fast ion losses.

1.6.2 Impurity production

The first ICRF experiments in ASDEX indicate that also with a divertor ICRF operation is accompanied by a significant increase in impurity production. Z_{eff} increases from about 1.4 in the ohmic discharge phase to 1.7 to 2.5 with an HF-power of 450 kW. The main impurity component in the plasma centre is found to be iron, while titanium, probably originating from the TiC/TiN-coating of the Faraday screen, contributes little to the central radiation. Soft X-ray profile measurements ($h\upsilon > 40$ eV) show that the central radiation increases more strongly than the edge radiation. Since the central SX signal rises much more slowly, when ICRF is switched on, compared to the relatively fast slope of the edge radiation, the observations indicate some kind of high-Z impurity transport into the plasma centre. At the plasma edge lines of essentially oxygen and carbon are found. In some discharge conditions the impurity signals (Fig. 43) and even the soft X-ray radiation (Fig. 44) become stationary when the HF-power has reached its final value. It is noteworthy that the HF pulse length is not limited by impurity production.

An interesting dependence of the impurity behaviour on the resonance layer position (see insert of Fig. 45) which is possibly related to the geometry of the ASDEX divertor entrance has been observed.

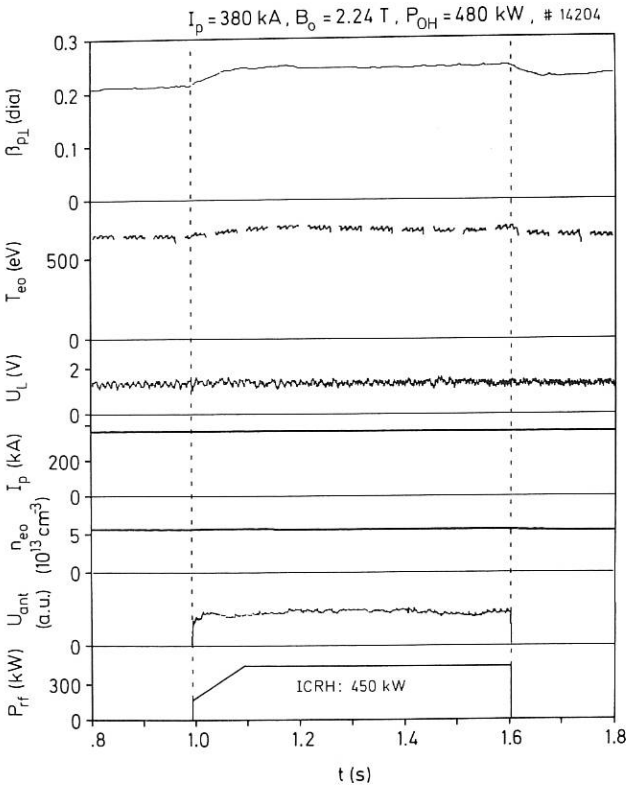

Fig.42: Set of typical traces of plasma data during ICRH (U_{ant} denotes the voltage at the antenna, P_{rf} is the high frequency power delivered by the RF-generator).

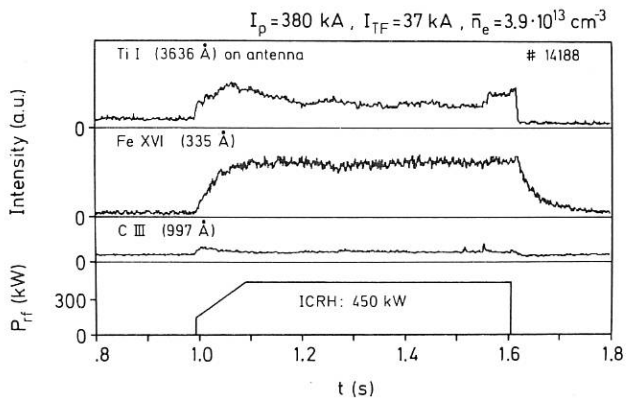

Fig.43: Impurity line densities from different species during ICRH.

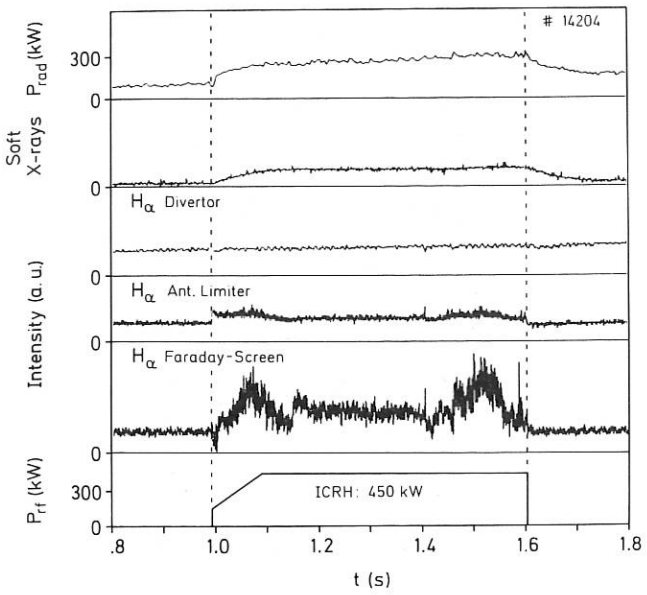

Fig.44: Set of typical traces corresponding to radiation during ICRH. H_α-radiation is observed in the divertor chambers, at the antenna guard limiter and in front of the Faraday-screen.

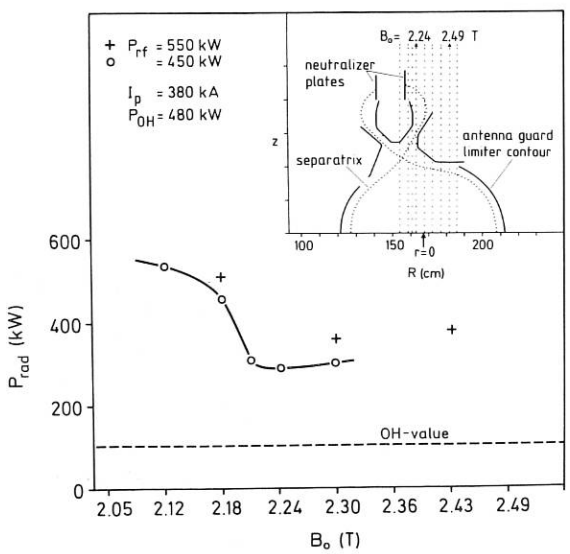

Fig.45: Total radiated power versus toroidal magnetic field.

Figure 45 shows the dependence of the total radiation P_{rad} on the toroidal magnetic field. The radiation level is high when the vertical projection of the resonance layer position intersects the protection of the central divertor coil. The flat minimum in Fig. 45 seems to be correlated to the resonance layer "passing" through the divertor entrance slit. At this position bolometer radiation profiles are much less centrally peaked than in other positions (Fig. 46) indicating a smaller concentration of medium and high-Z impurities on axis.

With ICRF a change in the plasma edge density profiles was also observed by means of the lithium beam diagnostics. For $B_o < 2.24$ T the scrape-off layer (SOL) density decreased continuously throughout the 600 ms ICRF pulse by a factor of about two while the SOL density profile is not changed. The density decrease - also recorded by the microwave interferometer monitoring the SOL line density in the divertor throat - was accompanied by a reduction in the H_α-divertor recycling signal and an increase in impurity flux. In contrast, at $B_o = 2.24$ T the SOL density is only slightly decreased ($\leq$25 %) within 50 ms after initiation of the ICRH and remains constant thereafter for the entire pulse length.

As a preliminary hypothesis, vertically drifting ions accelerated in the resonance layer might release impurities at structural elements close to the upper stagnation point and could thus be responsible for the observed central impurity radiation. In fact, the ICRF-induced relative increase of SX-radiation from the upper plasma boundary is about 25 % higher than from the lower part (see also Sec. 1.4.1). A significant impurity release in front of the divertor throat could additionally cool down the scrape-off layer, resulting in reduced impurity screening efficiency accompanied by the small (about 1 cm) shrinking of the plasma radius observed by the Li-beam diagnostic. Obviously these questions have to be addressed in more detail in the forthcoming experiments.

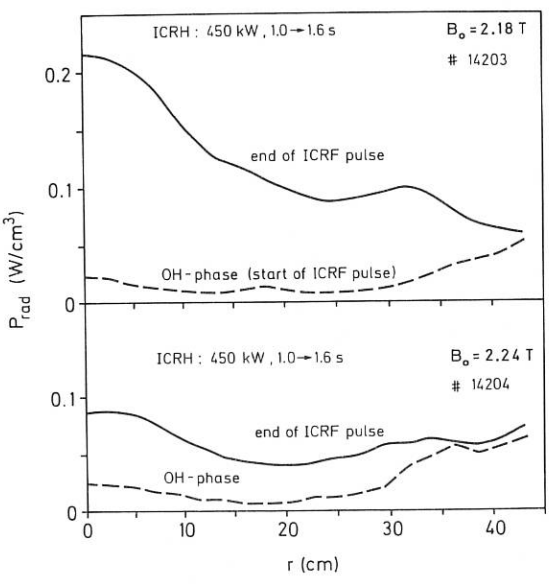

Fig.46: Power radiation profiles at two different resonance layer positions (circular symmetry is assumed).

1.7 Pellet Ablation in ASDEX Discharges with Ohmic, Neutral Injection and Lower Hybrid Heating

(In collaboration with K. Büchl, W. Sandmann, E. Oberlander; JET Diagnostic and Pellet group)

Deuterium and hydrogen pellets 1.0 mm (occasionally also 1.8 mm) in diameter were injected at velocities of 400 to 1100 m/s into ASDEX discharges with ohmic (OH), neutral injection (NI) and lower hybrid (LH) heating or with lower hybrid current drive. Dependent on these conditions three types of pellet ablation can be distinguished according to the signals of the space-integrated H_α-emission (Fig. 47) or time-integrated photographs of the ablation traces.

In ohmically heated discharges the ablation of a pellet starts near the plasma edge and increases slowly along its path up to that radius where the pellet is completely evaporated and the H_α-emission suddenly drops. The fluctuatios in the H_α-signals can be explained by the influence of rational q-surfaces and will not be discussed here. The smoothed signal is in fair agreement with calculations using the neutral gas shielding model. In addition, the model gives the penetration depth to within a few cm of the measured value. The ablation properties of pellets is the same in neutral beam heated plasmas in the L-regime and in plasma with lower hybrid heating at high densities. This agreement is also obtained with large pellets (1.8 mm Ø).

In NI-heated plasmas in the H-regime the H_α-emission during pellet ablation is similar to that of OH plasmas, but the rise of the line intensity is substantially steeper than in OH plasmas. The H_α-signal becomes rectangular in shape. It is not yet clear whether the evolution of the H_α-emission can be explained solely by the steep temperature rise at the plasma edge or whether the ablation by the fast ions also has to be taken into consideration.

In very low-density OH plasmas and in low-density plasmas with LH, during the pulse and within 200 ms of its termination the H_α-emission due to pellet ablation shows totally different characteristics. The rise of H_α-radiation is very fast. It is followed by a slow decay for several milliseconds. This is much longer than the transit time of the pellet through the plasma column would be. If information on the line density and suprathermal electrons in these discharges is included, one can conclude that the pellets explode near the edge of the plasma by intense volume heating with suprathermal electrons. The pellet thus acts like a super gas puff.

The results of H_α-emission measurements are confirmed by photographs of the ablation traces. The penetration depth of the pellets was calculated from H_α-signals and the photographed traces. It is shown in Fig. 48 as a function of the pellet velocity. The penetration depth can be described by linear function of the pellet velocity. For a

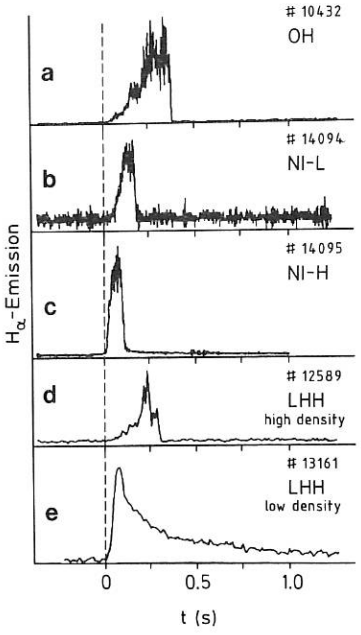

Fig.47: H_α-emission during pellet injection for different types of discharges in ASDEX. a) ohmically heated plasma; b) NI-heated plasma: L-regime; c) NI-heated plasma: H-regime; d) high-density plasma with LH; e) low-density plasma with LH (current drive)
D_2 pellets 1.0 mm Ø, v_p = 700 ... 1100 m/s

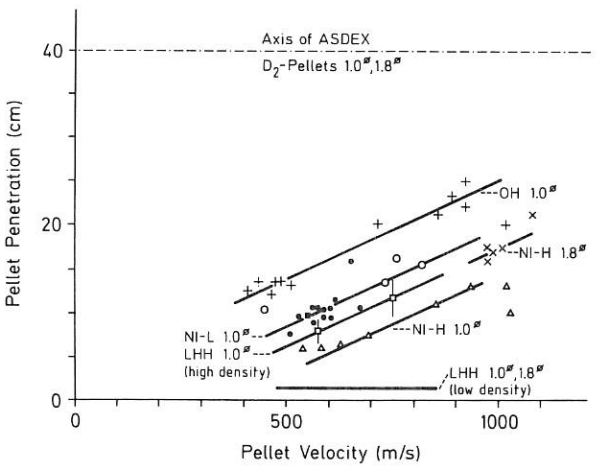

Fig.48: Penetration depth of pellets into plasmas of different types versus pellet velocity.

---

certain type of discharge n_e and T_e do not change much, but for different types of discharges the temperature is varied in a wide range.

Improvement of energy confinement by pellet injection was observed in just a few OH discharges, where β_p was increased by approx. 50 %, and in an

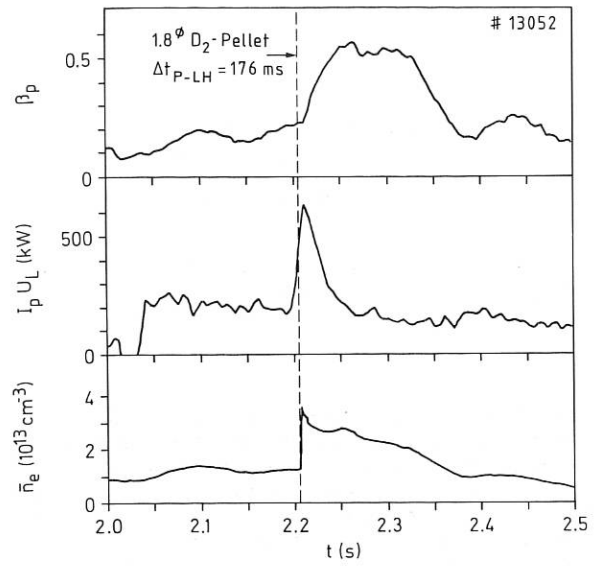

Fig.49: Pellet injection into a low-density ohmically heated plasma 176 ms after the end of the lower hybrid pulse. β_p, ohmic heating power $I_p \cdot U_L$ and line density $\bar{n}_e$ versus time.

exotic OH discharge with a large contribution of suprathermal electrons to the electron distribution. In this case the pellet was injected into a low-density discharge 176 ms after the end of LH pulse (Fig. 49). The number of nonthermal electrons decreases as a result of pellet injection. During enhanced ohmic heating β_p increases and afterwards stays on this level for approx. 100 ms.

2. IMPROVEMENT OF DIAGNOSTICS

2.1 Electron Cyclotron Emission

(A. Eberhagen, S.E. Kissel[1], V. Mertens[2])

For broad-band absolute calibration of the ASDEX ECE diagnostics (four-channel polychromator and Michelson interferometer) a black-body radiation source has been developed for the spectral range $1 \leq \lambda \leq 3$ mm on the basis of a heated Macor block radiating at about 800 K across a useful area 17 cm in diameter. Its so-called grey factor $g(\lambda)$ was determined ($0.83 \leq g(\lambda) \leq 0.92$ between $1 \leq \lambda \leq 3$ mm). The broad-band calibration of the respective diagnostic is done by measuring the difference in the spectra of this source and of the background radiation (at $\simeq$300 K) and by subsequently comparing it with the black-body radiation calculated for the difference temperature of $\simeq$500 K (Rayleigh-Jeans approximation!). The extremely low intensities to be recorded called for a huge number of individual measurements (typically 10^5 - 10^6) to overcome the noise level of the detector electronics and therefore involved special data acquisition techniques. In the upper part of Fig. 50 the spectra are shown, as an example, of the broad-band source and of the background radiation as recorded with the Michelson diagnostic (corresponding measurements with the polychromator have not yet been completed), and in the lower part of Fig. 50 the curve of the inverse calibration factor, derived from the spectra in the manner described, is presented between $0.7 \leq \lambda \leq 4$ mm. The heavy reductions in the spectra at ~550 GHz ($\lambda \simeq 0.55$ mm) and ~750 GHz ($\lambda \simeq 0.4$ mm) are caused by absorption by atmospheric water vapour along the diagnostic path. Together with the decrease in the inverse calibration factor towards high frequencies, they limit the meaningful application of our Michelson diagnostic to wavelengths $\lambda \gtrsim 0.6$ mm (corresponding to the 8th harmonic of ECE at B_T = 2.2 T).

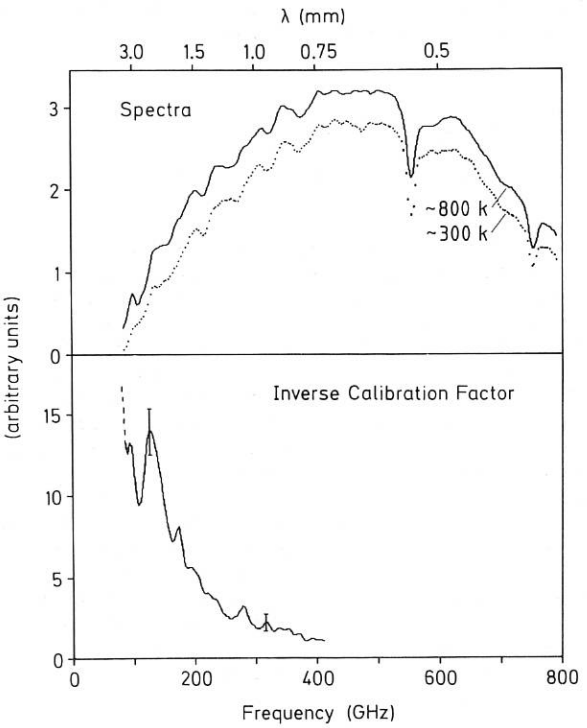

Fig.50: Broadband absolute calibration of Michelson Interferometer, source plus background radiation spectra and inverse calibration factor derived.

2.2 Development of Charged Fusion Product Diagnostics

(H.-S. Bosch)

The properties of the charged fusion products escaping from the plasma bear important information on the plasma parameters. The diagnostic of fusion protons and tritons from D-D and D-He^3 reactions is therefore being developed for ASDEX discharges with

[1] now JET Joint Undertaking
[2] ASDEX-Upgrade Group

additional heating. The ion temperature and the beam-target reactions can be deduced from the fluxes or from the energy spectra of the fusion protons or tritons.

For these measurements two different diagnostic methods are being developed:

- The energy spectra of protons for different time intervals during the discharge are obtained with surface barrier detectors. The work was concentrated on the design of the detector electronics.
- Time-integrated proton and triton fluxes and spectra are measured with nuclear emulsion foils (PM 355).

In preliminary measurements with these foils in ASDEX deuterium discharges with deuteron neutral injection, it was possible for the first time to detect tritons escaping from a tokamak. The spectra of the tritons and protons are obtained by applying these foils together with absorber foils (aluminium) of different thicknesses.

2.3 60 Hz Thomson Scattering

(D. Meisel, H. Murmann, H. Röhr[1], K.-H. Steuer)

The 60 Hz Nd:YAG scattering system tested on ASDEX in the last two years was expanded to measure electron density and temperature profiles. We therefore built a multipoint optical system capable of measuring simultaneously at 16 points along the vertical laser beam in a range of $-40\ \text{cm} \lesssim r \lesssim +20\ \text{cm}$. The spatial resolution is 2.8 cm (beam diameter 0.4 cm) matched to the active area of the avalanche diodes in connection with a f/1.2 lense. The distance between two measuring points is 4 cm. Each scattered spectrum is analysed by means of 3 interference filters and silicon avalanche diodes as detectors. The calibration of the spatial channels for absolute density measurements is done with antistokes Raman scattering from H_2 filled into the ASDEX vessel. First measurements with 4 channels show that signal to noise ratios are sufficiently high for reliable profile measurements.

Now, the diagnostic system is completed and the data acquisition and evaluation programs are tested.

2.4 Johann Spectrometer

(G. Fußmann, M. Hesse[2])

To improve the flexibility of the spectrometer we implemented in 1984 a software system for accurate wavelength adjustment (control of 5 step motors).

[1] Experimental Division 1
[2] CEN Grenoble

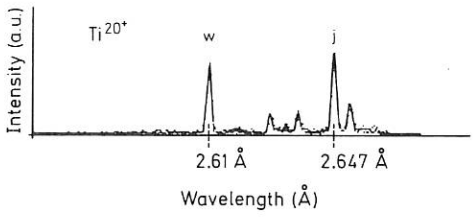

Fig.51: He-like spectrum of Ti^{+20} measured with Johann spectrometer on ASDEX.

Furthermore a data readout program was installed that allows plotting and computer manipulation of the measured spectra. The spectrometer was already routinely used for the acquisition of time resolved He- and H-like spectra of Fe, S, Cl, Ti and Ar impurities in ASDEX. An example of Ti^{+20}-spectrum measured during neutral injection is shown in Fig. 51. First results from Doppler broadening measurements of the S^{+14} line yielded ion temperatures of 3 keV in case of a NI-heated plasma (3.2 MW, H-phase).

2.5 Lithium Beam Diagnostic

(K. McCormick)

The optical system to measure, in conjunction with the Li-beam[3] the ASDEX poloidal magnetic field was installed in 1984, and preliminary tests begun. The WVII-a Li-beam results (Annual Report 1981, p.87) that the beam penetration depth in the plasma does not improve significantly with increasing energy was confirmed on ASDEX during tests carried out with beam energies 40 - 80 keV.

Figure 52 shows the experimentally determined Li [2p-2s] light intensity along a 60 keV/ 0.3 mA neutral beam for line densities of 0.5, 1 and 1.5 x $10^{13}\ \text{cm}^{-3}$, in a double-null diverted ASDEX discharge. The intensity is expressed in terms of the number of photons emitted in 4π steradians per cm of beam per sec. The absolute values are the result of an indirect calibration and hence must be taken as approximate. Nevertheless, they furnish the basis for estimating the resolution $\delta\theta$ of the magnetic field line pitch angle as a function of radius and line density on ASDEX. This prediction is for an integration time constant of 10 msec under the assumption that $\delta\theta$ is governed by photon statistics only.

It is seen that relatively good angular resolution ($\delta\theta < 3$ mrad) should be possible over a large portion of the plasma for the density regime ($\bar{n}_e < 10^{13}\ \text{cm}^{-3}$) associated with effective LH

[3] K. McCormick, M. Kick and J. Olivain, 8th Eur. Conf. on Contr. Fusion and Plasma Physics, Prague (1977) 40.

current drive on ASDEX. Higher densities restrict practical use of the method to the region closer to the plasma boundary.

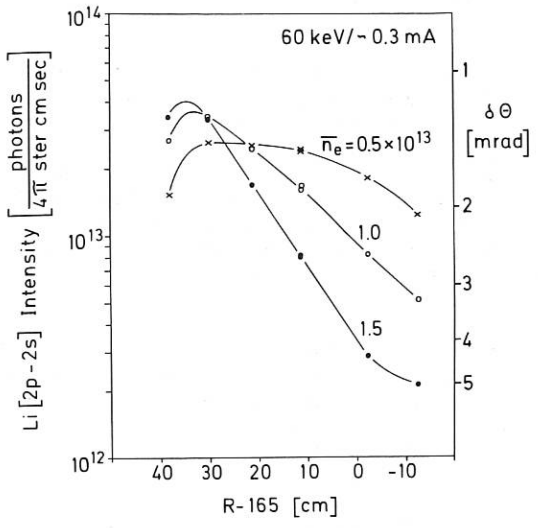

Fig.52: Li[2p-2s] light intensity along a 60 keV/~ 0.3 mA neutral beam injected into a double-null diverted ASDEX discharge for line densities $\bar{n}_e$ = 0.5, 1, and 1.5 x 10^{13} cm^{-3}. R - 165 = 40 cm corresponds approximately to the position of the outer separatrix. The predicted angular resolution δθ of the magnetic field pitch angle is given on the right-hand ordinate for an integration time constant of 10 msec, whereby δθ is assumed to be determined by photon statistics alone.

3. DATA ACQUISITION AND ELECTRONICS

3.1 Data Acquisition

(N. Ruhs, H. Hohenöcker, D. Zimmermann, H. Bauer, M. Harnau, A. Kus, J.G. Müller, E. Karl, T. Wendt)

The data acquisition system for ASDEX was upgraded during 1984. A VAX 11/780 was added to the configuration to relieve the PDP 11/70 of coordination and most preliminary data analysis responsibilities, and a Local Area Network based on DECnet and Ethernet was put into operation (Fig. 53).

In 1977, when the system was designed, a much smaller number of data and diagnostics had been envisaged. In Fig. 54 the evolution of diagnostics and data is shown. After only one year of operation, however, the number of diagnostics, the quality and quantity of data analysis, and the amount of data had already reached the limits imposed by the computing power available. Transfer of data to the IPP computer centre (line RZG in Fig. 53) and complex analysis on the mainframes enhanced the response for the user, the other bottlenecks being eliminated by the introduction of the VAX.

At the end of February, five weeks after installation, all 45 user terminals were switched to the new computer. Conversion of programs imposed no problems because of the similar structures of VAX and PDP. The programming effort on the new computer could be reduced by a factor of up to 5. The ASD

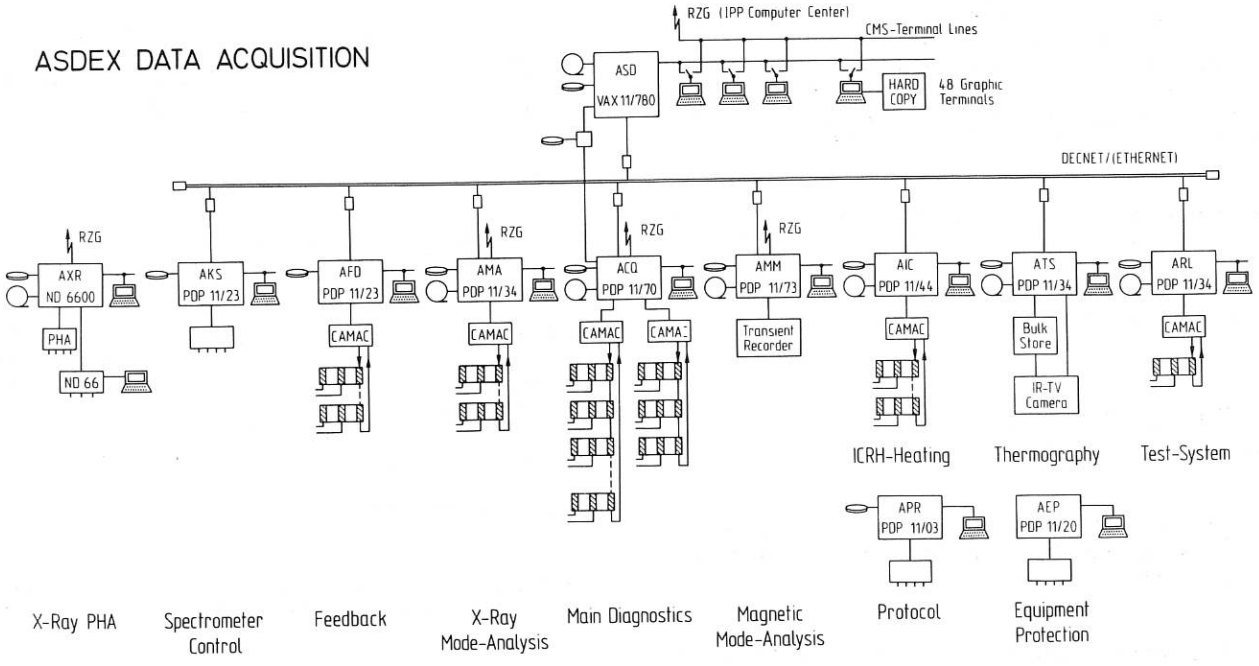

Fig. 53: Configuration.

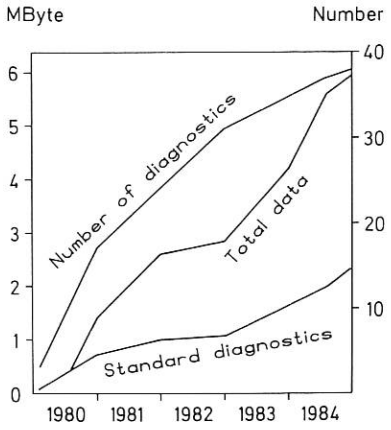

Fig.54: Number of diagnostics and data.

main computer took over coordination of subsystems and first data analysis, the ACQ system now being dedicated to data acquisition for the main diagnostics.

With the aid of the Local Area Network, functions of an operating system are spread over the whole network. This provides for transparency in the system but the network software imposes an additional load on the computers. Using the complete set of network functions of DECnet has produced a throughput of 20 kbyte/s between two PDP 11 computers. Software is being developed to increase the throughput rate up to 100 kbytes/s for special tasks such as data file transfer; facilities utilizing the bottom layers of the network protocol for this purpose are contained in the DECnet software. On the line to the IPP computer centre a simple transport software is used, but since the data format has to be converted, the effective transfer rate is also limited to 20 kbytes/s. The Local Area Network has considerably improved the functions of the data acquisition system and has proved to be reliable and easy to use.

New diagnostics were connected to the system during 1984: expanded quasistationary Thomson scattering, crystal spectrometer control and diagnostic (both microprocessor-controlled), Johann spectrometer and active charge-exchange spectroscopy.

3.2 Electronics Development

(F. Schneider, H. Czich, H. Horbach)

For plasma profile measurements several diagnostics had to be extended from a few measuring signals to a large array system.

The bolometers, with 48 channels successfully in operation, have been followed by the soft-X-ray system with up to 64 slow and 24 fast channels, which are used for computer tomography. More resolution is needed and new wide-band amplifiers (designed by the central electronics group) had to be remotely controlled and adapted to the system. A CAMAC module was designed capable of changing 8 control bits of any of these 80 amplifiers individually and several times during a shot via a single pair of wires of RS 232 standard.

Very important design work was the 48 channels of the 50 Hz Thompson scattering system. Not only had the signal amplifiers (rise time 5 ns) to be developed, but also the light-sensitive gate unit, with very short delay and a jitter of less than 2 nanoseconds for the measuring window. The large dynamic range of the electronics allows the system to be tested with the laser as well as with a simple light-emitting diode.

Further electronic channels have also been added to the interferometers and to the magnetic and diamagnetic systems. The lithium diagnostic has been fitted with new specially designed anti-aliasing filters for all 12 channels.

For the spectroscopy systems more geometric resolution will be obtained by scanning a mirror. Since the conventional stepping motor drives available on the market cannot be used for this application a stepping motor drive was developed with an automatic, crystal-clock-stabilized accelerator and decelerator to move the mirror reproducibly and without interruption at optimum speed. For this purpose a special CAMAC module was designed allowing a preprogrammed curve with up to 2000 positions loaded by the computer to control the stepping motors.

4. ENGINEERING

(H. Rapp, R. Allgeyer, H. Finkelmeyer, J. Franzspeck[1], J. Gernhardt, F. Gresser, F. Hartz, G. Herppich, G. Klement, P. Krüger, H. Niedermeyer, B. Quiel[2], F. Schneider, S. Schraub)

4.1 Operation of the Experiment

ASDEX was in operation for 66 days. A total of 3300 discharges were carried out, roughly 2/3 of them with additional heating (Neutral Injection, Lower Hybrid Heating, and, at the end of the year, Ion Cyclotron Heating). Experiments with ICRH started in November after installation of two antennae during the summer. No disturbance of machine control due to HF noise was observed up to the present power level of 700 KW.

Problems with the contacts between current leads and multipole coils again caused lengthy interrup-

[1] Up to November 1984
[2] Since November 1984

tions of the experiment during March/April and in December. Continuous monitoring of the contact resistance reliably prevented damage to the coils. The shut-down periods were used for modifications of the vacuum vessel walls and limiters and for preparations relating to the planned long-pulse heating programme. A major effort was the replacement of approximately 3000 stainless-steel bars at the multipole protection plates by about 400 graphite bars to reduce the metal impurity production in high-ß discharges.

For better control of the plasma shape the divertor coil circuit was rearranged to allow, within certain limits, individual control of the currents in the three divertor coils. The arrangement of the controlled rectifiers (see Fig. 55) was determined by the existing coil connections and was based on the good experience with the bypass operation of rectifiers.

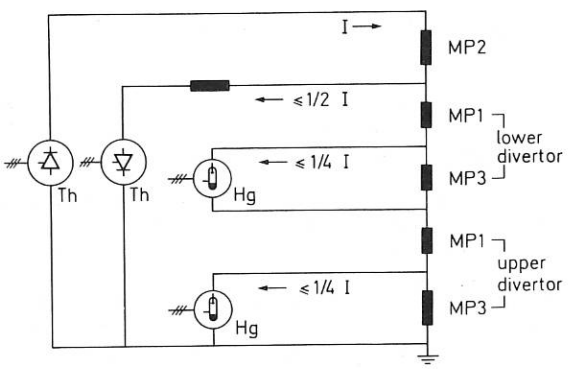

Fig.55: Circuit diagram for plasma shape control.

4.2 Preparation for Long-pulse Heating

The design of all essential divertor modifications to permit long-pulse heating with 6 MW/10 s has been completed and manufacturing is making progress.

Figure 56 shows a cross-section of the upper half of the discharge vessel with the divertor consolidated for long-pulse heating. Neutralizer plates and thermal shielding of the centre divertor coil (MP2) will be replaced by one integral heat shield. It consists of a copper-stainless-steel compound structured in meanders by vertical slits. The structure is necessary to reduce eddy currents and resulting forces during disruptions. Remaining forces are taken up by the stainless-steel backing of the soft copper facing the plasma. Heat is being removed during the pulses by water flowing in a cooling channel inside the copper. Special shaping of the surface prevents particles from impinging at steep angles.

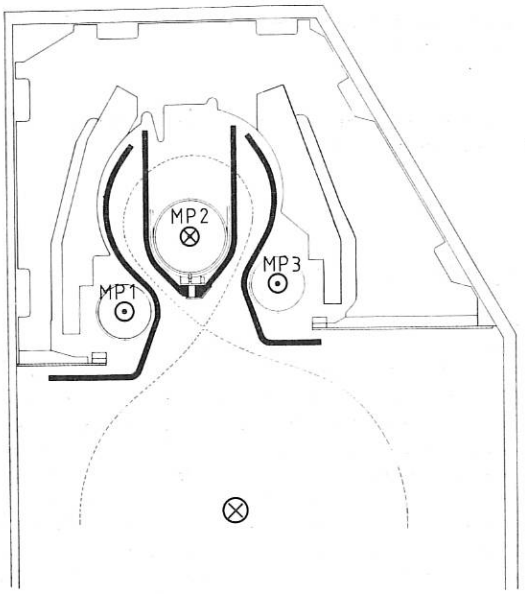

Fig.56: Water-cooled protection plates for long-pulse heating of ASDEX.

To protect the coils MP1 and MP3 and all other installations inside the divertor from the high-power neutral particle radiation emitted from the scrape-off layer, the new MP1 and MP3 shields have been enlarged and designed with direct water cooling. As a consequence of this different shape, energetic particles will be confined to a much smaller volume than in the old divertor. Numerical calculations performed by the Tokamak Physics Group (see Sec. 1.4.2) show that neutral hydrogen retention properties will not significantly change.

Getter pumping will still be possible at a reduced pumping speed by sublimating titanium on the rear sides of the heat shields and the vessel walls. The cooled getter panels provided on the present divertor for an increased pumping speed will be removed.

Many special apertures are provided in the heat shield to meet all diagnostic requirements. Some of the diagnostics in the main chamber exposed to the plasma radiation will have to be modified to cope with the strongly increased heat load. All necessary technical investigations have been performed and design is under way.

Deionized cooling water will be delivered from a newly designed system which will serve the ASDEX divertor installations and the new long pulse neutral beam sources. A contract for manufacturing the cooling systems has been placed with industry.

Water cooling of the divertor installations will be used for a calorimetric determinaton of energy flows. Flow speeds and temperatures of the water in several circuits will be measured and recorded by a

computerized system, the specification of which has been completed.

It is expected that assembly can commence in the first few months of 1986.

5. AUXILIARY HEATING AND REFUELLING

The production of a hot plasma and the investigation of its behaviour on a time scale large compared to the skin time will be the main objective of ASDEX during its remaining period of operation. For this purpose the divertor will be modified (see Sec. 4.2) to allow long-pulse (~10 s) auxiliary heating at power levels of up to 6 MW, and the Neutral Injection (Sec. 5.1) and Ion Cyclotron Heating (Sec. 5.3) systems will be extended to 10 s pulse lengths. Together with the existing Lower Hybrid Heating system (Sec. 5.2) this will also allow a realistic comparison of the prospects of these three heating methods in one machine.

In the past year the centrifuge for genuine particle refuelling has achieved most promising results in the laboratory (Sec. 5.4) and is now being installed on ASDEX.

5.1 Neutral Injection

(E. Speth, J.H. Feist, K. Freudenberger, J. Kolos, R.C. Kunze, H. Lohnert, W. Melkus[1], P. Mikolajczak[2], W. Ott, F.P. Penningsfeld, P.J. Schneider, A. Stäbler, O. Vollmer, K. Wittenbecher, G. Wulff; Neutral Injection Group (Technology Division))

5.1.1 Neutral injection with short pulses (≤ 0.5 s)

In 1984 neutral injection was - as in previous years - the dominant heating method in ASDEX. The emphasis was therefore to provide high neutral powers with high reliability.

A major step in the performance of the system was achieved by accelerating deuterium instead of hydrogen for the first time. While for hydrogen beams the neutral power is limited to 3.5 MW by the current capability of the HV power supplies, operation with deuterium allows the higher voltage available to be used without reaching the current limit of the supplies. With this advantage, combined with the higher neutralization efficiency of the deuterium ions, the system could be enhanced up to a neutral power of 4.3 MW into the torus. This high power level strongly supported the extensive ß-limit studies performed in ASDEX in summer 1984.

In addition to the increased power, the availability of the NI system was significantly improved. The total of 8 ion sources has been available throughout the experimental period of ASDEX in 1984. In spite of the more extensive use of the capability for longer pulse lengths (≤ 0.5 s), the reliability of the ion sources increased from 75 % to 85 %: Only 15 % of the neutral-beam-heated discharges exhibit reduced pulse length due to HV breakdowns in the accelerating system of one or more ion sources. This corresponds to an averaged single-source reliability of 98 %.

Besides numerous minor modifications an "arc-notching"-system was implemented and commissioned. This system allows to switch the beam on again after HV breakdown and will improve the ion source reliability. In addition, a beam restart during one pulse is now possible, giving considerably more freedom in modelling the time dependence of the neutral beam power during an ASDEX discharge.

5.1.2 Variation of neutral beam deposition

A few experiments were conducted in which different beam deposition profiles were applied to identical ohmic target plasmas in order

- to study the effect of different power deposition profiles on heating, confinement and impurity response
- to derive a "minimum required beam energy" for ASDEX below which heating, confinement and impurity behaviour degrade, and, consequently,
- to attempt an experimental assessment of neutral beam penetration requirements for larger toroidal plasmas.

Three different beam voltages as well as H_2 and D_2 in the beam sources were used (40 kV H_2, 45 kV D_2, 29 kV D_2) in order to vary the deposition profiles, while the injected neutral power, the plasma density, the plasma current and the divertor configuration were kept constant. Since the extracted ion beams of the ASDEX injectors contain a large fraction of molecular ions ($H^+ : H_2^+ : H_3^+ \simeq 40 : 50 : 10$), the penetration characteristics of the beams are more adequately described by a species-averaged beam energy rather than by the beam voltage.

A typical result is shown in Fig. 2. For a line-averaged density of $\simeq 6 \times 10^{13}$ cm^{-3}, a plasma current of 420 kA, a neutral power of between 1.1 and 1.3 MW and a single-null configuration the global energy confinement time τ_E does not show any deterioration between averaged beam energies of 25 keV/AMU and 9 keV/AMU. This is surprising since for the lowest energy the deposition profiles as computed with the FREYA code are peaked around r = a/2, as shown in the same figure. For such hollow profiles one would expect some deterioration of τ_E (compared with the centre-peaked case), assuming constant electron heat conduction. Since electron heating does not show any significant dependence on the deposition profile either, as shown in Fig. 57, the experiments clearly call for

[1] ZTE
[2] Visiting scientist from University of Lublin, Poland

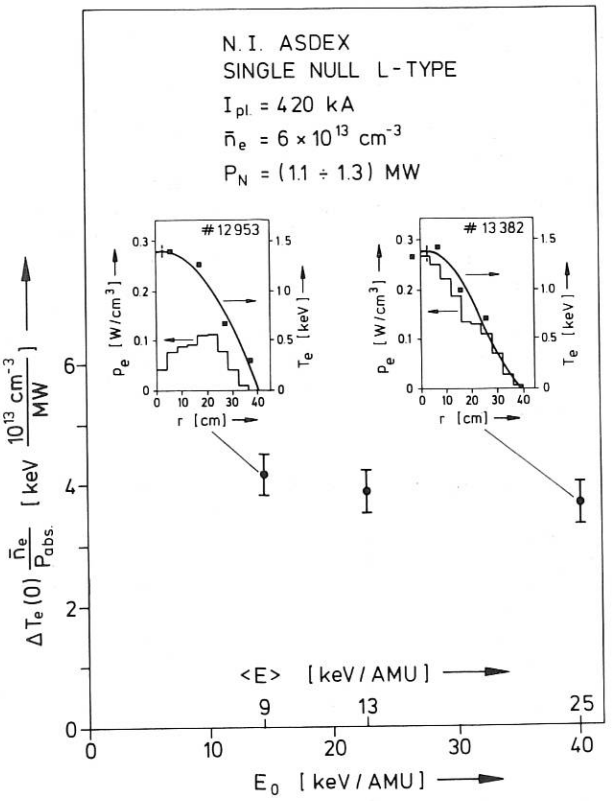

Fig.57: Electron heating efficiency vs. full beam energy and species-averaged beam energy <E> respectively;
I_{pl} = plasma current;
$\bar{n}_e$ = line-averaged density;
P_N = neutral power into the torus;
$\Delta T_e(0)$ = central electron temperature rise;
$P_{abs} = P_N - P_{cx}$;
P_{cx} = charge exchange loss ≃ 0.15 P_N (FREYA-code);
inserted are electron temperature profiles as measured by ECE and power deposition profiles (as computed with FREYA) for the two extreme cases.

---

a more detailed transport analysis, which still has to be done.

From the heating and confinement point of view an average energy of 9 keV/AMU is acceptable for ASDEX at $\bar{n}_e \simeq 6 \times 10^{13}$ cm^{-3}. The situation is more complicated with respect to impurity behaviour. For the parameters quoted above, the total radiated power was also found to be insensitive to the beam deposition profile. However, for different conditions ($n_e \leq 5 \times 10^{13}$ cm^{-3} and/or $P_N \geq 1.3$MW) enhanced impurity radiation (iron) with subsequent radiation collapse has been observed.

Scaling up the results to larger toroidal plasmas (NET) means extrapolating to $n_e a$ values which are a factor of about 6 higher. (ASDEX: at present $n_e a = 2.5 \times 10^{15}$ cm^{-2}, NET: $n_e a = 1.5 \times 10^{16}$ cm^{-2}). Applying the conventional wisdom that a/λ = const. (a = minor plasma radius, λ = mean free path of the injected fast neutrals), one can derive a value of E < 95 keV/AMU for a full-bore, full-density scenario in NET. If, however, changes in transport due to off-axis-peaked power deposition profiles occur as the present results seem to indicate, the scaling law a/λ = const. probably becomes less meaningful.

Clearly these experiments should be continued in ASDEX and other machines towards higher $n_e a$ values in order to establish the limits in degradation of confinement and heating and create a better basis for extrapolations.

5.1.3 Preparation for long-pulse neutral injection

Overview

Designing and testing of all components for upgrading the present neutral-beam injection system to 55 kV, 22 A, pulse length 10 s per source are proceeding well. A water-cooled panel has been successfully tested to full specifications. Extensive 3D calculations of the reflection magnet and all the magnetic shielding problems have given valuable information for the design of these components. The fabrication of most parts, especially those manufactured in the central workshop, has been proceeding very well. Problems arose with the manufacture of several parts by industry, especially during the transition from prototype development to series production. Consequently, some delays have occurred, but without any serious effects on the overall programme of ASDEX.

Ion source and water-cooled grids

The prototype plasma grid conforming to the fabrication technique chosen for series production has been used for more than 15,000 thermal cycles. (This also proves to be the necessary lifetime of these grids.) However, owing to many problems with the fabrication of the series grids a complete arrangement of these grids has not yet been tested. Nevertheless, first operation with completely water-cooled grids was possible with a prototype set manufactured by KFA Jülich. Despite some mechanical imperfections it was possible to condition these grids up to 55 kV, 20 A operation. The more important experience, however, was long-pulse operation (45 kV, 15.5 A, 10 s and 50 kV, 18.5 A, 5 s), limited only by the inertially cooled calorimeter. The only problem encountered during these tests was the temperature of the back plate of the source, where the cooling has to be improved. A new magnetic shielding for the source has been designed: testing of its mechanical and high-voltage properties is in progress.

Water-cooled panels

Testing of the prototypes of these panels began in February 1984. In the first step it was verified that the panel could handle the maximum design value of the power density of 2.75 kW/cm^{-2} at the

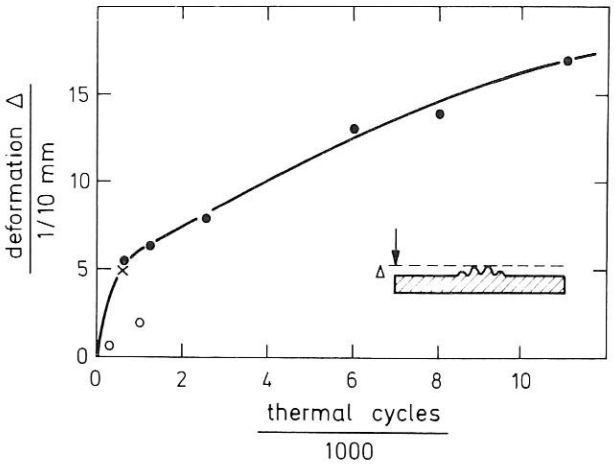

Fig.58: Deformation of the surface at the point of the maximum heat flux as a fucntion of the number of thermal cycles. The open circles represent the result for a modified design.

specified position on the surface. The next step was a lifetime test, where a design value of 25,000 thermal cycles had been specified. In order to save time, a pulsed beam was used with 500 ms pulses, 500 ms interrupt time, 8 cycles in a row. The time duration of 500 ms should be long enough to reach a temperature distribution in the panel close to steady state. The main observation during this procedure was a deformation of the front surface in the hottest region. Figure 58 shows the amount of distortion as a function of the number of thermal cycles. After a rather strong initial increase, which may even have occurred initially after a few pulses only, the deformation grows almost linearly but at a reduced rate. After 11,000 pulses, when the test was stopped, the panel was still working reliably. A second test with an improved panel design showed a much smaller deformation in the start-up phase (open circles in Fig. 58). A final test was to find the "burn-out" limit. A maximum power density of up to 4.3 kW/cm^{-2}, limited by the ion source and the geometry, was applied for 1 s. The only observation made was the onset of boiling of the water (probably at the hottest region) with increasing power density. Since no other negative effect could be detected series production was started and the first panels are expected at the end of February 1985. For the test stand a small calorimeter with four panels from a preseries production has been put together and will be installed in early 1985 to allow full-power tests of the ion sources to be conditioned.

Reflection magnet and ion dump

The design calculations for the reflection magnet have been considerably improved by using the PROFI real 3D iron magnet code. This program allowed the influence of various factors such as the ASDEX stray field, position of the neutralizer, magnetic shielding of the drift space, and special 3D modifications of the magnet to be investigated. As a very encouraging result it turned out that the design of the magnet itself, so far based on 2D or pseudo 3D calculations (see last annual report) was completely correct. The power density on the various parts of the magnet and on the ion dump was determined by following the trajectories of up to 700,000 particles, representing the full phase space of the beam, including the beam divergence, the focal point, and the relative distribution of power between the three different energy components. A contour plot of the power density on the ion dump is shown in Fig. 59. The maximum power density is less than 2 kW/cm^{-2}, which is well below the capability of the actively cooled part of the dump. For the inertially cooled section thick copper bars are envisaged, which should handle up to 300 W/cm^{-2} for the pulse length of 10 s.

The effect of the ASDEX stray field, which would have a considerable influence on the particle trajectories and especially on the power loading on the pole faces of the magnet, was minimized by an appropriately designed magnetic screen between the end of the neutralizer and the magnet. This shield will be built in such a way that it does not influence the pumping in this region.
The same program was also used to verify the design of a new magnetic shield for the ion source.

Cooling-water system

For the cooling of the extraction grids, the panels and the reflection magnet, a high-power cooling system is needed. An engineering study has been performed for the design of two 130 m^3/h, 23-bar systems with variable-speed pumps to cool away the appr. 45,000 kJ/shot for each beam line. These systems have meanwhile been ordered and the first one should be available in September 1985.

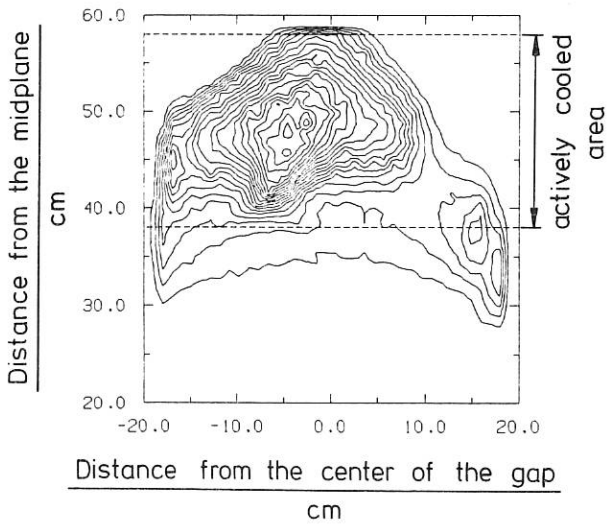

Fig.59: Power density contours in steps of 100 W/cm^2 on the surface of the ion dump. The actively cooled plates (2 plates, V-shaped) are represented by the dashed lines. The remaining part of the dumps will be of thick copper.

5.2 Lower Hybrid Experiments

(D. Eckhartt, M. Brambilla, H. Brinkschulte[1], H. Derfler, M. Hesse[2], F. Leuterer, R. Magne[3], M. Münich, F. Ryter[2], K.H. Schmitter, T. Vien, F. v. Woyna, M. Zouhar; Lower Hybrid Group (Technology Division))

The Lower Hybrid Heating (LH) system (1.3 GHz, 2.4 MW, 1.5 s) was commissioned in November 1983 and has been in operation since. The experimental results obtained up to now are reported in Sec. 1.5. Minor modifications and improvements of the system were made during the past year. A new front-piece to the 8-waveguide grill was built, emitting a symmetric power spectrum around $N_{\parallel} = 6$. Construction work for the new 16-waveguide grill for preferential heating of electrons was begun. Preparation and execution of the LH experiment was carried out under the terms of a cooperation contract with CEN Grenoble which expired at the end of 1984.

5.2.1 Transmitter and supplies

The transmitter /174/ has been running at full availability and without any noticeable down times. Re-starting of the klystron amplifiers after a long stand-still (3 months), which was originally considered rather difficult owing to the necessary conditioning of the tubes, proved to be easier than expected. It was possible, while LH experiments were running, to put the amplitude control system into operation by including the klystron amplifiers in the control loop.

A number of modifications were introduced by developing and constructing new electronic devices:

-a circuit for automatically switching on the HF power in the klystrons after a power trip, with pre-programming of the power levels (in steps) in the 8 klystrons (facilitating the procedure of conditioning the grill antenna),
-various modulators for the electronic attenuators for shaping and programming the HF pulse,
-an LED matrix monitor for diagnosing the frequency and time sequence of HF breakdowns in the individual grill waveguides,
-a PIN photodiode monitoring system with opto-preamplifiers of small rise times to detect light signals from plasma formations and breakdowns in the individual grill waveguides.

The data acquisition relating to the HF powers in forward and reflected waves has now been implemented in the ASDEX system. A number of data evaluation programs via CMS now exist but could not yet be tested under experimental conditions.

5.2.2 8-waveguide grill coupler with exchangeable front-pieces

The grill coupler for preferential ion heating was used with either one of two front-pieces: a straight one emitting a symmetric power spectrum with $N_{\parallel} = 3 \pm 0.75$, and a slightly tapered one with $N_{\parallel} = 4 \pm 1$. The waveguide inside walls of these front-pieces are covered with a thin, coarsely structured gold layer (as are the waveguides in the antenna proper) in order to suppress multipactor discharges /67,143/. In accordance with a proposal from CEN Grenoble a strongly tapered front-piece with $N_{\parallel} = 6 \pm 1.5$ was built. Its inside walls are covered with an antimultipactor layer of colloidal graphite ("Hydrokollag") which was found to be applicable in the high magnetic field regions where the front-piece is located. Although the conditioning of the grill outside ASDEX (i.e. without magnetic fields) did not show any multipactor discharges at all, there is the problem of power limitation to about 100 kW per waveguide which could not yet be identified (see Sec. 1.5.3).

After the experience gained during the first series of LH experiments a number of measures were taken:

- the grill antenna as a whole was displaced radially outwards by 15 mm, so that the foremost parts of the front-pieces, facing the plasma, remain in the "shadow" of the fixed ASDEX limiters (to protect them against runaway electrons), as well as to protect the fingerstock contacts between the ASDEX vacuum vessel and the movable antenna against thermal plasma bombardment.
- the foremost parts of the front-pieces were machined to a toroidally shaped contour adjusted to the curvature of the main magnetic field lines. The $\langle N_{\parallel} \rangle = 3$ front-piece was given a poloidal shape as well.

The standard-size vacuum windows at the grill entrance proved to be a critical item. Several of them had to be replaced since their antimultipactor coating (in most cases now made of colloidal graphite) was found to be damaged. A new technique for depositing antimultipactor gold coatings on the curved parts of these windows is under development.

The eightfold UHV-tight microwave window section (developed and built by the Vacuum and Material Sciences Group of the Central Technical Services) was completed and tested on the HF test bench (see Fig. 60). For this conditioning the grill antenna proper was used as an interface between the klystron amplifier and the microwave power dump. The window section passed the usual tests with full HF power (H_2 at 2×10^{-4} mbar, magnetic fields variable up to 1 tesla). It is now ready to be inserted between a (shortened) front-piece with straight waveguides and the grill antenna so that the rear part of the grill antenna can be pressurized (to avoid HF-breakdowns).

[1] Till 31.8.1984
[2] CEN Grenoble
[3] CEN Grenoble, till 31.7.1984

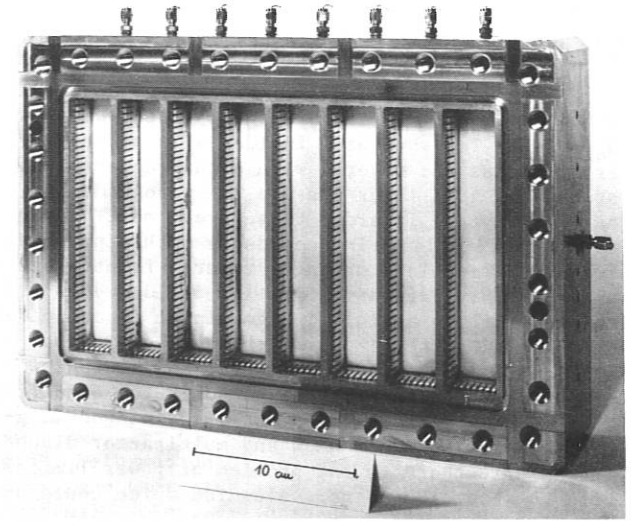

Fig.60: Microwave window section with eight UHV-tight alumina windows which can be replaced individually in case of failure.

5.2.3 16-waveguide coupler

The plans to build the 16-waveguide grill for preferential electron heating were approved. A proposal, jointly submitted by CEN Grenoble and IPP Garching, was granted EURATOM Preferential Support. The coupler will be built under IPP responsibility with microwave components purchased by our French partner. The antenna is designed to fit the existing interface to the ASDEX vacuum vessel. It will emit a power spectrum with $\langle N_{\parallel} \rangle = 6.4$. The waveguides will be made of OHF-copper. When they are connected to the 8 klystron amplifiers, the necessary power splitting and phase shifting will be accomplished by adjusting external waveguide components. The 16 entrance vacuum windows will be of the same type as those used in the eightfold window section (see Sec. 5.2.2.).

The company selected after an international call for tender to build this grill coupler failed to meet the quality standards for the brazing tests of the copper parts required in the first stage of the manufacturing contract. A second call for tender had to be issued and a number of bids were received by the end of the year. One company proposes to make the 16 narrow grill waveguides from seamless copper tubes of rectangular cross-section.

5.2.4 RF test bench /143/

During one of the shut down periods of the ASDEX machine the whole grill antenna was brought over to the test bench in order to check whether it had been damaged by internal HF breakdowns. After a few of the standard-size entrance windows had been replaced the antenna waveguides were found to transmit the full available HF power again. Various $\lambda/2$ vacuum windows of reduced height, built by IPP as well as by outside manufacturers, were tested and conditioned. They will be needed as entrance windows of the 16-waveguide grill antenna under development (see Sec. 5.2.3 above).

5.2.5 LH theory

In addition to routine ray tracing and coupling calculations, a few new problems suggested by the experiments on LH current drive were explored.

In the first place, we investigated the possibility that scattering of the externally excited waves could explain the brodening of the $N_{\parallel}$-spectrum, which is required to interpret the observed interactions with the electrons. The ray-tracing code has been adapted to take into account irregularities of the magnetic field configuration (magnetic braiding, islands, ripple). The resulting broadening (10 % to 30 %) is too small to explain the observations. An extension to include the more effective scattering on density fluctuations is in progress.

In the second place, we re-formulated the theory of parametric decay within the formalism of geometric optics. This should make it possible in future to extend the ray tracing code to describe also modifications of the spectrum due to parametric decay.

5.3 Ion Cyclotron Resonance Heating (ICRH)

(F. Wesner, J. Bäumler, F. Braun, R. Fritsch, F. Hofmeister, E. v. Mark, J.-M. Noterdaeme, S. Puri, M. Söll, K. Steinmetz, H. Wedler; ICRH Group (Technology Division))

The HF technical equipment for ICRH in ASDEX and W VII (HF generators and transmission lines to the experiments[1,2] was completed in 1984. In ASDEX two antennas have been installed and first heating experiments have been carried out (see Sec. 1.6).

Further work on ICRH is described in the sections on the Technology Division, the W VII experiment, and of the ASDEX-Upgrade design.

[1] F. Wesner, et al., Proc. 3rd Joint Grenoble-Varenna Intern. Symposium on Heating in Toroidal Plasmas, pp. 429-435, March 1982

[2] F. Braun, et al., Proc. 12th Symposium on Fusion Technology, (1982), pp. 1393-1398

5.3.1 HF-Generators and transmission lines

The two 1.5 MW generators[1], developed by industry, have been installed and tested at full nominal power and with pulse lengths of up to 10 s. They are tunable within a frequency range of 30 - 115 MHz, the full output power being available up to 80 MHz. Twelve discrete frequencies are to be preprogrammed in order to allow easy and fast frequency changes. The high-power amplifier stage is of strong coaxial design, the input and output circuits and the grid-screen-grid circuitry consisting of coaxial lines with different impedances and adjustable lengths. Water and high-voltage feeding lines are made from $\lambda/4$ stubs.

Coaxial lines transmit the HF-power to the two experiments, where large double-stub tuner systems are arranged to match the line impedance to that of the antennas. DC breaks, built of coaxial foil capacitors, insulate the experiment and generator against low frequencies. The generators can be optionally switched to either of the two experiments, to dummy ohmic loads or to the test bed by means of coaxial switches.

5.3.2 Antennas

Two uncooled loop antennas for ASDEX have been completed, tested and installed (Fig. 61). They are arranged at the low-field side of the plasma, fed at both ends, and short-circuited in the midplane, being capable of launching 1.5 MW each. Their design is based on two- and three-dimensional calculations[2]. The loops are made of silver coated stainless-steel plates. The optically opaque Faraday screens, for polarizing the radiated waves and shielding the antennas against the plasma, are composed of T-shaped stainless-steel rods coated primarily with copper to reduce the HF losses and then with a plasma compatible titanium carbide layer. To investigate the influence of the geometry or materials on the antenna characteristics, Farady screen elements and central loop conductors can be changed within the vacuum vessel. The electrical length of the antennas can be varied by additional capacitive elements. For the first experiments it was adjusted to about $\lambda/4$ for each half-antenna. To allow 10 s HF pulses, water-cooled elements are being developed.

5.3.3 Control system, data acquisition

A control system has been developed which allows the HF system to be operated not only at the generator site, but also remotely from the W VII control room and from the test bed. Primary functions, including personnel and equipment safety, are implemented by a free-programmable control and relay circuitry.+ Parameter settings for timers and remote displays are handled by microcomputer circuitry and asynchronous data links.++ The power output of the generators and a frequency offset (relative to the mid-frequency of one of the 12 present frequency channels) can be controlled as time functions according to computer-stored tables.

An autonomous data acquisition system with a PDP 11/44 was installed. Its task is the data acquisition and archiving of mainly technical data, such as there are detector data of voltage probes and directional couplers and data from thermal or pressure sensors. These data serve for calculating the antenna impedances and the power delivered to the antenna via the matching network taking into account various frequency-dependent corretion factors. The computer is located near the HF-generators. A CAMAC Serial Highway System links it with the remotely located equipment at the experiment sites. This high-speed optically coupled link gives fast access to the experimental data. The

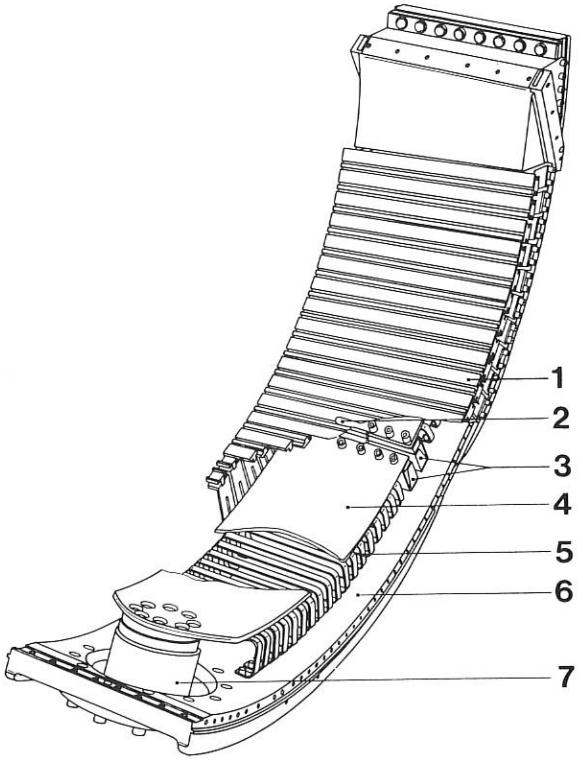

Fig.61: Schematic view of one ASDEX antenna (1 Faraday screen, 2 diagnostic window, 3 short-circuits, 4 central conductor, 5 capacitive loading, 6 return conductor, 7 feeding point).

[1] W. Schminke, F. Hofmeister, F. Wesner: Proc. 10th Symp. on Fusion Engineering, Philadelphia 1983

[2] M. Söll, F. Wesner, Proc. 10th Symp. on Eng. Problems of Fusion Research, Philadelphia, 1983

+ in cooperation with W.Jakobus, and F.Lollert / ZTE (Central Technical Services)

++ in cooperation with R.Ammer / ZTE

computer is compatible with the experiment computers. Technical and physical data can thus be requested by users at both computers.

Both the ASDEX and the W VII ICRH data acquisition were in operation at the end of 1984, but a large part of the software needed for tuner positioning and possible closed-loop matching has still to be completed.

5.3.4 Diagnostics

Particular attention is paid to HF related diagnostics to measure the electrical and thermal characteristics of the antennas or possible discharges in them as well as the physical phenomena in front of the antennas and in connection with wave propagation, absorption and impurity production. In addition to the extensive standard diagnostics of ASDEX, the following main methods are available: Fast monitor diodes observe the development of the H_α-light (i.e. essentially the neutral gas density) in front of the Faraday screen of the antenna, and in front of the carbon tiles of the antenna guard limiter. The impurity production at the antenna surface is observed with a multi-channel spectrometer looking directly onto the Faraday screen, while the impurity concentration of the plasma is measured separately. A high-speed cine film camera (time resolution of up to 1 ms) and a motorized standard camera (3 pictures per second) view the antenna from an opposite position on the torus. Several small B-field coils are installed around the torus to collect information on the HF mode structure. The antenna itself has built-in current and voltage probes as well as several temperature probes (thermocouples) at various positions of the Faraday screen and short circuits. Gas puffing is also possible through the midplane of one antenna.

5.4 A Centrifugal Pellet Accelerator for Quasi-continuous D_2-Pellet Injection into ASDEX

(W. Amenda, H. Birkmeier, D. Jakobi, R.S. Lang, G. Prausner, JDP Group, R. Ammer, ZTE)

The centrifugal pellet injector with a new, fast direct pellet feed has been constructed and tested (Fig. 62). The new concept of the D_2-rod feed results in a feeding time lower than 2 ms. Thus the centrifuge can now be fed up to a rotation frequency of 500 Hz. Till now the results are:

pellet velocity $v_p \leq 720$ m s^{-1};
pellet frequency $f_p \leq 50$ Hz (pellets per second);
pellet exit scattering angle of less than $\pm$ 1.4°;
series of pellets with up to 65 pellets have been accelerated.

Furthermore, we injected the pellets into a microwave tube (7 x 3.5 mm^2). Such a guiding tube reduced the exit scattering angle to $\pm$ 0.5°.

In January 1985 the pellet injector will be installed on ASDEX for fuelling and plasma profile shaping experiments.

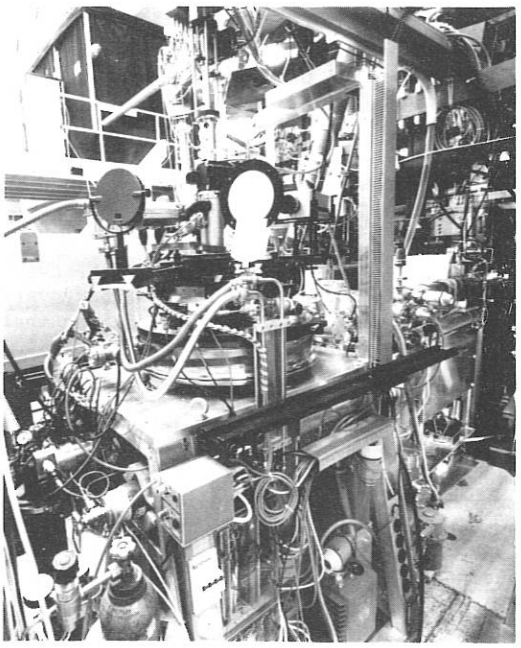

Fig.62: Centrifugal pellet injector for ASDEX.

ASDEX UPGRADE PROJECT

Head of Project: W. Köppendörfer

ASDEX Upgrade

M. Blaumoser, S. Cha, R. Chodura, K. Ennen,
J. Gruber, O. Gruber, O. Jandl, H. Kollotzek,
M. Kottmair, H. Kotzlowski, E. Lackner, K. Lackner,
M. Mahl, G. Mannhardt, P. Martin, J. Neuhauser,
J.-M. Noterdaeme, M. Pillsticker, R. Pöhlchen,
H. Preis, H. Röhr, G. Ryll, W. Schneider,
H. Schneider[1], U. Seidel, B. Streibl, M. Troppmann,
H. Vernickel, F. Werner, F. Wesner, A. Wieczorek,
R. Wunderlich, H.-P. Zehrfeld

[1] Interatom Bensberg

1. STATUS OF PROJECT

ASDEX Upgrade, the next step poloidal divertor experiment at IPP after ASDEX, has been designed to match the benefical divertor properties found in ASDEX with reactor requirements. The physical aims and the design principle of ASDEX Upgrade were described e.g. in/102/.

The time schedule for construction of ASDEX Upgrade aims at assembly of the tokamak system in 1987 and at the start of operation at the end of the same year. This meant freezing the tokamak system design in 1984 and placing the orders for all main tokamak components. Accordingly, construction of the shielding house had to be started. Considerable effort was necessary in order to conform to the reference data of the system because the detailed designs proved to be difficult for reasons of space and material stress, particularly with regard to the poloidal field coil system and its interference with the TF magnet and vacuum vessel.

By the end of 1984 all major components had been ordered: the TF coils, the TF coil turn-over support structure, the ohmic heating coils OH1 and OH2, the divertor coils V1, the poloidal field coil support structure and the vacuum vessel. The calls for tender of the V2 and V3 coils were formulated.

Several reasons favoured an extension of the flywheel generator energy supply of IPP. Although the layout of ASDEX Upgrade took into account the existing energy supply facility, the power and energy requirements became more stringent especially owing to the incorporation of neutral injection heating and increased power as required for plasma stabilization. A call for tender of a 220 MVA, 650 MJ generator was therefore issued. It was ordered in December 1984 from Siemens. This now allows the electrical circuits of the different coil systems to be simplified and separated, thus providing more flexibility of operation.

Since the different coils and the support structure will not be manufactured exactly in accordance with the time schedule originally envisaged, an assembly procedure was worked out which is largely independent of the exact delivery time of the vertical field coils. This was achieved by providing assembly of the toroidal field magnet and vacuum vessel without the lower poloidal spoke wheel and V-coils being in place already.

On the short time scale the vertical plasma position control relies on a passive saddle coil inside the vacuum vessel. The detailed design of this coil has been completed. It is adjusted to the single-null (SN) $\beta_p = 2$ configuration and therefore, since it has to be close to the plasma, it is not symmetric to the torus midplane. This fact complicates plasma control and stabilization by coupling radial and vertical plasma motion. It affects the torus assembly considerably because the loops have to be composed of half sections, which also requires that the torus be assembled in separate halves.

The following work on the periphery of the tokamak system was done: Construction of the shielding house (2 m thick walls, 1.8 m thick ceiling) was started in August 1984. The doors and openings for supply and diagnostics were optimized by KWU for shielding a yearly neutron flux fluence of 10^{19}. This corresponds to about 500 discharge seconds in deuterium

at full plasma parameters. The building in which the shielding house is at present being erected is also being adapted to the needs of preassembly, diagnostic preparations, cooling supply, electric circuits, machine control and data acquisition installations. The planning of the tokamak system periphery was concerned with the compatible arrangement of electric power connections, cooling pipes, ICRH and NI heating systems and diagnostic apparatus.

The machine control and safety system is being conceptually worked out by IPP and Siemens. This started with the definition of component control and the location of measuring gauges with which the coils and support structures have to be equipped. The programmed control system is still under discussion.

A plasma heating power of 12 MW for up to 7 s provides the required energy flux density of 0.3 MW m^{-2} in the plasma boundary. At present all possible heating methods are again being discussed with regard to the application for EURATOM preferential support. The intention is to alter the original preference for 12 MW 2nd harmonic ICRH to half neutral injection and half ICRH. Although good heating results with ICRH have been reported from other tokamaks, the experimental basis still does not seem solid enough to rely solely on 2nd harmonic ICRH. The development work on ICRH generators, transmission lines and antenna design is described below. For neutral injection the use of 2 boxes of the TORE SUPRA type injection with 2 sources each and a H° particle energy of $\leq$ 80 keV is being considered.

In October 1984 the diagnostics needed for ASDEX Upgrade were discussed in a workshop at "Schloss Ringberg" attended by experts from ASDEX, ASDEX Upgrade, and PWW and a few from foreign laboratories. The outcome was a classification of diagnostics into three groups. The first encompasses what is necessary to start plasma operation including configuration control and stabilization. The second covers what is actually needed to achieve the physical aims of ASDEX Upgrade as defined by the EURATOM proposals[1,2,3]. The third group addresses diagnostics needed for further analysis of the plasma.

The diagnostic data acquisition system is being worked out by the Computer Science Division of IPP. The hardware and software development is concerned with an autonomous diagnostic subsystem (AD) and a central data analysis system (CDAS). The systems are interconnected by fast transfer lines. The AMOS/D file structure allows easy and distributed access to all data. In 1984 a diagnostic substation, using a CADMUS computer, was installed for testing the subsystem and the transfer line of 100 kbyte/s to a communication node which has to interlink the approx. 20 subsystems with the XA main computer.

In the following, details of more important results of the work in 1984 on ASDEX Upgrade are described. The tokamak system and the components are described with respect to those problems whose solution required special attention and effort. Experimental results on ß-limits in tokamaks /122/emphasized the necessity of taking measure to achieve larger ß. The possibility of producing bean-shaped plasmas as well as larger elongated $\kappa \leq 2$ plasmas was therefore investigated. However, the boundary condition was not to degrade the reference SN (I_p = 1.6 MA) plasma configuration. Otherwise all measures are taken to allow for these options.

The problem of plasma positional control and stabilization was tackled with an ideal two-dimensional MHD code with a complex system of external conductors and a lumped parameter model for the electromagnetic interactions between the plasma motion and external passive structure and active coils.

2. THE ASDEX UPGRADE TOKAMAK SYSTEM

2.1 Toroidal Field (TF Magnet)

2.1.1 TF coils

The TF coils have been under construction at ANSALDO since January 1984. There was an option between winding (like the JET coils) and assembling already bent half-turns (prebending method, PBM).

The PBM, proposed by ANSALDO, calls for joining the half-turns by brazing them to elevate the last turn assembled about 30 cm from the coil former. After tests with a 6-turn model the PBM was chosen and it was decided to assemble the lower and upper pancakes of a coil simultaneously. This avoids the large elevation displacement of 70 cm otherwise required for the innermost turn of the upper pancake (pancake thickness 40 cm).The simultaneous assembly of the two pancakes requires a combined turn and pancake insulation. Extra glass fabric tapes forming the pancake insulation are fixed along the short edge of a conductor during taping of the turn insulation. Additionally, there will be a glass rope inserted between adjacent turns of the coil midplane (Fig. 1).

To prevent gas bubbles forming during vacuum impregnation, ANSALDO will flush the coils with carbon dioxide, since the solubility of this gas in resin is 20 times better than in air. The impregnation of a beam with the original coil cross-section and a length of 2 m has demonstrated the usefulness of this method. It is therefore no longer necessary to keep the lid of the mould open during vacuum impregnation.

A resin system combining high strength and large ductility was developed by means of a test series. The tensile strength of the resin at a strain velocity of 3 %/min is shown in Fig. 2. The tensile rupture strain reaches more than 9 % throughout.

Rupture tests with a JET shear specimen yield for the glass epoxy insulation a remarkable rupture strain of over 30 %. The rupture is still determined by adhesion to the copper surface. To improve adhesion, first the diluting agent of the DZ 80 N primer was investigated. Best results were obtained with butilic alcohol at the main working temperature of 40° C, the shear strength obtained being 51 Mpa with a scatter of $\pm$ 2 Mpa. In a second step the sand-blasting parameters will be investigated.

---

1 IPP Report No. 1/197 (1982)
2 IPP Report No. 1/211 (1982)
3 IPP Report No. 1/217 (1983)

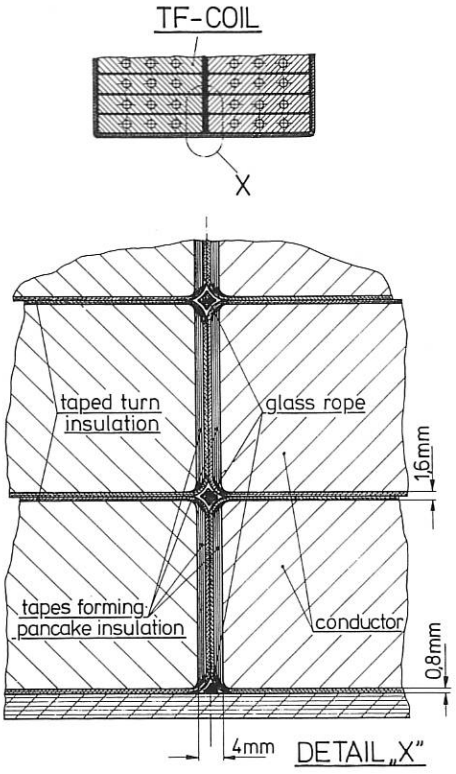

Fig. 1: TF-coil insulation.

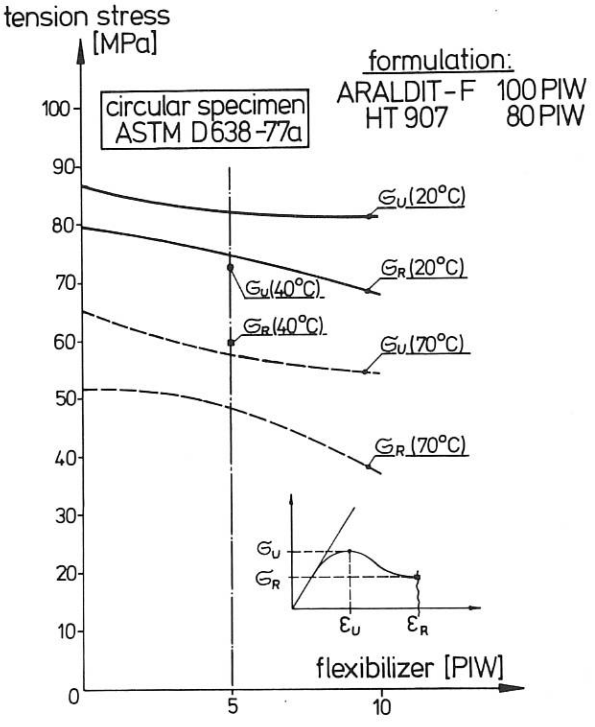

Fig. 2: Tensile strength in dependence on flexibilizer content.

It is known from JET that high-strength brazing of large copper cross-sections is difficult. The turn cross-sections of these TF coils are even larger (180 mm x 32 mm). ANSALDO have not yet achieved the specified rupture strength (200 Mpa). The main reason for the lower strength obtained (150 Mpa) is to be found in the excessive temperature gradients, which cause gaps and misalignement of a joint during inductive heating and brazing. It is expected that the improved design of the split coil antenna, limiting the temperature differences to ± 15° C, will increase the strength of the brazed joints.

ANSALDO have bought a new brazing generator. First tests are in good agreement with computations for the annealed length of the brazed joint. The annealed length can be kept below ± 70 mm with this generator.

2.1.2 Turn-over structure (TOS)

The TOS has been under construction since August 1984. The German company MAN is the main contractor, being responsible for the final machining and preassembly of the structure. The subcontractor for casting and proof machining is the French company FAM near Rouen.

In order to keep the stressing of the TF coils as small as possible, an austenitic steel casting was chosen and a high Young's modulus E ≥ 190 GPa valid within a stress level of 150 Mpa was specified.

To achieve a large region of linear stress-strain behaviour, FAM first tried to block dislocations by filling the interstitial lattice locations of a basically Cr-Ni alloy with small atoms such as carbon and nitrogen. In addition, the effect of creating precipitations by means of small fractions of Nb and Mo in conjunction with suitable heat treatment was studied. The efforts resulted in a pronounced increase of the yield and rupture strength.

The E-modulus is mainly influenced by the elements at the main lattice sites. Best results were obtained by substituting part of the Ni by Mn, which also stabilizes the austenitic phase. The resulting alloy, similar to the American standard AISI 202 or to the German standard 1.3965, shows good homogeneity of the E-modulus over the wall thickness. After heat treatment E = 200 Gpa is established within ± 5 %, the yield limit reaches 300 Mpa, the rupture stress becomes almost 600 Mpa, and the rupture strain (A_5) shows about 50 %. The material properties achieved are thus very satisfactory.

2.2 The Poloidal Field System

2.2.1 Poloidal field coils

More exact calculations considering the vacuum vessel eddy currents when the plasma is formed showed the need for an additional OH compensation coil. The poloidal field system now consists of (Fig. 3)
- ohmic heating coils OH1, OH2, OH3
- vertical field coils V1, V2, V3
- internal and external coils for stabilization and compensation CoI, CoA, CoOH.

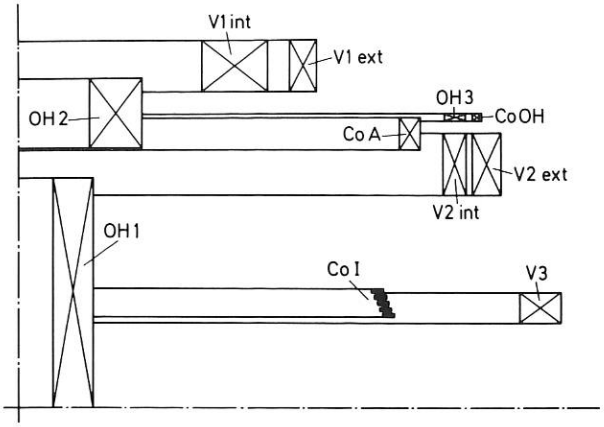

Fig. 3: Poloidal field coil distribution, upper half.

The ohmic heating coils OH1 and OH2 are being manufactured by BBC. Various electrical and mechanical tests with insulation and brazing of conductors were conducted as a part of the manufacturing contract. The results meet the requirements. A considerable decrease in dynamic strength within the insulation (five times less than the static strength) was observed for a high number of pulses. In comparison with other results, we evidently have to take into account inter-relations between the strength and load pulse frequency. Additional tests will be carried out in order to determine this interdependence for the coil insulation chosen (glass fibre, kapton, epoxy resin).

An advantage is gained by winding the OH1 coil directly on the cylinder as part of the PF coil support structure. The force to be applied for correct bending of the conductors is about 12 x 10^4 N. The current feeds and water inlets and outlets are applied to the front ends of the OH1 coil: Assembly problems due to lack of space forced us to develop complicated connection systems for current and water.

High control currents for plasma stabilization in the V and Co coils induce electromagnetic forces which cause changes in the design of the V coils and holders.

In the mean-time a contract for manufacturing the V1 coils has been signed with BBC. The V1 coils consist of two coil units each, separately mounted to the 16 beams of the PF support structure. The holders guarantee central positioning and also allow moving of the coils in accordance with thermal and magnetic forces, thus causing an insignificant increase in stress. The insulation system of the V1 coils will be glass fibre-kapton-epoxy resin. All the current connections and water inlets and outlets will be applied to the front ends of the coils. The connection to the transmission lines are therefore above or below the PF support structure.

Characteristic data of the V1 coils are:

	V1 internal	V1 external
Design	cylindrical coils	
Number of cylinders	10	4
Central radius (mm)	1486,5	1952
Coil cross-section (mm^2)	451 x 366	190 x 366
Number of windings	66	27
Max. current density (kA cm^{-2})	3.25	
Max. temperature difference (Kelvin)	45	

For the V2 coils, the OH3 coil, and the CoOH coil the latest design provides for a coil formation which will be supported by 32 holders moveably attached to the PF support structure. Stresses caused by thermal effects can thus be avoided. The insulation system of all coils mentioned is identical to that of the V1 coil.

Characteristic data of the coils are:

	V2 internal	V2 external
Design	cylindrical coils	
Number of cylinders	4	4
Central radius (mm)	3015	3232
Coil cross-section (mm^2)	168 x 442	207 x 442
Number of windings	40	48
Max. current density (kA cm^{-2})	3.9	
Max. temperature difference (Kelvin)	48	

The coils OH3 and CoOH consist of 5 and 2 windings, respectively, designed as pancake coils which will be assembled above or below the V2 coils. The V2 and OH coils must be separate from each other for sliding in the event of different loading.

The CoA coils will be separately attached to the PF support structure by 16 holders. Moveable holders avoid coil stresses by thermal effects. The main data of the coil are:

	CoA
Design	cylindrical coils
Number of cylinders	4
Central radius (mm)	2700
Coil cross-section (mm^2)	150 x 220
Number of windings	24
Max. current density (kA m^{-2})	1.5
Max. temperature difference (Kelvin)	35

The concept of the CoI coil has not been changed (see Annual Report 1983). Tests performed on winding joints of this coil supported the design and led to several improvements.

2.2.2 The poloidal field coil support structure

Production of the poloidal field (PF) coil support structure was awarded to the DWE Company, Deggendorf, Germany. Of the cast and welded steel versions the latter was chosen. As already described, this consists of two spoke wheels connected by 16 vertical beams, all with double-T profile. The central hub, which carries the OH1 and OH2 coils, is being made from cast austenitic steel by a subcontractor to DWE. Sixteen columns support the framework on the floor (Figs. 4 and 5).

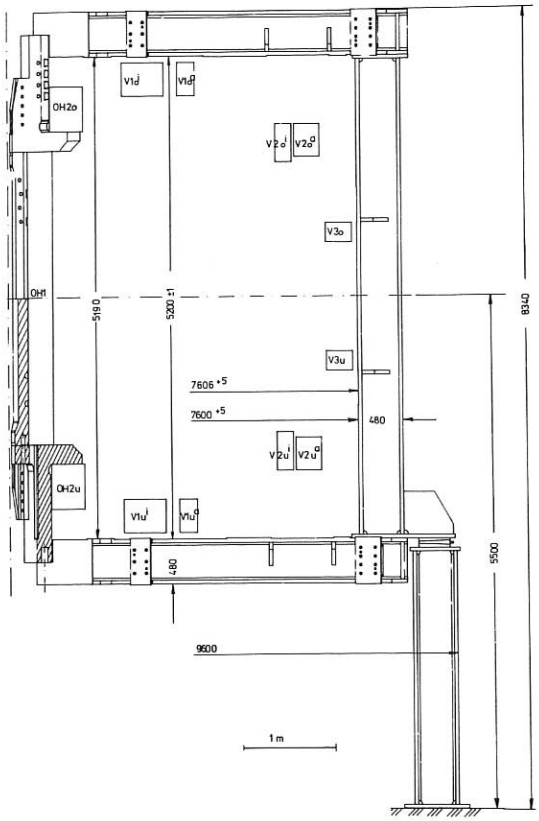

Fig. 4: Vertical cross-section of the PF support framework.

The design was based on extensive FE calculations for the numerous load cases of single-null, double-null and limiter-controlled plasma configurations. The structure was idealized by means of beam and shell elements. Because of the symmetry it was sufficient to model just one octant. For the maximum load and infinite load cycles a safety factor of 1.5 was chosen. The largest deformation, a vertical displacement of the V1 coil, does not exceed 8 mm in any of the load cases.

Construction of the PF support framework with welded beams required manufacture of a test beam 4 m in length. This was done in order to test the deformation by welding, the form stability during machining, and the welded seams. Test samples from this beam were examined by metallography, notched bar impact tests, tensile stress tests and cyclic load tests. Satisfactory results allowed the start of series production of this beam.

2.3 The Vacuum Vessel System

2.3.1 Vacuum vessel

The design of the vacuum vessel as described in the Annual Report 1983 was finalized, the call for tender released and the contract signed. The major change of the design concerns the connection of the octants. The flange connection with Helicoflex O-rings was replaced by a welding seam. This change was prompted by the fact that the passive stabilization loop prevents replacement of the O-rings in the event of a leak.

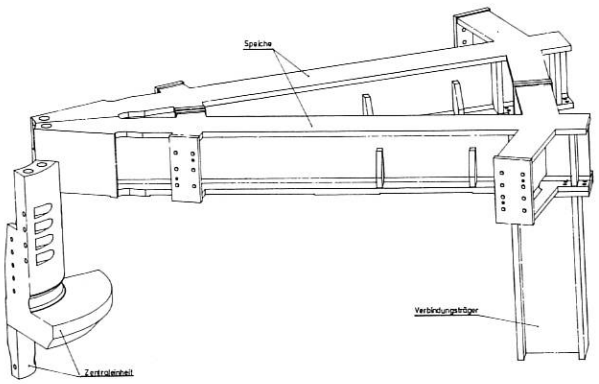

Fig. 5: View of two spokes of the upper part of the support showing also a section of the central OH2 support.

As in all tokamaks, the major mechanical load occurs during a hard disruption. This was studied in more detail as an extension of earlier calculations[1]. The eddy current distribution and the magnetic forces were calculated by the FEDIFF FE-code[2]. For the single-null case the code has to be extended to include cases without up-down symmetry. The distribution of eddy currents and the resulting forces were calculated on the assumption of a linear current decay with $\dot{I}_p = 4 \times 10^8$ A s^{-1}. It turns out that all force components reach their maximum at about the same time around the end of the current decay. They then decay (non-exponentially) on a time scale of 10 to 30 ms. The calculated current distribution is a superpositioning of a toroidal current which is a function of just the poloidal position and the saddle current which develops on each octant. The forces are considerable. For example, the force component directed normally to the vessel surface can locally attain 2 MPa. Stress calculations were performed with the forces at the time of their maximum as static load. This is on the safe side. The calculations (performed by CDC) confirm the soundness of the design. In the single-null case additional forces occur on the vessel support owing to the lack of up-down symmetry; they are also within tolerable limits.

2.3.2 In-vessel components

For the divertor plates an alternative design with active cooling of the graphite was developed. In this design graphite tiles are brazed to cooling tubes of Mo. Figure 6 illustrates this design[3]. Thermal tests were performed in a vacuum test stand with radiation heater. The maximum power available was 3.8 MW/m² on the surface of the graphite, which could be removed in the steady state. The tests

[1] O. Jandl, H. Kotzlowski, P. Martin, F. Werner, Fusion Technology, 309 (1982)
[2] H. Preis, Archiv für Elektrotechnik 65, 233 (1982)
[3] Brazing technology developed by Metallwerke Plansee, Reutte, Austria

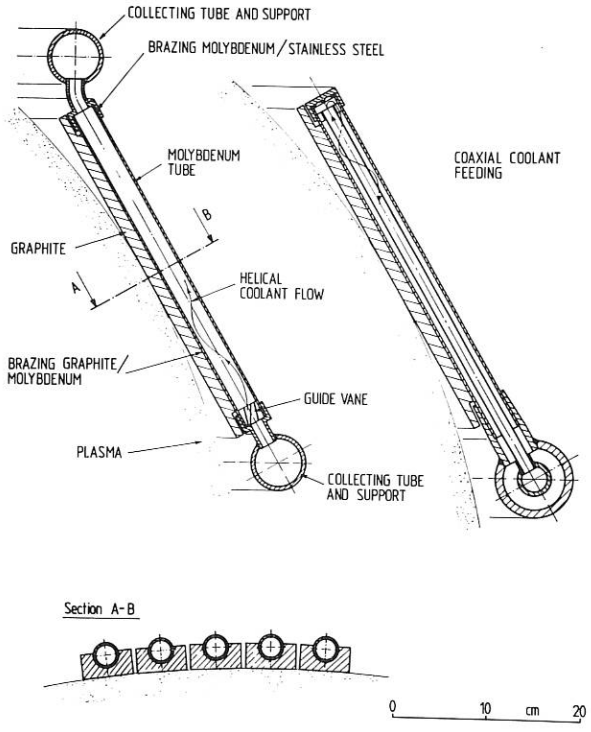

Fig. 6: Concept of the active cooling of the graphite target plates.

were supplemented by FE-calculations of the temperature distribution and stress. The calculations indicate that fluxes of up to 5.5 WM/m^2 should be possible without surpassing the maximum permissible temperature of the braze. More details may be found in /135/.

Stress analysis for the in-vessel components in the case of a plasma disruption was performed. The components are subdivided into sections in order to reduce thermal stress and eddy currents. This facilitates estimates of the disruption forces, since the L/R time constant of the individual parts are usually small compared with the duration of the disruption t_D. The sections may thus be treated as loops carrying a constant induced current during t_D, which in turn gives rise to torque. The resulting stresses have been shown to be within tolerable limits. The high electrical resistivity of graphite is favourable for reducing the induced currents compared with metal plates of similar thermal capacity.

2.3.3 Pumping system

The pumping system has been planned in more detail, no important changes having been made. The stray field of the poloidal field coils is so large at the position of the turbo-molecular pumps that magnetic shielding is necessary. Calculations allowing for the necessary openings indicate that a box of 4 cm thick soft iron sufficiently reduces the magnetic field.

2.3.4 Theoretical investigations of the plasma in the divertor and neutral gas in the divertor chamber

The calculations mentioned in the Annual Report 1983 have been improved by calculating the plasma parameters self-consistently with the SOLID code coupled to the DEGAS neutral particle code. The procedure is described in the section on ASDEX. The conclusions presented last year did not change significantly. In particular, it was confirmed that, for sufficient energy input to the divertor region, a high-density, low-temperature plasma develops in that region, closing the divertor to neutral hydrogen in spite of the open geometry. It was also confirmed that only 20 % of the energy input to the divertor region is distributed to the walls of the divertor chamber, while 80 % is deposited on the divertor plates. The behaviour of He, which was treated as a minority, was also studied. In contrast to all other impurities He neutralized at the DP is re-ionized outside the region of strong recycling. This is illustrated in Fig. 7. This effect may be of significance for the pumping of He "ash".

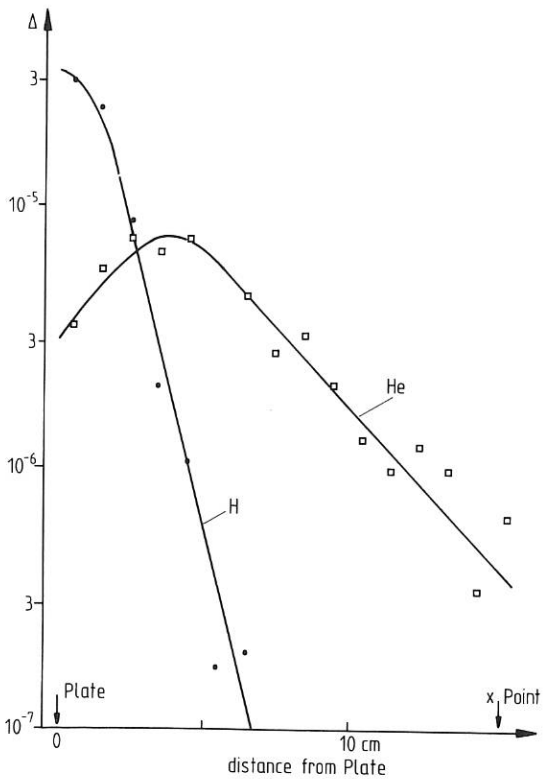

Fig. 7: Ionization rate Δ/cm^3 s and per ion neutralized at the target plate. The abscissa is the distance from the plate along the separatrix.

2.4 The Energy Supply of ASDEX Upgrade

ASDEX Upgrade was designed under the boundary condition of utilizing the existing IPP flywheel generator energy. Considerable effort and investment for rectifiers and switching gear were required in order to reach marginally the reference data. This additional installation brought no advantage for other users of the generator facility.

A change in heating power from ICRH to half ICRH and half neutral injection requires an additional pulse power of 25 MVA and a pulse energy of 100 MJ.

The energy supply concept for ADSDEX Upgrade was therefore altered as follows:
- supply of each coil system, TF and PF, by a separate generator to avoid switching between diffe-

rent coil systems;
- provision of a sufficient margin of power and energy for safe operation at the reference data, including the neutral injection heating option;
- increased availability of the pulse energy supply, e.g. to compensate for servicing and repair of the older installations.

This led to the issue of a call for tenders for an additional flywheel generator with the following data:

Pulse power	220 MVA
Pulse peak power	260 MVA
Pulse energy	650 MJ
Frequency	86 - 110 Hz
Motor power	7.5 MW

In December 1984 a horizontal-shaft generator meeting the above data was ordered from Siemens. At the end of 1987 a pulse power of 500 MVA and a pulse energy of 2.5 GJ will be available for ASDEX Upgrade. The main switching installations are located close to the experiment in the experimental hall L6.

The NETASIM nonlinear network program was bought from AEG Berlin in order to simulate the poloidal field coil supply circuits. At present the OH circuit is being optimized with vacuum tube breakers and alternatively with multiple thyristor switches. Offers from industry were obtained for both versions. The requirements for the supply of the plasma position control coils (V and Co coils) are still the subject of theoretical calculations for minimizing the required peak power. Phase-controlled or force-commutated rectifiers are under discussion. Experts from industry and research institutions have been contacted.

2.5 Crane for Tokamak System Assembly

In August 1984 the main crane for torus assembly was ordered from the Häupler-Werke company. It is a specially designed crane meeting the following requirements:
- minimized distances from hook to walls in order to cover a large area;
- large clearance in height in order to allow OH1 coil assembly from top;
- starting and stopping without jerks in order to avoid swinging of the loads;
- motion velocities down to 0.5 mm/s in order to fit parts precisely during assembly;
- total carrying load capacity of 64 tons.

A one-beam bridge crane with two trolleys of 32 tons capacity was chosen to meet the demands.

Perpendicular and parallel horizontal and vertical motion of 0.03 to 2.5 m/min are provided by an infinitely variable D.C. motor. Velocities of 12 m/min are possible by means of additional induction motors. The two trolleys can be moved separately or together with one control lever.

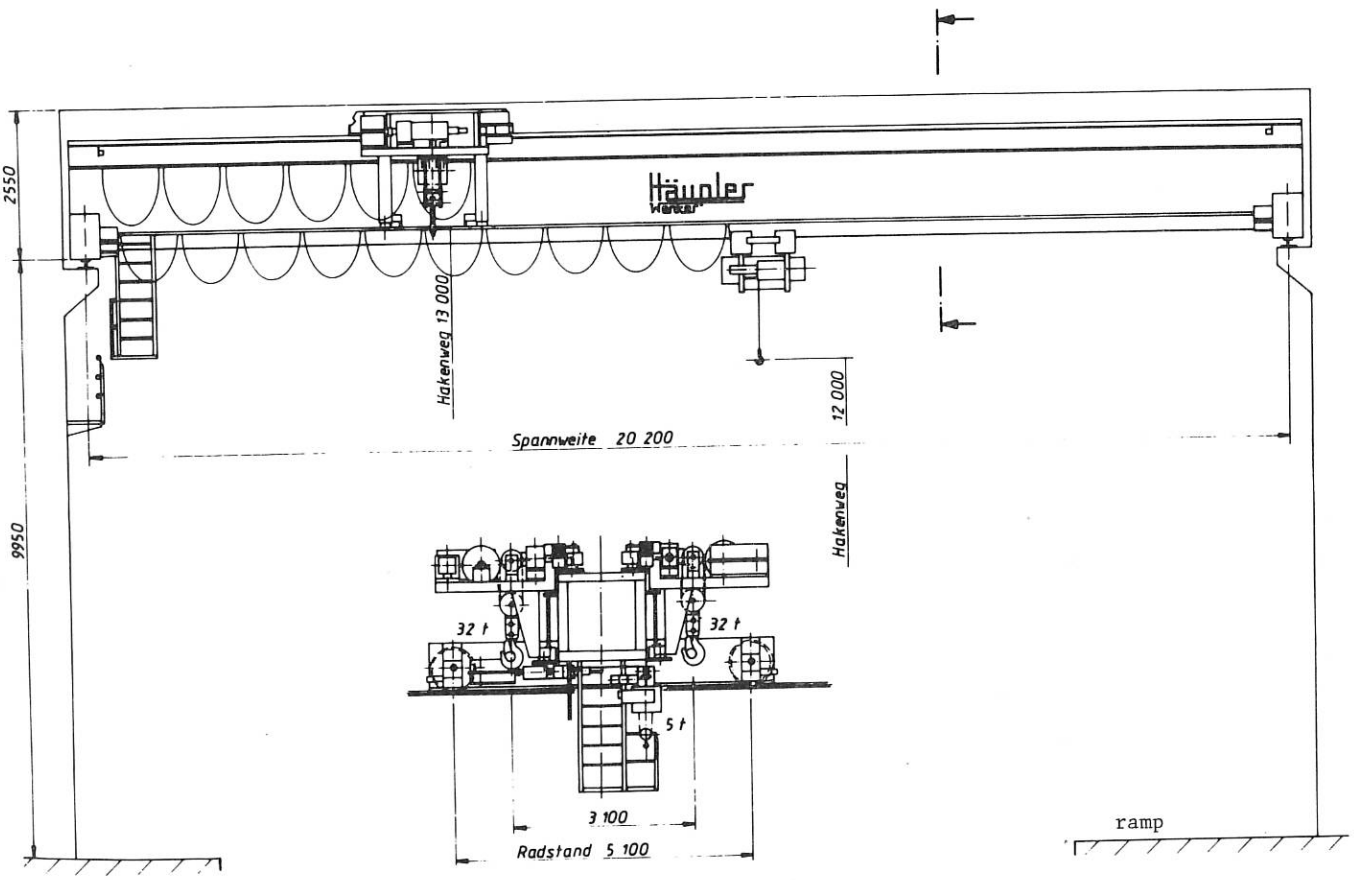

Fig. 8: The 2 x 32 ton crane of the torus hall.

For maximum vertical clearance the distance between hook and ceiling is 2100 mm. The hook is a special design which can be taken off so that the load can be connected to a bolt. The clearance can thus be increased by 620 mm to reduce the bolt (hook)-to-ceiling distance to 1480 mm (Figs. 8 and 9).

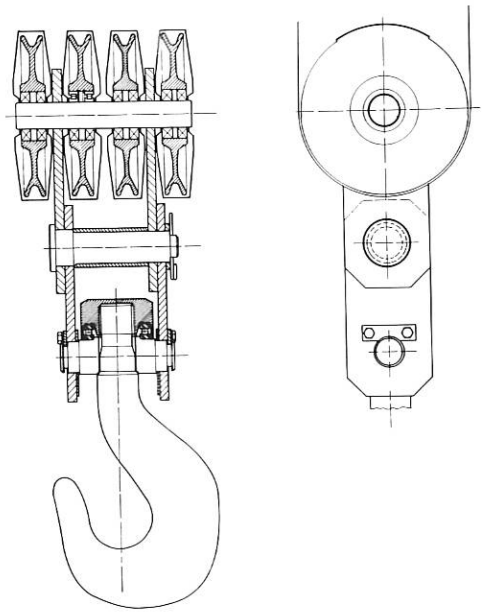

Fig. 9: The hook arrangement. The hook can be taken off and load connected to the bolt in order to gain clearance for OH1 coil assembly.

Control is achieved optionally by cable or wireless with a Theimeg transmitter. The crane is equipped with a 5-ton auxiliary hoist, separately moveable with a load and excess load monitor and limit switches.

The crane is accessible for servicing through gangways which are installed around all four walls of the torus hall.

Delivery and commissioning will be in spring 1985.

3. PLASMA CONFIGURATIONS AND POSITION CONTROL

3.1 High-ß Plasma Configurations for ASDEX Upgrade

Ideal MHD theory and experiments with additional heating power showed the existence of a ß-limit $ß \leq 0.03\, I/aB_t$ [MA, m, T], yielding for ASDEX Upgrade ß-values of 3.5 % for the SN reference case. Strongly elongated (with half-axis ratio $b/a \geq 2$) and bean-shaped plasmas allow for fixed q-value at the plasma boundary, essentially higher toroidal plasma currents I compared with circular ones with the same plasma cross-section, and, therefore, higher ß-values. Moreover bean-shaped plasmas offer the possibility of reaching the second region of ideal MHD stability. But resistive modes are still unstable and kink modes need strong wall stabilization. An additional problem is the positional n = 0 instability, which calls for passive stabilization elements near the tips of the bean.

The realization of bean-shaped and strongly elongated plasma configurations in ASDEX Upgrade was investigated by using also the OH2 coils as divertor coils and only one additional coil in the torus midplane (at R = 1.30 m) as pusher coil for the bean-shaped plasmas. For the latter, indentations $i = \frac{R_{min}\ (z = 0) - R_{min}\ (abs)}{R_{max} - R_{min}\ (abs)}$ of up to 0.3 can be produced (see Fig. 10). The stagnation points are inside the vessel structures (necessary for achieving the H-mode). The vertical forces acting on the OH and V coils have been calculated and are compatible with the coil supports envisaged. The MHD stability for the n = 0 and n ≠ 0 modes has to be calculated next.

If the passive stabilization of the n = 0 instability is taken into account, it is possible to have plasma configurations with increased elongation compared with that of the standard configurations, without additional coils being needed. The equilibrium parameters of the reference SN, a bean-shaped and a highly elongated SN plasma are given in the following for $q_s = 3.3$ and for ß values at the ideal MHD limit.

	Reference SN	High elongated SN	Bean-shaped
b/a	1.6	1.9	--
q_a	2.6	2.6	--
q_s	3.3	3.3	3.3
$ß_p$	1.6	1.6	1.6
ß %	3.3	4.2	7.4
$\frac{B_t\ [T]}{I\ [MA]}$	1.92	1.59	1.10

($q_a = \frac{5\, B_t\, a^2\, (b^2/a^2 + 1)}{I\, R\, 2}$; q_s = flux-surface-averaged q-value at the flux surface containing 95 % of the closed poloidal flux).

As the forces on the toroidal field coils exerted by the poloidal field limit the maximum achievable $I \cdot B_t$-values, the particular values of I and B_t cannot be given at present except for the case SN ($I = 1.5$ MA; $B_t = 2.9$ T). At the same plasma current the total plasma energy and hence the necessary heating power is about equal for all three configurations given in the table.

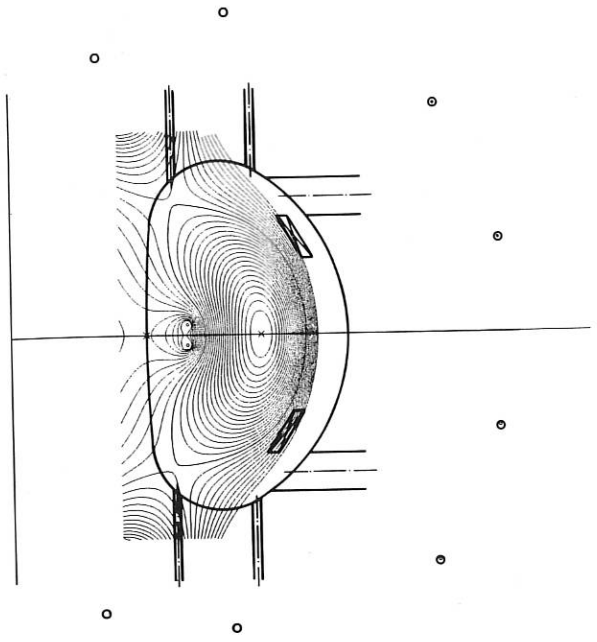

Fig. 10: A bean-shaped plasma fitted into the ASDEX Upgrade vacuum vessel using the existing PF-coils and one additional coil inside the vacuum vessel.

3.2 Free Boundary Flow Equilibria for ASDEX Upgrade

With the planned high-power neutral beam injection into ASDEX Upgrade, the possibility that the plasma may be far from motionless, and that it may not be in a static equilibrium but rather in a stationary flow regime has become more than mere speculation. Recent results obtained in PDX have shown features which are irreconcilable with a static state. Another reason for increasing interest in plasma flow equilibria is the possibility that flow may stabilize some MHD instabilities and allow operation at higher ß-values. Finally, there is evidence that some other heating schemes may also lead to plasma rotation. This has been the motivation for work on a free boundary flow equilibrium code capable of computing stationary plasma flow states maintained by the external magnetic field of the ASDEX Upgrade conductor configuration. At present, in the testing phase, equilibrium states up to toroidal Mach numbers M = 0.7 are under consideration.

3.3 MHD Equilibrium Sequences for ASDEX Upgrade

For studies of positional control and stability of high-beta plasmas we considered the time evolution of two-dimensional ideal MHD equilibria in magnetic fields of complex external conductor structures. Time variations were introduced into the system by resistive decay of the induced conductor currents as well as by active external (current or voltage) control. A systematic eigenvalue analysis of the homogeneous part of the system of tokamak circuit equations describing the passively conducting elements (including both discrete coils and continuous structures such as the vacuum vessel) leads to a quasi-analytic solution of the complete inhomogeneous system and a concise description of the nonlinear interaction between the continuous plasma medium and a certain set of individual external circuits. A numerical realization of this concept was applied to the ASDEX Upgrade configuration. The corresponding code, in its present state, is able to perform the following steps: (I) to calculate different plasma equilibria for constant circuit source voltages (dependent on the assumed initial distributions of poloidal current and plasma pressure). The flux contours for a particular ASDEX Upgrade single-null equilibrium are shown in Fig.11 (I = 1.0 MA, q_A = 1.0, $ß_p$ = 2.20, toroidal vacuum field at the position of the magnetic axis 1.74 T); (II) to determine isentropic and flux-conserving current density fields required for calculating the poloidal flux function, and to calculate all induced voltages; (III) to calculate the transient currents of the ASDEX Upgrade electrical circuit based on the eigenvalue analysis mentioned above.

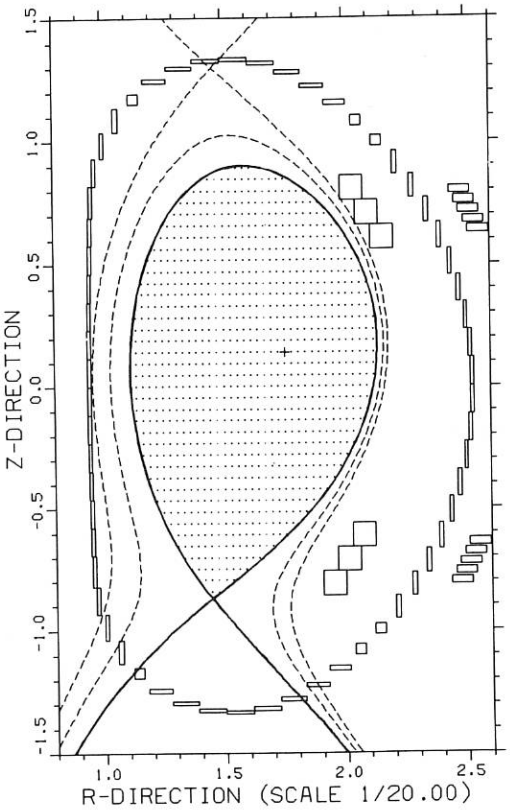

Fig. 11: ASDEX Upgrade single-null equilibrium configuration.

3.4 Plasma Position Control

The problems relating to the power and energy consumption of the fast plasma position control were investigated in more detail. For this purpose, a lumped parameter model of the electromagnetic interaction between the plasma motion and the outer poloidal field coils (including the fundamental modes of the vacuum vessel current) was combined

with an idealized PID controller model and the response of the system to a change in poloidal ß was analyzed. Besides the obvious influence of the uncertainties of the assumed disturbances, the results show a strong dependence on the plasma operation mode (high or low ß). The effort needed to control the unstable vertical plasma position increases as ß decreases.

To control the plasma position completely (R and Z) with the 2 control coils inside the TF coils CoI a power requirement of about 5 MVA for each coil was found to be sufficient for dealing with a change of - 0.2 of $ß + l_i/2$ in a 2 MA plasma. If for any reason position control has to be accomplished with outside coils, it proves advantageous to apply R-control with the V2 vertical field coils and Z-control with a pair of separate outer control coils CoA.

In any case, control of the plasma current proves indispensable for satisfactory position control action. A margin of 1 .. 1.5 kV in the OH voltage must be available for this purpose.

A collaboration contract with TU München was recently been concluded for the conceptual and detailed design of an overall control system suitable for coordinating all the control actions for proper guidance of the plasma discharge.

The detailed design of the passive stabilization loop system inside the vessel has been completed. Certain details concerning diagnostic openings and assembly problems are being investigated by means of real-size models of a vacuum vessel quadrant and a 180° stabilizing loop section.

4. ION CYCLOTRON RESONANCE HEATING (ICRH)

An additional heating power of 12 MW is required for ASDEX Upgrade, 6 MW to be provided by neutral injection, 6 MW by ICRH.

The preferred ICRH method is second-harmonic heating of hydrogen at frequencies of 80 to 120 MHz corresponding to the magnetic field of the experiment, the full power being necessary up to 100 MHz. An extension of this frequency range down to 60 MHz or even lower to allow minority heating too, is under discussion. The 6 MW HF power will be provided by 4 generators of 1.5 MW to 4 antenna pairs. The option to increase the power up to 12 MW ICRH by using all of the eight antenna ports envisaged is being kept open.

4.1 HF Generators

Generators for long 1.5 MW pulses in the 100 MHz range are not yet available, the limitation being the HF losses in the power tetrodes. A large tunable frequency range has already been achieved by the generator development for ASDEX/WVII (see ASDEX Sec. 5.3.1). In order to allow economic generator devices, study contracts have been placed with several companies to check the real limitations of available tetrodes or to study the possibilities of further development of valves and corresponding generators. Theoretical and first experimental investigations (the latter not yet being completed) have already given confidence that the new valve generation can provide the required parameters. These study contracts were instrumental in encouraging the industry to further developments.

4.2 Antennas

Each generator will feed one antenna pair. They are of the all-metal type and situated at the low-field side of the plasma. In the case of a dipole antenna, calculations were performed for the maximum voltage needed to couple 0.75 MW pro antenna (1.5 MW pro antenna pair) as a function of the antenna width and distance central conductor - return conductor.

For a distance central conductor - return conductor of 16 cm, this voltage varies from 39 kV to 15 kV when the width of the antenna goes from 4 cm to 32 cm. Slightly higher voltages (49 kV to 16 kV) are obtained when the distance central conductor - return conductor is decreased to 4 cm. Ray-tracing calculations are used to investigate the influence of the two parameters(width and distance central conductor to return conductor) on the absorbed power (rather than the coupled power only). Combination of the two calculation will result, within the constraints, in the optimal dipole configuration. Similar calculations will be performed for a quadrupole antenna.

Although only 4 of the 8 antenna boxes (B port plane) will be atfirst occupied by antennas, provision is made for fitting the 4 additional planes with antennas as well.

Each antenna box has 8 bushing with tapped holes on which the return conductor can be mounted. This return conductor serves at the same time as the structural base on which side pieces with limiters (graphite) and a cooled Faraday screen can be mounted (see Fig. 12).

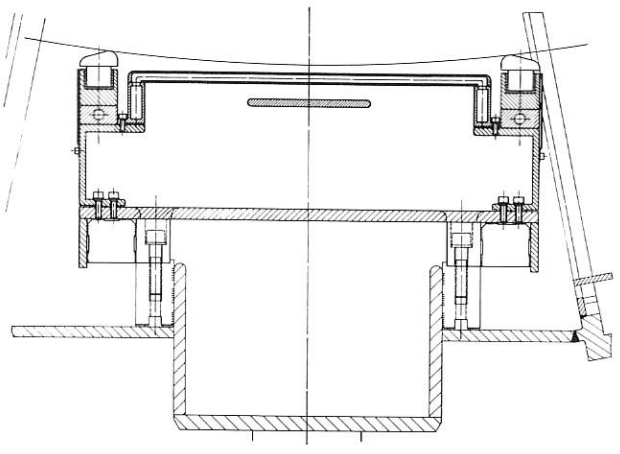

Fig. 12: Cross-section of the ICRH antenna.

By changing the side-pieces limited adaptation to the plasma contour can be realized without the need of new limiter pieces or a Faraday screen. Full use will be made of the experience gained from ASDEX

in choosing the configuration (open/closed Faraday screen) and the cooling of the Faraday screen.

4.3 Transmission Lines and Line-antenna Interfaces

To transmit the power from the generator to the antenna pairs 9-inch coaxial transmission lines are envisaged.

From each generator a single line goes to two stub tuners before splitting into separate lines to each of the antenna in the antenna box. An alternative solution with only one stub per line and frequency variation is being investigated.

Bellows in the inner and outer conductor of the transmission line are at present favoured to take up the thermal expansion of the vacuum chamber. Contacts with industry on cost and manufacture have been started and tests are envisaged for next year.

In-house development of a low-priced detachable feed-through is being pursued, while the possibility of using the design developed by Princeton or ORNL is being kept open.

5. IMPLEMENTING AGREEMENT ASDEX/ASDEX UPGRADE

A collaboration of IPP and US-DOE Laboratories is agreed for the investigation of toroidal plasma physics in and technology of tokamaks with poloidal field divertor. This collaboration will be formalized in an IEA implementing agreement between EURATOM and DOE. Letters of intent have already been exchanged. The agreement itself is drafted and negotiations are in their final stage.

The general objectives of the collaboration are to investigate toroidal physics and the plasma boundary physics in tokamaks with poloidal field divertor as a means of optimizing plasma performance, controlling the plasma boundary, protecting the first wall, reducing impurities, and exhausting ash from the plasma, and to prepare a common data base in these areas.

The joint programme shall concentrate on investigations in the ASDEX Upgrade experiment, and in ASDEX while the ASDEX Upgrade facility is being prepared. The joint investigation shall include surface physics and technology of surface materials. The programme shall consist of:

1 exchanges of information and computer codes
2 exchanges of personnel
3 exchanges of equipment, materials and instrumentation
4 jointly performed experiments
5 joint development and construction of plasma diagnostics, limiter and divertor components.

In 1984 a provisional Executive Committee was established, which in accordance with the draft agreement decided on the proposed program of the near-term collaboration. In 1984 a few exchanges of scientific personnel took place, and the cooperation was concentrated in the following areas:

5.1 Boundary Physics

The main subject of this collaboration was the use and the application of the DEGAS code. The IPP Tokamak Physics group also introduced a number of improvements in the code, which PPPL incorporated. A further topic was the discussion of data analysis issues with the ASDEX group, particularly on analysis of the divertor performance data and the comparison of codes and numerical techniques.

5.2 Transport Codes

Several projects including a model for the H-mode and newer models for neutral reflection were the subject of this topic. In particular a model was developed for low energy reflection of neutral atoms. A self-consistent pumped limiter calculation could be completed in collaboration with IPP staff.

5.3 Pellet Injection

The main subject of this collaboration in 1984 was the investigation of pellet penetration into ASDEX. For pellets shots in ohmic, neutral beam and lower hybrid heated plasmas in a wide range of parameters a scaling law was found for the penetration depth in partial agreement with the neutral gas shielding model.

JET COOPERATION PROJECT

Head of Project: M. Kaufmann

The JET (Joint European Torus) experiment at Culham (U.K.) went into operation in 1983 and has since been conducting a major experimentation programme.

About 700 high-current discharges have been performed in the purely ohmic heating phase. Here the plasma was limited by four carbon limiters mounted symmetrically to the midplane. The plasma current was increased to 3.7 MA and the toroidal magnetic field reached its full design value of 3.4 tesla.

The first discharges were made in hydrogen. Later deuterium was used in a small number of shots. This yielded a 20 % improvement of the confinement time under otherwise equal conditions for the current, toroidal field and electron density.

The elongation of the plasma was usually between 1.1 and 1.7. At larger values the control fields were no longer capable of controlling the plasma position.

The data obtained so far are world records for operation with purely ohmic heating. The energy confinement times of 0.7 s and the ion and electron temperatures of 3 keV are twice as high as the values expected. This result shows that the confinement of plasma strongly improves as the machine is enlarged. However, the value of $Z_{eff} = 3$ for the impurities in these discharges is much higher than expected. The main impurities are nickel, oxygen and carbon.

IPP involvement in the joint European experiment takes various forms. Several IPP employees have been seconded to JET for long terms and are integrated in the JET team. IPP also continue to develop and build diagnostics essential for investigating the JET plasma. So far IPP have supplied JET with three bolometer cameras, a provisional soft-X-ray camera and IPP have designed the cassette probe system for investigating surface samples, all of which are in operation. Still under construction are the final soft-X-ray camera, the surface analysis station, a pellet injection system for diagnostic purposes and two crystal spectrometers for the X-ray region.

Besides having taken part in the construction of JET and providing diagnostics for it, IPP are also participating in the experiments. For this purpose IPP have concluded task agreements with JET which define the the cooperation of IPP in certain areas and are concerned with, in particular, the operation of IPP-built diagnostics. Under the terms of these task agreements IPP assign personnel to JET. Three task agreements are now in force. The first provides for investigations in impurity physics, the second is concerned with plasma-wall interaction, and the third covers the area of plasma position control. In 1984 several staff members of IPP were active with JET in the context of these task agreements.

Apart from this work on diagnostics and assignments under the task agreements, IPP also supported JET with theoretical work and numerical calculations in various fields.

1. CONTRIBUTIONS OF THE JET DIAGNOSTIC AND PELLET INJECTION GROUP (JDP)

C. Andelfinger, E. Buchelt, K. Büchl, C. Dorn,
A. El-Sharnouby[1], H.U. Fahrbach, J. Fink,
K. Follmer, H. Frischmuth, K. Hilber, D. Jacobi,
H. Krause[2], F. Mast[2], E. Oberlander, D. Pohl,
G. Prausner, H. Röhr, G. Rupprecht, M. Salvat
W. Sandmann, H.B. Schilling, G. Schramm,
U. Schumacher, J. Sommer, A. Stimmelmayr,
M. Ulrich, G. Weber, H. Weichselgartner, D. Zasche

The status of design and construction work for JET diagnostics and pellet launchers is as follows:

- During 1984 the complete bolometer diagnostic, two horizontal cameras, one vertical camera and 8 individual bolometers were put into operation and yielded important results on impurity radiation in JET plasmas. The results will be presented in the contribution of Task Agreement No. 1.
- For the soft X-ray diagnostic the vertical camera was constructed, the horizontal camera designed in detail and the data acquisition system nearly completed. Installation at the JET site is planned for June/July 1985.
- The two X-ray double-crystal monochromators are in the detailed design phase. Laboratory tests with various components of these have been performed. The construction phase should start in early summer 1985. Completion will be expected for spring 1986.
- The design study for LIDAR Thomson scattering was completed in collaboration with IPF Stuttgart and MPQ Garching. Final design and construction will be carried out by JET and IPF Stuttgart.
- The detailed design of the diagnostic pellet launcher was approved. Construction has now started.
- Tests with a prototype pellet centrifuge are proceeding. The pellet feed-in mechanism worked successfully. Material and fabrication of the rotor must still be improved.
- Investigations on tritium interaction with and analysis at metallic surfaces have begun. Work on testing and completing the technological equipment was continued.

1.1 Soft X-ray Diagnostic with Diode Pinhole Cameras

This diagnostic can deliver information on the absolute intensity and the coarse spectral character of the plasma soft X-ray emission with high time and space resolution. It is to be used to investigate plasma instabilities and fluctuations, to locate rational q-surfaces and to measure the position and radial profile of the JET plasma. Quantitative analysis will help to study the distributions of impurities to identify impurity transport phenomena and thus to facilitate optimization of plasma conditions. Application of 11 different absorption filters will allow comparison of the emission in adjacent spectral intervals.

In 1984 the vertical camera with 38 diodes (Fig. 1) was constructed. A leaking bellows and three electrical feedthroughs (3×10^{-8} mbl/s) have made some revision necessary. Final tests are scheduled for the end of January 1985.

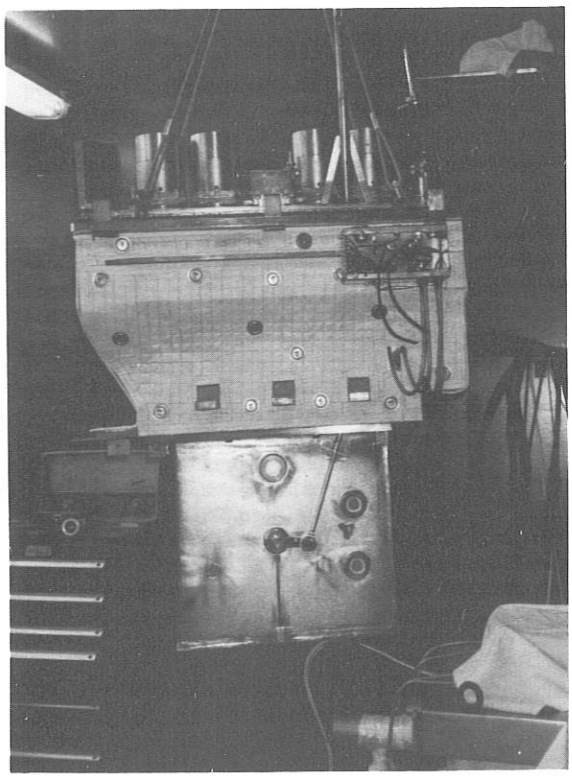

Fig. 1: Vertical camera.

Detailed design of the horizontal camera with 62 diodes has been completed and construction is under way. Both cameras are expected to be installed in the summer break of JET operations. The 100 channel data acquisition system has been delivered and successfully tested. The camera control electronics and the vertical camera will be available in February 1985 for final tests of the complete system including software.

117 Quantrad Si diodes were delivered in the second half of the year. These diodes were selected for use in this diagnostic because of their good radiation stability, which was confirmed by n-irradiation experiments in 1982. Extensive tests had to be performed on this batch because a previous batch of detectors had shown that there are detectors with good properties which deteriorate during operation within a few days. A test facility was therefore built which allows 10 detectors to be simultaneously operated in vacuum and their noise levels and leakage currents to be recorded. Each detector was tested for at least one week, then heated to 150° C and retested. Several detectors are now being tested for a period of several weeks. About 15 % show increasing noise or leakage current or are otherwise defective.

Calibration was performed with 6 keV photons of a 50 mCi Fe55 X-ray source (Amersham). The photon flux was chopped by a 90 Hz chopper. An aperture just in front of the detector defined the solid angle.

[1] Guest, Nuclear Research Centre, Cairo, Egypt
[2] Now assigned to JET

The signal was about 140 pA. It was converted to a voltage, amplified and measured with a lock-in amplifier. With an integration time of 400 s the statistical error was ± 0.1 to 0.5 % of the signal. Within this accuracy all diodes show the same relative responsivity. The total systematic error is estimated to be 10 %. The absolute responsivity calculated from the measurements, is only 4 % lower than the value of 0.28 A/W ≙ 3.6 eV per electron-hole pair given in the literature and thus in good agreement. The main contribution to the systematic error is the uncertainty of the X-ray source photon output specified by Amersham. Other contributions include errors in the solid angle, the transmission, the gain and offsets in the electronics. The result is shown in Fig. 2.

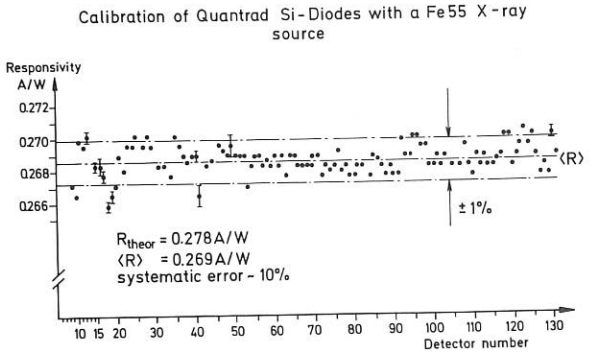

Fig. 2: Results of the Si-diode calibration. The indicated error bars are typical values and show the single standard deviation. The accuracy of the absolute value is about 10 %.

1.2 Spectroscopy of Soft X-rays with Double-crystal Monochromators

The spectroscopy of soft X-rays in the photon energy range from about 0.5 to 10 keV (about 0.1 nm to 2.5 nm in wavelength) is well suited for the identification, quantitative determination of concentrations and the transport of impurities in hot JET plasmas.

A time and space-resolved spectrum of JET plasmas of all phases (including DT operation) can be obtained by applying a double-crystal monochromator for the nearly perfect shielding afforded by the labyrinth beam path, for its mechanical handiness due to the fixed detector position and for its flexibility in wavelength range and resolution by changing crystals and collimators. The device, however, calls for high mechanical accuracy during fast wavelength scan and for homogeneity of crystal reflection.

In spring the scientific and engineering design of two double-crystal monochromators was completed (IPP 1/225 and IPP 1/226). The first device for the "active phase" will be located behind the shielding wall of the JET experimental hall. It will be connected via a long vacuum pipe to the horizontal port 6 of the JET vacuum vessel. It should allow scanning of a large spectral range with a frequency of a few hertz for one line of sight through the midplane of the JET plasma. It is designed to operate also in the active phase of JET (D-T operation).

The second device is the "spatial scan" double-crystal monochromator, which is to be placed on top of vertical port 3 of the JET vacuum vessel to allow a continuous spatial scan over more than the half-axis of the JET plasma.

Contracts for detailed design and construction were concluded on the basis of these designs. Completion of the devices is expected for the beginning of 1986.

Major parts will be performed by industry, e.g.
- mechanical components such as the linear displacement units, the rotating tables, angular encoders and vacuum vessels;
- the control systems for the crystal motion and vacuum systems.

Components which need further investigation in the laboratory are to be developed by IPP:
- multi-wire proportional counter
- X-ray calibration source
- windows for separation of spectrometer vacuum from torus and detector (2 µm Hostaphan covered with 300 nm Al).

Major effort was expended on measuring the crystal properties, such as rocking curves, which are important for the monochromator resolution and for the mechanical accuracy, and dependencies of peak reflectivity on the location on the crystal surface with double-crystal arrangement, which give the crystal homogeneity. Figure 3 gives examples of the rocking curves of topaz (303) measured at CuK_α and CrK_α in non-dispersive (parallel) orientation. The widths are sufficient for line profile measurements but do not call for extremely high mechanical accuracy. Figure 4 shows the peak reflectivity of Si (111) versus its surface location, indicating that Si (111) is a very homogeneous crystal.

A test apparatus for simulation of the swivel motion of crystal 1 in the spatial scan monochromator was built. Preliminary tests were undertaken with an autocollimator and a diffraction grating instead of the crystal. Up to 5 Hz, the bending of the grating was less than 13".

Final tests of the spatial scan monochromator operation will be done with an extended X-ray source.

Testing of the important condition of parallelism of both crystals and its control was done with the crystal rotation units in conjunction with a Michelson interferometer. This showed that with some restrictions the required parallelism of 12 seconds of arc can be achieved.

The detector prototype is being tested using the X-ray tube with the Cu anode as well as a Fe^{55} source emitting MnK_α. The present mechanical design comprises the aluminium vessel with the (at present) 6 µm thin Hostaphan window, which contains an anode mesh with 88 wires of gold-covered tungsten 10 µm in diameter with 1 mm spacing plus thicker edge wires for continuously decreasing the electric field strength towards the edge. The anode wire area is surrounded on both sides by cathode meshes, each

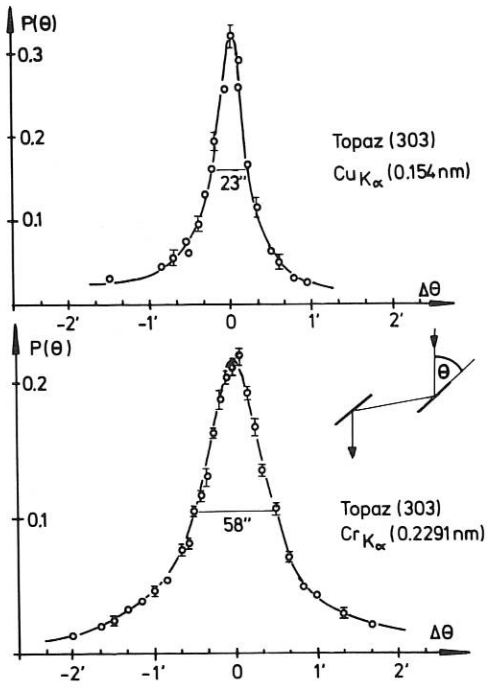

Fig. 3: Rocking curves of Topaz (303) in non-dispersive (parallel) double crystal arrangement for two different wavelengths.

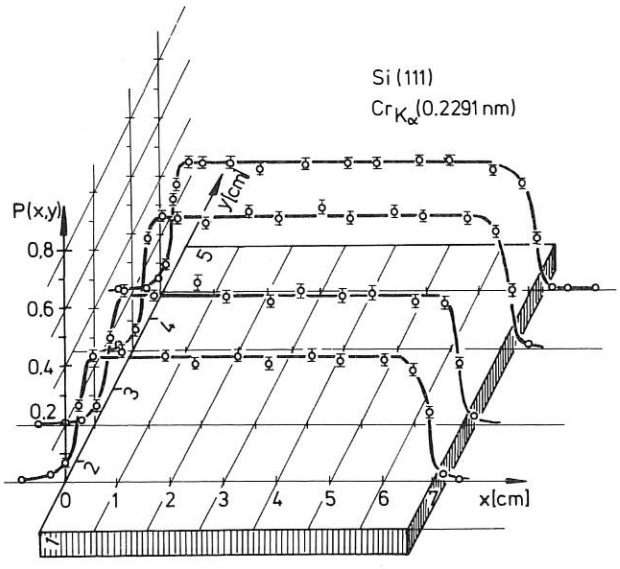

Fig. 4: Peak reflectivity of Si (111) versus location on crystal surface demonstrates that the condition for homogeneous reflection in double crystal arrangement is fulfilled.

---

made from about 200 wires of gold-covered tungsten 50 µm in diameter with 0.5 mm spacing.

The distance of the cathode meshes to the anode mesh is 16 mm each. The tests are being performed mainly to determine and increase the maximum count rate at which the detector can operate, and to find out the influence of the background radiation level.

A Soller collimator built from 150 blades of CuBe will be compared with respect to transmission, angular resolution, reflection and wavelength dependence with a grid collimator of the same resolution now under construction.

Test samples for the window design were successfully loaded with 1 bar up to 180° for many load cycles.

1.3 LIDAR Thomson Scattering

The design study for a Thomson back-scattering diagnostic with time-of-flight analysis was completed in close collaboration between IPF Stuttgart, MPQ Garching and IPP (IPP-JET-Report No. 25, IPP 1/299, IPF-84-3). A more detailed description of the system is given in the report of IPF Stuttgart). A scattering system is proposed that uses an iodine laser (15 J at 657 nm, pulse length 300 ps), microchannel plate photomultipliers (response time 400 ps) in connection with a 1 GHz oscilloscope. The repetition rate of the system should be up to 1 Hz. Statistical errors are expected to be $\Delta T_e/T_e \leq 10$ % at $n_e = 10^{19}$ m^{-3} in the range of 0.7 keV $\leq T_e \leq$ 15 keV.

The realization of such a system for JET will be done by JET in collaboration with IPF Stuttgart.

1.4 Diagnostic Pellet Launcher for JET

A single-shot pneumatic pellet injector was designed in detail and has been approved by JET. It is for accelerating hydrogen or deuterium pellets to velocities of up to 1.5 km/s. These single-shot pellets can be very useful for influencing and diagnosing basic properties of the plasma, such as density profile and transport. Construction of the injector can now start. A test facility is in operation for testing the manufactured pellet guns of different sizes.

Pellets 2.6, 3.6 and 4.6 mm in diameter and of equal length have been ordered. The velocity ranges from 1500 to 1200 m/s, depending on the size. In the same test facility the portion of propellant gas flowing to the torus was found to be smaller than 1 % of the pellet mass.

For the pellet diagnostic the following were prepared:
- the electronics for two-channel D_α measurement
- the system for measuring the pellet velocity and mass (by Risø, Denmark)
- the solid-state TV camera, memory and hard copy unit were tested.

System control will be done with a programmable Simatic S5-150. The flow charts have been written and manufacturing can start. The data acquisition system based on JET standard CAMAC units has been approved by CODAS and ordered.

Installation at the JET site is expected for the end of 1985.

1.5 Tests with the JET Prototype Centrifuge Pellet Launcher

After design work of a centrifuge for JET in an Art. 14 Contract there were two problems that required additional tests with a prototype centrifuge:
- the pellet production and feed-in procedure
- the centrifugal load of full-size centrifuge rotors.

These tests were carried out during an extension of the scientific design phase. The production of solid D_2 rods with the Leybold-Heraeus extrusion cryostat is working very well after some optimization of the temperature control. For the feed-in procedure pellets must be cut from the rod and ejected to the centrifuge rotor. First experiments resulted in unacceptable stray angles of the pellets. Separation of the cutting and ejection processes improved this short-coming. Test runs with a small Al rotor (R = 12 cm) show that all pellets survive the feed-in at a rotor frequency of 300 Hz. Only very precisely placed pellets survive 400 Hz. A major difficulty was the balancing procedure of the full-size carbon fibre rotor (R = 45 cm). Finally, an imbalance of $\leq$ 10 gmm was left. In former centrifuge load tests with full size carbon-fibre-compound (CFC) test rotors the rotors crashed at a rotor frequency of 480 Hz and 470 Hz respectively. Those crashes probably resulted from too high tensile stress in the CFC material. The new rotors made from CFC-material allowing even higher tensile stress were intended to be run at 400 Hz only but tumbled at 230 Hz already. These rotors were manufactured in two pieces and stuck together. We have to assume that some epoxy from the adhesive was lost, producing a sudden imbalance which excited a deadly precision oscillation. After this experience we recommend metallic rotors instead of compound materials, until technological problems connected with CFC materials are solved.

1.6 Tritium Technology

Investigations on tritium interaction with and tritium analysis at metallic surfaces will become a major part of the future work to be done in the tritium laboratory. The technical equipment of the laboratory needed for these investigations was completed and tested with tritium in 1984.

Separation of hydrogen isotopes has successfully been investigated in 1983 with H_2, HD and D_2. Now, after completion of the glove-boxes, tests with the addition of tritium have been carried out. Figure 5 shows an example of separated species. The composition introduced was 20 ml H_2, 40 ml HD, 20 ml D_2 and 15 ml T_2 (38.5 Ci). HT and DT originate from contaminations in T_2. The retention times of these species are close to those of D_2 and T_2, respectively. To enhance the efficiency of separation of HT and D_2, and of DT and T_2, the chemical composition of the filling material of the separation columns has been modified. Improved separation efficiency was found in 1.5 cm Ø columns. Tests with the 5 cm Ø columns are under way.

Removal of tritium from the glove-box: The tritium removal system is based on the TROC method and consits of a SS reaction column (h = 2 m, d = 20 cm).

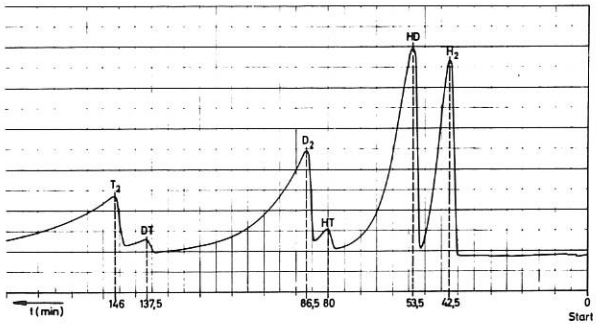

Fig. 5: Gas chromatogram of the hydrogen isotopes (test no. 9 with 38.5 Ci T_2).

The contaminated glove-box atmosphere is circulated countercurrently through the column by a centrifugal blower (20 m^3/H^{-1}) and the tritium becomes chemically bonded to unsaturated organic acids (IPP 1/227).

An emergency case was simulated with hydrogen: 600 ml H_2, equivalent to about 1500 Ci of tritium was injected into the glove-box, and the hydrogen concentration (10^{-4}) was measured during operation of the TROC by an analytical gas chromatograph. Within 30 to 45 minutes more than 99 % of the H_2 disappeared from the glove-box atmosphere.

During tritium testing of the preparative gas chromatograph tritium was released into the glove-box. In Fig. 6 the tritium activity in the glove-box during three test runs is shown. The TROC was set in operation when the maximum activity was reached.

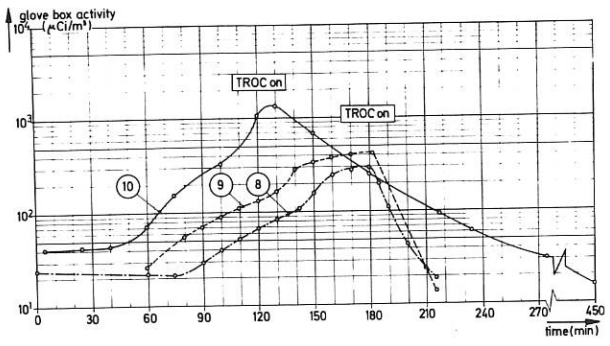

Fig. 6: T_2 activity in the glove-box during T_2 tests.

The best result was obtained in test run No. 9, where a maximum activity of 430 $\mu Ci/m^3$ and a T_2 activity of 380 $\mu Ci/m^3$ were reduced within 35 min to 55 μCi (THO+T_2) and 12 $\mu Ci/m^3$ (T_2), respectively. Test No. 10 also represents an interesting result: the T_2 activity (max. value more than 1300 $\mu Ci/m^3$) decreased within 150 min to 30 $\mu Ci/m^3$; a final value of 15 $\mu Ci/m^3$ (= 1.5 x 10^{-5} Ci/m^3) was reached within 330 min. Obviously, the removal plant works much more effectively in removing gaseous T_2 than THO. It is estimated that the organic medium, which is not mixable with water, displaces the THO from the reaction column. Part

of the THO therefore circulates further in the glove-box atmosphere. This effect will be diminished by adding a solvent which is able to pick up THO.

Numerous laboratory tests (IPP 1/234) were conducted in order to investigate this problem; the most promising results will be applied with the pilot plant.

An experimental set-up for investigating tritium interactions and analysis on metallic surfaces was installed. Small metallic samples will be exposed to tritium at different pressures and temperatures and both the activity at the surface and at a depth of about 1000 Å will be measured. First experiments have been started at a tritium partial pressure of 3 to 100 Pa at room temperature; the exposure time was 3 to 4 hours. A surface activity of 3 to 4.5×10^{-9} Ci/cm^2 was monitored with a proportional counter. Depth profiles have not yet been determined. These experiments will be continued and several decontamination methods will be investigated.

2. CONTRIBUTION OF THE TOKAMAK PHYSICS GROUP

The following theoretical work was carried out either by IPP members during their stay as associated staff at JET or at IPP under JET contract.

2.1 Impurity Transport Code

(K. Lackner, R. Wunderlich)

Development of the code describing the flux-surface-averaged, time-dependent impurity transport at finite reaction rates was continued by extension to general flux surface geometries and the inclusion of the Pfirsch-Schlüter contributions to the impurity fluxes.

2.2 Numerical Simulation of Ergodic Boundary Layers

(W. Feneberg)

A 3D numerical code was written for the plasma transport in boundary layers where magnetic surfaces are intentionally destroyed by superimposed perturbation fields. In the present formulation, which includes anomalous viscosity in the plasma equation of motion but assumes given, time-independent temperature profiles, these calculations result in an unphysical, explosive runaway of plasma parameters over a limited region, which can be attributed to the not enforced energy conservation. In future work, the temperature profiles will therefore be determined self-consistently from the energy conservation law.

2.3 Classical Cross Field Transport in Scrape-off Layers

(W. Feneberg)

The classical effects contributing to the finite thickness of the scrape-off layer of a toroidal limiter or an axisymmetric divertor were investigated.

It was found that the gradient of the temperature along the field lines will produce a high perpendicular transport velocity resulting in a classical layer thickness which could become of the same order as that due to typically assumed anomalous diffusion. This effect is due to the coefficient of thermo-diffusion of the electrons generating an electric field in the toroidal direction. This field is compensated by a perpendicular motion of the electrons. This classical effect is largest in divertor experiments of reactor dimensions where the temperature difference between the divertor plates and the plasma midplane is large enough to give a classical thickness of the order of 10 cm. The classical boundary layer leads to an asymmetry in the energy load of the limiter or the divertor plates which depends on the direction of the main field.

3. CONTRIBUTIONS OF THE LHRH GROUP

3.1 Ion Cyclotron Heating Studies for JET

(M. Brambilla)

During 1984 the RAYIC code was completed and documented (IPP-JET-Report No. 18), and installed in the JET computer facility. This code models coupling, propagation and absorption of electromagnetic waves in large tokamak plasmas in the ion cyclotron frequency domain.

The code has also been used to investigate three IC heating scenarios of the JET plasma (IPP-JET-Report No. 22): He_3^{++} minority in a hydrogen plasma, first-harmonic resonance of deuterium, and H^+ minority in a deuterium plasma. The dependence of absorption on the discharge parameters (density, temperature, minority concentration, etc.) and on the antenna configuration (dipole or quadrupole) was obtained, and understood in terms of elementary damping mechanisms (wave conversion, IC damping, electron transit time damping). All three methods were found to be satisfactorily efficient for typical JET extended-phase performances.

4. CONTRIBUTIONS OF THE PLASMA WALL INTERACTION GROUP

Head: R. Behrisch

Under the terms of JET contracts surface collector probes to be used in JET have been designed and constructed, and the surface analysis system is being built for installation at the JET site. Beryllium was investigated with respect to its hydrogen retention and sputtering properties at temperatures of up to 750° C.

4.1 Surface Analysis System (SAS)

For the investigation of the collector probes as well as the long-term samples, a surface analysis system (SAS) using different surface analysis methods is being built. The collector probes can be transferred in vacuum to the SAS either by a fast transfer system (FTS) or via vacuum cassetts. The detailed design of the mechanical and vacuum system of the SAS has been completed in cooperation with industry. A detailed specification of the local control system has been prepared by IPP allowing fully computer-controlled operation of the system. The ion beam analysis equipment to be used with chamber I has been defined. Manufacture of the mechancial and vacuum components and the control system has commenced. The system is expected to be ready for operation at JET late in 1985. (Phase II Contract No. JE2/0687.)
(Ch.Dorn, W.Möller)

4.2 Surface Collector Probes for JET

The design of the collector probes to be used for plasma boundary and surface diagnostics at JET was completed and several probes have been manufactured. (Art. 14 Contract No. JB2/9014)
(J.Ehrenberg, Ch.Dorn)

4.3 Sputtering of Beryllium

The erosion of Be under ion irradiation was investigated by the weight loss method. The sputtering yield was measured for H^+, D^+ and He^+ ions in the energy range from 60 eV to 3 keV at normal ion incidence at target temperatures of 100° C, 650° C, and, for D^+ also at 750° C. At the highest temperature thermal evaporation of Be is about the same as the erosion rate by sputtering with an ion flux of 1.5×10^{16} cm^{-2} s^{-1} at an energy of 100 eV.

The sputtering yield measured for high incident ion energies ($E \gtrsim 500$ eV) with the Be probes supplied by JET (Brush-Wellmann Corp. type 565) gave the same results as previous ones measured on cast beryllium (Fig. 1). At low ion energies ($\lesssim 100$ eV) and higher temperatures (> 100° C), the yields are higher than at room temperature. The data were found to scatter, which was attributed to the formation of different oxide layers on the surface; the highest yields being attributed to clean surfaces. The investigations also showed a dependence of the erosion on the ion flux. At an ion flux of 1.5×10^{16} cm^{-2} s^{-1} a needle-like structure developes, which is not the case for a flux of 3×10^{15} cm^{-2} s^{-1} (see Fig. 2). For the higher flux the sputtering yield is reduced by a factor of about 2 relative to the lower flux condition. Further the angular dependence of the sputtering yield was investigated. The measured yields normalized to the yield at normal incidence are given in Fig. 3. The data generally show an increase with the angle of incidence with depends on the target temperature. This temperature dependence may be caused by different surface structures which are developed under irradiation. (Art. 14 Contract No. JD3/9005.)
(J.Bohdansky, J.Roth, W.Ottenberger)

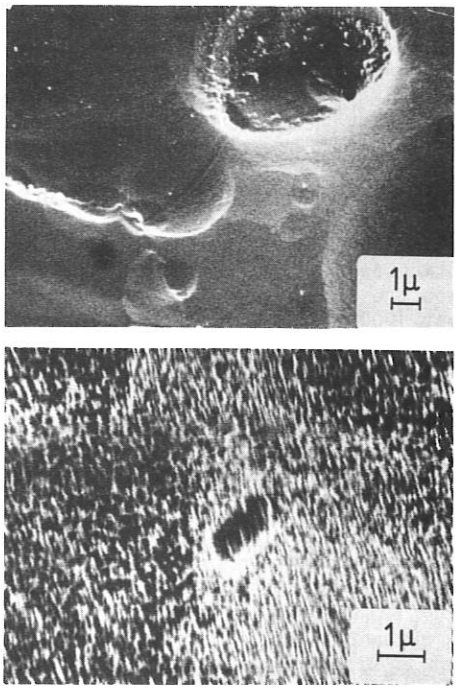

Fig. 2: Surface structure of Be (Brush-Wellmann Corp. type 565) irradiated at 100° C with normal incident 100 eV D^+ ions at a fluence of 10^{20} D/cm² and a flux of 3×10^{15} D/cm² s (top) and 1.5×10^{16} D/cm² s (bottom).

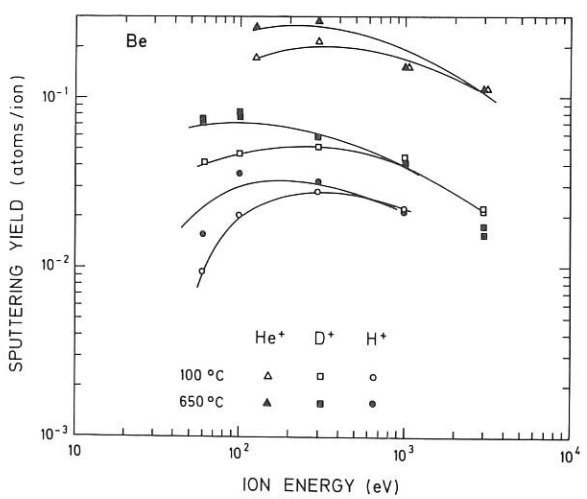

Fig. 1: Sputtering yields of Be (Brush-Wellmann Corp. type 565) at temperatures of 100° C and 650° C as a function of the incident energy for light ions and normal incidence.

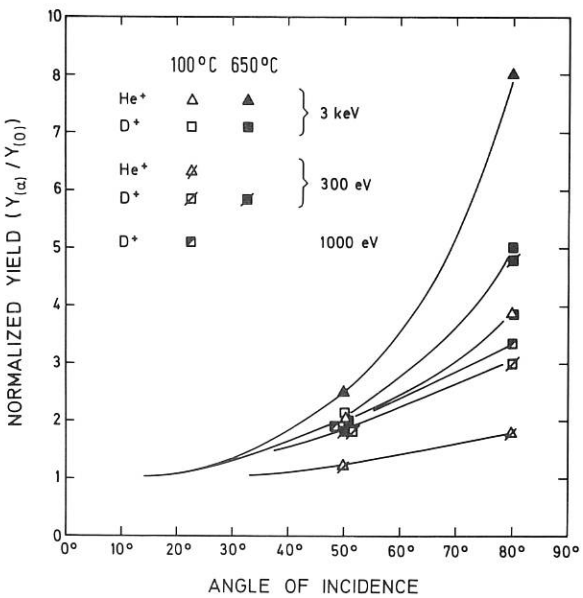

Fig. 3: Relative increase of the sputtering yield of Be at temperatures of 100° and 650° C for light ions as a function of the angle of incidence.

4.4 Retention and Release of Deuterium Implanted into Beryllium

For the Be probes supplied by JET retention and release of implanted deuterium was also investigated. Implantations were carried out between room temperature and 920 K in an energy range of 60 eV to 10 keV, with subsequent remote nuclear reaction analysis for the lower energies (60 eV to 1 keV), and in-situ gas reemission measurements, nuclear reaction analysis and thermal release experiments at the higher energies ($\gtrsim$1 keV). The operating vacuum for the in situ measurements was about 1×10^{-8} mbar with a water partial pressure of 10^{-10} mbar, which is comparable to present JET conditions. Nevertheless, an oxygen contamination of $\sim$1 to 8 x 10^{16} O/cm^2 was always present on the sample surfaces.

It was found that the amount of deuterium retained after high fluence bombardment (in saturation) scales approximately linearly with the implantation depth, with 7 x 10^{17} D/cm^2 and 1 x 10^{17} D/cm^2 for implantations at room temperature and 720 K, respectively, at an energy of 10 keV. No significant retention is found at 920 K.

Only around 720 K is instantaneous partial release observed after terminating the implantation, with a time constant scaling linearly with the implantation depth and ranging up to 130 s for a bombardment energy of 10 keV.

The thermal release spectra (see Fig. 4) show two different release stages, the low-temperature one only being present after room temperature irradiation to saturation. The second stage is completely suppressed for the lowest energies ($\lesssim$ 100 eV). Implantation at an elevated temperature leads to a larger retained amount compared to that left after room temperature implantation and annealing to the same temperature. (Art. 14 Contract No. JD3/9005.) (W.Möller, B.M.U.Scherzer).

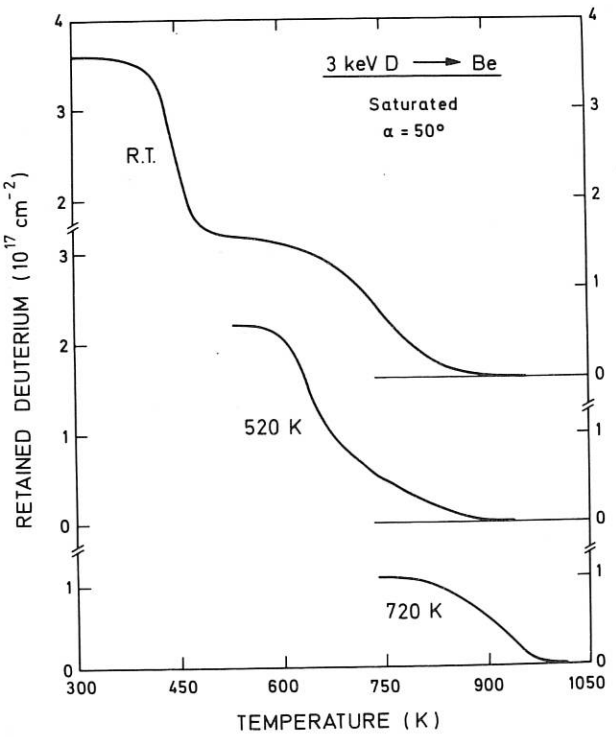

Fig. 4: Thermal release plots for 4° C/s annealing of Be implanted with deuterium of saturation of different temperatures.

5. TASK AGREEMENT NO. 1

H. Krause[1], F. Mast[1], K. Hilber[2], G. Schramm[2], C. Dorn[2], A. Richmond[3], A. Ainsworth[4], K. Behringer[4], J.L. Bonnerue[4], A. Bulliard[4], A. Edwards[4], W. Engelhardt[4], R.D. Gill[4], A. Gondhalekar[4], N. Gottardi[4], J. Holm[4], E. Oord[4], J. Ryan[4]

Under Task Agreement No. 1 IPP undertake to "contribute significantly to the exploitation of JET in the area of: Bulk Impurity Physics and Impurity-Related Diagnostics". In 1984 two diagnostic systems developed by IPP were used at JET for that purpose, the bolometer diagnostic and the provisional soft X-ray diagnostic. Both diagnostics were operated jointly by JET staff and IPP personnel on long-term assignments. IPP contributed to installation and commissioning by assigning key personnel on short time contracts.

The provisional soft X-ray system, an array of four Si diodes, observes the plasma on narrowly collimated horizontal chords. Three of the diodes are covered with beryllium filters of different thickness and thus allow some crude spectral information to be obtained. The diagnostic was installed in 1983, already, and continued to monitor the plasma in 1984. Figure 1 shows a trace of soft X-ray sawteeth activity and a corresponding trace of H_α light from one limiter. The time delay ($\sim$ 20 ms) from a soft X-ray sawtooth to the onset of light emission at the limiter can be interpreted as the propagation time of the heat pulse emitted at the q = 1 surface to the plasma periphery.

The provisional soft X-ray diagnostic will be replaced by the full system of two pin-hole cameras with together 100 channels in the summer shut-down 1985, since production delays made it impossible to install the first camera as planned in 1984.

In January/February 1984 the installation of the bolometer diagnostic was completed. The previous temporary system of 16 channels, only, which fed data into spare ADC's of another diagnostic system was dismantled. The assembly of the final electronics in three cubicles, the interfacing with the CODAS cubicle and the installation of the IPP-written control software proceeded smoothly. At the same time the two horizontal bolometer cameras were

1 assignment to JET
2 short-term assignment to JET
3 work contract with JET
4 JET Joint Undertaking, Abingdon, UK

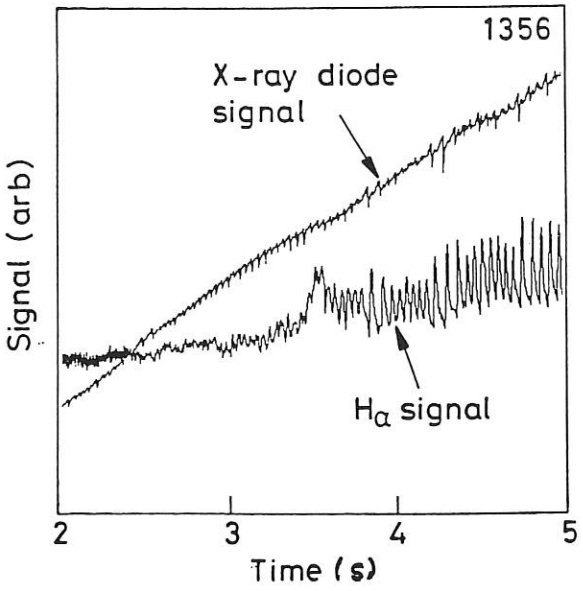

Fig. 1: Soft X-ray sawteeth signal and correlated H_α light signal showing sawteeth.

inserted into the horizontal port at octant 2. At the onset of plasma pulsing in March 1984 the bolometer diagnostic was commissioned with 42 channels, three of which were not operational because of damage to the bolometer heads caused by water influx into the vertical camera at torus wash-out.

During the current flat-top the majority of discharges radiated away 70 % to 100 % of the ohmic input power. No obvious relation could be found between the power ratio P_{rad}/P_Ω and Z_{eff}, the plasma shape, or the density. Figure 2 shows for a series of discharges the radiated power and the ohmic input power. There are indications that higher toroidal fields generally go with the lower power ratios.

During the last weeks of operation in 1984 the Inconel walls of the vacuum vessel were "carbonized" by running a glow discharge in a gas filling of H_2 with a few per cent of CH_4 added. This spectacularly reduced the metal content of the plasma and improved the radiated power to only $\sim$ 40 % of the input power. Under these conditions there is a weak dependence of the power ratio on the density over most of the range and a rapid transition to $\sim$ 100 % radiated power when the density limit is approached.

Measured profiles of the chord-averaged intensities were Abel-inverted to give local emissivities using a simple variation to the standard method which assumes constant emissivity on nested circles. In this case a set of nested ellipses with one common centre and constant ellipticity is assumed. The characteristics of these ellipses are taken from the shape of the outermost flux surface as determined from magnetic measurements. While this procedure is a good approximation to the actual flux surfaces at present, later available additional heating and intensionally D-shaped plasmas will require a more general approach. A code which solves the inversion problem for an arbitrary set of nested surfaces was therefore written by the JET Theory Division

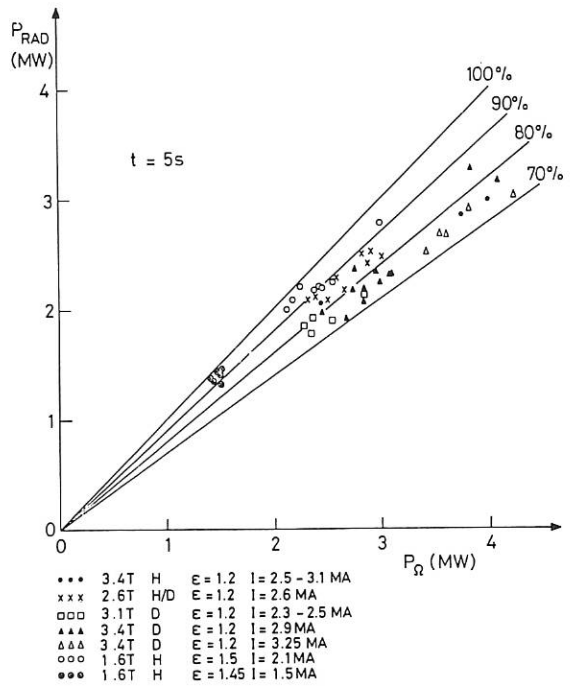

Fig. 2: Radiated power and ohmic input power for the flat-top of various discharges.

and installed on the Harwell IBM computer. The nested surfaces of assumed equal emissivity are taken from another code which outputs the nested flux surfaces as determined from magnetic measurements, physical restraints, and the condition of magnetic equilibrium. As could be expected, this code and the simple one assuming nested ellipses agree well for the present plasmas.

Figure 3 shows an example of an inversion using the IBM code. The upper part of the figure gives the measured intensities from all three cameras. The vertical camera data and the lower horizontal camera data are transformed into the viewing frame of the upper horizontal camera and thus can be drawn over the same coordinate which is the viewing angle of the upper horizontal camera. The plasma centre is normalized to a viewing angle of 0 rad. The lower part of the figure gives the result of the inversion, the local plasma radiation profile. The profile is hollow, which is typical of JET discharges, and the central radiation losses at $\sim$ 5 kW/m^3 are just an insignificant fraction of the central ohmic heating.

Generally, lines of equal emissivity closely follow the plasma flux surfaces for discharges well below the density limit. In the vicinity of the density limit strong deviations sometimes occur. Figure 4 gives an example showing the measured intensity of the 20 channels of both horizontal cameras. Up to t = 5.6 s the upper half-profile and the lower half-profile agree well, and then a strongly radiating "blob" of plasma develops at the plasma edge initially near the equatorial plane at the plasma inside. This blob then spreads upward (but not downward) along the plasma periphery until the whole plasma is surrounded by a strongly radiating mantle. At this stage the plasma radiates away $\sim$ 120 % of

its ohmic input power. After $t \approx 8.5$ s the plasma starts to shrink in size and terminates disruptively.

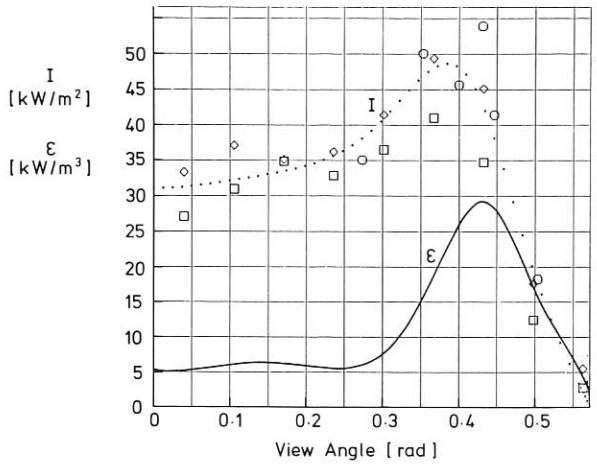

Fig. 3: Measured intensities and inverted profile for pulse #3001. Circles indicate vertical camera data, diamonds upper horizontal camera data, and squares lower horizontal camera data.

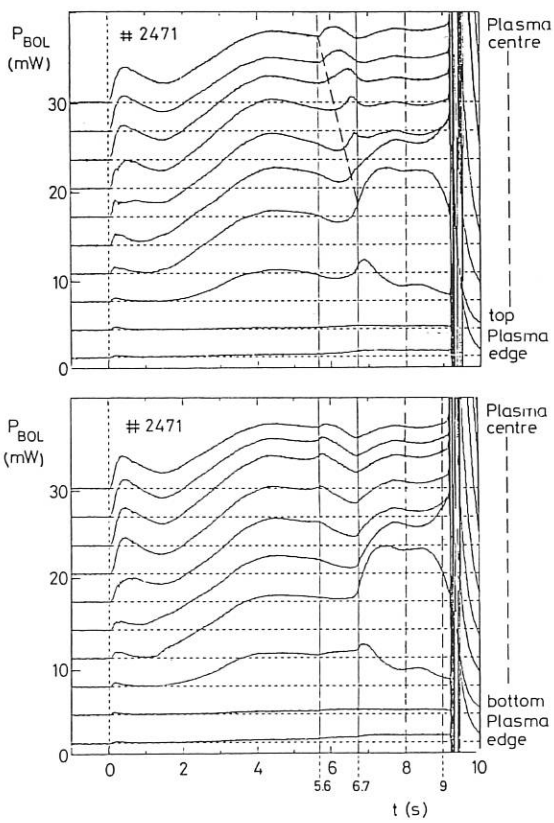

Fig. 4: Bolometer signals for all channels of the two horizontal cameras showing up/down asymmetries.

6. TASK AGREEMENT No. 2

R. Behrisch, P. Børgesen, J. Bohdansky, Ch. Dorn, J. Ehrenberg, A.P. Martinelli, W. Möller, J. Roth, B.M.U. Scherzer

Task Agreement 2 was agreed in 1984 between IPP and JET to investigate plasma-wall interaction in the JET torus with collector probes. These probes allow time-resolved deposition and erosion measurements at a top position and a position at the outer circumference of the boundary plasma. Further detailed investigations were performed on limiter tiles as well as on long-term samples located in all interesting areas of the vessel walls.

6.1 Surface Layer Analysis of the JET Limiters and of Long-Term Samples from the JET Vessel

The central tiles of the carbon limiters removed after the first (June to December 1983) and second (March to October 1984) periods of operation were analyzed by PIXE, RBS and SEM. No major damage of the limiter tiles was found after the two periods of operation. The surface was rough in the 10 µm range and a total deposition of about 10^{17} Ni, Cr, Fe/cm², about 10^{17} Mo/cm² and a lower deposition of O, Ca, K, Cl, S and Ti were measured (Fig. 1).

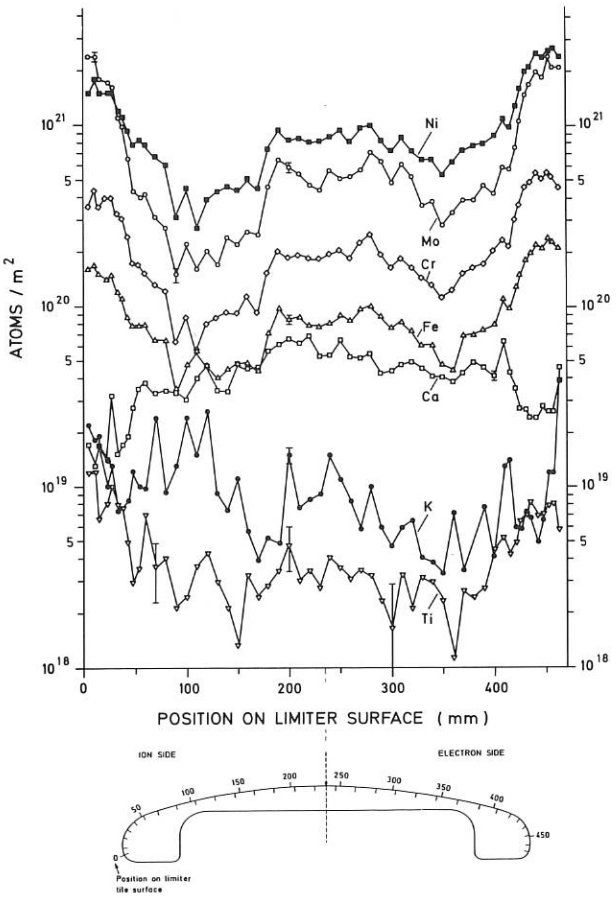

Fig. 1: Distribution of different impurities in atoms/m² across the surface of a carbon limiter tile after the first period of operation.

The deposition showed maxima, being a factor of 2 to 4 higher at the sides of the limiters, where magnetic field lines are incident normal to the surface. On the limiter used in the first period of operation the metal deposits are agglomerated to small droplets, mostly in holes of the carbon (Fig. 2). On the limiter tile used during the second period of operation no droplets are found, but in addition a deep minimum of deposition is seen in the central area. The D-concentration measured at this limiter tile corresponds to 5 x 10^{16} to 10^{18} D/cm². The highest deuterium concentration was found at the sides of the limiter. This cannot be explained as being due to deuterium implantation, but due to co-deposition of carbon and deuterium.

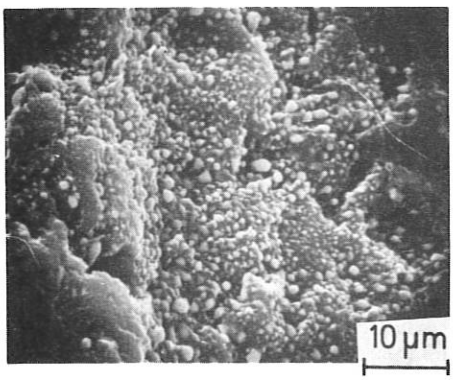

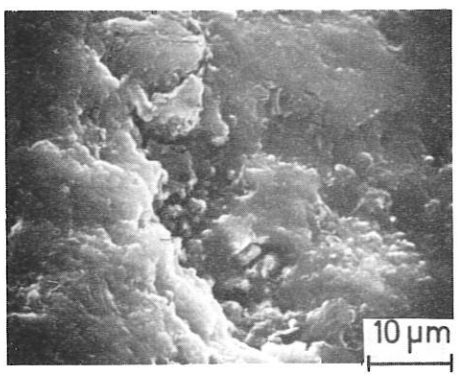

Fig. 2: SEM micrographs of two surface positions (top high deposition, bottom low deposition) of the carbon limiter tile. The droplets contain inconel and molybdenum.

Another small maximum of the Deuterium deposition is found in the central area. The minima in deuterium deposition are associated with the high heat loads in these areas. The amount of molybdenum found on the carbon limiter tiles is highest for the first period of operation and very likely originates from baking the tiles in an oven with Mo-surrounded heating elements.

Long-term samples were installed at the walls only during the second operation period. The carbon samples showed a metal (Inconel components) and deuterium deposition with large poloidal but only slight toroidal variations.

The total deposition was about 6 x 10^{16} Ni, Cr, Fe/cm² on the top and bottom, about 10^{17} Ni, Cr, Fe/cm² on the outer wall and about 5 x 10^{17} Ni, Cr, Fe/cm² on the inner wall. The metal is deposited partly in the form of a thin film which is sometimes cracked and flanked and partly in the form of 20 to 40 µm splashes (Fig. 3). The amount of deuterium found on the carbon samples was up to 8 x 10^{15} D/cm², while on the metal long-term samples about 3 to 4 x 10^{17} C/cm² are found.
(J. Ehrenberg, H. Kukral, A.P. Martinelli, P. Børgesen, R. Behrisch)

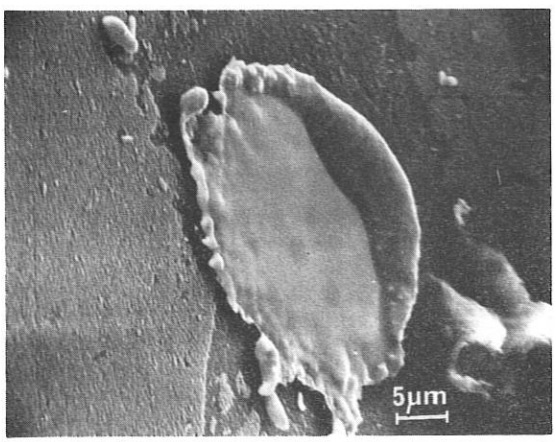

Fig. 3: Small metal splashes and uniform metal film on a carbon long term surface.

6.2 Isotope Exchange

A model was tested to explain isotope exchange experiments in JET. The major contribution comes from the hydrogen trapping and exchange in the surface area of the carbon limiter, while the contribution of the hot metal walls is not significant. Reasonable agreement was found for the ratio of the H to D fluxes with the measured H_α/D_α ratio and the charge exchange neutral measurements.
(J. Ehrenberg)

7. TASK AGREEMENT No. 3

Control of Plasma Shape

H.Niedermeyer, The Physics Operations Group:
F. Schueller[1], P. Lomas[1], A. Tanga[1], P. Thomas[1];
The Power Supplies Division[1];P. Noll[1] (Torus Division) and J. Wesson[1] (Theory Division)

Equilibrium studies with the Blum code, already begun in 1983, were continued. The Blum code (J. Blum, CEA, Fontenay-aux-Roses) is a finite-element program which allows computation of magnetic vacuum field configurations and MHD-equilibrium configurations taking into account nonlinear effects of the iron core.

A set of equilibria with different turn ratios of the poloidal-field coil system corresponding to different plasma elongations has been worked out as a proposal for the stepwise experimental transition from weakly elongated cross-sections to the full-size plasma. The influence of several parameters such as current density profile and plasma position was studied and the stabilizing or destabilizing force on a vertically displaced plasma was calculated. The proposed turn ratios were used as a guideline for the experimental programme.

As a contribution to the working party on magnetic limiter configurations, equilibria with one and with two stagnation points were computed and the growth rates for vertical instability were estimated.

At an elongation of 1.7, reached unintentionally with a high plasma current, the feedback system lost control and the vessel was heavily shaken by a vertical instability of the plasma. An analysis of the force balance supported by Blum code calculations indicated a vertical force on the vessel due to interaction between the toroidal magnetic field and a poloidal vessel current which must have been closed by a radial plasma current.

To determine the reason of the loss of stability, measurements on the radial field system were made. Calculated mutual inductances used for the previous stability analysis could be confirmed experimentally. The sine wave response of the power amplifier, however, was much slower than anticipated. It was possible to identify the internal voltage feedback loop (an I-controller acting on the poorly linearized thyristor amplifier) as the element which reduced the amplifier's speed.

---

[1] JET Joint Undertaking, Abingdon, UK

NET COOPERATION PROJECT

Head of Project: G. Grieger

It is the task of the European NET Study Group at the IPP to define the objectives of NET, the Next European Torus, and to prepare its design. The IPP contributes to this subject by direct secondment of personnel to the NET Study Group and by performing NET-supporting work mainly via NET study contracts. In doing so the IPP exploits its particular experience in edge plasma physics, divertor performance, pellet injection, etc.. Together with additional work directly related to the INTOR activities this work also serves as input to the INTOR Workshops.

1. SHORT PROGRESS REPORT OF THE NET STUDY GROUP

(The following members of the NET Team are seconded to NET by the IPP:
K. Borrass, R. Buende, W. Daenner, J. Raeder, J.-G. Wegrowe)

1.1 Definition of NET Objectives and Reference Parameter Set

The approach to defined objectives is characterized by iterative use of systems studies, component design and evaluation of the knowledge available in physics and technology. The target values of the neutron fluence remain uncertain because of the difficulties in anticipating the availability and breeding capability of NET. The systems studies for defining the parameter set led to one reference study point which gives acceptable performance for most of today's physics scalings for ß and energy confinement.

It is planned to conclude the internal work for the definition of NET, on which the predesign phase is to be based, by about summer 1985.

1.2 Design

Design work on essential components of the basic machine has progressed, yielding information needed for the system analysis codes, for guiding the work in the associated laboratories and in industry, and for identifying critical issues having an impact on the NET objectives.

1.3 Elaboration of the "European NET Technology Programme 1985/89"

The work on the "European NET Technology Programme 1985/89" was done in close cooperation with experts from the associated laboratories. In a step-by-step procedure this led to identification of the tasks, schedules, and resources necessary for providing the technology data base for the design of NET during the coming years.

1.4 Contribution to INTOR

Several members of the NET Team are also members of the INTOR Workshop in Vienna and are in charge of providing the European contributions.

2. AVAILABILITY OF NEUTRAL BEAM INJECTION

O. Vollmer

In the context of availability assurance work for NET, the performance of the neutral injection heating system of the ASDEX tokamak was analyzed. A period of two years (October 1982- August 1984) has been traced to derive the availability achieved by the neutral injection system. Within the considered period about 40 % of the intended ASDEX discharges with neutral beam heating were prevented by limited availability of the neutral injection system.

For the more stringent operation conditions envisaged in NET, failure rates and mean down-times were estimated. The HV power supplies and circuits could be identified as the most critical components. The outage times caused by intrinsic problems of the ion source technology turned out to be negligible.

From the study it can be concluded that the performance of a heating system like ASDEX neutral injection may be acceptable for experimental devices. To meet the requirements for plasma heating in NET, however, the availability of the system would not be adequate.

3. THERMOMECHANICAL LAYOUT OF THE NET FIRST WALL ASSEMBLY

S.B. Mukherjee

Under the terms of a NET contract, a first finite-element analysis for the "Thermomechanical Layout of the NET First Wall Assembly" was carried out at IPP.

The two-dimensional finite-element (FE) method is applied for the first wall structure to compute the quasi-harmonic steady-state temperature distribution within the wall and to determine the stresses under thermomechanical loads.

Basically, the first wall assembly consists of a steel structure with a total width of 35 mm. Water coolant tubes are contained within rectangular ducts, the interspace being filled with 17Li83Pb eutectic breeder material in liquid phase. This provides good thermal bonding and additionally contributes to the tritium breeding capability of the blanket.

For the FE computation the wall's support conditions, nonlinear material and thermal parameters are varied. The hydrostatic liquid lead pressure within a breeder duct is considered. The power density distribution within the first wall structure is shown in Fig. 1. It corresponds to a neutron wall loading of about 1.3 MW/m^2. The external heat flow on the plasma-oriented side is 13 W/cm^2. The thermal data and material properties are supplied by the NET team. The finite-element analysis was carried out with the STRUDL code.

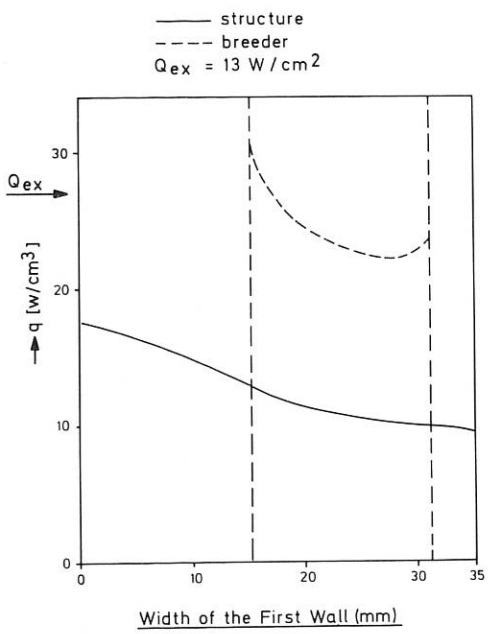

Fig. 1: Power density distribution within the first wall.

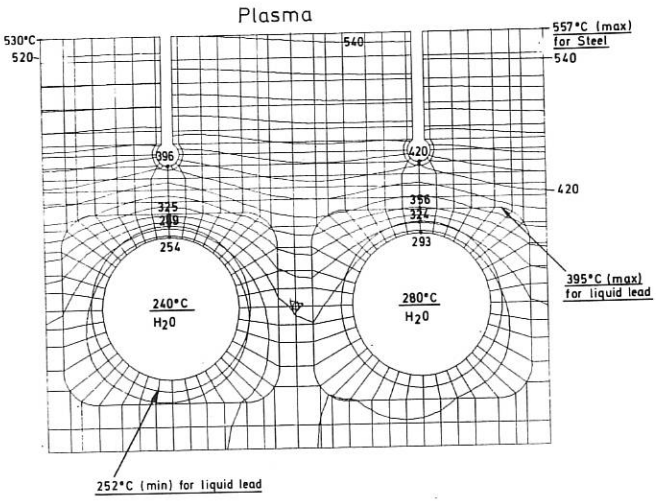

Fig. 2: Contours of temperature distribution within the "grooved" first wall structure.

The contours of the temperature distribution within the "grooved" first wall are shown in Fig. 2. As far as the thermo-elastic stresses are concerned, they depend significantly on the support conditions of the wall structure.

4. PELLET REFUELLING

Deep refuelling of thermonuclear plasmas imposes extreme technological requirements which not only justify extensive critical studies of its actual necessity and of the advantages to be gained for quasistationary tokamak operation, but also call for quantitatively reliable models linking ablation rates with local plasma parameters and pellet dimensions. Both points have been theoretically examined at IPP - partly under a NET contract - using expected NET/INTOR conditions for target parameters. Although the assessment of the fuel and helium ash balance of a quasistationary burning plasma indicates only a need for rather shallow pellet penetration, the possibly different situation during transient phases with devices of shorter pulse length and the unexplained improvement in tokamak energy confinement observed with pellet injection still justify the study of scenarios involving deep refuelling as well.

4.1 Helium Pumping and Pellet Refuelling

M. Kaufmann, K. Lackner, J. Neuhauser
H. Vernickel

The pellet refuelling and hydrogen and helium pumping requirements for a reactor with poloidal field divertor were discussed. On the assumption that there is sufficiently high friction between the hydrogen and helium flows parallel to the field lines in the boundary layer, both species are strongly coupled. Assuming a flat central density profile, one can easily derive the following relation [1]: the shallower the penetration is (slow

[1] M. Kaufmann, J. Neuhauser, K. Lackner, H. Vernickel, to be published in Nucl.Fusion 25 (1), 1985

pellets), the more hydrogen flows through the boundary. The enhanced hydrogen throughput reduces the helium concentration at the boundary and hence in the centre as well. If realistic numbers for INTOR are used in this model, relatively shallow refuelling is found.

Discussion of the optimum profiles for reactor does not alter this conclusion: for maximum ß the pressure profile has to be flat and the current profile peaked [1]. For the steady-state conditions a peaked current profile also calls for a peaked temperature profile. Besides the pressure profile requirement, it would thus be desirable to have a hollow density profile. Deep refuelling thus tends to go in the wrong direction.

4.2 Advanced Pellet Ablation Model

M. Kaufmann, K. Lackner, L. Lengyel, W. Schneider

The observation of H_α-radiation extending along the magnetic field in the case of pellet injection led to renewed discussion of the ablation model. It was argued that the ablated mass is frozen in the magnetic field somewhere beyond the Mach = 1 radius [2]. There is therefore no feedback of the ablated material on the central core of the neutral gas cloud, which is responsible for the shielding. The frozen-in gas flowing away along the field lines was followed with the PELLET 1D hydrodynamic code (similar to the SOLID code used for scrape-off simulation). It is found that an extended (of the order of several metres) high-density (up to 100 times the background plasma density) plasma hose forms along the field lines /119/. The temperature in this plasma is much lower than in the background plasma (in a computation for ASDEX the temperature dropped from 500 eV to approx. 40 eV). This should lead to a distinct decrease in the ablation. In determining the electron heat conduction it was necessary to replace the classical Spitzer-Härm law by a non-local expression taking into account large mean free path effects[3]. As yet the model does not describe the transition from spherical expansion to 1D channel flow in a completely self-consistent manner. Another effect not yet quantitatively treated is the toroidal drift of the ablation hose due to the high ß-value.

4.3 Assessment of Pellet Injection for NET/INTOR

L. Lengyel

In the first part of this study, penetration depth calculations were made by coupling an ablation model to a 1D tokamak transport code. Particular attention was paid to the question of pellet sizes and pellet velocities required for central fuelling of NET or INTOR. The major part of the calculations was made by means of the neutral gas shielding ablation model, in which it is assumed that the ablatant leaving the pellet surface expands in a spherically symmetric manner. In a number of calculations, the magnetic constriction of the ablatant flow was taken into account by means of an ad hoc assumption. Results of penetration depth calculations are summarized in Table 1.

Pellet radius (cm)	Pellet velocity (10^3 m/s)	Penetration depths (cm) 1st pellet (D_2)	2nd pellet (T_2)
Neutral gas shielding model			
0.3	10.	73.	73.
0.3	18.	87.	90.
0.5	14.	125.	162.
0.5	16.	131.	171.
0.525	10.	119.	148.
0.6	10.	142.	325.
0.7	10.	206.	325.
Allowance for magnetic field effects			
0.3	3.	90.	96.
0.3	5.	113.	125.
0.3	6.	125.	142.
0.3	7.	137.	154.
0.3	8.	148.	165.
0.4	5.	160.	177.
0.4	6.	182.	194.
0.4	7.	200.	217.
0.52	3.	171.	200.

Table 1: Data on pellet sizes and injection velocities required for central fuelling of a burning thermonuclear plasma in INTOR.
Plasma radius: a = 162.4 cm.
Time delay between 1st and 2nd pellets: 1 s.

As can be seen, if only neutral gas shielding takes place, central fuelling with realistic pellet velocities is not possible. The presence of magnetic shielding, if effective, may reduce the velocity requirements to technically feasible values.

The large differences in pellet penetration depths resulting from different ablation models have focussed attention on the accuracy and reliability of the existing ablation theories. An analysis of the existing ablation models is therefore given in the second part of this study. The results of this analysis indicate that the neutral gas shielding approximation may yield acceptable results for thermal plasma at low and intermediate temperatures. Care should be exercised in extrapolating these results to thermonuclear plasma because of the two major limitations inherent in these models:

1) F. Troyon et al., Plasma Phys. and Contr. Fusion 26 (1984) 209

2) P.B. Parks, Nucl.Fusion 20, 311 (1980)

3) Luciani, J.F., Mora, P., Virmont, J., Phys.Rev. Letters 51 (1983), 1664

(i) The neglect of nonlocal phenomena in the energy transport, such as the spectrum of stopping lengths or penetration depths corresponding to different energy carrier species and to different energy groups of a single species;

(ii) the neglect of the change of the initially spherical expansion of the pellet substance into a constricted channel flow along magnetic surfaces and the associated changes in gas-dynamic and magnetic shielding.

In the third part of this study, the effects of high-energy electrons, neutral beam ions, and alpha particles on the ablation rate are estimated under fusion plasma conditions. The results show that in certain parameter ranges the effect of non-thermal particles may be significant.

4.4 Numerical Model for Pellet Ablation Studies

L. Lengyel, P. Lalousis

In the framework of some studies complementary to the pellet injection assessment performed for NET, a one-dimensional Eulerian hydrodynamic code was developed for investigating the radial and axial expansions of the ablatant in a magnetic field. The conservation equations for mass, momentum, and energy are solved for a partially ionized gas by taking the ionization dynamics fully into account. The heavy particles, i.e. ions and neutrals, are assumed to be of the same temperature, but the two constituents may move with different velocities. The electrons and ions move with equal velocities. The electron temperature is allowed to be different from the heavy particle temperature.

Figure 3 shows the deceleration of the transverse motion of the ablated mass: the heavy particle density (ions and neutrals) times the volume differential is plotted vs. the logarithm of the radial coordinate. Owing to the initial pressure distribution specified, the centre of mass is first shifted towards the axis and then outwards until it comes to a stop at approximately R $\simeq$ 2.8. cm. The initial peak of ndv was located at R $\simeq$ 2.2 cm. The initial data used in this calculation are as follows:

$n_{ablatant} = 10^{26}$ m^{-3}; $T_{ablatant}$ = 0.09 eV;

$n_{plasma} = 10^{20}$ m^{-3}; T_{plasma} = 500 eV, and

B = 2 tesla.

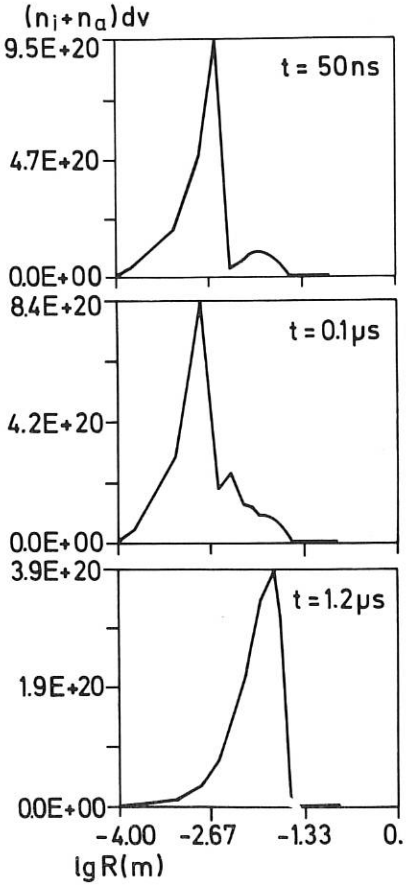

Fig. 3: Deceleration of the transverse motion of the ablated pellet mass in a magnetic field: density times volume differential as a function of lg(r).

5. TECHNICAL BENEFIT OF INTERNATIONAL PARTITIONING IN THE INTOR PROGRAMME

A. Knobloch

The European contribution to a study on the above topic was compiled on the basis of internationally agreed questionnaires - which had to be completed by experts. A number of assumptions were selected, such as the scenario of partitioning in the design and construction phases (Table 2), a reference organisation scheme, an existing cost estimate and the INTOR schedule. As shown in Table 3 it turned out that an INTOR machine built internationally by four partners could be 57 to 67 % cheaper for each participant (compared with one national "INTOR" per partner), depending on the form of partitioning. Owing to the necessary international coordination and some overlapping of activities the period for fabrication, assembly and commissioning increases from 7 to 9.5, possibly 8.5 years. A partitioning scheme with somewhat smaller savings and longer realization time is considered suitable for gaining the complete industrial know-how needed to build a fusion reactor. Reports on experience gained in multinational projects such as JET, LCT, and isotope separation plants and comments on partitioning in INTOR were collected.

A	B (advanced technology components split, conventional technology components branch)	C (branch)
Four nations each build their own "INTOR" based on their national R & D = reference case for benefit evaluation	One international machine is built by four nations based on four national R & D programs sharing fabrication of multiple high technology components and of the different conventional components.	One international machine is built by four nations based on four national R & D programs sharing fabrication of different components.

Table 2: Three scenarios for realizing INTOR.

n	Item	N_n	N_{fac}	N_{facI}	reason+	Scenario B: c_n(%)	f_n	p_n	$c_n \cdot f_n$(%)	$1.2 \cdot 0.3 \cdot c_n \cdot f_n \cdot p_n$(%)	Scenario C: c_n(%)	f_n	p_n	$c_n \cdot f_n$(%)	$1.2 \cdot 0.3 \cdot c_n$(%)
1.	Torus	12	4	4	time	9.89	1.02	4	10.09	14.79	9.89	1	1		
2.	Magnets TF	12	3	3	time	18.81	1.02	3	19.19	21.09	18.81	1	1		
3.	" PF ring	6	2	2	site	8.57	1	1	8.57	3.14	8.57	1	1		
4.	" PF sol.	16	3	1	techn.	4.29	1.10	3	4.72	5.18	4.29	1	1		
5.	Magn. structure	12	3	3	time	1.43	1	3	1.43	1.57	1.43	1	1		
6.	Divertor	12	4	4	time	1.32	1.02	4	1.34	1.97	1.32	1	1		
7.	Heating	12	4	1	techn.	4.52	1.10	4	4.97	7.29	4.52	1	1		
8.	Fueling	1	1	1	unit	0.46	1	1	0.46	0.17	0.46	1	1		
9.	Electrical TF	1	1	1	unit	1.12	1	1	1.12	0.41	1.12	1	1	Σc_n	$1.2 \cdot 30.53/100 \cdot \Sigma c_n$
10.	" PF	20	3	3	bal.	10.09	1.01	3	10.19	11.20	10.09	1	1		
11.	" RF	1	1	1	unit	2.74	1	1	2.74	1.01	2.74	1	1		
12.	Tritium	4	4	1	techn.	6.86	1.36	4	9.33	13.68	6.86	1	1		
13.	Cooling	3	3	3	bal.	6.23	1.05	3	6.54	7.19	6.23	1	1		
14.	Instrumentation	4	4	1	techn.	5.89	1.27	4	7.48	10.96	5.89	1	1		
15.	Maintenance	4	4	4	techn.	3.37	1.06	4	3.58	5.24	3.37	1	1		
16.	El. generation	1	1	1	unit	0.63	1	1	0.63	0.23	0.63	1	1		
17.	Reactor hall	1	1	1	unit	8.00	1	1	8.00	2.93	8.00	1	1		
18.	Other facil.		1	1	unit	5.78	1	1	5.78	2.12	5.78	1	1		
Direct costs						100.00%			106.16% →		100.00%			100.00% →	
Engineering						30.53% ·	$1.2 \cdot \Sigma c_n \cdot f_n \cdot p_n/100$			110.16%	30.53% ·	1.2			36.64%
Installation, assembly						15.78% ·	$1.2 \cdot \Sigma c_n \cdot f_n/100$			20.10%	15.78% ·	1.2			18.94%
Contingency						46.14% ·	$1.2 \cdot \Sigma c_n \cdot f_n/100$			58.78%	46.14% ·	1.2			55.37%
Design specific R and D						15.10% · 4				60.40%	15.10% · 4				60.40%
Total capital costs					(1 national INTOR)	207.55%	(1 international INTOR)			→ 355.60%	207.55%	(1 international INTOR)			→ 271.35%

+reasons for N_{fac} = number of fabrication lines
- time : to restrict total fabrication time
- site : fabrication on site, restrict time
- techn: to share high technology fabrication
- unit : single "unit" item
- bal. : to balance cost contributions

Cost effect for each participant (1 international INTOR)
- cost ratio $\frac{1 \text{ international INTOR}}{1 \text{ national INTOR}}$ = 1.71
- cost ratio $\frac{1 \text{ INTOR share (of 4)}}{1 \text{ national INTOR}}$ = 0.43

Cost effect for each participant (1 int. INTOR)
- cost ratio $\frac{1 \text{ international INTOR}}{1 \text{ national INTOR}}$ = 1.31
- cost ratio $\frac{1 \text{ INTOR share (of 4)}}{1 \text{ national INTOR}}$ = 0.33

N_n = number of individual components
N_{facI} = number of fabrication lines needed for a national INTOR
c_n = component cost fraction
f_n = correction factor for splitting fabrication/testing
p_n = number of participants sharing fabrication/testing of component n

Table 3: INTOR design/construction cost for partitioning in scenarios B and C.

Stellarators

The stellarator line of magnetic confinement uses only external electric currents to produce the magnetic field in which a ring of plasma is passively contained. This line has been pursued since the foundation of IPP and during the last 10 years the operation of the W VII-A device has been the centre of this activity. The success of the operation of this device - inspite of its relatively small plasma cross-section - and of a few other machines in other countries has made the stellarator line the most serious contender to the tokamak as the future fusion reactor principle. Some of the most important apparent difficulties with the stellarator concept have greatly been reduced by the results of the last years. So the predicted poor containement of ions in "classical" stellarators (like W VII-A) was found to be drastically improved by the action of the electrical polarization of the confined plasma. The progress in the construction of the "Advanced Stellarator" Upgrade of the present W VII, which will be called W VII-AS, demonstrates that the technical difficulties of producing the complicated external magnetic fields can be overcome in a way which should be applicable to full-size fusion reactors. Theoretical work is continuing to tackle the greatest single remaining problem of stellarators, namely to increase its effective confinement power, as expressed by the value of ß. It seems likely that the stability limit to ß of otherwise acceptable stellarator configurations might exceed that of tokamaks.

During 1984 the steady experimental progress of W VII-A has centered around electron cyclotron resonance heating (ECRH) and neutral particle injection heating (NI) to produce and sustain net-current free stellarator discharges. ECRH has further expanded the available parameter range which now includes densities from $5 \cdot 10^{12}$ to 10^{14} cm^{-3} and electron temperatures of up to 1.5 keV.

Deeper insight into the power transport through the electron channel was possible for the first time in ECRH plasmas since contributions by the ion channel are rather negligible under these circumstances. Using the 28 GHz gyrotron (B = 1 T) it was found that inside 2/3 of the plasma radius the power losses are fully consistent with neo-classical predictions if also the ripple of the magnetic field is properly taken into account. Outside this radius the well documented anomaly of the electron heat conduction is found again. Since this particular effect decreases with both increasing density and temperature ($\chi_e \sim n^{-1} T^{2/3}$) it is shifted more and more towards the plasma edge and should thus become less and less important the higher our plasma parameters grow.

Also experiments with 70 GHz (2.5 T) have demonstrated that a plasma can be generated and heated to significant levels by ECRH alone. This is an important step for the start of W VII-AS. Also for this frequency it was found that the power available to the bulk of the plasma stems only from single pass O-mode absorption. This supports the intention of clean mode irradiation.

With the help of neutral injection values of half the equilibrium beta were reached. Up to the highest power available beta was still rising linearly with power and no MHD instabilities were observed.

It is now well established that both heating methods produce plasma currents of up to 1 kA or so. In case of NI this current grows with the plasma pressure. In case of ECRH the pressure-driven component is small. Here the observed current consists mainly of RF-driven high energy electrons and can be changed or even be reserved upon variation of the vertical magnetic field. This current has good and bad consequences. On the average its contribution to iota has to be compensated dynamically by a corresponding variation of the external iota to avoid the occurrance of resonances, whereas the small shear resulting from the plasma current seems to be beneficial in broadening the maxima of confinement.

Careful studies of the power balances of the individual species have led to the conclusion that the electric field arising from the perpendicular neutral particle injection reduces the perpendicular ion heat conduction to values much below those which are calculated neo-classically assuming only the equilibrium value for the electric field. This effect is also found numerically. Experiments on the dynamic behaviour of impurities have shown agreement with neo-classical predictions except for some intervals in space or time.

Ion cyclotron resonance heating (ICRH) is still under test. Two antennae, one with and the other without Faraday shield are inserted into the device. A power of up to 150 kW was applied to the plasma but increased radiation losses counteracted observable heating. Also observed was a tail of high energetic ions thermalized among themselves at 3 keV.

With all the above informations the main part of the data base for the start of operation of W VII-AS is at hand.

All essential components needed for upgrading WENDELSTEIN VII-A (W VII-A) towards WENDELSTEIN VII-AS (W VII-AS) are now under construction in industry. A prototype coil and a full-scale prototype segment of the vacuum vessel were built and successfully tested so that series production could be initiated. It is planned to shut down W VII-A in August 1985 and to start commissioning W VII-AS in autumn 1986. Neutral particle injection (1.5 MW, 45 keV, 3 s), ECRH (0.6 - 0.8 MW, 70 GHz, 3 s), and ICRH (3 MW, 30 - 115 MHz, 3 s) will be available when W VII-AS starts operation. The technical preparations for these heating devices are running and are in line with the construction schedule of W VII-AS.

Work oriented towards the definition of W VII-X, the next step in the WENDELSTEIN line after W VII-AS, was concentrated on deeper investigations of the reactor properties of W VII-AS type configurations. This was done with the aim to identify those problems which need to be studied in W VII-X and thus influence its definition. With respect to all those questions involving the mechanical structure, blanket and shielding, superconducting technology, etc., the cooperation with the Kernforschungszentrum Karlsruhe (KfK) was intensified.

Further W VII-X-related work aims at studying the full variety of Stellarator configurations in order to provide a data base sufficiently detailed for the subsequent selection of the configuration preferred for W VII-X. During 1984 configurations possessing a helical magnetic axis were preferentially studied. These were improved by reducing the magnetic mirror ratio in order to diminish the number of trapped particles.

The 5th International Stellarator Workshop was organised at Schloß Ringberg (near Lake Tegernsee) from 24 to 28 September 1984, immediately following the London IAEA Conference. It was the aim of the workshop to present and to discuss the latest achievements of experimental and theoretical investigations of stellarator physics, as well as the prospects for the development of stellarator fusion reactors, in greater detail as it was possible at the London Conference. More than 50 contributions from 16 laboratories of seven countries covered the following topics: overview of experimental results; topical details of experiments and their interpretation: heating, transport, impurities; theory: equilibrium and stability, transport; machines under construction or approved; configuration and reactor studies.

WENDELSTEIN VII-A PROJECT

Head of Project: H. Renner

W VII-A

G. Cattanei, D. Dorst, A. Elsner, V. Erckmann, G. Grieger, P. Grigull, H. Hacker, H.J. Hartfuß, H. Jäckel, R. Jaenicke, J. Junker, M. Kick, H. Kroiss, K. Krusch, G. Kühner, H. Maaßberg, C. Mahn, S. Marlier, G. Müller, W. Ohlendorf, F. Rau, H. Renner, H. Ringler, F. Sardei, M. Tutter, A. Weller, H. Wobig, A. Wootton [1], E. Würsching, M. Zippe.

Neutral Injection

K. Freudenberger, G.G. Lister, W. Ott, F.-P. Penningsfeld, E. Speth (Technology Division).

ECRH (Electron Cycl. Resonance Heating)

R. Wilhelm, G. Janzen, W. Kasparek, G. Müller, P.G. Schüller, K. Schwörer, M. Thumm (IPF Stuttgart)

ICRH (Ion Cyclotron Resonance Heating)

F. Wesner, F. Braun, R. Fritsch, F. Hofmeister, E. V. Mark, S. Puri, M. Söll, K. Steinmetz, H. Wedler (Technology Division).

Pellet Injection

K. Büchl (Division E1)

1. INTRODUCTION

The investigations in the W VII-A stellarator are concentrated on the description of plasma behaviour during "currentless" operation. For this purpose plasma can be produced in an extended parameter range: By neutral injection (NI) at a main field of 2 - 3.5 T with densities $n_e \gtrsim 10^{14}$ cm^{-3} and temperatures of $T_e < T_i \sim 1$ keV; at a main field of 1 T with densities $n < 10^{13}$ cm^{-3} and temperatures of $T_i < T_e \sim 1.5$ keV by electron cyclotron resonance heating (ECRH) using a gyrotron (28 GHz, 200 kW). First experiments for plasma build up and heating have been initiated at a main field of 2.5 T by means of the new VARIAN gyrotron (70 GHz, 200 kW, 0.1 s). The accessible range of higher density $n > 10^{13}$ cm^{-3} will allow combined heating with NI and rf-heating at the ion cyclotron resonance (ICRH). Two different antenna systems have been tested. For this the connection to the new generator (2 x 1.5 MW, 30-110 MHz, 3 s) has been completed.

To analyze the experimental results theoretical models have been developed and numerical codes have been used for the description of

- heating efficiency, power deposition
- energy transport with transition to the collisionless regime (ECRH)
- impurity transport and radiative losses
- stability and equilibrium
- influence of error fields on the magnetic configuration.

The main results have been reported at the IAEA meeting in London and during the IAEA Workshop on Stellarators held at Ringberg. In the following section the main results are summarized.

1.1 Stability and Equilibrium

- In the almost shearless W VII-A ($\Delta t/t \sim 1$ %) the confinement is determined by the external transform ι_o and the residual plasma current I_p.
- For optimum confinement at $\iota \neq m/n$ ß proportional to the heating power P_{IN} has so far been demonstrated. No MHD instabilities have been observed within the accessible ß range. The

1) Oak Ridge National Laboratory

highest ß value corresponds to about half the equilibrium ß at W VII-A.

- Both heating methods lead to a plasma current $I_p \lesssim 2$ kA. By careful control of the edge value of the rotational transform - either by modifying the plasma current or the current of the helical windings - good confinement properties are maintained.

- The deterioration of the confinement at the "resonances" $\iota = m/n$: e.g. 1/2, 1/3, 2/3, is rather an effect of island formation and convection at resonance surfaces.

- The extent and location of perturbed regions seem to be influenced by shear. The current density distribution of the residual current I_p and the plasma pressure profiles thus modify the confinement in W VII-A .

1.2 Transport

1.2.1 Electron heat conduction

- Transport studies of the ECRH plasma lead to reasonable agreement with theoretical predictions. The measured temperature profiles can be fitted by taking into account the local electron heat conductivity: $\kappa_e = \kappa_{e,HH} + \kappa_{e,rip} + \kappa_{eOH}$ (κ_{eHH} resulting from axisymmetric theory). $\kappa_{e,rip}$ becomes important in the central region due to magnetic ripple effects on the "collisionless" electrons. The heat conduction at the edge of the plasma $r/a > 0.6$ has to be enhanced according to $\kappa_{eOH} \sim 1/T$ 0.6, as derived for ohmic discharges in W VII-A.

1.2.2 Ion heat conduction

For the energy balance of NI heated plasma a strong influence of radial electric fields on the ion heat conduction is indicated.

The measured high ion temperatures appear feasible, if the ion heat conduction is less than the neoclassical plateau theory predicts.

With radial electric fields taken into account, the heat conduction even in the plateau regime approaches the lower PS values. Such electric fields may be generated by the orbit losses of the injected particles to achieve ambipolarity. For the measured high ExB velocities almost no banana-type orbits of thermal ions exist.

1.2.3 Impurities

- Al ablation experiments to study the impurity transport have be seen in good agreement with neoclassical models.

- Time resolved measurements of Al lines have been compared with calculations of the radiative power. For this purpose measured density and temperature profiles are taken to calculate the impurity flux: $\Gamma_z = D\partial n_z/\partial r - v(r)\, n_z$

1.3 Neutral injection

- Experiments with an inverted magnetic field geometry (counter injection) exhibit no significant difference between co- and counter injection.

- The increased heating efficiency influenced by electric fields may be confirmed by the observation of even higher poloidal velocities with a reversed sign of the rotation.

- The residual plasma current ($U_L = 0$), which is observed to be proportional to the energy content, changes direction with the field ("bootstrap current").

- The high ion temperatures $T_{io} \simeq 1$ keV, both parallel and perpendicular to B_o, have been confirmed by Doppler measurements analyzing an OVIII line at 2976 A produced by charge exchange effects.

- Classical collisional slowing-down has been verified by analyzing the neutron production rate of $D^o \rightarrow D^+$ injection experiments with power modulation. The measured neutron flux and charge exchange flux fit very well to the collisional slowing down model.

- Theoretically, only the transient slowing-down distribution during switch on of the beam has been found to be unstable for low harmonic ion cyclotron modes.

- Consequently, the earlier hypothesis of preferential ion heating during NI ($P_{bi} \sim P_{IN}$) has been not supported. (P_{IN}: total power absorbed, P_{bi}: power transfered to the ions)

- Laser fluorescence measurements of the iron concentration near particular wall areas describe the loss mechanism of injected particles depending on the confinement conditions.

1.4 ECRH (Electron Cycl. Resonance Heating)

The experiments, using a 28 GHz gyrotron, have been finished (cooperation with IPF Stuttgart).

- To replace ohmic heating a plasma can be generated and heated with densities of $n \lesssim n_{cutoff} < 10^{13}$ cm^{-3} and temperatures of up to $T_e \sim 1.5$ keV at a magnetic field of 1 T.

- The advanced irradiation with the polarized TE11, HE11 mode leads to a concentrated power deposition and temperature increase compared with TE02 mode launching.

- Bulk plasma heating only by absorption of the ordinary mode seems to be indicated. A heating efficiency of 50 % has been achieved. A flat temperature profile ($T_e \sim 400$ eV) can be maintained by power deposition at the edge (ω_{ce} resonance 4 cm off axis).

- Rf measurements by means of a spectrum analyzer indicate parametric decay of the incident wave: According to the power absorbed at the lower hybrid frequency a high energetic ion tail may be generated.

1.5 ICRH (Ion Cyclotron Resonance Heating)

- First experiments have been started with 50 MHz to heat an ohmic target plasma: H minority heating at D_2, H_e plasma.
- Up to a power of $P_N < 150$ kW two different antenna systems have been tested.
- A strong increase of radiative losses (O, Fe), which counteracts the heating has been observed.
- High energetic ions, thermalized at $T_i \sim 3$ keV, have been measured.

2. PHYSICS IN W VII-A STELLARATOR

2.1 Parameter range, ß-limits

The helical winding system of W VII-A (l = 2, m = 5) produces a magnetic configuration with an external rotational transform $\iota_o < 0.6$ and low shear $\Delta\iota_o/\iota_o \sim 1$ %.

Currentless plasmas with NI ($P_N \sim 1$ MW) - typically $H^o \rightarrow D^+$ - have been studied for various ι values. At optimum confinement for $\iota \neq m/n$, close to ι = 1/2, 1/3, central ß-values versus the heating power actually coupled to the plasma are presented in Fig. 1. With NI for the conditions in W VII-A a maximum heating efficiency $\eta \sim 50$ % is obtained. So far Fig. 1 represents the accessible ß range: the maximum ß-values are shown to be proportional to the heating power, slightly dependent on the rotational transform. Experimental data derived from ECRH - generated plasma at 1 T are also included. Only a significant increase of the heating power would allow critical ß-values to be approached. The highest ß-values already correspond to about half the equilibrium limit of W VII-A.

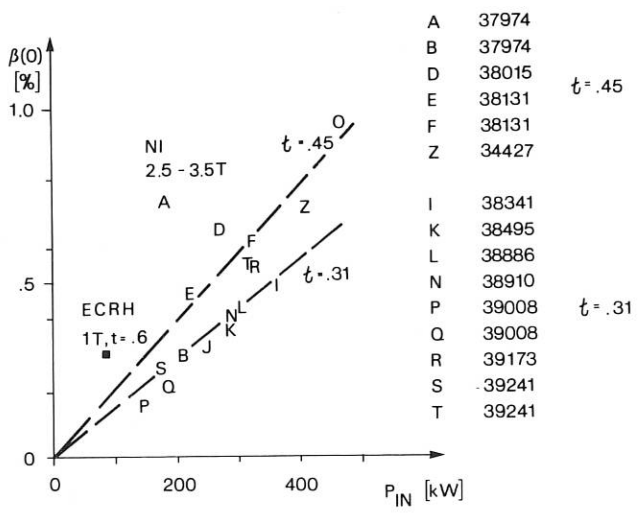

Fig. 1: Maximum ß values in W VII-A depending on effective heating power P_{IN}. Data for NI (2.5 - 3.5 T) and ECRH (1 T) are included.

In Fig. 2 theoretical predictions for stability ß are compared with experimental data. For particular values of the rotational transform ß limits are calculated according to the ANANIA, JOHNSON [1] code. Tokamak data based on the ß-limits postulated by TROYON and SYKES [2,3] are included. The edge value of the transform has been related to an equivalent plasma current. Calculations for $ß_s$ and $ß_n$ limitations by NÜHRENBERG, LORTZ [4] in W VII-A are also plotted. No MHD instabilities have been observed in W VII-A so far. Critical tests of the theoretical predictions seem to be restricted by the lack of heating power in W VII-A.

2.2 Effect of Rotational Transform and Residual Plasma Current on Confinement

Good confinement in W VII-A can only be established for certain values of the rotational transform . This strong dependence of confinement is similar to phenomena observed earlier in the low-ß Ba plasma of W II-A [5]. Although the ß-values in W VII-A are 5 orders of magnitude higher similar minima ("resonances") of confinement have been measured by variation of shot by shot. Figure 3 presents the

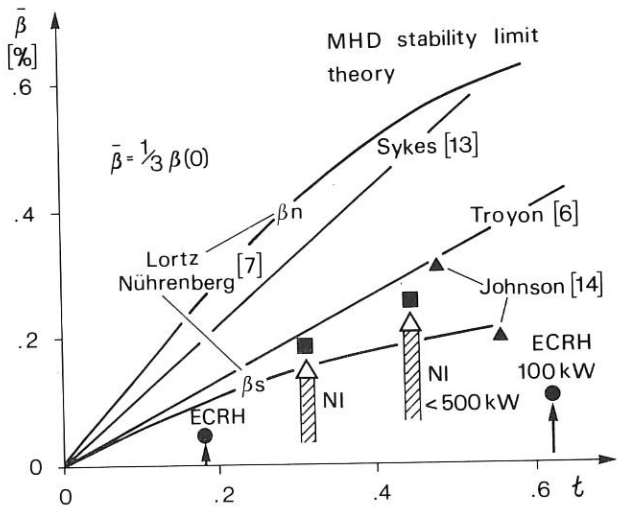

Fig. 2: Comparison of ß-limits for stability in W VII-A as predicted by theory with experimental data.

energy content for a main field of 1 T using ECRH at 28 GHz depending on the rotational transform at the plasma edge. Minima and maxima of confinement occur, the minima being related to low order rational numbers of ι = m/n, e.g. 1/2, 1/3, 2/3 .

1) Anania, G., Johnson, J.L., Phys. Fluids 26 (10) 1983, 3070
2) Troyon, f. et. al., Plasma Physics, Vol. 26 No 1A, 209 (1984)
3) Sykes, A. et al., 11th Europ. Conf. Contr. Fusion and Plasma Physics, Aachen 1983, Vol. 7D, 363
4) Lortz, D., Nührenberg, J., Nucl. Fusion 17 (1977) 125
5) Grieger, G., Ohlendorf, W., Pacher, H.D., Wobig, H., Wolf, G.H., in Plasma Physics and Controlled Nuclear Fusion Research (Proc. 4th Int. conf. Madison 1971) Vol. 3, IAEA, Vienna (1971) 37.

Significant maxima appear close to ι = 1/2, 2/3, where the number of low order rational values is less dense.

Variation of the external transform ι_o for different values of the remaining plasma current show that mainly the edge value of the transform $\iota = \iota_o + \iota_p$ determines the gross plasma behaviour. In addition, the confinement seems to be influenced even by the entire profile, modified by the residual current density distribution and the plasma pressure. Both pressure and current introduce shear.

By controlling the edge values of the transform - either by control of I_p, which is generated by the plasma pressure and by the heating mechanism, or by control of ι_o - good confinement at $\iota \neq$ m/n can be maintained.

The entire ι profiles are not directly measurable. But first experiments slightly modulating the external transform $\iota_o + \tilde{\iota}_o$ indicate a localization of perturbed regions on resonant surfaces. Soft X and ECE measurements with high spatial and temporal

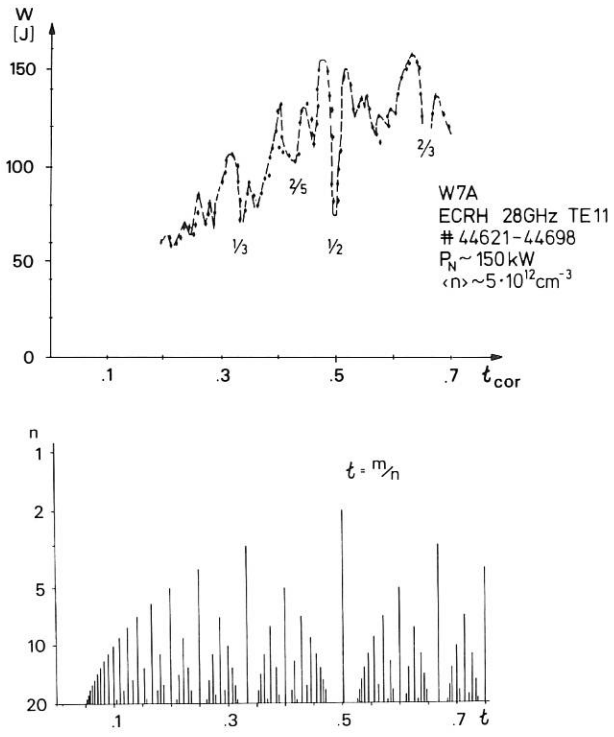

Fig. 3: Energy content depending on the rotational transform $\iota = \iota_o + \iota_p$ obtained for ECRH. For correlation rational values of ι = m/n are given and marked for low n,m.

resolution allow an analysis of the correlated positional shift of the perturbations. Finally fine adjustment of the transform may allow the impurity flow and plasma pressure profiles to be modified.

At rational values of the rotational transform islands can be formed by small perturbing fields. A combined effect of island formation and plasma convection may be responsible for the enhanced losses at ι = m/n, rather than being the result of instabilities.

Small shear evidently influences the width of these islands. The position of perturbed regions at the edge is most dangerous for the global confinement of the shearless W VII-A with a rather small plasma radius.

2.3 Neutral Injection

2.3.1 Neutral injection into W VII-A

As reliable operation of the injectors had been ensured in the previous years, the main task now was to keep the injectors running and in good condition. Fig. 4 shows the development of the overall injector reliability during the last three years of operation. "Overall reliability" is defined here as the ratio of good shots (all injectors worked as intended) to the total number of shots. The possibility of modulating the beam was mainly used for diagnostic purposes. An example is shown in Fig.10. Interrupting all beams together and reinjecting them into the afterglow did not postpone the radiation collapse of the W VII-A plasma. Seemingly, the impurities were confined during the afterglow at least as well as or even better than hydrogen ions.

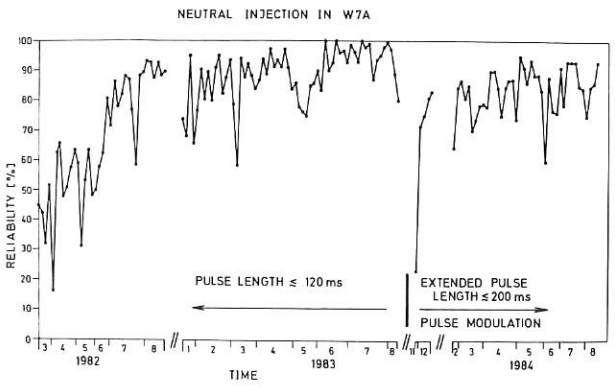

Fig. 4

The question of fast particle slowing-down was extensively studied in W VII. Both beam modulation and injection of deuterium instead of hydrogen provided additional diagnostic tools. Details are described below. It should be stated here, however, that it could be clearly shown that during the main part of the pulse the injected ions slowed down as a result of Coulomb friction. Nonclassical effects may have occurred only during a transient phase at the beginning of a beam pulse when the emission of high-frequency waves was observed for a period of about one slowing-down time.

The importance of radial electric fields for the confinement of the injected ions was re-affirmed. It is thought that this electric field is produced by the loss of some fast ions, which improves the confinement of the rest. A beneficial effect of the electric field on the plasma ion confinement also

had to be postulated in order to obtain a reasonable energy balance.

The main reason for the generation of electric fields as strong as observed in W VII-A is the almost perpendicular injection geometry. In W VII-AS, where injection will be tangential, little fast particle losses and therefore no enhanced electric fields are to be expected.

2.3.2 Energy balance

A major problem in the energy transport analysis of currentless, neutral beam heated discharges is to understand the high ion temperatures measured. In the past a model has been used where the neoclassical expression for the ion heat conductivity without radial electric fields has been applied. As a consequence, it had to be postulated that the plasma ions get almost the total beam heating power by some unknown anomalous heating mechanism. However, it has been shown in the meantime (see 2.3.3.2) that the slowing-down of the injected hot ions is collisional, which excludes such an anomalous interaction.

If the beam heating efficiency is calculated on the basis of Coulomb collisions between injected ions and plasma particles, the beam power is approximately equally distributed between ions and electrons for plasma parameters of W VII-A. Because of the almost perpendicular injection, radial electric fields derived from the observed poloidal plasma rotation increase the total heating efficiency considerably in agreement with the experiment. These fields change not only the particle trajectories of the injected hot ions, but influence even more the trajectories of trapped plasma ions, which dominate the ion heat transport at the achieved temperatures and densities. Taking potential differences between the plasma center and edge of the order of a few kV into account in the neoclassical calculation of the plateau ion heat conductivity, it can be shown that the resulting total ion heat conduction coefficient is close to the Pfirsch-Schlüter value in the center of the discharge. With such a corrected, i.e. reduced neoclassical ion heat conduction the observed ion temperatures in the center of the discharge could also be explained in the presence of collisional beam-plasma interaction in some first test discharges.

The electron energy transport is not changed significantly. In the center where the electrons are now also heated by the beam, a heat conduction coefficient $_e$ is needed which is about an order larger than the sum of the neoclassical and the anomalous values. Both terms are of the same order of magnitude. The anomalous one is taken as derived from ohmically heated discharges. Since the electron temperature profiles are strikingly flat in the center, resonant magnetic surface effects such as magnetic islands and convective cells are a possible explanation of this enhancement. At mid radii, where T_e has its maximum, the anomalous $_e$ is dominant and gives a good description of the electron energy transport.

The validity of the modified energy transport model will be further investigated by analyzing additional discharges. Especially the strong variation of the electron temperature profiles by minor changes of impurity concentration seems to be in contradiction to the high power transfer of the beam to the electrons.

2.3.3.1 Ion temperature

An ion temperature of 1 keV as measured by energy analysis of CX neutrals perpendicular to B has been confirmed by measurements of Doppler broadening of the OVIII line both perpendicular and parallel to B, and by the neutron flux from thermal D-D reactions. Fig. 5 shows a current-free discharge with 3 injectors for 130 ms and 1 injector pulsed for 40 ms. CX measurements show the ions to be heated from 200 eV during the ohmic phase to 900 eV with all injectors running. The maximum temperature from the neutron flux agrees within 10 %. Even better agreement has been achieved with the Doppler broadening measurement (see 2.3.5).

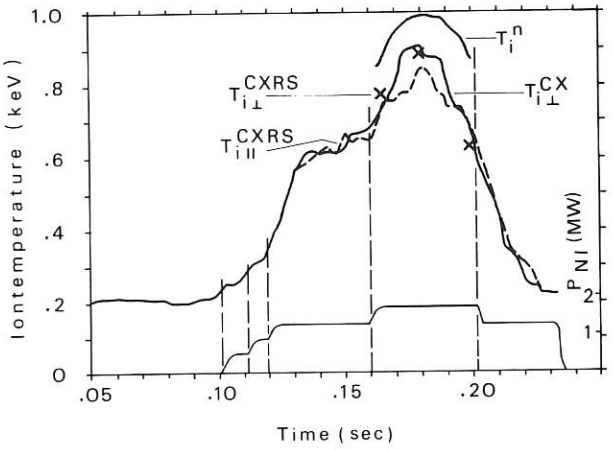

Fig. 5: Comparison of various ion-temperature results:
T_i^{CXRS}: Parallel temperature from OVIII (Doppler).
T_i^{CXRS}: Perpendicular temperature from OVIII (Doppler).
T_i^{CX}: Perpendicular temperature from charge exchange.
T_i^n: Temperature from neutron flux.

Due to the H^+ slowing-down distribution of the high density NI, the distribution of the thermal D^+ component may be disturbed (suprathermal tail). To investigate this, the nonlinear Fokker-Planck equation based on Coulomb interaction had been solved by Monte Carlo technique for H^o injection in a H^+/D^+ plasma mixture. Strong pressure anisotropy was found based on the H^+ distribution. However, the D^+ distribution was nearly unaffected (isotropic Maxwellian). The small deviations in the suprathermal tail of the D^+ spectrum are due to electron cooling ($T_e < T_i$) see Fig. 6.

2.3.3.2 Heating efficiency

The stationary energy spectrum of the hydrogen particles injected into a deuterium plasma has been measured. A Monte Carlo calculation of the high energy ion population assuming collisional slowing

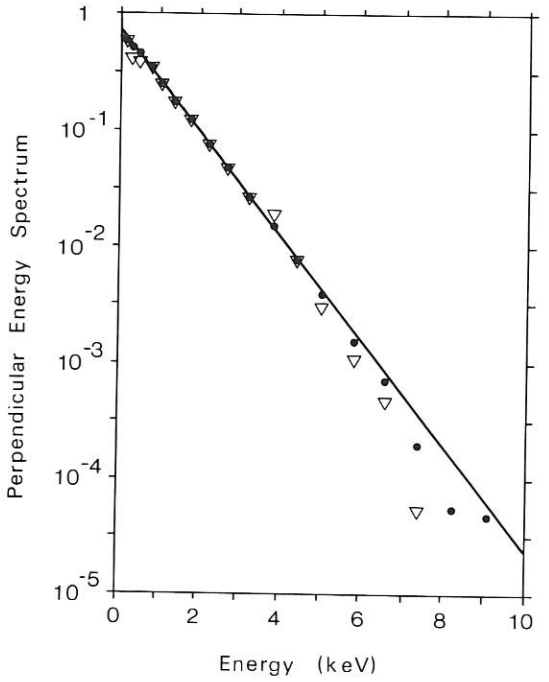

Fig. 6: Perpendicular energy spectrum of D^+ with injection of H^0 into H^+/D^+ plasma mixture.

down leads to the solid line distribution of Fig. 7, which shows good agreement with the measured data. At the injection voltage of 27 kV the beam power composition was assumed to be 40:30:30 for particles with 27, 13.5, and 9 keV.

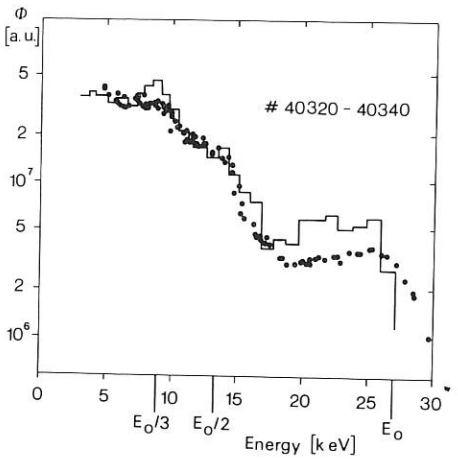

Fig. 7: Measured stationary energy spectrum of H^0 particles injected into D^+ plasma compared with Monte Carlo calculations for collisional slowing down.

For deuterium injection the neutron yield has been measured and found to be in agreement with the high energy (27 to 17 keV) deuteron density yielded by collisional slowing-down calculations. For various plasma parameters (T_i, n_i) the measured neutron yield varies as expected from the collisional slowing-down time.

The neutron flux follows the decay of the high energy deuteron density calculated for collisional slowing-down after switching off the deuterium injector. The deuterium target plasma was heated by 3 hydrogen injectors. By varying the plasma parameters from T_i = 1200 eV, n_i = 3.5×10^{13} cm^{-3} to T_i = 475 eV, n_i = 8.3×10^{13} cm^{-3} excellent agreement between the measured flux decay and the calculated one is obtained (Fig. 8).

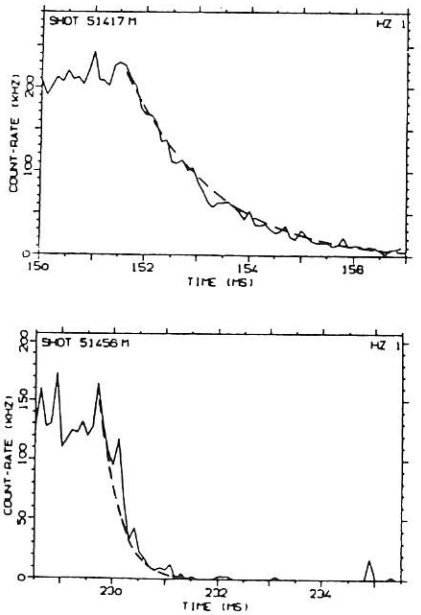

Fig. 8: Decay of neutron flux compared with collisional slowing-down calculations of the high energy deuteron density.

A detailed comparison between the CX particle flux decay at specific energies (28.6 to 6.3 keV) and the calculated decay of the deuteron density shows agreement within a factor 2 on the assumption of collisional slowing-down. Table I shows the measured and calculated decay times for two different plasma parameters (low and high slowing down times).

2.3.3.3 Heating efficiency (diamagnetic signal)

After the NI is switched off, the diamagnetic signal yields an enhanced decrease of the internal

Table I: Decay time (msec)

E(keV)	measured	calculated	measured	calculated
28.6 ± 3.9	0.4 ± 0.1	1.05 ± 0.25	—	0.5 ± 0.1
20.5 ± 2.3	2.45 ± 0.45	3.1 ± 0.5	1.3 ± 0.1	1.2 ± 0.3
12.7 ± 1.2	1.3 ± 0.3	1.6 ± 0.5	0.95 ± 0.25	1.25 ± 0.25
8.8 ± 0.7	2.6 ± 0.2	2.75 ± 0.3	1.75 ± 0.25	1.25 ± 0.25
6.3 ±0.5	4.35 ± 0.75	4.8 ± 0.9	2.15 ± 0.4	2.35 ± 0.5
Plasma Parameters	n_{eo} = 5×10^{13} cm^{-3} T_{eo} = 540 eV T_{io} = 1200 eV		n_{eo} = 9×10^{13} cm^{-3} T_{eo} = 360 eV T_{io} = 475 eV	

Energies of injected particles: E_o = 27 keV; 1/2 E_o = 13.5 keV, 1/3 E_o = 9 keV

energy production within an average slowing-down time. From this additional non-thermal part, the contribution of the slowing-down distribution to the internal energy $W_\perp$ was estimated and a pressure anisotropy of more than 10 % was deduced. The magnitude of this anisotropy is in agreement with Monte Carlo calculations based on collisional slowing down of the NI.

2.3.3.4 Ion cyclotron instabilities

A code has been developed for solving the linear electromagnetic dispersion relation for ion waves in a beam-plasma system with the beam distribution function, f_b, calculated by Monte-Carlo technique based on Coulomb interactions /153/. The ion cyclotron modes driven by nearly perpendicular NI have been analyzed for both transient and stationary conditions.

For stationary f_b, the low ion cyclotron harmonics are stable, instabilities being found only at the plasma resonance near the lower-hybrid frequency. These instabilities are highly localized in $\underline{k}$-space, i.e. they are driven only by regions in $v_\perp$ near the injection peaks, where $\partial f_b/\partial v > 0$. As the bulk of f_b is stable, the distribution function will be smoothed near the injection peaks by quasilinear effects. Thus the energy transfer is expected to be mainly collisional. For bad confinement properties (particle confinement time of the order of magnitude of the slowing down time), however, nonresonant instabilities at higher harmonics were found. These instabilities are mainly driven by the loss cone which enlarges the region of $\partial f_b/\partial v > 0$.

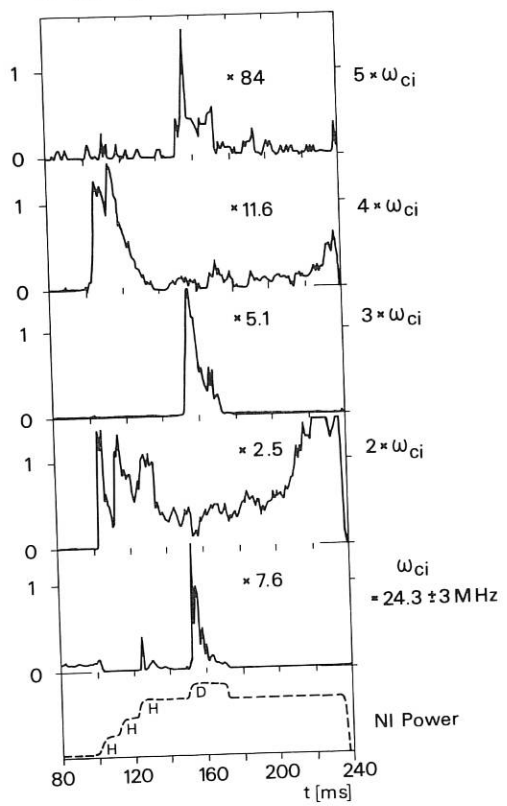

Fig. 9: Emission at low harmonics of the deuterium ion cyclotron frequency.

After the NI is switched off regions with $\partial f_b/\partial v > 0$ vanish. The slowing-down distribution is characterized by the broad near-thermal component, which has a stabilizing effect on the ion cyclotron modes. In this case, no instabilities are expected.

After the NI is switched on, the low harmonics were found to be weakly unstable. Strong instability, however, was found at higher harmonics even below the lower hybrid frequency. As the growth distances are small, one would expect energy transfer to the thermal ions through these ion cyclotron modes. This is consistent with a simultaneous increase of T_i in the experiment after the 4th injector is switched on, whereas T_e remains constant. A further indication of instabilities in the switching on phase are ICE signals in the low harmonic range (see Fig. 9), suggesting quasilinear or parametric effects.

2.3.4 Neutron flux measurements

2.3.4.1 Determination of the ion temperature

For the analysis of the energy balance it is desirable to check the ion temperature by different methods.

The central temperature of neutral beam heated (H^0 injection) deuterium plasmas is derived from neutron flux measurements with a He^3 proportional counter. The input parameters for the calculation are:

- The radial density profiles of the D^+ ions. These are taken from the measured electron density profiles using estimates of Z_{eff} and the content of hydrogen ions in the plasma.
- The shape of the ion temperature profiles.
- The response function of the detector, which is measured with a Pu-Be neutron source.

Typically the values of the ion temperature from this method are up to 10-15 % higher than those obtained from other measurements (see 2.3.3.1, Fig. 5).

2.3.4.2 Deuterium injection experiments

Also important with respect to the energy balance are the characteristic slowing-down times of the neutral beam injected particles. In addition to measurements of the neutral particle fluxes the neutron production originating from injecting a D^0 beam into a deuterium plasma provides a method of determining the slowing-down time from the injection energy ($\sim$ 27 keV) down to $\sim$15 keV.

Information about the slowing-down process can be derived from:

- The toroidal distribution of the neutron production rate in the case of local injection with 1 D^0 injector.
- The absolute value of the stationary neutron flux.
- The transient behaviour of the neutron flux after switch on/off of 1 D^0 injector.

For the absolute neutron flux measurements the calibrated He^3 - counter was used. Additionally a NE 213 liquid scintillator detector with fast electronics served to rule out possible count rate losses of the He^3 - counter since the neutron fluxes due to beam-plasma interaction exceed the fluxes generated from plasma-ion interaction by a factor of $\sim$20. A second He^3 - counter was moved in the toroidal direction. This detector in particular allowed to determine the neutron flux produced by the interaction of the injected deuterium not absorbed from the plasma with the deuterium absorbed on the beam dump plates. At the injection port this fraction is comparable with the neutron flux from beam-plasma reactions, but this local production does not interfere with the measurements made at some distance from the injection port.

The results of the measurements can be summarized as follows:

- The neutron production (from beam-plasma reactions) is toroidally homogeneous. This means that the time for the slowing-down of the fast ions is long compared with the transit time of these ions around the torus.

- The former result also allows to give the absolute neutron flux, which agrees with calculations based on collisional slowing-down within a factor of $\sim$2. Typical values are $2 - 4 \times 10^{10}$ n/s.

- Also the transient response of the neutron fluxes is in good agreement with the calculations assuming Coulomb collisions of fast injected D^+ ions with the plasma (see 2.3.3.2, Fig. 8).

2.3.5 Doppler measurements of ion temperature and mass flow

For a better understanding of the energy balance during neutral injection, it was necessary to gain information on the ion temperature and mass flow parallel to the magnetic field.

Recently it was proposed to use for this purpose Doppler measurements of impurity lines in the visible or near UV, where these lines are produced in the process of charge exchange recombination, involving high-energy injected neutral hydrogen and e.g., fully stripped oxygen [1),2),3)].

The experimental setup was therefore changed, thus allowing toroidal observation of the plasma, the line of sight intersecting a beam of injected neutral hydrogen (energy 27 keV).
The line used results from a transition of O VIII (hydrogen-like oxygen, n = 8 n = 7), at 297.6 nm. In order to ensure observation of the desired line, the neutral beam was switched off for a few ms (Fig. 10). Since the observed signal practically disappeared and reappeared instantaneously with the switching off and on of the beam, it was concluded that the observed line-radiation indeed resulted from the CXRS line, described above.

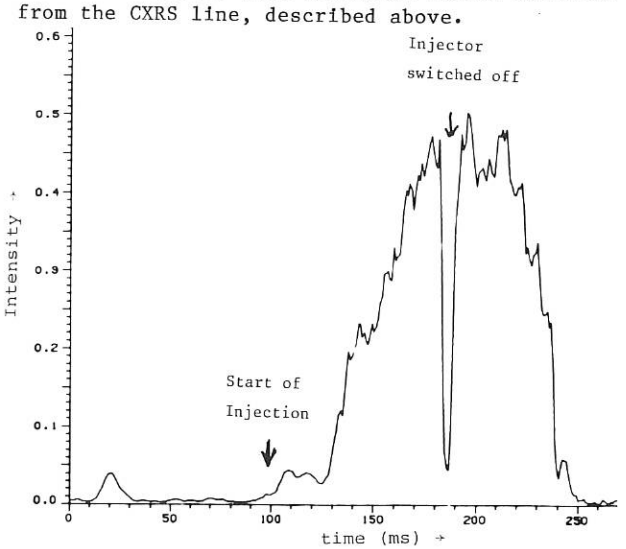

Fig. 10: Intensity of the OVIII line.
Injector switched off for a few ms .

With this line it was possible to deduce the central ion temperature and the central mass velocity. The angle of observation with respect to the magnetic field was roughly 10 degrees. Therefore both results represented a good approximation of the parallel values of temperature and velocity.

The observed parallel mass velocities were always smaller than 3×10^4 m/s. Thus it was confirmed that the formerly observed poloidal velocities were indeed not just components of toroidal ones.
Fig. 5, 2.3.3.1, gives a comparison of ion temperatures deduced from charge exchange analysis, yielding the component perpendicular to the magnetic field, and deduced from Doppler width measurements of the O VIII line for the parallel component.

Also included are temperatures deduced from Doppler measurements of the O VIII line perpendicular to the magnetic field and temperatures resulting from neutron measurements.

Within the experimental errors the agreement is excellent.

2.3.6 Impurity transport studies

2.3.6.1 Experiments

In neutral beam heated discharges with good confinement properties ($\tau_p \sim$100 ms) high radiation losses are observed. Typically the currentless phase can be maintained for about 100 - 150 ms. After this time radiation losses from accumulated impurities, also enhanced by the increased electron density, have increased so much that they lead to a significant decay of the electron temperature.

The dominant part of the radiation losses in the plasma center (up to 80 %) consists of line

1) Isler, R.C. et al., Appl. Phys. Lett. 42, 355 (1983)
2) Fonck, R.J. et al., PPPL-Report, Nr. 2067, Dec. 1983
3) Suckewer, S. et al., PPPL-Report, Nr. 2081, Feb. 1984

radiation from He- und H-like oxygen impurities [1].

Four different types of plasma discharges have been studied in particular /198/:

Discharges with relatively low density and narrow density profiles (without gas puff) are compared with high-density discharges characterized by significantly broader density profiles (with steady gas flow), which are expected to have a beneficial influence on the retardation of the central impurity density build-up.

A second comparison was made between experiments corresponding to "co" and "counter" neutral beam injection.

Total radiation measurements were performed with a 10-channel bolometer system and a soft X-ray camera composed of 30 surface barrier diodes which are sensitive to radiation $\gtrsim 400$ eV. The radiances of

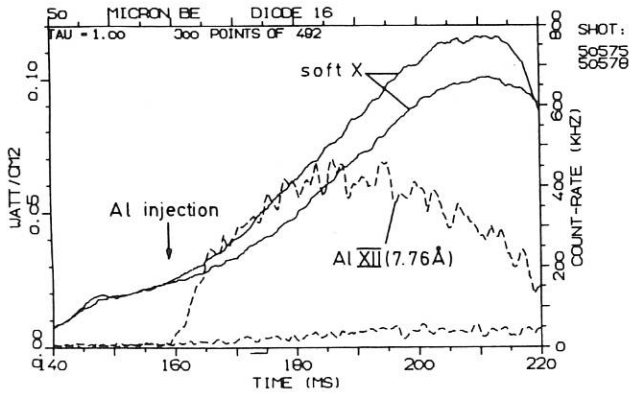

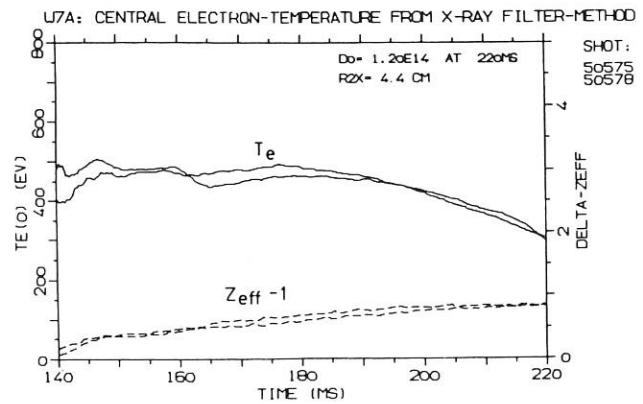

Fig. 11: a) Signals of central soft-X-ray diode and signals of Al XII from crystal spectrometer for discharges with and without Al injection.
b) T_e and Z_{eff} from soft-X continuum radiation.

1) W VII-A Team, NI Group, Plasma Physics and Controlled Nuclear Fusion Research (1982), Baltimore, IAEA CN 41/L5

various resonance lines along a chord through the plasma center were recorded with a flat crystal spectrometer operating between 7 - 20 Å and a grazing incidence spectrometer. Another VUV-spectrometer supplied with a rotating mirror can also provide radial scans of resonance radiation from lower ionization states. But generally the radiation originating near the plasma edge shows significant asymmetries which do not allow the measurements to be compared with 1-dimensional transport calculations.

The transport of Al trace impurities injected by the laser blow-off technique was experimentally studied by soft-X measurements. Radial and time resolved data on the combined radiation power from Al-XII and Al-XIII resonance lines are derived from the soft-X radiation through a 50 μm Be filter which compared to the case without filter attenuates the radiation by a factor of about 100, whereas the Al radiation at about 7 Å is only reduced by a factor of ~ 5. Typically, a 10 - 30 % increase of the filtered X-radiation has been observed when Al was injected into the plasma in tolerable doses by laser blow off (Fig. 11).

The local power of the Al radiation can be evaluated by taking the difference between similar shots with and without Al injection after Abel-inversion. In order to correct for small n_e, T_e, Z_{eff} deviations of the shots taken for subtraction, HCN-laser interferometer signals and T_e and Z_{eff} measurements from X-continuum radiation were used. Oxygen continuum radiation has been assumed to be responsible for producing the radiation without Al injection

2.3.6.2 Impurity transport code

The one-dimensional simulation code for impurity transport and radiation, SITAR [1], has been used to describe the total radiation observed by soft-X and bolometer measurements as well as line radiation from oxygen and aluminium, the latter injected as a tracer impurity. The neoclassical transport fluxes due to collisions of the impurity ions with the background plasma have been taken from [2]. The Pfirsch-Schlüter fluxes including the interaction of impurity ions in different charge states have been evaluated using the formalism given in [3] with the modification proposed in [4] to account for the mixed collisionality of background and impurity ions. For our standard calculations, however, the following approximate expression for the PS fluxes due to collisions between different charge states has been used:

$$\Gamma_z^{add.} = \sum_{z' \neq z} \frac{\varrho_{z'}^2}{\tau_{z'z}} \cdot \frac{1}{\sqrt{2}} \cdot \frac{z'}{z} (0.5 + q^2) \cdot$$

$$\left(\frac{\partial n_{z'}}{\partial r} - \frac{n_{z'} \cdot z' \partial n_z}{n_z \cdot z \partial r} - \frac{1}{4} \cdot \left(\frac{z'}{z} - 1 \right) \frac{n_{z'}}{T} \frac{\partial T}{\partial r} \right)$$

1) F. Sardei, A. Weller publication in preparation
2) TFR Group, Nuclear Fusion 22 (1982) 1182
3) S.P. Hirshman, Phys. Fluids 20 (1977) 589
4) R.J. Hawryluk, S. Suckewer, S.P. Hirshman, Nuclear Fusion 19 1 (1979) 607

This representation allows a substantial saving of computing time without loss of accuracy for typical W VII-A experimental conditions.

Particularly in the case when oxygen concentrations exceed ~1 %, this term leads to a considerable enhancement of the transport fluxes. They were separated into a diffusive and a convective term ($\Gamma_z = -D_z \partial n_z/\partial r - v_z n_z$). Also the anomalous transport, if it applies, is modelled this way, with D and v equal for all charge states. Fig. 12 gives an example of the calculated neoclassical diffusion coefficients and convective drift velocities for various Al charge states. For typical density and temperature profiles in W VII-A the velocity is generally inward.

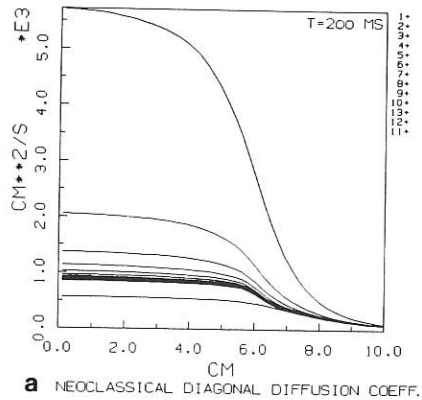

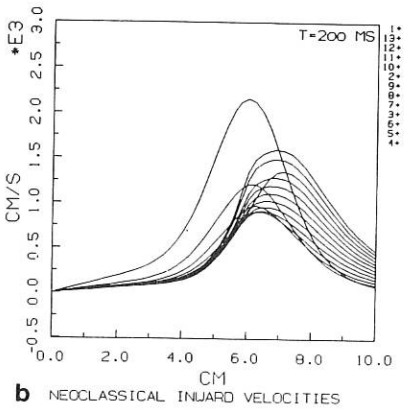

Fig. 12: Calculated radial distribution of neoclassical diffusion coefficient and inward drift velocity (sum of classical, Pfirsch-Schlüter and plateau terms) for a particular time (200 ms) of a high-density discharge.

The source term of neutral beam injected impurities was calculated by a Monte Carlo beam injection code [1]. Charge exchange recombination of the impurity ions with the injected hydrogen neutrals is included. The excitation rate coefficients are taken in the form given in [2].

1) G.G. Lister, W. Ott, E. Speth, Proc. of the Joint Varenna-Grenoble Int. Symp. on Heating in Toroidal Plasmas, Grenoble, Vol. I (1982) 103
2) T. Kato, Report IPPJ-AM-2 (1977)

2.3.6.3 Results of Al laser blow off experiments

Fig. 13a shows the evolution of the spatial distribution of the radiation power density of Al XII and Al XIII after laser blow-off ($\sim 3\times10^{16}$ Al atoms). At the beginning, a peak of Al density is formed at ~5 cm, as indicated by the hollow radiation profiles. After 10 - 15 ms a transition to peaked Al density profiles occurs. In Fig. 13b a code calculation is presented which simulates quite well the measured intensity. For this particular high-density discharge hollow plasma density profiles are maintained by strong gas feed during the Al penetration phase. Therefore, the relatively small neoclassical diffusion coefficient in the plasma center of about 500 cm ^{2} s^{-1} in combination with a small outward convection velocity implies a relatively slow transport to the plasma center. In order to simulate the faster increase of the central radiation and the accelerated transition to peaked profiles, an additional anomalous diffusion coefficient of the order of 2000 - 3000 cm^2 s^{-1} had to be added at particular radial ranges. This rather local deviation from neoclassical transport may possibly be caused by magnetic island formation near the plasma center. This hypothesis is based on investigations of the dependence of the energy and particle confinement on the external rotational transform and residual current (see 2.2). Moreover, for typical discharges fairly flat temperature and density profiles are always observed around the plasma center.

The decay of the Al radiation intensity is almost entirely caused by the electron temperature reduction at the end of the discharge. This is illustrated in Figs. 13c,d where the Al density corresponding to the calculation of the radiation intensity (Fig. 13b) is plotted. The measurement is thus consistent with only negligible losses of Al ions for the whole duration of the discharge. In the plasma center even a steady increase of the Al density can be observed which seems to be an effect of the neoclassical inward velocity in combination with the continuous steepening of the plasma density in the plasma center.

Regarding the Al transport in the low-density discharge which always shows fairly peaked plasma density profiles, good agreement is obtained between the experimentally observed Al radiation and code predictions based only on neoclassical transport. The absolute values of the measured central Al radiation power are reproduced by the simulations within a factor of ~2.

With respect to the comparison of "co" and "counter" experiments, no significant difference has been found in their behaviour. Possible modifications of the impurity fluxes caused by the different momentum transfer of "co" and "counter" neutral beam injection are apparently very small owing to the nearly perpendicular injection. Also no strong toroidal rotation and no significant difference of the basic plasma parameters is observed.

Sudden redistributions of the Al ion density occurring within short time intervals (some ms) could be detected by varying the Al injection time.

This is particularly evident during the existence of hollow Al radial profiles with steep gradients. Qualitatively, this behaviour was modelled by anomalous transport fluxes which shift Al impurities outward, flattening the Al density peak at about 5 cm. This effect seems to be correlated with small modulations of the plasma pressure observed during maximum energy content. The structure of the magnetic surface may be affected by critical values of pressure-driven currents which can produce localized magnetic islands at rational ι-values.

2.3.6.4 Simulation of the total radiation

In order to check the transport terms with a different impurity species for the same discharges investigated with Al tracer impurities, the total radiation losses were also calculated by summation over the relevant resonance lines. In Fig. 14 the local soft-X radiation (14a) is compared with a simulation based on neoclassical transport and the same anomalous term already used in Fig. 13 (14b).

The need for including additional anomalous transport is not very stringent. Almost all oxygen calculations with neoclassical transport lead to good agreement with the measurements. In this calculation a 1 % oxygen content in the neutral beams and an influx of $\sim 3 \times 10^{13}$ cm^{-2} s^{-1} from the walls ($\hat{=}\ 2.8 \times 10^{18}$ s^{-1}) can explain the observed central radiation power. These two impurity sources contribute in almost equal parts.

Z_{eff} derived experimentally from the soft-X continuum reaches a value of about 1.8, corresponding to an oxygen concentration of about 2.2 % of the electron density.

The low-density discharges (without gas puff during NI) are characterized by significantly higher central radiation losses with Z_{eff} up to 4.5 and n_o/n_e increasing up to 7 %. The oxygen influx from the walls has to be increased up to 8×10^{13} cm^{-2} s^{-1} ($\hat{=}\ 7.5 \times 10^{18}$ s^{-1}) in the calculations. In this case 1 % beam impurities contribute only 15 % of the central impurity content.

2.3.6.5 Summary and conclusions

The main features of the impurity transport in W VII-A seem to be consistent with neoclassical predictions. Localized additional anomalous transport during particularly short time intervals improves the agreement of code calculations with the experimental data for certain types of discharges. These regions of enhanced impurity transport may be caused by modifications either of the ι-profile (change of the residual current distribution) or of ι(a) (modulations of the helical field). Simulations with Al and O impurities provide a consistent description of the transport. The analysis of the total radiation in discharges with and without additional D gas feed indicate a reduction of the impurity radiation level in the plasma center due to broad plasma density profiles. This is to be expected with neoclassical transport theory because of the low inward convection velocity in the plasma center. Al injection experiments also show a higher central Al density for discharges without gas puff. The penetration of impurities to the plasma center can be studied by the laser blow-off technique. The characteristic behaviour of different discharge types, as expected from neoclassical theory, seems to be masked by contributions of anomalous transport. A dependence of the neutral beam induced

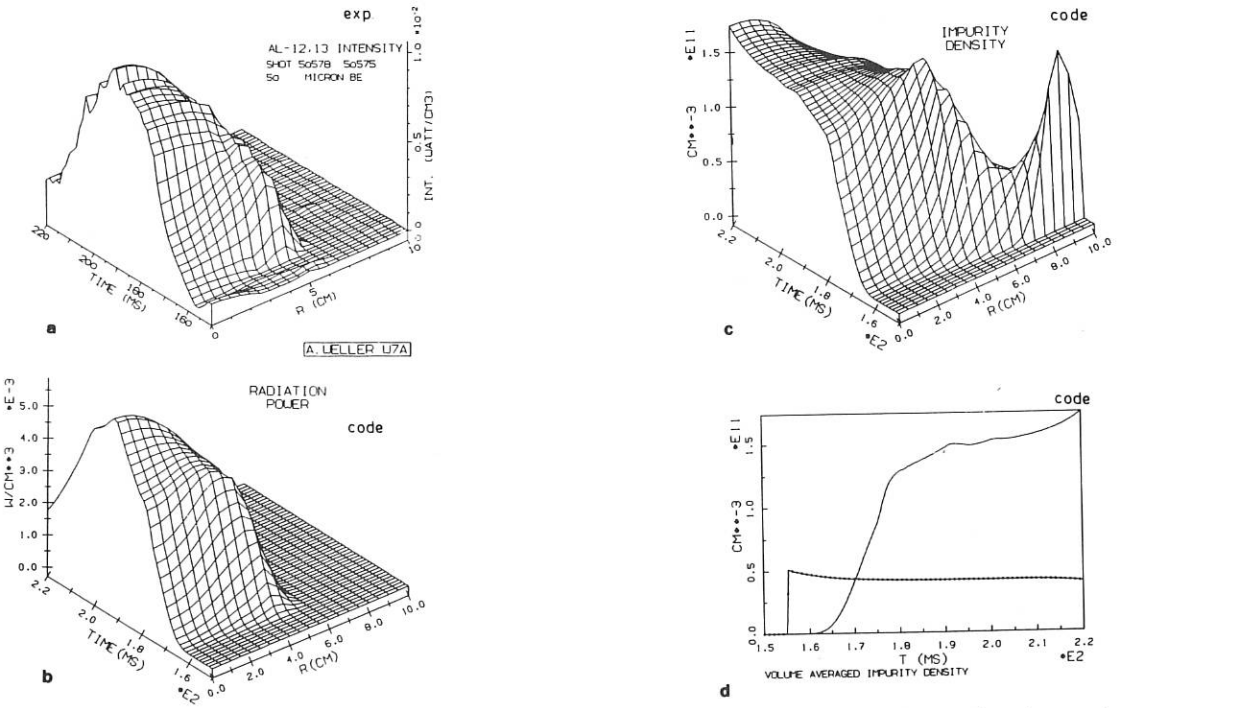

Fig. 13: a) Evolution of Al XII, XIII radiation power from soft-X measurements after Al injection into a high-density discharge.
b) Code simulation of a)
c) Evolution of Al ion density and
d) central and volume-averaged Al ion density, as predicted by the code.

transport on the toroidal momentum transfer could not be observed, probably due to the almost perpendicular neutral beam injection.

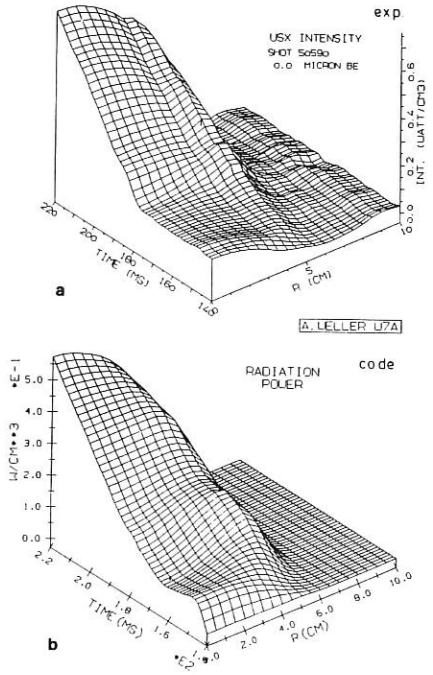

Fig. 14: a) Soft-X radiation ($E \gtrsim 400$ eV) for the same experimental conditions as in Figs. 12, 13.
b) Code simulation of soft-X radiation with oxygen

2.3.7 RF probe measurements

AC and DC probe measurements with a shielded Langmuir probe at a position inside the limiter shadow were continued during this year. Particularly the ion cyclotron instability at frequencies $\omega = n \cdot \omega_{ci}$ (ω_{ci} = ion cyclotron frequency of target and injected particles, n = 1, 2, 3,...) observed during the NB injection into OH, net-current-free and EC-heated plasmas was investigated in more detail.

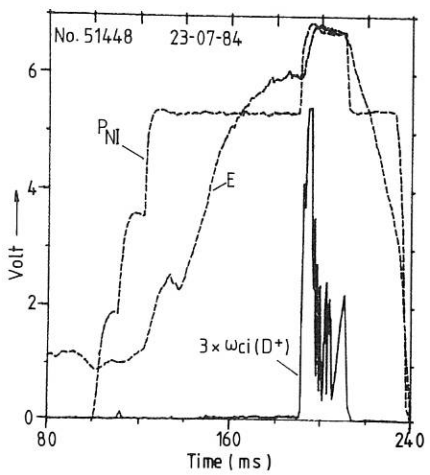

Fig. 15: $3\omega_{ci}(D^+)$ signal, total NB power and plasma energy vs. time, 3 NB injectors with H, build-up net-current-free D plasma, test NB injector with D, Shot No,: 51448 (23.7.84).

The typical variation in time of the amplitude of the $n\omega_{ci}$ signals (see Fig. 15 and Fig. 9, 2.3.3.4) is a fast rise of the signal to a high level at the start of NB injection, which is followed by a slowly varying reduction of the signal to a low level or even to a level vanishing in the noise, depending on the actual plasma parameters. The signal rise time is of the order of the NB switching-on time, while the decay time can be up to 10 ms. The transient peak amplitude of the $n\omega_{ci}$ signals varies also with the actual target plasma parameters. It is the smaller, the earlier the test injector is started into the net-current-free plasma build-up phase and it is the larger, the later the test injector is fired into the target plasma, where both the plasma density and energy are higher.

Parts of the observed behaviour of the $n\omega_{ci}$ signals in connection with CX measurements may be understood by stability investigations of such a plasma-beam system (see 2.3.3.4).

In 28 GHz EC-heated plasmas the low-frequency parametric wave decay spectrum could be measured with RF probes (Fig. 21, 2.4.1.3). This spectrum shows a growing amplitude with frequency and a $n\omega_{ci}$-modulation and has a sharp upper frequency

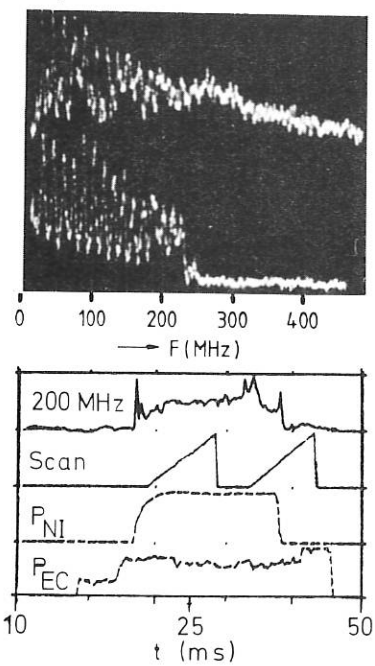

Fig. 16: Low frequency spectra (f: 0 to 500 MHz, 10 db/div, top, trace 1/2) at 2 scan times and 200 MHz signal (trace 3), spectrum analyzer scan (trace 4), NBI- and ECRH-power (trace 5/6) vs. time during 28 GHz ECRH and NBI-heating. Shot No: 49303 (23.5.84), 1.0 T, D plasma, 4 Inj. (H), 28 GHz HE11-mode.

limit at the "lower hybrid" frequency of the target plasma. A strong amplification of the n_{ci} signals as well as an expansion of the spectrum to higher frequencies is observed, when the NB's are injected into the EC-heated target plasma (Fig. 16).

2.4 Electron Cyclotron Resonance Heating

The ECRH activities in 1984 are characterized by two different phases:

a) The heating experiments at 28 GHz (B_{res} = 1 T, $n_{e,crit} = 10^{19}$ m^{-3}) were continued until the summer break. The main interest in these experiments was focussed on a comparison of the plasma behaviour for different kinds of wave launching and the associated plasma phenomena.

b) Within the second experimental period a 70 GHz ECRH-system (200 kW, 0.1 s) was installed and successfully tested. The gyrotron was specially developed for IPP to fit the nominal field of the future W VII-AS (B_{res} = 2.5 T, $n_{e,crit} = 6\times10^{19}$ m^{-3}) and will be part of the final W VII-AS heating system (1 MW). First plasma experiments were performed exactly on schedule in December 1984.

2.4.1 28 GHz experiments

2.4.1.1 Plasma parameters for different wave launching

Once the experiments with simple irradiation of the gyrotron mode mixture, containing mainly the axisymmetric TE_{02} mode (see annual report 1983) were finished, the transmission line and the launching system were successively modified (see annual report of IPF Stuttgart, this volume). Detailed studies were performed irradiating the axisymmetric TE_{01} mode and the almost linearly polarized TE_{11} and HE_{11} modes. As can be seen in Table 1, these modes are mainly characterized by their beam divergence and polarization with respect to the main field, i.e. the ordinary (O) and extra-ordinary (X) mode fractions.

	TE_{02}	TE_{01}	TE_{11}	HE_{11}
Beam divergence (3 dB)	25°	14°	6°	6°
Power deposition	broad		narrow	
Polarization $\tilde{E} \parallel B_o$	50 %	50 %	90 %	96 %

Table 1: Main characteristics of the different modes launched into the plasma.

For both axisymmetric modes half of the power is in X-mode orientation and this fraction is reflected back from the X-mode cut-off layer at the outer edge of the plasma. Penetration of this part towards the resonance layer can only be expected via multiple reflections from the torus walls. For both linearly polarized modes the beam quality is about the same and no distinction will be made in the discussion of the results later on. Nevertheless, the HE_{11} mode is of great technical interest because of its low damping and the possibility of optical treatment (Gaussian-like beam). In all cases, the waves are launched from the low-field side of the torus in the equatorial plane perpendicular to the direction of the main field B_o. For the linearly polarized irradiation (O-mode), a polarization twist reflector was mounted at the inner torus wall to focus the non-absorbed fraction of the incident power back to the plasma in X-mode polarization. This mirror is equipped with rf-measuring ports at 3 different positions giving access to a direct measurement of the rf-power absorbed by the plasma in a single path.

In the shearless W VII-A Stellarator the plasma parameters are strongly dependent on the rotational transform ι. Optimum confinement conditions for OH-current-free plasmas were found slightly below and above the rational ι-numbers 1/2 and 2/3. Most of the experiments reported later on were therefore performed at $\iota = 0.46$ and $\iota = 0.64$. The plasma density was externally controlled by gas puffing and kept constant during the discharges at central densities of $n_{eo} \simeq 5\times10^{18}$ m^{-3}, which is half the cut-off density $n_{e,crit}$. For this density, deflection of the beam and thus broadening of the power deposition profile can be neglected while the O-mode single-pass absorption is still near to optimum value at $n_{eo} \simeq 0.7 n_{e,crit}$ for a given electron temperature. As seen from Table 2, a doubling of the central electron temperature T_{eo} from 0.6 to 1.2 keV is observed when going from the simple to the advanced coupling system, whereas the total plasma energy content W_p increases only slightly. The ions remain at low temperatures and are almost decoupled from the hot electrons due to the low density.

	T_{eo} /keV/	T_{io} /keV/	W_p /J/	η
TE_{02}	0.6 ± 0.06	0.15	110	0.4
TE_{01}	0.9 ± 0.1	0.14	100	0.45
TE_{11}	1.1 ± 0.1	0.17	150	0.55
HE_{11}	1.2 ± 0.1	0.17	150	0.55

Table 2: Comparison of the central temperatures of electrons (T_{eo}) and ions (T_{io}) as well as the total plasma energy content W_p and the global heating efficiency η for the different modes (incident rf-power P_{RF} = 180 kW).

The heating efficiency defined by

$$\eta = \frac{P_{ABS}}{P_{INC}} = \frac{dW_p/dt}{\Delta P_{INC}},$$

where P_{ABS} is the absorbed rf-power and ΔP_{INC} is the modulation depth of the incident power, was determined by pulse modulation techiques.

As seen from Fig. 17, the measured heating efficiency at different temperatures T_{eo} can be explained by ray-tracing calculations of the ordinary-mode single-pass absorption only. An upper boundary is given by the simple formula for the optical thickness of a plasma with homogeneous temperature T_{eo} and density n_{eo}, which is also indicated in the figure.

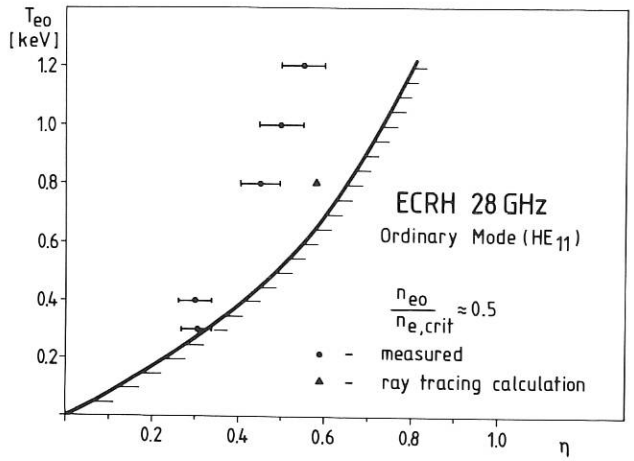

Fig. 17: Central electron temperature T_{eo} versus the measured overall heating efficiency for $n_{eo}/n_{e,crit} = 0.5$. The upper boundary is determined from the optical thickness of a plasma with uniform temperature T_{eo} and density n_{eo}. One ray tracing calculation based on measured profiles is also shown.

The measurement of the power distribution incident on the polarization twist reflector gives direct access to the ordinary-mode single-pass absorption and is shown in Fig. 18 for discharges at two different central electron temperatures.

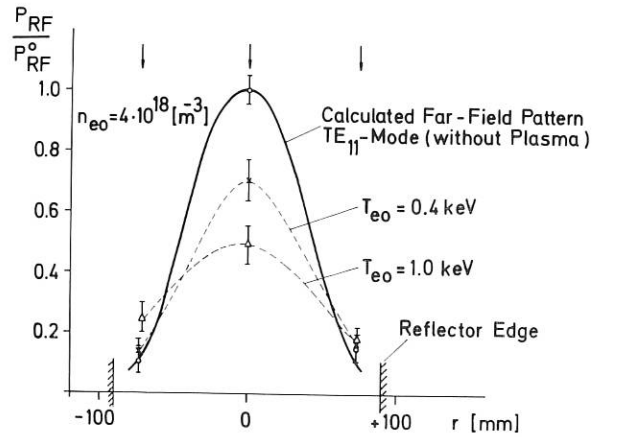

Fig. 18: Normalized rf-power distribution incident on the reflector at the inner torus wall. The positions of the three rf-measuring ports are indicated by arrows, r = 0 is in the equatorial plane.

The fraction of power absorbed in a single pass derived from this measurement is equal to the measured total absorbed power within the experimental errors. This shows that the overall heating efficiency can be explained by the ordinary mode single-pass absorption alone.

For the advanced coupling system (TE_{11}, HE_{11}) this heating efficiency is less than expected from theoretical considerations. According to theory, the nonabsorbed fraction of the incident power (O-mode), which is reflected to the plasma in X-mode polarization from the high-field side, should undergo mode conversion to backward travelling electron Bernstein modes near the upper hybrid layer, which should then be absorbed in the plasma centre.

One possible explanation for the weak contribution of the extraordinary wave to the total heating efficiency as found in the experiments may be disturbance of the upper hybrid (UH) layer by density fluctuations. For the resonance layer on axis the UH-layer is positioned close to the outer plasma edge. Spatial disturbance (which would be stationary on the wave frequency time scale) of the UH-layer would lead to a wide angular spread of the electron Bernstein modes, which would then be absorbed favourably near the plasma boundary, where the confinement is bad and a weak contribution to bulk plasma heating is expected. A second explanation would be parametric decay of the X-mode pump wave near the UH-layer. This phenomenon was clearly identified and will be discussed later (see 2.4.1.3).

2.4.1.2 Transport considerations

The ECR-heated plasmas are characterized by high electron temperatures and low densities. The ions are only weakly coupled to the electrons and play a minor role in the energy balance. These plasmas therefore give access to electron heat transport studies in the long mean free path regime. The measured temperature and density profiles were modelled by transport calculations using the Garching TEMPL steady-state code and the Princeton BALDUR code modified at IPF Stuttgart for net-current-free Stellarator application. Excellent agreement with the measured profiles was obtained using the following expression for the electron heat diffusivity χ_e:

$$\chi_e = \chi_{e,HH} + \chi_{e,rip} + \chi_{e,OH},$$

where $\chi_{e,HH}$ is the axisymmetric Hazeltine Hinton term

$$\chi_{e,HH} \propto \frac{T_e^{3/2}}{R\,B^2 \ell}$$

and $\chi_{e,rip}$ gives the neoclassical losses induced by a helical magnetic field ripple ε_H

$$\chi_{e,rip} \propto \chi_{e,HH} \cdot \varepsilon_H^{3/2} \cdot \lambda \ell / R,$$

λ is the mean free path of the electrons.

Finally, an anomalous term $\chi_{e,OH}$ has to be added, which was previously obtained empirically from ohmic discharges in W VII-A and gives the contribution at the plasma edge:

$$\chi_{e,OH} \propto \frac{1}{n_e T_e^{2/3}}$$

Optimum agreement with the measured temperature profiles was obtained with a proportinality factor of 2×10^{18} as compared to 3.8×10^{18} for OH-discharges at 3.5 T.

Radiation losses were found to be 10 kW and are

also included in the calculations. The ion heat conduction was treated as neoclassical, charge exchange losses being included. Fig. 19 shows the comparison of measured and calculated profiles for the TE_{02} and TE_{11} irradiation.

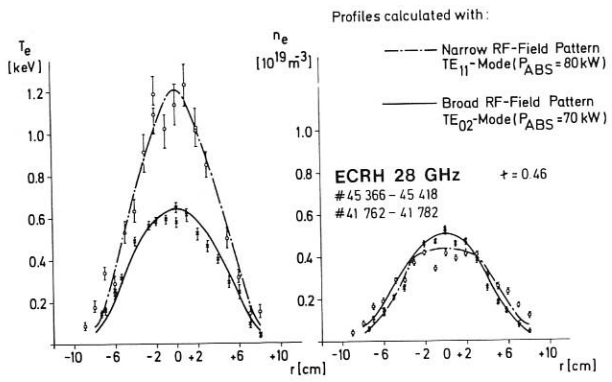

Fig. 19: Comparison of measured and calculated profiles of electron temperature and density for both the TE_{02} mode and TE_{11} mode irradiation.

Excellent agreement between measured and calculated profiles for both cases is obtained just by changing the power deposition profile, which is modelled by the parabolic expression,

$$P(r) = P\,(1 - (\frac{r}{a})^2)^{\beta}\ ,$$

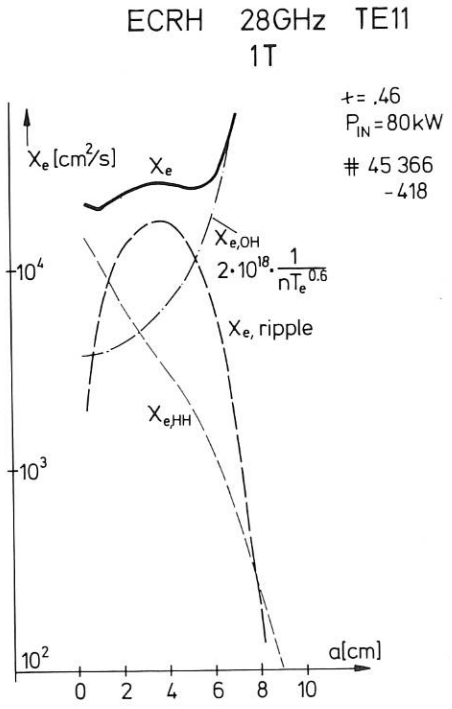

Fig. 20: Radial dependence of the axisymmetric diffusivity $\chi_{e,HH}$, the ripple-induced diffusivity $\chi_{e,rip}$ and the anomalous term $\chi_{e,OH}$. The line gives the sum of the three terms.

from a broad (β = 2, TE_{02} case) to a narrow (β = 14, TE_{11} case) profile, corresponding to the natural width of the radiation pattern at the resonance layer. This result gives strong support to the assumption, that the improvement of the electron temperature is due to the narrow power deposition profile rather than to the slight increase of the absorbed power.

In Fig. 20 the three terms of the electron heat diffusivity are plotted versus the plasma radius for the TE_{11}-case.
The centre of the plasma ($r/a \lesssim 0.7$) is seen to be governed by neoclassical heat transport, whereas the anomalous term dominates near the plasma edge, where temperature and density are low.

2.4.1.3 Parametric wave decay

Decay of an extraordinary EC-pump wave into daughter waves becomes possible near the X-mode resonace (UH-resonance) if a certain threshold power density of the pump wave is exceeded. The simplest case to be considered is decay into two daughter waves. This process was observed in several ECR-heated plasmas [1,2] where the decay waves were identified to be a low-frequency lower hybrid mode and a high-frequency electron Bernstein mode.

In W VII-A a 10-channel superhet system with tunable local oscillator was installed, the microwave horn looking to the plasma in the horizontal plane from the low-field side. A typical spectrum obtained from discharges where the HE_{11} mode was launched is shown in Fig. 21a.

The pump wave frequency is indicated by an arrow. The total natural line width of the gyrotron was measured to be 40 MHz.

Upper and lower side-bands were detected, the intensity of the downshifted one being almost two orders of magnitude higher than the upshifted one and showing a sharp drop in the range 200-250 MHz below the pump frequency. Simultaneously, the low frequency spectrum was followed by Langmuir probes. An example is given in Fig. 21b. These spectra show a sharp drop around 220 MHz and are "empty" above that frequency, which is the lower hybrid frequency near the upper hybrid resonance. The spectra show sharp spikes at high harmonics of the ion cyclotron frequency. Both high and low-frequency spectra fit well to the picture of parametric decay of the extraordinary wave near the upper hybrid resonance. The threshold power is estimated by McDermott et al. [1] to be 0.5 kW/cm^2. The actual power density in the experiments ranges from 1.5 to 10 kW/cm^2 and exceeds the necessary threshold clearly. A strong

1) McDermott, F.S., et al., Phys. Fluids, 25, 9 1488 (1982).
2) Bulyginsky, P.G., et al., Proc. 11th Europ. Conf. Contr. Fusion and Plasma Physics, Aachen, FRG, part I, p. 457 (1983).

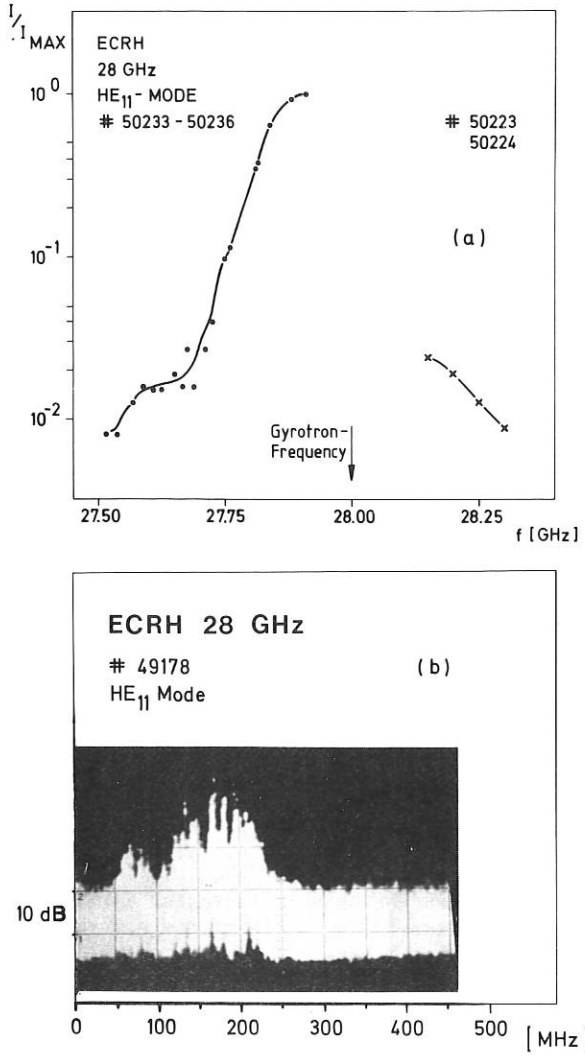

Fig. 21: High frequency side-bands detected by a 10-channel superhet receiver (a) and low frequency spectrum detected by Langmuir probes (b).

correlation between the lower side-band activity and the occurrence of high-energetic ion tails measured by charge-exchange diagnostics was found.

These ion tails vanish in the TE_{02} case, where no extraordinary wave is launched from the high-field side. A comparison of the ion spectra for the two cases is shown in Fig. 22.

The ion spectra can be treated as bi-Maxwellian, giving a bulk temperature of 170 eV and a tail temperature of about 500 eV. The population of the tail is about 1 % of the total particle number.

These ion tails are explained by absorption of the low-frequency waves generated by the wave decay.

The low frequency waves can carry 1 kW of power (from frequency ratio), which is sufficient to maintain the ion tail if classical coupling to the bulk ions and complete absorption of the waves is assumed.

During pulse modulation experiments, where the rf-power is repetitively pulsed down to about half of the maximum power for short intervals, the ion tail energy decays (rises) in phase, whereas the ion bulk temperature remains unaffected. An example is given in Fig. 23.

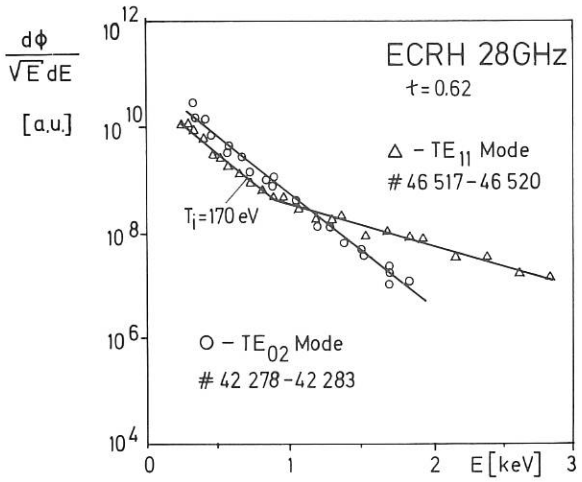

Fig. 22: Comparison of the ion energy distribution obtained from charge-exchange diagnostics for the TE_{11} and the TE_{02} mode.

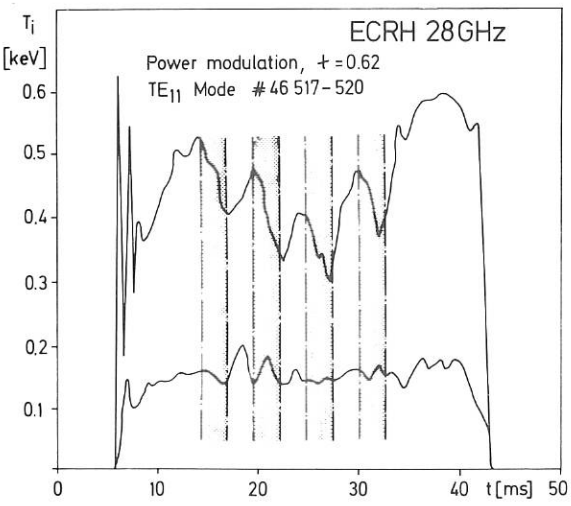

Fig. 23: Time behaviour of the bulk temperature (lower trace) and the tail energy (in terms of temperature, upper trace). The shaded areas indicate intervals of down-pulsed rf-power.

Whereas the bulk ions gain energy from the electrons on a time scale given by Coulomb collisions, a much faster time scale for the energy gain of the tail ions is necessary, which supports the assumption of wave absorption. The rapid decay of the tail energy during the down-pulsed interval can be explained by classical slowing-down and/or by particles on lost orbits (note that the high energetic particles are assumed to be generated near the plasma edge, where wave decay and absorption occur).

2.4.1.4 Experiments with resonance off axis

By tuning the main magnetic field, the resonance layer can be shifted apart from the magnetic axis. With the narrow power deposition profile of the HE_{11} mode, discharges were realized with a displacement of the resonance layer by up to $\pm$ 6 cm. Fig. 24 shows a sequence of profiles obtained from soft-X-ray emission with the resonance layer shifted successively outward.

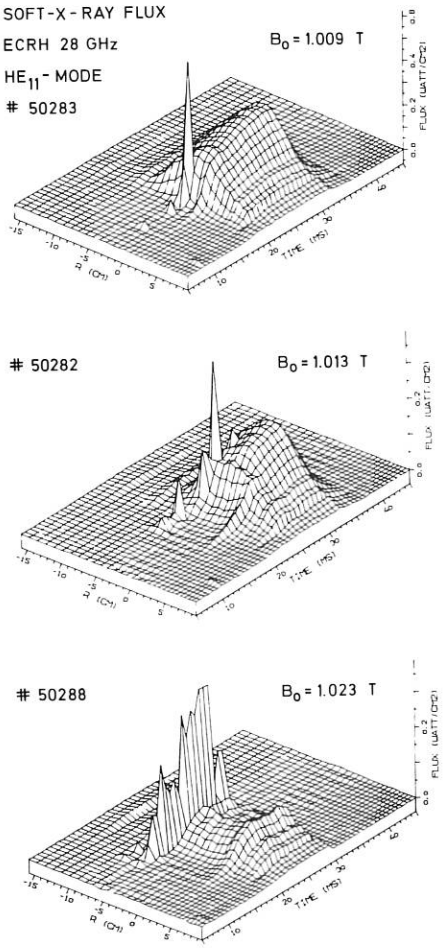

Fig. 24: Soft-X-ray emission profiles for three discharges, where the resonance layer is successively shifted towards the outer plasma edge.

The position of the plasma breakdown is seen several milliseconds before the final profile is established. The fast electrons generated at the resonance layer are distributed around a flux surface leading to X-ray emission of high spatial symmetry with respect to the magnetic axis. As seen from Fig. 25, plotting the magnetic field B_o on axis versus position of plasma breakdown fits well to the expected 1/R dependence.

Off-axis and on-axis experiments were performed at a fixed total plasma energy content W_{pl} = 55 J. In the off-axis case (r_{ECR} = - 5 cm) an incident rf-power of 180 kW giving an absorbed power of 58 kW was necessary to maintain the discharge, whereas in the on-axis case an incident power of only 65 kW with an absorbed power of 28 kW was sufficient.

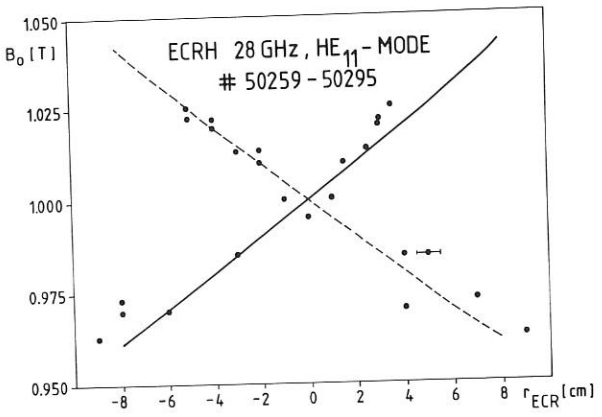

Fig. 25: Magnetic field B_o on axis versus position of plasma breakdown from soft-X-emission. The solid line indicates the position of the ECR-layer, the dashed line gives the position of the second intersection of a flux surface containing the resonance position with the equatorial plane.

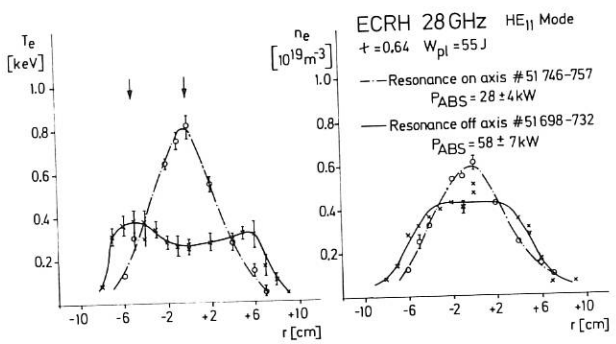

Fig. 26: Comparison of the temperature and density profiles from Thomson scattering of discharges with resonance on axis and off axis. The total plasma energy is kept constant in both cases. The arrows indicate the position of the resonance layer.

Fig. 26 shows a comparison of the temperature and density profiles for both cases. A hollow temperature profile is observed in the off axis discharge, which may be caused by impurity line radiation in the plasma centre.

2.4.2 70 GHz experiments

In September 1984 a 70 GHz, 100 ms, 200 kW pulse gyrotron was delivered by VARIAN together with the superconducting magnet. Installation of the system and technical tests were successfully finished in October. The transmission line was developed by IPF Stuttgart (see this volume, annual report of IPF) and was shown to transmit the full power emitted by the gyrotron (power densities of up to 35 kW/cm^2 in the waveguide). First plasma experiments were started in November by launching the TE_{02} gyrotron mode into the plasma. In contrast to the 28 GHz experiments the divergence angle of the 70 GHz

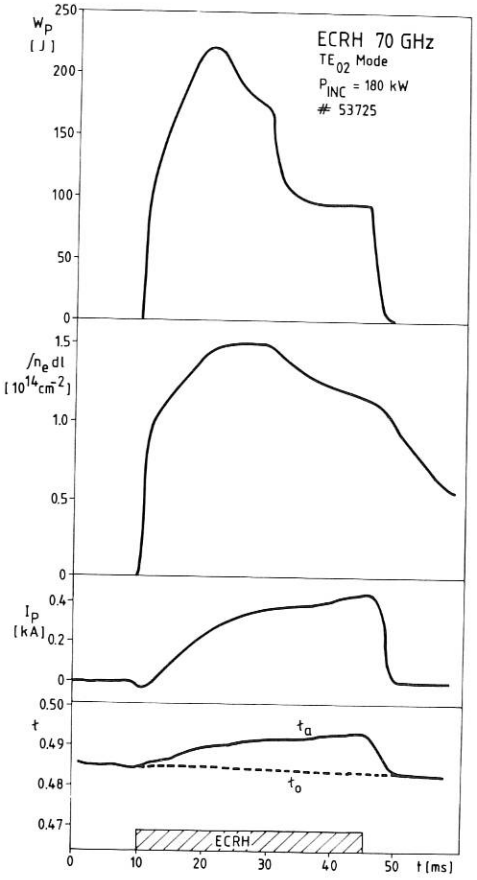

Fig. 27. Plasma energy content W_p, line density $n_e dl$, plasma current I_p and rotational transform as functions of time.

TE_{02}-mode radiation pattern is comparable to the 28 GHz HE_{11} mode pattern (plasma center in the near field). Therefore, narrow power deposition profiles are achieved even with the simple irradiation. The time behaviour of some plasma parameters for a typical discharge is shown in Fig. 27.

The non-stationary behaviour of the discharge is due to the current driven by the rf, leading to an edge value of the rotational transform ι_a which increases with time. This result is similar to the situation found in the 28 GHz experiments. Maintaining stationary plasma conditions requires careful feedback control of the external rotational transform ι_o to keep the edge value constant. At the optimum ι_a the energy content of the plasma is 220 J, and the correlated temperature and density on the axis are found to be 1.1 keV and 8×10^{18} m^{-3} respectively. The main interest in the forthcoming experimental period will be focussed on linearly polarized irradiation and combination of ECRH with the other heating methods available, such as ion cyclotron heating, neutral injection and ohmic heating.

2.5 ICRH

This year ICRH experiments have been started in W VII-A. A small HF generator $P \lesssim 100$ kW, $t \lesssim 100$ ms, f = 50 MHz was used. The HF power was first coupled to the plasma with a conventional antenna (see Annual Report 1983). It turned out, however, that the coupling efficiency of this antenna was too poor. No significant change could be observed in the plasma parameters. It was assumed that most of the HF power was lost in the double-layered Faraday shield. The antenna was therefore removed in order to take away one of the layers of the Faraday shield. In the meantime a new antenna has been designed and manufactured (see Fig. 28).
The new antenna is much broader (d = 70 cm) than the previous one (d = 6 cm). It has no Faraday shield, is fed in the middle and short-circuited at both ends. Both antennas were installed in W VII-A and the new one was successfully tested up to the maximum power delivered by the small generator. By the end of the year experiments could be started with an ohmically heated target plasma. First results show that the new antenna has a much better

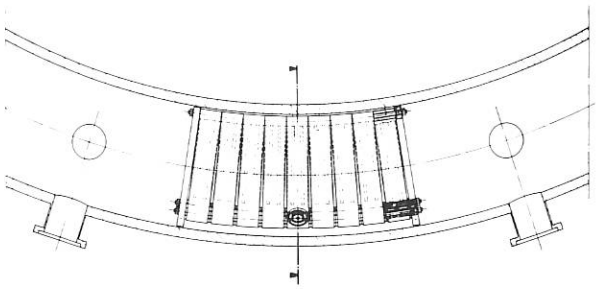

Fig. 28: Schematic view of the new antenna.

coupling efficiency than the old one. The plasma energy content increases during the first 2-3 ms of the HF pulse and than decreases below the value reached before the HF pulse. The diamagnetic signal decreases almost linearly during the HF pulses, irrespective of the position of the ion cyclotron resonance with respect to the midplane of the plasma column. For short HF pulses of $t \lesssim 10$ ms the plasma energy content recovers its original value after the end of the HF pulse, while for longer pulses it remains at the low value reached at the end of the HF pulse for the remainder of the discharge, i.e. $t \sim 50$ ms. This is due to an increase of the impurity influx and, possibly, to the onset of MHD instabilities caused by a change in the ohmic current distribution. These results have too preliminary a character since the experiments were soon interrupted in order to allow connection to the large HF generator $P \lesssim 1.5$ MW, $t \leq 10$ s, f = 30 MHz, to 115 MHz. A more systematic study of the impurity source and ICRH in a current-free stellarator plasma will be the next task.

3. DIAGNOSTICS

3.1 Investigations of Orbit Losses by Fluorescence spectroscopy

(in collaboration with KFA Jülich)

From 1981 and throughout 1984 laser fluorescence spectroscopy was used to study various topics and has proved to be a very useful diagnostic.

The activity on W VII-A had to be terminated at the end of 1984, because the ports on the machine are being used for ICRH heating during the last period of the experiment.

The measurements of sputtered Fe-atoms by laser fluorescence, using a flashlamp pumped dye laser, have been closely connected with the energy balance in neutral beam heated currentless discharges. Measurements of the power input agree with code predictions if electric fields deduced from poloidal plasma rotation measurements are induced [1] /184/. For the almost perpendicular injection, radial electric fields have a strong influence on particle trajectories and thus on lost orbits, which in turn determine the electric field to achieve ambipolarity. By measuring sputtered Fe-atom densities, via laser fluorescence, the existence of orbit losses has been shown in positions of the vacuum vessel where the calculations predict the orbits to intersect the stainless-steel wall of the vacuum vessel.

In addition, experiments were conducted with all currents and magnetic fields reversed, which leaves the magnetic configuration unchanged. In this case however, both ∇B drift and ExB poloidal rotation have to change sign, whereas the radial electric field remains unchanged. The orbit losses are now deposited on the opposite side of the vacuum vessel. This has been verified experimentally by fluorescence spectroscopy; a change of sign in the poloidal velocity was also found /184/ [2]

Absolute values of neutral atom densities are estimated [2] to be $n_{Fe} \sim 1.5 \times 10^8$ cm^{-3}. With a mean velocity of the sputtered atoms of $v = 2.4 \times 10^5$ cm s^{-1} this leads to a flux density $\phi_{Fe} = n_{Fe} \cdot v = 3.6 \times 10^{13}$ cm^{-2} s^{-1}.

From Monte Carlo calculations the area where orbit losses are expected to intersect the vacuum vessel is found to be $F \approx 5 \times 10^3$ cm^2. The total flux of Fe atoms then amounts to $\Gamma_{Fe} = \phi_{Fe} \cdot F = 1.8 \times 10^{17}$ s^{-1}.

Using the sputtering yield Y ($\underline{H}^+$) for stainless steel, the total flux of orbit losses $\Gamma_{\underline{H}+}$ (fast ions) can be calculated from $\Gamma_{Fe} = \Gamma_{\underline{H}^+} \cdot Y(\underline{H}^+)$.

Since particles on lost orbits leave the plasma with almost full injection energy, we take the sputtering yield to be Y ($\underline{H}^+$) = 3 x 10^{-3} 3).

Then the total flux of high energetic protons to the wall of the vacuum chamber turns out to be $\Gamma_{\underline{H}^+} = 6 \times 10^{19}$ s^{-1}.

This has to be compared with the total number of beam particles

$$\Gamma_{\underline{H}} = 3 \times 10^{20} \text{ s}^{-1}.$$

1) W VII-A Team, Neutral Injection Group, in Plasma Physics and Controlled Nuclear Fusion Research (Proc. 9th Int. Conf. Baltimore 1982) Vol. 2, IAEA, Vienna (1983) 241
2) Schweer, B. et al., J. Nucl. Matt. 93 + 94 (1980)
3) Bodhansky, private communication

The measured fraction of $\eta = 0.2$ for the orbit losses is in good agreement with experimental results at high line densities $\int n_e dl = 1.5 \times 10^{15}$ cm^{-2} 1).

3.2 Spectroscopy in the Soft-X-ray and VUV Regions

The main tasks were:

- routinely recording the line radiation of the most important impurity species in W VII-A plasmas heated in different ways (OH, NB, ECRH, ICRH)
- investigating the time histories of the densities of highly ionized impurity atoms, e.g. O^{8+}, N^{7+}, C^{6+}, by means of Charge Exchange Recombination Spectroscopy (CXRS)
- to develop crystal spectrometers with fairly good resolution and high luminosity, for UHV-operation and for the spectral region 0.5 to 3.0 nm, where the main part of the radiation of W VII-A plasmas is emitted.

For comparison with the predictions of an impurity transport code, the line-integrated light fluxes of OIV-OVIII and FeX-FeXVIII resonance lines were measured for different types of NB-heated discharges. Spatial profile measurements by means of a fast rotating mirror showed strong poloidal asymmetries of the radiances of the lower ionization states, especially during the neutral injection phase. Therefore, experimental data and code predictions concerning the edge radiation should be compared with caution. Additionally, the temporal behaviour of the radiances of AlX to AlXII lines after injection by laser blow off were recorded. For results and detailed discussion see 2.3.6. The spectrometers used for these experiments are: (1) a flat crystal (KAP) spectrometer for 0.6-1.9 nm with $\lambda/\Delta\lambda \approx 100$, supplied with proportional counter, (2) a 0.33 m grazing-incidence (Jobin-Yvon LHT30) spectrometer for 10-120 nm and a 1 m normal-incidence spectrometer with rotating mirror system for 40-140 nm.

The CXRS experiments were performed making use of a neutral beam line. The fixed chord of view of a LHT-30 spectrometer crossed the beam perpendicularly in the plasma centre.
Additionally switching on this injector for about 10-20 ms was found to be the most sensitive way of identifying CXR lines. More than 20 "CXR sensitive" lines in the VUV spectral region could be assigned, e.g. lines of OVIII, OVI, NVII, FeXV, CVI, SiXII, AlXI, TiX, TiXII. Most of them are related to $\Delta n = 1$ (d-f) transitions, as predicted by theory [1]. The advantage of short time switching-on of the beam is that one can easily distinguish small CXRS signals from a high background of stray light and electron impact excited lines.

Fig. 29 shows some examples of CXRS line detection. The drawback of the present experimental setup at W VII-A is the large aperture of the beam and the lack of spatially resolved measurements because of

1) Salop, A., J. Phys. B: Atom. Molec. Phys., 12, 6, 1979

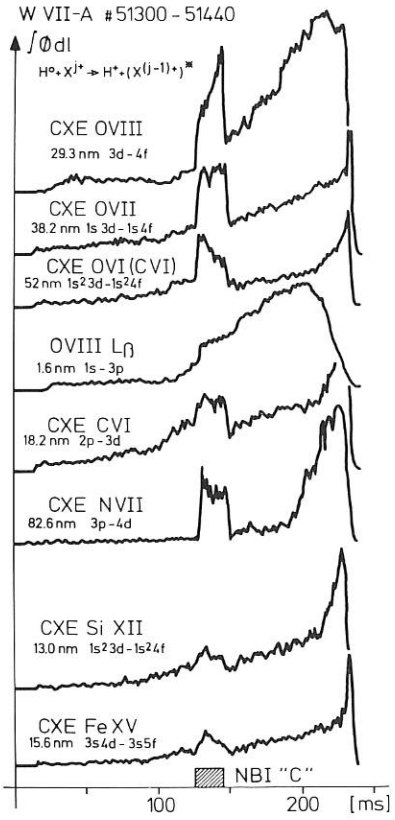

Fig. 29: Examples of CXR emission of different impurities and ionization states during the NBI phase. Comparison of OVIII resonance line emission shows a small ascent mainly resulting from the increase of n_e, caused by adding the fourth beam, which is intersected by the line of observation.

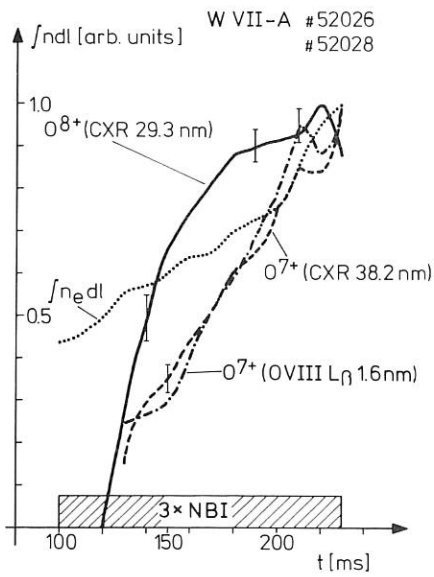

Fig. 30: Evolution of line-integrated densities of O^{7+} and O^{8+} during the current-free 3xNB heated plasma phase.

geometric constraints. As an example of CXRS's usefulness in Fig. 30 the time histories of the line integrated densities of the O^{8+} and O^{7+} ions, measured by CXRS, are compared with those of the electrons and the O^{7+} ions, as derived from the OVIII L_β line. The agreement of the O^{7+} density evolution measured by two methods, seems good. The steep increase of the ion density compared with the electron density confirms impurity accumulation as predicted by the transport code.

The more or less flat part of the O^{8+} density curve as well as the very steep increase before 150 ms can be explained by $T_e < 500$ eV. By means of CXRS, too, the confinement behaviour of He atoms injected by a short gas puff in the early OH phase was studied. During the current-free plasma phase the density of He^{++} remains nearly constant and long particle confinement times, as derived from ablation experiments, were confirmed.

The performance of two crystal spectrometers, a polychromator for space-resolving measurements and a fast scanning flat crystal spectrometer, was tested. Both instruments have been designed for ultra-high vacuum conditions and are equipped with channeltron/channelplate detectors. The objective was to expand the spectral region to lower energies down to about 300 eV for recording CVI, OVII, OVIII resonance lines. This was only partially achieved. A strong stray light background of plasma radiation of about 100-300 eV and secondary X-ray emission with energies of around 2 keV intensively blends the line radiation to be investigated with a moderate resolution of $\lambda/\Delta\lambda \geq 500$ and without strongly absorbing filter foils.

3.3 Microwave Scattering and Plasma Fluctuations

Microwave scattering measurements at 2 mm were continued during the past experimental period. This diagnostic provides access to coherent plasma fluctuations in the region of $60 \leq f(\mathrm{kHz}) \leq 5500$, $8 \lesssim k_\perp(\mathrm{cm}^{-1}) \lesssim 35$, $k_\parallel < 1.5\ \mathrm{cm}^{-1}$ propagating in the radial and poloidal directions in one half of the plasma cross-sectional plane.

Enhanced plasma fluctuation activities are observed in plasma phases with deteriorated confinement, caused either by large MHD-activities or by magnetic islands at a low-order rational rotational transform. The behaviour of the fluctuation amplitude in OH discharges both in the absence and presence of tearing-modes was described in the IPP Annual Report 1981.

The typical behaviour of the plasma fluctuations through the transition phase from the OH discharge to the net-current-free NB-heated plasma phase and as a function of the rotational transform is shown in Fig. 31.

In the net-current-free phase the plasma fluctuations have much lower amplitudes than in the OH-discharge when no low-order rational rotational transform magnetic surface crosses the microwave scattering volume. Under the conditions of Fig. 31, however, the rotational transform ι was changed in time by variation of the helical coil current and

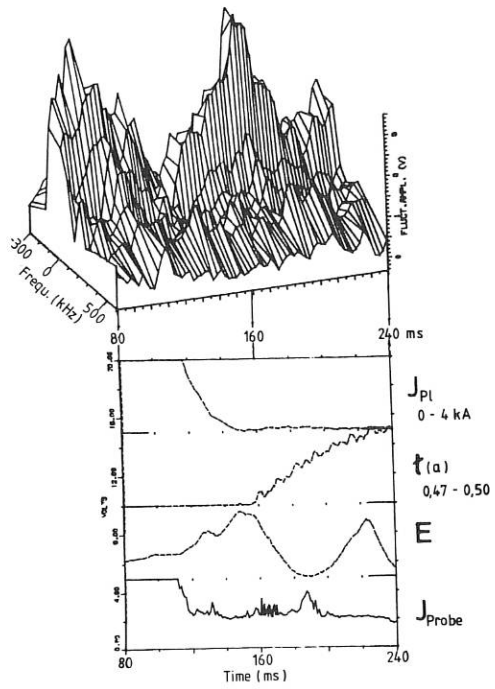

Fig. 31: 3D-plot of fluctuation spectra ($-300 \leq f(kHz) \leq 600$ plasma current I_{Pl}, rotational transform $\iota(a)$: 0.47 to 0.50, plasma energy E and Langmuir probe current I_{pr} vs. time.
Shot-No: 48266 (2.5.84), B(o) = 3.2 T, D, 3 Inj.(H).

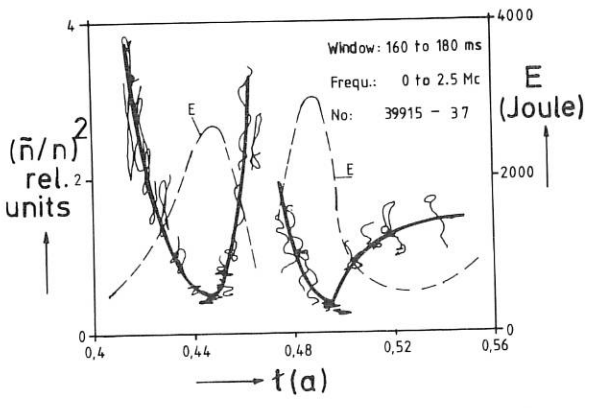

Fig. 32: Normalized fluctuation power $(\tilde{n}/n)^2$ and plasma energy E vs. total rotational transform $\iota(a)$, $0.40 \leq \iota(a) \leq 0.56$.
Shot-No: 39915-37, B(o) = 3.0 t, D, 3 Inj.(H).

passes $\iota(a) = 0.5$. As a result of this ι-variation the fluctuation amplitudes and the plasma confinement show a reciprocal behaviour when the rotational transform passes from below to above the rational rotational transform $\iota(a) = 0.5$. Close to $\iota(a) = 0.5$ the fluctuation amplitudes are largest, while the energy content of the plasma is lowest. On the neighbouring sides around $\iota(a) = 0.5$, where the highest plasma energies are found, the two fluctuation amplitudes have a minimum.

However, such a fluctuation increase at $\iota(a) = 0.5$ is not observed under experimental conditions with a small residual plasma current. As a result of the residual current shear is produced and the magnetic islands extend only over a narrow edge region.

Fig. 32 shows the fluctuation power together with the plasma energy as a function of the rotational transform (a) around (a) = 0.5 again measured in the net-current-free plasma phase but under stationary plasma conditions on a shot to shot basis. These experimental results demonstrate the strong correlation between low-frequency plasma fluctuations and plasma confinement.

3.4 Scattering of CO_2 Laser Radiation from Fluctuations

The 9-element detector system for simultaneous measurements at different angles has been bought and is being installed. In the meantime we borrowed a 5-element system in order to test the procedure: the beat signal on each detector is frequency selected - as before with 1 detector - and for each frequency the signals of the 5 detectors - corresponding to 5 different scattering angles - are made to best fit a theoretically expected curve, the parameters of which deliver the fluctuation wavelength at that particular frequency. The wavelength Λ accessible that way ranges from 0.2 cm to 6 cm (drift-type fluctuations, for example, are generally assumed to be widely spread around $\Lambda \approx$ 1-2 cm, according to $k\rho_i \approx 0.5$-1).

The method is sensitively dependent on the quality of the radial intensity profile of the laser beam. Because of the narrowness of the entrance window there were deviations from a perfect Gaussian profile, which deteriorates the curve fit procedure.

Preliminary results confirmed that the fluctuations detected exist in the cm wavelength region rather than in the mm region. First indications of dispersion relations have been obtained as well.

Our experience further supports the need for more than 5 detectors.

3.5 W VII-A Bolometer Diagnostic

Two different bolometer diagnostic systems were installed at W VII-A:

- a turnable 10-channel system at an unperturbed position (porthole plane without auxiliary heating)
- a turnable 2-channel system looking from above onto a region where the neutral beam (NB) penetrates the plasma

The bolometers of the 10-channel system with individual collimators have fixed viewing angles with respect to each other (Fig. 33). The whole system can be turned poloidally, so that any region within the plasma cross-section can be observed.

The radial resolution is $\Delta r \approx 2$ cm, and the time resolution depends on the perturbation level, ranging from $\Delta t \approx 2$ ms to $\Delta t \approx 6$ ms. The rise time of the bolometer itself is less than 10 μs.

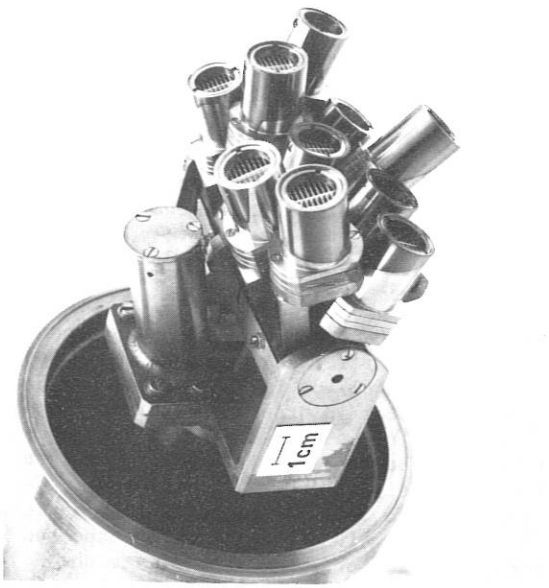

Fig. 33: Turnable 10-channel bolometer system with individual reflection-free collimators.

As the 10-channel system is mounted at a position (unperturbed porthole plane) which is assumed to be representative of the plasma, the total radiation power and, by Abel inversion, local radiation levels are derived from the measurements.

The radiation losses of the plasma depend strongly on the auxiliary heating method (NB or ECRH). In the NB-heated plasma the total radiation losses increase up to about 200 kW, thus terminating the discharge. In the ECRH plasma the radiation loss remains nearly constant during the discharge and is less than 15 % of the deposited heating power. This is not necessarily due to a low impurity content, since the impurity confinement time may be of the order of the ionization times for the high ionization states of central impurities ($\tau_E \leq 2$ ms).

The 2-channel system has detectors and collimators of the same type as the 10-channel system. The bolometers have parallel viewing chords and are moved simultaneously. One of the bolometers looks through a 500 A (7.2 $\mu g/cm^2$) carbon filter, screening off the low-energy fraction of particles and photons for a rough energy discrimination. The system can be turned poloidally and after remounting, toroidally, thus being able to scan in two perpendicular directions across the penetration region of the NB. The measured power losses are one order of magnitude higher than in the unperturbed plasma. Assuming radiation as the main contribution to these losses would lead to extremely high impurity concentrations in this region. Calculations have shown that these power losses can be explained by charge exchange losses due to interaction of the high-energy particles of the slowing down distribution with the high neutral density at the injection plane. Contributions to the neutral density are the H^0 neutrals, the D^0 halo and the cold gas streaming out of the beamline. For the cold gas density the following radial dependence is assumed:

$$n_{cold}(r) = 10^{(7+0.5r)}\ cm^{-3}$$

The agreement between measurement and calculation is within a factor of two. The spatial distribution of the CX-neutrals is anisotropic. The maximum of the distribution is given by the injection angle, the width by the pitch angle scattering. The total power loss at the position of an injector is about 5 kW, depending on the discharge conditions.

3.6 Electron Cyclotron Emission (ECE) Diagnostic

ECE measurements have been carried out using an independantly calibrated eight-channel heterodyne radiometer which allows within known limits of electron temperature and density the electron temperature $T_e(t,r_i)$ to be determined as a function of time at eight discrete plasma radii r_i. The system can now be used for both first and second harmonic measurements of ECE in the frequency range 50 to 180 GHz by interchanging the radiometer's front-end mixer and the corresponding local oscillator [1]. To avoid density cut-off, most of the observations are done at the extraordinary mode of the second harmonic ECE. By introducing sharp notch filters into the transmission line between the plasma and radiometer at 56 GHz to reject the strong gyrotron second harmonic, ECE measurements became possible during electron cyclotron resonance heating at 28 GHz. The receiving channels are staggered almost symmetrically to the plasma axis, which corresponds to 56 GHz. It was found that the signals as monitored by the individual channels are superpositions of three contributions:

a) Electron cyclotron emission from the thermalized bulk of the plasma electrons. The signals obtained by the four inner or high field side channels mainly reflect this contributions. They can be evaluated for electron temperature in reasonable agreement with the electron temperature profile as determined by Thomson scattering of a laser beam.

b) Electron cyclotron emission of a small amount of weakly relativistic suprathermal electrons. Radiation of this contribution dominates the signals obtained by the outer or low field side channels. By comparison with simulated emission spectra, the average energy and density of the suprathermal population can approximately be determined to be 5 to 15 keV and about 0.3 % of the central electron density of the thermalized bulk. The suprathermal density is assumed to be constant between the limiter radii (see below). Fig. 34 gives an example.

c) The third contribution of completely different nature is due to lower sideband emission of the second harmonic of the gyrotron line around 56 GHz superimposed on the ECE band.

1) Hartfuß, H.J., Tutter, M., Fast Multichannel Heterodyne Radiometer for Electron Cyclotron Emission Measurement at the Stellarator W VII-A, to be published in Rev. Sci. Instr. (1985)

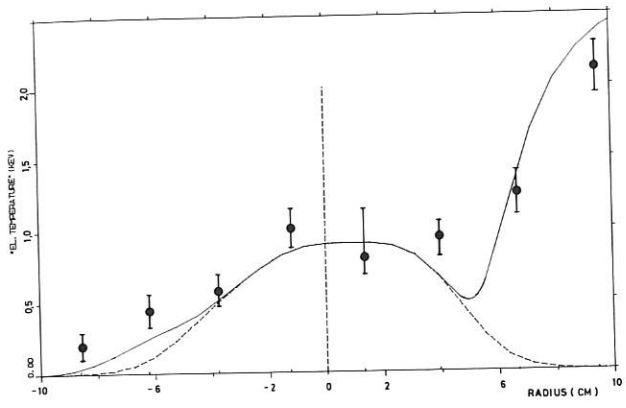

Fig. 34: Measured "temperature profile" (points) obtained via ECE during ECRH in comparison with a computed "profile", the solid line assuming a small amount of weakly relativistic electrons in addition to the thermalized bulk (dashed curve).

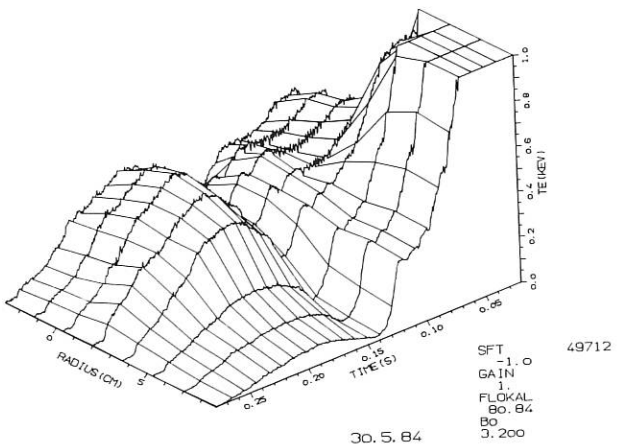

Fig. 35: Evolution of temperature profile as measured during a neutral injection heated discharge at 3.2 T. The discharge starts up by ohmic heating. During this phase suprathermal electrons cause the additional maximum around 6 cm radius. When the neutral injection is switched on at about 100 ms, the suprathermal population disappears due to the increase of density.

A possible generation process may be the parametic wave decay (including harmonic generation) of the X-mode pump wave at the upper hybrid layer.

As a result of the parametric wave decay, a high energetic tail in the ion energy distribution is found by the charge exchange diagnostic. The occurrence of the sideband emission at about 56 GHz - 300 MHz and the flux of high energetic (2.2 keV) neutral atoms are well correlated, as can be seen from Fig. 36.

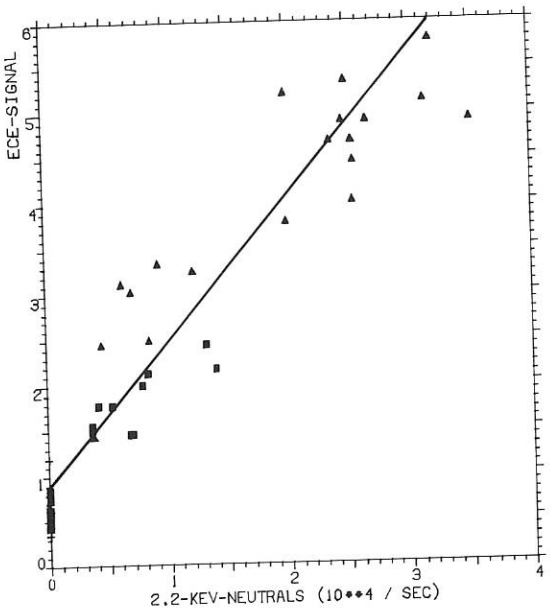

Fig. 36: Correlation between the intensity obtained at the lower sideband of the gyrotron's second harmonic and high energetic flux, indicating parametric wave decay.

The computer program for calculation of the cyclotron emission of the suprathermal plasma /235/ was extended to directions of observation oblique to the main magnetic field. Observing a gyrating electron with an axial velocity such that it approaches the receiving horn, one gets (below a certain energy of the electron) an increase of the emission frequency beyond the cyclotron frequency because the positive Doppler effect overcompensates the relativistic frequency lowering. The spectrum of a suprathermal electron population with a continuous energy distribution has a pronounced peak at the largest frequency which depends on the angle of observation. Radiation with this frequency is not reabsorbed by the Maxwellian background plasma on its way to the receiver. This holds for each emission radius with its inherent magnetic field, and so one gets a picture of the radial density distribution of the suprathermal electrons superimposed on the radial temperature profile of the Maxwellian plasma.

To measure the electron cyclotron emission perpendicularly from above the torus axis, microwave horns have been installed into that plane where ECRH power is launched. The contours of the total magnetic field in this plane are shaped such that the radiation passes zones of monotonically increasing magnetic field on the way from its origin to the horn, and has therefore no reabsorption in the thermal background plasma. Thermal emission on the other hand is received only in a narrow frequency band and there is very little overlap with the suprathermal spectrum.

The spectra to be expected with W VII-A parameters were calculated with computer codes.

A new Michelson-interferometer with a rotating helically shaped mirror was prepared for measuring more than 10 interferograms during one plasma discharge, with the same radial and time resolution as the present interferometer.

4. TECHNICAL OPERATION

By the end of 1984 shot number 53922 since commissioning of the WENDELSTEIN VII-A experiment in December 1975 was recorded by the data acquisition system. The number of load pulses exceeds the number of shots by some thousands as the pulses required for commissioning of the system were not recorded by the data acquisition system.

The maximum loads for the most important systems were the following:

Toroidal field coils: B_o = 3.8 T, mainly 3.2 T (design: 4 T)

Helical windings: I_{HX} = 48 kA for 1 s; $I_{HX} \cdot B_o$ = 155 kN/m (design: 40 kA for 3 s; 160 kN/m).

The displacement of the helical windings on the torus caused by the magnetic and thermal forces has beem continuously recorded at various points since 1977, by means of linear film potentiometers in a bridge connection. For some months a critical point in the region of the current leads to the helical windings showed an increasing displacement of the conductors in the range of 0.1 mm. The reason was found, and after repair and some improvements this displacement could be kept within tolerable values.

In September 1984 the 28 GHz gyrotron for the electron cyclotron resonance heating (ECRH) was replaced by a new 70 GHz gyrotron. A new cooling system and the cryogenic equipment for the superconducting magnet (2.5 T) had to be designed and tested. Commissioning of the new gyrotron was successfully finished in October 1984.

W VII-AS Project

Head of Project: J. Sapper

WENDELSTEIN VII-AS

U. Brossmann[1], F. Kerl[1], J. Kisslinger,
T.v. Larcher[1], R. Mathis[1], H. Münch, J. Sapper,
I. Schoenewolf.

Neutral Beam Injection

E. Speth, J.H. Feist, K. Freudenberger, J. Kolos,
P. Mikolajcazk[2], W. Ott, F.P. Penningsfeld,
P.J. Schneider, G. Wulff.
Neutral Injection Group (Technology Division)

Electron Cyclotron Resonance Heating

IPF Stuttgart, W VII-A Team

Ion Cyclotron Resonance Heating

F. Wesner, J. Bäumler, F. Braun, R. Fritsch,
F. Hofmeister, E. v. Mark, J.M. Noterdaeme,
S. Puri, M. Söll, K. Steinmetz, H. Wedler.
ICRH Group (Technology Division)

1. INTRODUCTION

In 1984 all essential machine components of W VII-AS were under construction in various industrial companies. Detailed experience with the envisaged fabrication methods was gained. A prototype coil for the modular field system was delivered to IPP in November. At IPP the coil test bed was prepared and current tests were started.

The planning for the assembly of the machine was carried out. Devices and tools which are necessary for the assembly are under design.

The technical concept and the status of W VII-AS were presented at the Jahrestagung Kerntechnik '84 in Frankfurt and at the 5th International Workshop on Stellarators, Lake Tegernsee /46, 209/. Investigations on the physics in W VII-AS were reported also at the 5th Intern. Workshop on Stellarators, Lake Tegernsee /196/.

2. ENGINEERING IN WENDELSTEIN VII-AS

2.1 Modular Coil System

As already reported last year, a two-stage contract was placed with industry for the modular coils. Stage 2 was released at the end of 1983 after sufficient development work had been performed.

A first prototype coil was manufactured and was ready for the current test in April. At the beginning of that test an inter-turn short circuit was detected in the coil and it was not accepted by IPP. Analysis of the manufacturing and quality control stages of the coil showed that the defect arose during the final closing operation of the coil-backing mould, before impregnation. During this operation the pressure on the edge of one of the cooling conductors could be so high that the glass texture insulation between the windings (or the pancakes) was cut through. Drawing on this experience, the company decided on the following improvements:

- New winding and backing moulds, with better handling during the various manufacturing steps.
- Improved arrangement of the conductors and the insulation layers, so that the operator can see all critical spots during the winding process.

---

1) ZTE (Central Technical Services)
2) Guest from the University of Lublin, Poland

- Improved inter-turn voltage test method, so that faults can be detected before impregnation in the winding mould.

A second prototype coil taking into account the above-mentioned alterations, was successfully manufactured, tested at 10 kA and full temperature rise (maximum temperature 80°) with 100 pulses, and delivered to IPP in November. The contour precision of the coil after impregnation is within a tolerance of 0.6 mm relative to the master model.

The series manufacturing of the modular coil system is being started at the time of this report. A delay of 3 1/2 months was caused by a lockout of workers by the contractor in summer 1984. A similar delay arose from the difficulties with the first prototype coil. Figure 1 shows a prototype coil removed from the backing mould.

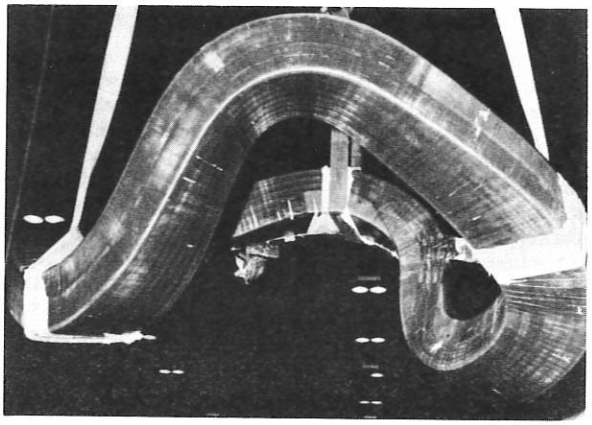

Fig. 1: Modular field prototype coil, after the resin impregnation.

2.2 Toroidal Field Coils

Ten planar TF coils of the W VII-A type are under construction in industry. Existing coil frames from W VII-A will be re-used. New pancakes with optimized performance dates were designed. The winding device is ready assembled and the winding process will start in February 1985, so that the first coil can be delivered to IPP in March 1985.

2.3. Vacuum Vessel

All five modules for the vacuum vessel are under construction. The manufacturing method which was derived from the test piece proved good. By the end of 1984 all wall segments had been welded. Also the connecting flanges, NI ports and diagnostic ports have been prepared for assembly. The machining work on several parts is in full swing. The first module can be delivered to IPP in March 1985, ready for assembly. An assembly test has already been carried out with the master models of the coils. Information for the preparation of the final assembly with original parts was gained.

2.4 Structure Shell and Coil Supporting Elements

The work on the structure shells and on the housing for the enlarged coil No. 5 is running on schedule. The first module of the shells and all 5 housings for the enlarged coils were accepted in December 1984. These parts are now waiting in the manufacturer's plant for preassembly with the coil supporting elements, which will be delivered in April 1985 from another company.

The supporting elements are cast stainless-steel bodies adapted to the space available between the coils and between the coils and the structure shell. All 22 different master models for the supporting elements were tested for geometrical accuracy together with the coil master models at IPP before being released for the final casting operation. The first set of supporting elements is expected in February 1985. Figure 2 shows the drawing of one of these pieces, which was completely designed by a CAD system (MEDUSA) from an IPP data set.

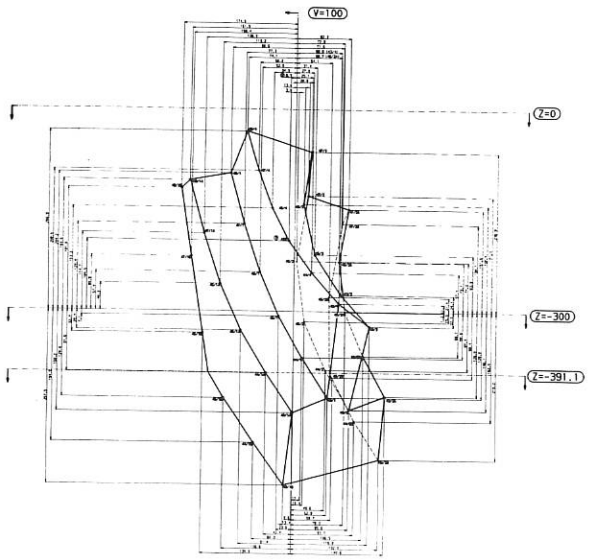

Fig. 2: Supporting element for modular field coil, designed with a CAD system.

2.5 Other Components

- The design for the W VII-AS cooling system was worked out. It is based on a closed cooling circuit for each coil system and for the torus, as well as for the external heating systems. A call for tender was released and the system will be ordered in February 1985 after evaluation of the offers. The order will include the dismantling of the existing system and the assembly and commissioning of the new circuits.

- The order for the 5 vacuum pumping sets is running on time. Extended calculations for the performance of the pumps in the magnetic fields of W VII-AS showed that it was not necessary to use a magnetic screen for normal operation. Only at a very high level of the applied vertical field is a moderate reduction of the specified

pulse frequency necessary, because the heating of the pump rotor by eddy current losses has to be reduced. The pump sets are expected at IPP by June 1985.

- The design of all current bridges and bus bar systems for the machine is completed. The call for tender has been out since December 1984.

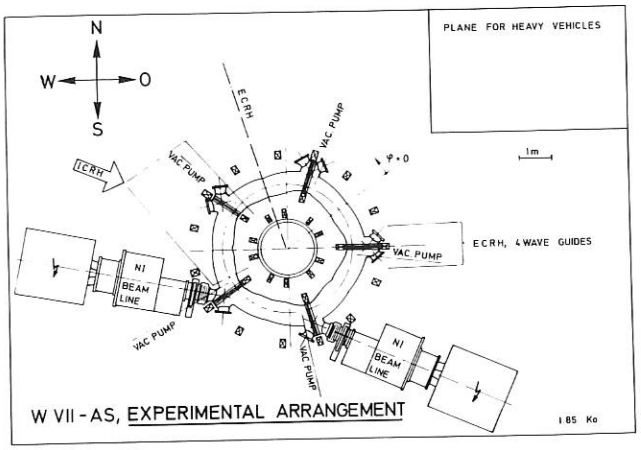

Fig. 3: Experimental arrangement of W VII-AS.

- The design of smaller structural parts is in progress.

- The integration of the external heating systems into the machine was checked in detail. Supports for larger parts (i.e. beam chambers) are under final design. Figure 3 shows the total arrangement of the device in the experimental hall.

2.6 Time Scale of Delivery and Assembly

In December 1984 the following delivery dates were scheduled by industry:

- Modular coil system: first coil in March 1985, last one in April 1986.

- TF coils: first one in March 1985, last one in November 1985.

- Vacuum vessel: first module in March 1985, last one in June 1985.

- Structure and supporting elements: first module in December 1984, last one in June 1985. The assembly of the supporting elements requires an additional 2 months for each.

- Vacuum pumping sets in June 1985.

The assembly of the first torus module will start when the first set of MF coils is completed. This is scheduled for May 1985. So the first assembled machine module will be ready in August 1985.

Depending on the MF coil delivery, the modules can be completed in May 1986. With an additional time of 3 months for the final assembly of the complete arrangement, technical commissioning of W VII-AS could start in September 1986. To achieve this date, it is necessary to close W VII-A in August 1985 and dismantle it by Dec. 1985.

3. EXTERNAL HEATING

3.1 Neutral Injection into W VII-AS

3.1.1 Overview

In the year 1984 the realization of the proposed neutral injection sytem for W VII-AS was well abreast of the fore of the activities. The two beam line boxes needed for co-injection and counter-injection are under construction in industry and should be delivered to IPP in August 1985.

The ion sources with inertially cooled grids were developed at Fontenay-aux-Roses. The acceptance test of the first series was performed on their test bed in January 1985. All sources will be delivered in the course of 1985.

Since the current operation of the W VII-A beam lines has had priority up to now, necessary modifications of the existing power supplies for the new ion sources could not begin. One prototype of these modules was therefore built with existing spare parts and is now being tested.

3.1.2 Beam lines

In parallel to the supervision of the beam line boxes, orders for the internal installations and additional parts were placed and supervised for both the ASDEX-LPNI and the W VII-AS injection. The actual status of the main components is given in the section of the report on the ASDEX-LPNI system.

Several diaphragms and scrapers of the W VII-AS system have to be different from the ASDEX-LPNI. They were designed and some are under construction and some already finished.

The tilted oval injection port of the W VII-AS vessel calls for a more complicated design of the duct liner compared with the ASDEX case. The sputtering of wall material due to beam losses in the duct region is the main criterion for the choice of the exact design and the suitable material for this liner (copper, graphite, molybdenum). This work is still in progress.

3.1.3 Delivery of ion sources

As already stated in earlier reports, it is intended to use periplasmatron ion sources (as used in ASDEX) together with edge-cooled accelerator grids such as are being developed at Fontenay-aux-Roses. The FAR ion source group of J.-F. Bonnal has made rapid progress in the last year. A prototype was developed and accepted in April. The acceptance test of the first series source was made in January 1985. The parameters obtained are 45 kV, 24 A, 2.7 s, 1.0 to 1.1°, power within the beam acceptance of W VII-AS 670 - 790 kW (ions and neutrals).

All sources will be delivered to Garching during 1985. According to the contract, only the first source will already be conditioned. The rest of the sources will have to be conditioned by Garching personnel.

3.1.4 Beam impurities

The negative influence of beam impurities on NI-heated plasma discharges is well known from W VII-A results and led to the application of titanium gettering of the ion sources. This approved method of reducing impurities will also be used for the new periplamatrons.

Doppler spectroscopic and mass spectroscopic measurements of beam impurities of a periplasmatron source on the test bed showed in good agreement that sources of this type produce relatively clean beams even without titanium gettering of the source volume: The relative impurity content of the beam decreases after 10 - 20 shots with a pulse length of about 0.2 s (i.e. conditioning) from 3.5 % to 1.0 % if the fast pumping system is activated (see Fig. 4).

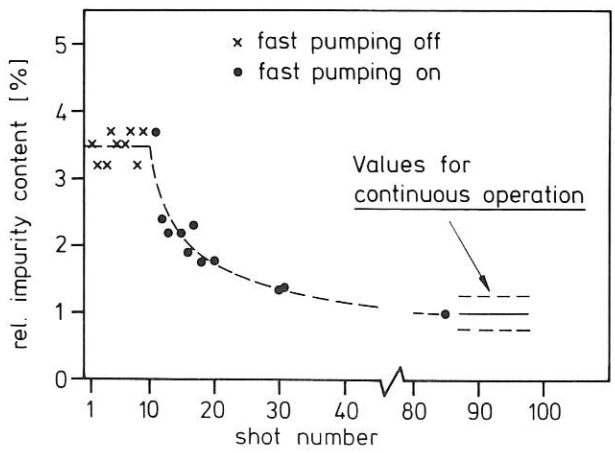

Fig. 4: Relative impurity content of a periplasmatron beam as measured by Doppler spectroscopy versus the shot number without titanium gettering of the source.

Such a self-cleaning effect could not be observed at the W VII-A sources probably because of the use of epoxy insulators. Tests for the operation of the periplasmatrons with an actively gettered source will be performed in 1985.

Despite these beam-cleaning methods, some residual fast impurities will reach the plasma during the heating period. To make a guess at the deposition of these ions, the FAFNER code was extended to calculate deposition profiles of the thermalized impurity ions (e.g. oxygen, molybdenum, titanium) /184/.

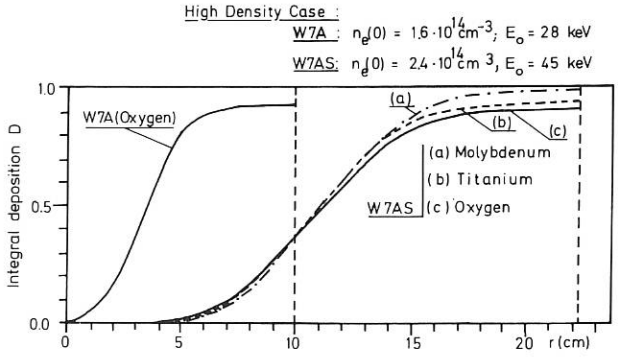

Fig. 5: Deposition D of fast injected ions integrated over the plasma volume as calculated by the FAFNER code for W VII-AS. Shine-through and orbit losses are subtracted. The corresponding ODIN result for oxygen in W VII-A is shown for comparison. (Deposition D(r) is defined as the ratio of the integrated - to radius r - rate of thermalized impurity ion input to the total neutral impurity input current)

$$D(r) = \frac{1}{V}\int_0^V H_T(r)\, dV - f_{Loss}$$

In Fig. 5 the deposition of fast injected ions integrated over the plasma volume is shown for the high-density case in W VII-AS. Shine-through and orbit losses are subtracted. For comparison the corresponding deposition for oxygen in W VII-A is also shown. As a result of the larger plasma cross-section, the plasma core in W VII-AS ($r < 6.0$ cm) should be effectively screened against injected impurity ions if thermal drift effects can be neglected.

3.2 ICRH for W VII-AS

The common HF system for W VII and ASDEX (see section on ASDEX) was completed, including the coaxial transmission lines to the W VII hall, and has been put into operation for W VII-A. Also the matching networks for W VII-AS are ready to be installed; only the line connections to the ultimate antenna sites have to be designed and fabricated. Two and three-dimensional calculations resulted in a basic design for a conventional loop antenna, capable of giving 750 kW of radiated power, while the final decision on the antenna principle is waiting for first experimental results with different antennae in W VII-A.

3.3 ECRH for W VII-AS

The application for preferential support, Phase II, was submitted in 1984 and approved by EURATOM. In Dec. 1984 orders for 4 cw gyrotrons, 200 kW, 70 GHz could be placed with industry. Preparations for the location of the gyrotrons in experimental hall L3 and for the transmission line support system from halls L3 to L7 are under way. For more details see report of IPF Stuttgart.

4. PHYSICS IN W VII-AS

Contributions to physical investigations are presented in Part A under Wendelstein VII-X Project in this report.

W VII-X Project

Head of Project: H. Wobig

The W VII-X project aims at a conceptual design of a Stellarator experiment capable of demonstrating - together with results from other experiments - the viability of the Stellarator line as an efficient fusion reactor concept. For this purpose extensive studies of Stellarator reactor problems were made: start-up scenario, heating and refuelling machines, mechanical problems of modular coils, geometry of the blanket. Critical issues of Stellarator reactor physics were identified for the purpose of including the investigation of them in the aims of the W VII-X experiment.

A basic problem of the experiment is the appropriate magnetic field configuration. Since configurations with a helical magnetic axis promise large critical ß-values, several configurations of this type were investigated. Special attention was paid to the geometry of the modular coils generating these fields. MHD equilibrium and stability of W VII-X-relevant configurations are being investigated by the Stellarator physics group of Theory Division 2.

After definition of the optimum magnetic field configuration, technical problems will be investigated in cooperation with the W VII-AS project team. First studies on neutral beam heating have been made in cooperation with the NBJ project. With respect to all those questions involving the mechanical structure, blanket and shielding, superconducting technology, etc., the cooperation with the Kernforschungszentrum Karlsruhe (KfK) was intensified.

CONTRIBUTIONS OF THE WENDELSTEIN VII-X GROUP

E. Harmeyer, J. Kisslinger, H. Maassberg,
F. Rau, H. Wobig.

1. ADVANCED STELLARATOR REACTOR AND BURNER COIL CONFIGURATION

Coil configurations of the W VII-AS type were extrapolated /104, 192, 260/ towards the dimensions of stellarator fusion reactors and burner experiments, i.e. devices with an estimated fusion power of about 4 and 0.4 GW, respectively. The scaling was done with an assumed distance of 1.8 m between the blanket and shield for the advanced stellarator reactor (ASR), and 1.2 m for the smaller burner device (ASB). Typical dimensions and characteristic data are given in Table 1.

TABLE 1

		ASR	ASB
Major radius	R_o =	25.5 m	15.2 m
Plasma radius	$\bar{a}$ =	1.6 m	0.9 m
Magnetic field on axis	B_o =	5.3 T	7 T
Maximum field on coils	B_{max} =	8.7 T	11-12.6 T
Rotational transform	t =	0.58	0.51
Aspect ratio		16	17
Coil aspect ratio		4.9	4.8
Coil current density	j_{max} =	9.8 MA/m^2	18 MA/m^2

In ASR, the maximum magnetic field of 8.7 T is within the scope of NbTi technology. Here ten coils per period are chosen in order to minimize the modular magnetic field ripple. Because of the tight arrangement of the coils maintenance and replacement of a single coil might be difficult or even impossible. A reduction to 4 coils per period eliminates this problem. On the other hand, the ratio B_{max}/B_o increases from 1.64 to 1.9 and a large modular ripple occurs. The ripple $1/2\,\Delta B/B$ on the magnetic axis is 1.9 % in the 10-coil case and 8.5 % in the 4-coil case. The increased ripple will certainly increase plasma losses. The rotational transform, the magnetic well depth and the plasma radius are also changed by this reduction.

In ASB coil sets comprising 18, 9 and 6 coils/field period are studied. The induction at the axis is increased to 7 T in order to improve the plasma confinement and lower the required value of ß. The maximum induction at the coils increases towards 11 to 12.6 T for the data sets of 18 to 6 coils/period. These values definitely call for Nb_3Sn as superconductor if operation of NbTi at reduced temperature is to be avoided. The current density of these data sets is chosen close to averaged values of INTOR.

Figure 1 shows in the upper row the ASR25T7 coil configuration (left) and the magnetic flux surfaces (vacuum fields) at toroidal positions of 0 and 1/2 field period along with the associated coils. In the lower row of the figure the coil systems of ASB are given on the same scale as above for the cases of 18, 9 and 6 coils/field period.

The data sets of ASB are also rescaled to the dimensions of ASR ($R \approx 25$ m), maintaining an elevated current density of 15 to 18 MA/m^2 averaged over the coil cross-section. Configurations with 6 coils/field period are now being considered as a reasonable compromise between magnetic field quality (ripple, magnetic well) and ease of maintenance.

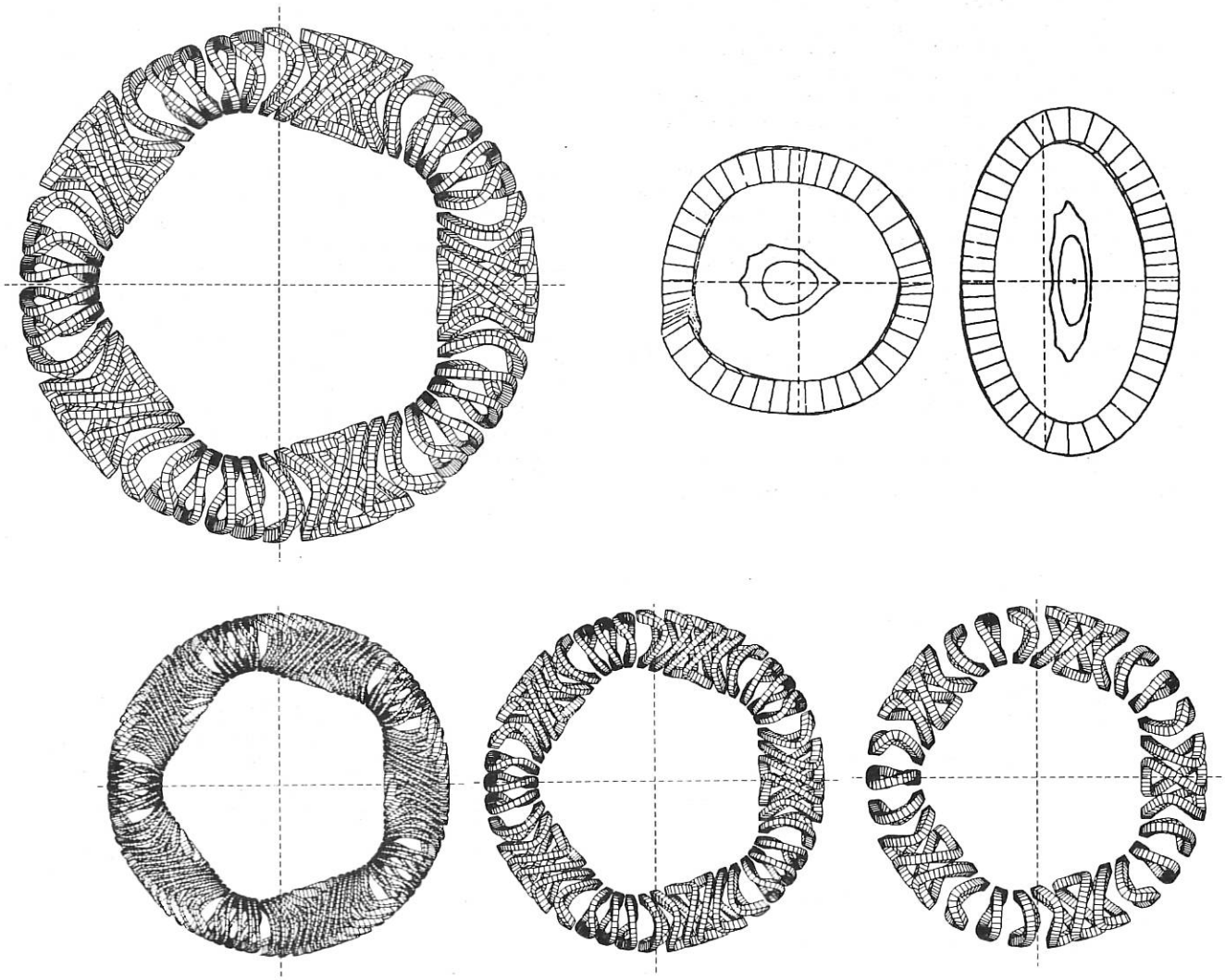

Fig. 1: Coil set of ASR25T7 and three ASB-systems shown on the same scale.

2. ELECTROMAGNETIC COMPUTATIONS AND SUPPORT SCHEMES

The mechanical stress calculations are mainly done for the ASB06E coil system with 6 coils per field period in comparison with the ASR25T7 system [1]. In the latter, a maximum force density of 41.2 MN/m^3 was found, whereas the corresponding value for ASB06E amounts to 88.4 MN/m^3. These values are averages over the coil cross-section ("macroelements"). The higher value for ASB06E is caused by the increased current density and the increased magnetic field at the coils. For a detailed investigation the distribution of the magnetic force density over the coil cross-section is made by dividing the coil cross-section into 3 radial and 2 lateral microelements. For coil No. 3 of ASB06E, Fig. 2 shows the radial and lateral components of the force density along the coil circumference.

Local maximum values of F'= 161 MN/m^3 are found for the microelements 1 and 4, at ARG = 20 and 30, resp., ARG being the length along the coil circumference.

To support the magnetic forces, the coils are surrounded by a suitably shaped support structure. The PADDING program, which generates input data for SAP, was extended to allow also for mutual support between the coils of one or more field periods. This more realistic support scheme avoids rigid boundary elements of the lateral support structure used in previous evaluations of stresses in single coils.

The presently used support scheme consists of 9 twisted coils (one and a half field periods) with lateral paddings and rings and a system of mutual support elements between the lateral support rings, which covers about 60 % of the circumference, in the example shown in Fig. 3. In addition, there are outer support rings with padding and rigid boundary elements (see Fig. 4). Rigid boundary elements are also located at the outer side rings of coils 1 and 9. Each coil is characterized by 48 macroelements loaded with the force density averaged over the coil cross-section. The SAP structure analysis program system treats 3244 elements with 6912 nodes.

[1]) Harmeyer, E. et al., Report IPP 2/269 (1983)

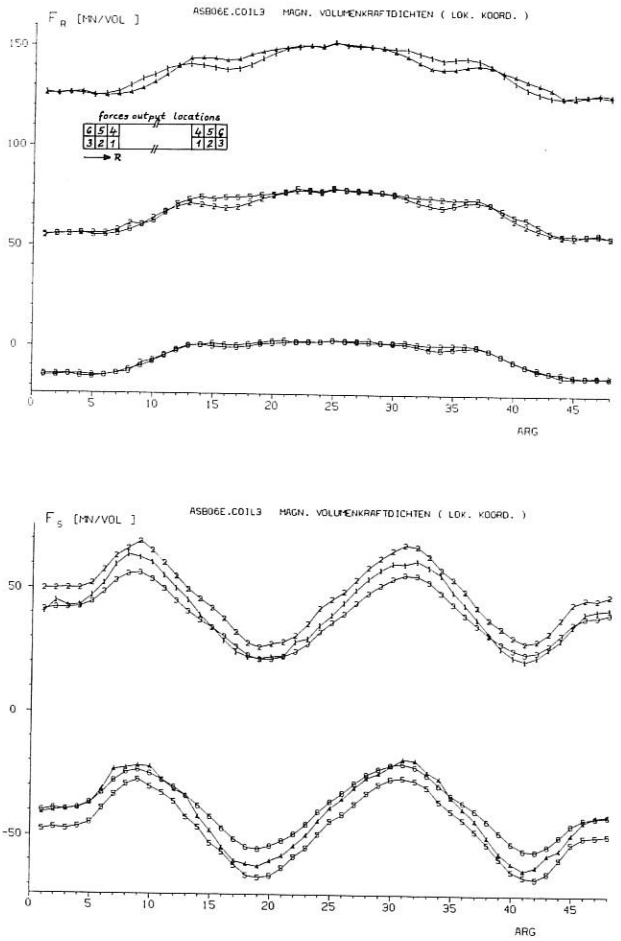

Fig. 2: ASB06E coil 3: magnetic force densities in the radial and lateral directions.

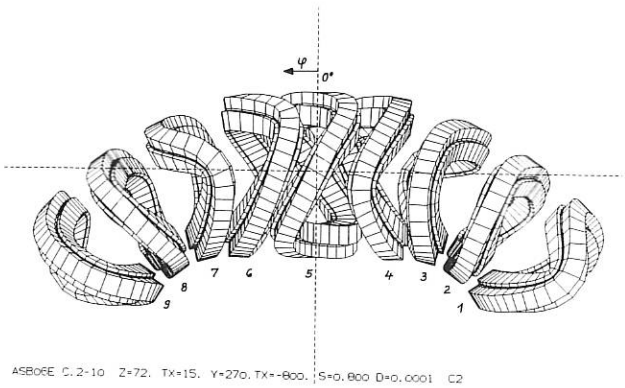

Fig. 3: ASB06E, coils 1-9.

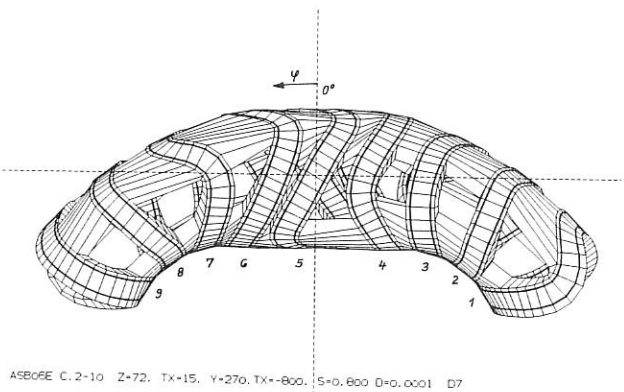

Fig. 4: ASB06E, mutual support.

Maximum values of about 200 - 220 MPa are found for the von Mises stresses, when a filling factor of 0.8 and further material constants as in [1] are used. A factor of about 2 is applied to take into account the increased edge values of the magnetic force density. Although the magnitude of the von Mises stresses is uncritical, comparatively large shear stresses are found at certain positions in the coils. Future studies aim to reduce the shear stresses.

3. PLASMA PARAMETERS IN A STELLARATOR REACTOR

The TEMPO modified transport code was used to study the start-up scenario of ASR with the parameters described above. Neoclassical transport as modelled by Shaing and Houlberg and an additional anomalous loss as found in W VII-A were introduced as loss mechanisms. The effective mirror ratio on the magnetic axis is ε_h = 2 % and on the plasma boundary 10 %. The radial power deposition of external heating is a given function, as also is the local particle production rate. The start-up procedure is investigated using a production rate centred in the plasma centre, thus modelling a refuelling mechanism with pellets penetrating deep into the plasma (Fig. 5). The temperature and density profiles of the ignited state are shown in Fig. 6. By increasing the refuelling rate the thermal output of the reactor can be raised to more than 3 GW.

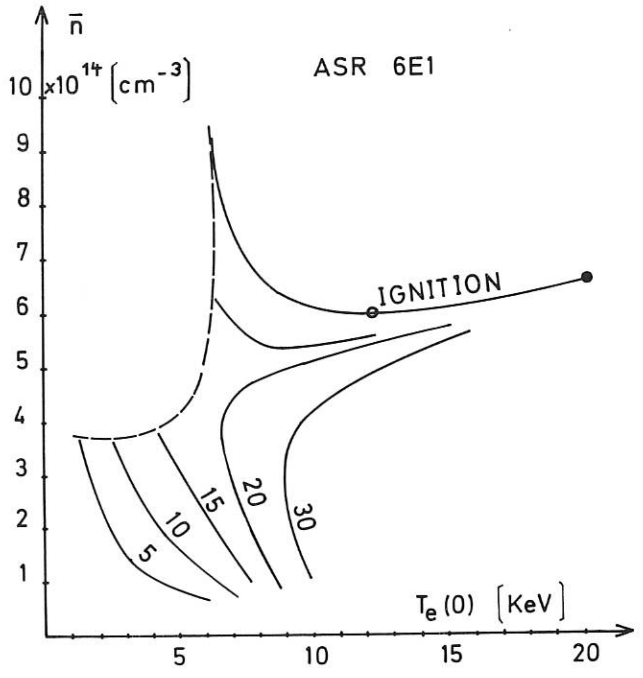

Fig. 5: Start-up scenario of ASR for net heating powers 5 to 30 MW.

In the case of refuelling in the boundary region described by a deposition profile peaked in the boundary region, conditions for ignition are more stringent than in the former case. The average density has to be raised to 1.6 x 10^{20} m^{-3} but the temperature remains around 12 keV. This state is shown in Fig. 7. The broken line Q_d indicates the local refuelling rate: the power output in this case is 3.2 GW.

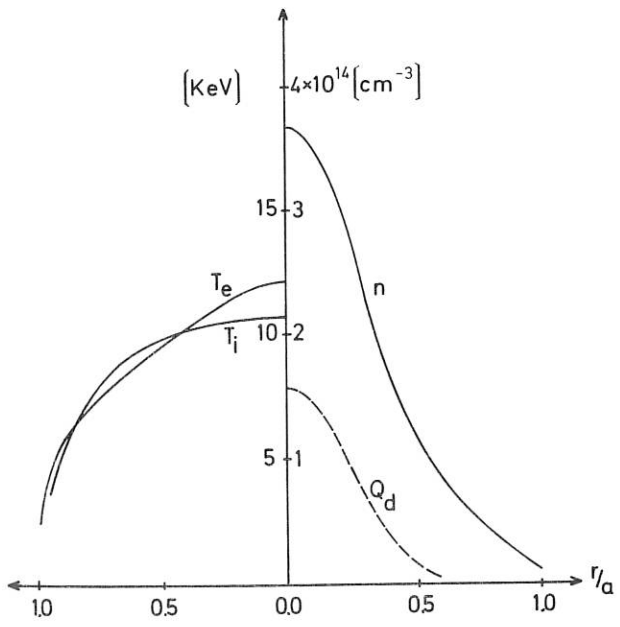

Fig. 6: Radial profiles of density, temperatures and centred production rate Q_d.

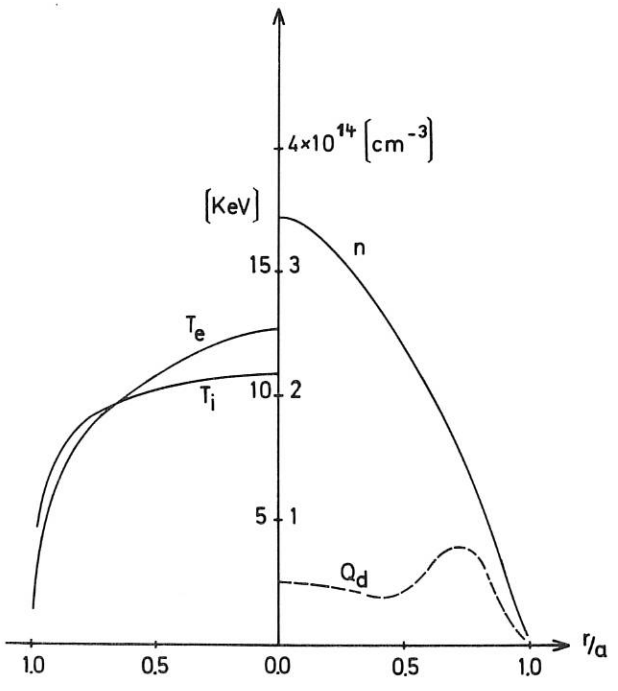

Fig. 7: Same as Fig. 6, deposition in the boundary region.

4. MAGNETIC FIELD STUDIES

With respect to W VII-X extensive studies of vacuum fields were made. Following the principle of minimizing Pfirsch-Schlüter currents, mainly configurations with helical magnetic axes were investigated. A special configuration of this type is the HELIAC configuration. Modular twisted coils were used in order to represent HELIAC configurations. As a figure of merit for comparing different magnetic fields the value

$$J^* = \frac{B_o^2}{B^2} \left\langle \left(1 + \frac{j_\parallel^2}{j_\perp^2}\right) \right\rangle$$

is used, where B_o is a reference field (average field on magnetic surface) and $\langle\ \rangle$ denotes the average on a magnetic surface. The ratio $j_\parallel / j_\perp$ only depends on the structure of the magnetic field and can also be calculated in a vacuum field. In W VII-A the number J^* is 11 and in W VII-AS $J^* = 6.3$.

The investigation of helical axis configurations starts from coils given by an analytic winding law. The centre of the coils is positioned on a helically and toroidally closed line, which is described by the following law:

$$R = R_o + A \cos(\varphi + S \sin\varphi)$$
$$z = B \sin(\varphi + S \sin\varphi)$$

R, z, φ are cylindrical coordinates, R_o = major radius, A,B are constants, and S is a parameter describing the pitch of the helix. The coil winding law is given in a Cartesian coordinate system with $t(\varphi)$, $b(\varphi)$, $n(\varphi)$ as base vectors. Under special conditions t, b, n, may coincide with the tangent and binormal and normal vectors of the central helix. In general, the t, b, n system is rotated with respect to the natural system.

In the b - n plane a closed curve is described in polar coordinates r, θ. With θ as the second independent variable, we obtain a toroidally closed surface $r = r_o(\varphi,\theta)$. The curve $\varphi = \varphi_c(\theta)$ on this surface is the centre of a twisted coil. The functions $r_o(\varphi,\theta)$ and $\varphi_c(\theta)$ are given in Fourier series. In the special case of circular plane coils we obtain HELIAC configurations. Figure 8 shows a HELIAC case with 8 field periods, $\iota \approx 3.4$ and an aspect ratio of about 10. The distance between adjacent coils is chosen so as to minimize the magnetic mirror on the magnetic axis. The figure of merit J^* in this case is $J^* = 2.1$.

Modular systems with 5 and 8 periods were extensively studied. The central circular conductor of a HELIAC can be replaced by appropriately twisting the TF coils. In the case of plane noncircular coils a magnetic well can only be obtained at large aspect ratio.

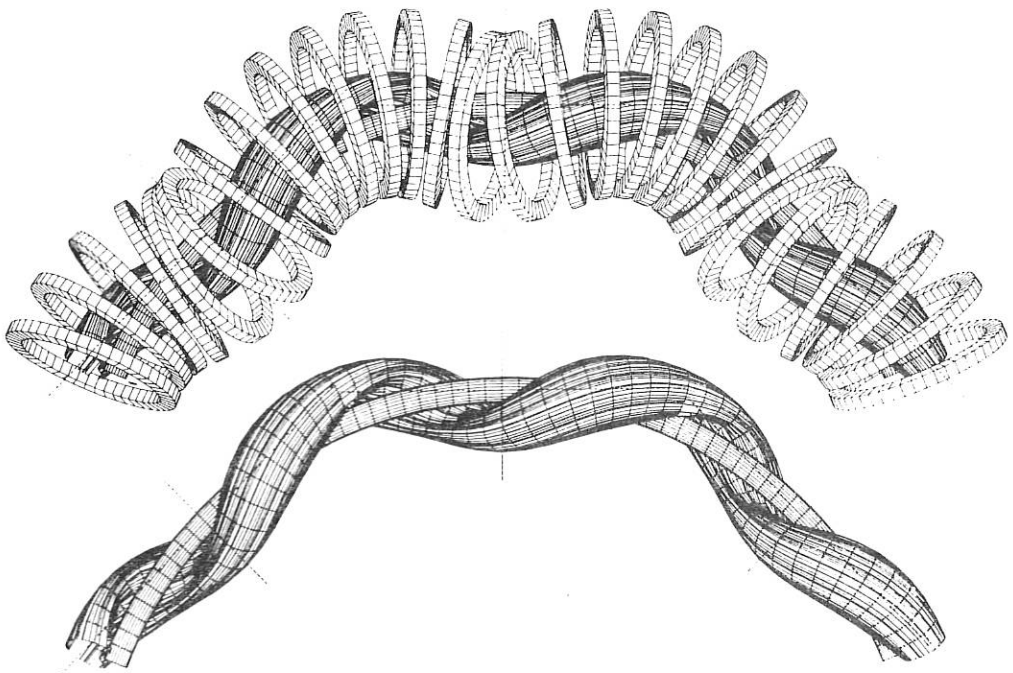

Fig. 8: Conventional HELIAC configuration, three of eight field periods shown.

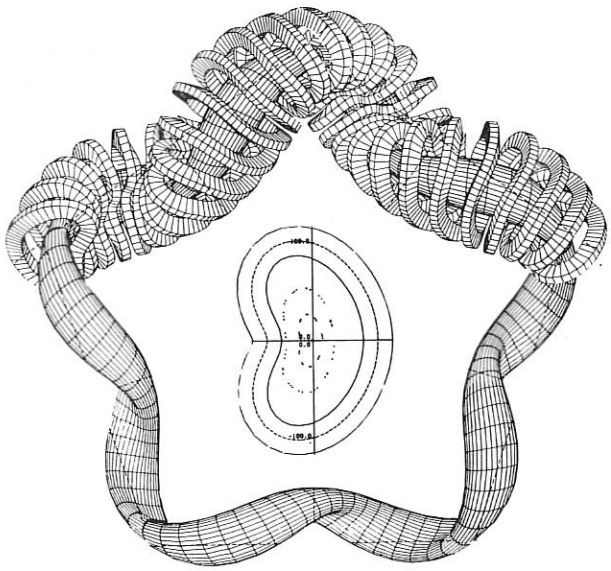

Fig 9: Modular coil system for a HELIAC with five field periods.

In Fig. 9 a 5-period modular system is shown which has an aspect ratio of A = 10, a rotational transform t = 2.3 - 2.1 and a magnetic well of - 2 %; J^* is 3.3. A deeper magnetic well requires more twist of the coils or less distance between the coils and plasma.

5. PLASMA EQUILIBRIUM IN STELLARATORS

A plasma equilibrium is calculated by the low-ß-expansion method, starting from a given vacuum field. This method, already proposed by L. Spitzer, calculates a sequence of magnetic fields resulting from $\nabla p_n = J_n \times B_{n-1}$, $\nabla \times B_n = J_n$, $\nabla \cdot B_n = 0$.

In each step of the interation the plasma currents J_n are determined from the equilibrium condition. The magnetic differential equation $B \cdot \nabla \nu = 1$ yields the current lines ν = const. on every magnetic surface, Fig. 10, bold lines. The magnetic field of these currents is obtained by Biot-Savart's law, and the iteration process is continued with this new field. Unlike in other equilibrium codes, no boundary conditions for the magnetic field are required, except B = 0 at infinity. The condition of zero toroidal current selects a special solution of the magnetic differential equation. A difficulty of the iteration process is the occurrence of islands. Since the pressure profile is an arbitrary function of the magnetic surface, it can be made constant in the island region. The code needs further development with respect to this problem.

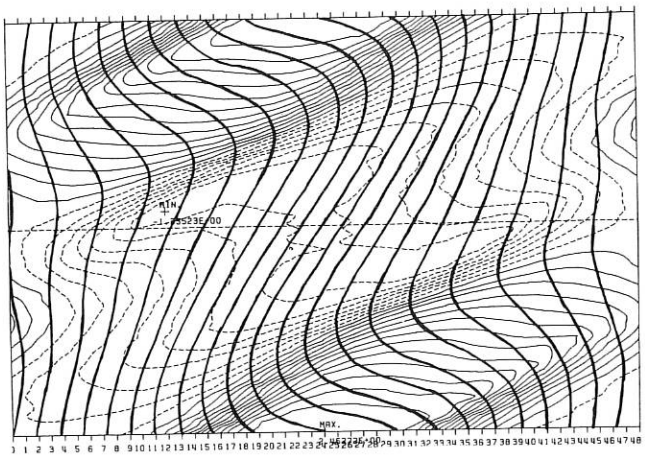

Fig. 10: Poloidally closed current lines on a magnetic surface (one period).

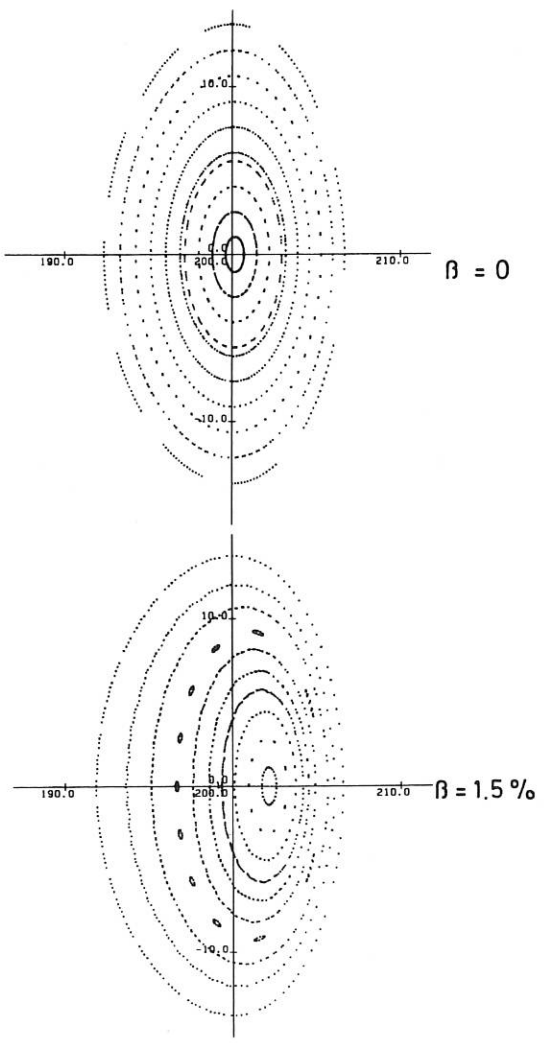

Fig. 11: Magnetic surfaces of the W VII-A Stellarator, vacuum field and at ß(o) = 1.5 %.

In Fig. 11 magnetic surfaces of the W VII-A stellarator are shown; at ß(o) = 1.5 % the Shafranov shift is 1/4 of the plasma radius. Similar calculations for W VII-AS verify the reduction of the Shafranov shift in this configuration. Future improvements of the code will combine the equilibrium code and the transport code.

Cooperation with W VII-X and KfK Karlsruhe

Cooperation with KfK Karlsruhe was initiated in the field of superconductivity and stellarator reactor studies. In several discussion meetings between July 1983 and November 1984 members of the W VII-X group presented their work on stellarator reactor and burner magnetic field configurations, on finite element computations of electromagnetic forces and stresses, as well as on start-up and burning scenarios of such devices. Details are given above. The activity of KfK is concentrated on studies of superconducting coil design - possibly at a later time also including the construction of a test coil with about twice the dimensions of the normal conducting W VII-AS coils - as well as on the layout and maintenance schemes for blanket, shield and coils with their associated structure requirements. For further information see the Annual Report of KfK, Institut für Technische Physik, especially regarding their cooperation with the University of Wisconsin on fusion reactor studies.

CONTRIBUTIONS OF THE STELLARATOR PHYSICS GROUP

W. Dommaschk, F. Herrnegger, W. Lotz, P. Merkel, J. Nührenberg, A. Schlüter, U. Schwenn
Guests: J. Cary [1], P. Garabedian [2], J. Johnson [3], G. Kuo-Petravic [4], J. Rome [5]

MHD equilibrium and stability as well as neoclassical transport in stellarators have been the main concerns. Results of these efforts are meant to be used in selecting optimal configurations for future stellarator devices of IPP.
Some of the new codes mentioned in Table 1 of the Annual Report 1983 are now being routinely used. As far as Monte Carlo simulations of neoclassical transport are concerned, the Fourier analysis of $|B|$ on magnetic surfaces together with Monte-Carlo simulations in magnetic coordinates are now being performed without and with electric potential, as well as without and with finite β. As to MHD calculations, which were the primary concern in 1984, the BETA 3D code and the PPPL stellarator expansion code are now being used for equilibrium and mode analyses, supplemented by evaluation of the Mercier and the resistive interchange criteria. The BETA and FIT codes successfully underwent mutual tests, so that the systematic use of FIT is now being prepared.

1. Evaluation of the resistive interchange criterion for toroidal stellarators

Subsequent to the application of the Mercier criterion to 3D code stellarator equilibria, the analogous resistive criterion [6] was considered /181/. In the case of vanishing net longitudinal current typical of stellarators, this criterion reduces to ($' = \frac{d}{ds}$, $s \propto$ toroidal flux, $\langle \ldots \rangle = \int \ldots \sqrt{g}\, du\, dv \,/ \int \sqrt{g}\, du\, dv$)

$$\frac{V''}{V'} P' - P'^2 \langle B^{-2} \rangle - \langle j_\parallel^2 / |\nabla s|^2 \rangle > 0$$

which clearly exhibits the dominating role of the stabilizing magnetic well and the destabilizing parallel current density for these instabilities. W VII-AS, ATF, Heliacs and those $\ell = 1, 2, 3$ equilibria in which the classical PS component of the parallel current density is eliminated, exhibit quite different stability behaviour. W VII-AS becomes (ideally and resistively) unstable at $\langle \beta \rangle \approx 0.01$ because the destabilizing current density grows faster with β than the depth of the well.

Although ATF remains ideally stable up to $\langle \beta \rangle \approx 0.03$, it is resistively unstable for β as low as $\langle \beta \rangle \approx 0.01$, because resistivity eliminates the stabilizing influences of the shear and the interaction between shear and averaged parallel current density. For Heliacs and $\ell = 1, 2, 3$ equilibria, the difference between the ideal and the resistive criteria virtually vanishes. Some results are shown in detail in Fig.1.

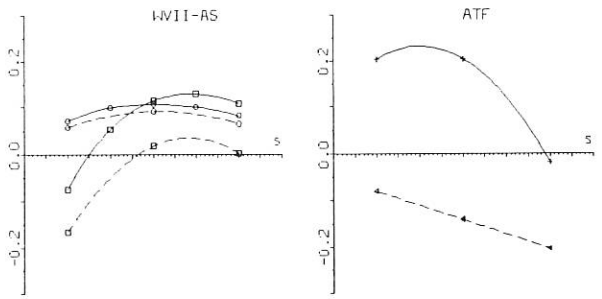

Fig.1: The Mercier (—) and resistive (- - -) stability criteria as functions of the radial label s for W VII-AS and ATF with parabolic pressure profile. The stable result in W VII-AS is obtained for $\langle \beta \rangle \approx 0.7\%$, the marginal one for 1.4%. In the ATF-cases, $\langle \beta \rangle \approx 3\%$ (—), $\langle \beta \rangle \approx 1\%$ (- - -).

[1] Visiting scientist from IFS
[2] Visiting scientist from CIMS
[3] Visiting scientist from PPPL
[4] Visiting scientist from PPPL
[5] Visiting scientist from ORNL
[6] A.H. Glasser, J.M. Greene, J.L. Johnson, Phys.Fluids 18 (1975) 875

2. Elimination of pressure-driven singular current density

Evaluation of Mercier's criterion may also be used to assess the singular pressure-driven current density near rational magnetic surfaces as well as its elimination by a flattened profile or a finite separation $\delta\iota$ in twist ι. Results obtained so far suggest that low order resonances, e.g. $\iota_p = \frac{1}{3}, \frac{1}{4}$ (ι per period), have to be avoided. A detailed study /100/ of a strongly three-dimensional $\ell = 1, 2, 3$ equilibrium with $\iota_p \approx \frac{1}{6}$ investigated the effective width Δs of the singular current as a function of β, position in s, and shear as measured by the difference $\Delta\iota$ from the axis to the boundary. The results can be summarized by

$$\Delta s \approx \langle\beta\rangle^2 s^{\frac{3}{2}}/\Delta\iota \qquad (\text{for } \iota_p = \frac{1}{6})$$

Figures 2, 3 show examples. The elimination of the singular current by a flattened pressure profile is demonstrated in Fig.4 and suggests that the spacing between comparable resonances $[\sim 0(\iota_p^2)]$ allows sufficient shear $[\Delta\iota/\iota \sim 0(\iota_p)]$ for a solution with an acceptably thin, flattened pressure profile region. The other possibility, elimination of the singular current by avoiding the resonance, is demonstrated in Fig.5. Applying these results to W VII-AS, where the resonant effects of ι_p (e.g. $\frac{1}{12}$) are beyond the reliable resolution of the finite-β codes, one may hope that the crossing of one or several of these high-order resonances, e.g. by raising β (see Fig.6) /109/ will be harmless.

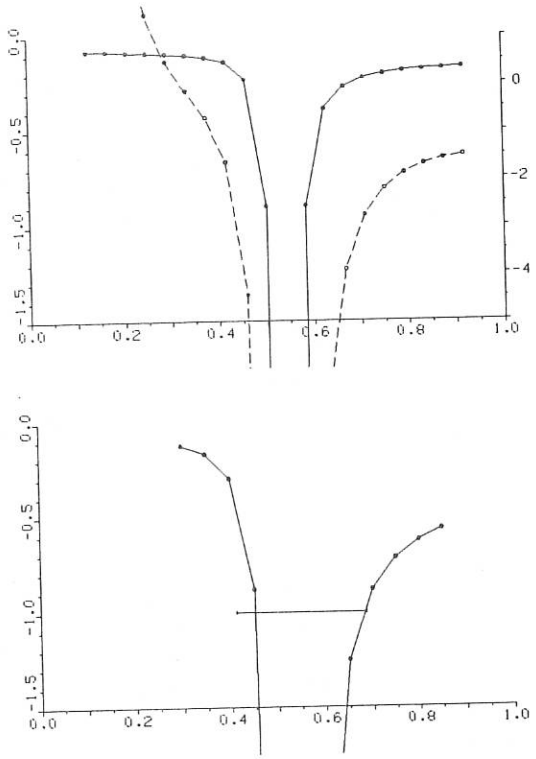

Fig.2: The Mercier criterion (- - -, right ordinate) and a measure of $\langle j_\parallel^2\rangle$ (—, left ordinate) as functions of s for $\langle\beta\rangle = 4.5\%$ in an $\ell = 1, 2, 3$ case with $\iota_p \approx \frac{1}{6}$. In the upper part, the shear may be characterized by $\Delta\iota/\iota = 0.06$, in the lower part by 0.02.

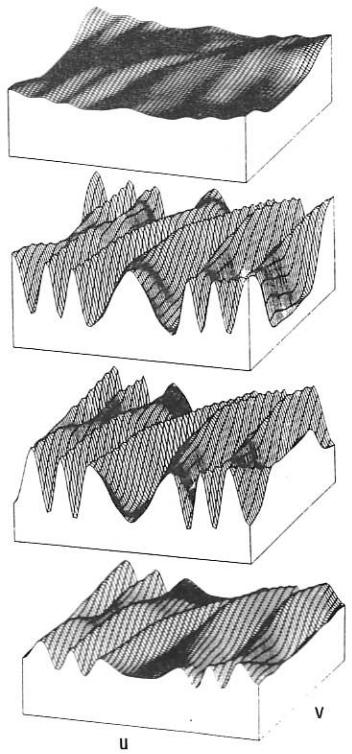

Fig.3: The parallel current density as a function of u (poloidal) and v (toroidal) at (from top to bottom) $s = 0.3, \frac{12}{24}, \frac{14}{24}, 0.75$ in the case of Fig.2a.

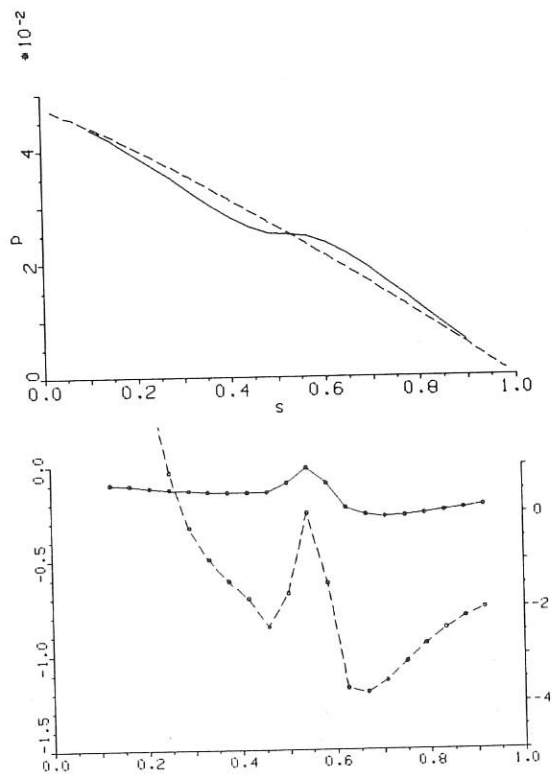

Fig.4: The upper part shows a flattened pressure profile as a function of the flux label. The lower part, Mercier criterion (—) and $\langle j_\parallel^2\rangle$ (- - -), shows that this profile eliminates the pressure-driven singular parallel current.

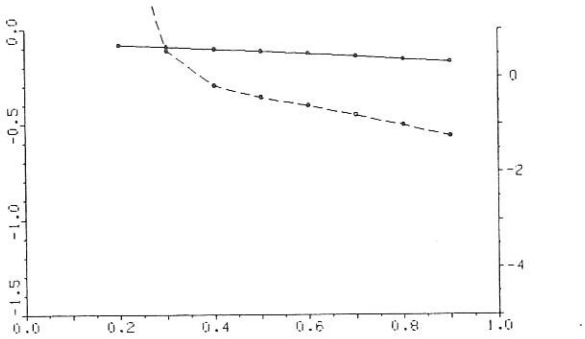

Fig.5: The same plot as in Fig.4b. The singular behaviour at $\iota_R = \frac{1}{6}$ is avoided by $\iota_p - \iota_R \approx 0.005$.

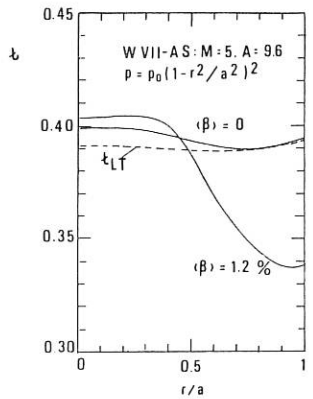

Fig.6: ι-profile in W VII-AS as obtained with the BBG code.

3. Case studies of 3D configurations

Some progress was made in the search for a suitable configuration for the next-generation stellarator. In the following some results are listed which show that improvements beyond the previous W VII-AS results on local stability criteria can be obtained.

For W VII-AS a rough optimization of the pressure profile leads to the result that $\langle\beta\rangle \approx 1.6\%$ is approximately Mercier marginal, while a bell-shaped profile leads to a marginal value of $\langle\beta\rangle \approx 0.5\%$. Thus, the profile dependence leads to a variation of the marginal $\langle\beta\rangle$ value of a factor ≈ 3, which shows that for this reason alone a reliable prediction of the β-limit is not possible (Fig.7a).

An $\ell = 1, 2, 3$ configuration with $\langle\beta\rangle \approx 2.1\%$ and a parabolic pressure distribution which is approximately marginal except in the vicinity of the $\iota_p = \frac{1}{4}$ resonance is shown in Fig.7b.

A Heliac configuration with $\iota_p = \frac{1}{4} \rightarrow \frac{1}{3}$ which is approximately marginal at $\langle\beta\rangle = 1.3\%$ is given in Fig.7c.

A configuration which geometrically interpolates between the above two configurations is presented in Fig.7d. It avoids $\iota_p = \frac{1}{5}$ and $\frac{1}{4}$, and is approximately marginal at $\langle\beta\rangle = 1.9\%$ for a bell-shaped pressure profile.

A configuration with identical ι profile, significantly smaller contributions from both the magnetic well and the parallel current density, but approximately the same stability result is given in Fig.7e. The magnetic well is only marginal, so that, formally, instability prevails. Configurations of this type stress the as yet unsolved question to which degree violation of the Mercier (or resistive) criterion will be acceptable.

The main conclusion from the above results seems that significant improvements of the admissible β-value in advanced stellarators may well be possible, but are difficult to demonstrate because of the vastness of the configuration space.

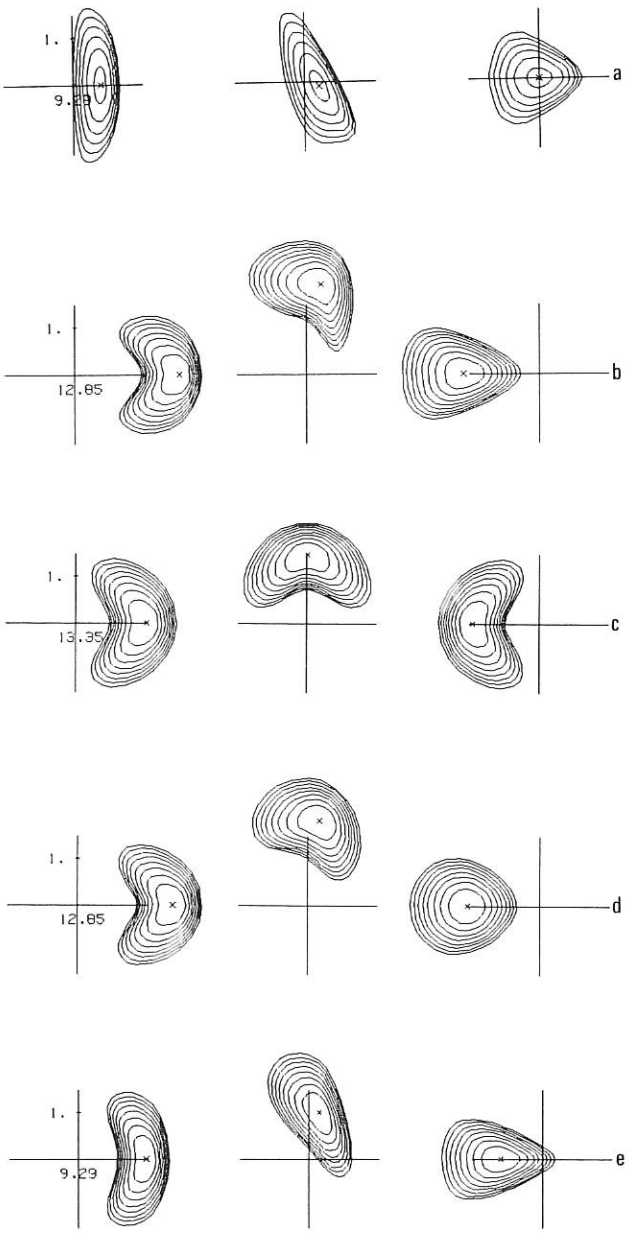

Fig.7: Various stellarator configurations with approximately marginal Mercier criterion: a) W VII-AS, b) $\ell = 1, 2, 3$ stellarator, c) Heliac, d) Hel123, e) AS123 with the following values characterizing the twist (inside $\rightarrow$ outside), the $\langle\beta\rangle$ value, the magnetic well $\Delta V'/V'$, and $\langle j_\parallel^2\rangle$, respectively:

a) .09 $\rightarrow$ .06, 1.6%, 7.4%, .077;
b) .22 $\rightarrow$ .29, 2.1%, 9.2%, .030;
c) .25 $\rightarrow$ .33, 1.3%, 6.0%, .006;
d) .20 $\rightarrow$ .23, 1.9%, 9.0%, .044;
e) .21 $\rightarrow$ .24, 1.1%, 0.0%, .002.

The numbers at the axes indicate the plasma radius (normalized to 1) and the aspect ratio; all configurations have 5 periods.

4. Nonlocal modes

The BETA code and the PPPL code based on the stellarator expansion were used to study linear growth rates and (in the case of BETA) nonlinear saturation of ideal MHD modes.
Figure 8 shows a comparison of eigenvalues of an m = 2, n = 1 mode in a sequence of straight and toroidal $\ell = 2$ stellarator equilibria (considered as topological tori with five periods) in which ι was varied to study the instability window [1]. Very good agreement was obtained with all three codes used. The expected scaling of the maximal eigenvalues $\propto A_P^{-2}\beta$ with aspect ratio and β was verified.
A toroidal $\ell = 2$ case with many periods was selected /182/ to study the nonlinear saturation of modes of the above type in the framework of ideal MHD. Figure 9 shows the saturated distortion at a finite mesh size (14/28/140). Extrapolation to zero mesh size shows that the true distortion is much larger, so that saturation may not occur in a more realistic model (e.g. free boundary calculation or resistive MHD).

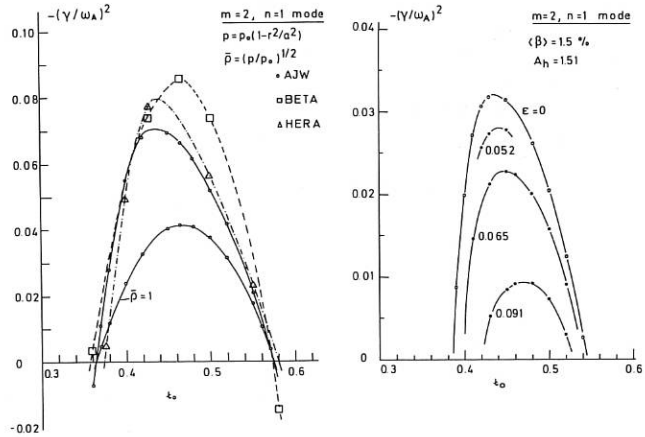

Fig.8: Normalized eigenvalues versus twist as computed by three codes for a straight $\ell = 2$ configuration (left: $\langle\beta\rangle = 3\%, L_P/2\pi = 1.51, M = 5$). Right: the unstable $m = 2$ mode will be stabilized by increasing the torus curvature $\epsilon = 1/A$ (asymptotic code).

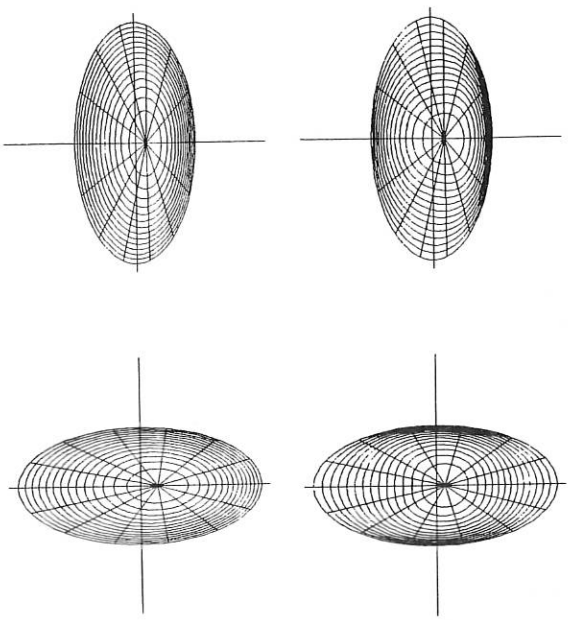

Fig.9: The left column shows a toroidal $\ell = 2$ equilibrium with $\langle\beta\rangle \approx 18\%, N = 70, A = 50$; the right column shows the bifurcated state due to a nonlinearly saturated $m = 2$ mode.

5. The FIT 3D MHD Code

The FIT code /216/ designed to compute ideal MHD equilibria, was modified as follows: 1) The previous iteration methods were extended by a conjugate gradient method capable of varying all three dependent variables r, z, and λ simultaneously, where λ is defined by the magnetic flux function $\psi = -uF_T' + vF_P' + \lambda$. 2) The redundancy of these variables has been reduced by coupling some of the $r-$ and $z-$coefficients in the Fourier series [2].
FIT was tested on six configurations /215/: 1) an axisymmetric Solov'ev equilibrium; 2) an axisymmetric high-beta equilibrium; 3) a low-aspect-ratio ($A \approx 4$) $\ell = 2$ configuration; 4) an ATF model; 5) a W VII-AS; and 6) a Heliac. Figure 10 shows the final state of a W VII-AS case with a boundary given by 39 Fourier coefficients.
The results obtained with FIT were compared with those of other codes. The accuracy was checked by two scalars, the energy and the mean axis shift. In most cases 20...26 coefficients in the r, z and λ series were sufficient to reduce the poloidal and toroidal discretization errors to the accuracy of the radial extrapolation. In the W VII-AS case the energy values are reliable in the leading five figures.

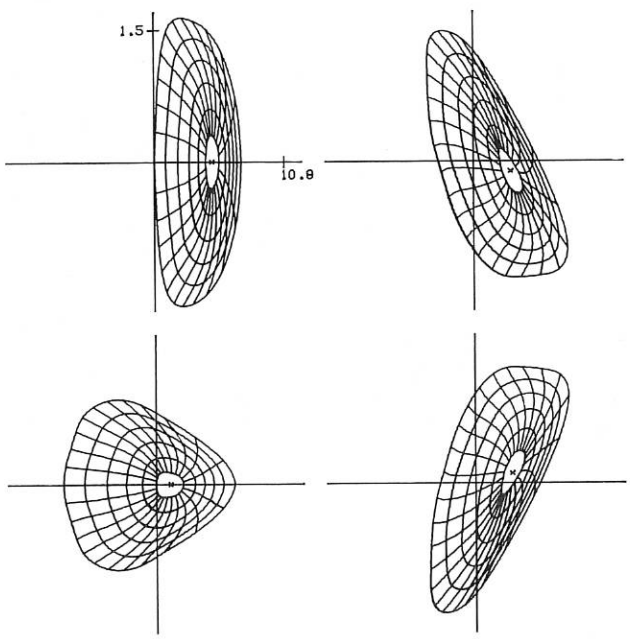

Fig.10: A finite-β case of W VII-AS as obtained with FIT.

Owing to the radial (s) difference approximations, the extrapolation in the mesh size for the energy and the axis shift was done with a polynomial in Δs^2, i.e. $f(\Delta s) = f_0 + f_2\Delta s^2 + f_4\Delta s^4$. Grids of 8...20 points turned out to be sufficient. Typically the relative errors in the energy are $\approx 10^{-4}$, in the position of the axis $< 10^{-1}$

[1] O. Betancourt, F. Herrnegger, P. Merkel, J. Nührenberg, R. Gruber, F. Troyon, J.Comp.Phys. **52** (1983) 187

[2] F. Bauer, O. Betancourt, and P. Garabedian, Magnetohydrodynamic Equilibrium and Stability of Stellarators (Springer, New York 1984);
S. Hirshman, H.K. Meier, ORNL/TM-9300

already on the coarsest grids. With respect to the energy this is more than one order of magnitude below the respective values usually obtained with codes based on difference methods in all dimensions. Within the accuracy of either FIT or BBG/BETA results the agreement is excellent, as in the cases treated by Hirshman [1] and Lao [2].

6. An integral equation technique for the exterior and interior Neumann problem in toroidal regions

For a given magnetic field $\vec{B}_0(\mathrm{div}\vec{B}_0 = 0, \mathrm{curl}\vec{B}_0 = \vec{j})$ in a toroidal region bounded by a surface a magnetic vacuum field $\vec{B}_1 = \nabla\Phi$ can be calculated so that the superposition of the two fields $\vec{B} = \vec{B}_0 + \nabla\Phi$ is tangential on the surface.
This leads for Φ to the Neumann problem of finding a function Φ which satisfies the Laplace's equation in a region, and whose normal derivative $\frac{\partial\Phi}{\partial n}$ takes given values on the boundary of the region. In the case of only one boundary one gets for Φ one integral equation

$$\Phi(\vec{x}) + \frac{1}{2\pi}\int \frac{\partial G(\vec{x},\vec{x}')}{\partial n'}\,\Phi(\vec{x}')\,df' = \\ = \frac{1}{2\pi}\int G(\vec{x},\vec{x}')\,\frac{\partial\Phi(\vec{x}')}{\partial n'}\,df'$$

where $\vec{x}, \vec{x}'$ are points on the surface and $G(\vec{x},\vec{x}') = 1/|\vec{x}-\vec{x}'|$ is Green's function.
The integral equation is solved /160/ by representing the toroidal surface and the potential Φ by Fourier series of two angle-like variables (u, v). A set of linear equations for the Fourier coefficients of the potential Φ is obtained. The singularity of Green's function and its derivative are treated by a subtraction method: functions with the same singularity are subtracted and their analytically calculated Fourier transforms are added again.
Two applications are of interest: 1. As solutions of the inner boundary value problem toroidal vacuum fields can be generated with a magnetic surface on the boundary. There are conjectures that for appropriate boundaries configurations with "good" magnetic surfaces in the whole region can be found.

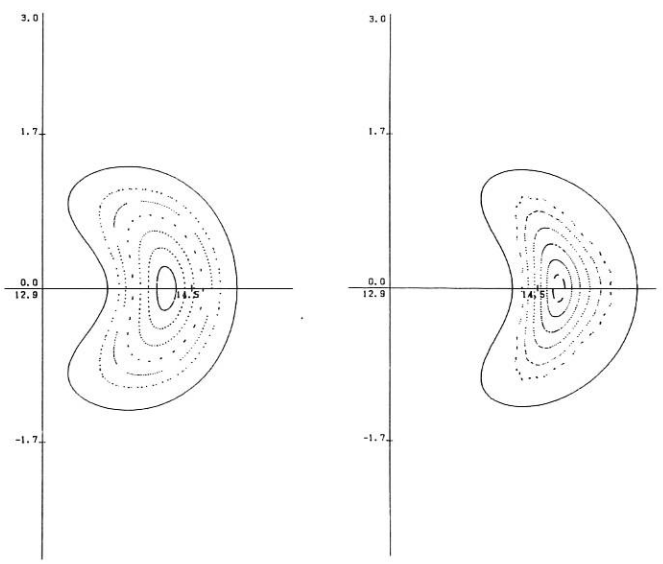

Fig.11: Section of surface plots obtained from the solution of the boundary value problem for a Heliac left and an $\ell = 1, 2, 3$ stellarator (right).

Figure 11 shows examples of a Heliac and an $\ell = 1, 2, 3$ configuration. Generating the solution in terms of Φ at the boundary takes seconds on a CRAY-1, so that the application of this method to systematic optimization of vacuum field configurations is being considered. 2. The vacuum field contribution in the 3D equilibrium problem can be calculated, with the fields produced by the external currents included. In this case an exterior Neumann problem is solved by considering the infinite region exterior to the toroidal surface, while in the 3D BETA code [3] the vacuum field is calculated by a variational method which requires an outer control surface to keep the region finite. Coupling of this code to FIT in order to compute free boundary equilibria is being prepared.

7. Vacuum field configurations with good surfaces

The method of Hanson and Cary [4] to eliminate stochasticity in stellarators was adapted to the use of Dommaschk potentials in optimizing the quality of magnetic surfaces. Figure 12 in which the elimination of island widths was applied to $\iota_p = \frac{1}{3}$ and $\iota_p = \frac{1}{4}$ shows that a satisfactory result can be obtained. Thus, it is not necessary to go back to coils and Biot-Savart's law to obtain good surfaces. Whether or not the method can be applied to more three-dimensional cases is being investigated. A preliminary example is shown in Fig.13, where a vertical field was added and the procedure still worked.
The evaluation of island widths with the PPPL code [5] determining the poloidal flux function is being prepared.

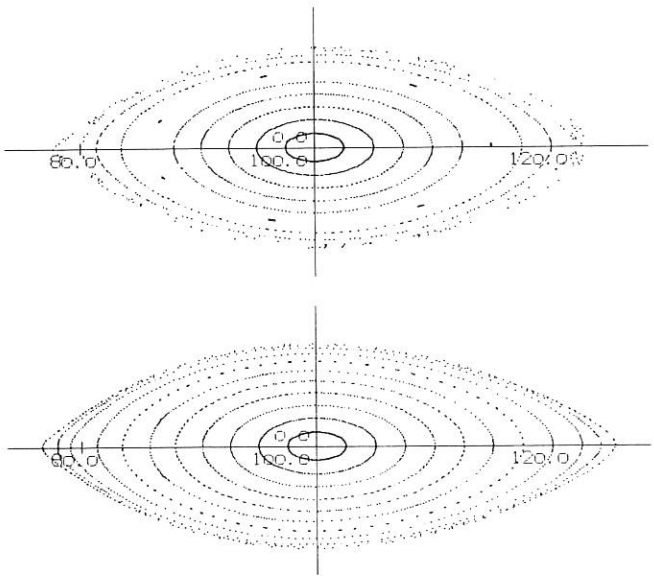

Fig.12: An $\ell = 2$ configuration as obtained with Dommaschk potentials before and after island elimination.

[1] S. Hirshman, priv.communication
[2] L. Lao, GA-A17188 and priv.communication
[3] F. Bauer, O. Betancourt, and P. Garabedian, Magnetohydrodynamic Equilibrium and Stability of Stellarators (Springer, New York 19840
[4] J.D. Hanson, J.R. Cary Phys.Fluids **27** (1984) 767
[5] G. Kuo-Petravic, A.H. Boozer, Proc.5th Int.Workshop on Stellarators, Vol.II, 463

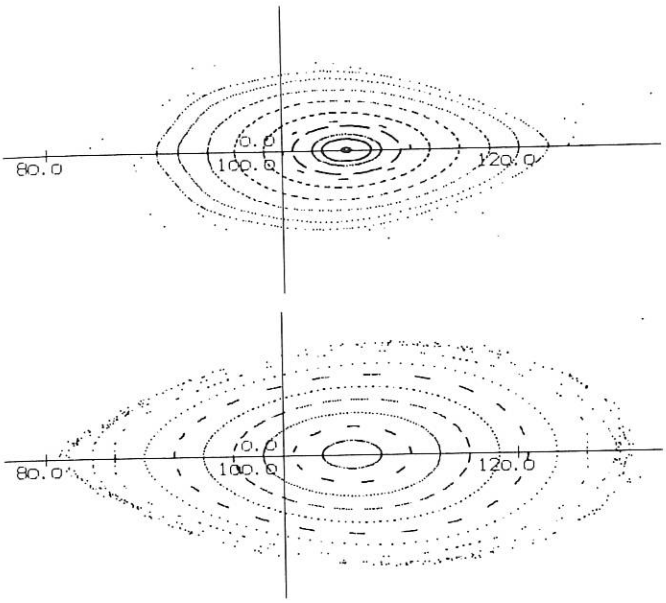

Fig.13: The $\ell = 2$ configuration of Fig.12b with vertical field and after reoptimization.

8. Monte Carlo simulation in magnetic coordinates

Two ORNL codes, the generation of the Fourier amplitudes of $|\vec{B}|$ in Boozer's coordinates from a given magnetic field [1] and the Monte Carlo simulation of neoclassical transport [2], which needs these Fourier amplitudes, have been tested and are now in use. In addition, the JMC code was modified to yield these amplitudes in finite-β equilibria. Figure 14 shows a comparison of the vacuum field and a finite-β case of W VII-AS. Figure 15 shows the good agreement of transport coefficients as obtained from the MC simulation in Cartesian coordinates /70, 148/ and with the above codes. A preliminary result with non-vanishing electric potential is shown in Fig.16.

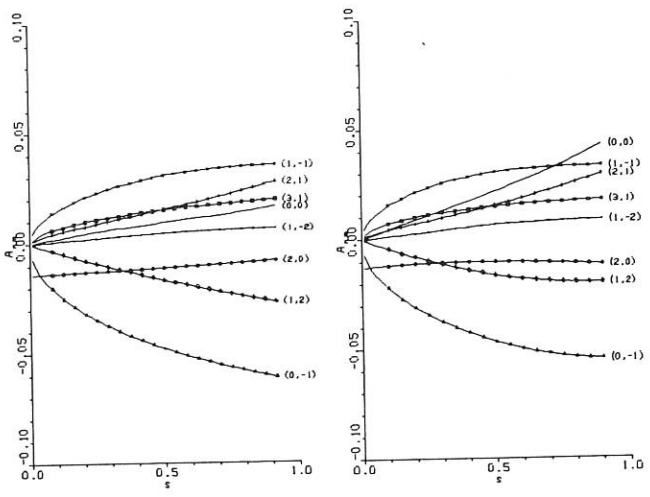

Fig.14: The left part shows Fourier coefficients of $|\vec{B}|$ as functions of s for the W VII-AS vacuum field, the right part shows the $\langle\beta\rangle \approx 1.4\%$ case.

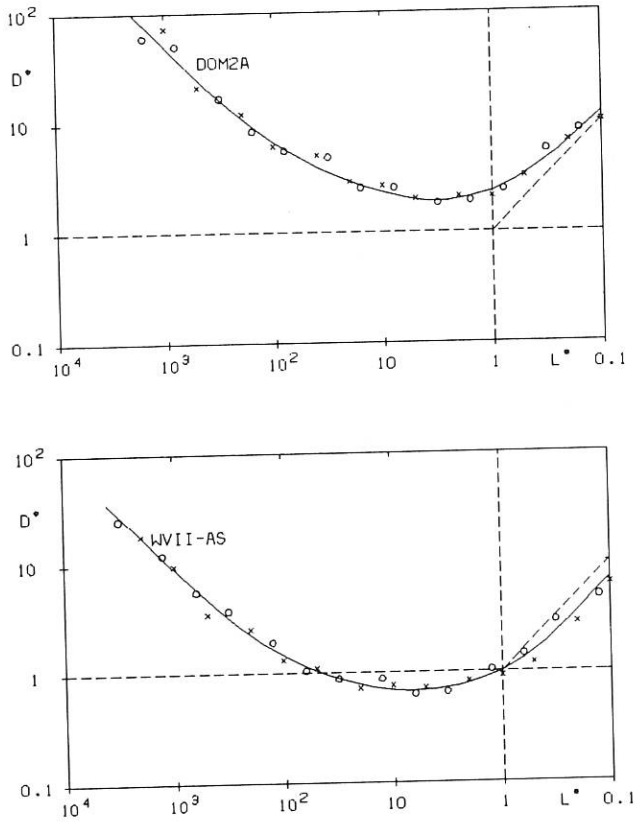

Fig.15: Normalized transport coefficients D^* as functions of normalized mean free path L^* in an $\ell = 2$ stellarator and in the W VII-AS vacuum field. ○ MC-simulation in Cartesian coordinates, × in magnetic coordinates.

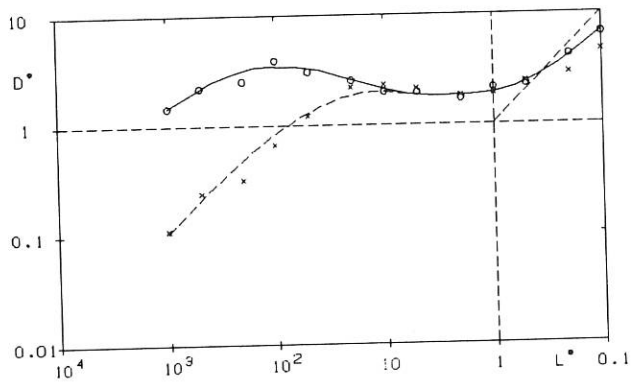

Fig.16: Transport coefficients as functions of mean free path for the $\ell = 2$ stellarator case of Fig.15a without electric potential (○), so that a loss cone develops at large mean free paths, and with an electric potential (×) of $-5E_{kin}$ and, accordingly, without collisionless losses.

1) G. Kuo-Petravic, A.H. Boozer, J.A. Rome, R.H. Fowler, J.Comp.Phys.**51** (1983) 261

2) R.H. Fowler, J.A. Rome, IAEA, London 1984

Part B:
Divisions and Groups

THE SCIENTIFIC DIVISIONS OF IPP

Experimental Plasma Physics Division 1

Director Dr. M. Kaufmann

ASDEX Upgrade
- construction of a follow-up to the ASDEX experiment for investigating the NET divertor and a reactor-relevant plasma boundary

JET diagnostics and pellet injection
- development and construction of diagnostics and pellet injection for JET and IPP

Tokamak physics
(In 1985 this work will be performed in Theory Division 3.)
- experiment-oriented theoretical work for interpreting and designing tokamak experiments such as ASDEX, ASDEX Upgrade, JET and NET

Experimental Plasma Physics Division 2 (Stellarators)

Director: Dr. G. Grieger

Wendelstein VII-A
- toroidal plasma confinement in the stellarator
- net-current-free plasmas, plasma production and heating by neutral injection, high-frequency and ohmic heating
- plasma stability and impurity effects

Wendelstein VII-AS (Advanced Stellarator)
- construction and operation of a stellarator with improved confinement conditions

Wendelstein VII-X
- preliminary investigations

Contributions to stellarator reactor systems studies

Contributions to NET studies

Technology Division

Director: Dipl.-Ing. K.H. Schmitter

Neutral Injection
- development and construction of the injection systems for W VII-AS and ASDEX
- implementation of injection experiments

Lower hybrid heating
- preparation and implementation of LH heating and current drive experiments

Ion cyclotron resonance heating
- preparation and implementaiton of ICRH experiments

Contributions to INTOR studies

Studies of reactor systems

Experimental Plasma Physics Division 3 (ASDEX)

Director: Dr. G. von Gierke

ASDEX
- tokamak experiment with axisymmetric divertor at ion temperatures in the keV range
- energy confinement with auxiliary heating
- beta, density, and q-limits
- current drive with lower hybrid waves
- comparative studies of heating methods: neutral injection and HF waves at the ion cyclotron and lower hybrid frequencies
- pellet injection: refuelling and plasma profile shaping

Theory Division 1

Director: Prof. D. Pfirsch

Theoretical basis of plasma physics
- toroidal plasma equilibria
- anomalous transport
- macroinstabilities and microinstabilities
- plasma turbulence
- multi-fluid codes
- high-frequency current drive

Theory Division 2

Director: Prof. A. Schlüter

Stellarator physics
- numerical methods of investigating equilibrium, stability and transport in three-dimensional toroidal configurations

Surface Physics Division

Director: Prof. D. Pfirsch (provisional)

Plasma-wall interaction
- interactions of ions and electrons with solid surfaces
- wall fluxes in the boundary layer of plasma devices
- limiter and wall analyses

Computer Science Division

Director: Prof. F. Hertweck

Development of the AMOS/2 operating system

Development of data acquisition sytems for experiments at IPP

EXPERIMENTAL PLASMA PHYSICS DIVISION 1

(Dr. M. Kaufmann)

Division E1 comprises three groups:

1. JET DIAGNOSTICS AND PELLET INJECTION (JDP)

Head: C. Andelfinger

Deputy Head: H. Röhr

Team: E. Buchelt, K. Büchl, C. Dorn A. El-Sharnouby[1], H.U. Fahrbach, J. Fink, K. Follmer, H. Frischmuth, K. Hilber, D. Jacobi, H. Krause[2], F. Mast[2], E. Oberlander, D. Pohl, G. Prausner, G. Rupprecht, M. Salvat, W. Sandmann, H.B. Schilling, G. Schramm, U. Schumacher, J. Sommer, A. Stimmelmayr, M. Ulrich, G. Weber, H. Weichselgartner, D. Zasche

This group is responsible for designing and producing plasma diagnostics and pellet injectors for JET and is also involved in a Task Agreement on the investigation of impurities in the JET plasma. These activities are detailed under the JET Cooperation Project. Other work is concerned with the development and operation of pellet injectors for ASDEX and W VII-A.

2. ASDEX Upgrade

Head: W. Köppendörfer

Deputy Head: M. Blaumoser

Team: S. Cha, K. Ennen, T. Grave, O. Jandl, H. Kollotzek, H. Kotzlowski, E. Lackner, V. Mertens, M. Pillsticker, R. Pöhlchen, H. Preis, U. Seidel, B. Streibl, M. Troppmann, H. Vernickel, F. Werner, A. Wieczorek

This group is concerned with the construction for the follow-up experiment to ASDEX. This work is described under the ASDEX Upgrade project.

3. TOKAMAK PHYSICS

Head: K. Lackner

Deputy Head: J. Neuhauser

Team: B.J. Braams[1], R. Chodura, W. Feneberg, O. Gruber, W. Jilge, L. Lengyel, P. Martin, K.G. Rauh, W. Schneider, R. Wunderlich, H.P. Zehrfeld

Most of the activities of the Tokamak Physics Group are in the form of directly project-oriented work and are therefore described in the respective section of this report. In particular, this concerns the plasma scrape-off layer and divertor physics modelling (ASDEX project), high-ß configuration studies and models for the dynamics of axisymmetrically unstable plasmas (ASDEX Upgrade), modelling of ergodized field regions in tokamak boundary layers, and development of impurity transport code packages (JET) and studies of the need for and of the technical requirements of pellet injection in fusion devices (NET/INTOR). Only those investigations not yet specifically relating to a single device (or carried out under a specific contract) are described in the following section.

3.1 Tokamak Equilibrium Studies

The achievement of high-$ß_p$ plasmas in ASDEX, the substantial input of angular momentum by powerful neutral injection, and the pronounced elongated shape of the flux surfaces in ASDEX Upgrade have motivated new studies of axisymmetric equilibria.

---

1 Guest, Nuclear Research Centre, Cairo, Egypt
2 presently assigned to JET

1 FOM, Nieuwegein, The Netherlands

One purpose of these was to derive relations between externally measured magnetic signals and macroscopic plasma parameters (such as position, shape and magnetic and thermal energy content) for more complex situations in which the usual expressions of Shafranov are quantitatively unsatisfactory. This effort has demonstrated to us the potential of the method of principal component analysis and function parametrization, which we plan to expand in the future to exploit also information from other diagnostics. As this method, in the preparatory step, involves extensive equilibrium calculations, we have also further optimized our respective algorithms.

The requirements and expected operating conditions of ASDEX Upgrade also call for a refined description of plasma dynamics during feedback control of the intrinsic axisymmetric instability, in order to check the conclusions of the simplified models used in the design of the control system. The development of such a code as well as configuration studies assessing the capability of ASDEX Upgrade to implement alternative high-ß stable plasma shapes are reported in the ASDEX Upgrade section. Neutral injection heated tokamaks are also expected to store significant energy in the form of macroscopic rotation, requiring for device-oriented studies the development of a corresponding free-boundary equilibrium code like that described in the same section.

3.1.1 Interpretation of tokamak diagnostics by function parametrization

Commonly, measurements made in the course of an experiment do not immediately correspond to the physical parameters to be determined but require for their interpretation a complicated, multidimensional parameter fitting procedure. In these cases, the real-time interpretation of the data and their possible use for feedback control have so far been excluded by the complexity of the required analysis.

A technique, originally developed by H. Wind (CERN) for the interpretation of spark chamber data, aims at the derivation of some relatively simple functional representation for the relation between experimental data and physical parameters. This representation, which gives the estimated physical parameters as an explicit function of the measurements, is found by analysis of a large data set of simulated experiments. Statistical methods for dimension reduction and multiple regression are involved. A substantial effort may be involved in generating and analyzing the data base, but is justified when the data interpretation is required many times for the same experimental set-up. As first use of this technique in fusion research we applied it to the interpretation of axisymmetric magnetic signals in ASDEX. The plasma parameters to be determined are: position of the magnetic and geometric axis; radius, area and elongation of the plasma column, position of the saddle-point; intersection point of the separatrix with the divertor plates; normalized safety factor, and $ß_p + l_i/2$. The diagnostics used are: 4 magnetic flux and 4 magnetic field measurements in a poloidal plane, the total plasma current, and the multipole current. The derivation of the desired functional relations proceeded in three steps.

(1) A data base was generated with the Garching equilibrium code covering the ASDEX operating regime, containing simulated data for nearly 6000 different experimental situations. Using a CRAY-optimized code version (see below), these calculations were carried out at a total expense of only 35 min of CPU time.

(2) The number of independent variables was reduced by a principal component analysis, the original diagnostic signals being replaced by a set of (at present) 6 linear combinations.

(3) A functional relation between the above-mentioned plasma parameters and these principal components was derived by performing a multiple regression analysis on a second-order polynomial model in the principal components.

Mean errors of the plasma parameters, as determined with these functions, were calculated by means of a test data base. Depending on the specific parameter, these errors vary between 0.04 % and 1.5 %, which is a very promising result. Now, in a real experimental situation, only two short calculations are involved in the determination of plasma parameters: (1) transformation of the magnetic measurements into their principal components and (2) evaluation of the above-mentioned simple functional relations, which could both be performed in real time.

On the basis of this experience, we expect function parametrization to become a powerful tool in tokamak interpretation, in particular when signals of different diagnostic systems are combined.

3.1.2 Finite element methods for fixed boundary MHD flow equilibria in tokamaks

(In cooperation with R. Gruber, R. Iacono and S. Semenzato, C.R.P.P. Lausanne)

The MHD equations which describe a stationary equilibrium in axisymmetric geometry lead to a quasilinear partial differential equation for the poloidal magnetic flux and one nonlinear and three linear algebraic equations for the mass density, poloidal current and two tangential velocity components. These equations are solved numerically by a continuation method, a Picard iteration and finite element approaches using conforming and nonconforming (hybrid) finite elements. The nodal points are redistributed iteratively so that they fall on initially prescribed constant flux surfaces. For different coordinate systems the different finite element approaches are applied to a static case and compared. The influence of flow is shown by applying the CLIO fixed boundary code to a particular plasma configuration (PDX tokamak).

3.1.3 CRAY optimization of numerical algorithms for equilibrium calculations

Re-consideration of some numerical algorithms required for the calculation of two-dimensional MHD equilibria with respect to their effective use on the CRAY-1 computer has led to a considerable reduction of the corresponding CPU time requirements. The Garching Buneman solver (in its first form developed by v.Hagenow) which is used in form of a flux computing routine was re-written and now requires for the evaluation of a 64 x 64 grid about 11 ms (originally (on the CRAY) 50 ms). This progress was made

possible by extensive use of vectorizing techniques and application of CRAY-specific routines such as ISRCH, FOLR and others. By extenting this technique to other routines of the Garching equilibrium code the CPU time for its execution could be reduced from originally 3.5 s on the CRAY to the present 500 ms (standard version; 64 x 64 grid).

Fast two-dimensional spline and flux surface averaging routines are under investigation for calculating free boundary flow equilibria and time-dependent ideal MHD equilibria. Here the devlopment of vectorized procedures for the solution of systems of ordinary differential equations and of tridiagonal systems of linear equations has also led to a remarkable decrease in CPU time (factors of 3 - 20 relative to conventional adaptations).

3.2 Plasma Boundary Physics

(Edge modelling studies directly related to ASDEX and ASDEX Upgrade are described in the respective sections.)

3.2.1 A 2D edge plasma transport code

The earlier two-dimensional edge plasma code (see Annual Report 1983) was improved in various points: inclusion of viscous heating in the ion energy equation, a corrected treatment of the electron-ion thermal coupling, a more satisfactory recycling model, a change to toroidal geometry, and improved graphical output. The code was applied for the planned parameters of a Princeton Tokamak Fusion Core Experiment (with C.E. Singer) and indicated that a limiter configuration may be viable for a reactor, provided one can attain a sufficiently high separatrix density ($n_i \sim 10^{20}/m^3$ and sufficiently strong radial energy transport ($\chi_e \sim 5\ m^2/s$). The same code was used, together with members of the Culham Laboratory Exhaust Physics Group, for modelling of the INTOR divertor. The numerical methods used in the code were written up.

3.2.2 Structure of ergodic fields near material walls

Starting from the field line mapping of Taylor and Martin[1] we studied specific questions arising in a real tokamak with ergodizing external coils. The mapping was extended to allow for two separate diffusor coils with different poloidal extent and mode number and an arbitrary q-profile. A random field line wandering with prescribed average displacement can be superimposed as a rough representation of inherent ergodicity (fluctuations) or of particle diffusion, if the field lines are interpreted as guiding-centre particle orbits. Besides affording a general overview of ergodic structures, this model is used to study, for a specific geometry, the degree of ordering of field lines near the wall, the length of field lines between successive limiter or wall intersections and the competition with anomalous diffusion of the order of that observed in experiments. Clear deviations from the usual view of ergodically enhanced transport are to be expected near the limiter radius and in the geometric limiter shadow, since the field line length between material intersections becomes small and the ergodization becomes irrelevant for a plasma attached to those lines.

[1] T.J. Martin, J.B. Taylor, Plasma Phys. Contr. Fusion 26, 321 (1984)

EXPERIMENTAL PLASMA PHYSICS DIVISION 2 (Stellarators)

(Dr. Günter Grieger)

IPP acitvity in the field of Stellarator physics is mainly done in Division 2 and Theory Division 2 (see there).

The relevant teams are:

1. W VII-A
   G. Cattanei, D. Dorst, A. Elsner, V. Erckmann, G. Grieger, P. Grigull, H. Hacker, H.J. Hartfuß, H. Jäckel, R. Jaenicke, J. Junker, M. Kick, H. Kroiss, K. Krusch, G. Kühner, H. Maaßberg, C. Mahn, S. Marlier, G. Müller, W. Ohlendorf, F. Rau, H. Renner, H. Ringler, F. Sardei, M. Tutter, A. Weller, H. Wobig, A. Wootton [1], E. Würsching, M. Zippe.

2. W VII-AS
   U. Brossmann[2], F. Kerl[2], J. Kisslinger, T.v.Larcher[2], R. Mathis[2], H. Münch, J. Sapper, I. Schoenewolf

3. W VII-X
   E. Harmeyer, J. Kisslinger, H. Maassberg, F. Rau, H. Wobig.

The contributions of these teams are described in Part A of this Report in the sections on W VII-A, W VII-AS and W VII-X.

---

1) Oak Ridge National Laboratory
2) Central Technical Services

EXPERIMENTAL PLASMA PHYSICS DIVISION 3 (ASDEX)

(Dr. Gerhart von Gierke)

Experimental Plasma Physics Division 3 comprises the ASDEX group, the work of which is fully reported in the section "ASDEX Project". The members of this group are as follows:

Head: M. Keilhacker
Deputy Head: H. Niedermeyer

Team: G. Becker, K. Bernhardi, H.-S. Bosch, H. Brocken, A. Eberhagen, U. Ditte, G. Fussmann, O. Gehre, J. Gernhardt, G. v. Gierke, E. Glock, M. Hesse[1], G. Haas, G. Herppich, H. Hohenöcker, G. Janeschitz, A. Izvozchikov[2], F. Karger, S. Kissel[3], O. Klüber, M. Kornherr, P. Kotzé[4], M. Lenoci[5], G. Lisitano, H.M. Mayer, K. McCormick, D. Meisel, E.R. Müller, H. Murmann, N. Ruhs, F. Ryter[1], H. Rapp, F. Schneider, G. Siller, P. Smeulders, F. Söldner, K.H. Steuer, Z. Szymanski[6], D. Zimmermann, G. Vlases[7], F. Wagner.

---

[1] CEN Grenoble, France
[2] Academy of Sciences, Leningrad, USSR
[3] now JET Joint Undertaking, England
[4] Nuclear Development Corp. of South Africa, Pretoria
[5] Frascati, Italy
[6] Institute of Fundamental Technological Research, Warsaw, Poland
[7] University of Washington, USA

THEORY DIVISION 1

(Prof. Dr. Dieter Pfirsch)

The work of Theory Division 1 covers a number of topics of relevance in fusion-oriented plasma physics, such as resistive magnetohydrodynamics and ß-limits, drift wave turbulence and anomalous transport, and HF heating and current drive. In addition, further fundamental problems are being treated: energy-conserving drift kinetic theories, turbulence and chaotic motions. Certain problems can only be solved by means of big computer codes, and the development of new codes for three-dimensional nonlinear problems in resistive magnetohydrodynamics and for non-Hermitian eigenvalue problems represents at present one of the major activities. These codes should allow disruptions and the problem of ß-limits in tokamaks to be investigated in a more realistic way than has been possible up to now. In particular, the analytic result that the so-called second linear stability regime does not exist, because there are resistive ballooning and interchange modes,could be tested on the basis of the full set of the nonlinear equations. This would also provide an answer to the question whether these instabilities are serious or not.

1. MHD THEORY

1.1. Semi-implicit Method of MHD Simulation

A semi-implicit method of solving the full compressible MHD equations in three dimensions was developed. The MHD equations are written in difference form, the usual predictor-corrector method being used for the integration in time. A term of the same form as the fast compressible modes, but with a constant coefficient A, is then subtracted from both sides of the corrector equation for the velocity. The additional term on the r.h.s. is treated explicitly at the old time, and that on the l.h.s. implicitly at the new time. With sufficiently large A, the method is unconditionally stable with respect to the fast, compressible modes. The time step is only limited by the slower shear Alfvén dynamics. The numerical stability limits were derived and computationally verified. The computing time required for a time step is comparable with that for explicit methods. On the basis of this method D. Harned developed a code for MHD simulation in cylindrical geometry. A comparison of the stability limits and growth rates of tearing modes with Lerbinger's resistive eigenvalue code yielded very good agreement for time steps exceeding the usual Courant-Friedrichs-Lewy condition by a factor of 200. The nonlinear development of perturbations was also investigated, good agreement with results of Biskamp and Welter being obtained. (D.S. Harned [+], W. Kerner, E. Schwarz)

1.2. 3D Nonlinear MHD Simulation in Toroidal Geometry

Development started on a code for solving the full compressible and resistive MHD equations. Modified cylindrical coordinates x, z, ϕ are used, these being much simpler than Hamada-like coordinates adapted to an initial equilibrium. All quantities are expanded in a Fourier series with respect to the toroidal angle ϕ. A predictor-corrector method is used for time discretization. As Harned and Kerner's semi-implicit method is implemented, the limitation of the time step is governed by the shear Alfvén wave and not by the fast compression wave. The corresponding implicit velocity equation in the corrector step is very efficiently solved by fast Fourier transform. In addition, two scalar elliptic equations for potentials have to be solved in each time step, this also being done by fast Fourier transform. The code is intended to describe the macroscopic dynamic behaviour of realistic plasma configurations, particularly near the ß-limit.
(W. Kerner, H. Welter and D. Biskamp)

[+] Courant Institute, New York

1.3. Calculation of Complex Eigenvalues

Non-ideal MHD theory generally involves complex eigenvalues. The complex eigenvalue problem $A \underline{x} = \lambda B \underline{x}$ was therefore treated with a general, non-Hermitian matrix A and a Hermitian, positive-definite matrix B and was solved by inverse vector iteration. The algorithm preserves the band structure of the matrices and, with external storage, requires just one complex matrix in the core storage. It is therefore possible to solve systems with very large dimension d, e.g. d = 3472, at a band width of b = 47. All complex eigenvalues for the resistive Alfvén spectrum were successively computed in the application. The algorithm is being partitioned into sub-problems with increased input/output on disc to develop a version in which the dimension of the matrices can be very much larger, e.g. d = 40,000.

The look-ahead Lanczos algorithm was implemented and successfully tested in collaboration with Prof. Parlett of the University of Berkeley. This method calculates several (approx. 50) eigenvalues simultaneously. (W. Kerner, K. Lerbinger, J. Steuerwald)

1.4. Spectral Code for Resistive MHD

The compressible, resistive MHD equations are linearized about an equilibrium in cylindrical geometry. The entire spectrum of normal modes is evaluated numerically by applying the Galerkin method in conjunction with finite elements, leading to a non-Hermitian matrix eigenvalue problem with complex eigenvalues. The entire spectrum is calculated with the QR algorithm for matrices of dimension up to d = 600. Much larger matrices, necessary for obtaining exact results, are treated with the I/O optimized eigenvalue solver based on inverse vector iteration (d = 3742).
The dependence of the current and pressure-driven instabilities on resistivity was studied. The growth rate of the internal kink mode becomes larger with resistivity for small beta equilibria (ß less than 2 %); it scales as $\eta^{1/3}$. For larger beta values the ideal MHD growth rate remains nearly unchanged.
Furthermore, the influence of resistivity has been studied on the ideal Alfvén and slow mode continua for tokamak-like equilibria with pressure and with resonant surfaces inside the plasma. For finite values of resistivity the continua are found to disappear. For small enough resistivity the eigenvalues lie on well-defined curves in the complex plane that are independent of resistivity. The structure with the corresponding branch points and the scaling of the damping of these modes depend on the ideal MHD dispersion relation, i.e. on the specific equilibrium. (K. Lerbinger)

1.5. Resistive Spectrum of Configurations without Magnetic Shear

The problem of determining the normal modes of a slightly resistive, incompressible plasma slab with unidirectional fields is reduced to quadratures. The eigenfrequencies are on a system of curves in the stable part of the complex plane which are independent of the resistivity η. For finite wave number the distance from the tip of the ideal Alfvén continuum of the nearest eigenvalue is $0\ (\eta^{1/3})$. The first correction to this is $0(1/|\ln \eta|)$, which thus only becomes small for unrealistically small values of η. Including this logarithmic correction yields quantitative agreement with numerical computations. (D. Lortz, G. Spies)

1.6. Localized Resistive MHD Modes

a) General results

A dispersion relation for the complex growth rate of resistive ballooning modes was derived that takes into account the effect of compressibility (known as the case of finite G in the literature). Contrary to former investigations, the normalized growth rate Q was not assumed to be small. Owing to this fact, this dispersion relation is suitable for investigating the stability properties near the ideal stability boundaries, where $Q \sim 1$.

Another result is the following: in order to determine the growth rates of resistive ballooning modes when $D_R < 0$ and $s > 1/2$ (D_R is the usual resistive interchange stability parameter and s is Mercier's exponent), the simple dispersion relation $\Delta' = \Delta(Q)$, where Δ' is obtained from the ideal marginal ballooning mode equations, does not hold. In this case, Δ' cannot be determined from the lowest-order ballooning mode equations alone (in an expansion with respect to small resistivity and inertia), it being necessary to include further terms in the inner expansion, up to terms of order ε^n, $n \leq (1+2s)/2$. As a consequence, Δ' also depends on Q, a fact which has not been considered before.

b) Application of the theory to a model of a tokamak

The investigation of localized resistive modes for self-consistent tokamak equilibria which have circular cross-sections near the magnetic axis was concluded. For these configurations, the ideal MHD ballooning mode theory predicts a second region of stability at high values of the poloidal beta, $ß_p$. These good stability properties at high $ß_p$ deteriorate in the presence of resistivity, which introduces both resistive interchange and resistive ballooning modes.

The stabilizing effect of $q > 1$ was investigated. This made it necessary to derive a new stability parameter Δ'.
Stability boundaries for resistive ballooning modes were computed (in the first ideally stable region) as a function of the mode number. These calculations were supplemented by computations of the growth rate as a function of $ß_p$.
(D. Correa-Restrepo)

1.7. Extrap Theory

Theoretical investigations of the Extrap experiment were performed under the contract with the Royal Institute of Technology, Stockholm. This experiment consists of a straight (or, in future, toroidal) Z-pinch immersed in an external octupole vacuum magnetic field. A typical mag-

netic field line pattern is sketched in Figure 1: The plasma (cross-hatched area) fills the whole

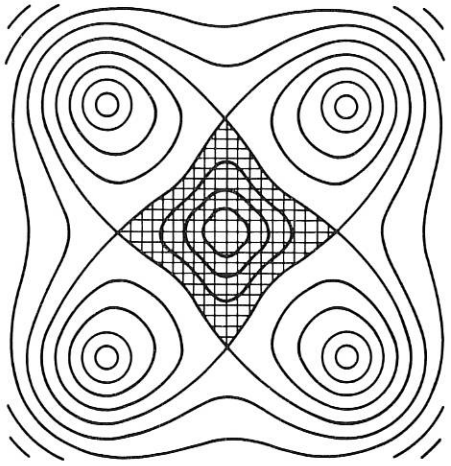

Figure 1: Magnetic field lines

interior of the square-like part of the separatrix; its current is opposite to the external currents. A typical feature is the presence of five magnetic stagnation points, viz. the axis and the four corners of the separatrix; most of the theory centres around these.

Experimentally, a stable plasma is observed as long as the ratio (plasma current/total external current) remains below a critical value of about 1/16. A firm theoretical explanation of this (which is the primary aim of the present studies, but which is still pending) involves constructing equilibrium states, determining how the configuration passes through a sequence of such states, and investigating their stability.

a) Equilibrium and its temporal evolution

Analytical investigations of Extrap suffer from two flaws: First, the one-dimensional model (circular cross-sections) is insufficient because it neglects the separatrix. For instance, the Bennet relation is totally different if the plasma boundary contains stagnation points, and the plasma current need not increase during adiabatic expansion towards the separatrix. Second, none of the known exact solutions of the two-dimensional Grad-Shafranov equation (with the exception of those with a pure surface current, which, however, are not suitable for describing transport) can be joined to the desired external vacuum field. Extrap equilibria must therefore be computed numerically as solutions of a free boundary problem. In collaboration with J. Scheffel (Royal Institute) and O. Ågren (University of Uppsala) a code is now being developed which uses Grad's method of alternating dimensions to compute such equilibria and their temporal evolution due to ionization, adiabatic changes of external parameters, or transport processes.

b) Stability

The observed stabilizing influence of the external currents is only partly explained by ideal magnetohydrodynamics: The circular Z-pinch (no external currents) is unstable to interchange modes near the plasma boundary, while for non-vanishing external currents these modes can be stabilized if the plasma boundary coincides with the separatrix. However, the ballooning modes are always unstable near the axis. We have shown that they are also unstable near the separatrix, i.e. that the stabilizing effect of good curvature is always dominated by the destabilizing effect of bad curvature near the stagnation points.

Since the unstable ideal modes are concentrated at the stagnation points, where the ideal theory is not valid, they should not be taken too seriously, and the observed stability must be explained by using some non-ideal theory. We have shown that the axis remains ballooning unstable for arbitrarily anisotropic pressures according to the guiding centre theory. This implies that large gyration radius effects must be invoked. As the simplest possibility, ballooning stability according to the Hall term model is being investigated in collaboration with M. Faghihi (Royal Institute). Ballooning stability near the axis is also being investigated within the more realistic Vlasov theory. As a crucial ingredient, we have developed an asymptotic orbit theory using a new adiabatic invariant which, unlike the magnetic moment, is uniformly valid, deviating from the latter only near the stagnation point. This line of studies is being continued by collaborators of E. Karlsson (University of Uppsala). (G. Spies)

2. DRIFT WAVES

2.1. Drift Wave Turbulence in Sheared Magnetic Fields

Small-scale density fluctuations appear to be ubiquitous in low-ß plasma discharges. They are generally associated with drift waves and believed to be directly or indirectly responsible for the anomalous transport processes observed. A numerical code had therefore previously been developed to study the nonlinear behaviour of drift waves in two and three dimensions. In contrast to similar numerical work performed elsewhere, magnetic shear, which is known to have a strong influence on linear drift mode properties, is taken into account explicitly. The code solves the simplest set of fluid equations for potential and parallel ion flow, assuming some phenomenological excitation coefficients. The major results obtained thus far are as follows:

a) Turbulence energy spectra W_k have a universal shape, rather independently of the particular choice of the excitation coefficients, i.e. the type of drift instability. There is a maximum of W_k at $k\rho \simeq \sqrt{L_n/L_s}$, a power law behaviour for higher k, $W_k \propto k^{-\nu}$, $\nu \simeq 3$, and a weaker decay for low k. These results agree well with recent experimental observations in TEXT and TFR.

b) Turbulent, i.e. strongly nonlinear drift waves are fundamentally different from their linear counterparts. Most importantly, the shear damping, an essential property of linear drift modes, is strongly reduced nonlinearly. As a consequence, finite turbulence levels exist without any apparent damping for parameters where all modes are linearily damped. Hence theories of drift wave turbulence relying on these properties of linear drift modes are restricted to relatively low turbulence levels. (D. Biskamp, M. Walter)

2.2. Three-drift-wave Interaction at Finite $k_{\parallel}$

In a sheared magnetic field drift waves have finite $k_{\parallel}$ almost everywhere. It is therefore interesting to generalize the work of Terry and Horton, which investigates the coupling of a triple of drift modes $\vec{k}_1 + \vec{k}_2 + \vec{k}_3 = 0$ at $k_{\parallel} = 0$, to finite $k_{\parallel}$. As it turns out, this effect considerably modifies the results of Terry and Horton.

a) While for $k_{\parallel}L_n \ll 1$ the turbulent amplitudes reach very large values, $e\phi/T_e \gg \rho_s/L_n$, finite $k_{\parallel} \sim 1/L_n$, which is typically satisfied for drift modes in a sheared magnetic field, leads to much lower turbulence levels, $e\phi/T_e \sim \rho_s/L_n$, as is also expected from general arguments.

b) The present model exhibits interesting bifurcation behaviour. Transition to chaos proceeds in precisely the manner postulated on general grounds by Ruelle and Takens, i.e. by the sequence stationary solution → periodic solution → doubly periodic solution → chaos. This behaviour is in strong contrast to the $k_{\parallel} = 0$ model by Terry and Horton. Since the transition occurs at very small $k_{\parallel}L_n$, the latter model must be considered as being rather singular. (D. Biskamp, He Kaifen[+])

3. PLASMA HEATING AND CURRENT DRIVE WITH LH WAVES

3.1. LH Waves in the Presence of Ponderomotive Density Fluctuations

We consider a uniform Cartesian plasma half-space in a B_{oz}-field which is accessible to a y-independent monochromatic LH wave launched at the $x = 0$ surface with a given k_z-spectrum (the Brambilla spectrum). The nonlinear steady-state 2D equation for the amplitude $E_z(\vec{r})$ of such a wave, including the ponderomotive density changes, has been analytically solved in the electrostatic, nondispersive, nondissipative "radiation" limit far from linear mode conversion. "Radiation" limit is used in the sense of inverse scattering theory to indicate absence of solitary waves in a low-amplitude field. Our model is thus complementary to that of CFF Karney et al., (Phys. Fluids 22 (1979) 940). Since thermal dispersion is neglected, there is a discontinuity surface for the electric field of the LH wave, and nonlinear LH-wave propagation can only be described in the region of space between the $x = 0$ boundary and such a discontinuity surface. An integration procedure derived from the Riemann method (or, in one case, separation of variables) is used to find solutions which reduce to the linearized ones when the small parameter $\gamma \propto |E_z|^2$ characterizing the ponderomotive effect vanishes. The linearized solutions are supposed to have lost their resonance-cone behaviour (in contrast to what is assumed in previous studies (E. Canobbio and R. Croci, IAEA Fusion Conf., London (1984), paper F-III-5)) and to permeate the whole plasma volume enclosed by the $\omega_p^2 = \omega^2$ cutoff surface. In the experiments, both direct absorption and linear mode conversion are indeed absent, so that at each point within the cutoff surface there will be superposition of guided modes going right and left along z and having the $\vec{k}$-values of the admitted Brambilla spectrum. It should be noted that guided modes confined within the cutoff surface do not imply vanishing power flux from the antenna. (E. Canobbio, R. Croci)

3.2. Ponderomotive Decay of a LH Two-wave Pump in a Torus

From the results mentioned under the previous heading we have shown that the nature and strength of the nonlinearity strongly depend on the kind and number of superposed modes. If there was one single travelling wave or two waves travelling along (across) $\vec{B}_o$ with equal amplitude and equal $k_z(k_x)$, but with opposite k_x's (k_z's), the solution would be periodic in space and the ratio of two successive $\vec{k}$-harmonics of the E-field amplitude would only be of order γ. Our main finding is that the nonlinear effects are strong when the LH pump consists of at least two waves travelling through the same region of space with parallel and/or antiparallel $\vec{k}$-vectors. The structure of the ponderomotive density change term is such that, in the case of a two-line k_z-spectrum, at least two LH waves with the same frequency as the pump interact resonantly with the two constituents of the pump. Even if the amplitude of the waves is small, the nonlinearity sufficiently deep in the plasma half-space is always strong because the effect is secular in space. Let the pump be expressed as $E_o/\bar{E} = \exp i(k_z z - k_x x) + a/\exp i K(k_z z - k_x x)$. The decay terms E_n $(n = 1,2,\ldots)$ are proportional to $(a\gamma k_x x \bar{E}^2)^n$, which exhibits the secular x-dependence. E_n contains the "harmonic" $(1+n(1+K))$ of the first term of the pump and the "harmonic" $(1+n(1+K^{-1}))$ of the second term of the pump.

In the case of a nondirectional antenna one has to set $K = a = 1$. It can be seen that $K \cong 1$ even in the case of a directional antenna. Indeed the parts of the Brambilla spectrum external to a certain $|k_z| = A$ value are absorbed by the particles on a single transit through the plasma and produce a weak current which can be in the "wrong" direction. The parts of the admitted spectrum which are well within $|k_z| = A$ are not directly absorbed and fill up the accessible plasma volume with a sufficiently high reactive power to produce a substantial nonlinear effect and the observed current. (E. Canobbio, R. Croci)

[+] Normal University of Peking

3.3. Production of Fast Particle Tails

The time average of the power absorbed by the electrons (ions) per unit volume $P_e(P_i)$ is the sum over the harmonics of the original $\vec{k}$-spectrum of the quasilinear expressions for electron Landau damping (Karney's stochastic ion heating). An interpolation of the expressions for the collision-dominated (linear) and HF-dominated (nonlinear) regime is used. The quantity $|E_z(\vec{r})|^2$ is simply related to the time mean value of the reactive electric energy per unit time, and to W, the time mean value of the HF power injected into the plasma. The injected waves are assumed to remain trapped in the plasma torus until $|E_1|, |E_2|, |E_3| \ldots$ become large enough to allow total power absorption: $W = V\,(P_e+P_i)$, where V is the plasma volume. However, there is an obvious upper bound to the absorbed power given by the nonlinear expression of (P_e+P_i). For plasma and HF parameters typical of LH heating and current drive experiments we have found that total power absorption implies an average $|E|^2$ value which is a fraction (0.03 to 1) of the value one would have in the resonance cone. It should be stressed that even in the case of directional antennae there are $\vec{k}$-harmonics corresponding to waves propagating in the "wrong" toroidal direction, thus creating fast tails opposite to the main electron drift (J. Stevens et al., 5th Topical APS Conf. on Radio Frequency Plasma Heating, Madison, Wisconsin (1983), paper B-L3).

The experimental observation of a density cutoff for current drive is related to the condition $P_i \cong P_e$.

Finally, wave propagation well inside the plasma is nonlinearly prevented when the discontinuity surface referred to before is located near the plasma surface. The maximum penetration depth l_o of a LH pump in the case of a nondirectional antenna is found to be $l_o \cong 1.89\ f\ (T_e+T_i)\ \varepsilon^2/N_z^2\phi$ where l_o is in m, f in GHz, T in keV, $\varepsilon \equiv 1 + \omega_{pe}^2/\omega_{ce}^2 - \omega_{pi}^2/\omega^2$, and ϕ is the HF power influx from the antenna in kW/cm^2. (E. Canobbio, R. Croci)

4. HAMILTONIAN DYNAMICS AND OTHER FORMAL DEVELOPMENTS

4.1. Investigation of Model Hamiltonians

In plasma physics Hamiltonian equations occur in the study of particle motion, wave propagation, magnetic surfaces, etc. If, apart from the Hamiltonian, $H(\underline{p},\underline{q},t)$, sufficiently many invariants $I(\underline{p},\underline{q},t)$ exist, H is called integrable, and the orbits in phase space or configuration space are smooth. In the opposite case H is non-integrable and the orbits are chaotic or turbulent.

The integrability of Hamiltonians of the type $H_L(\underline{P},\underline{Q}) = P_1 \cdot G_1(Q_1,Q_2) + P_2 \cdot G_2(Q_1,Q_2)$, $G_i = \omega_i + F_i(Q_1,Q_2)$, F_i 2π-periodic, $\langle F_i \rangle = 0$, $i = 1,2$ was investigated. This type occurs in Alfvén wave propagation.

Numerical results:
Poincaré surface-of-section plots for a variety of functions $F_i(Q_1,Q_2)$ show that H_L are, in general, integrable. For ω_1/ω_2 rational and div $\underline{F}(\underline{Q}) = 0$, $\underline{F} = (F_1,F_2)$, non-integrability may occur.

Analytical results:
For ω_1/ω_2 irrational there is always an invariant I of the type $I = P_1 \cdot J_1(Q_1,Q_2) + P_2 \cdot J_2(Q_1,Q_2)$, where J_i are doubly infinite Fourier series in Q_1,Q_2. They may be semiconvergent. For ω_1/ω_2 rational, however, they are useless owing to vanishing denominators. Nevertheless, other series J_i without vanishing denominators exist in this case, provided div $\underline{F} \neq 0$. The analytical results thus confirm the numerical ones in a particularly intriguing way.

In connection with the topics mentioned above it was investigated whether an important result obtained by Lewis [1] may be generalized. In [1] it was proved that the time-dependent oscillator Hamiltonian $H_{LL}(p,q,t) = p^2/2 + \Omega^2(t)q^2/2$ is integrable for arbitrary $\Omega(t)$. With a simple canonical transformation the invariant takes the form $I = P \cdot J(Q,t)$, $J = A_o(t) + A_2(t) \cos 2Q + B_2(t) \sin 2Q$, the same form as H_{LL} itself. – It has been shown that H_{LL} is a peculiar case: For all $H = P \cdot K(Q,t)$, where K contains more than two (complex) Fourier modes in Q, the invariant has infinitely many modes in general (provided it exists at all and is linear in P). (A. Salat)

4.2. Regularization of the Hamilton-Lagrange Guiding-centre Theories

The modern guiding-centre theories of Littlejohn, Wimmel, and Pfirsch can be derived from Lagrangians or Hamiltonians, and since Liouville's theorem is then valid, they allow useful kinetic equations to be constructed. However, in magnetic fields with a non-vanishing parallel component of their curl ($\underline{B} \cdot \mathrm{curl}\ \underline{B} \neq 0$) the drift velocity $\underline{v}$ and the acceleration $\dot{v}_{\parallel}$ then diverge on a hypersurface in phase space (at high values of $v_{\parallel}$). This leads to non-causal guiding-centre orbits, and particle conservation is violated. Without regularization this situation calls for the exclusion of all guiding-centre orbits intersecting (or being tangential to) the singular hypersurface. It is thus prohibited, for example, to use Maxwell distributions (in the equilibrium) or any other distribution function with arbitrarily high values of $v_{\parallel}$. The introduction of diffusion-like collision terms, e.g. a Fokker-Planck collision term, is also ruled out. It is attempted to eliminate this complication by regularizing the guiding-centre theories so that a singular hypersurface is no longer present. We seem to have found a useful regularization method, the details of which still have to be worked out. It is worth noting, moreover, that a similar phenomenon, viz. sudden breakdown of the gyromotion at a critical value of $v_{\parallel}$, also occurs in exact particle mechanics. This work is being continued. (H.K. Wimmel, D. Correa-Restrepo)

---

[1] H.R. Lewis, Jr., J. Math. Phys. 9 (1968) 1976.

4.3. Drift Kinetic Theory and Dirac's Hamiltonian Method

The new variational formalism for drift kinetic theories is based on a Hamiltonian description of the guiding-centre motion. Since the Lagrangian for this motion is of the non-standard type a certain limitation procedure was previously applied, starting with a standard type Lagrangian which allows a Hamiltonian to be constructed in the usual way. Dirac's method allows one to find a Hamiltonian without such a limitation procedure, and it was possible to arrive at the same drift kinetic theory as previously by means of this method. In general, however, Dirac's method can be rather inconvenient because of the occurrence of so-called primary, secondary and so on constraints. A new method has been developed which avoids these features and which allows Hamiltonians to be constructed in closed form in the general case. (D. Pfirsch)

4.4. Fluctuation Spectra in Nonhomogeneous Plasmas

A general formula for the fluctuation spectrum of nonhomogeneous plasmas and fluids in statistical equilibrium was derived. It is valid for linearized equations of conservative systems and uses a rigorous treatment within Gibbs statistics. Vlasov plasmas as well as macroscopic plasmas can, in principle, be handled in this way. Quantitative calculations should be possible in the 2-dimensional macroscopic case.
This method has been applied to the MHD equations including gyroviscosity. The main result is that gyroviscosity does not help to remove ultraviolet divergences. For a sub-class of observables (such as density fluctuation) it does not even show up. The full nonlinear problem may be needed.
(H. Tasso, I.L. Caldas [+])

4.5. Hamiltonian Formulation of Two-fluid Theory without and with Gyroviscosity

A variational principle for two-fluid plasmas was obtained by means of Clebsch variables. A Hamiltonian as well as canonical Poisson brackets are then defined.
On the other hand, gyroviscous MHD in two dimensions is shown to be a Hamiltonian field theory in terms of a noncanonical Poisson bracket. This bracket is of the Lie-Poisson type, but possesses an unfamiliar inner Lie algebra. Analysis of this algebra motivates a transformation allowing a Clebsch-like potential decomposition that makes Lagrangian and canonical Hamiltonian formulations possible. (P.J. Morrison [++], I.L. Caldas, H. Tasso)

4.6. Trapping in Turbulent Diffusion

The conventional statistical approach is based on the Hopf equation. Analytical solutions of this equation may lead to incorrect results, as can be shown by counter-examples allowing for trapping. A similar difficulty arises for stochastic shock waves. (P. Gräff)

4.7. Asymptotic Behavior of the Solutions of Certain Parabolic Equations

Some laws in physics describe the change of a flux and are represented by parabolic equations of the form

$$(*) \qquad \frac{\partial u}{\partial t} = \frac{\partial}{\partial x_j}\left(\eta \frac{\partial u}{\partial x_j} - v_j u \right), \quad j \leq m,$$

where η and v_j are functions of both space and time. We show under quite general assumptions that the solutions of equation (*) with homogeneous Dirichlet boundary conditions and initial condition $u(x,0) = u_o(x)$ satisfy

$$\| u \|_p \leq c(p)\, e^{-dt} \| u_o \|_p , \quad p = 2, \infty .$$

The decay rate $d > 0$ only depends on bounds for η, v and $G \subseteq \mathbb{R}^m$ the spatial domain, while the constant c depends additionally on which norm is considered. For the solutions of equation (*) with homogeneous Neumann boundary conditions and initial condition $u_o(x) \geq 0$ we derive bounds

$$d_1 u_1 \leq u(x,t) \leq d_2 u_2 ,$$

where d_i, $i = 1,2$, depend on bounds for η, v and G, and the u_i are bounds on the initial condition u_o.
(D. Lortz, R. Meyer-Spasche, E. Stredulinsky [+++])

[+] Universidade de Sao Paulo

[++] University of Texas, IFS Austin

[+++] University of Wisconsin, Madison

THEORY DIVISION 2
(Prof. A. Schlüter)

Theory Division 2 comprises the Stellarator Physics Group, the work of which is reported in the section "W VII-X Project".
The members of this group are W. Dommaschk, F. Herrnegger, W. Lotz, P. Merkel, J. Nührenberg, A. Schlüter, and U. Schwenn.

SURFACE PHYSICS DIVISION

(Acting Division Head: Prof. D. Pfirsch)

In order to understand and possibly control plasma-wall interaction in fusion experiments, it is necessary not only to investigate these phenomena in plasma machines but also to measure the different processes occurring on the first wall in separate experiments. These measurements concern plasma recycling like reflection, trapping, diffusion and re-emission of hydrogen and helium implanted into solids as well as erosion and surface changes of solids due to ion bombardment. The investigations were mainly performed with typical wall materials. Under the terms of a JET contract extensive measurements involving beryllium were made; the work on carbon and carbides and also on nickel, stainless steel and Inconel was continued and intensified. Limiter components of ASDEX and wall samples from JET were tested. Other major activities were again time-resolved measurements of wall fluxes and wall erosion in ASDEX and detailed investigations of wall and limiter samples from tokamaks, such as ASDEX, JET and UNITOR, the results of which are presented in the context of the respective projects. The scope of surface analysis was improved with respect to sensitivity and applicability to special problems.
In July/August the NATO Advanced Study Institute International Course of "PHYSICS OF PLASMA-WALL INTERACTION IN CONTROLLED FUSION" in Val Morin, Canada, was organized in collaboration with Dr. D. Post (Princeton).

Plasma Wall Interaction Group

Head: R. Behrisch; Deputy head: E. Taglauer
J. Appelt[1)], A. Bähr[2)], B. Baretzky[3)], J.Barth[4)], R.Becerra-Acevedo[2)], J. Berthold[4)], J. Bohdansky, P. Børgesen[4)], W. Eckstein, J. Ehrenberg[5)], W. Englert, G. Engelmann[2)], K. Ertl, W. Gries[6)], M. Hashmi, H. Liebl, R. Margraf[2)], A.P.Martinelli, W. Möller, E. Mühling[2)], D. Presinger[2)], W. Poschenrieder, J. Roth, B. Sawicka[7)], B.M.U. Scherzer, G. Staudenmaier, A. Turos[1)], P. Varga[8)], G. Venus, H. Verbeek, Y. Wang[9)], M. Wielunski[1)], Y. Yamamura[10)].

1) Guest, Institute of Nuclear Studies, Warsaw, Poland
2) Doctoral candidate
3) Undergraduate
4) Post doc
5) Assigned to JET since June 1984
6) Guest, National Physics Research Lab., Pretoria, South Africa
7) Guest, Institute of Nuclear Physics, Cracow, Poland
8) Humboldt Fellowship, Techn.Univ.of Vienna, Austria
9) Guest, Institute of Plasma Physics, Hefei, P.R. China
10) Guest Okayama Univ. of Science, Ridai-cho, Okayama, Japan

1. RECYCLING

The limited particle confinement in present plasma experiments causes all plasma particles to be recycled several times between the plasma and the wall during one discharge. The investigation of the different surface processes contributing to this recycling was continued.

1.1. Reflection of Light Ions

Advanced plasma sheath theories indicate a strong influence of the hydrogen reflection coefficient on the plasma parameters in the sheath and scrape-off layer. Up to now no measured, but only calculated (TRIM) data of such reflection coefficients exist in the relevant energy range below 1 keV. Experimental data at higher energy and the calculated data show that the reflection coefficient scales with an energy parameter ε. This scaling was confirmed by experimental results on Ti for energies down to 100 eV. In the energy range of 10 eV TRIM calculations have shown that the reflection coefficient is modified by the binding energy of hydrogen at the metal surface. In order to cover also this energy range with experimental data, devices have been constructed and first results have been obtained.

1.1.1 Total reflection coefficient of D^+ on Ti between 100 eV and 2 keV

Ti targets were bombarded by D^+ ions in the energy range from 100 eV to 2 keV. At temperatures between 20° C and 300° C Ti collects all implanted D up to high fluences (10^{20} particles) except those which are kinetically reflected. The reflection coefficient can therefore be measured from the weight change of the target if the weight loss by sputtering is taken into account. The oxide layer normally present on a Ti surface was removed by sputtering and by heating to temperatures of 250° C, where oxygen dissolves in Ti. Results for the backscattering coefficient measured are given in Fig. 1 and compared with calculated values.
(J. Bohdansky and J. Roth)

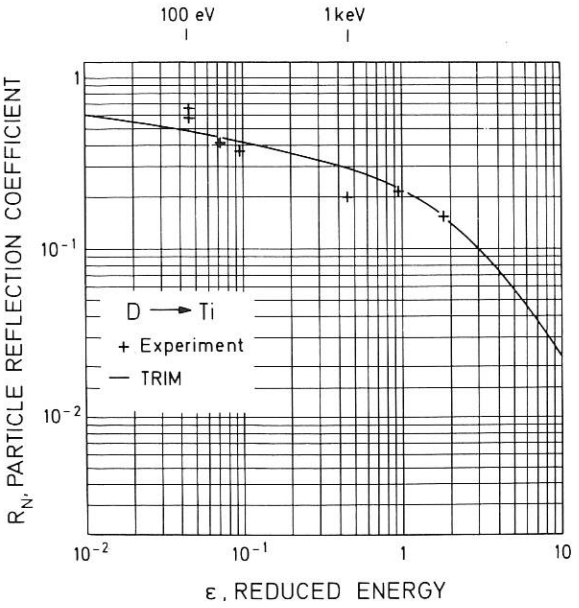

Fig. 1 Total particle reflection coefficients for D^+ on Ti versus ion energy and comparison with TRIM calculations; ε is the normalized energy according to Lindhard

1.1.2 Calculation of reflection data

The new TRIM version, TRSP1C, was used to calculate data on hydrogen reflection at energies down to 0.2 eV. Owing to the chemical binding of hydrogen to a surface, the particle and energy reflection coefficients of hydrogen decrease below a few eV (see Fig. 2). In addition, angular and energy distributions were calculated. The investigation covers all three hydrogen isotopes and C, Ni and W as targets. The calculated data do not take adsorbed hydrogen into account.
(W. Eckstein)

1.1.3 Reflection of H and D in the energy range of 10 to 1000 eV

Backscattering measurements were made with the low-energy hydrogen beam apparatus using positive and negative ions at energies down to 300 eV and neutrals down to 20 eV. The hydrogen atoms reflected as positive and negative ions from a nickel and an alkali-covered nickel surface show a decreasing

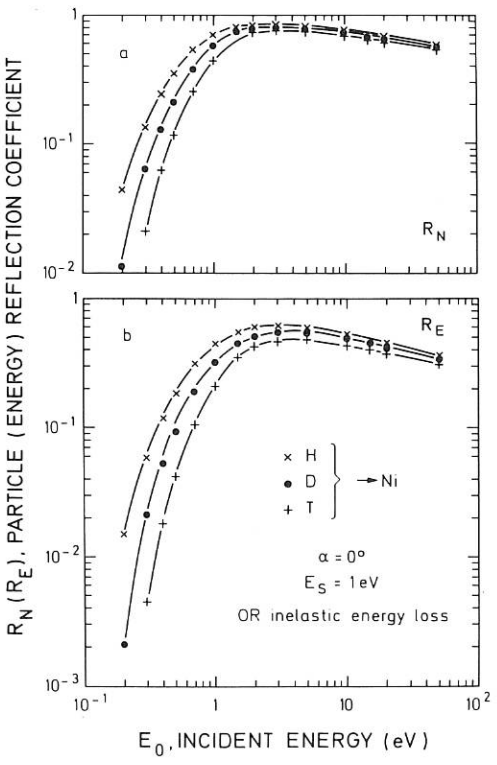

Fig. 2 Particle and energy reflection coefficient R_N and R_E versus the incident energy E_0. Ni is bombarded at normal incidence, $\alpha = 0°$, by the three hydrogen isotopes. A surface binding energy E_S = 1 eV is applied

width of the energy and the angular distributions and also of the charged fractions with decreasing incident energy.
(A. Bähr, H. Verbeek, W. Eckstein)

1.2 Re-Emission and Permeation

The re-emission of hydrogen implanted into the first wall is important for the particle balance in a fusion plasma. At temperatures well above RT the re-emission depends mainly on the recombination coefficient of hydrogen atoms to form molecules at the metal surface. The recombination coefficient and the importance of traps in hydrogen permeation was investigated experimentally for different temperatures. Analytical approximations for re-emission and permeation during temperature changes are derived which are useful for fusion reactor studies (INTOR, NET).

1.2.1 Re-emission from Ni bombarded with deuterium

The investigations on the re-emission of D_2-molecules after implantation in Ni metal were continued in the PHARAO accelerator for target temperatures of 200° C $\lesssim$ T $\lesssim$ 600° C. In this temperature regime, the recombination of D atoms on the Ni surface is the rate-limiting step of re-emission. It thus appears that above 200° C the time dependence of the re-emission is predominantly determined by the surface recombination rate coefficient K(T), which was evaluated from the experimental results in connection with computer models. The independent analysis of three different kinds of re-emission measurements (rise and decay of re-emission and reimplantation) generally leads to consistent results. These are in good agreement with those obtained in permeation measurements (see Sec. 1.2.2), but show a systematic deviation from existing theoretical calculations (Fig. 3).
(D. Presinger, P. Børgesen, W. Möller and B.M.U. Scherzer)

1.2.2 Permeation of implanted deuterium through Ni

The permeation of deuterons implanted with 2 - 22 keV into 25 µm thick cold-rolled Ni foils was studied at temperatures between 264 K and 600 K by collecting the permeating deuterium in a collector layer applied to the downstream side of the foils. The results show in comparison to theoretical calculations:
(i) a delayed permeation around RT due to the buildup of inventory at trapping sites throughout the foil. Traps, which probably originate from the cold work of the foils, are involved with binding energies 0.27 eV and 0.12 eV with atomic concentrations of 4×10^{-4} and 10^{-2}, respectively;
(ii) an enhanced permeation at high temperature since the outdiffusion through the upstream surface becomes limited by the surface recombination process. Surface recombination rate coefficients have been derived and found to be consistent with those obtained from re-emission measurements (see Sect. 1.2.1 and Fig. 3).
(P. Børgesen, B.M.U. Scherzer and W. Möller)

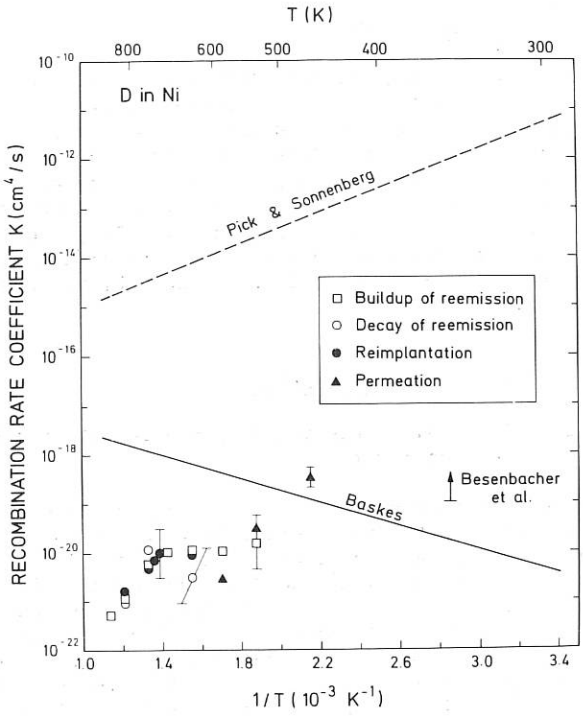

Fig. 3 Recombination rate coefficients as a function of inverse temperature; evaluation from re-emission and permeation measurements together with a lower limit obtained from desorption experiments (Besenbacher et al.). The curves indicate predictions of K versus T given by different models.

1.2.3. Gas re-emission and surface modification due to He implantation into Nb

Helium ions implanted into metals are completely trapped at damage sites up to a saturation concentration with a ratio of helium atoms to metal atoms close to one. Helium re-emission starts sharply when the saturation concentration is reached. It was shown that in niobium the onset of gas re-emission is accompanied by the appearance of surface blisters. This is in agreement with earlier results on Ni.
(B.M.U. Scherzer, P. Børgesen, J. Ehrenberg, W. Möller)

1.2.4 Analytical formulae for re-emission and permeation of hydrogen

Analytical approximation formulae are given for the concentration and the flux density of hydrogen diffusing through a plane metal slab. Concentration build-up during burn periods, degassing during dwell periods, steady-state solutions, permeation rates, etc. are described by formulae with characteristic parameters such as diffusion time, release time, SORET constant etc. Some of these parameters are of the type T^{-2}grad T in order to take into account the thermal load. The range of applicability of the formulae is tested by numerical calculations.
(F. Pohl, J. Bohdansky)

2. IMPURITY PRODUCTION

The impurity production during normal operation of tokamaks is mainly caused by energetic particle sputtering and ion-induced desorption. The investigations of both effects as well as surface composition changes were continued and the effort was concentrated on relevant materials such as Be (see section on JET), graphites, TiC, TiN, and Li-containing materials such as Cu/Li and Al/Li, where sputtering was expected to be reduced by Li segregation.

2.1 Sputtering of Graphite

2.1.1 Chemical sputtering of graphite with a metal surface layer

Graphite limiters are found to become covered by metal films after short operation. The amount of reduction of chemical sputtering by such films was measured for 500 eV H^+ and different metal films (Ni, Mo, Ti, Si) on a graphite target which was kept at 500° C (Ni) and 600° C (maximum of chemical sputtering). The results are plotted in Fig. 4 as a function of the metal yield normalized to the yield of pure metal. Each set of data for the different materials is obtained by sputtering through the metal film. The chemical erosion increases at a lower rate than the metal yield decreases. A linear superposition would be given by the dash-dotted line.
This reduction effect of chemical sputtering is not necessarily helpful for the impurity problem. The flux of carbon into the plasma is reduced but in addition metal enters the plasma.
(J. Roth, J. Bohdansky)

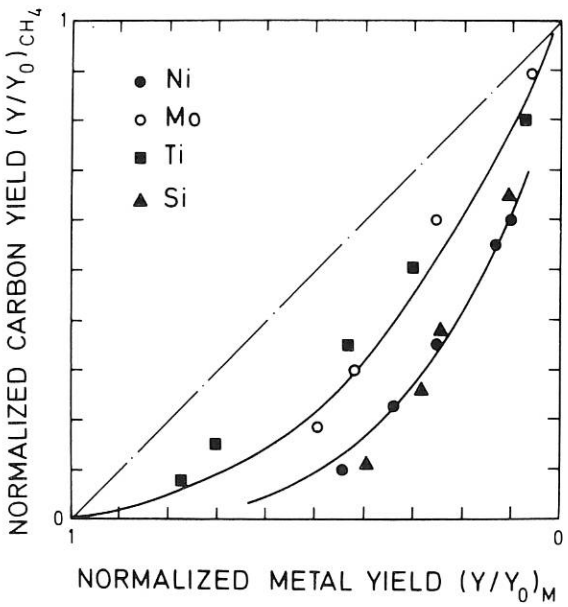

Fig. 4 Normalized carbon yield versus normalized metal yield for a metal film on a graphite target bombarded with 500 eV H^+ ions

2.1.2 Radiation enhanced sublimation of carbon above 1300 K

At temperatures above 1300 K, graphite shows a strong increase of the sputtering yield with increasing temperature which is proportional to the energy deposited into nuclear collisions in the surface layer. This enhancement of the sputtering yield can be described by a new model which was originally developed to explain the volume swelling of graphite under neutron bombardment, and which has now been modified for near-surface ion implantation. It assumes the formation of interstitial atoms and vacancies, which diffuse with different activation energies and recombine or annihilate according to various mechanisms. The flux of interstitials arriving at the surface is assumed to evaporate at the elevated temperature. The input data for the model calculations are taken from the literature. The calculated flux of interstitials through the surface is compared to experimental sputtering data in Fig. 5. The predictions of the model are found to be in good quantitative agreement with the experimental data. Both the temperature dependence and the scaling with ion mass is well reproduced. The results can be extrapolated to fusion-relevant conditions to predict the enhanced sputtering of carbon during low-energy

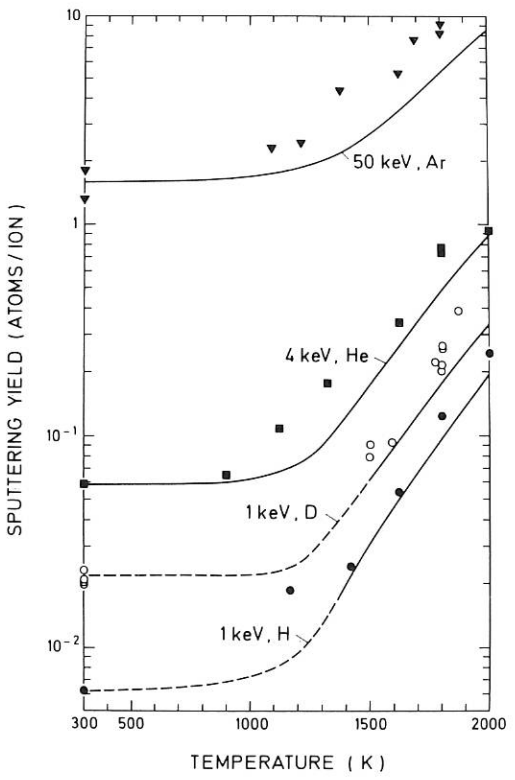

Fig. 5 Comparison of the temperature dependence of the measured erosion yield with the interstitial flux to the surface calculated by the present model. For the hydrogen isotopes the erosion peak due to chemical sputtering around 900 K has been omitted.

(10 to 1000 eV) deuterium and impurity ion bombardment. For deuterium fluxes and energies representative of limiter sputtering in JET an enhancement factor of 2 is obtained at 1800 K, while the self-sputtering yield is close to 1 at these temperatures.
(J. Roth, W. Möller)

2.2 Sputtering of Cu/Li and Al/Li Alloys

2.2.1 Sputtering yields

Cu/Li and Al/Li alloys have been proposed as materials with a low net erosion yield in magnetic fusion devices. Li segregates at elevated temperatures on the surface and should protect the bulk material from sputtering. In addition, Li is expected to be sputtered as ions, which would be deflected back to the surface by the magnetic field. First sputtering yield measurements of Cu/Li and Al/Li alloys with 500 eV D^+ at a current density of 10^{16} cm^{-2} s^{-1} using the weight loss method show no influence of the target temperature on the total yield, which was comparable with the yield of pure Cu or Al. With a negative bias voltage at the target no dependence on the voltage was found. It is concluded that at high ion fluxes the Li overlayer affords no significant protection, which is supported by ion desorption measurements (see Sec. 2.2.2).
(J. Bohdansky, J. Roth)

2.2.2 Ion desorption spectrometry (IDS) on a Cu/Li alloy

In order to know the surface composition of the Cu/Li alloy IDS experiments with a 5 keV Ar^+ beam at non-normal incidence were performed between 20° C and 430° C. From the behaviour of the binary collision peaks of sputtered Li and Cu we can derive the following results:
(i) At 430° C the total peak intensity of Li particles (Li^+,Li^0,Li^-) is greater than the total peak intensity at room temperature by a factor of 10 - 30 (depending on the scatter angle). This demonstrates the segregation of Li to the surface, especially above 200° C.
(ii) The number of sputtered neutral Li particles shows a dramatic increase with increasing temperature, i.e. with increasing Li coverage. At an exit angle ß = 60°, the positive charge fraction of sputtered Li particles decreases from 70 % at 24° C to 40 % at 430° C, while the neutral Li fraction increases at the same time from 30 % to 60 %. Negative Li was only observed at the highest temperatures, where negative charge fractions were below 1 %.
iii) The total peak intensity of Cu particles (i.e. the sum of Cu^+, Cu^0, Cu^-) sputtered in the binary collisions at the surface seems to be nearly independent of the Li coverage.
(H.J. Barth, E. Mühling, W. Eckstein)

2.3 Sputtering of Compounds

2.3.1 Change in surface composition of TiC and TiN coatings bombarded with H^+ and D^+

The changes in surface composition due to preferential sputtering by light ions (H^+ and D^+) was studied for compounds which are used for coatings in plasma machines, i.e. TiC and TiN. These coatings were formed by the CVD technique on graphite and Mo substrates. Bombardment with light ions results in the depletion of the lighter constituent into a certain depth T (see Fig. 6). The maximum concentration ratios and altered layer depths (given in units of Ar^+ fluence for sputter-profiling) for samples bombarded with 500 eV H^+ and samples exposed to the ASDEX divertor plasma are compared. The comparison shows that the C or N depletion can be very substantial to a depth equivalent to several hundred Angstroms. The ASDEX values are characteristic of a high fluence of low energy particles. Moreover, the high heat flux to the samples at the outer ASDEX divertor, which are exposed normally to the magnetic field lines, can cause damage, melting and disruptions at these coatings.
(E. Taglauer, P. Varga)

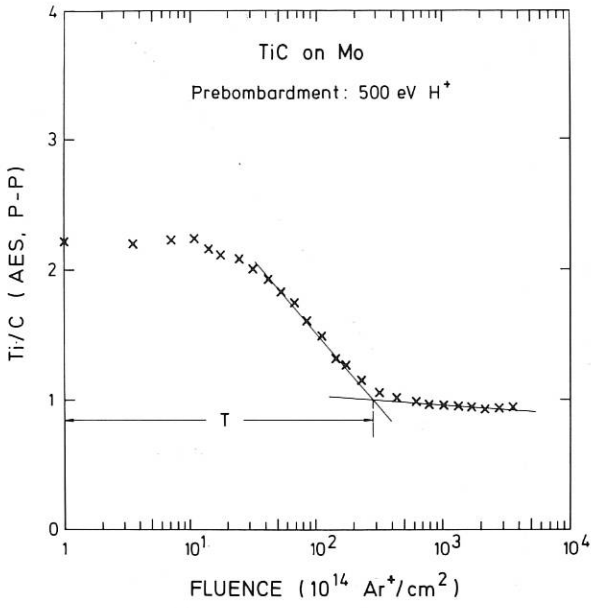

Fig. 6 AES depth profile (1 keV Ar^+) of a TiC layer on Mo with hydrogen prebombardment

2.3.2 Change in surface composition of Ta_2O_5 bombarded with He^+ at various angles of incidence

With the new ALI experimental facility surface compositions and depth profiles of Ta_2O_5 samples bombarded with 1.5 keV He^+ ions at different angles of incidence were measured by Auger electron spectroscopy. For more grazing incidence of the ion beam a significant decrease of the preferential sputtering effect is observed (Fig. 7).
(B. Baretzky, E. Taglauer)

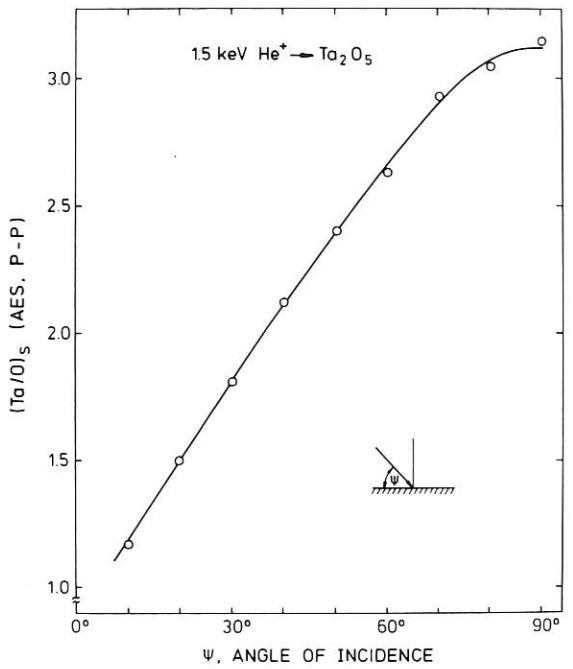

Fig. 7 Saturation values of the Ta/O Auger peak height ratio in the altered layer surface as a function of the angle of incidence

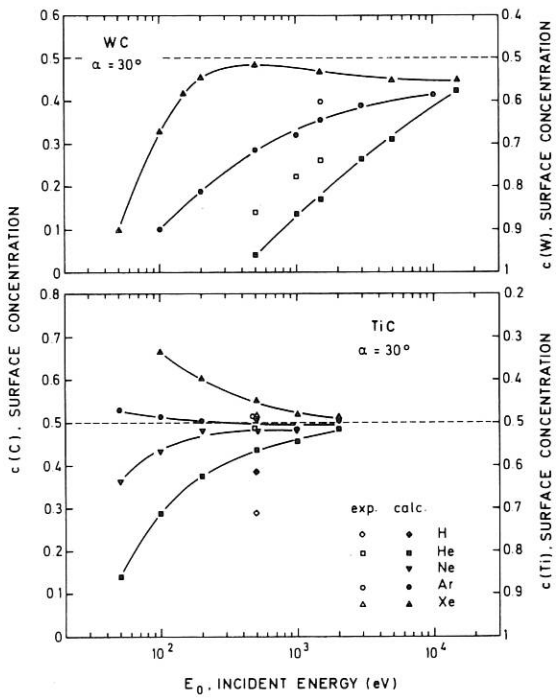

Fig. 8 Surface concentrations under steady-state conditions (stoichiometric sputtering) versus the incident energy E_0. WC and TiC are bombarded with H, ^{4}He, Ne, Ar and Xe at an angle of incidence $\alpha = 30^o$

2.3.3 Computer simulation of sputtering based on TRIM-SP

The TRIM-SP Monte Carlo program was extended to the sputtering of two-component targets. It was used to investigate preferential sputtering, partial sputtering yields, dependence of the yields on the angle of incidence, surface concentrations at low bombardment dose and in steady state, and sputtering of isotope mixtures. In addition, angular and energy distributions of the different sputtered target species were determined. Figure 8 shows the calculated surface concentrations in steady state for the bombardment of WC and TiC at an angle of incidence $\alpha = 30^o$. The calculated data show good agreement with experimental values.
(W. Eckstein, J.P. Biersack)

2.3.4 Computer simulation with the TRIDYN dynamic program

An investigation of surface composition and recoil mixing with the TRIDYN dynamic program has shown that some experimental mixing data can be reasonably well reproduced. It was shown that the surface concentrations in steady state determined with the static program are a good approximation.
(W. Möller, W. Eckstein)

2.4 Ion-induced Desorption

2.4.1 Oxygen desorption on TiC and TiN coatings

Ion impact desorption of oxygen on TiC and TiN coatings under 500 eV H^+ and He^+ bombardment was investigated. According to the heterogeneous structure of the CVD-deposited coatings the desorption cannot simply be characterized by one desorption cross-section, but the average values are close to those measured for metallic Ti samples, i.e. about 2×10^{-17} cm^2.
(E. Taglauer)

3. SPECIAL ANALYSIS

To investigate surfaces exposed to the fusion plasma and understand the important processes of plasma-wall interaction, special analysis techniques have to be tested and developed. Work in this field was continued. Existing devices have been improved and new devices constructed in order to enlarge the capability of necessary experimental investigations.

3.1 New Techniques and Improvements

3.1.1 Laser-induced fluorescence (LIF) for sputtering

A set-up for detecting sputtered atoms by means of laser-induced fluorescence (LIF) was constructed and tested. A pulsed dye laser (Candela) was modified with respect to the energy output, long-term stability and spectral properties of the laser light. The detection system for the fluorescence light was designed and optimized for maximum sensitivity, being now of the order of 10^6 atoms/cm^{-3}. The software for signal storage and data processing was developed.The sputtering yields measured for iron at different energies (see Fig. 9) show good

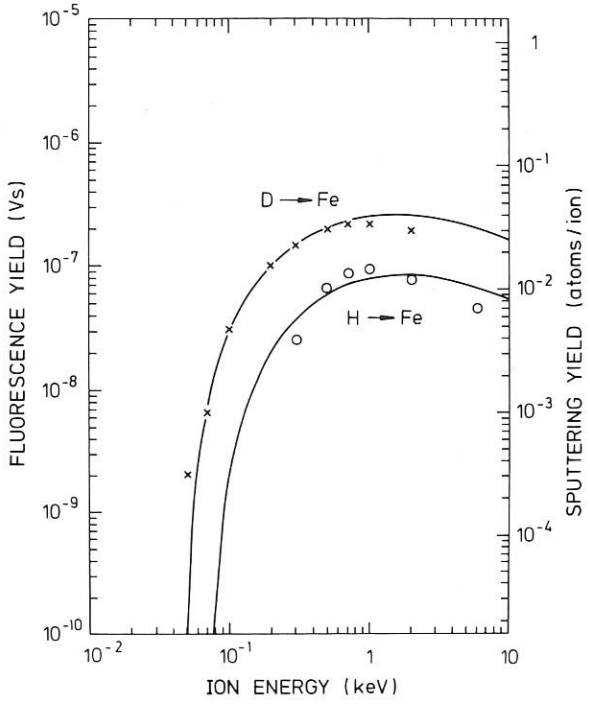

Fig. 9 The sputtering yield of iron versus D^+ ion energy measured by laser-induced fluorescence. Comparison is made with the data gained by weight loss measurements (solid line)

agreement with results from weight loss measurement and with the semi-empirical relation, previously given by Bohdansky. Further sputtering measurements were made on the ASDEX limiter (see ASDEX project).
(J. Appelt, J. Berthold)

3.1.2 Quantitative sub-monolayer analysis of metals and oxygen

To investigate the interaction of low-energy oxygen ions with metal surfaces, a simple electron probe analyzer combined with an oxygen ion source was built. The light elements boron, carbon, nitrogen and oxygen are detectable with a new window-less energy dispersive detector. The energy dependence of the X-ray intensities of various K and L shells was measured at thin metal layers on carbon and silicon. Corrected intensities are compared with theoretical values of the ionization cross-sections and allow optimization of the peak- to-background ratio.
(G. Staudenmaier)

3.1.3 COALA Apparatus for SIMS

The apparatus was modified so that the so-called "Köhler illumination" mode for the primary beam column can now be used. This mode allows higher current densities in the probe spot and also makes the probe spot independent of the size and shape of the virtual ion source (Fig. 10).
(H. Liebl)

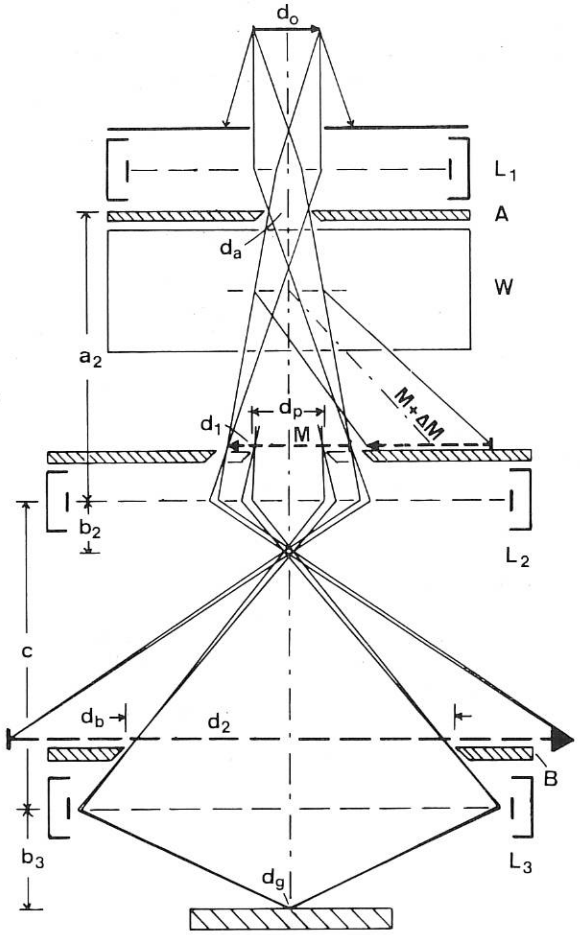

Fig. 10 Schematic of beam column with Wien filter and Köhler illumination. The condenser lenses L_1, L_2 image the source (diameter d_o) on aperture B (diameter d_b) of objective lens L_3. Mass separation at first image (diameter d_1) formed at entrance pupil (diameter d_p) of L_2, L_3. Image diameter $d_2 > d_b$, $d_1 > d_p$. Lenses L_2, L_3 image aperture A (diameter d_a) on sample. Spot diameter $d_g = d_a(b_3/a_2)/(c/b_2-1)$. Weak focusing action of Wien filter neglected

3.2 Surface Analysis

3.2.1 Surface analysis of the Be-limiters of UNITOR

The surfaces (3 x 6 cm^2) of the two beryllium limiters exposed to about 150 plasma discharges in the UNITOR tokamak (University of Düsseldorf, R =o,3 m a = 0.1 m, B_t = 1.7 T, I = 50 kA) were analyzed by RBS, PIXE and SEM. As in the observations of the ASDEX, JET and TFR limiters, Fe, Ni and Cr were found ($1\text{-}2 \times 10^{16}$ atoms/cm^2) in a ratio corresponding to the composition of the stainless-steel vessel. Furthermore Sn (5×10^{15} atoms/cm^2) and a large quantity of oxygen ($5 - 20 \times 10^{17}$ atoms/cm^2) were measured. The foreign atoms are almost uniformly distributed on the limiter surface, independently of its orientation to the magnetic field.
The Fe, Ni and Cr coverages presumably originate

from the vessel walls by plasma erosion and subsequent deposition on the limiters. The Sn coating must originate through similar processes from solder joints in the torus or from probes. The relatively thick oxide shows the good gettering effect of Be, which is likely the major reason for the long plasma discharges observed.
(A.P. Martinelli, R. Behrisch)

3.2.2 Charge fractions of sputtered Ni and Ti

The energy distributions of sputtered Ni and Ti ions (negative, single and double positive) and neutrals were measured by ion desorption spectroscopy (IDS) at non-normal incidence of Ne and Ar ions, and the charge fractions of the sputtered atoms were determined.The Ni and Ti particles sputtered in a binary collision together with Monte Carlo simulations (TRIM-SP) were used for absolute calibration. The charged fractions of the sputtered atoms are found to be less than 10 % for sputtered Ni with energies below 5 keV and less than 5 % for sputtered Ti below 5 keV (Fig. 11). The singly positively charged fraction is about an order of magnitude higher than the negative and doubly positively charged fractions. The positively charged fractions of Ni and Ti are smaller for sputtering with Ar ions compared with sputtering with Ne ions, whereas the negative fractions are independent of the nature of the primary beam.
(H.J. Barth, E. Mühling, W. Eckstein)

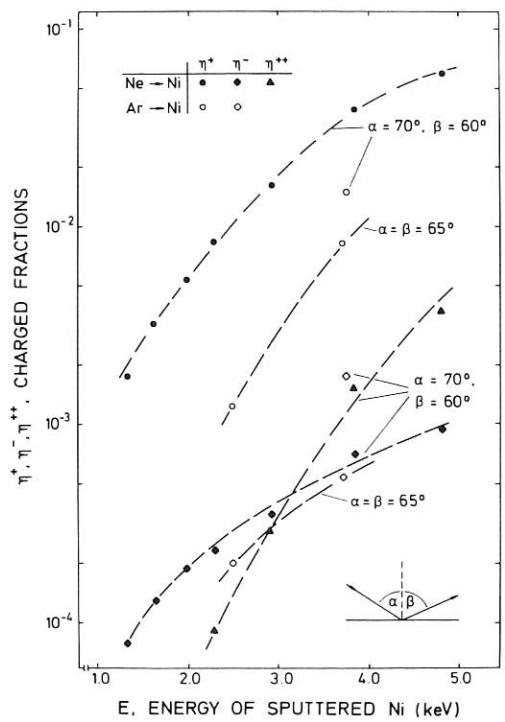

Fig. 11 Charged fractions of positive and negative Ni ions sputtered in one binary collision by Ne^+ and Ar^+ bombardment.

3.2.3 Surface analysis by ion scattering

Temperature effects on low-energy ion scattering are studied as part of the SFB 128 program. The variation of the Ne^+ single scattering intensity from a Cu(110) surface with temperature can be explained with a two-atom-model. In the temperature range of 100 K to 600 K, quantitative agreement is obtained for a Debye temperature of 150 K for vibrations perpendicular to the surface. The three-dimensional calculations using the ARGUS code support these results.
(G.Engelmann, D.P. Jackson, E. Taglauer)

Ion scattering studies of catalysts were extended to MoS_2 single crystals whose near-surface composition was investigated after various preparation procedures. These studies continue a collaboration with the University of Munich (LMU).
(H. Knözinger, R. Margraf, E. Taglauer)

3.2.4 Oxidation of oxygen-bombarded iron

The study of oxide formation due to ion bombardment is important for limiter and wall surfaces but it is also of interest in processes where sputtering and secondary ion formation occur in the presence of oxygen. In the present investigation ^{57}Fe was ion-implanted into a polycrystalline copper host and the valence state of the implant after oxygen treatment (annealing in oxygen, oxygen implantation) of the host was determined by Conversion Electron Mössbauer Spectroscopy (CEMS), X-ray Photoelectron Spectroscopy (XPS) and sputter-assisted Auger Electron Spectroscopy (AES). These measurements showed that in the absence of ion bombardment the oxidation of iron in a copper host proceeds only to the +2 valence state, despite the presence of sufficient oxygen for higher oxidation. Ion bombardment of the same system with oxygen results in complete transformation to the +3 valence state. It is suggested that iron oxide corresponding to the +2 valence state grows coherently in the host lattice of copper and Cu_2O, while oxides corresponding to the +3 valence state (e.g. Fe_2O_3 and $CuFeO_2$) have a different crystal structure than the host and grow incoherently at ion bombardment induced lattice defects.
(W.H. Gries, J. A. Sawicki, B.D. Sawicka)

3.2.5 Mössbauer analysis of Fe films on carbon

In order to simulate the processes leading to droplet formation on limiters, carbon probes were evaporated with an Fe film and heated up to 1000° C. The droplets formed on the surface were analyzed by Conversion Electron Mössbauer Spectroscopy. It was found that, after heating, iron was largely converted from its original metallic form (bcc-Fe) into austenitic iron (fcc-Fe with carbon interstitials), which allows a large number of carbon atoms to be accommodated within the iron structure. In the case where the contact area between the iron and carbon was large (graphite substrate with a rough surface) the droplets were found to contain also a substantial fraction of iron carbide Fe_3C. The results were significant for the interpretation of the CEMS data for metal deposits on graphite ASDEX limiters.
(B.D. Sawicka, J.A. Sawicki)

3.2.6 Surface modifications due to ion irradiation

The effect of irradiation of SS 304 by 7 keV deuterons near room temperature was investigated by Mössbauer spectroscopy. The implantation of 2.5×10^{19} ions/cm^2 was seen to result in a phase transformation near the irradiated surface to a ferromagnetic state, whereas the bulk remained austenitic.
(P. Børgesen, B.D. Sawicka, J.A. Sawicki)

3.2.7 Hydrogen beam modification of iron at 100 K

The Mössbauer spectra of 95 nm ^{57}Fe films vacuum deposited between two 35 nm copper films on a beryllium substrate were investigated after 60 keV D^+-ion bombardment up to a fluence of 1.2×10^{18} ions/cm^2. A considerable modification of Mössbauer time shapes was observed with the target kept at 100 K, which points to radiation damage during the beam operation and hydride formation after irradiation. Above 1400 K a complete recovery of the ordinary metallic iron properties is seen.
(B.D. Sawicka, J.A. Sawicki, F.E. Wagner, W. Möller, and P. Børgesen)

COMPUTER SCIENCE DIVISION

(Prof. F. Hertweck)

The main activities were the design of the ASDEX-Upgrade Data Acquisition System. It will be a "distributed system" of autonomous subsystem computers, a large central computer, and a powerful communications system connecting the subsystems to the central computer facility.

(F. Hertweck, H. Fisser, H. Friedrich, K.H. Goihl, A. Hackl, P. Heimann, J. Hellauer, J. Maier, R. Makowitz[1], I. Precht, U. Schneider, J. Steuerwald[2], D. Stolz)

[1] until 6-3o-84
[2] until 8- 1-84

DATA ACQUISITION for ASDEX Upgrade

The data acquisition and analysis concept for ASDEX Upgrade was designed and development was started. The system has to be capable of acquiring about 8 Mbytes (i.e. about 4 million) of experimental data and analyzing them between shots (i.e. within minutes). These requirements greatly exceed the data rates of present-day experiments (ASDEX and JET: about 2 - 3 Mbyte, 3 - 4 minutes till shot file available). In particular, the time needed to make the data available for analysis is to be greatly reduced.

To meet these requirements, a "distributed system" consisting of the following components was designed:

(1) A series of autonomous subsystems (in principle, one per diagnostic) which control the diagnostic hardware (mostly CAMAC units) and execute the first data acquisition (including "validation" and "selection") at a data rate of at least 25o KByte/s)

(2) A CDAS (central data analysis system: an IBM 4381 with 15 Mbyte main memory is envisaged), which is also responsible for archiving the data and on which the analysis programs run (each diagnostic program having access to the whole shot file)

(3) A powerful communication system that can transfer the shot data by glass-fibre at about loo Kbyte/s from the subsystems to a node computer (near the experiment) and from there (likewise by glass-fibre) at about 1 Mbyte /s to a further node computer (which also serves as interface to the IBM computer); of course, transfer to the subsystems (mostly plot data are involved) and between the subsystems is also envisaged.

It is thus an essentially star-shaped configuration, although the subsystems can also interchange data (without recourse to the CDAS) (see Fig. 1).

The shot data are analyzed with a large number of independent diagnostic programs. They will be run quasi-simultaneously on the CDAS as "parallel processes". As these programs not only have to rely on their own diagnostic data, but also require data from other diagnostics, a shot file structure has been defined that keeps all data available in certain normalized formats. Data objects were

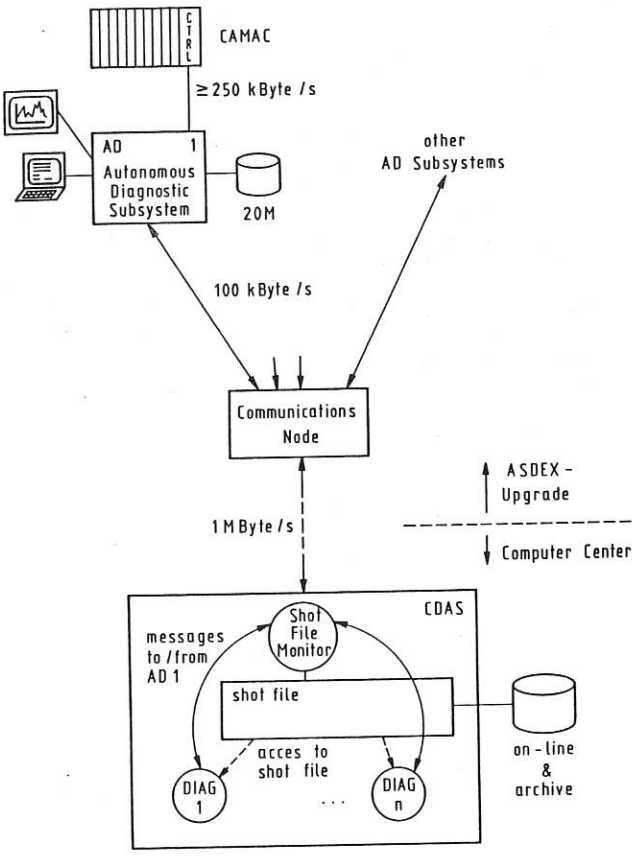

Fig. 1: ASDEX Upgrade Data Analysis System

therefore introduced which, though formally of the same structure, can represent a vide variety of objects (e.g. signals, time bases, CAMAC modules, mappings of CAMAC memories onto signals, etc.). In particular, relations between the objects can be defined (e.g. signal always points to the relevant time base). The experience available shows that very complex relations can be described in this way. In principle, a shot file should contain all data needed for interpretation.

FORTRAN-77 is the only user programming language envisaged; in the system area the C-language (on the UNIX system) and PLX (on the IBM) will also be used. The system is to be presented to users (physicists, diagnosticians) as a "FORTRAN machine", but their work will be facilitated by a large number of utility programs (e.g. access to shot data, control of CAMAC modules, plot procedures, user-friendly input/output interfaces, evaluating algorithms etc.).

The AMOS/2 system is to be used on the CDAS. In particular, the AMOS/2 file system, a further development of the AMOS/1 system, ensures clean structuring of the files, automatic long-term archiving, and efficient new access methods (virtual file I/O, which makes data available from the virtual memory management). Furthermore, AMOS/2 includes advanced process/process communication, file protection mechanisms, an efficient input/output system readily adapted to new requirements, implementation of the virtual terminal concept, the possibility of using re-enterable programs (both in PLX and FORTRAN), and very little overhead for the management of the users' programs and jobs.

CADMUS computers will probably serve as AD subsystem computers: basis Q-bus, Motorola 68010 CPU, 1 Mbyte main memory, 20 Mbyte Winchester disk, UNIX operating system. The first systems of this type have been successfully tested. These AD computers also serve as work stations for the CDAS.

In the course of 1984 the MSCC (medium speed communications controller) hardware was completed (on the basis of a 1 Mbit/s HDLC chip). A data rate of 118 Kbyte/s, i.e. 95 % of the nominal rate, was measured between a CADMUS system and the node computer (which is provided with an VME-bus system, containing a Motorola 68000).

To demonstracte the system concept, the prototype Thomson scattering diagnostic was set up by the end of the year (see Fig. 2).

PROTOTYPE "THOMSON" DIAGNOSTIC FOR ASDEX UPGRADE

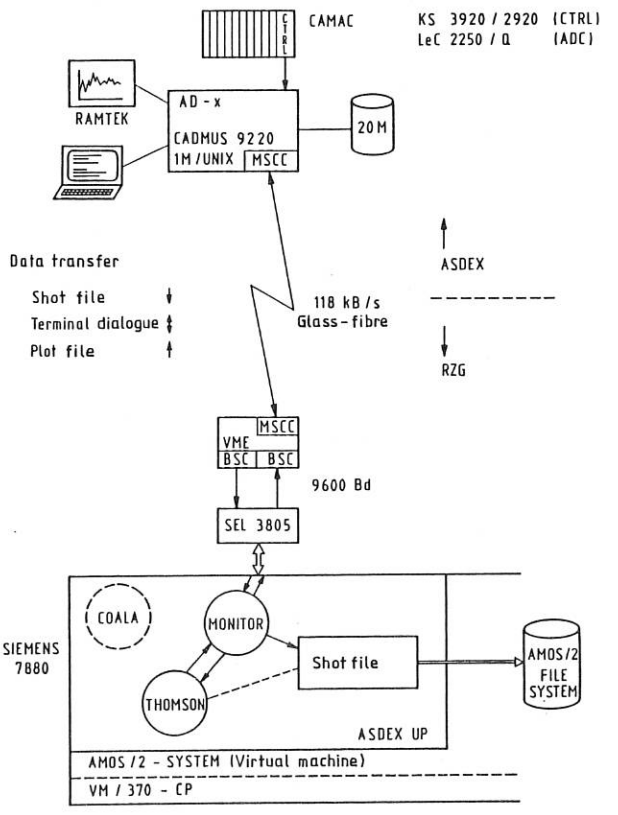

Fig. 2

The following subsidiary tasks were performed:

- commissioning of a CADMUS 9220 UNIX system
- driver software for CAMAC (real-time-like operation) and the MSCC interface
- first version of a data acquisition and transfer process which includes the design of a shot file on the principles stated
- plot software for output of an extended GKS metafile on a RAMTEK color screen monitor and implementation of an autonomous plot process (the plot files are received by the CDAS via the MSCC).
- terminal process, which connects the local CADMUS terminal to the central AMOS/D system
- software for the (provisional) node computer (which also serves as interface computer to the Computer Centre); as the HSCC (high speed communications controller for 10 Mbit/s) and the IBM channel interface are not yet available, it was only possible to attain a data rate of 9600 bit/s between the node and CDAS computers
- general work on the AMOS/2 system in support of the diagnostic programs (virtual memory management, file management, process/process communication, loader for re-enterable programs, FORTRAN input/output interface, use of FORTRAN compiler under AMOS/2, full-screen ACE editor)
- implementation of a first version of the SFM shot file monitor, which acquires the shot data, spreads them out in the memory, writes them on disk, and signals the diagnostic process ("THOMSON")
- implementation of the (most important) access routines to access the data of a diagnostic (they are transmitted as SIGNAL into an array of the diagnostic process, with simultaneous conversion from 16-bit integer to 32-bit floating-point)
- implementation of efficient basis plot routines which generate a GKS-like plot file which is transmitted to the AD subsystem
- integration of the THOMSON diagnostic program as process into the AMOS/2 system

In December 1984 the CADMUS system was installed at ASDEX, but only one signal group for one location was available (and as ASDEX was not in operation, only noise data could be recorded; genuine data acquisition is to be initiated in February 1985). The node computer, connected to the CADMUS by glass fibre, was installed in the Computer Centre and connected to the "AMOS/2" virtual machine on the SIEMENS 7.880 computer via the SEL 3805.

The following sequence of actions was demonstrated:

- data acquisition from the CAMAC ADC
- composition of a shot file
- transmission of the shot file to the central evaluating job in AMOS/2
- spreading of the shot file in the memory of the CDAS by the SFM; notification of the THOMSON process
- evaluation of the data; generation of a plot file from several frames
- interactive control of the THOMSON process from the terminal of the CADMUS system
- transfer of plot data to CADMUS system
- output of the plots on the RAMTEK colour screen monitor

The work schedule for 1984 was essentially completed. Departures of personnel prevented some assignments from being performed. On the other hand, progress in preparing the shot file structure was faster than expected.

In the course of 1985 a further diagnostic is to be installed (electron cyclotron emission being planned); this is to provide early practical experience with the system.

TECHNOLOGY DIVISION

(Dipl.Ing. K.H. Schmitter

The Technology Division comprises three groups, whose work, as in the preceding year, was an essential part of the Tokamak and Stellarator experiments at IPP. All of the groups provided interesting experimental results and, in addition, developed new technologies in their respective fields. Furthermore, contributions were made to the INTOR study, and work relating to systems studies was also performed.

1. NEUTRAL INJECTION

Group leader: E. Speth
Deputy: W. Ott

W.Ertl, J.H.Feist, K.Freudenberger, J.Kolos, R.-C.Kunze, H.Lohnert, P.Mikolajczak (guest from University Lublin, Poland), F.P.Penningsfeld, F.Probst, P.J.Schneider, A.Stäbler, R.Süß, O.Vollmer, K.Wittenbecher, G.Wulff

Field: Plasma-neutralbeam interaction

Objectives: Plasma heating by neutral injection. Development, construction, operation and experiments at the stellarator Wendelstein VII-A and Wendelstein VII-AS and the tokamaks ASDEX and ASDEX Upgrade.

See projects ASDEX, ASDEX Upgrade, W VII-A, and W VII-AS.

2. ION CYCLOTRON HEATING

Group leader: F.Wesner
Deputy: F.Hofmeister

J.Bäumler, F.Braun, R.Fritsch, E.van Mark, J.-M.Noterdaeme, S.Puri, M.Söll, K.Steinmetz, H.Wedler

Field: Plasma wave interaction in the ion gyroresonance range of frequency.

Objectives: Ion gyroresonance frequency heating on ASDEX, ASDEX Upgrade, Wendelstein VII-A, and Wendelstein VII-AS (development, design construction, operation of the heating system and heating experiments.)

See also projects ASDEX, ASDEX Upgrade, and W VII-A, JET Cooperation.

2.1 Ray-tracing Modelling of D(H)-Minority Heating in ASDEX

(K. Steinmetz, M. Brambilla)

One of the objectives of ICRH in ASDEX is to compare the heating efficiency, plasma confinement and impurity production in different heating regimes, such as the second harmonic hydrogen IC-resonance mode and D(H)-minority heating.

The ray-tracing modelling of the ASDEX second harmonic ion cyclotron resonance heating has already been described in the IPP Annual Report 1983 and in /IPP 4/219/, also have the models on which the calculations are based /IPP 4/210/. The same code has been used for calculating the D(H)-minority case.

The following ASDEX target plasma parameters are applied: minor radius a = 40 cm, major radius R = 165 cm, toroidal magnetic field B_T = 2.3 T, experimental electron density and temperature profiles. A power of P_{rf} = 1 MW at f = 35 MHz is launched by two loop antennae located on the low magnetic field side of the torus. The resonance layer is across the plasma axis.

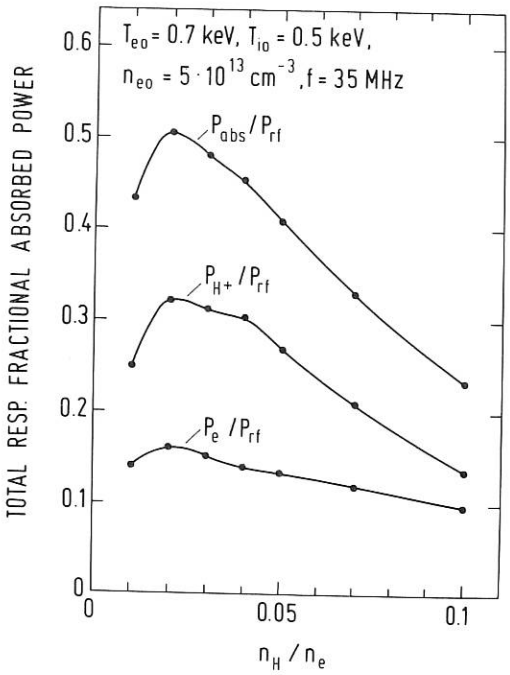

Fig.1: Single pass absorption versus minority species concentration.

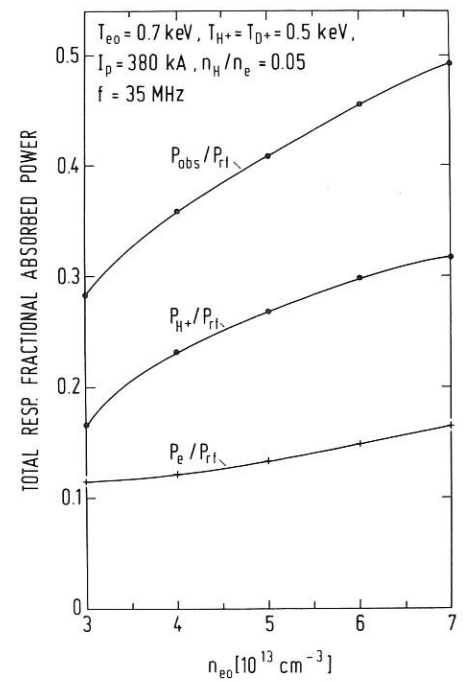

Fig.2: Single pass absorption for ohmic discharge parameters versus central electron density.

Figure 1 shows the single pass absorption of the various plasma species versus the density ratio of the minority ions H^+ to the electrons. For small H^+-concentrations the power absorbed by ions and electrons increases, while the absorption decreases when n_H+/n_e is larger than about 2 %. This typical dependence on the minority concentration has also been reported by others 2), 3). For ohmic discharge conditions (T_{eo}= 700 eV, T_{io}= 500 eV, n_{eo}= 5 x 10^{13} cm^{-3}) a maximum total single pass absorption of about 50% of the input rf power is found. This is a factor of about 3.6 higher than in the case of second harmonic heating under identical plasma conditions. At $n_H+/n_e \simeq 5\%$, which seems to be experimentally achievable, the total absorption is still about 40 %, i.e. 400 kW, of which about 260 kW is absorbed directly by the minority species, the rest goes to the electrons due to Landau damping of the excited ion Bernstein wave.

The dependence of the absorption on n_{eo} and T_{io} in case of D(H)-minority heating at $n_H+/n_e \simeq 5\%$ is illustrated in Figs. 2 and 3.

For ohmic discharge parameters the single pass absorption increases almost proportionally to the electron density (Fig. 2), the ratio P_{H^+}/P_{abs} being relatively independent of n_{eo} between 3 to 7 x 10^{13} cm^{-3}.

Figure 3 shows the behaviour of the absorption versus central ion temperature (at fixed electron density) where the central electron temperature floats from 0.7 keV to 1.5 keV in keeping with real experimental conditions. Increasing T_{io} enhances the absorption by electrons owing to a stronger overlapping of the evanescence layer with the Doppler broadened resonance layer. Absorption by the minority ions has a maximum around $T_{io} \simeq 1$ keV, so that the total single pass absorption tends to saturate for $T_{io} \geq 1$ keV at a value of $P_{abs}/P_{rf} \simeq 55\%$.

In summary, it is shown that ray-tracing calculations for ASDEX exhibit a significantly higher single pass absorption in the case of D(H)-minority heating at small minority concentrations than in the second harmonic hydrogen heating regime. At high target plasma temperatures ($T_{io} \geq 3$ keV), however, the total single pass absorption is not too different in the two modes (D(H): 55%, $2\omega_{CH}$: 44%, see IPP 4/219), although a larger fraction of direct ion heating is expected in the case of second harmonic heating (D(H): $P_{H^+}/P_{abs} \simeq 42\%$, $2\omega_{CH}$: $P_H/P_{abs} \simeq 77\%$).

1) P.L. Colestock, R.J. Kashuba, Nucl.Fusion 23 (1983) 763.

2) H. Kimura, K. Odajima, S. Jizuka et al., Proc. 8th IAEA Int. Conf. and Plasma Physics and Controlled Nucl. Fus. Research, Vol. II, Brussels, (1980) 105.

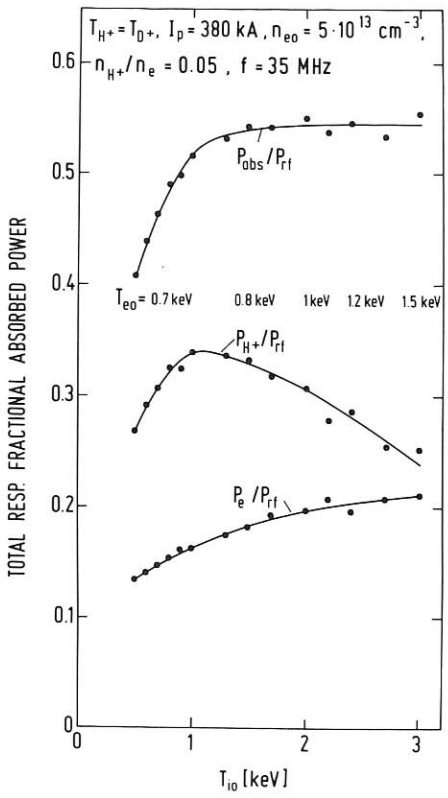

Fig.3: Single pass absorption versus central ion temperature.

2.2 ICRH Antennas

2.2.1 $k_{\parallel}$-shaping.

(M. Söll)

One of the main problems with ICRF heating is the production of impurities. There are some indications that impurities are produced by waves which propagate along the plasma edge before leaking into the plasma. The waves are: the coaxial mode, characterized by the dispersion relation $k_y^2 + k_z^2 = k_0^2$ propagating in the vacuum layer between the plasma and the metal wall, and the surface waves propagating in the plasma edge.

One method of suppressing the coaxial modes is to use antenna arrays producing a $k_{\parallel}$-spectrum which has a minimum at $k_{\parallel} = 0$. Model calculations were carried out to find optimal $k_{\parallel}$-spectra for ASDEX antennae; the calculations are based on the 2-D antenna model [1]. For the monopole ASDEX antenna used at present, the $k_{\parallel}$-spectrum is shown in Fig. 4 (curve a). The $k_{\parallel}$-spectrum (which is symmetrical with respect to $k_{\parallel}$) is peaked at $k_{\parallel}$=0.

The simplest way of producing a proper $k_{\parallel}$-spectrum with a maximum displaced from $k_{\parallel} = 0$ is to use the installed ASDEX antennae but to modify the central conductor. Instead of one central conductor two smaller central conductors are placed in the box built by the Faraday screen. The $k_{\parallel}$-spectrum for

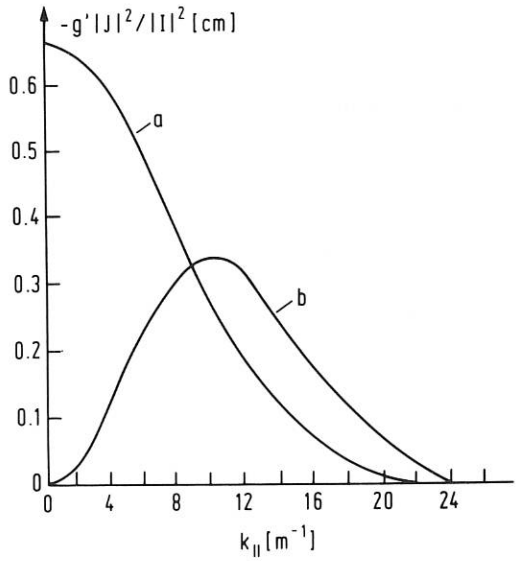

Fig. 4: $k_{\parallel}$-spectra for
a): monopol ASDEX antenna (width of the central conductor 18cm; antenna parameters are described in Ref.[3])
b): quadrupol antenna (width of one central conductor 6 cm; gap between the two central conductors 6 cm; phase difference $\Delta\phi = \pi$).

such a quadrupole antenna where the phase difference between the two currents is π is shown by the curve b) in Fig. 4 (the width of such conductors and the gap between them is 6cm). The spectrum shows a minimum at $k_{\parallel} = 0$ and a maximum at $k_{\parallel} = 10$ m^{-1}. The location of the maximum is not optimal with respect to the absorption spectrum, where the maximum is located at $k_{\parallel} = 6$ m^{-1} or lower, depending on the plasma temperature [2].
Variations of the conductor width within the space constraints of the given ASDEX antennae show only small changes of the location of the maximum.

To get the location of the $k_{\parallel}$ maximum in the range of 6 m^{-1} the distance between the two conductors has to be increased to about half a metre, as

1) M. Söll, E. Springmann: "ICRH programmes for antennas and for plasma dispersion relation", Report IPP 4/215, Feb. 1984

2) M. Brambilla, K. Steinmetz: "Ray tracing for first harmonic ion cyclotron resonance heating in ASDEX". Proc. 4th Intern. Symp. on heating in toroidal plasmas, Rome, 21-28. March 1984, Vol. I, 351

3) F. Wesner et al.: "ICRH components for ASDEX and W VII", ibid. Vol. II, 1103.

shown in Fig. 5. This situation can only be obtained with two completely separated antennae.

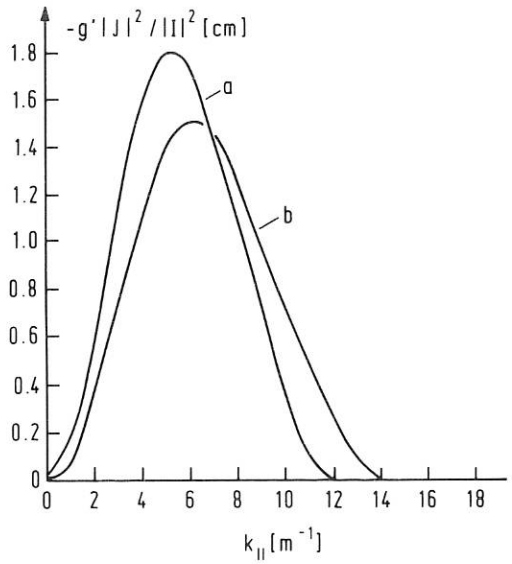

Fig. 5: $k_{\parallel}$-spectra for antenna systems consisting of two ASDEX antennae (for dimensions, see Ref. 2)) which are separated 40 cm (curve b) and 50 cm (curve a).

The antenna quality Q (defined by ωL/R) values are: 10 for the monopole antenna, about 50 for the quadrupole antenna with two small central conductors placed within the screen, and about 12 for the system with two complete ASDEX antennas separated by about half a metre. This indicates that the maximum voltage necessary to radiate equal amounts of power is considerably larger for the quadrupole system with small central conductors and a small distance between them than for the monopole ASDEX antenna.

2. Loop antenna with variable R, L, C
(J.M. Noterdaeme, M. Söll)

One common feature of all present antenna programmes is that the geometrical dimensions (distance between the central and return conductors, width of the central conductor) are constant along the antenna.

In order to treat antennae with varying geometrical dimension (for instance, the distance between the central and return conductors changes along the antenna length), the 2-D model /IPP 4/215/ was extended. The calculation procedure is as follows: first the R, L and C values are calculated with the 2-D model /IPP 4/215/ for different antenna sections where for each section the antenna geometry was kept constant; these R, L, C values then serve as the input data for a computer program modelling a transmission line with variable R, L and C. The antenna input impedance is the final result.

This calculation model was applied to a possible W VII-AS antenna where the distance between the central and return conductors varies from 2.5 cm at the antenna input to about 9 cm at the short-circuit.

2.3. Experimental Investigations of ICRH Antenna Models
(J.-M.Noterdaeme, F.Braun, M.Söll)

For long pulses the antenna must be actively cooled. This presents a problem for the Faraday screen in particular, since cooling the screen means that is has to be thicker, with a resulting increase in HF losses and reduction in coupling to the plasma because of the larger plasma-central conductor distance. In addition, a cooled antenna means a more complicated structure.

Solutions were therefore studied which could reduce the cooling requirements and avoid the coupling reduction resulting from thick Faraday screens. Two kinds of experiments were carried out: experiments with a conventional ICRH loop antenna where the Faraday screen was coated with high-conductivity material in order to reduce the HF losses, and experiments with an antenna where the Faraday screen is replaced by a fin-like screen placed between the central and return conductors 1). A schematic view of such a

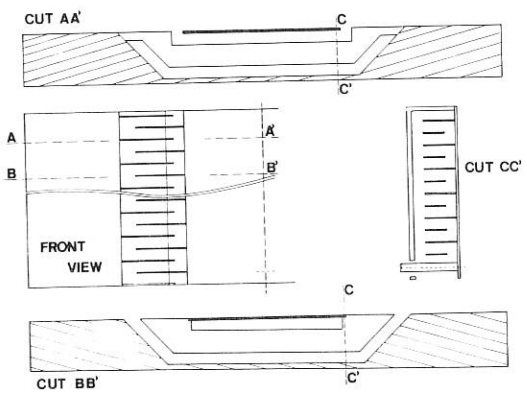

Fig.6 Model for an antenna with fin-type polarizing screen and capacitive loading.

"cross-fin antenna" is shown in Fig. 6 . With such an antenna the required additional capacitive loading can be provided and theory predicts that the correct polarization of the electromagnetic wave is attained 2). Variations of the internal capacitance could be achieved by varying the distance between the fins. Measurement of the antenna input impedance and resonance frequency yielded the following main results:

1) J.-M.Noterdaeme, F.Braun, M.Söll: "Innovative designs for long pulse ICRH antenna". Proc. 4th Intern. Symposium on Heating in Toroidal plasmas, Rome, March 21-28, 1984, Vol. II, 1109
2) S.Puri, Max-Planck-Institut für Plasmaphysik, Report IPP 4/205, Feb. 1982

- coating the Faraday screen with a high conductance material reduces HF losses,
- high capacitive loading can be obtained with a fin-type antenna,
- good agreement between the measured and calculated resonance frequencies as a function of the displacement of the fins.

2.4 Self-consistent, Analytic, Periodic-Loop-Antenna Theory

(S. Puri)

Loop-antenna coupling to toroidal plasmas is simulated in a flat geometry by an infinitely repeated array of finite loops in order to obtain a discrete spectrum along the y (azimuthal) and z (toroidal) directions. The electromagnetic field of the entire configuration, including the wall, the plasma, and the Faraday shield, is analytically expressed in terms of the antenna current. The self-consistent antenna current is determined by variational techniques which also yield the antenna impedance. Finally, the theory is specifically applied to the case of ion cyclotron wave coupling.

2.4.1 The antenna model

Figure 1 shows the idealized, periodic, loop antenna geometry. Each loop consists of an infinitesimally thin rectangular ribbon with height 2 l, breadth 2b, and width 2w and resistivity R_A per unit length. It is driven by a "slice generator" of voltage V situated at x = 0, y = 1, and $-w \leq z \leq w$. The antenna is imaged indefinitely with periodicities Λ_{yo} and Λ_{zo} along the y and z directions, respectively.

The plasma is replaced by a smooth boundary at x = a with the surface impedance matrix ζ_p. The wall and the Faraday shield are situated at x = -c and x = f, respectively.

2.4.2 The antenna field

It is convenient to introduce the cyclic antenna coordinate $-2(1+b) \leq \xi \leq 2(1+b)$ with the origin at x = 0, y = 1, as shown in Fig. 7a. The antenna current distribution $I(\xi)$ may be expressed as

$$I(\xi, z) = f_\xi(\xi) f_z(z). \qquad (1)$$

The solution for the antenna electomagnetic field may now be obtained from the Maxwell's equation in vacuum, subject to the boundary condition that the magnetic field component H_z be discontinuous at the location of the antenna current. The antenna field component θ^A_ν may be expressed in the form

$$\theta^A_\nu = \theta^{AF}_\nu + \theta^{AB}_\nu + \left[\theta^{ASb}_\nu + \theta^{AS-b}_\nu + \theta^{AST}_\nu\right], \qquad (2)$$

where θ^{AF}_ν, θ^{AB}_ν and θ^{AS}_ν pertain to the contributions from the antenna front surface, the antenna back, and the two antenna sides taken together, respectively. The field arising from the antenna sides has three distinct components corresponding to a transmission line field θ^{AST} plus the contributions θ^{ASb} and θ^{AS-b} from the open circuit terminations at x = b and x = -b, respectively.

The spectral distributions of the antenna current from the front and the back surfaces, may be obtained through straightforward Fourier decomposition. Application of the boundary conditions for the tangential components of the electromagnetic field then determines Θ^{AF} and Θ^{AB}.

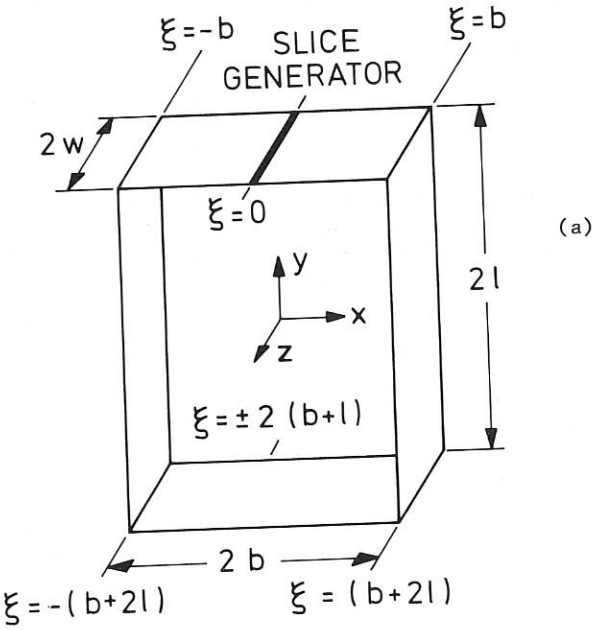

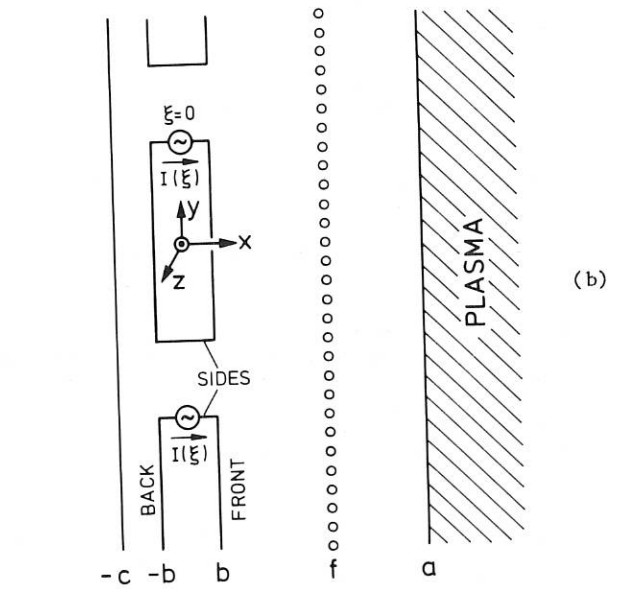

Fig.7: Geometry of the single loop (a) and of the system (b) comprised of the repeated loops (both along y and z directions at intervals Λ_{yo} and Λ_{zo}, respectively), the plasma, the wall, and the Faraday shield.

A somewhat more involved procedure is required to determine the field contributions due to the current components in the antenna sides. In the upper antenna arms $\xi = x$, so that the current

$$I(\xi) = I(x) \text{ for } b \leq \xi \leq b, \qquad (3)$$

One may express I(x) as the superposition integral

$$I(x) = \int_{-\infty}^{\infty} I(x-x')\, \delta(x')dx', \qquad (4)$$

where $\delta(x)$ is the Dirac delta funtion defined as

$$\delta(x) = (2\pi)^{-1} \int_{-\infty}^{\infty} \exp(in_x x)dn_x, \qquad (5)$$

consisting of "exponential excitations" $\exp(in_x x)$. The current I(x) and hence the "exponential excitations" constitute endlessly repeated current sheets at intervals Λ_{yo} in the y direction.

The procedure for obtaining θ^{AS} involves the following steps:

(i) Determining the electromagnetic field by solving Maxwell's, equations subject to the boundary conditions at the current sheets because of an exponential excitation.

(ii) Obtaining the Green's functions $G\theta\{\delta(x)\}$, i.e. the net response to the delta-function excitation (5), by integrating the fields of the exponential excitations over $-\infty \leq n_x \leq \infty$.

(iii) Using the superposition integral,

$$\int_{-\infty}^{\infty} I(x-x')\, G\theta\{\delta(x')\}\, dx', \qquad (6)$$

gives the electromagnetic field resulting from the current in (3).

(iv) Finally adding to (6) the field produced by the lower antenna arms yields the desired field θ^{AS}.

(v) Adding θ^{AF}, θ^{AB} and θ^{AS}, one obtains the composite antenna field.

Following are some significant observations regarding the structure of the antenna field:

(i) The field component pairs (θ^{AF}, θ^{ASb}) and (θ^{AB}, θ^{AS-b}) tend to cancel (with the exception of H_z^A), leaving a net contribution which is of the order $|n^{-2}|$ compared with the individual contributions, thereby confirming the importance of including the feeder currents in the analysis[1),2)].

(ii) Because of the delicate cancellation effects, an accurate determination of the self-consistent antenna current assumes importance[2)].

2.4.3 The boundary value solution

For the present case of boundaries uniform in the y and z directions, the effect of boundaries may be simulated by the surface current distribution

$$\underline{J} = |J_y^W, J_z^W, J_z^F, J_y^P, J_z^P, \qquad (7)$$

where the subscripts W, F and P refer to the wall, the Faraday shield and the plasma, respectively. The field components θ_ν^J caused by the surface current distribution $\underline{J}$ are readily determined using Maxwell's equations and the boundary conditions involving the discontinuity of the tangential magnetic field components at the location of the surface currents. Thereby one obtains the total electromagnetic field as

$$\theta_\nu = \theta_\nu^A + \theta_\nu^J. \qquad (8)$$

2.4.4 The self-consistent current

The electric field along the antenna loop is given by

$$E_\xi(\xi) = R_A I(\xi) - V\delta(\xi), \qquad (9)$$

Multiplying by $I(\xi)$ and integrating around the loop gives Storer's[3)] variational formulation

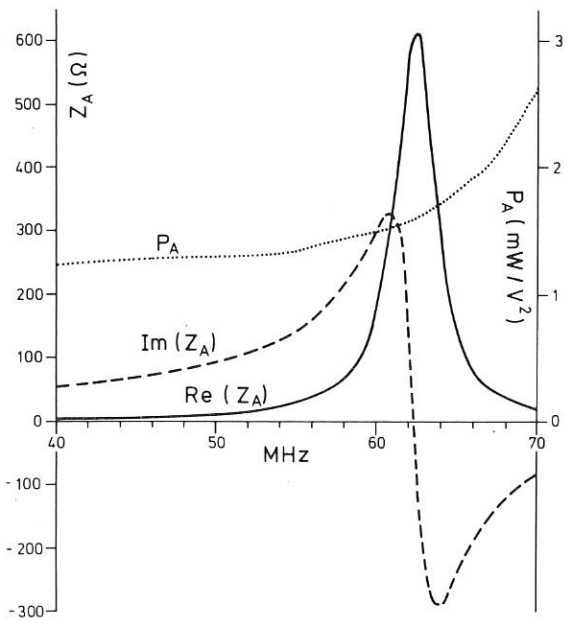

Fig.8: Antenna impedance and input power for unit applied voltage as a function of frequency.

1) V.P. Bhatnagar, R.Koch, A. Messiaen and R.R. Weynants, Nuclear Fusion 22, 280 (1982).

2) K. Theilhaber and J. Jaquinot, Nuclear Fusion 24, 541 (1984).

3) R.W.P. King in "The Theory of Linear Antennas", Harvard University Press, Cambridge, Massachusetts (1956)

$$Z_A I^2(0) + \oint E_\xi(\xi) I(\xi) d\xi - R_A \oint I^2(\xi) d\xi = 0, \quad (10)$$

where Z_A is the antenna impedance. Differentiating (10) with respect to the $F\xi$ (p_i) term in the Fourier expansion of $f_\xi(\xi)$ yields p_{max} simultaneous equations for determining the p_{max} unknown amplitudes $F\xi(p_i)$. This finally determines both Z_A and $I(\xi)$. The lateral antenna current profile $f_z(z)$ in (1) is assumed to be independently supplied.

2.4.5 Application to ICRF coupling

Figure 8 shows the antenna inpedance Z_A and the antenna input power P_A for parameters approximately corresponding to that of the ASDEX tokamak. A linear density profile was assumed. For these computations $m_{max} = n_{max} = 37$ and $p_{max} = 5$. Also the current was taken to be uniformly distributed over the antenna width 2w, and the alternate loops were oppositely phased.

2.5 ICRH Test Bed[1)]

(H.Wedler, E.van Mark, F.Fritsch, F.Wesner)

An ICRH test bed allowing HF power tests in vacuum and with a magnetic field up to 1 T has been installed. The HF generator power available until the end of 1984 was limited to 15 kW/100 ms at a frequency of 102 MHz. By means of a tunable coaxial resonator circuit voltages of between 15 and 30 kV peak were obtained, depending on the quality factor of the component tested. Installation of a coaxial line connection to one of the new 1.5 MW generators (see Sect.5.3.1 of the ASDEX Project) and assembly of a 12" double-stub tuner system has been started at the end of the year.

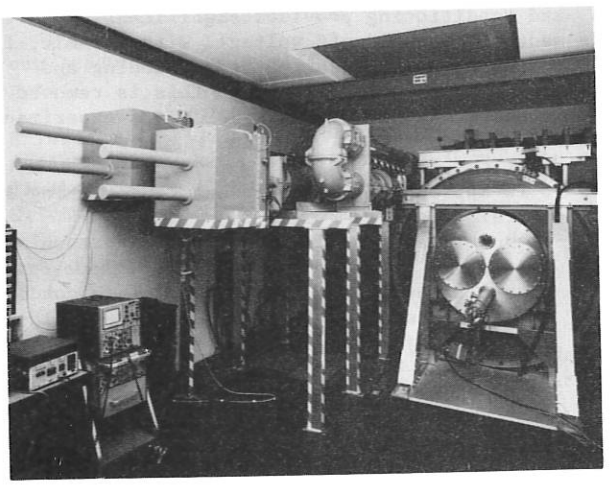

Fig. 9: Test bed with vacuum vessel, magnetic field coils and 12" double-stub tuner system.

1) H. Wedler, F. Fritsch, E. van Mark, F. Wesner, ICRH Test Bed and First Experimental Results, 13. SOFT, Varese, 1984.

HF-tests in vacuum and in the ICRH frequency range show multipactor discharges at relativly low voltages (up to several 100 V) and channel discharges and breakdown at higher voltages. All discharges are accompanied by a pressure rise. Conditioning with short pulses, primarily in the multipactor regime and then with higher power, normally leads to reduction of the gas production and improvement of the breakdown voltage. Critical points are metal-ceramic junctions. If these are not properly designed, their electrical strength cannot be improved to the same extent by conditioning.

2.5.1 Component Tests

In 1984 the following main components were tested:

- ASDEX half-antenna

Testing of the ASDEX half-antenna showed strong multipactors in the vacuum vessel at flanges and in port cavities outside the antenna, which caused high gas production. By improving the contacts at the flanges and with appropriate shielding of the cavities it was possible to eliminate these parasitic discharges.

Inside the antenna multipactors were observed at 102 MHz with a low CW power (1 W). They first occurred at the voltage maximum and then passed along the antenna towards the short-circuited end with increasing power (30 W).

With higher power and 50 µs pulses multipactors are just observed at the antenna input because of the voltage build-up and decay process (10µs) With 40 ms pulses the multipactors were observed at the current maximum, too. Gas production was very high after venting and could be strongly reduced by CW or pulsed conditioning. But it was never possible to operate the antenna completely without gas production. After the tests many components were found to be coated with a thin, yellowish film which could be abraded.
The following four versions of the half-antenna were tested:

- without Faraday shield, without additional capacitance
- without Faraday shield, with additional capacitance
- with Faraday shield, without additional capacitance
- with Faraday shield, with additional capacitance.

With good conditioning and appropriately low repetition rates there were no cases of breakdown up to the maximum attainable voltage of 20 kV_p. In general, gas production due to multipactors was higher in the three versions with additional capacitance or Faraday shield. Furthermore, discrete high-resistance channels were observed when additional capacitances (spacing 1 cm) were used. It is conceivable that these may become low-resistance arcs at higher voltages and longer pulses.

With a hydrogen filling an exact limit was found at 2×10^{-4} torr H^2. At higher pressures there was always breakdown.

With magnetic fields of up to 1.2 T the power reflexion increased, and the gas production in the vacuum vessel as well. Intense luminous phenomena were observed. It was not possible to detect the location inside or outside the antenna at which these luminous phenomena occurred.

- ASDEX vacuum feeder line

In the relatively short time available for tests of this line some critical points of this design were detected at the ceramic-metal junctions of ceramic rod spacers, where the dielectric flux is concentrated on small areas. Depending on the repetition rate and pulse length there is a danger of breakdown above about 15 kV. On the basis of this experience a modified version with a more uniform flux distribution was developed and fabricated for testing purposes.

2.5.2. Development of a Low-cost disc vacuum feedthrough

For ICRH experiments at ASDEX and W VII coaxial HF power vacuum feedthroughs with 6 1/8" diameter (25Ω) are needed. Up to now a feedthrough type with brazed metal-ceramic seals, developed at Fontenay-aux-Roses, has been used. Estimates show that this design is limited to relatively short pulses. New designs developed by JET and Oak Ridge on the same principle can be considered for 10 s pulses.

As an alternative to these expensive brazed feedthroughs, a relatively simple 6 1/8" disc feedthrough using Helicoflex seals was developed. This design can be dismantled and is relatively cheap. In first tests peak voltages of 36 kV/1ms or 30 kV/10ms and currents of 400 A/200 ms were attained without breakdown, limited by the test facility.

2.5.3. General remarks

The test results of one year of experiments with the test bed can be summarized as follows:

2.5.3.1 Pressurized lines

When HF transmission lines are put into operation, low-voltage breakdown already occurs at about 50% of the breakdown threshold proper, even at atmospheric pressure and overpressure, i.e. conditioning with short pulses, 50 µs if possible, is essential to prevent damage of the transmission line. This breakdown, which is particularly significant with HF pulses, is due to:

a) moisture in ceramic components, which leads to strong field divergences and losses,
b) dust particles, sharp protrusions, pollution etc.

2.5.3.2 Vacuum feeder lines

The breakdown strength in vacuum is excellent in principle (typically 20 kV/mm), but it is drastically reduced by various processes, which can cause enormous problems, particularly with long heating pulses. Besides effects known to cause vacuum breakdown, e.g. microprotrusions, loosely adhering microparticles and microreservoirs of occluded gas, the most important factors to emerge from our tests are the following:

- Multipactor discharges in the low-voltage regime result in pressure rises and collisional ionization and breakdown.
- Poor contact due to inferior surface quality, low contact pressure and lack of centring also lead to microdischarges accompanied by pressure rises.
- Metal-ceramic junctions can cause excessive rises in field strength and, as a result of inhomogenities in the current density and poor contact, pressure rises as well.
- High currents and long pulses result in strong heating of the surface accompanied by gas production. Thorough cleaning leaving no residue of solvent is necessary.
- At relatively low radiated power multipactors can be produced outside the antenna. Resonant structures can readily afford qualities of 1000, and voltages of 200 to 1000 V, which are critical for multipactors, can already be attained with a few watts. It is therefore important in all experiments with HF heating to avoid such multipactor traps.

To avoid all of these potential problems, it is essential that all components be tested at full power prior to installation. All structures should be evacuated with a high throughput, i.e. not only have the pump connections and pumps to be appropriately dimensioned, the actual HF coaxial line has to be suitably designed with a sufficiently large buffer volume.

Probably the most significant factor influencing the level of vacuum breakdown is the nature of contamination on the surface, especially with respect to multipactor discharges. This factor depends on the smoothness of the surface, the machining process, the techniques used to polish the surface and the cleaning processes. Cleaning and conditioning provides significant improvement in the hold-off voltage. With ceramic, for instance, carbon residue from grinding and polishing cannot be avoided. This is removed by subsequent annealing at 850° C, as experiments showed.

It is appropriate to carry out conditioning in several steps:

- Multipactor conditioning with short pulses (50 µs) to avoid damage. At the same time all transmission line sections are conditioned as a result of the voltage build-up and decay processes, and the surfaces are degassed by the multipactor discharges. The best test results were obtained by conditioning in methane with a pressure of 10^{-4} torr. This seems to cause deposition of a carbon layer with a SEE coefficient < 1. These two processes appreciably reduce the gas production.

- Spot knocking with 1 to 5 ms pulses in order to eliminate peaks, sharp edges and microscopic protrusions.

- Thermoshock conditioning with long pulses in order to degas the surfaces with high temperatures.

In Fig. 10 a typical conditioning process is shown. The gas production rises sharply whenever the RF pulse length is increased. This is followed by a decay due to conditioning.

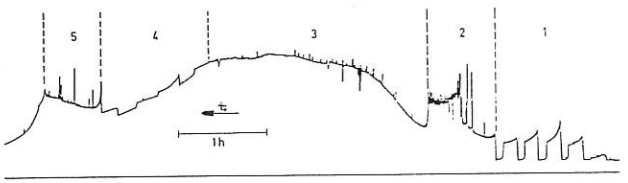

Fig.10: Gas production rate at a typical conditioning process with 50µs - 20ms pulses (multipactor and plasma conditioning in combination with spot knocking and heating).
1: 5 periods, the pulse length being increased from 50µs to 20ms pulses every 500ms, no breakdown
2: pressure rise due to heating at 20ms/500ms pulses and breakdown
3: Sudden stop of breakdown, pressure rise due to heating at 20ms/500ms
4: Pulse length reduced step by step to 1ms/500ms
5: 20ms/500ms as in (2), but with a largely reduced number of breakdowns.

3. LOWER HYBRID EXPERIMENTS

Group leader: D. Eckhartt
Deputy: F.Leuterer

H.Brinkschulte (till 31.8.1984), H.Derfler, M.Hesse (CEN Grenoble), R.Magne (CEN Grenoble, till 31.7.1984), M.Münich, F.Ryter (CEN Grenoble), K.H.Schmitter, T.Vien, F.v.Woyna, M.Zouhar;

Field: Plasma wave interaction in the lower hybrid frequency range

Objectives: Lower hybrid heating and/or current drive on ASDEX and ASDEX Upgrade (development, design, construction, operation of the system and experiments)

See also project ASDEX

3.1 Suppression of Multipactor Discharges in Waveguides

(H.Derfler, J. Perchermeier, F. Leuterer, H. Spitzer)

In view of the mysterious power limit of approx. 800kW which we observed in LH heating and LH current drive in ASDEX, parasitic discharges in waveguides were re-investigated more closely. This involved:

1. scaling of the maximum permissible power flux before the onset of HF secondary electron multiplication (multipactors) with polarization $\vec{E} \parallel B$ and $\vec{E} \perp B$, and
2. metal coating of ceramic surfaces to suppress multipactors in the window area of the waveguides.

3.1.1 Power limit before the onset of multipactors

The mean power density of a TE_{01} wave in the waveguide with rectangular cross-section a x b is given by 1)

$$P/ab = (K/4Z)\,|\vec{E}|^2, \qquad (1)$$

where
$K = \sqrt{1-(\lambda_o/2a)^2}$, $\lambda_o = c/f$, $Z = \sqrt{\mu_o/\varepsilon_o} = 377\Omega$hm

a) In the case of polarization $\vec{E} \parallel B$ the base and top side of the waveguide can give rise to secondary electron emission (SEE) if every electron traverses the width b of the waveguide in $t = (2n-1)\pi/\omega$ seconds. The primary energy eV_p thereby extracted from the HF wave is given implicitly by

$$(\hat{V}/V_o)^2 = V_p/V_o + (1 - 1/2\ \omega t \sqrt{V_p/V_o})^2 \qquad (2)$$

where $\hat{V} = -\hat{E}b$, and V_o is defined by the following reference energy:

$$eV_o = 1/2\ m\ (\omega b)^2, \qquad (3)$$

The voltage necessary for the onset of a multipactor (eq.2) becomes a minimum where $d\hat{V}/dV_p = 0$, i.e. for a transit angle of $\omega t \simeq 2\sqrt{V_o/V_p}$, with the result

$$\mathrm{Min}\,|\hat{V}|^2 \simeq V_o V_p \rightarrow \mathrm{Min}\,|\hat{E}^2| \simeq \frac{1}{2}\frac{m}{e}\omega^2 V_p \qquad (4)$$

When substituted in eq. (1), this gives the maximum permissible power density before the onset of a double-sided multipactor:

$$\frac{P}{ab} = \frac{\pi^2}{2}\frac{m}{e}\frac{K}{z} V_p f^2 = 7.4477\ KV_p\ f^2_{GHz}\ \ W/cm^2 \qquad (5)$$

where V_p is replaced by that primary energy at which the SEE becomes maximum: Max $\delta(V_p) > 1$. If Max $\delta(V_p) < 1$, as in the case of our rough gold coating[1], eq. (5) is of course not valid. In the absence of multipactors, the permissible power density is then very much higher and is presumably governed by the onset of field emission from extremely sharp peaks (spot knocking).

b) In the case of polarization $\vec{E} \perp B$ an emitted electron drops back on to the surface of its origin after $t = \pi/\Omega$ seconds, gaining in the resonance layer $\omega = 2n\Omega$ the following energy from the HF field:

---

1) Derfler, H. et al.: "The Suppression of Multipactors in Lower Hybrid Antennae", 4. Int.Syp. on Heating in Toroidal Plasmas, Rome Italy, March 21.-28., 1984; (see also Annual Report IPP 1983)

$$eV_p = \frac{2}{m}\left|\frac{e\tilde{E}}{\omega}\right|^2 \left(\frac{4n^2}{4n^2-1}\right)^2 \qquad (6)$$

This energy gain becomes maximum for n=1. If $|\tilde{E}|^2$ from this expression is substituted in eq. (1), this gives the maximum permissible power density before onset of a one-side multipactor:

$$\frac{P}{ab} = \frac{\pi^2}{2}\frac{m}{e}\frac{K}{z}\left(\frac{3}{4}\right)^2 V_p f^2 = 4.189\ KV_p f^2_{GHz}\left[\frac{W}{cm^2}\right] \qquad (7)$$

For the antennae in ASDEX we have

a = 16.5 cm; f = 1.3 GHz → K = 0.7153.

For example, with weakly oxidized copper Cu_2O, which must always be expected even in high vacuum, this gives
Max δ = 1.19 → 1.25 at V_p = 400 V,[2)]
P/ab = 3.601 kW/cm² in the case $\tilde{E} \parallel B$,
P/ab = 2.026 kW/cm² in the case $\tilde{E} \perp B$.

The values for the maximum permissible power flux per channel are thus as follows:

	a cm	b cm	$N_{..} = \lambda_0/2b$	MAX P in kW $\tilde{E}\parallel B$	$\tilde{E}\perp B$
Standard waveguide	16.57	8.25		490	276
Ion grill	"	3.00	3.84	178	100
Electron grill	"	1.40	8.24	83	47

The value required for the ion grill was P>330kW, and for the electron grill P > 150 kW. As the above table shows, the two requirements could only be met with a rough gold coating[1)]. This has meanwhile been experimentally demonstrated for the planned electron grill as well. As eqs. (5) and (7) show, the permissible power density increases as the frequency square. It should be noted however, that the total transmittable power remains constant when the frequency is scaled, because the cross-sectional areas of the waveguides themselves scale in proportion to f^{-2}.

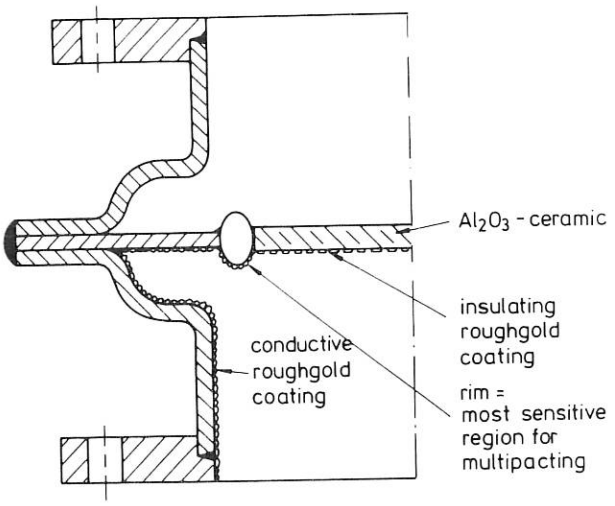

Fig.11:
Wave-Guide Vacuum Window

3.1.2 Coating of ceramic surfaces
The vacuum windows for connecting the antenna to the HF energy supply are made of an oxide ceramic (see Fig.11) which as insulator is necessarily subject to a secondary electron emission of $\delta > 1$, e.g. for high Alumina, Al_2O_3:

$1 < \delta < 1.5 \rightarrow 9$ in the range $350 < V_p < 1300$ V,[2)].

To eliminate the associated risk of multipactoring, we studied two methods of metallizing the surface with coatings transparent to HF and thus non-conducting.

a) Metallization by vapor deposition on rough Al_2O_3 surfaces
To give the surface a metallic character with the lowest possible SEE, the layer thickness d of the deposited metal has to exceed the penetration depth of the primary electrons of approx. 50 Å. To maintain the transparency, the layer thickness must not exceed this value by much. This is seen from Fig. 12 where the resistivity of gold coatings deposited on Al_2O_3 is plotted versus the layer thickness d. As can be seen, this techniques allow a maximum layer thickness of d = 100 Å. Figure 13 shows that in the case of d = 50 Å gold on Al_2O_3 the SEE is in fact $\delta < 1$, in the case of d = 50 Å titanium on Al_2O_3 as well. This is no longer the case with d = 400 Å and d = 10,000 Å gold on Al_2O_3. As expected, the SEE for thick layers approaches the values of compact metal surfaces. This of course results also in the insultation being lost, as can be seen from Fig.12. The values of $\delta \simeq 1$ for insulating layers of thickness d = 50 Å should be viewed with some caution. These were measured by a DC method, in which static charges on the surface can cause its potential to stay at the upper crossing-point of the SEE where $\delta(V_p) = 1$. This difficulty can only be circumvented by using a pulse method with two electron beams[3)], which is unfortunately not available to us at present. To manufacture the windows shown in Fig. 11, the frames had to be coated with galvanic rough gold before the ceramic was coated. To make sure that the SEE of the frame does not rise again when the coating is applied, we measured the SEE coefficient of galvanic rough gold layers after vapor deposition. As can be seen from Fig.14, no

2) D.Hackenberg and W.Bauer in "Advances in Electronics and Electron Physics", Vol XI, Ed.L.Marten, Academic Press 1959, S.438."

3) Salow, H.: "On the secondary electron emission of insulators irradiated by electron beams", Z. Tech.Phys. Vol. 21, p. 8, and: Phys. Zs. Vol. 19, p. 434

change of the SEE due to subsequent coating with gold is to be expected within the measuring accuracy.

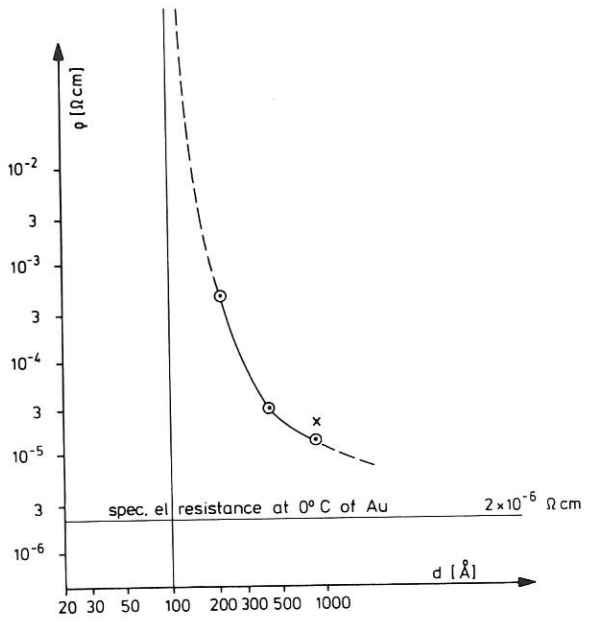

Fig.12:
Resistivity of gold evaporated on Al_2O_3 Vs. depth d of coating

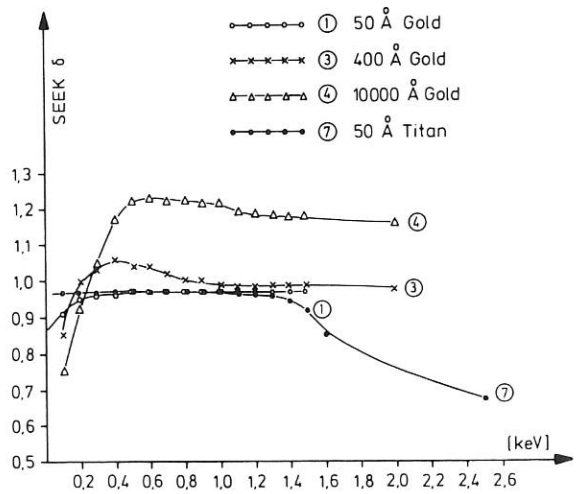

Fig.13:
Secondary Electron Emission of Gold and Titanium evaporated on high Alumina.

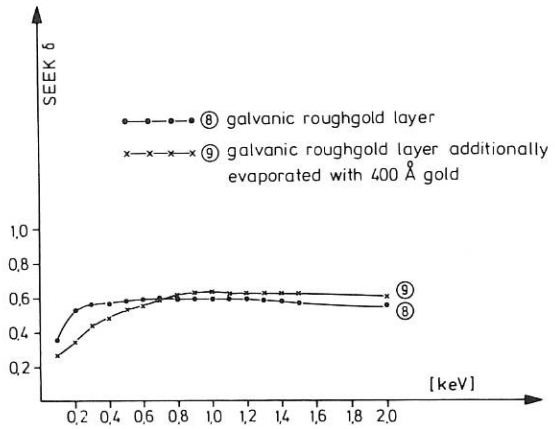

Fig.14:
Secondary Electron Emission of galvanic roughgold layers.

b. Rough gold coating of Al_2O_3 surfaces

To eliminate the problem of the critical layer thickness of approx. d < 100 Å for transparency, and the problem of its dependence on the surface quality of the bare oxide ceramic, we developed a rough metal coating produced by chemical reduction of an electrolyte. Gold in colloidal form is precipitated very fast from an 0,25% aqueous or methanolic solution onto the ceramic by means of a reducing agent. The resulting by-products should be as volatile as possible so as not to leave behind on the ceramic any impurities which would increase the SEE.

Hydrazine and dimethyl hydrazine are the best means of ensuring both fast precipitation, to prevent epitaxial growth of the gold, and the formation of volatile by-products.

The chemical process of reductive gold precipitation, without the intermediate reactions, can be formulated as follows:

$$3N_2H_4 + 4H\ AuCl_4 \rightarrow 4Au\downarrow(\text{rough}) + 3N_2\uparrow + 16HCl\uparrow$$

or

$$3N_2H_2(CH_3)_2 + 2H\ AuCl_4 \rightarrow 2Au\downarrow(\text{rough}) + 3N_2\uparrow + 3C_2H_2\uparrow + 8HCl\uparrow.$$

First the gold solution is painted onto the ceramic and allowed to dry slightly before it is painted over with a 5% hydrazine solution. The gold precipitated on the ceramic is finally dried at 100° C.

The conductance of the coating thus produced was in fact unmeasurable up to a layer thickness of 1µm. As shown in Fig.15, the SEE values then measured were just below 1, i.e. much higher than the values of $\delta \simeq 0.5$ found in Ref.1) for the conductive rough gold coating of metal surfaces. As already mentioned, these values are presumably also distorted during the DC measurements by static charging of the insulating surface, because the windows thus produced generally showed no multipactors on the test bench.

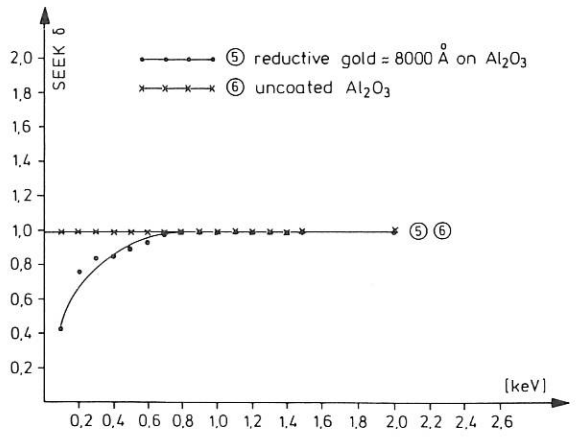

Fig.15:
Secondary Electron Emission of a roughgold coating on high Alumina.

In some cases, however, there was serious damage to the rim of the ceramic disc (see Fig.11). We are therefore not yet able to rule out with absolute certainty the possibility that a multipactor occasionally starts across the ceramic disc, and that the HF low-pressure discharge thus triggered migrates to the rim of the ceramic disc owing to the disc's poor conductivity. To clarify the situation properly, it would be absolutely necessary to use the pulse method of measuring the S.E.E of insulating surfaces as described in Ref.3).

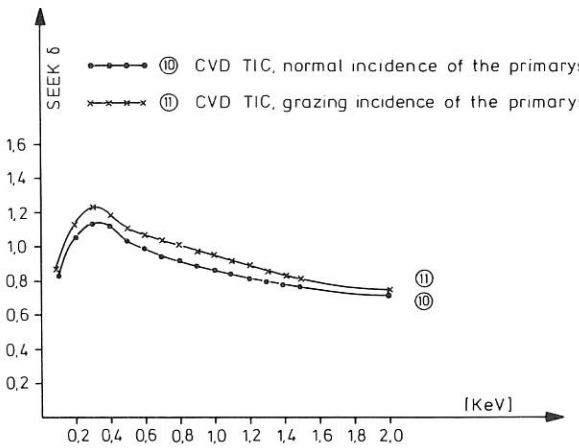

Fig.16:
Secondary Electron Emission of Titanium-Carbide layers in a Low Pressure Hydrogen Atmosphere p = 10^{-4} torr.

In the literature titanium carbide (TiC) is widely recommended as a means of suppressing SEE[4]. TiC is a refractive semi-conductor which insulates at room temperature. This material should therefore also be suitable for coating oxide ceramic surfaces. We were not sure, however, because hydrogen reacts in traces with TiC and may therefore increase the SEE. As our measurements on chemically precipitated TiC layers in Fig.16 show, this increase of the SEE in hydrogen does in fact occur. With max δ = 1.22, TiC is thus unsuitable for applications in plasma machines, unless it proves possible to increase the roughness of such layers so that max $\delta \leq 1$.

4. INTOR CONTRIBUTION
(A. Knobloch)

The European contribution to the INTOR study "Technical Benefit of partitioning INTOR component design and fabrication" was established. A further description is included in Section A under NET Cooperation Project.

5. REACTOR STUDIES
(D. Pfirsch[1], K.H. Schmitter)

The power density limits of tokamak reactors were estimated both from the permissible thermal stress in the first wall and from the ß-limits for standard tokamaks at present regarded as valid. The two limits roughly coincide under INTOR Phase 1 and Phase 2A sputtering assumptions. These limits indicate that the fission suppressed fusion breeder should be considered as a very interesting option on the way towards fusion energy.

An invariance principle for harvesting factors and energy payback times was established. It concerns the splitting of the power needed to operate a power plant, e.g. for fuel, heating, pumping etc., into that provided internally and that provided externally. Statements found in the literature on the harvesting factor of fusion electric power stations in comparison to fission reactors are partly due to erroneous definitions of these quantities not possessing the required invariance property.

1) Theory Division 1

4) Vierstra, A. and Butman,R.C.: Secondary, Emission Characteristics of high Power Mocrowave Tube Surfaces, MIT-Lincoln-Lab. Technical Report No 257, Febr.20,1962.

Publications, Conference Reports, Author Index

Part C: PUBLICATIONS AND CONFERENCE REPORTS

1 ASDEX Team and NI Team, presented by F.Wagner:
Energy confinement studies on ASDEX. Proc. 2nd European Tokamak Programme Workshop, Saulx-les-Chartreux 1983, CEA, Centre d'Etudes Nucléaires de Fontenay aux Roses 1984, XII/65/84, 45.

2 ASDEX Team and NI Team, presented by F.Wagner:
β_{pol}-studies on ASDEX. Proc. 2nd European Tokamak Programme Workshop, Saulx-les-Chartreux 1983, CEA, Centre d'Etudes Nucléaires de Fontenay aux Roses 1984, XII/65/84, 26.

3 ASDEX Team and NI Team, presented by M.Keilhacker:
Global energy balance for various types of ASDEX discharges. Proc. 2nd European Tokamak Programme Workshop, Saulx-les-Chartreux 1983, CEA, Centre d'Etudes Nucléaires de Fontenay aux Roses 1984, XII/65/84, 159.

4 ASDEX Team and NI Team, presented by M.Keilhacker:
Scrape-off parameters in ASDEX divertor discharges. Proc. 2nd European Tokamak Programme Workshop, Saulx-les-Chartreux 1983, CEA, Centre d'Etudes Nucléaires de Fontenay aux Roses 1984, XII/65/84, 161.

5 ASDEX Team, presented by F.Karger:
ASDEX divertor tokamak results of significance for large fusion experiments. Annual Meeting 1984, New Orleans, Lousiana, Transactions of the Americal Nuclear Society 46, 185 (1984).

6 ASDEX Team, presented by G.Haas:
Refuelling of diverted ASDEX discharges. Proc. 2nd Europ. Tokamak Programme Workshop, Saulx-les-Chartreux 1983, CEA, Centre d'Etudes Nucléaires de Fontenay aux Roses 1984, XII/65/84, 154.

7 ASDEX Team, vorgetragen durch F.Karger:
ASDEX, ein Experiment auf dem Weg zur Kernfusion.
Tagungsbericht Jahrestagung Kerntechnik 84, Frankfurt, Deutsches Atomforum, Bonn 1984, 617.

8 Amenda, W. and R.S.Lang:
A centrifugal D_2 pellet injector for refuelling plasma machines. Proc. 13th SOFT, Varese 1984, Comm. EC, 1P03.

9 Andelfinger, C., K.Büchl, W.Sandmann and H.-B.Schilling:
Pellet injector for JET. Proc. 13th SOFT, Varese 1984, Comm. EC, 1P906.

10 Bauer, P.[1)], F.Aumayer[1)], D.Semrad[1)] and B.M.U.Scherzer:
Measurements of the stopping cross section for protons in copper by backscattering using methods for foil-thickness determination.
Nucl. Instr. & Meth. in Phys. Res. B1, 1 (1984).

11 Becerra-Acevedo, R., J.Bohdansky, W.Eckstein and J.Roth:
Spherical angular distribution of atoms, sputtered with energetic deuterium at grazing incidence. Nucl. Instr. & Meth. in Phys. Research B2, 632 (1984).

12 Becker, G., K.Borras and O.Gruber:
Energy and Particle Confinement. In: Europ-Contr. Group F. INTOR-Workshop, 10th Symp. of Phase IIA, Part 2, 1984.

13 Becker, G.:
Scaling of transport coefficients in neutral-beam-heated ASDEX plasmas. Nucl. Fusion 24, 1364 (1984).

14 Behringer, K.[1], J.Bonnerue[1], A.Bulliard[1]. W.Engelhardt, R.Gill[1], A.Gondhalekar[1], G.Magyar[1], P.Morgan[1], J.O'Rourke[1], M.Stamp[1], P.Carolan[1], G.Cottrell[1], M.Forrest[1], N.Peacock[1], H.Krause und F.K.Mast:
Verunreinigungen und Strahlung in JET.
Verhandl. DPG (VI) 19, 1195 (1984).

15 Behringer, K.H.[1] et al. (from IPP: J.Ehrenberg, H.Krause and F.K.Mast):
Impurity studies and transport code modelling of JET plasmas. Proc. 10th Int. Conf. on Plasma Physics and Contr. Nucl. Fus. Res., London 1984, IAEA, Vienna, IAEA-CN-44/A-V-2-1/2.

16 Behrisch, R.:
Wechselwirkungen von Plasmen mit Oberflächen im Weltraum und bei Fusionsexperimenten.
Verhandl. DPG (VI) 19. 123 (1984).

17 Behrisch, R.:
Plasma wall interactions in fusion devices. Proc. 11th Int. Symp. on Discharges and Electrical Insulation in Vacuum, Eds. P. Bachmann,
H. Kastelewicz, Berlin/DDR 1984, 1, 123.

18 Behrisch, R., P.Børgesen, J.Ehrenberg, B.M.U.Scherzer und ASDEX Team:
Oberflächenzusammensetzung eines Graphitlimiters von ASDEX. Verhandl. DPG (VI) 19, 1244 (1984).

19 Behrisch, R., P.Børgesen, J.Ehrenberg, B.M.U.Scherzer, B.D.Sawicka, J.A.Sawicki and ASDEX Team:
Surface composition and topography of the graphite limiter in ASDEX. J. Nucl. Mat. 128 & 129, 470 (1984).

20 Behrisch, R. and J.B.Roberto[1]:
Plasma surface interaction processes and possible synergisms. Proc. Workshop on Synergistic Effects in Surface Phenomena Related to Plasma Wall Interactions, Eds. N. Itoh, K. Kamada, H. Tawara, Nagoya 1984, IPPJ-AM-35, 11.

21 Biersack, J.P.[1] and W. Eckstein:
Sputtering studies with the Monte Carlo-Program TRIM.SP. Appl. Phys. A 34, 73 (1984).

22 Bilbao, L.[1], J.P.Rager[1], B.V.Robouch[1] and K.Steinmetz:
Proprietà dell'emissione neutronica e della dinamica del plasma nell'esperienza 'plasma focus'da 1MJ di Frascati.
Proc. 2° Congresso Nazionale dei Elettronica Quantistica e Plasmi, Palermo 1983, CNR Roma 1984, 465.

23 Biskamp, D.:
Anomalous resistivity and viscosity due to small-scale magnetic turbulence.
Plasma Physics 26, 311 (1984).

24 Biskamp, D.:
How fast is fast magnetic reconnection across an
X-type neutral point?
Proc. Sherwood Theory Conf., 1984, paper 1R 16.

25 Biskamp, D.:
Magnetic reconnection across an X-type neutral point-slow shocks versus current sheets.
Phys. Letter 105A, 124 (1984).

26 Biskamp, D.:
Validity of the Petschek model. Magnetic Reconnection in Space and Laboratory Geophysical Monograph 30, 369 (1984).

27 Biskamp, D. and F.Pohl:
Effect of radial structure of eletrostatic or magnetic perturbations on the diffusion of test particles in a sheared magnetic field.
Proc. Sherwood Theory Conf., 1984, paper 2S 15.

28 Biskamp, D. and M.Walter:
Drift wave turbulence in a sheared magnetic field. Proc. Sherwood Theory Conf., 1984, paper 2R 5.

29 Børgesen, P., B.M.U.Scherzer und W.Möller:
Permeation implantierten Deuteriums durch Ni.
Verhandl. DPG (VI), 19, 297 (1984).

30 Bohdansky, J.:
A universal relation for the sputtering yield of monoatomic solids at normal ion incidence.
Nucl. Instr. & Methods in Physics Research B2, 587 (1984).

31 Bohdansky, J.:
Sputtering. Nucl. Fusion, Special Issue: Data Compendium for Plasma Surface Interactions, 61 (1984).

32 Bohdansky, J.:
Sputtering and its importance for the thermonuclear fusion. Symp. on Atomic and Surface Physics, Eds. F.Howarka et al., Maria Alm/Österreich 1984, 261.

33 Bohdansky, J. and J.Roth:
Light ion sputtering of different low Z-materials in the temperature range. 20-1100°C,
J. Nucl. Mater. 128 & 129, 1417 (1984).

34 Bohdansky, J. and J.Roth:
Synergisms on surface erosion (Session summary). Proc. Workshop on Synergistic Effects in Surface Phenomena Related to Plasma Wall Interactions, Eds. N. Itoh, K. Kamada, H. Tawara, Nagoya 1984, IPPJ-AM-35.

35 Borrass, K. and M.Söll:
Burn stabilization via feedback ripple regulation in an ignited tokamak.
Proc. 13th SOFT, Varese 1984, Comm. EC.

36 Braams, B.[1]):
MHD equilibrium determination. Bull. Am. Phys. Soc. 29, 1374 (1984).

37 Braams, B.[1]):
Modelling of a transport problem in plasma physics. Topics in Appl. Num. Analysis 1, No. 4, 149-164 (1984).

38 Braams, B.[1]):
Multigrid Solution of the Grad-Shafranov Equation.
Verhandl. DPG (VI) 19, 1238 (1984).

39 Braams, B.[1]):
Status of Fluid Modelling of the Edge Plasma.
Verhandl. DPG (VI) 19, 1211 (1984).

40 Braams, B.[1]), P.J.Harbour[1]), M.F.A.Harrison[1]), E.S.Hotson[1]) and J.G.Morgan[1]):
Modelling of the boundary plasma of large tokamaks. J.Nucl. Mater. 121, 75 (1984).

41 Braams, B.[1]) and M.F.A.Harrison[1]):
Tentative results of 2-D plasma modelling of the limiter edge plasma in INTOR. INTOR-Phase IIa Workshop, Comm. EC Brussels 1984, Europ. Contr. to the 9th Workshop Meeting, EURFUBRU/XII-1/84/EDV20.

42 Braams, B.[1]), M.F.A.Harrison[1]), E.S.Hotson[1]) and J.G.Morgan[1]):
Application of two dimensional modelling to the scrape-off and the single null poloidal divertor plasma of INTOR. Proc. 10th Int. Conf. on Plasma Phys. and Contr. Nucl. Fus. Res., London 1984, IAEA-CN-44/E-2-5.

43 Braams, B.[1]), M.F.A.Harrison[1]), E.S.Hotson[1]) and J.G.Morgan[1]):
Preliminary results of 2-D modelling of the INTOR boundary plasma. INTOR-Phase IIa Workshop, Comm. EC Brussels 1984, Europ. Contr. to the 8th Workshop Meeting, EURFUBRU/XII-1/84/EDV10.

44 Brambilla, M. and K.Steinmetz:
Ray tracing for first harmonic ion cyclotron resonance heating in ASDEX. Proc. 4th Int. Symp.on Heating in Toroidal Plasmas, Eds. H.Knoepfel, E.Sidoni, Rom 1984, EUR 9341 EN, I, 351.

45 Brocken, H.J.B.M., H.DeKluiver[1]) and F.B.Hendriks[1]):
Active ion temperature determination by energetic neutral beam probing critically discussed. Plasma Physics and Controlled Fusion 26, 749 (1984).

46 Brossmann, U., E.Harmeyer, J.Kißlinger, F.Rau, J.Sapper, H.Wobig und H.Bieder[1]):
Wendelstein V II-AS, die Realisierung eines modularen Stellarators mit nichtebenen Spulen.
Tagungsbericht Jahrestagung Kerntechnik, Frankfurt 1984, Deutsches Atomforum , Bonn 1984, ISSN 0720-9207, 625-628.

47 Brzosko, J.[1]), H.Conrads[1]), J.P.Rager[1]), B.V.Tobouch[1]) and K.Steinmetz:
Investigations of high-energy deuterons in a dense plasma focus device by means of neutrons emitted in the ^{7}Li+D process.
Nuclear Technology/Fusion 5, 209 (1984).

48 Büchl, K., A.Eberhagen, D.Eckhartt, F.Leuterer, V.Mertens, W.Sandmann and F.Söldner:
Pellet ablation on LH heated plasmas.
Bull. Am. Phys. Soc. 29, 1367 (1984).

49 Büchl, K., A.Eberhagen und S.Kissel[1]):
Pelletinjektion als Mittel der Plasmadiagnostik in ASDEX. Verhandl. DPG (VI) 19, 1237 (1984).

50 Campbell, D.J.[1]), A.Eberhagen and S.E.Kissel[1]):
Analysis of electron cyclotron emision from non-thermal discharges in ASDEX tokamak.
Nucl. Fus. 24, 297 (1984).

51 Campbell, D.J.[1]) and A.Eberhagen:
Studies of electron cyclotron emission from high density discharges in the ASDEX tokamak. Plasma Physics and Contr. Nucl. Fus. 26, 689 (1984)

52 Canobbio, E.:
Introduction to the theory of RF plasma heating and current drive. In: Radiation in Plasmas,
Ed. B. McNamara, World Scientific Publishing Co. Pte. Ltd., 1984, I, 207-258.

53 Canobbio, E.:
Review of the theory papers in: Non-inductive current drive in tokamaks. Proc. IAEA Technical Meeting, Ed. D.F.H. Start, Culham Lab/UK 1983,
CLM-CD, II, 546-550.

54 Canobbio, E. and R.Croci:
LH k-spectrum upshift and resonance-cone disruption as competing ponderomotive effects. 26th Annual Meeting of the Div. of Plasma Physics, APS, Boston 1984, paper 12 - 11.

55 Canobbio, E. and R.Croci:
On the interpretation of lower hybrid current drive experiments. Proc. IAEA Technical Meeting, Ed. D.F.H. Start, Culham Lab/UK 1983, CLM-CD, II, 155-160.

56 Canobbio, E. and R.Croci:
Ponderomotive production of fast ion and fast electron tails by LH waves. Proc. 10th Int. Conf. on Plasma Physics and Contr. Nucl. Fus. Res., London 1984, IAEA-CN-44/F-III-5.

57 Canobbio, E. and R.Croci:
Progress in lower hybrid current drive and heating theory. Proc. 4th Int. Symp. on Heating in Toroidal Plasmas, Eds. H. Knoepfel, E. Sindoni, Rom 1984, EUR 9341 EN, I, 583-592.

58 Canobbio, E. and R.Croci:
RF current drive in the presence of a DC electric field. Proc. IAEA Technical Meeting, Ed. D.F.H. Start, Culham Lab/UK, 1983, CLM-CD, II, 196-201.

59 Cattanei, G.:
Mode conversion and wave damping in a two-ion-component toroidal plasma near the ion cyclotron frequency. Proc. 4th Int. Symp. on Heating in Toroid. Plasmas, Eds. H.Knoepfel, E.Sidoni, Rom 1984, EUR 9341 EN, I, 343.

60 Chen, C.K., B.M.U.Scherzer and W.Eckstein:
Trapping and reflection coefficients for deuterium in graphite at oblique incidence. Appl. Phys. A 33, 265 (1984).

61 Chen, C.K., J.Bohdansky, W.Eckstein and M.T.Robinson[1]:
Energy reflection of H^+-ions at energies between 10 and 80 keV. J. Nucl. Mater. 128 & 129, 687 (1984).

62 Chodura, R.:
Sheath and presheath of a scrape-off layer. Intern. Course: Physics of Plasma Wall Interactions in Controlled Fusion, NATO Advanced Study Institute, Val Morin, Quebec/Canada 1984, NATO ASI, Series B.

63 Cordey, J.G.[1] et al. (from IPP: H.Krause, F.K.Mast):
Particle and energy confinement in ohmically heated JET plasmas. Proc. 10th Int. Conf. on Plasma Physics and Controlled Nuclear Fusion Research, London 1984, IAEA, Vienna.

64 Correa-Restrepo, D.:
Comments on ballooning mode calculations in stellarators. Phys. Fluids 27, 1341 (1984).

65 Dorst, D., W.Melkus, G.Müller[1], V.Erckmann[1], M.Thumm[1], R.Wilhelm[1] and ECRH Team (IPF Stuttgart)[7]:
Control and modulation of gyrotron rf power for ECRH at 28 GHz and 70 GHz. Proc. 13th SOFT 1984, Varese 1984, Comm. EC.

66 Harned, D.S.[1] and W.Kerner:
Semi-implicit simulation method for 3D resistive MHD. Bull. Am. Phys. Soc. 29, 1207 (1984).

67 Derfler, H., H.Brinkschulte, F.Leuterer, J.Perchermeier and H.Spitzer:
The suppression of multipactors in Lower Hybrid Antennae. Proc. 4th Int. Symp.on Heating in Toroidal Plasmas, Eds. H.Knoepfel, E.Sidoni, Rom 1984, EUR 9341 EN, II, 1261-1269.

68 Dietz, K.J.[1] et al. (from IPP: H.Krause and F.K.Mast):
Start up and initial operation of JET. Proc. 6th Conf. on Plasma Surface Interactions in Controlled Fusion Devices, Nagoya 1984

69 Dodel, G.[1], H.Hailer[1], E.Holzhauer[1], P.N.Ignacz[1], J.H.Massig[1], H.P.Röser[1], H.Salzmann[1], F.Söldner and T.Vogel[1]:
A 119 μm scattering system for the investigation of lower hybrid waves in the ASDEX tokamak. Proc. 9th Int. Conf. on Infrared and Millimeter Waves, Osaka 1984, 407.

70 Dommaschk, W., W.Lotz and J.Nührenberg:
Monte Carlo simulation of neoclassical transport in stellarators. Nucl. Fus. 24, No.6, 794 (1984).

71 Dorst, D. and W VII-A Team[3]:
Power supplies for the various systems at the W VII-A-experiment.
Proc. U.S.-Japan Stellarator/Heliotron Workshop on Experimental Planning, Oak Ridge/USA 1984, II.

72 Dorst, D. and W VII-A Team[3]:
The ohmic heating system of W VII-A and the plasma current regulation.Proc. U.S.-Japan Stellarator/Heliotron Workshop on Experimental Planning, Oak Ridge 1984, II.

73 Dorst, D. and W VII-A Team[3]:
WENDELSTEIN VII-A and its machine diagnostics. Proc. U.S.-Japan Stellarator/Heliotron Workshop on Experimental Planning, Oak Ridge 1984, III.

74 Düchs, D.F.:
Ergebnisse aus der ersten Betriebsphase des europäischen Tokamaks JET. Verhandl. DPG (VI) 19, 1200 (1984).

75 Eberhagen, A., D.J.Campbell[1], S.E.Kissel[1] and V.Mertens:
ECE-diagnostics of the ASDEX-tokamak plasmas. Proc. 4th Int. Symp. on ECE and ECR, Rom 1984, I4.

76 Eckhartt, D., F.Leuterer, M.Münich, A.Izvoztchikov[1], F.Ryter[1], F.Söldner, M.Keilhacker, G.Becker, K.Bernhardi, M.Brambilla, H.Brinkschulte, H.Derfler, U.Ditte, A.Eberhagen, M.ElShaer[1], G.Fußmann, O.Gehre, J.Gernhardt, G.v.Gierke, E.Glock, T.Grave, O.Gruber, M.Hesse[1], G.Haas, G.Janeschitz, F.Karger, S.Kissel[1], O.Klüber, M.Kornherr, G.Lisitano, R.Magne[1], H.M.Mayer, K.McCormick, D.Meisel, E.R.Müller, H.Murmann, W.Poschenrieder, H.Rapp, K.-H.Schmitter, F.Schneider, G.Siller, P.Smeulders, E.Speth, A.Stäbler, K.-H.Steuer, Z.Szymanski[1], G.Venus, T.Vien, O.Vollmer, F.Wagner, F.v.Woyna and M.Zouhar:
Lower Hybrid experiments in ASDEX. Proc. 4th Int. Symp.on Heating in Toroidal Plasmas, Eds. H.Knoepfel, E.Sidoni, Rom 1984, EUR 9341 EN, I, 501-512.

77 Eckhartt, D.:
Lower Hybrid Heizung im ASDEX Tokamak. Tagungsbericht Jahrestagung Kerntechnik , Frankfurt 1984, Deutsches Atomforum, Bonn 1984, ISSN 0720-9207, 633-636.

78 Eckstein, W. and H.Verbeek:
Light ion reflection from solids. Nucl. Fusion, Special Issue: Data Compendium for Plasma Surface Interactions, 12 (1984).

79 Eckstein, W. and J.Biersack[1]:
Sputtering investigations with the Monte Carlo Program TRIM.SP. Nucl. Instr. & Methods in Phys. Res. B 2, 550 (1984).

80 Engelmann, G. and E.Taglauer:
Temperature effects in low energy ion scattering from copper. Nucl. Instr. & Methods in Phys. Res. B2, 230, 436 (1984).

81 Engelmann, G. und E.Taglauer:
Einfluß der Oberflächentemperatur auf die Streuung niederenergetischer Ionen an Kupfer (110).
Verhandl. DPG (VI), 19, 345 (1984).

82 Erckmann, V.[1], ECRH Team (IPF Stuttgart)[7] and W VII-A Team[3]:
ECRH on the WENDELSTEIN W VII-A stellarator with different kinds of wave launching. Proc. 4th Int. Symp. on Heating in Toroid. Plasmas, Eds. H.Knoepfel, E.Sidoni, Rom 1984, EUR 9341 EN, II, 846.

83 Erckmann, V.[1], ECRH Team (IPF Stuttgart)[7] and W VII-A Team[3]:
Wave absorption and transport studies on ECR heated stellarator plasmas in W VII-A. Proc. 10th Int. Conf. on Plasma Physics and Controlled Nuclear Fusion Research, London 1984, IAEA, Vienna, paper CN-44/D-I-5.

84 Erckmann, V.[1], W VII-A Team[3] and ECRH Team (IPF Stuttgart)[7]:
ECRH experiments in WENDELSTEIN VII-A using different modes. 5th Int. Workshop on Stellarators, Schloß Ringberg/BRD 1984, Proc. IAEA Technical Committee Meeting on Plasma Confinement and Heating in Stellarators, Comm. EC, 1, 591.

85 Ertl, K. and ASDEX Team:
Heat flux measurements in the ASDEX edge plasma.
J. Nucl. Mat. 128 & 129, 163 (1984).

86 Ertl, K. und ASDEX Team:
Messungen des parallelen Energieflusses in der ASDEX-Randschicht. Verhandl. DPG (VI), 19, 1207 (1984).

87 Feist, J.-H., J.Kolos, P.Mikolajczak[1], P.-J. Schneider, E.Speth and G.Wulff:
The performance of watercooled grids for ASDEX long pulse neutral injection. Proc. 10th Symp. on Fusion Engineering, Philadelphia/USA 1983, 1494.

88 Feist, J.-H., K.Freudenberger, J.Kolos, P.Mikolajczak[1], W.Ott, F.-P.Penningsfeld, P.-J.Schneider, E.Speth and G.Wulff:
Long pulse injector design for ASDEX and Wendelstein VII-AS. Proc. 4th Int. Symp.on Heating in Toroidal Plasmas, Eds. H.Knoepfel, E.Sidoni, Rom 1984, EUR 9341 EN, 1051.

89 Feneberg, W., K.Lackner and P.Martin:
Fast control of the plasma surface.
Com. Phys. Communic. 31, 143 (1984).

90 Fußmann, G., ASDEX-Team[2] und NI-Team (ASDEX)[4]:
Untersuchungen zur Physik des Divertors an ASDEX. Verhandl. DPG (VI) 19, P7 (1984).

91 Fußmann, G., G.Haas, K.Bernhardi, U.Ditte, A.Eberhagen, O.Gehre, J.Gernhardt, G.v.Gierke, E.Glock, T.Grave, O.Gruber, M.Hesse[1], G.Janeschitz, F.Karger, M.Keilhacker, S.Kissel[1], O.Klüber, M.Kornherr, G.Lisitano, H.M.Mayer, K.McCormick, D.Meisel, V.Mertens, E.R.Müller, H.Murmann, W.Poschenrieder, H.Rapp, F.Ryter[1], F.Schneider, G.Siller, P.Smeulders, F.Söldner, E.Speth, A.Stäbler, K.-H.Steuer, Z.Szymanski[1], O.Vollmer and F.Wagner:
Impurity control and heat removal by the ASDEX divertor. Proc. 13th SOFT, Varese 1984, Comm. EC, I.08.

92 Fußmann, G., K.Behringer, E.Taglauer and ASDEX Team:
Impurity investigations in ASDEX. Proc. 2nd European Tokamak Programme Workshop, Saulx-les-Chartreux 1983, CEA, Centre d'Etudes Nucléaires de Fontenay aux Roses 1984, XII/65/84, 152.

93 Fußmann, G., U.Ditte, W.Eckstein, T.Grave, M.Keilhacker, K.McCormick, H.Murmann, H.Röhr, M.ElShaer[1], K.-H.Steuer, Z.Szymanski[1], F.Wagner, G.Becker, K.Bernhardi, A.Eberhagen, O.Gehre, J.Gernhardt, G.v.Gierke, E.Glock, O.Gruber, G.Haas, M.Hesse, G.Janeschitz, F.Karger, S.Kissel[1], O.Klüber, M.Kornherr, G.Lisitano, H.M.Mayer, D.Meisel, E.R.Müller, W.Poschenrieder, F.Ryter[1], H.Rapp, F.Schneider, G.Siller, P.Smeulders, F.Söldner, E.Speth, A.Stäbler and O.Vollmer:
Divertor parameters and divertor operation in ASDEX. 6th Int. Conf. on Plasma Surface Interactions in Contr. Fusion Devices, Nagoya 1984, J. Nucl. Mater. 128 & 129, 350 (1984).

94 Gill, R.D.[1], G.Decker[1], E.Kallne[1], H.Krause, J.O'Rourke[1] and T.E.Stringer[1]:
Soft X-ray measurements on JET.
Bull. Am. Phys. Soc. 29, No. 8, 1305 (1984).

95 Gräff, P. and J.J.Henning:
Pathological aspects of the Hopf-equation. CERNCOR-NUCOR, Pretoria 1984, Report PIN 815 B/R.

96 Grave, T.[1], K.Steinmetz, E.R.Müller, ASDEX Team und NI Team:
Thermographische Messungen des Energieflusses auf die Prallplatten des ASDEX-Divertors.
Verhandl. DPG (VI) 19, P 11 (1984).

97 Grieger, G.:
INTOR und NET - Stand der Entwicklung von Tokamak-Reaktoren. Tagungsbericht Jahrestagung Kerntechnik '84, Fachsitzung Kernphysikalische u. thermodynamische Methoden der Kernauslegung - Kontrollierte Kernfusion, Frankfurt, Deutsches Atomforum, Bonn 1984, 86 ff.

98 Grieger, G.:
Stand und Aussichten der Fusionsforschung. In: Forschung für die Kerntechnik: Die Rolle der Großforschung. Eds. Hans-Henning Hennies, Thomas Roser. Hrsg. BMFT, TÜV Rheinland, Köln, 1984, 194 ff.

99 Grieger, G. and INTOR Group[11]:
The evolution of the INTOR concept. Proc. 10th Int. Conf. on Plasma Physics and Controlled Nuclear Fusion Research, London 1984, IAEA, Vienna, CN/G-II-4.

100 Großmann, R. and J.Nührenberg:
Computational evidence for singular parallel current densities in 3D flux-conserving equilibria. Proc. Int. Conf. on Plasma Physics, Lausanne/ Switzerland 1984, I, 117 P 9-10.

101 Gruber, O.:
Confinement regimes in ohmically and auxiliary heated tokamaks. Proc. (Invited Papers) Int. Conf. on Plasma Physics Lausanne, Switzerland 1984, I, 67.

102 Gruber, O., M.Kaufmann, W.Köppendörfer, K.Lackner and J.Neuhauser:
Physics background of the ASDEX Upgrade project.
J. Nucl. Mater. 121, 407 (1984).

103 Gruber, R.[1], R.Iacono[1], S.Semenzato[1] and H.-P.Zehrfeld:
Finite element methods to calculate ideal magnetohydrodynamic. Proc. (Extended Abstracts) 3rd Int. Conf. on Finite Elements in Nonlinear Mechanics, Stuttgart 1984, Paper VII/3 (to be published in Comp. Methods in Appl. Mechanics and Engineering).

104 Harmeyer, E., J.Kisslinger, F.Rau and H.Wobig:
On modular stellarator coils of the W VII-AS type with reactor dimensions. Proc. 13th SOFT, Varese 1984, Comm. EC, 6P28.

105 Hartfuß, H.J., W VII-A Team[3] and ECRH Team (IPF Stuttgart)[7]:
ECE measurements and power modulation in WENDELSTEIN VII-A. 5th Int. Workshop on Stellarators, Schloß Ringberg/BRD 1984, Proc. IAEA Technical Committee Meeting on Plasma Confinement and Heating in Stellarators, Comm. EC, II, 449.

106 Hartfuß, H.J., W VII-A Team[3] und Neutralinjektionsteam (W VII-A)[5]:
ECE-Messungen mit einem 8-Kanal-Radiometer. Verhandl. DPG (VI) 19, P 204 (1984).

107 Hartfuß, H.J. and M.Tutter:
Minimum noise temperature of a practical SIS quantum mixer. Int. J. of Infrared and Millim. Waves 5, P 717 (1984).

108 Hechtl, E.[1] and J.Bohdansky:
Sputtering behaviour of graphite and molybdenum energies. J. Nucl. Mater. 128 & 129, 1431 (1984).

109 Herrnegger, F.:
Dependence of rotational transform on beta in currentless stellarators - Comparison of stellarators expansion and 3D-code results. 5th Int. Workshop on Stellarators, Schloß Ringberg/BRD 1984, Proc. IAEA Technical Comm. Meeting on Plasma Confinement and Heating in Stellarators, Comm. EC, I, 401.

110 Hertweck, F.:
Using a vector processor in a research environment. Proc. Int. Conf. on Parallel Computing 83, FU Berlin 1983, Eds. M.Feilmeier, J.Joubert, U.Schendel, North-Holland, Amsterdam 1984, 57-66.

111 Jäckel, H., W VII-A Team[3], ECRH Team (IPF Stuttgart)[7] and NI Group (W VII-A)[5]:
Heating facilities in W VII-A/W VII-AS. Proc. U.S.-Japan Stellarator/Heliotron Workshop on Experimental Planning, Oak Ridge 1984, III.

112 Jäckel, H., W VII-A Team[3] and W VII-AS Project Team[10]:
Present status of W VII-A and W VII-AS stellarators. Proc. U.S.-Japan Stellarator/Heliotron Workshop on Experimental Planning, Oak Ridge 1984, II.

113 Jäckel, H. and W VII-A Team[3]:
New diagnostic installations at W VII-A. Proc. U.S.-Japan Stellarator/Heliotron Workshop on Experimental Planning, Oak Ridge 1984, III.

114 Jaenicke, R., W VII-A Team[3] and Neutralinjektionsteam (W VII-A)[5]:
Energy and particle confinement in WENDELSTEIN VII-A: NI Plasma. 5th Int. Workshop on Stellarators, Schloß Ringberg/BRD 1984, Proc. IAEA Technical Committee Meeting on Plasma Confinement and Heating in Stellarators, Comm. EC, I, 219.

115 Janeschitz, G., G.Fußmann, ASDEX-Team[2] und NI-Team (ASDEX)[4]:
Plasmaverunreinigungen in ASDEX-Entladungen mit Neutralinjektionsheizung. Verhandl. DPG (VI) 19, P6, 1984.

116 Junker, J., W VII-A Team[3] and Neutralinjektionsteam (W VII-A)[5]:
Ion heating and orbit losses in NI experiments on WENDELSTEIN VII-A. 5th Int. Workshop on Stellarators, Schloß Ringberg/BRD 1984, Proc. IAEA Technical Committee Meeting on Plasma Confinement and Heating in Stellarators, Comm. EC, I, 179.

117 Junker, J., W VII-A Team[3] and Neutralinjektionsteam (W VII-A)[5]: Ionenheizung im W VII-A Stellarator. Verhandl. DPG (VI) 19, P 1203 (1984).

118 Kaleck, A.[1] und H.-P.Zehrfeld: Zweidimensionale Plasmabewegungen im Tokamak. Verhandl. DPG (VI) 19, 1239 (1984).

119 Kaufmann, M., K.Lackner, L.Lengyel und W.Schneider: Die Erwärmung der Kaltgaswolke bei Pelletinjektion. Verhandl. DPG (VI) 19, 1210 (1984).

120 Kaufmann, M., K.Lackner und J.Neuhauser: Heliumpumpen und Pelletinjektion. Verhandl. DPG (VI) 19, 1210 (1984).

121 Kaufmann, M. und K.Lackner: Divertor-Konzept gegen Plasma-Verunreinigungen. Spektrum der Wissenschaft, August 1984, S.14.

122 Keilhacker, M., G.Fußmann, G.v.Gierke, G.Janeschitz, M.Kornherr, K.Lackner, E.R.Müller, P.Smeulders, F.Wagner, G.Becker, K.Bernhardi, U.Ditte, A.Eberhagen, O.Gehre, J.Gernhardt, E.Glock, T.Grave, O.Gruber, G.Haas, M.Hesse[1], F.Karger, S.Kissel[1], O.Klüber, G.Lisitano, H.M.Mayer, K.McCormick, D.Meisel, V.Mertens, H.Murmann, H.Niedermeyer, W.Poschenrieder, H.Rapp, F.Ryter[1], F.Schneider, G.Siller, F.Söldner, E.Speth, A.Stäbler, K.-H.Steuer and O.Vollmer: Confinement and beta-limit studies in ASDEX H-mode discharges. Proc. 10th Int. Conf. on Plasma Physics and Contr. Nucl. Fus. Research, London 1984, Nucl.Fus., Supplement 1, 71 (1985).

123 Kerner, W. and H.Weitzner[1]: Axisymmetric, non-ideal MHD states with steady flow. Comput. Phys. Comm. 31, 249 (1984).

124 Kerner, W. and H.Weitzner[1]: Neoclassical tokamak transport with toroidal flow. Proc. Sherwood Theory Conf., Incline Village/Nevada 1984, paper 2P8.

125 Kerner, W. and K.Lerbinger: The resistive MHD spectrum. Proc. Int. Conf. on Plasma Physics, Lausanne/Switzerland, 1984, paper P16-6.

126 Kerner, W. and O.Jandl: Axisymmetric MHD equilibria with flow. Comput. Phys. Comm. 31, 269 (1984).

127 Kissel, S.E.[1] and A.Eberhagen: Calibration of ECE Diagnostics. Proc. 4th Int. Symp. on ECE and ECR, Rom 1984, C19.

128 Knobloch, A.F.: Technical benefit. INTOR Phase IIA. (Draft EC report). Europ. Contributions to the 10th Workshop-Meeting, Vienna, Comm. EC, Brussels 1984, II, Group E, EURFUBRU/XII-1/84/EDV30.

129 Knobloch, A.F.: Technical benefit. INTOR Phase IIA. Europ. Contributions to the 9th Workshop-Meeting, Vienna, Comm. EC, Brussels 1984, II, Group E, EURFUBRU/XII-1/84/EDV20.

130 Knobloch, A.F. and G.Grieger: Technical benefit of partitioning INTOR design, production, and assembly between four nations. INTOR Phase IIA. Europ. Contributions to the 8th Workshop-Meeting,Vienna, Comm. EC , Brussels 1984, Group E, EURFUBRU/XII-1/84/EDV10.

131 Koch, A.W.[1], A.W.Nürnberg[1] and R.Behrisch: Investigation of vacuum arcs on graphite cathodes. J. Nucl. Mat. 128 & 129, 1437 (1984).

132 Köppendörfer, W.: ASDEX Upgrade, ein Reaktorbedingungen angepaßtes Divertor-Tokamakexperiment. Tagungsbericht Jahrestagung Kerntechnik, Frankfurt 1984, Deutsches Atomforum, Bonn 1984, 633-636.

133 Köppendörfer, W. and ASDEX Upgrade Design Team[6]: Status and Progress of ASDEX Upgrade. Proc. 13th SOFT, Varese 1984, Comm. EC, O.08.

134 Kornherr, M., ASDEX-Team[2] und NI-Team (ASDEX)[4]: Strahlungsprofile des Röntgenlichts und MHD-Studien an ASDEX. Verhandl. DPG (VI) 19, P101, 1984.

135 Kotzlowski, H.: Actively cooled graphite limiter. Proc. 13th SOFT, Varese 1984, Comm. EC, 5P06.

136 Krause, H., F.K.Mast, K.Behringer[1], J.Bonnerue[1], A. Buillard[1], W.Engelhardt, A.Gondhalekar[1], R.Grill[1] und J.O'Rourke[1]: Breitband Strahlungsmessungen an JET. Verhandl. DPG (VI) 19, 1196 (1984).

137 Kühner, G., W VII-A Team[3] and NI Group (W VII-A)[5]: Bolometry in WENDELSTEIN VII-A. 5th Int. Workshop on Stellarators, Schloß Ringberg/BRD 1984, Proc. IAEA Technical Committee Meeting on Plasma Confinement and Heating in Stellarators, Comm. EC, II, 427.

138 Lackner, K., R.Chodura, M.Kaufmann, J.Neuhauser, K.-G.Rauh and W.Schneider: Control of particle and energy transport across the boundary of a tokamak plasma. Plasma Phys. and Contr. Fusion 26, 105 (1984).

139 Lackner, K., U.Ditte, G.Fußmann, T.Grave, G.Janeschitz, M.Keilhacker, H.Murmann, J.Neuhauser, W.Poschenrieder, W.Schneider, K.-H.Steuer, G.Becker, K.Bernhardi, B.Braams[1)], R.Chodura, A.Eberhagen, O.Gehre, J.Gernhardt, G.v.Gierke, E.Glock, O.Gruber, G.Haas, D.Heifetz[1)], M.Hesse[1)], F.Karger, M.Kaufmann, S.Kissel[1)]. O.Klüber, M.Kornherr, G.Lisitano, H.-M.Mayer, K.McCormick, D.Meisel, V.Mertens, E.R.Müller, K.-G.Rauh, H.Röhr, F.Ryter[1)], G.Siller, P.Smeulders, F.Söldner, E.Speth, O.Vollmer, F.Wagner and R.Wunderlich: Experimental and theoretical investigation of the ASDEX divertor scrape-off layer. Proc. 10th Int. conf. on Plasma Phys. and Contr. Nucl. Fusion Res., London 1984, IAEA-CN-44/A-V-4.

140 Lackner, K. and M.Keilhacker: Divertor physics: Summary of modelling and experiments. 6th Int. Conf. on Plasma Surface Interactions in Contr. Fusion Devices, Nagoya 1984, J. Nucl.Mater.128&129, 368 (1984).

141 Lengyel, L.L., H.Brinkschulte and I.Bozsik[1)]: Laser pellet plasmas for filling magnetic confinement configurations. Laser Interac. and Related Plasma Phenomena 6, 369 (1984).

142 Leuterer, F., F.Söldner, K.Bernhardi, M.Brambilla, A.Eberhagen, D.Eckhartt, O.Gehre, J.Gernhardt, M.Hesse[1)], M.Keilhacker, S.Kissel[1)], M.Kornherr, E.R.Müller, M.Münich, F.Ryter[1)], P.Smeulders, M.Zouhar, G.Becker, H.Brinkschulte, H.Derfler, U.Ditte, M.ElShaer[1)], G.Fußmann, G.v.Gierke, E.Glock, O.Gruber, G.Haas, A.Izvoztchikov[1)], H.M.Meyer, K.McCormick, R.Magne[1)], D.Meisel, H.Murmann, W.Poschenrieder, H.Rapp, K.-H.Schmitter, F.Schneider, G.Siller, K.-H.Steuer, Z.Szymanski[1)], G.Venus, T.Vien, F.Wagner and F.v.Woyna: Lower hybrid heating and current drive experiments in ASDEX. Proc. 10th Int. Conf. on Plasma Physics and Contr. Nucl. Fusion Res., London 1984, Nucl. Fus., Supplement 1, 597 (1985).

143 Leuterer, F. and LH Group[9)]: Teststand experiments for the Lower Hybrid Heating in ASDEX. Proc. 4th Int. Symp.on Heating in Toroidal Plasmas, Eds. H.Knoepfel, E.Sidoni, Rom 1984, EUR 9341 EN, II, 1293-1299.

144 Liebl, H.: High-resolution scanning ion microscopy and secondary-ion mass spectrometry: Problems and solutions. Scanning Electron Microsc. II, 519, (1984).

145 Lisitano, G.: Antennamare. A method of radio-frequency conditioning of fusion plasma for both linear and toroidal magnetic traps. Proc. Workshop on Mirror-Based and Field-Reversed Approaches to Magnetic Fusion, Varenna 1983, 229.

146 Lortz, D., R.Meyer-Spasche, and E.Stredulinsky: Asymptotic behaviour of the solutions of certain parabolic equations. Comm. Pure Appl. Math. 37, 677 (1984).

147 Lortz, D. and G.O.Spies: Spectrum of a resistive plasma slab. Phys. Lett. 101A, 335 (1984).

148 Lotz, W.: Monte Carlo simulation of neoclassical transport in stellarator vacuum fields. 5th Int. Workshop on Stellarators, Schloß Ringberg/BRD 1984, Proc. IAEA Technical Comm. Meeting on Plasma Confinement and Heating in Stellarators, Comm. EC, II, 493.

149 Maaßberg, H.: A model of plasma cloud expansion generated by a dust particle impact. The Giotto Spacecraft Impact - Induced Plasma Environment, ESA SP-224, 59 (1984).

150 Maaßberg, H.: Electrostatic charging of the giotto spacecraft due to neutral gas impact. The Giotto Spacecraft Impact - Induced Plasma Environment, ESA SP-224, 55 (1984).

151 Maaßberg, H.: Slowing down of neutral injected particles and heating efficiency in Wendelstein VII-A. 5th Int. Workshop on Stellarators, Schloß Ringberg/BRD 1984, Proc. IAEA Technical Committee Meeting on Plasma Confinement and Heating in Stellarators, Comm. EC, II, 507.

152 Maaßberg, H. and M.A.Hellberg[1)]: Ion cyclotron modes driven by perpendicular neutral injection. Proc. (Contributed papers) Int. Conf. on Plasma Physics, Lausanne 1984, P 55.

153 Maaßberg, H. und M.A.Hellberg[1)]: NI-getriebene Ionenzyklotron-Moden in W VII-A. Verhandl. DPG (VI) 19, P 1205 (1984).

154 Mahn, C. und W VII-A Team[3)]: Streung von CO_2-Laser-Strahlung an Fluktuationen im Stellarator-Plasma. Verhandl. DPG (VI) 19, P 1203 (1984).

155 Martinelli, A.P., J.Roth and ASDEX Team: Plasma ion fluxes in the ASDEX edge plasma during neutral beam heated discharges. J. Nucl. Mat. 128 & 129, 225 (1984).

156 Mast, F.K., H.Krause, K.Behringer[1)], A.Bulliard[1)] and G.Magyar[1)]:

Bolometric diagnostics in JET. Proc. 5th Top. Conf. on High Temp. Plasma Diagn., Tahoe/USA 1984 (to be published in Review Scientific Instruments).

157 McCormick, K., ASDEX-Team[2] und NI-Team (ASDEX)[4]:
Die zeitliche Entwicklung des Randschicht-Dichteprofils an ASDEX.
Verhandl. DPG (VI) 19, P24, 1984.

158 McCormick, K.:
Dichteprofilmessungen im niedrig-Dichtebereich mittels eines hochenergetischen Lithiumstrahls.
Verhandl. DPG (VI) 19, P103 (1984).

159 McCormick, K.:
Measurement of the scrape-off layer density profile on ASDEX via an energetic neutral lithium beam. Proc. 5th Topical Con. on High Temperature Plasma Diagnostics, Tahoe City/USA 1984 (to be published in Rev. of Scientific Instruments).

160 Merkel, P.:
An integral equation technique for the exterior and interior Neumann problem in toroidal regions.
5th Int. Workshop on Stellarators, Schloß Ringberg/BRD 1984, Proc. IAEA Technical Comm. Meeting on Plasma Confinement and Heating in Stellarators, Comm. EC, I, 387.

161 Merkel, P. and J.Nührenberg:
HASE - a quasi-analytical 2D MHD equlibria code.
Computer Phys. Comm. 31, 115 (1984).

162 Meservey, E.[1], G.Siller, U.Ditte, ASDEX-Team[2] and NI-Team (ASDEX)[4]:
Probe and microwave measurements of n_e and T_e in the ASDEX divertor plasma. Verhandl. DPG (VI) 19, P8. 1984.

163 Möller, W., K.G.Rauh, W.Schneider und H.Vernickel:
Einfluß von Recycling und Reemission auf Divertorplasmen. Verhandl. DPG (VI) 19, 1209 (1984).

164 Möller, W. and W.Eckstein:
TRIDYN - a TRIM simulation code including dynamic composition changes. Nucl. Instr. & Methods in Phys. Research B 2, 814 (1984).

165 Morrison, P.J., I.L.Caldas and H.Tasso:
Hamiltonian formulation and two-dimensional gyroviscos MHD. Z. Naturforsch. 39a, 1023 (1984).

166 Mühling, E., U.Schumacher and H.G.Paretzke[1]:
Thermonuclear fusion product diagnostics by nuclear track detectors. Nucl. Tracks 9, 113 (1984).

167 Mühling, E., W.Eckstein und H.Verbeek:
ISS und IDS - zwei sich ergänzende Oberflächenmethoden. Verhandl. DPG (VI) 19, 345 (1984).

168 Mukherjee, S.B., W.Dänner and G.Vieider[1]:
2D-finite element stress analysis of NET first wall designs. Proc. 13th SOFT, Varese 1984, Comm. EC, 1P26.

169 Mukherjee, S., H.Gorenflo and E.Springmann:
Support optimization of nonplanar magnetic coils for fusion experiments. Proc. 4th World Congress nd Exhibition on Finite Element Methods, Interlaken 1984 (to be published in Finite Element News).

170 Müller, E.R., M.Keilhacker, K.Steinmetz, ASDEX Team and NI Teams:
Power balance of neutral-beam heated divertor discharges in the ASDEX tokamak.
J. Nucl. Mater. 121, 138 (1984).

171 Müller, E.R. and F.K.Mast:
A new metal resistor bolometer for measuring vacuum ultraviolet and soft X radiation. J. Appl. Phys. 55, (7), 2635 (1984).

172 Müller, G., W VII-A Team[3], NI Group (W VII-A)[5], ICRH Team[8] and ECRH Team (IPF Stuttgart)[7]:
Fluctuation measurements in Wendelstein VII-A. 5th Int. Workshop on Stellarators, Schloß Ringberg/BRD 1984, Proc. IAEA Technical Committee Meeting on Plasma Confinement and Heating in Stellarators, Comm. EC, II, 437.

173 Müller, G., W VII-A Team[3] und Neutralinjektionsteam (W VII-A)[5]:
Neuere Meßergebnisse zu Plasmafluktuationen im W VII-A Stellarator. Verhandl. DPG (VI) 19, P 1204 (1984).

174 Münich, M.J. and LH Group[9]:
The Lower Hybrid rf heating system for the ASDEX tokamak. Proc. 4th Int. Symp.on Heating in Toroidal Plasmas, Eds. H.Knoepfel, E.Sidoni, Rom 1984, EUR 9341 EN, II, 1183-1190.

175 Murmann, H., M.Kornherr, ASDEX-Team[2] und NI-Team (ASDEX)[4]:
Entwicklung der Elektronentemperatur und Wärmeleitung am Plasmarand. Verhandl. DPG (VI) 19, P25, 1984.

176 Neuhauser, J., W.Schneider, R.Wunderlich and K.Lackner:
Modelling of impurity flow in the tokamak scrape-off layer. Nucl. Fusion 24, 39 (1984).

177 Neuhauser, J., W.Schneider, R.Wunderlich and K.Lackner:
Modelling of the impurity pumping by a tokamak scrape-off layer. J. Nucl. Mater. 121, 194 (1984).

178 Neuhauser, J. and ASDEX Upgrade Design Team[6]:
Power Handling in the ASDEX Upgrade Divertor Experiment. Proc. 4th Int. Symp. on Heating in Toroid. Plasmas, Eds. H.Knoepfel, E.Sidoni, Rom 1984, EUR 9341 EN, II, 1365.

179 Niedermeyer, H. and ASDEX Team:
Density disruptions in ASDEX. Proc. 2nd European Tokamak Programme Workshop, Saulx-les-Chartreux 1983, CEA, Centre d'Etudes Nucléaires de Fontenay aux Roses 1984, XII/65/84, 35.

180 Noterdaeme, J.-M., F.Braun and M.Söll:
Innovative designs for long pulse ICRH antennae.
Proc. 4th Int. Symp.on Heating in Toroidal Plasmas, Eds. H.Knoepfel, E.Sidoni, Rom 1984, EUR 9341 EN, II, 1109.

181 Nührenberg, J. and R.Großmann:
Resistive interchange instability in 3D code stellarator equilibria. Proc. Sherwood Theory Conf., Incline Village/USA 1984, 2RG.

182 Nührenberg, J. and R.Zille:
Mercier and resistive interchange instabilities in 3D code stellarator equilibria. 5th Int. Workshop on Stellarators, Schloß Ringberg/BRD 1984, Proc. IAEA Technical Comm. Meeting on Plasma Confinement and Heating in Stellarators, Comm. EC, I, 339.

183 Onsgaard, J.[1] and E.Taglauer:
Depth profiling of thin films of Ag and Au on Mo deposited on a quartz crystal microbalance.
J. Vacuum 34, 831 (1984).

184 Penningsfeld, F.-P., G.G.Lister, W.Ott and E.Speth:
Deposition of neutral beam impurities in the stellarators W VII-A and W VII-AS. Proc. 4th Int. Symp.on Heating in Toroidal Plasmas, Eds. H.Knoepfel, E.Sidoni, Rom 1984, EUR 9341 EN, 89.

185 Pfirsch, D.:
New variational formulation of Maxwell-Vlasov and guiding center theories. Local charge and energy conservation laws. Z. Naturforsch. 39a, 1 (1984)

186 Pfirsch, D. and K.-H.Schmitter:
Some critical observations on the prospects of fusion power. Bull. Am. Phys. Soc. 29, 8, 1286 (1984).

187 Pfirsch, D. and K.-H.Schmitter:
Some critical observations on the prospects of fusion power. 4th Int. Conf. on Energy Options - The Role of Alternative in the World Energy Scene, London 1984, IEE Conf. Publ. No. 233.

188 Pillsticker, M. and F.Werner:
Aspects for optimization of the ASDEX Upgrade OH-system. Proc. 13th SOFT, Varese 1984, Comm. EC, 6P20.

189 Preis, H. and H.-P.Zehrfeld:
Modelling of plasma dynamics in conducting shells.
Proc. 13th SOFT, Varese 1984, Comm. EC, 2P02.

190 Presinger, D., W.Möller und B.M.U.Scherzer:
Reemission implantierter Deuterium-Atome von Nickel-Oberflächen. Verhandl. DPG (VI), 19, 297 (1984).

191 Puri, S.:
Self-Consistent analytic periodic-loop-antenna theory. Physics of Fluids 27, 2156 (1984).

192 Rau, F., E.Harmeyer, J.Kisslinger and H.Wobig:
On modular stellarator reactor coils. 5th Int. Workshop on Stellarators, Schloß Ringberg/BRD 1984, Proc. IAEA Technical Committee Meeting on Plasma Confinement and Heating in Stellarators, Comm. EC, II, 763.

193 Rau, F., J.Kisslinger, H.Wobig und W VII-A Team[3]:
Über rationale t-Werte im Vakuumfeld des Stellarators W VII-A. Verhandl. DPG (VI) 19, P 1234 (1984).

194 Rau, F. and G.G.Leotta[1]:
5th Int. Workshop on Stellarators, Schloß Ringberg/BRD 1984, Proc. IAEA Technical Committee Meeting on Plasma Confinement and Heating in Stellarators, Comm. EC, EUR 9618 EN.

195 Rebut, D.V.[1] et al: (from IPP: R.Behrisch, H.Krause, F.K.Mast, H.Niedermeyer):
First experiments in JET. Proc. 10th Int.Conf. on Plasma Physics in Contr. Nucl. Fusion Research, London 1984, IAEA-CN 44/A-I-1.

196 Renner, H., W VII-A Team[3], ECRH Team (IPF Stuttgart)[7] and NI Group (W VII-A)[5]:
Heating in WENDELSTEIN VII-AS. 5th Int. Workshop on Stellarators, Schloß Ringberg/BRD 1984, Proc. IAEA Technical Committee Meeting on Plasma Confinement and Heating in Stellarators, Comm. EC, II, 625.

197 Renner, H., W VII-A Team[3], NI Group (W VII-A)[5], ICRH Team[8] and ECRH Team (IPF Stuttgart)[7]:
Status of WENDELSTEIN VII-A. 5th Int. Workshop on Stellarators, Schloß Ringberg/BRD 1984, Proc. IAEA Technical Committee Meeting on Plasma Confinement and Heating in Stellarators, Comm. EC, I, 79.

198 Renner, H., W VII-A Team[3], NI Group (W VII-A)[5] and Pellet Injection Group (K.Büchl):
Plasma confinement and the effect of rotational transform in the WENDELSTEIN VII-A stellarator. Proc. 10th Int. Conf. on Plasma Physics and Contr. Nucl. Fus. Res., London 1984, IAEA, Vienna, CN-44/D-I-1.

199 Ringler, H., S.Marlier, W VII-A Team[3] und Neutralinjektionsteam (W VII-A)[5]:
Messung von zerstäubten Eisenatomen durch Laser-induzierte Fluoreszenz im W VII-A Stellarator. Verhandl. DPG (VI) 19, P 1235 (1984).

200 Roberto, J.[1], J.Roth, E.Taglauer and O.Holland[1]:
The use of isotopically-enriched carbon probes for erosion/deposition measurements in the ASDEX-Divertor. J. Nucl. Mater. 128 & 129, 244 (1984).

201 Roberto, J.[1] and R.Behrisch:
Synergistic effects in plasma-surface interactions.
J. Nucl. Mater. 128 & 129, 764 (1984).

202 Röhr, H., K.-H.Steuer, ASDEX-Team[2] und NI-Team (ASDEX)[4]:
Thomsonstreuung vor den Divertorplatten in ASDEX. Verhandl. DPG (VI) 19, P10, 1984.

203 Roth, J.:
Chemical effects in sputtering. Nucl. Fusion, Special Issue: Data Compendium for Plasma Surface Interactions, 72 (1984).

204 Roth, J., J.Bohdansky and J.Roberto[1]:
On the influence of impurities on the high temperatured sputtering yield of graphite.
J. Nucl. Mat. 128 & 129, 534 (1984).

205 Roth, J., J.Roberto[1] and K.L.Wilson[1]:
Enhanced sputtering of graphite at high temperature. J. Nucl. Mater. 128 & 129, 1347 (1984).

206 Roth, J. and W.Möller:
Mechanisms of the enhanced sputtering yield of carbon at temperatures above 1200°C.
Nucl. Instr. Meth. B3, 122 (1984).

207 Ruhs, N., H.Hohenöcker and D.Zimmermann:
Distributed processing in the ASDEX data acquisition system. Proc. 13th SOFT, Varese 1984, Comm. EC, 4P46.

208 Salat, A.:
Integrability of non-KAM Hamiltonians.
Z. Naturforsch. 39a, 830 (1984).

209 Sapper, J.:
Technical progress report on W VII-AS. 5th Int. Workshop on Stellarators, Schloß Ringberg/BRD 1984, Proc. IAEA Technical Committee Meeting on Plasma Confinement and Heating in Stellarators, Comm. EC, II, 643.

210 Sardei, F., W VII-A Team[3] and NI Group (W VII-A)[5]:
Impurity transport studies in WENDELSTEIN VII-A. 5th Int. Workshop on Stellarators, Schloß Ringberg/BRD 1984, Proc. IAEA Technical Committee Meeting on Plasma Confinement and Heating in Stellarators, Comm. EC, I, 259.

211 Schneider, P.-J., J.-H.Feist and P.Mikolajczak[1]:
Calculations for the reflection magnet for the ASDEX long pulse neutral injection beamline.
Proc. 10th Symp. on Fusion Engineering, Philadelphia/USA 1983, 530.

212 Schneider, P.J., W.Eckstein and H.Verbeek:
Energy distribution of oxygen desorbed from a nickel surface through ion bombardment: Comparison of computer simulation with experiment.
Nucl. Instr. Meth. in Phys. Research B2, 655 (1984).

213 Schneider, P.J., W.Eckstein and H.Verbeek:
Trajectory effects in the negative charge-state fraction of ^{3}He and ^{4}He reflected from a sodium target. Nucl. Instr. & Methods in Physics Research B2, 525 (1984).

214 Schneider, W., D.B. Heifetz[1], K.Lackner, J.Neuhauser, D.Post[1] and K.G. Rauh:
Modelling of the ASDEX scrape-off and divertor.
J. Nucl. Mater. 121, 178 (1984).

215 Schwenn, U.:
Convergence and extrapolation studies with the FIT 3D code. 5th Int. Workshop on Stellarators, Schloß Ringberg/BRD 1984, Proc. IAEA Technical Comm. Meetingon Plasma Confinement and Heating in Stellarators, Comm. EC, I, 377.

216 Schwenn, U.:
Fourier versus difference methods in computing three-dimensional MHD equilibria.
Computer Phys. Comm. 31, 167 (1984).

217 Semenzato, S.[1], R.Gruber[1], F.Troyon[1] and H.-P.Zehrfeld :
Influence of a stationary flow on tokamak equilibria. Proc. (Contr. Papers) Int. Conf. on Plasma Physics, Lausanne/Switzerland 1984, I, 109.

218 Singer, C.E.[1] and B.Braams[1]:
Low temperature plasma near a limiter - a solution for the tokamak fusion core experiment. Applied Phys. Div., PPPL/USA 1984, Rep. No. 30.

219 Singer, C.E.[1] and B.Braams[1]:
Low temperature plasma near a limiter.
Bull. Am. Phys. Soc. 29, 1246 (1984).

220 Smeulders, P., M.Kornherr, E.R.Müller, G.Fußmann, G.Janeschitz, G.Becker, K.Bernhardi, H.Brocken, U.Ditte, A.Eberhagen, O.Gehre, J.Gernhardt,

G.v.Gierke, E.Glock, T.Grave, O.Gruber, G.Haas, M.Hesse[1], F.Karger, M.Keilhacker, S.Kissel[1], O.Klüber, K.Lackner, G.Lisitano, G.G.Lister[1], H.M.Mayer, K.McCormick, D.Meisel, V.Mertens, H.Murmann, W.Poschenrieder, H.Rapp, H.Röhr, F.Ryter[1], G.Siller, F.Söldner, E.Speth, A.Stäbler, K.-H.Steuer, Z.Szymanski[1], O.Vollmer and F.Wagner: Radiation characteristics of H-discharges in ASDEX. Proc. 10th Int. Conf. on Plasma Physics and Contr. Nucl. Fus. Res., London 1984, IAEA, Vienna.

221 Speth, E., J.-H.Feist, J.Kolos und G.Wulff: Entwicklung wassergekühlter Gitter für Neutralinjektion mit langen Pulsen. Tagungsbericht Jahrestagung Kerntechnik, Frankfurt 1984, Deutsches Atomforum, Bonn 1984, ISSN 0720-9207, 641.

222 Stäbler, A., F.Wagner, G.Becker, K.Bernhardi, U.Ditte, A.Eberhagen, G.Fußmann, O.Gehre, J.Gernhardt, G.v.Gierke, E.Glock, T.Grave, O.Gruber, G.Haas, M.Hesse[1], G.Janeschitz, K.Karger, M.Keilhacker, S.Kissel[1], O.Klüber, M.Kornherr, K.Lackner, G.Lisitano, G.G.Lister[1], H.M.Mayer, K.McCormick, D.Meisel, V.Mertens, E.R.Müller, H.Murmann, W.Poschenrieder, H.Rapp, H.Röhr, F.Ryter[1], G.Siller, P.Smeulders, F.Söldner, E.Speth, K.-H.Steuer, Z.Szymanski[1] and O.Vollmer: Energy confinement scaling of ASDEX L- und H-discharges. Proc. 4th Int. Symp. on Heating in Toroidal Plasmas, Eds. H.Knoepfel and H.Sindoni, Rom 1984, EUR 9341 EN, 1, 3.

223 Staudenmaier, G.: Neue Erosionsmessungen an Limiter und Wand. Verhandl. DPG (VI) 19, 50 (1984).

224 Steininger, H.[1], B.Willerding[1], K.Snowdon[1], N.H.Tolk[1] and W.Eckstein: Light emission from hydrogen copper interaction at grazing incidence. Nucl. Instr. & Methods, Phys. Research B2, 484 (1984).

225 Streibl, B., O.Jandl and R.Pöhlchen: Fabrication of the ASDEX Upgrade toroidal field coils - results of manufacturing tests. Proc. 13th SOFT, Varese 1984, Comm. EC, 6P05.

226 Szymanski, Z.[1], G.Fußmann, ASDEX-Team[2] und NI-Team (ASDEX)[4]: Spektroskopische Untersuchungen im Divertorraum. Verhandl. DPG (VI) 19, P9, 1984.

227 Taglauer, E.: Desorption. Nucl. Fusion, Special Issue: Data Compendium for Plasma Surface Interactions 72 (1984).

228 Taglauer, E.: Edge plasma experiments and material surface effects. J. Nucl. Mat. 128 & 129, 141 (1984).

229 Taglauer, E. and J.Onsgaard[1]: Depth profiling of very thin films deposited on a quartz crystal microbalance. Proc. 6th Int. Conf. on thin films, Stockholm, Swedish Vac. Soc., 1984, 214.

230 Tasso, H.: On the fluctuations spectrum of inhomogeneous plasmas and fluids. Phys. Lett. 102A, 200 (1984).

231 Tasso, H. and I.L.Caldas: Fluctuations spectrum for linear gyroviscous MHD. Phys. Lett. 104A, 423 (1984).

232 Tasso, H. and I.L.Caldas: Variational formulation for two-fluid plasmas in Clebsch variables. Z. Naturforsch. 39a, 9 (1984).

233 Tendler, M.[1], J.Neuhauser and R.Wunderlich: Simulation of the oxygen transport at the periphery in a tokamak. Nucl. Fus. 24, 989 (1984).

234 Thomas, P.R.[1] et al. (from IPP: F.K.Mast, H.Niedermeyer): MHD behaviour and discharge optimisation in JET. Proc. 10th Int. Conf. on Plasma Physics and Controlled Nuclear Fusion Research, London 1984, IAEA, Vienna.

235 Tutter, M., H.J.Hartfuß, W VII-A Team[3] and NI Group (W VII-A)[5]: Effect of suprathermal electrons on ECE-spectra in W VII-A. 4th Int. Workshop on Electron Cyclotron Emission and Electron Cyclotron Resonance Heating, Rom 1984.

236 Tutter, M., W VII-A Team[3] und Neutralinjektionsteam (W VII-A)[5]: Einfluß überthermischer Elektronen auf Elektronenzyklotron-Emissionsspektren. Verhandl. DPG (VI) 1248, P 204 (1984).

237 Varga, P.[1] and E.Taglauer: Depth profiling of the altered layer in Ta_2O_5 produced by sputtering with He ions. J. Nucl. Instr. & Methods in Phys. Research B2, 800 (1984).

238 Verbeek, H., W.Eckstein and P.J.Schneider: The negative fraction of deuterium and helium scattered from a sodium surface. Proc. AIP Conf. No. 111, 3rd Int. Symp. on the Production and Neutralization of Negative Ions and Beams, Brookhaven/USA 1984, 273.

239 Verbeek, H. und W.Eckstein: Messung des langsamen Neutralteilchenflusses auf die Wand von ASDEX. Verhandl. DPG (VI) 19, 1207 (1984).

240 Vernickel, H., M.Blaumoser, K.Ennen, J.Gruber, O.Gruber, O.Jandl, M.Kaufmann, H.Kollotzek, W.Köppendörfer, H.Kotzlowski, E.Lackner, K.Lackner, J.Neuhauser, J.-M.Noterdaeme, M.Pillsticker, R.Pöhlchen, H.Preis, K.-G.Rauh, H.Röhr, H.Schneider[1], W.Schneider, U.Seidel, B.Sombach, B.Streibl, G.Venus, F.Wesner and A.Wieczorek:
ASDEX Upgrade: a poloidal divertor tokamak adapted to reactor requirements. J. Nucl. Mater. 128, 71 (1984).

241 Vernickel, H.:
The influence of plasma-induced heating on re-emission of hydrogen from graphite targets.
J. Nucl. Mater. 128, 708 (1984).

242 Vernickel, H., W.Möller, K.-G.Rauh und W.Schneider:
Einfluß von Recycling und Reemission auf Divertorplatten. Verhandl. DPG (VI) 19, 1209 (1984).

243 W VII-A Team[3] and NI Group (W VII-A)[5]:
CO and counter - Injection heating in W VII-A stellarator. Proc. 4th Symp. on Heating in Toroidal Plasmas, Eds. H.Knoepfel, E.Sindoni, Rom 1984, EUR 9341 EN, I, 95.

244 W VII-A Team[3] and NI Group (W VII-A)[5]:
Neutral injection heating of ions and electrons in W VII-A stellarator. Proc. 4th Int. Workshop on Electron Cyclotron Emission and Electron Cyclotron Resonance Heating, Rom 1984.

245 Wagner, F., ASDEX-Team[2] und NI-Team (ASDEX)[4]:
Die Bedeutung des Divertors für das Einschlußverhalten injektionsgeheizter ASDEX-Plasmen. Verhandl. DPG (VI) 19, P13, 1984.

246 Wagner, F., G.Fußmann, T.Grave, M.Keilhacker, M.Kornherr, K.Lackner, K.McCormick, E.R.Müller, A.Stäbler, G.Becker, K.Bernhardi, U.Ditte, A.Eberhagen, O.Gehre, J.Gernhardt, G.v.Gierke, E.Glock, O.Gruber, G.Haas, M.Hesse[1], G.Janeschitz, F.Karger, S.Kissel[1], O.Klüber, G.Lisitano, H.-M.Mayer, D.Meisel, V.Mertens, H.Murmann, W.Poschenrieder, H.Rapp, H.Röhr, F.Ryter[1], F.Schneider, G.Siller, P.Smeulders, F.Söldner, E.Speth, K.H.Steuer, Z.Szymanski[1] and O.Vollmer:
Development of an edge transport barrier at the H-mode transition of ASDEX.
Phys. Rev. Lett. 53, 1453 (1984).

247 Wagner, F. and K.Lackner:
Divertor tokamak experiments. Nato Advanced Study Institutes Programme, Val-Morin/Canada 1984. In: Physics of Plasma-Wall Interactions in Controlled Fusion, Eds. R. Behrisch and D. Post.

248 Wedler, H., R.Fritsch, E.v.Mark und F. Wesner:
ICRH test bed and first experimental results.
Proc. 13th SOFT, Varese 1984, Comm. EC.

249 Weichselgartner, H., A.El-Sharnouby, H.Frischmuth and A.Stimmelmayr:
Tritium operation of a gas chromatographic isotope separation plant - first results.
Proc. 13th SOFT, Varese 1984, Comm. EC, 1P38.

250 Weichselgartner, H.:
Anwendungsorientierte Tritiumtechnologie am IPP. Die Umschau 24, 420 (1984).

251 Weller, A., W VII-A Team[3] and NI Group (W VII-A)[5]:
Impurity Transport in the WENDELSTEIN VII-A Stellarator. Proc. 10th Int. Conf. on Plasma Physics and Contr. Nucl. Fus. Res., London 1984, IAEA, Vienna, CN-44/D-IV-5.

252 Weller, A., W VII-A Team[3] und Neutralinjektionsteam (W VII-A)[5]:
Verunreinigungsstrahlung und -transport im stromfreien Betrieb am W VII-A Stellarator. Verhandl. DPG (VI) 19, P 1196 (1984).

253 Wesner, F., F.Braun, R.Fritsch, F.Hofmeister, E.v.Mark, J.-M.Noterdaeme, S.Puri, M.Söll, K.Steinmetz and H.Wedler:
ICRH components for ASDEX and W VII.
Proc. 4th Int. Symp.on Heating in Toroidal Plasmas, Eds. H.Knoepfel, E.Sidoni, Rom 1984, EUR 9341 EN, II, 1103.

254 Wesner, F.:
Ion Cyclotron Resonance Heating for ASDEX Upgrade.
Proc. 4th Int. Symp.on Heating in Toroidal Plasmas, Eds. H.Knoepfel, E.Sidoni, Rom 1984, EUR 9341 EN, II, 1393.

255 Wesner, F. und W.Schminke:
Anordnung zur Hochfrequenzheiung von Plasmen im Bereich der Ionenzyklotron-Resonanzen.
Tagungsbericht Jahrestagung Kerntechnik , Frankfurt 1984, Deutsches Atomforum, Bonn 1984, ISSN 0720-9207, 629.

256 Wilhelm, R.[1], ECRH Team (IPF Stuttgart)[7] and W VII-A Team[3]:
Energy and particle confinement in WENDELSTEIN
VII-A: ECRH plasma. 5th Int. Workshop on Stellarators, Schloß Ringberg/BRD 1984, Proc. IAEA Technical Committee Meeting on Plasma Confinement and Heating in Stellarators, Comm. EC, I, 233.

257 Wilhelm, R.[1], V.Erckmann[1], G.Janzen[1], W.Kasparek[1], G.Müller[1], P.G.Schüller[1], K.Schwörer[1], M.Thumm[1] and W VII-A Team[3]:
Electron cyclotron resonance heating on the W VII-A Stellarator. Proc. Int. Conf. on Plasma Physics, Lausanne/Switzerland 1984.

258 Wimmel, H.K.:
Kinetic guiding-center equations for the theory of drift instabilities and anomalous transport. Physica Scripta 29, 141-145 (1984).

259 Wobig, H., E.Harmeyer, J.Kisslinger and F.Rau:
Configuration studies with respect to Wendelstein VII-X. 5th Int. Workshop on Stellarators, Schloß Ringberg/BRD 1984, Proc. IAEA Technical Committee Meeting on Plasma Confinement and Heating in Stellarators, Comm. EC, II, 749.

260 Wobig, H., E.Harmeyer, J.Kisslinger and F.Rau:
Some aspects of modular stellarator reactors. Proc. 10th Int. Conf. on Plasma Physics in Contr. Nucl. Fusion Research, London 1984, IAEA-CN 44/H-II-4.

261 Wobig, H.:
Plasma behaviour at rational rotational transform in Wendelstein VII-A. 5th Int. Workshop on Stellarators, Schloß Ringberg/BRD 1984, Proc. IAEA Technical Committee Meeting on Plasma Confinement and Heating in Stellarators, Comm. EC, I, 363.

262 Wobig, H.:
Status of stellarator research. Proc. Int. Conf. on Plasma Physics, Lausanne /Switzerland 1984.

263 Wobig, H., W VII-A Team[3] und Neutralinjektionsteam (W VII-A)[5]:
Stationäre Konvektion im Stellarator. Verhandl. DPG (VI) 19, P 1234 (1984).

264 Zasche, D., H.-U.Fahrbach and E.Harmeyer:
Front-end data reduction of diagnostic signals by real-time digital filtering. Proc. 13th SOFT, Varese 1984, Comm. EC, 4P27.

265 Zasche, D. und H.-U.Fahrbach:
Röntgendiagnostik für JET.Verhandl. DPG (VI) 19, 1247 (1984).

266 Zehrfeld, H.-P., R.Gruber[1] und S.Semenzato[1]:
Stationäre Strömungen in axialsymmetrischen Plasmen. Verhandl. DPG (VI) 19, 1238 (1984).

267 Zhao, W.H.[1], A.Koch[1], U.H.Bauder[1] and R.Behrisch:
First wall erosion by arcing. J. Nucl. Mater. 128 & 129, 613 (1984)

268 Zimmermann, D.:
Computer communication in control and data acquisition systems for fusion experiments. Proc. 13th SOFT, Varese 1984, Comm. EC, 4P47.

DISSERTATIONEN

269 Becerra-Acevedo, R.:
Untersuchung der räumlichen Winkelverteilung von zerstäubten Atomen bei schrägem Ioneneinfall. Johann-Wolfgang-Goethe-Universität, Frankfurt/Main 1984.

PATENTE

270 Betzler, P. and F.K.Mast:
Strahlungsmeßgerät und unter Verwendung desselben ausgebildetes, aus einem der Strahlung ausgesetzten Meßgerät und einem gegen die Strahlung abgeschirmten Referenzgerät bestehenden Meßsystem. (MO 7924). P 34 08 724.9; angemeldet 9.3.1984.

271 Frischmuth, H., J.Perchermeier, A.Stimmelmayr und H.Weichselgartner:
Auf dem Prinzip der Gaschromatographie arbeitende Einrichtung zum Gewinnen von Wasserstoffisotopen aus einem Gasgemisch. (11307). P 32 44 325.0; offengelegt 30.5.1984.

272 Kotzlowski, H.:
Abschälwerkzeug für Standardbolzen (11537) P 34 02 173.6; angemeldet 23.1.1984.

273 Kotzlowski, H.:
Aktiv gekühlter Hitzeschild. (11571) P 34 16 843.5; angemeldet 7.5.1984.

274 Kotzlowski, H.:
Werkzeug zum Abdrehen eines zylindrischen Werkstücks. (11540) P 34 04 643.7; angemeldet 9.2.1984.

275 Liebl, H.:
Kombinierte elektrostatische Objektiv- und Emissionslinse. (11299) P 32 31 036.6; offengelegt 23.3.1984.

276 Spensberger, W.:
Hohlleiterelement für Mikrowellen (11635) P 34 27 283.6; angemeldet 24.7.1984.

277 Weichselgartner, H.:
Abziehbare Beizfolie. (11654) P 34 46 931.1; angemeldet 21.12.1984.

LABORATORY REPORTS

IPP 1/225 Andelfinger, C., Fink, J., Fußmann, G., Krause, H., Röhr, H., Schilling, H.-B., Schumacher, U., Becker, P.[1)], Siegert, H.[1)], Abel, P.[1)], Keul, J.[1)]: Active Phase Double Crystal Monochromator for JET (Diagnostic System KS1. (1984)

IPP 1/226 Andelfinger, C., Fink, J., Fußmann, G., Krause, H., Röhr, H., Schilling, H.-B., Schumacher, U., Becker, P.[1)], Siegert, H.[1)], Belzig, H.[1)], Berghausen, A.[1)], Veigel, R.[1)], Zech, H.[1)]: Spatial Scan Double Crystal Monochromator for JET (Diagnostic System KS2). (1984)

IPP 1/227 Weichselgartner, H., El-Sharnouby, A.: Untersuchungen zur Beseitigung von Tritium mittels organischer Verbindungen, TROC-Prozeß. Teil 1: Katalytische Hydrierung von Erucasäure. (1984)

IPP 1/228 Braams, B.[1)], Lackner, K.: A proposed method for fast determination of plasma parameters. (1984)

IPP 1/231 Lengyel, L.L.: Assessment of Pellet Injection for NET. Part I: Penetration depth calculations for single pellets on the basis of available ablation models. Part II: Pellet sizes and velocities required for central fueling based on available ablation models: feasibility considerations. (1984)

IPP 1/232 Lengyel, L.L.: Assessment of Pellet Injection for NET. Part III: Uncertainties Inherent in Present Ablation Models. (1984)

IPP 1/233 Lengyel, L.L.: Assessment of Pellet Injection for NET. Part IV: An Estimate of the Effect of Energy carriers other than Thermal Electrons on the Ablation of Pellets in Plasmas. (1984)

IPP 1/234 El-Sharnouby, A., Weichselgartner, H.: Investigation of Tritium Removal by means of Organic Compounds. Catalytic Hydrogenation (Tritiation) of Linoleic Acid. (1984)

IPP 1/299 Brederlow, G.[1)], Gruber, J., Hirsch, K.[1)], Röhr, H., Salzmann, H.[1)], Witte, K.J.[1)]: JET Art. 14-Contract JE 3/9009 "Lidar-Thomson Scattering" Final Report. (1984) (IPP-JET-Ber. Nr. 25).

IPP 2/271 Mukherjee, S.B.: Ring-Type Support Concept for Twisted Coils (Finite Element Simulation). (1984)

IPP 2/272 Cattanei, G.: The influence of the poloidal magnetic field on mode conversion of the fast magnetoronic Wave in a Two component Toroidal Plasma. (1984)

IPP III/90 Niedermeyer, H., Behringer, K.[1)], Bernhardi, K., Eberhagen, A., Fußmann, G., Gehre, O., Gernhardt, J., Haas, G., Keilhacker, M., Kissel, S.[1)], Kornherr, M., Lisitano, G., Massig, J.H.[1)], McCormick, K., Meisel, D., Müller, E.R., Murmann, H., Neuhauser, J., Poschenrieder, W., Richter, B.[1)], Siller, G., Söldner, F., Steuer, K.-H., Szymanski, Z.[1)]: Change of plasma properties prior to high density disruptions in ASDEX. (1984)

IPP III/91 Khadra, L.: First results of time series analysis of MHD fluctuation in the ASDEX tokamak. (1984)

IPP III/95 Murmann, H., Huang, M.[1)]: Thomson scattering diagnostic in the boundary layer of ASDEX. (1984)

IPP III/96 ElShaer, M.[1)]: Probe measurements in the ASDEX boundary layer and the effect of neutral beam injection and lower hybrid heating. (1984)

IPP III/97 Müller, E.R., Bein, B.K.[1)], Steinmetz, K.: Time and space-resolved energy flux measurements in the divertor of the ASDEX tokamak by computerized infrared thermography. (1984)

IPP III/98 Becker, G., Bernhardi, K., Eberhagen, A., Fußmann, G., Gehre, O., Gernhardt, J., Gierke, v.G., Glock, E., Haas, G., Karger, F., Keilhacker, M., Kissel, S., Klüber, O., Kornherr, M., Lackner, K. Lisitano, G., Mayer, H.M., McCormick, K., Meisel, D., Müller, E.R., Murmann, H., Niedermeyer, H., Poschenrieder, W., Rapp, H., Röhr, H., Schneider, F., Siller, G., Smeulders, P., Söldner, F., Steuer, K.-H., Wagner, F., Lister, G.G., Speth, E., Stäbler, A., Vollmer, O.: Analysis of local transport in neutral-beam-heated L and H Plasmas of ASDEX. (1984)

IPP III/99 Becker, G., Bernhardi, K., Eberhagen, A., Fußmann, G., Gehre, O., Gernhardt, J., Gierke, v.G., Glock, E., Gruber, O., Haas, G., Karger, F., Keilhacker, M., Kissel, S., Klüber, O., Kornherr, M., Lackner, K. Lisitano, G., Mayer, H.M., McCormick, K., Meisel, D., Müller, E.R., Murmann, H., Poschenrieder, W., Rapp, H., Röhr, H., Schneider, F., Siller, G., Smeulders, P., Söldner, F., Steuer, K.-H., Wagner, F., Speth, E., Stäbler, A., Vollmer, O.: Local energy and particle transport in burst-free H-phases of ASDEX. (1984)

IPP 4/215 Söll, M., Springmann ,E.: ICRH Programmes for Antennas and for Plasma Dispersion Relation. (1984)

IPP 4/216 Brambilla, M.: Rayic - A Numerical Code for the Study of Ion Cyclotron Heating of Large Tokamak Plasmas. (1984)
(IPP-JET-18)

IPP 4/217 Brambilla, M.: Ion Cyclotron Heating of the JET Plasma. (1984)
(IPP-JET-22)

IPP 4/218 Zouhar, M.: Beschreibung des Niederleistungsteils des HF-Systems für die LH-Experimente in ASDEX. (1984)

IPP 4/219 Steinmetz, K., Brambilla, M.: Second Harmonic Ion Cyclotron Resonance Heating in ASDEX: Results of Ray Tracing Calculations. (1984)

IPP 6/233 Kaifen, H., Biskamp, D.: Effect of Parallel Ion Motion in Three-drift-wave Interaction. (1984)

IPP 6/234 Harned, D., Kerner, W.: Semi-Implicit Method for Three-Dimensional Compressible MHD Simulation. (1984)

IPP 6/235 Kerner, W., Lerbinger, K., Gruber, R.[1)], Tsunematsu, T.[1)]: Normal Mode Analysis for Linear Resistive Magnetohydrodynamics. (1984)

IPP 6/236 Kerner, W., Lerbinger, K., Steuerwald, J.: Computing Complex Eigenvalues of Large Non-Hermitian Matrices. (1984)

IPP 6/237 Caldas, I.L., Tasso, H.: Fluctuation Spectrum for Linear Gyroviscous MHD. (1984)

IPP 6/238 Salat, A.: Integrability of Non KAM Hamiltonians. (1984)

IPP 6/239 Morrison, P., Caldas, I.L., Tasso, H.: Hamiltonian Formulation of Two-Dimensional Gyroviscous MHD. (1984)

IPP 6/240 Correa-Restrepo, D.: Localized Resistive Modes in the Circular Tokamak. (1984)

IPP 6/241 Biskamp, D., Kaifen, H.: Three-Drift-Wave Interaction at Finite Parallel Wavelength-Bifurcations and Transition to Turbulence. (1984)

IPP 6/242 Lortz, D., Spies, G.: Resistive Spectrum of Configurations without Magnetic Shear. (1984)

IPP 6/243 Canobbio, E., Croci, R.: Ponderomotive LH k-Spectrum Upshift and Production of Fast Particle Tails. (1984)

IPP 6/244 Pfirsch, D., Gräff, P.: Stochastic Runaway of Dynamical Systems. (1984)

IPP 6/245 Pohl, F., Bohdansky, J.: Analytical Approximation Formulae for Hydrogen Diffusion in a Metal Slab. (1984)

IPP 9/48 Bohdansky, J., DeMatteis, A.[1)]: Approximations in modelling of light-ion reflection in numerical simulations planning for calorimetric measurements. (1984)

IPP 9/50 Verbeek, H.: Low energy neutral particle analysis at the ASDEX Tokamak. (1984)

IPP 9/51 Becerra-Acevedo, R.: Untersuchung der räumlichen Winkelverteilung von zerstäubten Atomen bei schrägem Ioneneinfall. (1984)

IPP 9/52 Ehrenberg J., Behrisch R.: Time-resolving collector probes. (1984)

IPP 0/48 Dommaschk, W., Lotz, W., Nührenberg, J.: Detailed Results of Monte Carlo Simulation of Neoclassical Transport in Stellarators. (1984)

IPP-JET-Berichte

Nr. 17 Gruber, J.: Electrical Tests for LIDAR Laser Systems. (1984)

Nr. 18 Brambilla, M.: RAYIC - A Numerical Code for the Study of Ion Cyclotron Heating of Large Tokamak Plasmas. (1984)
(IPP 4/216)

Nr. 19 Andelfinger, C., Fink, J., Fußmann, G., Krause, H., Röhr, H., Schilling, H.-B., Schumacher, U., Becker, P.[1], Siegert, H.[1], Abel, P.[1], Keul, J.[1]: Active Phase Double Crystal Monochromator for JET (Diagnostic System KS1). (1984)

Nr. 20 Andelfinger, C., Fink, J., Fußmann, G., Krause, H., Röhr, H., Schilling, H.-B., Schumacher, U., Becker, P.[1], Siegert, H.[1], Belzig, H.[1], Berghausen, A.[1], Veigel, R.[1], Zech, H.[1]: Spatial Scan Double Crystal Monochromator for JET (Diagnostic System KS2). (1984)

Nr. 21 Bohdansky, J., Chen, C.K.: Sputtering and energy reflection measurements with hydrogen ions on different target materials. (1984)

Nr. 22 Brambilla, M.: Ion Cyclotron Heating of the JET Plasma. (1984)
(IPP 4/217)

Nr. 23 Ehrenberg, J., Behrisch, R.: Surface Analysis of a Central Part of the JET Graphite Limiter. (1984)

Nr. 24 Ehrenberg, J., Bøgesen, P., Dorn, C.: Time-Resolving Collector Probes, Basic Investigations, Design and Construction. (1984)

Nr. 25 Brederlow G.[1], Gruber, J., Hirsch, K.[1], Röhr, H., Salzmann, H.[1], Witte, K.J.[1]: JET Art. 14 - Contract JE 3/9009 "LIDAR-Thomson Scattering" Final Report (1984).
(IPP 1/299)

---

1) No member of Max-Planck-Institut für Plasmaphysik

2) ASDEX-Team: G.Becker, K.Bernhardi, H.Brocken, A.Eberhagen, M.ElShaer, G.Fußmann, O.Gehre, J.Gernhardt, G.v.Gierke, E.Glock, T.Grave, O.Gruber, G.Haas, M.Hesse, G.Janeschitz, F.Karger, M.Keilhacker, S.Kissel, O.Klüber, M.Kornherr, G.Lisitano, H.M.Mayer, K.McCormick, D.Meisel, V.Mertens, E.Meservey, F.Söldner, K.-H.Steuer, Z.Szymanski, G.Venus, F.Wagner

3) W VII-A Team: G.Cattanei, D.Dorst, A.Elsner, V. Erckmann, G.Grieger, P.Grigull, H.Hacker, H.J.Hartfuß, H.Jäckel, R.Jaenicke, J.Junker, M.Kick, H.Kroiss, G.Kuehner, H.Maaßberg, C.Mahn, S.Marlier, G.Müller, W.Ohlendorf, F.Rau, H.Renner, H.Ringler, F.Sardei, M.Tutter, A.Weller, H.Wobig, E.Würsching, M.Zippe

4) NI-Team (ASDEX):
G.G.Lister, E.Speth, A.Stäbler, O.Vollmer

5) NI Group (W VII-A):
K.Freudenberger, W.Ott, F.-P.Penningsfeld, E.Speth

6) ASDEX Upgrade Design Team:
M.Blaumoser, K.Ennen, J.Gruber, O.Gruber, O.Jandl, M.Kaufmann, H.Kollotzek, W.Köppendörfer, H.Kotzlowski, E.Lackner, K.Larcher, T.v.Larcher, J.Neuhauser, J.-M.Noterdaeme, M.Pillsticker, R.Pöhlchen, H.Preis, K.-G.Rauh, H.Röhr, H.Schneider, W.Schneider, U.Seidel, B.Sombach, B.Streibl, G.Venus, H.Vernickel, F.Werner, F.Wesner, A.Wieczorek

7) ECRH-Team (IPF Stuttgart):
V.Erckmann, G.Janzen, W.Kasparek, G.Müller, P.G.Schüller, K.Schwörer, M.Thumm, R.Wilhelm

8) ICRH-Team:
F.Braun, R.Fritsch, F.Hofmeister, E.v.Mark, S.Puri, M.Söll, K. Steinmetz, H. Wedler, F.Wesner

9) LH Group:
H.Brinkschulte, H.Derfler, D.Eckhartt, F.Leuterer, R.Magne[1], M.Münich, K.-H.Schmitter, T.Vien, F.v.Woyna, M.Zouhar

10) W VII-AS Project Team:
U.Broßmann, F.Kerl, J.Kißlinger, T.v.Larcher, R.Mathis, H.Münch, J.Sapper, I.Schoenewolf

11) INTOR Group:
EC: G.Grieger, M.Chazalon, F.Engelmann, F.Farfaletti-Casali, M.Harrison, A.Knobloch, D.Leger, P.Reynolds, E.Sapietro, P.Schiller;
Japan: S.Mori, N.Fujisawa, T.Honda, H.Iida, S.Itoh, H.Kimura, T.Kobayashi, K.Miyamoto, M.Seki, K.Tomabechi, T.Tone, K.Ueda;
USA: W.M.Stacey, C.C.Baker, P.L.Colestock, C.A.Flanagan, R.F.Mattas, M.K.Peng, D.E.Post, T.E.Shannon, P.T.Spampinato, J.M.Tarrh, R.J.Thome;
USSR: B.B.Kadomtsev, B.Kolbasov, A.Kostenko, A.Kukushkin, V.Pistunovich, V.Sadakov, D.Serebrennikov, G.Shatalov

AUTHOR INDEX 1984

University Contributions to IPP Programme

INSTITUT FÜR PLASMAFORSCHUNG (IPF)
DER UNIVERSITÄT STUTTGART
(Prof. Dr. H. Zwicker)

In 1984 the cooperation with the IPP has been continued mainly on the basis of the contracts concerning electron cyclotron resonance frequency heating (ECRH) of the W VII-A stellarator and far-infrared (FIR) scattering diagnostics on the ASDEX experiment.

New 28 GHz-components for the transmission line were developed resulting in a 98 % linearly polarized and narrow microwave beam arriving at the plasma with power densities of more than 50 kW/cm^2 . In O-mode orientation a doubling of the central electron temperature (T_{emax} = 1.5 keV) compared to previous experiments at W VII-A could be obtained in this way.

Equivalent microwave components for 70 GHz operation have been developed, produced, and put into operation.

Ray-tracing calculations were carried out for the W VII-A and -AS configurations and compared to experimental results in the case of W VII-A.

Besides special developments for 10.6 µm laser-scattering and FIR-lasers, the set-up for the 119 µm CW scattering experiment was constructed, tested, and installed on ASDEX. Additionally the LIDAR-Thomson scattering developed at the IPF resulted in a JET Art. 14 contract.

At the POSEIDON Plasma Focus experiment various simultaneously applied diagnostics gave further information on two distinguished dynamic phases concerning the mechanism of neutron production.

1. ELECTRON CYCLOTRON RESONANCE HEATING (ECRH)

(R. Wilhelm, V. Erckmann , G. Janzen, W. Kasparek, G. Müller, P.G. Schüller, K. Schwörer, H. Sturm[1)], M. Thumm).

First ECRH experiments were started on the Wendelstein VII A stellarator in summer 1983 at a frequency of 28 GHz. These experiments were continued until summer 1984 by using various kinds of improved wave irradiation in combination with RF diagnostics in the torus. In course of operation linearly polarized waves at a power level far beyond the up-to-date values could be produced by means of special RF components developed at the IPF (P/A=50 kW/cm^2). As a result of the high power deposition in the plasma core (P_{abs}/V = 10 kW/cm^3) a doubling of the central electron temperature was observed. In other experiments with off-axis resonance a specific shaping of the pressure profile could be achieved in spite of the small plasma dimensions (a ≈ 10 cm). A summary of the physics results obtained in the 28 GHz experiments is given in the Wendelstein VII-A part of this annual report.

[1)] graduate student

In parallel to the 28 GHz ECRH experiments in the IPP, various components for the planned 70 GHz system were developed, fabricated, and successfully tested at the IPF Stuttgart. The first (pulsed) 70 GHz Gyrotron (P ≅ 200 kW, τ = 100 ms) was delivered by VARIAN in summer 1984. After the assembly and test phase of the new system, full power operation into the torus load was achieved. First experimental results at 70 GHz are given in the Wendelstein VII-A section of this report, too.

The following sections deal with the theoretical and technical work on the 28 and 70 GHz ECRH-systems performed at the IPF Stuttgart.

1.1 Gyrotron Facility

1.1.1 Power Modulation of the 28 GHz Gyrotron

An amplitude modulation of the microwave output power up to a frequency of 10 kHz was used in the experiments to study the heating efficiency of ECRH and the propagation of thermal waves. Modulation was achieved by varying the voltage of the gun anode. The gun anode supply is a linear HV amplifier; the time behaviour of the RF power is controlled by the amplifier input voltage; see Fig.1.

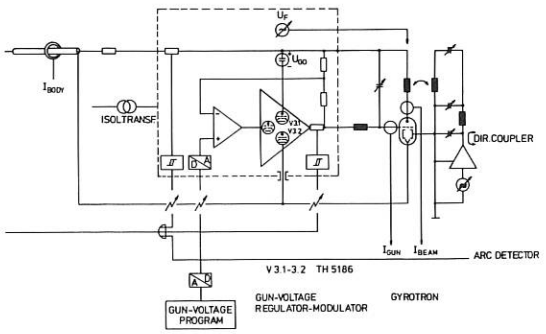

Fig.1 Circuit of the gun anode voltage supply

An example for square wave modulation is given in Fig. 2. In a further experiment a modulation frequency of 15 MHz was used. In this case an additional resonant transformer circuit matched to the output impedance of a 1 kW RF source was added to the output of the gun supply as shown in Fig. 1. A modulation degree of up to 50 % could be reached without deterioration of the gyrotron operation.

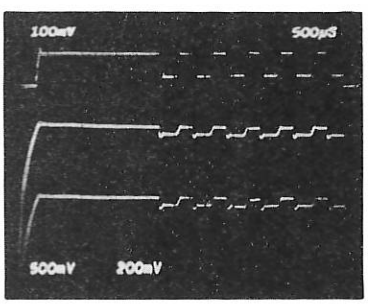

Fig.2 Response of RF power P_{rf}, beam current I_b, and gun anode voltage U_g to a square wave modulation of the amplifier input voltage.

The modulated RF power and the spectrum of harmonic distortion is given in Fig. 3.

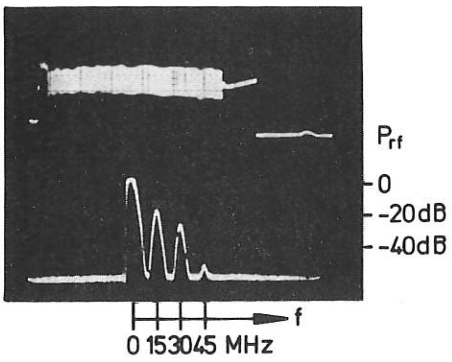

Fig.3 Response of RF power P_{rf} to a 15 MHz modulation of the gun anode voltage and the spectrum of the demodulated power signal.

1.1.2 70 GHz Gyrotron Installation

A new 70 GHz Gyrotron VGE-8070 from VARIAN was ordered by the IPP and could be accepted in Palo Alto in July 84. The tube parameters are in full agreement with the specifications concerning power (200 kW), pulse length (100 ms), and mode purity (> 85 % TE02 mode).

A support structure for the gyrotron and its cryogenic magnet containing the HV feedthrough was built together with a more powerful water cooling system than that of the 28 GHz tube. This installation was put in place of the old 28 GHz gyrotron mounting using the HV power supply of the former installation.

After one week of tube conditioning the tube was ready for operation at full specifications. In contrast to the 28 GHz gyrotron the 70 GHz tube reacts much more sensitively to unstable gun voltage values and to microwave reflections caused by imperfect waveguide components or by boiling water in the dummy load. As a consequence of this behaviour filtering of unwanted waveguide modes is compulsory and new types of dummy loads have to be developed.

1.2 70 GHz Transmission Line System for W VII-A

In the 70 GHz transmission line for the W VII-A stellarator the output mode mixture of the Varian gyrotron VGE-8070 (70 GHz, 200 kW, 100 ms) containing mainly the TE02 mode is first converted into a pure TE01 mode. This mode is used for the long distance propagation because it suffers the lowest damping. In front of the access port to the experiment this mode is converted into the almost linearly polarized TE11 mode and finally transferred into the linearly polarized HE11 mode which has nearly no cross polarization and low sidelobe levels. Therefore this mode is ideal for quasi-optical propagation. The waves are irradiated in a pencil beam from an open-ended corrugated waveguide from the low field side in O-mode polarization. The wave power which is not absorbed by the

plasma is reflected in the extraordinary (X-mode) wave polarization by a corrugated and focussing polarization twist reflector which is mounted to the inner torus wall.

The overmoded waveguide components like diameter tapers, corrugated waveguide bends, mode converters, and mode filters are described in the following paragraphs. The components have been tested by means of far-field pattern, insertion loss, and directional coupler measurements at low power levels.

1.2.1 Waveguide Diameter Tapers

Tapered transitions are needed for the interconnection of oversized waveguides with different diameters which do not generate spurious modes above a certain tolerable level. A reduction of the waveguide diameter D from 63.4 mm to 27.8 mm is necessary, because the arc length of optimally designed corrugated waveguide bends is proportional to D^3, and the lengths of high-power millimeter wave mode converters using periodic wall perturbations and of directional couplers in oversized waveguides are proportional to D^2. The efficiencies of circumferentially corrugated TE11 to HE11 mode converters and anisotropic-wall mode filters also increase with decreasing D. The reduced waveguide diameter has to be extended to 63.4 mm again for the BeO barrier window at the W VII-A stellarator, however. Very low mode conversion into unwanted modes can be obtained by employing relatively short nonlinear tapers with a gradual change of the cone angle. The numerically calculated optimum taper contours with approximate Tschebycheff mode conversion response depend on the propagating mode of interest and are described by Fourier series. These synthesized contours are analyzed by numerical integration of the coupled-modes equations. The properties of tapers (electroformed copper) developed for the 70 GHz W VII-A transmission line are summarized in Tab.1.

propagating mode	TE02	TE01	TE11	HE11
waveguide surface	smooth	smooth	smooth	corrugated
main coupled modes	TE01 TE03	TE02	TM11 TE12	HE12 EH12
taper length	705 mm	705 mm	1095 mm	700 mm
suppression of spurious modes; calculated : measured :	 37 dB ≥25 dB	 40 dB (36±5)dB	 25 dB (23±2)dB	 30 dB ≥25 dB

Tab.1 Data of 70 GHz waveguide diameter tapers for transitions from D=63.4 to 27.8 mm.

1.2.2 Corrugated Waveguide Bends

Changes in the direction of the waveguide transmission system are accomplished by circumferentially corrugated waveguide bends which are well suited for high-power applications with frequencies up to 70 GHz. In these normal-mode bends a pure propagating mode can be made the dominant one by proper choice of the surface reactance (matched corrugations). According to coupled-modes calculations optimum electrical slot depths appear at values of around $(0.2\text{-}0.3)\cdot\lambda/4$ for TE0n mode bends and at $1\cdot\lambda/4$ for HE11 bends.

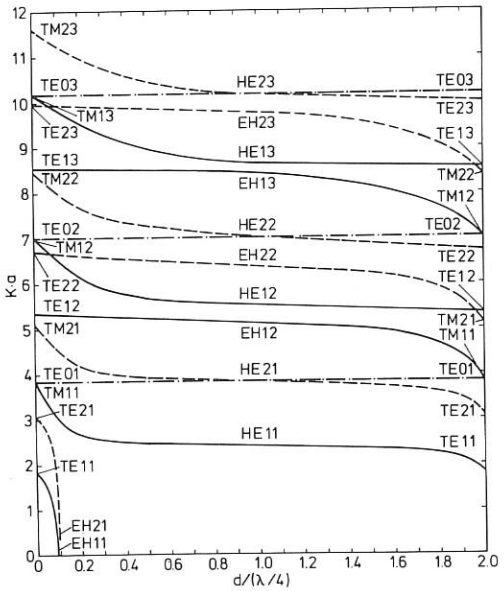

Fig.4 Eigenvalues k·a versus normalized electrical slot depth $d/(\lambda/4)$ for different modes in a 27.8 mm I.D. circumferentially corrugated circular waveguide (70 GHz).

In the case of TE0n mode bends a matched corrugation removes the degeneracy of the mode pairs TE0n/TM1n (as in smooth-walled waveguides), and it prevents a degeneracy between the hybrid HE2n and the original TE0n modes (at corrugation depths of about $\lambda/4$, see Fig.4). The properties of the bends were optimized using numerical integration of the coupled-mode equations. Unintentional conversion

propagating mode	TE02	TE01	HE11
curvature distribution	sin	sin	$\sin^2$
arc length	1.75 m	2.4 m	1.5 m
angle	90°	90°	52°
unintentional mode conversion; calculated: measured:	 <1% ≲2%	 <1%	 <1%

Tab.2 Data of 70 GHz corrugated waveguide bends with I.D. = 27.8 mm.

to spurious modes can be reduced by changing the curvature distribution sinusoidally or $\sin^2$-shaped instead of abruptly. The data of various waveguide bends with maximum internal unwanted mode levels lower than about 20 % (in order to avoid possible arcing in the bend) are given in Tab. 2. The bends are made of electroformed corrugated copper waveguides which are restrained and protected by stable aluminium cases. The depth of the corrugations is tapered at each end of the bends to avoid unwanted mode conversion and return losses.

1.2.3 Mode Converters

Axisymmetric mode transducers with sinusoidal m= 0 radius perturbation convert a TE0n mode into the TE0,n-1 mode, if the converter structure is periodic with the beat wavelength λ_B of the two modes considered. In the case of small waveguide distortions reflections can be ignored and the requirements on perturbation amplitude ($\varepsilon_o a_o$) and converter length (i.e. number of beat- wavelength sections) necessary for complete conversion are computed from a first order perturbation theory of coupled wave fields. Modes up to TE06 are included in the analysis. Results of the coupled differential equations calculations for six-period 70 GHz TE0n to TE0,n-1 mode converters (n=2,3,4) with average radius a_o= 13.9 mm are summarized in Tab.3 together with measured conversion efficiencies.

mode	TE04 to TE03 ε_o= 0.023 L = 234 mm	TE03 to TE02 ε_o= 0.032 L = 355 mm	TE02 to TE01 ε_o= 0.054 L = 594 mm
TE01	4.0 %	0.2 %	99.0 %
TE02	0.2 %	98.4 %	0.3 %
TE03	94.4 %	0.5 %	0.6 %
TE04	0.6 %	0.7 %	-
TE05	0.4 %	-	-
η(exp)	(96±2)%	(98±1)%	(99±1)%

Tab. 3 Conversion efficiencies η and unwanted mode levels of six-period TE0n to TE0,n-1 mode converters at 70 GHz.

A phase-locked gyrotron mode mixture containing 92% TE02, 4% TE03,and 4% TE01 can be cleaned without power losses by using a short and phase-matched TE03 to TE02 converter section ($L=1\cdot\lambda_B, \varepsilon_o=0.025$) at a specified axial position of the beat structure in the waveguide. The resulting TE02/TE01 mode composition can finally be converted into an almost pure TE01 mode by the same method ($L=7\lambda_B$, $\varepsilon_o=0.04$). The measured overall conversion efficiency is close to 98%.

Conversion of the unpolarized TE01 mode to the almost linearly polarized TE11 mode is achieved by a non-axisymmetric mode transformer with constant radius and with periodically modulated curvature in one plane (m=1 distortion). In this converter the E-field plane of the TE11 wave is perpendicular to the plane of curvature thus allowing the free choice of the polarization plane of the millimeter-wave beam at the antenna aperture. By choosing an appropriate waveguide radius, the number of beat wavelengths, and the amplitude of waveguide modulation (ε_o=0.049), the content of spurious modes (TE01, TE12, TE21, TM11, and TM21) was minimized resulting in a measured conversion efficiency of 96% and ohmic losses of about 2% at 70 GHz (a=13.9 mm, L=3.12 m).

Fig. 5 shows measured far-field H- and E-plane and cross-polar (XP) patterns of the generated TE11 mode. The agreement of these patterns with computed ones is good and consistent with the measured efficiency. Fig. 6 gives the computed power transmission and mode conversion efficiencies versus normalized converter length. The strong influence of unwanted modes decreases with increasing converter length (i.e. with reduced perturbation amplitude). The rather significant attenuation of the TE11 mode ultimately limits the efficiency. A converter length of 10 periods is most favourable with respect to power transmission, mode conversion efficiency, and bandwidth. According to the multimode calculations the predicted ten-period conversion efficiency of 92.5 % (2.8 % TE01, 0.2 % TM11, 2.1 % TE12, 0.5 % TE21) can be improved to almost 94.5 % by a 0.8 % increase of the perturbation period which reduces the remaining TE01 mode content.

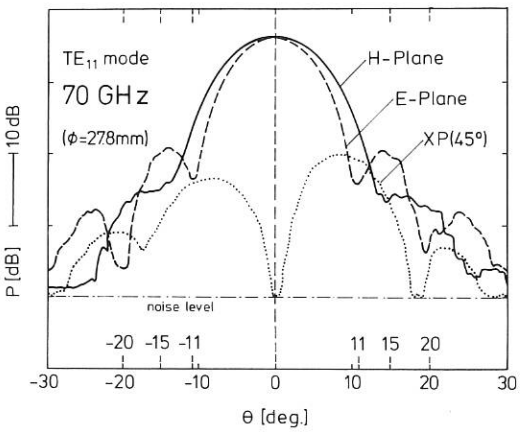

Fig.5 Measured H- and E-plane and cross-polarization (XP) far-field patterns of the TE11 mode produced by the TE01 to TE11 mode converter at 70 GHz.

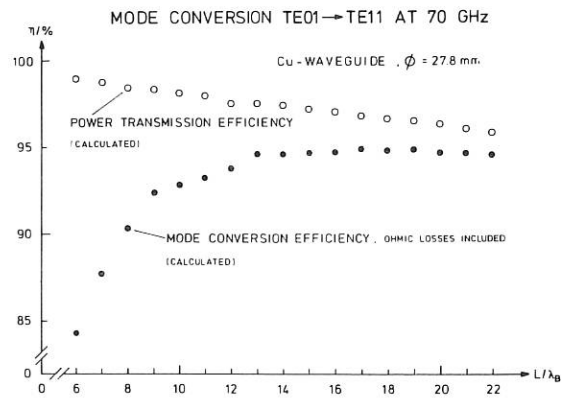

Fig.6 Computed power transmission and mode conversion efficiencies of the 70 GHz TE01 to TE11 converter versus normalized converter length.

The TE11 to HE11 mode conversion is achieved in a straight circumferentially corrugated waveguide section (a_o =13.9 mm) in which the electrical depth of the annular slots gradually decreases from an initial value of almost $\lambda/2$ to a final slot depth of approximately $\lambda/4$ (see Fig.4). Unwanted mode conversion into spurious modes is associated primarily with the entirely cross-polarized EH12 mode. Computer-aided optimization of converter length, shape of corrugations, and slot depth variation is achieved with the "Modular Analysis Concept" MAC [1] . Circumferentially slotted waveguides show a modular structure. Each of the modules merely consists of a junction of two circular waveguides of different diameters. In each region the electromagnetic field can be expanded in terms of complete sets of known eigenfunctions. If the converter is excited by the TE11 mode in the feeding waveguide, these eigenfunctions are represented by the corresponding forward and backward travelling TE1n and TM1n modes in the two waveguides. The boundary conditions for the tangential electric and magnetic fields lead to an individual scattering matrix of each module. In addition to the propagating modes, evanescent TE1n/TM1n modes have to be taken into account. The propagation behaviour of modes close to cutoff is influenced to some extent by the finite conductivity of the waveguide wall which is included in the computer code to model the performance of the converter accurately. The scattering matrix valid for reference planes located at the throut and at the end of the converter are determined by cascading module by module via the corresponding scattering matrices following an iterative algorithm. From the overall scattering matrix the input reflection, the near-field in the converter output aperture, and the various far-field patterns can be computed. The advantage offered by this MAC over the convenient wall impedance concept is that it incorporates all geometrical parameters of the corrugated mode converter and does not impose any restrictions on them. This allows to arbitrarily choose the depths and widths of the slots along the converter wall in order to fit manufacturing requirements, and for a parametric study to find the optimum corrugation geometry. The reduction of the effective corrugation depth (electrical depth) due to the finite space between the slots is accurately taken into account. The free parameters of the converter were optimized for high co-polar pattern symmetry, low cross-polar levels, and low return loss. In Fig. 7 the cross polarization of the HE11 mode obtainable at 70 GHz with two kinds of linearly tapered mechanical slot depths (slot period p= $\lambda/5$, slot width w= $\lambda/10$ and p=$\lambda/3$, w = $\lambda/8$, respectively) is plotted versus the converter length. The second corrugation profile results in a softer nonlinear variation of the effective corrugation depth and therefore leads to lower cross-polar levels. In this case of a high ka-value (ka=20.39, k being the free space propagating constant), nonlinear tapering of the mechanical slot depth is absolutely necessary for obtaining a mode purity of about 99% and cross-polar levels of $\lesssim$-28 dB with a converter length of 370 mm. The measured insertion loss of the 70 GHz TE11 to HE11 mode converter is (1.5 ±0.5)%, which is in good agreement with the calculated value of about 1 %. Fig. 8 shows the measured almost identical output H- and E-plane far-field patterns, the asymmetric TE11 input mode, and corresponding cross-polarization patterns together with the calculated patterns.

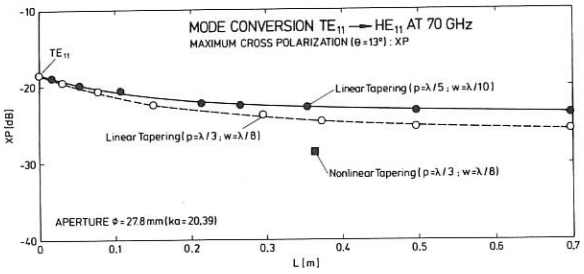

Fig.7 Computed cross polarization achievable with different kinds of linear and nonlinear tapering of mechanical slot depth versus converter length.

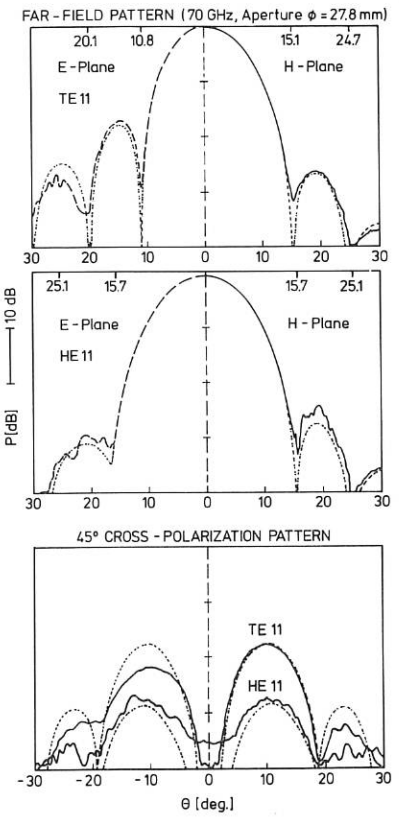

Fig.8 Measured H-plane (right side) and E-plane (left side) and cross-polarization patterns of the HE11 mode generated from the TE11 input mode (dotted curves = computed patterns).

1.2.4 Selective Mode Filters

Special selective mode absorbers for asymmetric modes are used in order to protect the gyrotron from excessive reflections and to avoid arcing in

1) Kühn, E., Hombach, V., IEEE Conf. Publ. 219 (ICAP 83), 1983, Part 1, 127.

the waveguide components caused by trapped mode resonances. Disturbing backward travelling non-circular modes are generated by reflections of some spurious higher-order asymmetric gyrotron modes from the down-taper in front of the first 90°-bend and by reflections from a non-ideal load (e.g. plasma torus, water load boiling). Optimum mode filtering results have been achieved with a new concept: circumferentially corrugated stainless steel filters with tapered slot depth convert non-circular modes into the corresponding EH-surface waves (step by step conversion, e.g. TE13 to TM12 to TE12 to TM11 to TE11 to EH11, see Fig. 4). These modes are highly damped by the special wall structure, while the attenuation of the transmitted TE01 mode is negligible. As in the case of the TE11 to HE11 mode converter, computer-aided optimization of total length, shape of corrugation, and slot depth variation is achieved with the scattering matrix formalism (MAC concept). The measured attenuation of different modes by such numerically optimized anisotropic wall mode filters (a_o = 13.9 mm) is 7 dB/m for TE11, 8.5 dB/m for TM11, and about 20 dB for high-order asymmetric modes (close to cutoff), whereas the attenuation of the TE01 mode is lower than 0.04 dB/m. The efficiency of these mode selective absorbers decreases with increasing values of k·a .

1.3 RF Diagnostics

1.3.1 Mode Selective Directional Couplers

Design, construction, and tests of mode selective directional couplers were extended from the frequency of 28 GHz to 70 GHz. Two types of directional couplers are used for overmoded waveguide systems, the short coupler with few pairs of holes and the multihole coupler with a great number of equally spaced holes.

The performance of those directional couplers can be considerably improved by combining their hole structures. The improvement may be aimed at directivity or at suppression of certain unwanted modes propagating either in forward or backward direction. Fig. 9 shows the hole structure of the combined couplers of the short and of the multihole type.

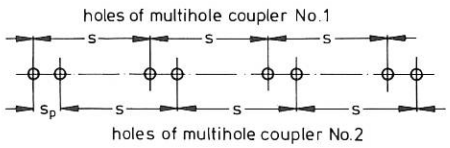

Fig. 9 Arrangement of holes of combined multihole and short coupler.

The influence of a second multihole structure shifted against the first one on the properties of a mode selective directional coupler is given in Fig.10. Comparisons are made between calculated data for one-hole and double-hole arrays of a TE11 coupler designed for 70 GHz and a waveguide diameter of 27.79 mm.

This coupler in the simpler one-hole array design showed insufficient suppression of the TE14 mode in forward direction, Fig. 10a. Marked suppression of the TE14 mode with a shifted structure removed this deficiency and also considerably improved the directivity by about 25 dB, mode suppression of

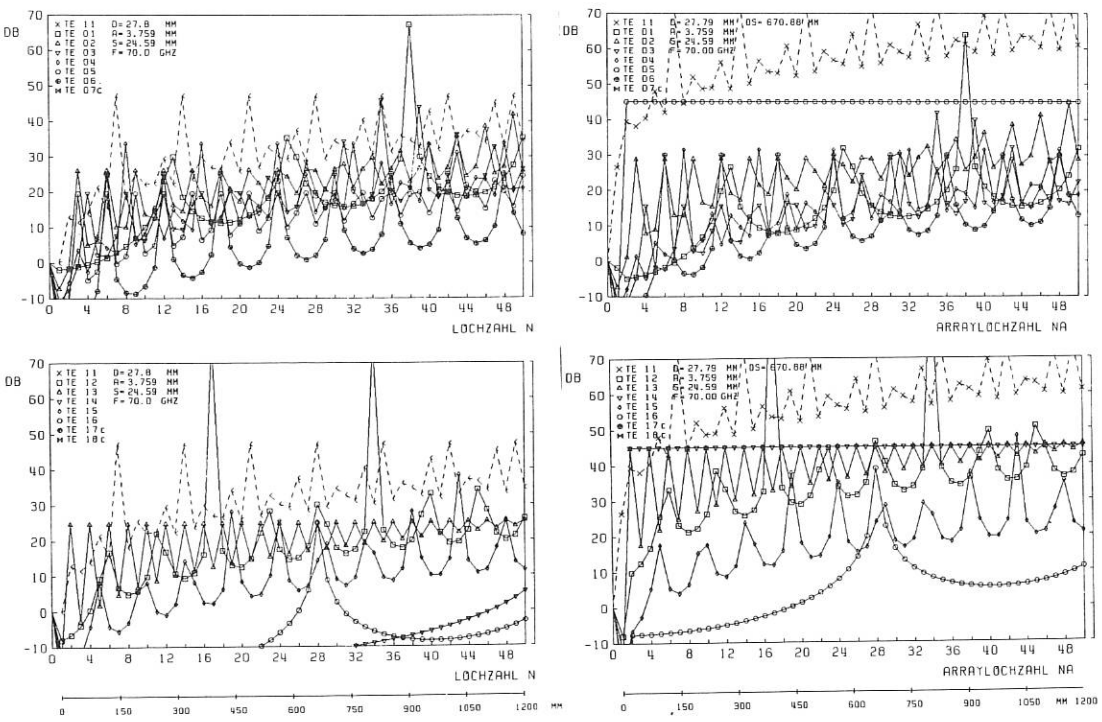

Fig.10 TE11 coupler for 70 GHz, 27.79 mm waveguide diameter: directivity and forward mode suppression of TE0m (above) and TE1m modes (below) versus number N of coupling holes.
a) single-hole structure b) double-hole structure

TE16 by 14 dB, mode suppression of TE05 by more than 30 dB, and suppression of other modes by 5 to 10 dB, Fig. 10b.

Experimental results obtained from double-hole array mode selective directional couplers for the modes TE01,02,03,04 at 70 GHz, 63.4 mm ∅, are given in Fig. 11. Initially the couplers were fed with a pure TE01 wave. This mode was then converted into a pure TE02 wave in six intermediate steps by consecutively adding six λ_{beat} — sections of a mode converter generating power fractions of 6.7%, 25%, 50%, 75%, 93.3%, 100% of the new mode, respectively. Further six λ_{beat} — sections converted the TE02 mode stepwise into the TE03 mode and then with another six sections into the TE04 mode. Signals in the coupling waveguides were measured with a heterodyne receiver of high sensitivity and wide dynamic range.

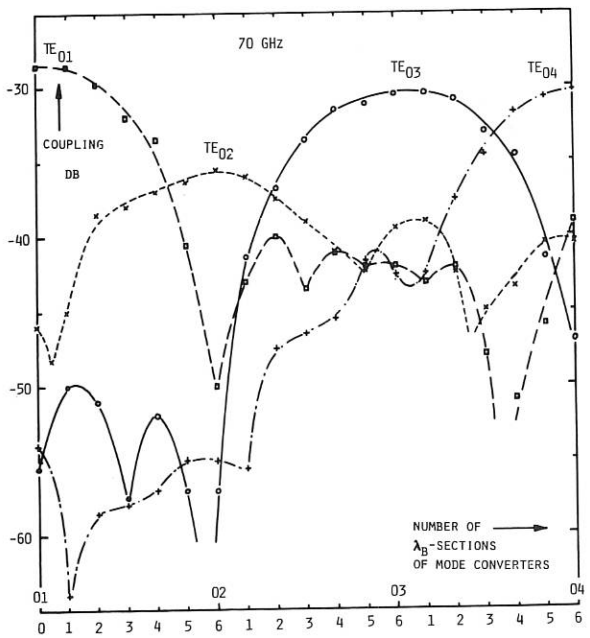

Fig.11 Response of mode selective couplers TE01 to TE04 to stepwise converted modes TE01 to TE04 propagating in the main waveguide (63.4 mm ∅) at 70 GHz.

Signal outputs of the four coupling guides attributed to one of the modes TE01,02,03,04 follow the growing responses for mode mixtures containing increasingly more amplitude of the mode under consideration. Maximum output is reached for the pure modes, respectively. The coupler output signals then follow the decreasing mode amplitude again.

1.3.2 Mode pattern analyzer

Burn patterns taken at high power behind each of the mode converters give a qualitative information on the efficiency of mode conversion in the transmission line. For 28 GHz Fig. 12 shows the increase in power concentration which was achieved by converting the TE11 mode into the almost completely linearly polarized HE11 mode which was irradiated into the plasma via a corrugated open-ended waveguide as antenna.

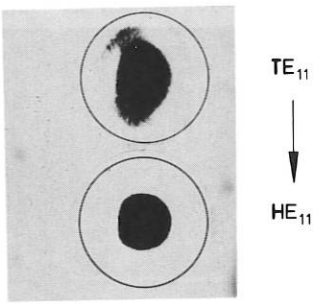

Fig.12 Burn patterns of the TE11 and HE11 mode at 28 GHz.

Burn pattern measurements with stacked thermographic papers revealed the mode composition of the 70 GHz VARIAN gyrotron VGE-8070-S/N 1 to be 90-94% TE02, the remaining power being distributed between TE03 and TE01.

1.3.3 Reflector signals

At the inner torus wall the incident RF power distribution was measured by three coupling holes in the surface of the polarization twist reflector. Thus an information on the power concentration of the radiated antenna beam could be obtained. Fig. 13 shows the signals received by the three coupling holes for the TE11 mode and HE11 mode at 28 GHz, respectively. The measured power density for the TE11 mode in the centre of the beam at the position of the reflector amounts to about 10 kW/cm^2 with a gyrotron output power of 200 kW. The signals (outer holes 74 mm off the centre) agree with the calculated patterns. For the HE11 mode, however, the central power density goes up to 14 kW/cm^2 with no signal at the outer part of the reflector. This confirms the character of a pencil beam for the HE11 mode in the near field.

During plasma experiments information on absorption and deflection of the RF beam by the plasma could be derived from the coupling hole signals. In order to sustain an interpretation of these measurements ray tracing calculations were performed.

In Fig. 14 the ratio of power incident on the reflector and radiated power (P_{inc}/P_o) for plasma conditions with constant central electron density $n_{eo} \cong 4 \cdot 10^{12} cm^{-3}$ is compared with the calculated and measured far field pattern for the TE11 mode without plasma. These experiments show that an increase of the electron temperature is caused by O-mode absorption.

In order to increase the accuracy of measuring the radial profile of the radiated or absorbed RF-beam the polarization twist reflector now installed in

W VII-A for the 70 GHz experiments is provided with 5 coupling holes. This reflector can also be tilted so that the direction of the reflected beam can be varied for the study of RF current drive experiments.

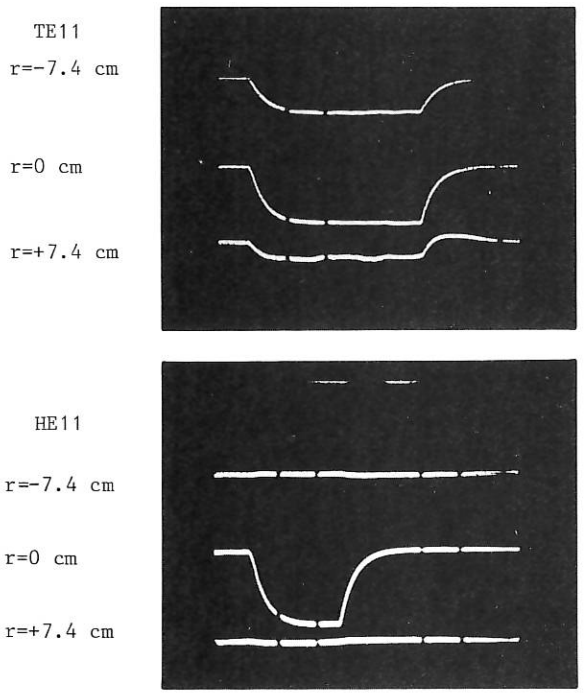

Fig.13 Coupling hole signals on the surface of the polarization twist reflector for the TE11 and HE11 mode without plasma (28 GHz).

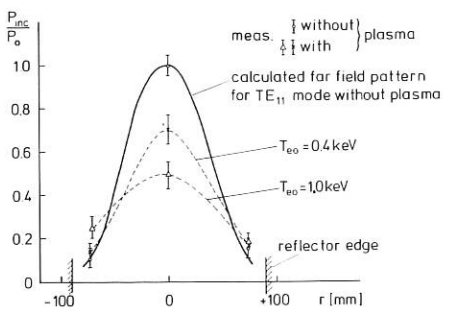

Fig.14 Ratio of incident power to radiated power for different electron temperatures at constant central density $n_{eo} \cong 4 \cdot 10^{12} cm^{-3}$.

1.3.4 Wave Decay

Different measurements show that the X-mode generated by the polarization twist reflector undergoes parametric decay at the upper hybrid layer into a high (ω_h) and a low-frequency wave (ω_ℓ), where $\omega_h + \omega_\ell = \omega_{gyrotron}$. The high frequency component of the decay waves was deduced from microwave emission of the plasma received by an antenna inside the torus. Direct gyrotron radiation was blocked off by a 28 GHz notch-filter. A heterodyne receiver with a tunable local oscillator followed by a ten-channel filter bank served as spectrum analyzer. Typical spectra of the observed microwave radiation contain an upper and a lower sideband of the 28 GHz pump wave (Fig. 15). The dominant lower sideband corresponds to the high frequency component with a frequency range of 27.7 - 28 GHz. This is consistent with the observation of low frequency decay waves detected by Langmuir probes at the plasma boundary. The low-frequency spectrum shows a sharp drop at a frequency of 230 MHz, which is equal to the lower hybrid frequency close to the upper hybrid layer.

Simultaneously with the occurance of wave decay a highly energetic ion tail is observed, where the flux of these ions is strongly correlated to the amplitude of the decay waves.

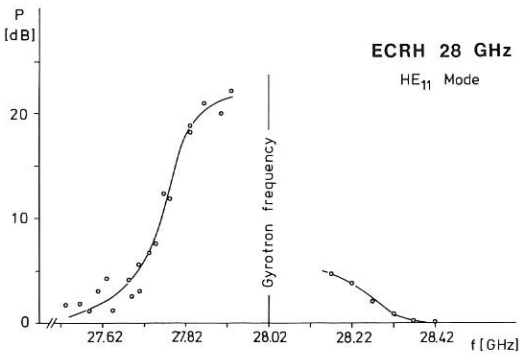

Fig.15 High frequency decay spectrum as detected by a microwave heterodyne receiver.

1.4 Overmoded Waveguide Mode Converters for ECRH at 140 GHz

One possible solution for high-frequency ($\geq$140 GHz) and high-power ($\geq$200 kW) gyrotrons for ECRH on large fusion devices might be a TE03-mode gyrotron with less than a 5% contribution from other circular electric modes[2]. As described in chapter 1.2.3 the TE03 output mode can be converted into the low-loss TE01 mode by a set of two axisymmetric ripple converters (TE03 → TE02 → TE01) whose lengths in an oversized high-power waveguide system with internal radius a_o = 13.9 mm would be about 0.71m and 1.19 m, respectively. Because beat wavelengths scale with $a_o^2 f$ and because the ohmic losses of the linearly polarized TE11 mode increase with $\sqrt{f}/a_o$, the serpentine TE01 to TE11 mode converter with periodically modulated curvature becomes impractical for 140 GHz transmission line systems. Fortunately the perfectly linearly polarized near-Gaussian HE11 mode can be generated in an alternative two-step mode conver-

[2] Felch, K., et al., Bull. Am. Phys. Soc. 29, 1255 (1984)

sion process, namely: TE01 to TM11 to HE11[1] . A schematic of the corresponding converters is shown in Fig. 16.

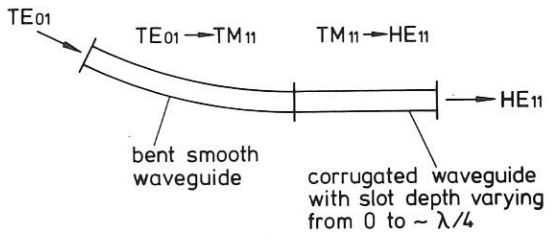

Fig.16 Principle of the generation of HE11 from TE01 via TM11. TM11 and HE11 are polarized perpendicular to the plane of the bend.

Because TE01 and TM11 modes are degenerated in smooth-walled circular waveguides (propagation constant is identical, see Fig. 4) power is continuously coupled from TE01 to TM11 along the curvature. A waveguide bend of angle θ_c will convert all the power from one mode to the other if

$$\theta_c = k_{01} \cdot \lambda / (2\sqrt{2}\, a_o)$$

where $k_{01} = 3.8317$ is the root of the Bessel-function for TE01 and TM11, and $\lambda = 2\pi/k$ is the free space wavelength. The bend must be long enough to avoid unwanted mode conversion to modes such as TE11, TE12, TE21 and TM21 but ought to be as short as possible to minimize ohmic (wall) losses from the high-loss TM11 mode.

The second converter (circumferentially corrugated waveguide) "adiabatically" converts TM11 to HE11 by increasing the corrugation depths from zero to a value of about $\lambda/4$ (see Fig. 4). This converter has to be long enough ($\cong$ 0.7 m at 140 GHz) to suppress mode hopping to the TE11-EH11 surface mode branch as well as to the TM11-EH12 branch. A disadvantage of this mode converter sequence is that it incorporates a bend which does not easily allow a free choice of polarization. Nevertheless this converter will be very useful for a 140 GHz ECRH system.

Bent TE01 to TM11 mode converters with I.D. = 27.8 mm for 70 and 140 GHz were optimized by means of numerical integration of the coupled-modes equations for six coupled modes (TE01, TM11, TE11, TE12, TE21, TM21). In both cases lowest spurious mode level is achieved using a sinusoidal curvature distribution instead of constant curvature as used in ref.[1] . The calculated data of the two converters are given in Tab. 4.

TE01 to TM11 mode converters for 70 and 140 GHz were fabricated by bending commercially available WC109 waveguide in a preassembled frame with a shape defining the curve. No ellipticity in the plane perpendicular to the bend could be measured ($\lesssim$ 0.01 mm). The experimentally determined efficiencies are in good agreement with the theoretical ones. Fig.17 shows the measured E- and H-plane far-field patterns of the TM11 mode generated at 70 GHz. The H-plane power distribution represents the residual unwanted modes, since a pure TM11-mode far-field pattern has no intensity in the H-plane. These excellent results show that such bent smooth waveguide TE01 to TM11 converters are very suitable for future high frequency ECRH system and that they are also appropriate to produce the TM11 mode for low-power tests of waveguide components (e.g. mode filters etc.).

	70 GHz	140 GHz
θ_c	24.0 °	12.1 °
Arc length	1.305 m	2.520 m
normalized power in:		
TE01	0.9%	0.1%
TM11	96.9%	95.2%
TE11	-	-
TE12	-	-
TM21	0.2%	0.1%
TE21	0.4%	0.2%
Normalized transmitted power	98.4%	95.6%

Tab.4 Theoretical conversion efficiencies and unwanted mode levels of bent TE01 to TM11 mode converters at 70 and 140 GHz.

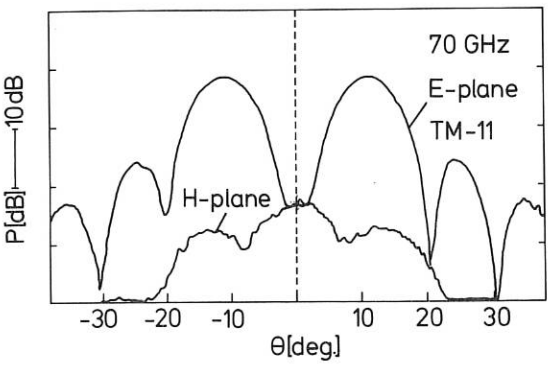

Fig.17 Measured E- and H-plane far-field patterns of the TM11 mode generated from the TE01 mode at 70 GHz.

2. PLASMA THEORY

(E. Räuchle, U. Erz, F. Moser, W. Konle[1] , J. Mayer-Stöhr[1]).

2.1 Ray Tracing Calculations for Electron Cyclotron Heating.

The propagation of electromagnetic waves in inhomogeneous plasmas is investigated numerically within the approximation of geometrical optics. Applications concern the propagation and

[1] Doane, J.L., Proc. 10th Symp. Fusion Engineering, Philadelphia, 1983, p. 1459

[1] Doktoranden

absorption of electron cyclotron waves in the stellarators W7A and W7AS. For an ordinary electromagnetic wave propagating perpendicular to the magnetic field the absorption is determined by the relativistic effect. This case is investigated experimentally in W7A. There is a good agreement between experimental and theoretical results.

2.2 Stochastic Effects

The interaction of three waves is investigated for the case where one wave is externally driven. The amplitude b of the pump wave is modulated in time. This system shows bifurcations, intermittency (Fig.1) and chaotic behaviour depending on b and the degree of modulation as control parameters.

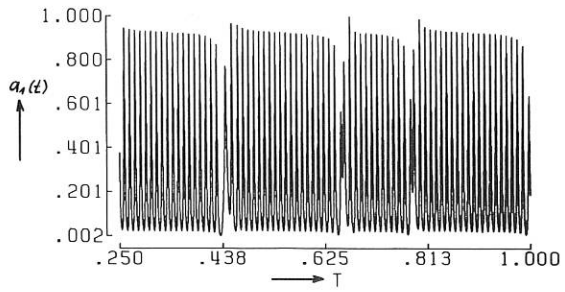

Fig.1 Intermittency in a driven three wave system.

2.3 Numerical plasma simulation.

a) Numerical solution of the Vlasov-equation as an initial value problem.

The developed code for the numerical solution of the Vlasov-equation is applied to the investigation of strong plasma waves. The distribution function for electrons and ions is investigated for the case of the formation of cavitons and ion acoustic solitons (Fig.2).
In order to obtain a direct information of the excitation of waves a numerical code was developed on the basis of Fourier and Hermite series expansion. It will be used to obtain coefficients of nonlinear wave interaction.

In order to investigate waves propagating in magnetic fields an extension to further dimensions is necessary. A suitable code has been developed.

b) Numerical solution of the Vlasov-equation as a boundary value problem.

The propagation of electrostatic waves, periodic in time, excited at a spatial boundary is investigated numerically. A solution technique based on tracing the characteristics of the Vlasov-equation in space is developed. First applications concern spatial Landau damping and spatial echoes.

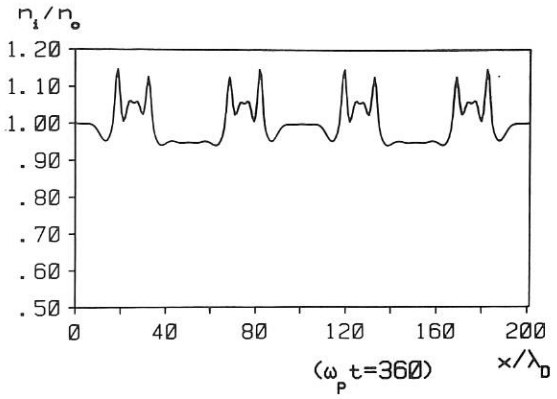

Fig.2 Ion density of decaying solitary waves

3. L A S E R D I A G N O S T I C S

(H. S a l z m a n n, G. Dodel, P. Engelfried [1], H. Hailer, J. Heppner, K. Hirsch, E. Holzhauer, M. Köchel [1], J. Massig, Z. Solajic [2], W. Kasparek, G. Merkle [3], F. Schuler [1], J. Singethan [3], T. Vogel [3])

The work of this group deals with the development of laser diagnostics for fusion devices and the application of such diagnostics to tokamak and stellarator devices.

3.1 LIDAR-Thomson scattering for measuring spatial n_e, T_e-profiles in large fusion devices.

The investigation done under JET Art. 14 contract JE 3/9009 showed that all relevant problems with regard to a possible application to JET can be solved : With available laser, detector and registration technology measurements can be performed along a 2.5 m long vertical spatial chord with a spatial resolution of 13 cm. The expected statistical errors at $n_e = 1 \times 10^{13} cm^{-3}$ and $T_e = 5$ keV are $\Delta T_e/T_e = 4$ % and $\Delta n_e/n_e = 2.6$ %. Experiments at the MPQ Garching (Dr. Witte, Dr. Brederlow) demonstrated that the required 15 J/ 300 ps frequency-doubled iodine laser can be operated with 1 Hz repetition rate for a burst duration of 10 ns. The detector tests at the IPF Stuttgart yielded that the chosen MCP Photomultiplier (ITT F4128) meets all the requirements concerning sensitivity bandwidth, gating properties and saturation recovery properties: At full gain of 1×10^5 a risetime of 180 ps was measured, the FWHM response to a short light pulse being less than 400 ps. The gating tests showed that light pulses containing at least up to 10^9 photons within the response time of the PMT can be tolerated 18 ns in front of the measu-

[1] Diplomand
[2] Institute of Physics, Beograd, Yugoslavia
[3] Doktorand

ring signal. This time interval corresponds to the time lapse between the stray light pulse from the entrance window and the scattering signal from the plasma boundary.

Stray light measurements were performed on a full-scale optical set-up using a small frequency doubled 1 ns iodine laser in order to predict the stray light level in the real experiment. The measurements yield that the entrance window will cause $2x10^{10}$ stray light photons incident on the detector. Thus the polychromator only needs to discriminate the stray light by a factor of ≈ 20.

The results were approved on a workshop at JET. In a subsequent study a modification of the proposed set-up was investigated. This modification consists in sharing the existing KE1 single point Thomson scattering collection optics, thus using a radial line of sight in the equatorial plane. The modification simplifies considerably the application to JET. Due to the much larger solid angle of collection the required laser energy is only ≈ 5 J (at 2 ω). The investigations showed that the total plasma diameter will be accessible for the measurements.

The described modification will be realized on JET.

3.2 Laser diagnostics at 10.6 µm. Scattering with heterodyne detection.

The possibility to measure the magnetic field direction in plasmas with CO_2-laser scattering and heterodyne detection has been investigatèd numerically. Ion spectra calculated on the basis of scattering geometries with elliptical beam-cross sections show that the direction of the magnetic field can be determined with an accuracy of about $\pm 1°$. This result will be checked by a corresponding scattering experiment on a magnetically confined hydrogen arc.

In previous experiments, the local oscillator was derived from the pulsed CO_2-hybrid laser. The fast rise of this laserpulse and the connected high frequency Fourier components did not allow to detect mixing signals below 10 MHz. To get access to this frequency range, which is essential for the measurement of the narrow spectra from magnetized plasmas, a quasi-cw low-pressure CO_2 - laser will be used as a separate local oscillator.

To investigate the frequency characteristics of the CO_2-hybrid laser, mixing experiments with the low-pressure laser were performed. The results show, that the chirping of the laser frequency during the pulse is reproducible. The corresponding bandwidth of the laser line is below 6 MHz and will therefore not affect the spectral resulution of the heterodyne receiver. The drift of the difference frequency of the two lasers was reduced by passive stabilization methods to 10 MHz/hour and can be controlled by piezoelectric length adjustment of the resonators.

3.3 Far infrared lasers

3.3.1 Far infrared modulation

a) Acousto-optic modulation

Due to the inverse λ^2-dependence (λ = wavelength) of the acousto-optic modulation efficiency a practically relevant modulation degree can be achieved in the far infrared only by selecting a material with good transmission and ultra sound properties and by applying high ultra sound intensity. Previous attempts with TPX as modulator material (annual report 1982) were substantially improved by using different materials and increasing the ultrasonic intensity both by raising the RF power and focussing the ultrasonic wave with a half cylindric transducer. The best modulation efficiency of 1.5 % for 119 µm radiation was achieved by exciting a 780 kHz acoustic wave in liquid cyclo-hexane with 2 ms, 150 W RF pulses[1] (Fig. 1). This efficiency is sufficient to provide, for example, the reference beam of a FIR heterodyne interferometer or polarimeter. The possibility of longer pulse durations or cw operation, however, remains to be investigated.

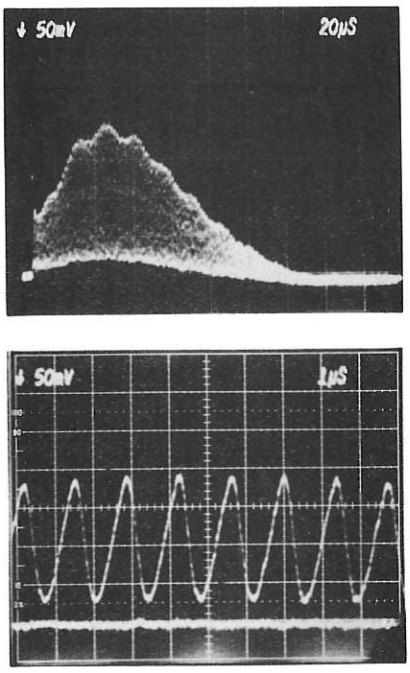

a)

b)

Fig.1 780 kHz beat note obtained by mixing the acousto-optically deflected beam with the carrier beam. The envelope of the beat signal (a) (time scale = 20 µs /div) presents the shape of a 119 um CH_3OH laser pulse. In(b) (time scale = 1 µs/div) the lower trace is the baseline obtained with radiation blocked.

1) T. Vogel and G.Dodel, Infrared Phys.,25,315 (1985)

b) Electrical switching of far infrared radiation

119 μm radiation from a CH_3OH laser was switched off in 0.5 ns by electrically exciting a LN-cooled, 60 μm thick InSb wafer (Fig. 2). 100 percent modulation was achieved by applying 900 V, 0.5 ns risetime, 3-15 ns long voltage pulses from a transmission line pulser. The reflected beam responds to the voltage pulse also with a steep intensity decrease to ≈ 50 % of its initial value. This is in contrast to what was observed in the case of optical switching (annual report 1983) and suggests that the carrier density produced by the current pulse in the wafer is still below the cut-off density.

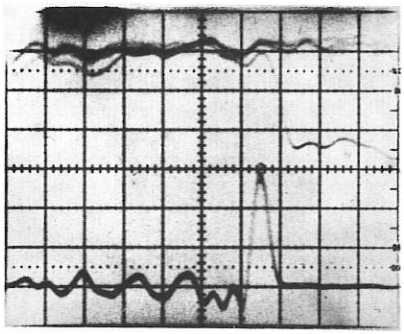

Fig.2 Switching of 119 μm radiation in transmission. Time scale 2 ns/div.; upper half: current monitor signal; lower half: detector signal transmitted beam and baseline with radiation blocked. Risetime of oscilloscope 0.9 ns.

3.3.2 Pumping of far infrared laser transitions with a CW waveguide CO_2 laser

For investigations of FIR molecular gases, quantitative absorption measurements in CH_2F_2, CH_3F and CH_3OH in the vicinity of CO_2 laser lines have been done using a 300 MHz tunable waveguide CO_2 laser with output powers of about 3 W. Information on frequency offsets from the CO_2 line centers, small signal and saturated absorption coefficients of FIR laser pump transitions have been obtained. Some stronger pump transitions with frequency offsets larger than 50 MHz gave rise to the observation of 8 new FIR emission lines in CH_3OH with wavelengths from 43 to 125 μm and of 6 new emission lines in CH_2F_2 at offsets larger than 100 MHz with wavelengths from 127 to 281 μm. The strength of two of these lines is comparable with that of the strongest transitions reported so far in CH_2F_2. Four of the lines in CH_2F_2 have been assigned to molecular transitions.

An example for multiple laser action in CH_3OH at different pump offsets within ± 150 MHz is shown in Fig. 3. The results have proved that a cw waveguide CO_2 laser is a very useful tool for resonant pumping of FIR laser transitions. Recent developments of a new waveguide CO_2 laser with an intracavity mode selector and an extended gain length, to overcome the frequency tuning range usually being restricted by the free spectral range of the laser cavity length, give rise to the possibility of pumping a lot new FIR laser transitions with frequency offsets larger than 150 MHz.

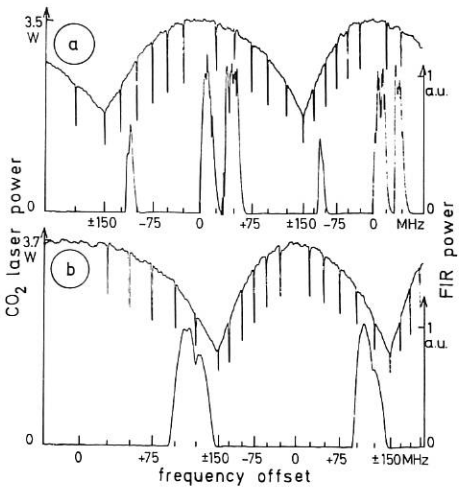

Fig.3 FIR Emission from CH_3OH and CO_2 laser output power versus detuning of the waveguide CO_2 laser frequency from 9P (34) line center:

a) 51.7 μm emission at -115 MHz pump offset,
70.5 μm emission at +15 and +45 MHz offset corresponding to the forward and backward gain in the FIR laser pumped below and above line center at +30 MHz in a non optimized cavity;

b) for a different FIR cavity setting 205.6 μm emission is observed at +125 MHz pump offset.

3.4 119 μm scattering system for the investigation of lower hybrid waves in ASDEX.

The CW scattering experiment designed last year (annual report 1983) was constructed and tested in a full scale model experiment at the IPF in Stuttgart and installed on ASDEX during the last quarter of 1984. It is now operative and will be run along with the lower hybrid heating experiments in 1985. In the following the performance of the principal components and the results of preparatory experiments are summarized.

Optical set up:

An overall view of the scattering system is shown in Fig. 4. The beam of the scattering laser is directed into the plasma vessel and reflected back from an internal mirror with a slight tilt. Radiation scattered from the reflected beam is observed at angles $-13° < \theta < +13°$ making the predicted range of $k_\perp$-fluctuations ($20\ cm^{-1} \leq k \leq 125\ cm^{-1}$) accessible to investigation. The scattering volume is imaged by a spherical mirror (f = 1380 mm, size 800 x 50 mm) onto a plane mirror which can be

rotated to select the scattering angle. The system is designed to allow a k-scan within one tokamak discharge and a shot-to-shot spatial scan of the major part of a poloidal plasma section 90° away from the lower hybrid antenna grill. To avoid absorption of the 119 μm radiation through atmospheric water vapour (typically 1 dB/m at 70% humidity for the CH_3OH laser line) the optical system is flushed with dry air.

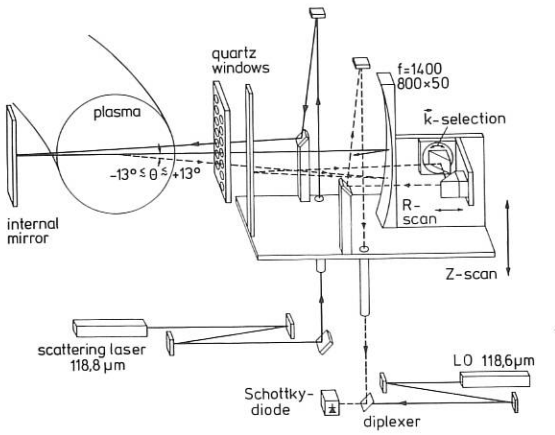

Fig.4 Optical set up.

Lasers

The construction of the CO_2 laser pumped 118.8 μm CH_3OH laser used for scattering was completed. It is equipped with a Si-etalon-coupled, ZERODUR stabilized waveguide FIR resonator (Duran glass, 2150 mm x 25 mm i.d.) and yields typically 100 mW in a Gaussian beam at 40 W pump power delivered by a commercial CO_2-laser. A 118.6 μm discharge pumped H_2O-laser supplied by the Association Euratom-CEA, Fontenay-aux-Roses, serves as the local oscillator. Its power is 60 mW, linearly polarized in a Gaussian mode. Due to the frequency difference (5.17 GHz) between these lasers the scattering signals can be discriminated in frequency against possible pick-up from the 1.3 GHz, megawatt power lower hybrid transmitter. In addition, the propagation direction of the electron density fluctuations can be determined.

Detection system:

A GaAs Schottky barrier diode mounted in an open structure mixer as well as a second mixer stage which downconverts the scattering signals expected at 5.17 ± 1.3 GHz to 150 MHz was supplied by and tested in collaboration with the MPI für Radioastronomie, Bonn. In a hot/cold black body experiment the NEP of the system was measured to be 10^{-18} W/Hz in the IF bands of interest (3.87 GHz and 6.47 GHz). The suitable LO power was found to be approximately 30 mW. The mixing efficiency saturates in this range and further increase of the LO power does not improve the NEP of the system.

Alignment tests.

The alignment of the detection system was achieved by setting the k-selecting mirror to the scattering angle $\theta = 0°$ and optimizing the detector signal for both the LO and the scattering laser beam. The performance of the system for scattering angles $\leq 13°$ was then tested by moving a thin wire (0.3 mm diameter, mounted on a rotating disc) across the scattering laser beam. The Doppler shifted radiation diffracted by the wire is collected by the scattering optics and mixed on the Schottky diode with radiation obtained from the scattering laser via a beam splitter. Figs. 5a and 5b show the results measured when the k-selecting mirror was adjusted for scattering angles $\theta = 8°$ and $\theta = 2°$, respectively. The temporal width of the envelope of the beat signal is proportional to the transverse dimension of the scattering volume, the proportionality factor being the inverse of the wire speed. Similarly the duration of one beat period is connected with the fluctuation wavelength by this proportionality factor. The amplitudes of the beat signal reflect the weighting function across the scattering volume determined by the beam profile of the scattering laser and the antenna beam of the detector. Thus the rotating wire experiment immediately yields the k-resolution for a specific scattering geometry. By translating the rotating wire along the scattering beam the length of the scattering volume can be determined as well.

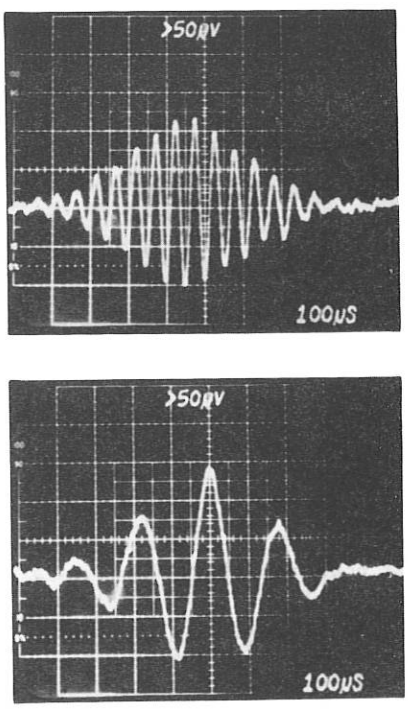

Fig.5 Beat signals obtained by scanning the scattering volume with a moving wire for $\theta = 8°$ in a) and $\theta = 2°$ in b). (One division corresponds to 1.6 mm).

3.5 Laser spectroscopy

The possibility to measure plasma parameters such as electric and magnetic fields, ion temperature etc. in a fusion plasma by means of Doppler free spectroscopy is investigated. The experimental set-up for the laser spectroscopy of a hydrogen model plasma has been completed.

A radially movable Langmuir probe has been prepared to measure the electron temperature and density profile of the plasma. With a special cathode flange of the vacuum vessel the cathodes can be changed easily and different cathode designs (cold and hot cathodes, hollow cathodes) have been tested. Best results with respect to a quiescent discharge at low pressure ($p \cong 0.1$ Pa) in a magnetic field of $B = 0.2$ T have been achieved with an array of Barium-Strontium-Oxide matrix cathodes at currents up to 100 mA.

The laser system consisting of an Ar laser pumped single mode dye laser has been aligned for single mode scan of the dye laser in the region of a few GHz around the H_α line centre. For absolute wavelength calibration a frequency stabilized He-Ne laser is required. For this purpose we are developing a modification of an inexpensive internal mirror He-Ne laser (Spectra-Physics 155) to yield a linewidth stability of less than 10 MHz. The application of both a transverse and an axial magnetic field to the laser discharge results in a modulation of the laser output which is frequency-shifted when the He-Ne laser is detuned from its line centre. This effect can be used to stabilize the laser by modulating the optical length of the laser and measuring the beat frequency. A mechanical length modulation with the help of piezotransducers has been tested successfully. The electronic feedback circuitry is under development.

4. PLASMA FOCUS

(H. Herold, W. Biermayer, H.J. Kaeppeler, H.Schmidt, M. Shakhatre, A. Shyam[1]. Doktoranden U. Jäger, R. Schmidt)

[1] Bhabba Atomic Research Center, Trombay, India.

4.1 Poseidon Plasma Focus.

The measurements on the Poseidon device concerned turbulence and nonlinear phenomena associated with ion acceleration and neutron production in the two dynamic phases of the focus pinch. The experiments were carried out at 280 kJ, 60 kV with pinch currents of 1 MA and neutron yields up to 10^{11}. The laser light scattering experiments were terminated in the first quarter of 1984. In the following, an extensive program of simultaneous measurements was carried out, concerning mainly radiation and particle emission in temporal, spatial and partly spectral resolution. Fusion reaction products (neutrons and protons), fast plasma ions and deuterons, soft and hard x-rays were investigated.

1) The methods developed in the past for investigation of energy spectra and source structure of accelerated deuterons and reaction protons by etchable plastic films (CR39) were applied. A proton energy resolution of $\Delta E = 50$ to 70 keV was achieved with a 54 step filter method. The spatial resolution in proton pinhole pictures was $\approx$ 3 mm. These time integrated measurements were supplemented by time and spectral resolved fast deuteron measurements with a magnetic spectrometer.

To explain the mechanismus of neutron production a new model, the "Gyrating Particle Model" (GPM) has been developed. The main feature of the GPM is the calculation of fast ion trajectories in the focus pinch in presence of time varying profiles of n_e, T_e and j, adapted to experimental results. Initial distribution functions for the deuterons are assumed. Energy loss of the deuterons by elastic collisions and fusion collisions are taken into account by Monte Carlo treatment, and the deflection of the fusion protons by the focus magnetic field is regarded. With the GPM, measurable quantities such as proton and neutron spectra, angular distributions of protons and neutron flux anisotropy have been calculated and compared with experimental results. It turns out that the agreement is best when the deuterons have a forward directed anisotropic emission with an initial quasi-temperature of $T_i = 40$ to 100 keV. In such cases about 10^{17} fast deuterons (≈ 0.1 to 1 % of the particle content) with an energy up to 10 % of the thermal plasma energy are needed to explain the observed fusion reaction yield (Fig. 1 and 2). 60 to 90 % of the model fusion reactions take place in the dense focus plasma in agreement with experimental results. A hard deuteron component of $T_i \cong 200$ keV appears to be present presumably in the 2nd dynamic phase. It has no marked influence on the neu-

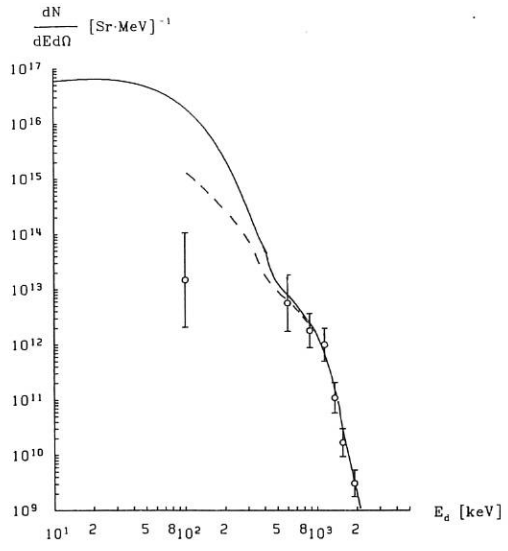

Fig.1 Measured and fitted (solid line) spectrum of accelerated deuterons in axial direction from a plasma focus discharge. Two temperatures $T_{i,1} = 40$ keV and $T_{i,2} = 200$ keV are assumed.

tron production. From proton pinhole pictures and from the observed angular proton distribution in comparison to GPM results the pinch current could be deduced. It was about 0.7 to 1 MA. Furthermore, the occurence of axial B-components of $B_z \leq 0.3\, B_{\varphi max}$ could be found from radial shifts of the proton source.

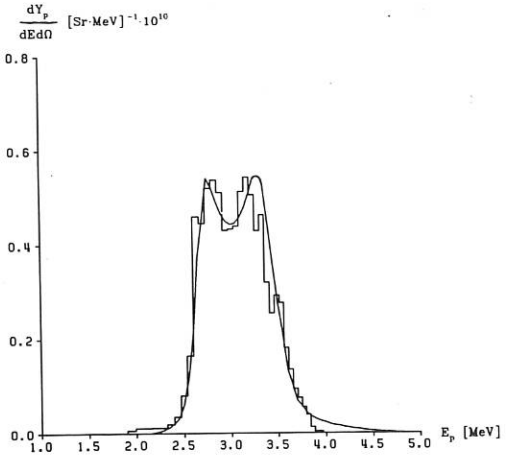

Fig.2 Measured spectrum of reaction protons compared with a calculated spectrum (continuous line). The fitted ion distribution of Fig. 1 with particle numbers $N_{b,1} = 6.8 \cdot 10^{16}$ (40 keV) and $N_{b,2} = 4 \cdot 10^{14}$ (200 keV) is taken for the calculation.

2) The time dependent electron emission in anode direction (θ = 180°) was measured with a Cerenkov detector consisting of a lucite cone. A rough energy resolution was achieved by aluminium filters covering the detector. In most of the discharges two electron pulses were observed. They have a time distance of about 150 ns. The signals are time correlated to x-ray and neutron pulses. The correlation to ion pulses, particularly in the pinch phase, is not so well established. The energy distributions drop exponentially between 200 keV (lower measuring limit) and 500 keV, exhibiting more energetic distributions (up to 1 MeV) at lower filling pressures.

3) A neutron pinhole equipped with a detecting array of scintillators was developed and used to determine the time development of the source in single shots. The spatial resolution at the source was about 2 cm. The results show that the source of the first neutron pulse extends only over the pinch region from z =-2 to 5 cm, whereas the source of the 2nd pulse grows in +z direction and extends over the whole length of the neutron emitting region up to z = 12 to 14 cm (z = 0 : anode end). Time of flight measurements assign a higher energy to the front neutrons (z = 5 to 12 cm) pointing to a beam target process in the instability phase (m = 0) of the focus.

4) Soft x-ray pinhole pictures revealed a filamentary structure of the focus pinch. In the neutron optimized regime (p ≅ 5 mbar) there occured distinct axially oriented continuous filaments grouped around a central filament. First framing pictures with a gated channel plate and time resolved measurements with a small scintillator showed that the filamentation exists in the compressed focus pinch and that the central filament lives up to 70 ns. At lower and higher filling pressures the central filament dominates and has either a diffuse (2 mbar) or a narrow high intensity appearance. The physical nature of the filaments (temperature, density) and their origin are not yet clarified.

5) A novel method was developed which should yield information about the time resolved energy spectrum of the neutrons from the plasma focus or from other fast time-varying fusion plasmas. The signals of detectors placed in various distances (5 to 70 m) from the plasma focus are combined using Laplace transformation to yield the source emission function. Reconstruction of realistic examples by computer simulation shows that 5 to 8 detectors are sufficient to get a meaningful information (Fig.3). Experiments with 8 detectors at optimized distances are in progress.

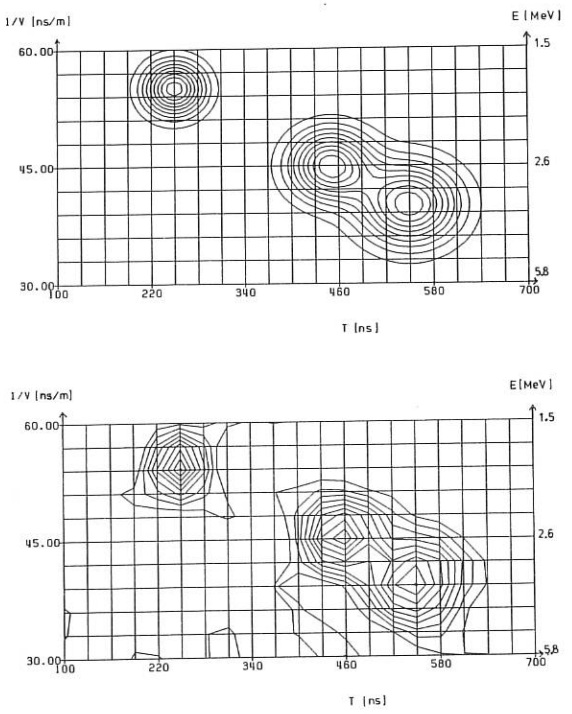

Fig.3 Computer experiment with 8 detectors. A neutron emitter with a given source function F(E,t) causes synthetic signals in detectors placed in 5 to 80 m distance. F(E,t) is reconstructed from the signals by means of Laplace transformations
a) Source function $F(Et) = \sum_{i=1}^{8} \exp(a_i E - b_i t)$
b) Reconstruction

6) At the end of 1984, a new enlarged electrode system with a hollow central anode (ϕ= 20.8 cm) was installed. The system should be usable for the full nominal bank energy of 500 kJ at 80 kV. First focus discharges with neutron emission have been obtained, but the strongly increased currents ($\approx$3.5 MA entering the electrodes) cause serious troubles with electrode erosion and insulator shattering.

4.2 Plasma focus theory

The development of the four-fluid REDUCE/FORTRAN hybrid code for the calculation of plasma focus behavior was continued. Particularly, several improvements in the basic mathematical formalism were made. It was found that transformation of the fluid equations in cylindrical coordinates results in difficulties for the k-integration, as the dispersion relation is explicitly r-dependent then. The fluid equations will now be expressed in cartesian coordinates and the boundaries will be described by a method proposed by E. Halter of Kernforschungszentrum Karlsruhe. Furthermore, a new FORTRAN part for the hybrid code will be developed. The present one used here is suited for soliton solutions but unfavorable for k-integration.

IPF UNIVERSITÄT STUTTGART

PUBLICATIONS AND CONFERENCE REPORTS

Heppner, J., Z. Solajic, G. Merkle:
Bistability and passive Q-switching of a CO_2 - laser with saturable absorber.
Applied Physics B 35, 77-82 (1984).

Janzen, G., H. Stickel:
Mode selective directional couplers for overmoded waveguide systems.
Int. J. Infrared and Millimeter Waves 5, 887 (1984).

Janzen, G., H. Stickel:
Improved directional couplers for overmoded waveguide systems:
Int. J. Infrared and Millimeter Waves 5, 1405 (1984).

Kasparek, W., E. Holzhauer:
Collective laser light scattering from thermal fluctuations in a collision dominated plasma.
Plasma Physics and Contr. Fusion 26 (9) 1133 (1984).

Merkle, G., J. Heppner:
Efficient far-infrared laser lines from CH_3F_2 pumped continuous wave waveguide CO_2 laser.
Optics Letters 9,(12), 542 (1984).

Merkle, G., J. Heppner:
IR absorption measurements and new FIR emission lines in CH_3OH by use of a frequency tunable CW waveguide CO_2 laser.
Optics Communications 51,(4), 265 (1984).

Wilhelm, R., V. Erckmann, G. Janzen, W. Kasparek, G. Müller, E. Räuchle, P.G. Schüller, K. Schwörer, M. Thumm, W VII-A Team:
Electron cyclotron resonance heating and confinement in the W VII-A stellarator,
Plasma Phys. and Contr. Fusion 26, 1433 (1984).

W VII-A Team, X. Zhang. K. Büchl, NI Group, R. Wilhelm, G. Janzen, G. Müller, P.G. Schüller, K. Schwörer, M. Thumm:
Recent results on plasma behaviour in the W VII-A stellarator,
Plasma Phys. and Contr. Fusion 26, 183 (1984).

Salzmann, H., K. Hirsch:
Proposal for a time-of-flight Thomson backscattering technique for large fusion devices.
Rev. Sci. Instr. 55 (4), 457 (1984).

Solajic, Z., J. Heppner:
CW and pulsed FIR-CO_2 hybrid laser with improved efficiency and amplitude stability at short FIR wavelengths.
Appl. Phys. B 33, 23-27 (1984).

Wilhelm, R., G. Janzen, G. Müller, P.G. Schüller, K. Schwörer, M. Thumm, V. Erckmann, W VII-A Team:
First ECRH-experiments on the W VII-A Stellarator,
Plasma Phys. and Contr. Fusion 26, 259 (1984).

10th International Conference on Plasma Physics and Controlled Nuclear Fusion Research, London, 1984.

Erckmann, V., G. Janzen, W. Kasparek, G. Müller, E. Räuchle, P.G. Schüller, K.Schwörer, M. Thumm, R. Wilhelm, W VII-A Team:
Wave absorption and transport studies on ECRH heated stellarator plasmas in W VII-A,
IAEA-CN-44 / D-I-5.

Herold, H. et al.:
Two Phases of neutron production in the Poseidon plasma focus,
IAEA-CN-44 / D-III-6.

4th International Symposium on Heating in Toroidal Plasmas, Rom, 1984.

Erckmann, V., G.Janzen, G. Müller,P.G. Schüller, K. Schwörer, M. Thumm,R. Wilhelm, W VII-A Team:
ECRH on the Wendelstein W VII-A stellarator with different kinds of wave launching,
Proceedings, Vol. II, p. 846.

Thumm, M., V. Erckmann, G. Janzen, G. Müller, P.G. Schüller, R. Wilhelm:
ECRH Systems for linearly polarized plasma irradiation in the HE11 mode at 28 and 70 GHz,
Proceedings, Vol. II, p. 1461.

1984 International Conference on Plasma Physics, Lausanne, 1984.

Wilhelm, R., V. Erckmann, G. Janzen, W.Kasparek, G. Müller, P.G. Schüller, K. Schwörer, M. Thumm, W VII-A Team:
Electron cyclotron resonance heating on the W VII-A stellarator,
Proceedings, Vol. I, p. 271.

Hayd, A., H.J. Kaeppeler, M. Maurer, P. Meinke:
Results from four-fluid calculations of turbulent plasma focus dynamics using REDUCE.
Vol. I, p. 166.

9th International Conference on Infrared and Millimeter Waves, Takarazuka, Japan, 1984

Dodel, G., H. Hailer, E. Holzhauer, P.N. Ignacz, J.H. Massig, H.P. Röser, H. Salzmann, T. Vogel:
A 119 μm scattering system for the investigation of lower hybrid waves in the ASDEX-tokamak
Conf. Digest, p. 407.

Thumm, M., V. Erckmann, G. Janzen, W. Kasparek, G. Müller, P.G. Schüller, R. Wilhelm:
Generation of the HE11 mode from gyrotron TE0n mode mixtures at 70 GHz,
Conf. Digest, p. 522.

Thumm, M.:
Computer-aided analysis of corrugated TE11 to HE11 mode converters in overmoded waveguides,
Conf. Digest, p. 524

Janzen, G., H. Stickel:
Improved directional couplers for overmoded waveguide systems,
Conf. Digest, p. 526.

Vogel, T., G. Dodel. E. Gornik:
Subnanosecond electrical switching of far infrared radiation
Conf. Digest, p. 536.

5th APS Topical Conference on High - Temperature Plasma Diagnostics, Sept. 16-20 1984, Tahoe City, Calif., USA.

Holzhauer, E., W. Kasparek:
Measurement of the magnetic field direction in a plasma by collective scattering with a CO_2 laser.

Salzmann, H. , K. Hirsch, J. Gruber, H. Röhr, G. Brederlow, K. Witte:
Time-of-flight Thomson backscattering technique for large fusion devices.

Proceedings of the 3rd International Conference on Infrared Physics,
Ed. W. Ruegsegger, F.K. Kneubühl, Zürich, July 23-27, 1984.

Merkle, G., J. Heppner:
FIR laser transitions pumped a waveguide CO_2 laser.
Conf. Proc. p. 430-432.

Vogel, T., G. Dodel:
Acusto-optic modulation at the far-infrared.
Conf. Proc. p. 468-470.

Heppner, J., Z. Solajic:
Bistability and passive Q-switching of a CO_2 laser with saturable absorber.
Conf. Proc. p. 622-625.

Symposium on Gyrotron Development, Lausanne, 1984

Thumm, M.:
High-power Millimeter-wave mode converters in overmoded circular waveguides using periodic wall perturbations.
Paper 6.5, Int. J. Electronics, Special Issue on Gyrotrons III, in print.

Janzen, G.:
Mode converters from TE0m to TEm0 for high power applications in the frequency range 1 to 30 GHz.
Paper 6.6, Int. J. Electronics, Special Issue Gyrotrons III, in print.

Jahrestagung Kerntechnik, Kerntechnische Gesellschaft e.V., Deutsches Atomforum e.V., Frankfurt, 1984 .

Wilhelm, R., V. Erckmann, G. Janzen, G. Müller, P.G. Schüller, K. Schwörer, M. Thumm:
Erzeugung und Heizung eines Fusionsplasmas mit Elektron-Zyklotron-Wellen.
ISSN 0720-9207, p. 637, Tagungsbericht.

4th International Workshop on ECE and ECRH, Frascati, 1984.

Wilhelm, R., V. Erckmann, G. Janzen, G. Müller, P.G. Schüller, K. Schwörer, M. Thumm, W VII-A-Team:
ECRH experiments on the W VII-A stellarator.
Invited paper I-3.

Schüller, P.G., V. Erckmann, G. Janzen, G. Müller, E. Räuchle, M. Thumm, R. Wilhelm:
Application of a polarization twist reflector in ECRH experiments.
Contributed paper C-8.

13th Symposium on Fusion Technology, Varese, 1984

Erckmann, V., G. Janzen, W. Kasparek, G. Müller, P.G. Schüller, M. Thumm R. Wilhelm:
Overmoded waveguide components for 28 GHz and 70 GHz ECRH systems.
Paper 2 P 13.

Müller, G., V. Erckmann, M. Thumm, R. Wilhelm, D. Dorst, W. Mellkus:
Control and modulation of gyrotron RF power for ECRH at 28 GHz and 70 GHZ.
Paper 3 P 15.

5th International Workshop on Stellarator - TAEA Technical Committee Meeting on Plasma Confinement and Heating in Stellarators, Schloss Ringberg, 1984 .

W VII-A Team, NI Team, ICRH Team, MPI für Plasmaphysik, Garching; ECRH Team (V. Erckmann, G. Janzen, W. Kasparek, G. Müller, E. Räuchle, P.G. Schüller, K. Schwörer, M. Thumm, R. Wilhelm); IPF Stuttgart:
Status of Wendelstein VII-A,
Proceedings, Vol. I, p. 79.

W VII-A Team, ECRH Team:
ECRH experiments in W VII-A using different modes.
Proceedings, Vol. I, p. 191.

W VII-A Team, ECRH Team:
Energy and particle confinement in W VII-A ECRH plasma:
Proceedings, Vol. I, p. 233.

W VII-A Team, NI Team, ICRH Team, ECRH Team:
Fluctuation measurements in Wendelstein VII-A.
Proceedings, Vol. II, p. 437.

W VII-A Team, ECRH Team:
ECE measurements and power modulation in Wendelstein VII-A.
Proceedings, Vol. II, p. 449.

W VII-A Team, NI Team, ECRH Team:
Heating in W VII-AS.
Proceedings, Vol. II, p. 625.

Expertentreffen, Gyrotronentwicklung, Kernforschungszentrum Karlsruhe, 1984.

Janzen, G.:
Vodenselektive Messung der Ausgangsleistung eines 28 GHz Gyrotrons.

Thumm, M.:
Rundhohlleiter-Querschnittsübergänge (Taper) in Gyrotrons.

Wilhelm, R.:
ECR-Plasmaheizexperimente mit Gyrotrons.

Frühjahrstagung der Deutschen Physikaischen Gesellschaft, Kiel, 1984.

Erckmann, V., G. Janzen, G. Müller, P.G. Schüller, K. Schwörer, M. Thumm, R. Wilhelm, W VII-A Team:
Elektron-Zyklotron-Resonanz-Heizung am W VII-A Stellarator.
Verhandl. DPG (VI) 19, 1195 (1984)
Hauptvortrag P1

Hayd, A., H.J. Kaeppeler, M. Maurer, P. Meinke:
Vierflüssigkeitsbeschreibung turbulenter Vorgänge im Plasmafokus.
Verhandl. DPG (VI) 19, 32 (1984).

Jäger, U., R. Schmidt:
Orts-, zeit- und energieaufgelöste Messungen der Deuteronen und der DD-Reaktionsprodukte an POSEIDON.
Verhandl. DPG (VI) 19, 48 (1984).

Wenzel, N. et al.:
Lichtstreumessung am Plasmafokus POSEIDON.
Verhandl. DPG (VI) 19, 49 (1984).

Sadowski, M., H. Herold, H. Schmidt, M. Shakhatre.
Zur Feinstruktur und Filamentierung im Plasmafokus.
Verhandl. DPG (VI) 19, 51 (1984).

Frühjahrstagung der Deutschen Physikalischen Gesellschaft, Gießen 1984.

Heppner, J. und Z. Solajic:
Bistabilität und passive Güteschaltung eines Lasers mit sättigbarem Absorber.
Verhandl. DPG (VI) 19, 816.

Salzmann. H., T. Vogel und G. Dodel:
Optisches Schalten von Ferninfrarot-Strahlung im Subnanosekundenbereich.
Verhandl. DPG (VI) 19, 823.

Merkle, G. und J. Heppner:
Pumpen von FIR-Laserübergängen mit einem Wellenleiter-CO_2-Laser.
Verhandl. (VI) 19, 844.

DISSERTATION

Kasparek, W.:
Lichtstreuung an kollektiven, thermischen Fluktuationen der Elektronendichte in Plasmen mit mehreren Ionenkomponenten.

IPF UNIVERSITÄT STUTTGART

LABORATORY REPORTS

IPF-84-1 Janzen, G., H. Stickel: Improved directional couplers for overmoded waveguide systems.

IPF-84-2 Hayd. A., H.J. Kaeppeler, M. Maurer, P. Meinke. Vierflüssigkeits-Beschreibung turbulenter Vorgänge im Plasmafokus.

IPF-84-3 Brederlow, G., J.E. Gruber, K. Hirsch, H. Röhr, H. Salzmann, K.J. Witte: JET Art. 14-Contract JE 3/9009 "LIDAR-Thomson Scattering" Final Report / June 15, 1984.

IPF-84-4 Hayd, A., H.J. Kaeppeler, M. Maurer, P. Meinke: Four-fluid description of turbulent plasma focus dynamics.

IPF-84-5 Wilhelm, R., V. Erckmann, G. Janzen, W. Kasparek, G. Müller, P.G. Schüller, K. Schwörer, M. Thumm: Electron cyclotron resonance heating system for the stellarator W VII-AS.

IPF-84-6 Thumm, M: High-power millimeter-wave mode converters in overmoded circular waveguides using periodic wall perturbations.

IPF-84-7 Janzen, G.: Design of mode converters from TE0m modes in circular waveguides to TEm0 modes in rectangular waveguides for high power applications in the frequency range 1 to 30 GHz.

IPF-84-8 Kasparek, W.. Lichtstreuung an kollektiven thermischen Fluktuationen der Elektronendichte in Plasmen mit mehreren Ionenkomponenten.

IPF-84-9 Erckmann, V., G. Janzen, W. Kasparek, G. Müller, E. Räuchle, P.G. Schüller, K. Schwörer, M. Thumm, R. Wilhelm, W VII-A Team: Wave absorption and transport studies on ECR heated stellarator plasmas in W VII-A.

IPF-84-10 Herold, H., L. Bertalot, K. Hirano, U. Jäger, H.J. Kaeppeler, M. Sadowski. H. Schmidt, R. Schmidt, M. Shakhatre, A. Shyam, G. Böckle, K. Matl, N. Wenzel, R. Wolf, R. Bätzner, H. Hinsch. K. Hübner: Two phases of neutron production in the Poseidon plasma focus.

IPF-84-11 Räuchle, E.: Bifurcation, intermittency and chaos in a driven three wave system.

INVITED TALKS

Dodel, G.: Möglichkeiten und Mängel des ferninfraroten Spektralbereichs aus der Sicht der Plasmadiagnostik, Seminar über Probleme aus der Festkörperphysik und Optik, Universität Regensburg, 1984.

Dodel, G.: Plasma diagnostic work at the University of Stuttgart, Japanese Atomic Energy Research Institute (JAERI), Takai Mura, Japan, 1984.

Herold, H.: New results from the Poseidon plasma focus in Stuttgart, Institute for Nuclear Studies, Swierk, Poland, sept. 1984.

Herold, H.: Plasmafokus Poseidon. 9. DFG-Kolloquium im Schwerpunkt "Fusionsorientierte Plasmaphysik", Garching 1984.

Holzhauer, E. and E. Räuchle: The driven nonlinear Helmholtz oscillator: an experimental demonstration of chaotic behaviour in an electric circuit, Int. Workshop on Synergetics, 25.-27.5.1984, Elmau.

Janzen, G.: Mikrowellen-Höchstleistungsröhren (Gyrotrons) und ihre Anwendungen in der Plasmaphysik, Elektrotechnisches Kolloquium, Hochschule der Bundeswehr, München, 1984.

Janzen, G.: Transmission line system and microwave components for ECRH, Japanese Atomic Energy Research Institute (JAERI), Tokai Mura, Japan, 1984.

Janzen, G.: High power microwave components for electron cyclotron resonance heating of plasmas, Physics Seminar, National Tsing Hua University, Hsinchu, Taiwan, 1984.

Janzen, G.: Mode selective directional couplers for overmoded high power transmission systems, Seminar of the Department of Electrical Engineering, National Taiwan University, Taipei, Taiwan, 1984.

Kaeppeler, H.J., et. al.: Quasi-analytisches Lösungsverfahren für Systeme nichtlinearer Differentialgleichungen in der Strömungsphysik. Kolloquium, Lehrstuhl für Technomathematik, Univ. Kaiserslautern, 9. Juli 1984.

Kaeppeler, H.J., M.Maurer: Quasi-analytische Methode zur Lösung nichtlinearer Differentialgleichungssysteme in der turbulenten Magneto-Plasmadynamik. Koll. Inst. f. Datenverarbeitung, KfK, 9. Okt. 1984.

Merkle, G.: Frequency-tunable CW waveguide CO_2 lasers for optical pumping of FIR molecular lasers. Course on optically pumped lasers. Departemento Fisica Fundamental, Universidad Autonoma de Barcelona.

Müller, G.: Elektronenzyklotronheizung am WII-A Stellarator, Plasma-Kolloquium, Universität Essen, 1984.

Schmidt, H.: Prospects of plasma focus and Z-pinch as intense fusion neutron sources. Physics Colloquium, Bhaba Atomic Research Centre, Trombay, Bombay, India.

Schmidt, H.: Plasma focus research at Stuttgart. Plasma Physics Department, Physics Research Laboratory, Ahmedabad, India.

Schmidt, H.: The plasma focus as an intense fusion neutron source, Department for Materials Research, Reactor Research Centre, Kalpakkam, India.

Schmidt, H.. Series of 6 lectures on: X-ray, ion, optical and neutron diagnostics on plasma focus devices and on plasma laser interaction. Workshop on plasma diagnostics, Bhabba Atomic Research Centre, Febr. 1984.

Räuchle, E.: Wellenphänomene in Plasmen, Kolloquium, Inst. f. Angewandte Physik -Theorie- ,Techn. Hochschule Darmstadt, 1984.

Thumm, M.: Erzeugung und Heizung von Plasmen im WII-A Stellarator mittels ECR-Wellen, Plasma Seminar, Univerität Bochum, 1984.

Thumm, M.: Wave absorption, confinement and transport studies on ECR heated stellarator plasmas in W VII-A, Japanese Atomic Energy Research Institute (JAERI), Tokai Mura, Japan, 1984.

Thumm, M.: Plasma production and heating by electron cyclotron waves in the W VII-A stellarator, Physics Seminar, National Tsing Hua University, Hsinchu, Taiwan, 1984.

Thumm, M.: Mode converters, bends, diameter tapers and mode filters in oversized high-power ECRH transmission systems, Seminar of the Department Electrical Engineering, National Taiwan University, Taipei, Taiwan, 1984.

ISOTOPE SEPARATOR LABORATORY OF THE PHYSIKDEPARTMENT AT THE TECHNICAL UNIVERSITY MUNICH

(Dr. E. Hechtl)

The temperature dependence of physical sputtering close to the melting point was investigated with Ar^+ on copper. No change was found in the sputtering yield. The fusion relevant materials titanium and zirconium were bombarded with various plasma impurity ions and the sputtering yields were measured by the mass loss method. Furthermore, several implantations of ^{13}C, ^{18}O and ^{57}Fe in various targets were performed for further investigations at MPI and at JET.

Sputtering of Solid Surfaces with Heavy Ions

(E. Hechtl, H. Lindner)

Some investigations on sputtering in the literature show an increase in yield with increasing target temperature above 0.6 T_m (T_m melting point in K). This phenomenon is not understood, however. Experiments were therefore made to clarify this behaviour. Copper targets were bombarded with Ar^+ ions of 1 keV and 3 keV. The target temperatures used were between room temperature and 850° C (0.83 T_m). Since the evaporation of the target in the upper range of this temperature interval contributes a major part of the mass loss, the amount of evaporation had to be carefully determined. This was done in a pre-experiment without ion beam. The sputtering yields found after correction for the evaporation loss showed no increase with increasing target temperature up to 0.83 T_m. This result is in accordance with theoretical expectations.

Moreover, sputtering yields of the fusion relevant materials titanium and zirconium bombarded with plasma impurity ions were measured. The ion energies ranged from 100 eV to 20 keV. In the case of oxygen ions the sputtering yields were measured not only at room temperature but also at a target temperature of 550° C. This was done because chemical reactions caused by sputtering were expected which can be temperature dependent. However, a dependence on the target temperature was only found at bombarding energies greater than 5 keV (Fig. 1). Above this energy the sputtering yields of both materials are higher at 550° C than at room temperature. The surface modified by oxygen bombardment shows sputtering yields different from the pure material. For comparison, yield data of titanium and zirconium with Ne^+ ions were also taken. The cascade theory predicts nearly equal values for sputtering with O^+ and Ne^+ ions. The experimental data, however, show the sputtering yields of O^+ bombardment to be much smaller than the corresponding Ne^+ data. Self-sputtering data of zirconium were measured in the energy range of 250 eV to 20 keV (Fig. 2).

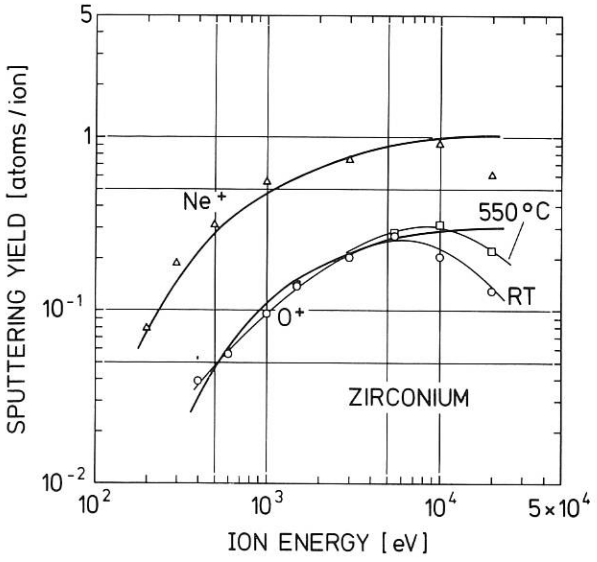

Fig. 1: Sputtering yields of zirconium versus ion energy. The projectiles are O^+ and Ne^+. The bold lines are drawn according to an analytical relation derived from a modified cascade theory. In the case of O^+ bombardment, thin lines of the best fit are also drawn.

The samples in these experiments were at room temperature only. The sputtering yield curve found in this experiments intersects the line Y = 1 at a bombarding energy close to 2 keV. This value was also found for titanium in an earlier investigation.

For further investigations at MPI and at JET some 30 graphite and copper samples were implanted with various isotopes. ^{13}C was implanted into pyrolytic

graphite with a fluence of 2 x 10^{17} atoms/cm^2. The bombarding energy was 10 keV. ^{18}O and ^{57}Fe were implanted into copper samples with energies of 10, 20, and 30 keV. The fluences ranged from 8 x 10^{15} to 2 x 10^{17} atoms/cm^2.

Conference contribution
Hechtl, E. and Bohdansky, J.:
Sputtering of Titanium and Zirconium by Fusion Plasma Impurity Ions, Int. Conf. on Fusion Reactor Materials -1, Tokyo, Japan, Dec. 3-6, 1984

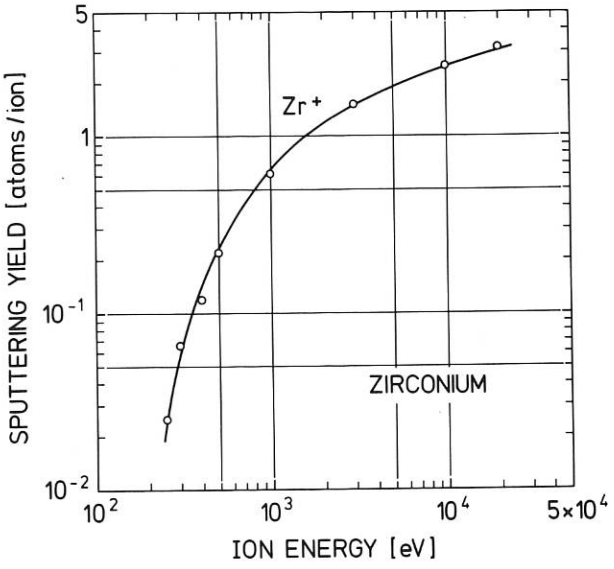

Fig. 2: Self-sputtering yields of zirconium at normal incidence and at room temperature as a function of ion energy. The solid line represents the result of model calculations.

LEHRSTUHL FÜR TECHNISCHE ELEKTROPHYSIK
DER TECHNISCHEN UNIVERSITÄT MÜNCHEN
(Prof. Dr. U. H. Bauder)

The ignition and operating conditions of plasma induced arcs found on first walls are studied by performing simulation experiments with arcs at low pressure.

Investigations related to unipolar arcing
(U.H. Bauder, A. Nürnberg, J. Prock, W.H. Zaho)

The hollow cathode apparatus described in the 1983 annual report was used for arc ignition experiments. Small copper rings were cleaned and conditioned by heating them to T ≦ 1000° C, bombarding them with argon ions (energies < 250 eV) and exposing them to cleaning arc discharges. These rings serve then as limiters to the hollow cathode plasma (Fig. 1).

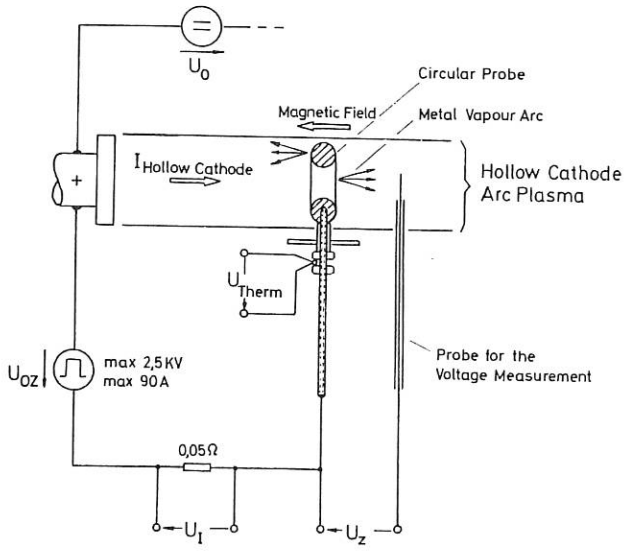

Fig. 1:
Schematic arrangement for the ignition studies in a low pressure hollow cathode arc.

By applying voltage pulses of 100 ms duration with different magnitudes to rings exposed to various hollow cathode background plasmas in axial magnetic inductions of varying magnitude (up to 1.2 T), the ignition probability of arcs may be determined. Fig. 2 shows examples of voltage current characteristics of the copper ring probe exposed to a 15 A hollow cathode argon plasma at 0.15 Pa pressure; the diagram also contains iso-probability lines for arc ignition (0%, 50% and 100% probability).

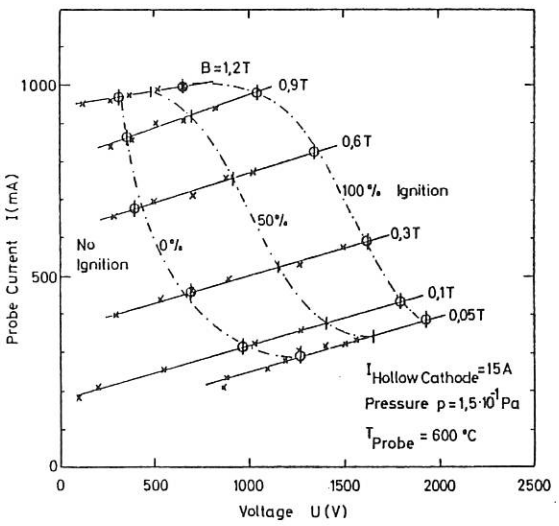

Fig. 2:
Current-voltage characteristics of a circular copper probe. Iso-probability ignition lines are included.

After cleaning the probes as well as after arcing them, protuberances similar to the ones shown in Figs. 3 and 4 can be found.

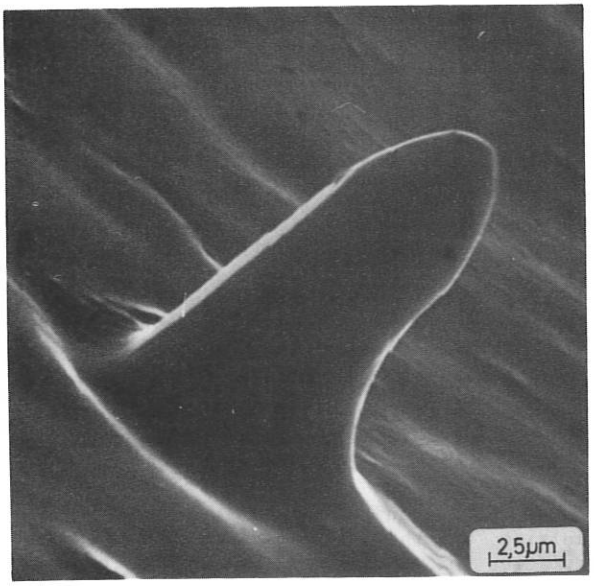

Fig. 3:
Structure on a copper probe after exposure to 250 eV argon ion bombardment.

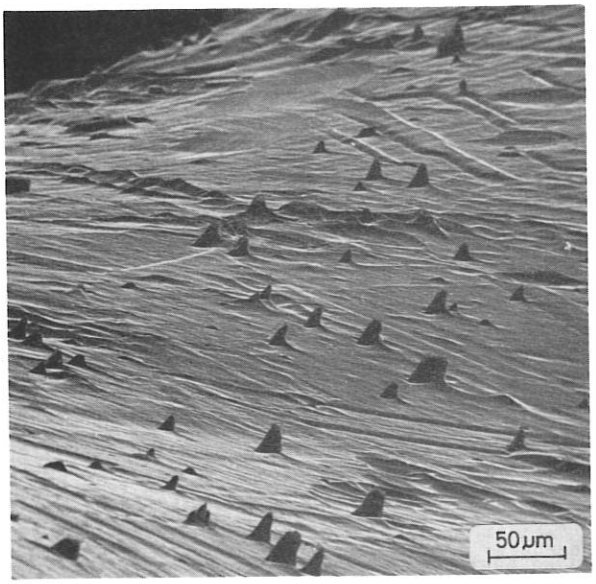

Fig. 4:
Structures on the probe of Fig. 3 at different magnification.

These protuberances are most probably identical with the ignition locations for the following arcs, where the ignition may be described by an explosive model of the protuberance. Parallel to the ignition studies, the work on the theoretical model of the vacuum arc cathode was continued. Using all known physical processes entering the power balance of the individual cathode spot of a metal vapor arc leads to expected values of crater radii, crater formation time and spot splitting limits which can be compared to measured values.

a) Crater radius R

	Cu	Cd
R/I_B(theor.)	$2...4\ 10^{-8}$	$1...3\ 10^{-7}$
R/I_B(exp./1/)	$5.7\ 10^{-8}$	$8.7\ 10^{-8}$
R/I_B(exp./2/)	$3...9\ 10^{-7}$	-

in [m/A]

b) Crater-formation time

	Cu	Cd
R^2/τ(theor.)	$0.7...1.5\ 10^{-3}$	$2...7\ 10^{-4}$
R^2/τ(exp.)	$2\ 10^{-3}$/3/	$6...8\ 10^{-4}$/4/

in [m^2/s]

c) Spot-splitting limit

	I_{SS}(theor.)	I_{SS}(exp./5/) [A]
Cd	25	8 .. 15
Cu	1500	75... 100
W	1000	250... 300

It is planned to extend these predictions to other cathode materials. The arc ignition studies could be continued by using He or H_2 hollow cathode background plasma.

Publication

W.H. Zhao, A. Koch, U.H. Bauder, R. Behrisch
First Wall Erosion by Arcing
J. of Nucl. Mat. 128 & 129 (1984) 613-617

References

/1/ Daalder J.E. Thesis Eindhoven 1978
/2/ Zhao W.H. J. Nucl. Mat. 128 & 129, 613, 1984 and priv. com.
/3/ Jüttner B. J. Phys. D14, 1265, 1981
/4/ Daalder J.E. J. Phys. D16, 17, 1983

IAP Universität Heidelberg

INSTITUT FÜR ANGEWANDTE PHYSIK II
DER UNIVERSITÄT HEIDELBERG
(Prof. Dr. Klaus Hübner)

Energy Resolution of Neutron Spectra Determined with Nuclear Emulsions

Besides minor mechanical modifications, the semi-automatic scanning apparatus for nuclear emulsions /1/ was essentially improved by installing a new TV camera (type Bosch T1VK9/B1). The contrast is enhanced by using a Pasecon-type image tube. This simplifies discrimination for digital images, which will be made in the near future.

The energy resolution of neutron spectra measured with nuclear plates depends both on the properties of the emulsion and on the errors of the track measurements. In order to determine the energy resolution achievable with our scanning equipment, plates were exposed in the test facilities at Princeton and Gothenburg, which are both using a deuteron beam impinging on a thin target. The data of these neutron sources communicated to us are given in Table 1.

With the scanning equipment the three coordinates of the start and end points of each proton track and the thickness of the emulsion are measured. We used one of the Gothenburg plates for systematic test measurements to determine the errors of the individual measurements and to get an impression of the reliability of the operators. The standard deviation of the projected track length l in the plane of the emulsion and of the dip z of the track were found to be $m_l = \pm 0.25\ \mu$ and $m_z = \pm 1.0\ \mu$. The relatively large error of the dip measurement results from individual differences between the operators in the focussing of the start and end points of the visual image on the monitor as well as from work fatigue of the operators. We are therefore going to include electronic focussing in our semi-automatic scanning equipment.

The measured dip of a track has to be corrected by a factor s for shrinkage of the emulsion during developing. The factor s is determined from the thickness of the emulsion as specified by the manufacturer and the measured depth of the emulsion at the time of scanning. The standard deviation of s is $m_s = \pm 0.065$ s. With relative values $\mu_x = m_x/x$, the error of the total range R of a track can be written as

$$\mu_R = \sqrt{\cos^4\varphi\ \mu_l^2 + \sin^4\varphi\ (\mu_z^2 + \mu_s^2)},$$

where φ is the dip angle of the track. The error of the cosine of the scattering angle Θ of the proton is

$$\mu_{\cos\Theta} = \sqrt{\mathrm{tg}^2\psi\ \mu_l^2 + \sin^2\varphi\ (\mu_l^2 + \mu_z^2 + \mu_s^2)}$$

Θ is related to the direction of incidence of the neutrons and ψ is the angle of the projection of the track to the plane of the emulsion.

The proton energy is determined from the track length by the energy-range relation $E_p = E_p(R)$ and then the neutron energy is found from $E_n = E_p/\cos^2\Theta$. Finally the total error of the neutron energy is

$$\mu_E = \sqrt{(R/E_p)^2 (dE_p/dR)^2\ \mu_R^2 + 4\mu_{\cos\Theta}^2 + \mu_{\mathrm{stragg}}^2}.$$

Here the contribution of the emulsion to the error is included, it arises from the range straggling, which is given in the literature /2/ as 1.7 .. 2.1 % (standard deviation) for protons with an energy of 2.5 MeV.

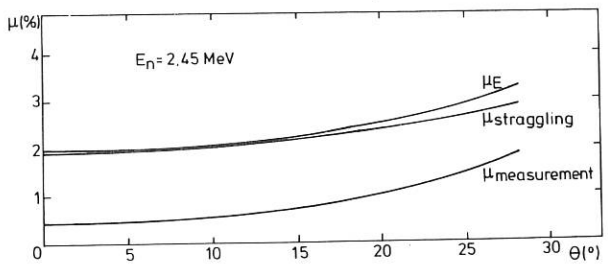

Fig. 1: Relative standard deviation as a function of scattering angle Θ.

Figure 1 shows for 2.5 MeV neutrons the error μ_E as well as the two contributions from the measurement and the straggling as a function of the scattering angle θ for the case $\psi = \varphi$ (note that $\cos\theta = \cos\psi\cos\varphi$). The two contributions increase with scattering angle and decreasing proton energy $E_p = E_n\cos^2\theta$, respectively.

The energy resolution δE is defined as the full half-width of the detector response to a monoenergetic neutron source. If the neutron energy is determined only from proton tracks with one fixed scattering angle θ, the energy resolution is

$$\delta E/E = 2\sqrt{2\ln 2}\ \mu_E.$$

Usually one takes all protons with a scattering angle below a certain maximum value and then the resulting energy resolution is found by integration over θ. Figure 2 shows, for example, the expected spectrum for monoenergetic neutrons with 2.45 MeV and maximum scanning angles $\psi_o = \varphi_o = 7^o$.

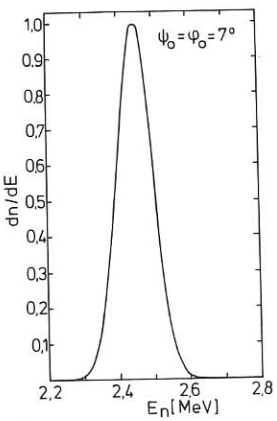

Fig. 2:
Expected spectrum.

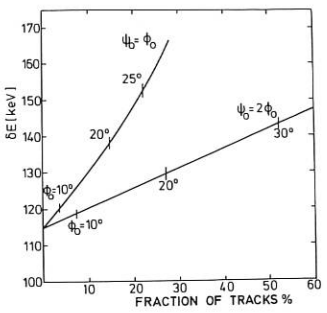

Fig. 3:
Expected full half-width.

The observed fraction of the tracks grows essentially with the maximum scanning angles. It is given by

$$P(\psi_o, \varphi_o) = (2/\pi)\sin\psi_o(\varphi_o + \sin\varphi_o\cos\varphi_o).$$

One therefore endeavours to take the maximum angles as large as possible. Owing to the large contribution of the dip measurement to the resulting half-width, the better way would be to limit the dip angle φ_o to smaller values than the plane angle ψ_o. Figure 3 gives the calculated full half-width for the two cases $\psi_o = \varphi_o$ and $\psi_o = 2\varphi_o$ as a function of the observed part of the tracks.

Figure 4 shows the energy spectra measured in the test facilities at Princeton and Gothenburg. The determination of the half-width of the spectrum T23 suffers from the fact that the low-energy wing is essentially broadened, which may be caused by some neutron scattering as well as by distorted tracks. This low-wing broadening needs further investigation. From the high-energy wing we found

E17 Princeton E = 120 keV ± 12 % ($\theta_o = 10^o$),
T23 Gothenburg E = 140 keV ± 5 % ($\theta_o = 10^o$).

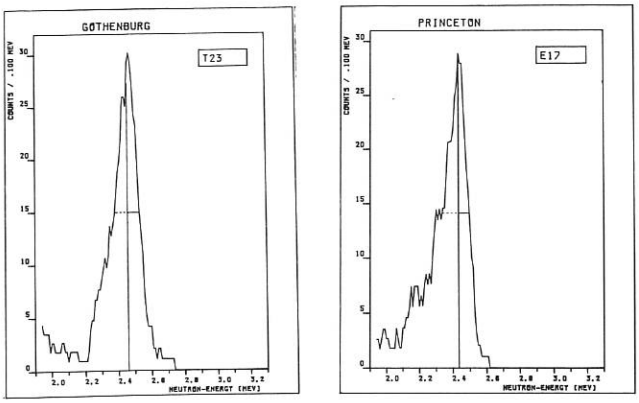

Fig. 4: Two measured spectra.

The scanning of T23 was done by 5 operators, whereas E17 was measured by one operator only. The enlarged half-width of T23 indicates the differences in dip measurements made by different operators, which will be eliminated by automatic electronic focussing. Figure 4 gives the number of counts in energy intervals of 100 keV. This is an integration over the real energy spectrum in 100 keV steps and enlarges the half width of the plot. Taking this effect and the energy spread of the neutron sources together, one gets the results given in Table 1, which agree very well with the values expected for the energy resolution, but they indicate that the values for the proton range straggling as given in the literature may be somewhat too high.

Table 1

	Princeton	Gothenburg
Date	May 1984	May 1984
No. of plate	E17	T23
Energy of beam	180 keV	300 keV
Exposure angle rel. to beam	100^o	100^o
Exposure time	2000 s	990 s
Distance source - plate	100 cm	100 cm
Neutron fluence at the plate	$1.25\times10^4 n_o/cm^2$	$5\times10^5 n_o/cm^2$
Neutron energy (source)	2.41 MeV	2.42 MeV
FWHM (source)	25 .. 50 keV	30 .. 60 keV
Neutron energy (spectra)	2.43 MeV	2.46 MeV
FWHM (spectra)	81 .. 92 keV	104 .. 116 keV
$\delta E/E$ (spectra)	3.3 .. 3.8 %	4.2 .. 4.7 %

/1/ Annual Report 1983, p. 193;
MPI für Plasmaphysik, Garching

/2/ W.H. Barkas et al., Physical Review,
Vol. 98, No. 3, p. 605, 1955

Frankfurt University

INSTITUT FÜR ANGEWANDTE PHYSIK
FRANKFURT UNIVERSITY

(Prof. Dr. R. Becker, Dr. J. Peschina)

ANALYSIS OF SPUTTERED PARTICLES USING A HIGH DENSITY ELECTRON TARGET FOR IONIZATION

In recent years, several high intensity electron targets as ionization devices were developed /1,2,3/ at Frankfurt University for measurements on ionization of ions by electron impact. The crucial point of all these devices is the variation of the potential within the interaction region, because the energy distribution is changed according to the potential in the ionization region. In 1981 the detection of 100...200 eV neutral hydrogen by ionization was performed at the IPP /4,5/, where no influence of the electron target on the energy distribution of the hydrogen could be found, although the ionization device was known to act as a weak electrostatic lens.
In the meantime several changes have been made. The current version of the ionization device does not show to the ions any inhomogeneities in potential neither in experiment nor in computer simulation. This outstanding inhomogeneity was reached by producing a full compensation of electron space charge with residual gas ions all over the ionization volume /3/. Therefore low energy ions are expected to be disturbed rather by the contact potential of partially covered walls than by potential inhomogeneity of the electron target. Due to the high intensity of the target the ionization probability is expected to be 10^{-2} for 1 eV tungsten atoms, so the intensity of the ionized beam passing a 2 mm aperture in a distance of 500 mm to the sputter target will be about 10^5 particles per second. If this ionizer is used for the detection and analysis of sputtered neutrals, the combination of electrostatic and magnetic deflection will provide energy analysis of sputtered neutrals and even molecules and fragments of compounds.
The analysis system is designed to perform full transmission of a beam of singly charged ions with masses as heavy as tungsten at an energy of 5 keV $\pm$ 0.5 %. It consists of two acceleration gap/einzel-lens combinations, one spherical condenser a double-focussing 90° dipole magnet and a CEM device for single particle detection (s.Fig.2). The resolution of the spherical condenser is set to 100 by the diameter of the exit aperture in combination with the bending radius. The 90° dipole magnet is used for mass analysis. A parallel beam at the entrance is focused at a distance of 200 mm to the exit, where a slit provides mass separation. The system can be set to two different detecting modes:

1. Mass analysis irrespective of energy distribution
2. Energy distribution of a selected mass.

In the first detection mode ionized particles are accelerated from 0.1 - 10 eV up to 5 keC within the first gap resulting in a diverging beam. The first lens converts to a parallel beam, which is necessary to obtain a focus at the exit of the spherical condenser. The condenser in this case only acts as a 90° deflector. The second gap is inactive in this mode, while the second lens makes the beam parallel again. The magnet finally performs the mass analysis.
In the second detection mode, the first lens and the first gap will be inactive, energy analysis is made by the spherical condenser. The selected particles are accelerated up to 5 keV by the second gap, the second lens again produces a parallel beam.
The whole system with exception of the magnet and the single particle detector will be housed in a special vacuum chamber, which fits to the sputtering facility of IPP. After assembly and test of all components in Frankfurt, the anaylsis system can be used in experiments in the second half of 1985.

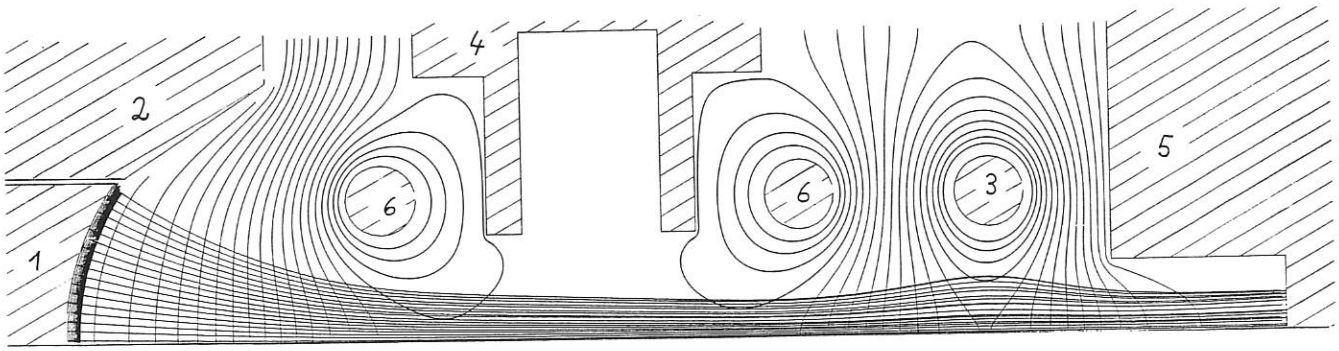

Fig. 1: Ionizing device

on cathode potential	1	cathode
	2	Pierce edge electrode
	3	secondary electron repeller rod
on interaction potential	4	center electrode
	5	electron collector
on highest potential	6	anode rods

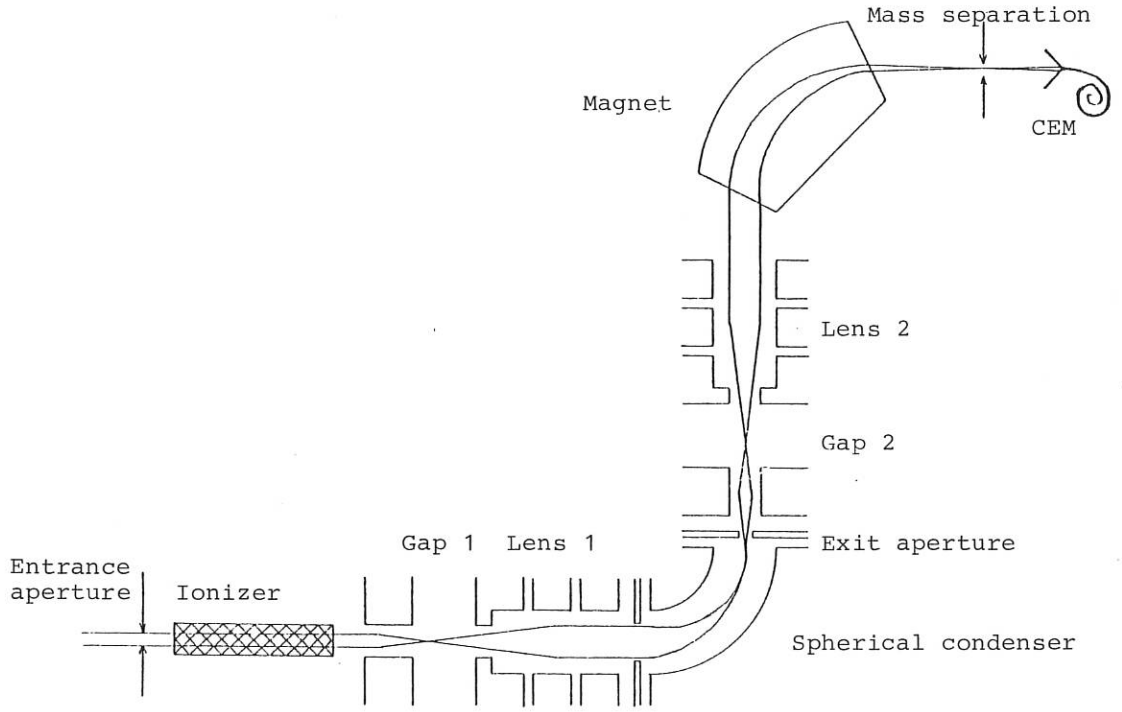

Fig. 2: Beam line of the detection system showing focusing properties for the mass analysis mode.

References:

/1/ A. Müller, E. Salzborn, R. Frodl, R. Becker, H. Klein and H. Winter: J. Phys. B: Atom. Molec. Phys. 13 (1980) 1877-1899

/2/ Ch. Achenbach, A. Müller, E. Salzborn, R. Becker: Phys. Rev. Letters 50 (1983) 2070

/3/ R. Becker, A. Müller, Ch. Achenbach. K. Tinschert and E. Salzborn: Proc. Conf. Phys. highly ionized atoms, Oxford 1984, to be published

/4/ R. Becker, R. Juergens: Annual Report 1980 (in German) Max-Planck-Institut für Plasmaphysik, Garching

/5/ R. Juergens, R. Becker and W. Eckstein, H. Verbeek: Annual Report 1982 Max-Planck-Institut für Plasmaphysik, Garching

University of Osnabrück

SURFACE SCIENCE GROUP AT THE UNIVERSITY OF OSNABRÜCK

Prof. Dr. W. Heiland

In 1984 the project "Light Emission from Ion-Surface Interaction" concentrated on the effects of the interaction of molecular ions with surfaces, molecule production by sputtering, and the positive and negative ionisation of scattered and desorbed hydrogen.

The interaction of molecular ions with surfaces is of some relevance for ion sources (see Proc. of the AIP Conf. on Production and Neutralization of Negative Ions and Beams). We studied the interaction of H_2^+ and N_2^+ with a Ni(111) surface with a newly developed time-of-flight (TOF) system. The TOF system permits the measurement of the energy distributions of reflected neutrals and ions. Fig. 1 shows results for H_2^+ as primary ions and Fig. 2 for N_2^+ as primary ions for two primary energies. The neutral part of the spectra is in all cases the major part of the reflected flux.

The narrow peak in the spectra can be interpreted as reflected H_2^+ (N_2^+) in the ionic part and as neutralized reflected H_2 (N_2) in the neutral part. At the lower primary energies H_2 reaches about the same yield as the neutralized dissociated H (broad peak), whereas in the N_2 case about 90 % of the reflected particles are N_2 molecules, the rest is dissociated neutral N.

In analogy to the neutralization processes for atomic ions we interpret these results as being caused by resonant neutralization and Auger neutralization. A consideration of the molecular energy levels shows that Auger neutralization is possible into the ground states of H_2 and N_2 with approximately the same efficiency as for atomic particles with comparable ionization energies. In case of H_2 resonant neutralization into the antibonding triplet state is recognized as the major cause for dissociation and the yield of neutral H-atoms. In case of N_2 the antibonding state with the lowest energy has a different core configuration from the N_2^+ groundstate. Therefore dissociation via this state is rather unlikely since an additional electronic excitation would be necessary. At primary energies above 1 keV (or about 10 eV perpendicular to the surface at grazing angles of 5°) other processes as proposed by Parilis et al. come into play (B. Willerding, K. Snowdon, H. Steininger).

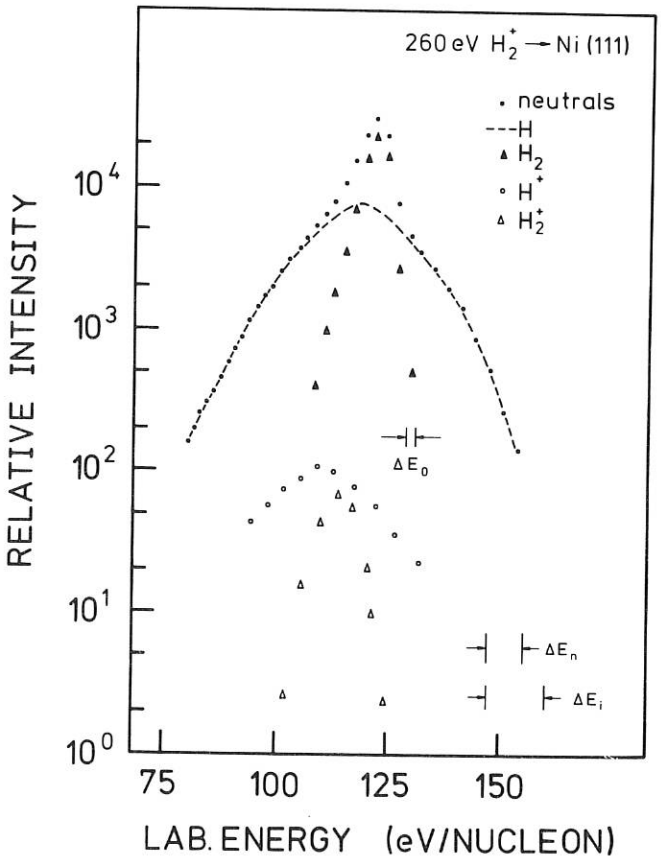

Fig. 1 : H_2^+ interaction at grazing incidence (5°) with a Ni(111) surface. ΔE_i, ΔE_n and ΔE_o are the error bars for the ionic spectra the neutral spectra and primary energy.

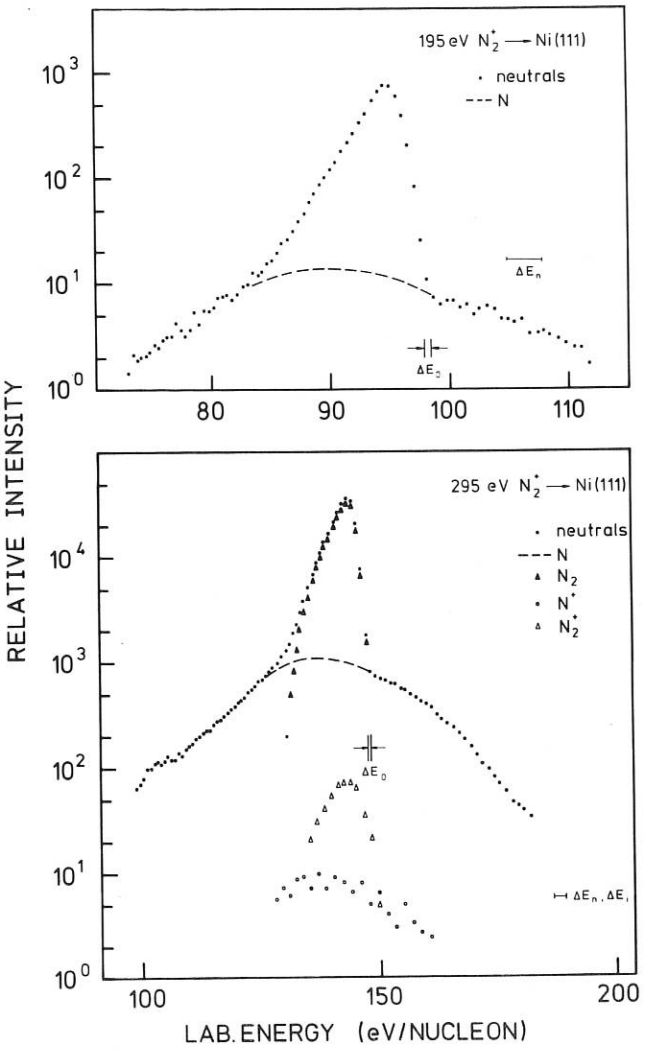

Fig. 2: N_2^+ interaction at grazing incidence (5°) with a Ni(111) surface: Top curve at low energies shows neutrals only, lower curve at higher energies shows neutrals and ions.

The problems connected with the production of molecules by sputtering centered around the observation of excited molecules during the bombardment of Si with N_2^+ ions. We developed a theory taking into account possible sputter mechanisms and the electronic, vibrational and rotational properties of the possible molecules, in our case N_2, N_2^+ and SiN. As a result of these calculations we identified the lines in the experimental spectra as excited SiN. The broad background is possibly due to N_2, whereas in other parts of the spectrum extending from 300 to 800 nm we found evidence for excited N_2^+.

The theoretical model gives very detailed information about the rovibrational distribution of the sputtered molecules, depending on the sputtering mechanism, the binding energy of the molecule, the surface binding energy etc. We expect that a careful analysis of the sputtered species will help to understand the sputtering process in general (K. Snowdon, R. Hentschke, P. Hertel).

Theoretical work on charged fractions of hydrogen scattered and desorbed from simple metals (K. Snowdon) is being extended. In progress is an attempt to explain $D^{\pm}$ charged fractions for reflection and desorption from Ti and Ni (measured by E. Mühling, Garching) using a time dependent solution of the Anderson-Newns Hamiltonian.

Publications

B. Willerding, H. Steininger, K.J. Snowdon and W. Heiland: Time-of-flight measurements of light molecular ions scattered at grazing incidence from a Ni(111) surface, Nucl. Instr. Meth. B2 (1984) 453

R. Hentschke, P. Hertel, W. Heiland and K. Snowdon: Rotational and vibrational excitation of sputtered dimers, Nucl. Instr. Meth. B2 (1984) 461

H. Steininger, B. Willerding, K. Snowdon, N.H. Tolk and W. Eckstein: Light emission from hydrogen copper interaction at grazing incidence, Nucl. Instr. Meth. B2 (1984) 484

W. Heiland: Radiation from atomic collisions with solids. "Electronic and Atomic Collisions", ed. I.V. Hertel et al. (Elsevier 1984) p. 511

K. Snowdon, R. Hentschke, W. Heiland and P. Hertel: Rotational and vibrational excitation of sputtered diatomic molecules - I. Theory, Z. Phys. A318 (1984) 261

K.J. Snowdon and W. Heiland: Rotational and vibrational excitation of sputtered diatomic molecules - II. Experiment, Z. Phys. A318 (1984) 275

B. Willerding, W. Heiland and K.J. Snowdon: Neutralization of fast molecular ions H_2^+ and N_2^+ at surfaces, Phys. Rev. Lett. 53 (1984) 2031

K. Snowdon: Trajectory and primary ion charge dependence of keV scattered and re-emitted $H^{\pm}$ charged fractions, Nucl. Instr. Meth. B2 (1984) 540

Conference Contributions

XII SPIG, Sibenik, Jugoslawien, 1984
W. Heiland and K. Snowdon: Surface Analysis by Low Energy Ion Beam Techniques (inv.)

DIET II, Elmau, Deutschland, 1984
K. Snowdon: Internal and translational energies of molecules desorbed by electronic transitions (inv.)

DPG-Frühjahrstagung, Münster, Deutschland 1984
K.J. Snowdon, W. Heiland, R. Hentschke und P. Hertel: Rotations- und Vibrationsanregung zerstäubter Moleküle.

B. Willerding, K.J. Snowdon und W. Heiland: Flugzeitmessungen an leichten Molekülen bei Oberflächenstreuung unter kleinen Winkeln

H. Obermeyer, K.J. Snowdon und W. Heiland: Polarisierte Strahlung bei der Streuung von He^+ an Ni(111)

Dissertation

B. Willerding: Neutralisation und Dissoziation schneller Molekülionen bei Streuung an Oberflächen

Diploma Thesis: H. Obermeyer: Ein Beitrag zur Messung polarisierter Strahlung bei der Ionen-Festkörperwechselwirkung.

SITE PLAN OF MAX-PLANCK-INSTITUT FÜR PLASMAPHYSIK

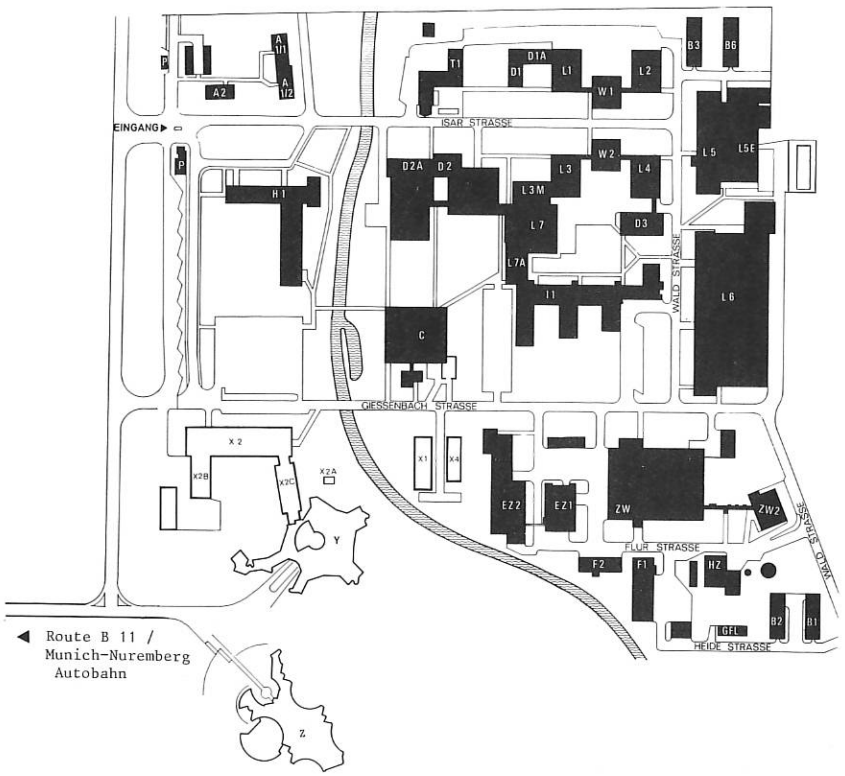

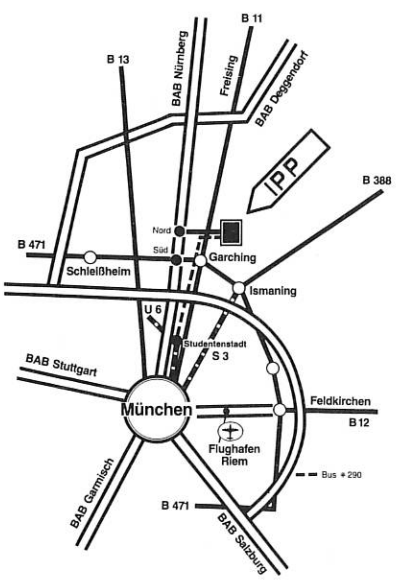

D1	Theory Division 2
W2, L4, D3	Plasma-Wall Interaction Division
L3, L3M, L7, L7A	Experimental Plasma Physics Division 2 (Stellarators)
D2, D2A	Theory Division 1
D2, D2A	Computer Science Division
L6	Experimental Plasma Physics Division 3 (ASDEX)
D1, D1A, L1, W1, L2, L6, D3	Experimental Plasma Physics Division 1
T1	NET Study Group
I1	Technology Division
ZW1, ZW2, I1	Central Technical Services
EZ, EZ2, L5E	Power Plants
B3, B6	Equipment Pool
H1	Directorate, Administration
B1, B2	Building Administration
C	Cafeteria
P	Main Entrance
F1, F2	Motor Pool
HZ	Heating Plant
A	Staff Quarters, Guest Accommodation
L5, L5E, L1, L2	Max-Planck-Institut für Quantenoptik
X1-X4, Y	Max-Planck-Institut für Physik und Astrophysik (Institut für Extraterrestrische Physik, Institut für Astrophysik)
Z	European Southern Observatory (ESO)

ANNUAL REPORT 1984

Max-Planck-Institut für Plasmaphysik (IPP) 8046 Garching bei München
Telephone (089) 3299-1, Telex 05215808

Editing and Layout: Dr. Winfried Herrmann
Printing: IPP and Kastner & Callwey, München

This work was performed under the terms of the agreement between Max-Planck-Institut für Plasmaphysik and the European Atomic Energy Community to conduct joint research in the field of plasma physics.

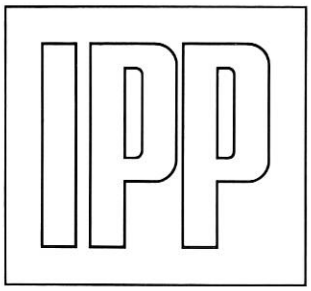
IPP